DEPARTAMENTO DE ASTROFÍSICA

Universidad de La Laguna

Spectroscopic and physical characterization of the Galactic O-type stars targeted by the IACOB & OWN surveys

Memoria que presenta
Don Gonzalo Holgado Alijo
para optar al grado de
Doctor por la Universidad de La Laguna.

INSTITUTO Đ ASTROFISICA Đ CANARIAS
diciembre de 2018

Examination date: January, 2019
Thesis supervisor: Dr. Sergio Simón-Díaz

Some of the material included in this document has been already published in *Astronomy & Astrophysics*.

Siempre adelante,

Resumen

Las estrellas O representan una fase fundamental en el zoológico de las estrellas masivas. Ionizan el material a su alrededor e inundan su entorno con material procesado a través de fuertes vientos estelares y explosiones de supernova. Además de la pérdida de masa, factores como la rotación y la multiplicidad (así como la interacción entre ellos) se han convertido en procesos clave para comprender su evolución. Una mejor comprensión de estos complejos objetos requiere de una mejor caracterización empírica de sus propiedades físicas, algo que solo se puede obtener a través del extenso estudio de grandes conjuntos de datos. Este ha sido el principal propósito de esta tesis, la exhaustiva caracterización empírica –principalmente mediante la espectroscopia cuantitativa, pero también teniendo en cuenta la información sobre fotometría y paralajes– de una muestra de 415 estrellas de tipo O Galácticas (lo que representa una muestra 5-10 veces más grande que las consideradas en estudios similares anteriores).

Una parte crucial del trabajo ha sido la compilación de una base de datos cuasi-homogénea de espectros ópticos de estrellas O Galácticas. El grueso de las observaciones proviene de las extensas bases de datos espectroscópicas recopiladas en el marco de los estudios IACOB y OWN. En total, hemos utilizado 2900 espectros de 415 estrellas de tipo O Galácticas, cubriendo los tipos espectrales entre O2 y O9.7 y todas las clases de luminosidad.

En un primer paso, la capacidad multi-época del conjunto de datos espectroscópicos compilados nos ha permitido evaluar la variabilidad espectroscópica de estas estrellas. Luego, realizamos un análisis espectroscópico detallado de aquellas estrellas (285) en la muestra no identificadas como binarias espectroscópicas de líneas dobles. Para hacer frente a la gran cantidad de objetos, utilizamos dos herramientas semiautomáticas (pero supervisadas) para el análisis espectroscópico cuantitativo, desarrolladas en el marco del proyecto IACOB. Primero, se utiliza un método combinado de la transformada de Fourier y ajuste de perfil para derivar $v \sin i$ y la cantidad de ensanchamiento de macroturbulencia que afecta a los perfiles de las líneas, usando el programa IACOB-BROAD. Luego, para derivar los parámetros de la atmósfera y el viento estelar, realizamos un minucioso análisis espectroscópico cuantitativo utilizando IACOB-GBAT, una herramienta semiautomatizada basada en una optimización χ^2 con una vasta red de modelos de atmósfera FASTWIND. El programa calcula de forma rápida, objetiva y reproducible, valores e incertidumbres para $T_{\rm eff}$, $\log g$, $Y_{\rm He}$, $\xi_{\rm t}$, y $\log Q$.

Como parte de este trabajo, inicialmente hemos seleccionado y analizado una submuestra de referencia (la red de estrellas estándar tipo O para clasificación espectral) para establecer un protocolo que seguir paso a paso en el

análisis de la muestra completa combinada de IACOB+OWN. Esta muestra también se usó para evaluar el nivel de acuerdo entre nuestros resultados y los proporcionados por los métodos más tradicionales "a ojo", y para construir nuevas calibraciones lineales de $T_{\rm eff}$ y $\log g$ en función de tipo espectral y clase de luminosidad para estrellas tipo O Galácticas.

Tras esto, extendimos nuestra investigación a toda la muestra de estrellas de tipo O Galácticas estudiadas por IACOB y OWN. Utilizamos los resultados del análisis espectroscópico para proporcionar una visión empírica global de los diversos parámetros investigados en varios diagramas de diagnóstico, así como para investigar algunos temas de interés en el campo de las estrellas masivas. En particular, introducimos una nueva versión independiente de la distancia de la relación de la luminosidad con el impulso del viento para evaluar nuestros resultados con respecto a estudios teóricos y empíricos anteriores. También evaluamos el desplazamiento aparente entre la edad-zero en secuencia principal teórica y empírica para estrellas más masivas que 32 $M_{\odot}$. Finalmente, estudiamos la distribución y evolución de la velocidad de rotación de las estrellas de tipo O, y comparamos la información empírica extraída con las predicciones de los modelos más avanzados de evolución estelar simples y binarios.

En el último capítulo, realizamos una exhaustiva evaluación de la información disponible sobre paralajes para nuestra muestra completa de estrellas tipo O Galácticas. Evaluamos, en términos de cantidad y precisión, la mejora desde el catálogo *Hipparcos-Tycho* a la reciente segunda publicación de datos de la misión *Gaia* (*Gaia*-DR2). Luego, nos beneficiamos de las paralajes provistas por *Gaia*-DR2 para obtener las magnitudes absolutas, radios, luminosidades y masas espectroscópicas de nuestra submuestra de referencia: la red de estrellas estándar de tipo O para la clasificación espectral.

Summary

O stars represent a fundamental phase in the zoo of massive stars. They ionize the material around them and flood their environment with processed material via strong stellar winds and supernova explosions. On top of the mass-loss, factors such as rotation and multiplicity (as well as the interplay between them) have become key processes to understand their evolution. A better understanding of these complex objects requires better empirical characterization of their physical properties, something that can only be obtained through extensive studies of large spectroscopic datasets. This has been the main purpose of this thesis, a thorough empirical characterization –mainly through quantitative spectroscopy but also taking into account information about photometry and parallaxes– of a sample of 415 Galactic O-type stars (i.e. representing a sample 5-10 times larger than those considered in previous similar studies).

A crucial part of the work has been the compilation of an (almost) homogeneous database of optical spectra of Galactic O stars. The bulk of the observations come from the extensive spectroscopic databases gathered in the framework of the IACOB and OWN surveys. In total, we have used 2900 spectra of 415 Galactic O-type stars, covering a range in spectral types from O2 to O9.7 and all luminosity classes.

In a first step, the multi-epoch character of the compiled spectroscopic dataset has allowed us to perform a spectroscopic variability assessment of the full sample of stars. Then, we have proceed with a detailed spectroscopic analysis of those (285) stars in the sample not identified as double-line spectroscopic binaries. To cope with the large amount of targets, we make use of two semi-automated (but supervised) tools for quantitative spectroscopic analysis developed in the framework of the IACOB project. First, a combined Fourier transform and profile fitting method is used to derive $v \sin i$ and the amount of *macroturbulence* broadening affecting the line-profiles using the IACOB-BROAD tool. Then, in order to derive the stellar atmosphere and wind parameters, we perform a detailed quantitative spectroscopic analysis using IACOB-GBAT, a semi-automatized tool based on χ^2 optimization with a vast grid of FASTWIND models. The program calculates in a fast, objective, and reproducible way, values and uncertainties for $T_{\rm eff}$, $\log g$, $Y_{\rm He}$, $\xi_{\rm t}$, and $\log Q$.

As part of this work, we have initially selected and analyzed a benchmark subsample (namely, the grid of O-type standard stars for spectral classification) to establish a step-by-step protocol to be followed in the analysis of the complete combined IACOB+OWN sample. This sample has been also used to assess the level of agreement between our results and those provided by more traditional "by-eye" techniques, and to construct new linear $T_{\rm eff}$ and $\log g$ calibrations as

a function of spectral type and luminosity class for Galactic O-type stars.

We then extend our investigation to the whole sample of Galactic O-type stars surveyed by IACOB and OWN. We use the results of the spectroscopic analysis to provide a global empirical overview of the various investigated parameters in several diagnostic diagrams, as well as to investigate some topics of interest in the field of massive stars. In particular, we introduce a distance-independent version of the wind-momentum luminosity relationship to evaluate our results with respect to previous theoretical and empirical studies. We also assess the apparent offset between the theoretical and empirical zero-age-main-sequence for stars more massive than 32 $M_{\odot}$. Last, we study the distribution and evolution of the spin rate of O-type stars, and compare the extracted empirical information with predictions by state-of-the-art models of single and binary star evolution.

In the last chapter we perform a thorough assessment of the available information about parallaxes for our complete sample of Galactic O-type stars. We evaluate, in terms of quantity and accuracy, the improvement from the *Hipparcos-Tycho* catalog to the recent second data release from the *Gaia* mission (*Gaia*-DR2). Then, we benefit from the parallaxes provided by *Gaia*-DR2 to derive the absolute magnitudes, radii, luminosities, and spectroscopic masses of our benchmark subsample: the grid of O-type standard stars for spectral classification.

Acknowledgments

Mi primer agradecimiento es a todos aquellos que no aparecen en esta página. Si ayudaste en la tesis, o ayudaste al doctorando, gracias. Si no estás aquí, pero sabes que lo mereces, ya sabes como soy y tienes que perdonarme.

My first token of gratitude is to all those who do not appear on this page. If you helped in the thesis, or you helped the doctoral student, thank you. If you're not here, but you know you deserve it, you know how I am and you have to forgive me.

∼∼∼∼∼∼∼∼∼∼∼∼∼∼∼∼

This thesis would have been impossible without the incalculable effort of my supervisor, Sergio Simón Díaz. I feel really honored to be his first doctoral student, and to be part of what will undoubtedly be a long list of academic "children". With only 10% of the help you have had to give me, I am sure that each of them will be very grateful for your invaluable help, attention to detail, ability to inspire, and even (in the last moments) total permission to hate/criticize your supervision. Thank you for trusting me and making me feel like a top priority from the start. I hope I have lived up to it.

I would like to thank Artemio Herrero as tutor of this thesis and, above all, for coordinating the group of massive stars at the IAC. Everyone who has been to Tenerife knows what I'm talking about when I say that Artemio does an incredible job at the forefront of all of us, allowing us to push in the same direction. In the same way, I want to thank all the colleagues who have passed through this group and who have always been willing to review with me any work, especially my PhD colleagues (Inés, Sara, Klaus) who have shared so much with me.

Now I would like to officially thank the IAC and its Resident Astrophysicist Programme (R) that have allowed me 4 years of an unbeatable working relationship. To all the staff, and especially Lourdes and Eva for their constant smile that could be felt even through the mail reminding you that you were missing some extra document.

For this piece of work I am indebted to the invaluable help and support of countless professionals over the past four years. Without their time and effort none of this work would have been possible. Giants shoulders' onto which I try to stood.

In particular to Rodolfo Barbá, and the entire group at La Serena University, for the joint work of IACOB and OWN that makes us together an incomparable team. To Carolina for her support and happiness despite explaining the same thing for the third time. And to all the people I met in La Serena for their great hospitality despite the fact that the ground did not stop trembling, and I trembled even more. I also want to thank Joachim Puls for inspiring me (at first a little out of fear). One day you said that this could be a great thesis, but only if I work a lot. I do not know if I've got it (I'm sure you'll tell me one way or the other) but I appreciate that you set the bar high. I also want to thank you for your attention and hospitality during our visit to Munich. Thanks to the great help from Jesús Maíz Apellániz, especially for his work in GOSC and GOSSS from which this work emanates. Thanks to our cousin group in Alicante, co-led by Ignacio and Amparo, and ultimately to the entire network of work colleagues (Miriam, Berto, Paco, Miguel, Pere, Emilio, María Fernanda, Lee, Nikolay, Ricardo, Javier, Hugo, ... ad infinitum) who have done nothing but encourage me to continue, I really appreciate you all. I also want to thank Sylvia and Cyril for their mini-master classes on evolutionary models, for all the help given, and for counting on me for the work group in Bern, a very productive experience at a professional and personal level.

I would also like to give sincere thanks to Lionel Haemmerle for the interesting work done with results from this thesis. And a very strong thanks to Carlos Allende, internal reviewer of this thesis, for a thorough review and always useful comments.

I want to congratulate the staff of the Mercator and NOT telescopes for their kindness and professionalism, and in general to all the staff at the Roque de los Muchachos that allows the long nights awake not to weigh on body or mind.

Finally I would like to apologize again to Jose Caballero and David Montes for leaving the field of exoplanets as soon as I had the opportunity and really thank them for how much they have helped ever since, real sportsmanship.

~~~~~~~~~~~~~~~~~

Aquí quiero dar gracias a toda mi familia por su apoyo incondicional. A mis padres, Fede y Carmen, que me han hecho sentir que podía llegar allí donde me propusiera; a la dedicación de mi hermano Fede, un espejo en el que reflejarme; a mis tíos y primos con los que siempre pude contar; y a mis abuelas, Rafaela y Dolores, que son el gran ejemplo a seguir en la familia y siempre, siempre, creyeron en mi. Sin todos vosotros esto habría sido imposible.

A toda mi gente en Córdoba muchas gracias. Al grupito del Carmen; Juan, Mega, Fer, Pepelu, Thayre, por tener siempre presente a los isleños. A los cafres de HST: Juanjo, Mr Rau, y Dani, por recordarme siempre que se pueden bajar dos tonos más al hacer metal. Al grupito Tardebuena del que tengo tanta suerte de formar parte. Y gracias a mi amiga Andrea, porque la distancia nunca fue un problema entre nosotros.

Gracias a mis compañeros, ya amigos, en el IAC. En particular a Marcos y Pablo por un curro increíble que jamás ninguno podremos olvidar ya, a toda la gente que vino al Domingo Jugetón semana tras semana (con ese nombre!): Alejandro(s), Efsan, David, Luis, María, Rafa, Amanda, Melania, Borja, Ignacio, Patri, Oliver, Pedro, Carlos, (...?) ; a todos los consortes, y en general a todos los que me hicieran descansar de estrellas masivas durante un rato en la isla. Sois todos increíbles.

Y por último gracias a Elena. Por ser como es y quererme como soy yo. Que quede por escrito lo muchísimo que (me) ha aguantado en esta tesis, y nunca perdió la fe. Doy gracias a su familia por cuidarla y ahora cuidarnos a los dos. Mientras todo lo demás gira a mi alrededor tú eres el centro de mi Universo, un punto al que mirar y saber cuál es la dirección a seguir.
~~~~~~~~~~~~~~~~~

Contents

1

Introduction

Whenever they ask you if you can do a job, answer yes and immediately go to learn how to do it.
Franklin D. Roosevelt

1.1 Massive stars

Massive stars play a prime role in the evolution of galaxies and, more generally, of the Universe. This is the reason why they have been many times claimed to be powerful "cosmic-engines" (Bresolin et al. 2008; Langer 2012). They are born with initial masses in excess of 8 $M_{\odot}$ (Maeder & Meynet 2000a; Smith 2014) and are associated with the most luminous stellar objects in the Universe. While they are in the main sequence[1] phase, where they spent most of their life as O and early-B type stars, they pour out large amounts of ionizing photons, creating H II regions. Their number is very low in comparison with lower mass stars (Salpeter 1955), and they also present much shorter lifetimes (5-20 Myr) than their less massive counterparts. The whole life of a massive star is marked by powerful stellar winds that flow supersonically expelling the outer layers, even passing occasionally through violent phases where they suffer from strong winds and stochastic eruptions (during, e.g., the so-called Wolf-Rayet and luminous blue variable phases, respectively). These winds help to distribute nuclear processed material throughout their parent galaxies and pol-

[1]The main sequence is the phase in the life of a star in which they spend the most time, characterized by the core burning of hydrogen into helium.

lute the interstellar medium (ISM) with heavy elements. In most cases they have a dramatic end as core-collapse supernovae (CCSN), leaving behind compact remnants such as neutron stars, black holes and, eventually, producing the most energetic cosmic flash, a Gamma-Ray-Burst (Woosley et al. 2002; Woosley & Bloom 2006; Savaglio et al. 2006; Ohkubo et al. 2009). These violent deaths produce a final spike of expelled photons, kinetic energy, and newly synthesized chemical elements.

In addition to the interest per se within the field of massive stars, these hot and luminous stellar objects are at the focus of attention in several fields of Astrophysics (e.g., star formation, chemodynamical evolution of galaxies, reionization of the Universe; see Herbig 1962; Elmegreen & Lada 1977; Elmegreen & Elmegreen 1980; Haiman & Loeb 1997; Tenorio-Tagle et al. 2006; Preibisch & Zinnecker 2007; Prantzos 2008; Bromm et al. 2009; Robertson et al. 2010). Indeed, massive stars are not only critical agents in the present-day Universe, but also in the early Universe. This makes the study of massive stars of fundamental importance for our understanding of the Universe.

To give a few examples, massive stars are key-players in the triggering of new generations of stars, as their feedback – via the intense ionizing radiation and stellar winds associated to the different evolutionary phases of these stars– produces remarkable effects over the star forming region that contains them. They are also commonly used as tracers of young populations, and to study the chemodynamical evolution of galaxies (Steidel et al. 1996; Pettini 2000; Steidel 2014). In any given star-forming galaxy, the massive star population dominates the light output across the full spectrum of light. In the UV and optical range the light is dominated by hot (up to $\sim$50 kK) massive stars (Kennicutt et al. 1998; Bestenlehner et al. 2011), whereas in the near infrared the light is dominated by the cool red supergiant stars evolved from these stars (Patrick et al. 2015). Their intense matter and photon outflows deposit huge amounts of mechanical and radiative energy in the ISM, enriching the interstellar medium by returning unprocessed and nuclear processed material, oxygen and other α-elements, during their whole lifetime. In this sense, their influence is not restricted to the surrounding medium, since their spectacular death as supernovae produces "chimneys" and "fountains" of material[2] which, afterwards, falls back to the main body of the star-forming galaxy.

With their high luminosities, strong stellar winds and violent deaths, they drive the evolution of galaxies in the near and far Universe. As a consequence of all the processes mentioned above, a proper characterization of the physical and evolutionary properties of massive star is vital to understand their contribution

[2]Large-scale outflows of interstellar material.

to the galaxy where they are formed. Moreover, before galaxies formed, the first massive stars are thought to have played an essential role in the reionization of the early universe at redshift beyond z∼6, and its early chemical evolution.

They are also the progenitors of the most extreme stellar objects known in the Universe (e.g., hyper-energetic supernovae, Wolf-Rayet stars, luminous blue variables, massive stellar black holes, neutron stars, magnetars, massive X- and γ-ray binaries), or the recently detected gravitational waves produced by a merger of two massive black holes (Abbott et al. 2016, incl. LIGO and Virgo Collaborations).

Finally, beyond their active role in the Universe, massive stars are visible out to large distances owing to their high luminosities and, as "gifts-of-nature", (Kudritzki & Puls 2000; Kudritzki et al. 2008), they have become powerful alternative tools to H II regions, cepheids, and SN Ia to obtain information about present-day chemical abundances in galaxies, as well as to infer extragalactic distances (Monteverde & Herrero 1998; Korn et al. 2005; Lennon et al. 2005; Urbaneja et al. 2005; Trundle & Lennon 2005; Evans et al. 2007; Kudritzki et al. 2008; Hunter et al. 2008; Bresolin et al. 2008; Castro et al. 2012, among others).

1.1.1 Massive stars in the HR diagram

Within the last decades, our understanding of the physical properties and evolution of massive stars has significantly improved due to theoretical, as well as observational, advances leading to a deeper knowledge of the physical processes taking place in their interiors, atmospheres, and winds.

An invaluable tool to study the evolution of massive stars is the Hertzsprung-Russell (HR) Diagram. It shows the relationship between the stars' absolute magnitudes or luminosities versus their spectral classification or effective temperature. Figure 1.1 (adapted from Castro et al. 2014) presents a global overview of the different type of stellar objects found in the massive star domain of the HR diagram. In its original version, it represents the probability density distribution of the location of a large sample of massive stars in the spectroscopic HR (sHR) diagram[3]. Their high masses and luminosities place all the stellar objects associated with massive star evolution in the upper part of the HR diagram. As indicated in Fig. 1.1, the massive star domain of the HR diagram is populated by OBA stars as well as other more extreme objects such as Red Supergiants (RSG), Wolf-Rayet stars (WR), Yellow Hyper Giants (YHG), and Luminous Blue Variables (LBV) (Conti et al. 1984; Smith et al.

[3]The spectroscopic HR diagram is a radius-free analogue to the conventional Hertzsprung-Russell diagram (see Langer & Kudritzki 2014).

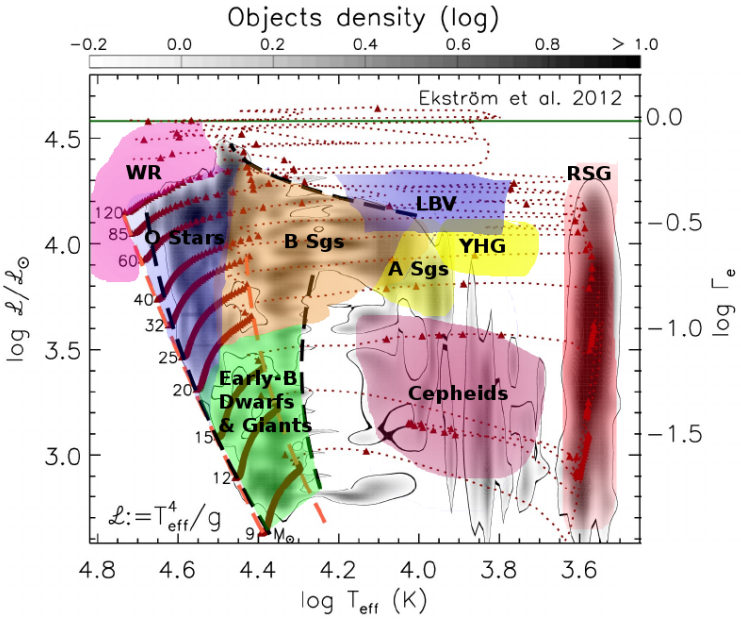

Figure 1.1: (adapted from Castro et al. 2014) Probability density distribution of the location of ∼600 stars in the spectroscopic HR diagram . The black dashed lines represent the limit between densely populated regions and empty regions. Overlayed in red are the Ekström et al. (2012) stellar evolution tracks for non-rotating stars with solar composition, including the zero-age main-sequence (ZAMS) and the end of the main-sequence in orange. Red triangles represent 0.1 Myr steps. The electron scattering Eddington factor (Γe) is given on the right ordinate axis. Defined as $\Gamma_e = L/L_{\rm Edd}$ it is a measure of how close a star is to its maximum luminosity (Castro et al. 2014). The Γe limit for hydrogen-rich composition at log $\mathcal{L}/\mathcal{L}$=4.6 is represented by a green horizontal line. The shaded areas represent the approximate regions where each type of object exists.

2004). On top of this density plot we have included as shaded areas with various colors the different regions where each type of object is presented. As indicated above, this empirical diagram allows us to assess the evolution that these stars follow.

In Crowther & Smartt (2007), a summary of the possible evolution scenarios of massive stars through the HR diagram is presented in a simplified way, based

on the "Conti scenario[4]" (Conti 1975):

- Stars with relatively low initial masses evolve redwards reaching a RSG phase and dying as a SNe. $8<M_{ini}<40$ $M_{\odot}$: OB star - RSG - SNIb
- Stars with higher initial masses reach the RSG/LBV phase and then return to the BSGs phase ("blue-loops"), becoming a WR before dying. $40<M_{ini}<60$ $M_{\odot}$: O star - LBV/RSG - WN(H poor) - SNIb
- The most massive stars experience extreme mass-loss and lose the convective equilibrium, contracting without reaching the RSGs phase. $M_{ini}>60$ $M_{\odot}$: O star - WN(H rich) - LBV - WN(H poor) - WC - SNIc

This qualitative empirical scenario linking the various types of objects thought (or confirmed) to be associated with massive stars evolution must be continuously confronted with new observations as well as the theoretical predictions by evolutionary models. In the following, I briefly summarize our present knowledge about the formation and evolution of massive stars (Sect. 1.1.2), also indicating factors which are known to be important fo the evolution of this type of stars (Sect. 1.1.3).

1.1.2 Formation and evolution of massive stars

Despite their importance, our current understanding of massive stars evolution is still limited. Given a specific metallicity, the very short lifetime of a massive star is critically dependent on the initial mass on the zero-age main-sequence (ZAMS) – or, equivalently, the mass it is able to accumulate during its formation– but there are also other important effects that need to be taken into account to properly understand and characterize the evolution of massive stars. Firstly, one of the primary facets of massive stellar life is mass loss. These stars can lose a significant fraction of their mass through their intense winds, modifying the specific evolutionary path followed in the HR diagram (Heap et al. 2006; Vink & Gräfener 2012; Crowther et al. 2017). This is particularly important for very luminous stars near the Eddington limit, or for objects in an advanced evolutionary phase, such as RSGs, WR stars, or LBVs. A second factor that could affect their internal structure and evolution is rotation, reducing the effective gravity through the associated (latitude-dependent) centrifugal acceleration, and contributing to the transport of chemical elements and angular momentum. This could influence the evolution, lifetime, and final fate of the star (Maeder & Meynet 2000a; Heger et al. 2000; Gray 2005; Brott

[4]This scenario needs to be taken very cautiously, as the effect of rotation is not included.

et al. 2011). In addition, the fact that the majority of massive stars are found in binary systems makes it necessary to include binarity as a decisive factor in their formation and evolution. It affects the rotation and chemical composition of the stellar atmosphere by means of mass transfer and/or mergers (Sana et al. 2012). Finally, magnetic fields may also have an effect on the formation and evolution of these interesting objects (Morel et al. 2015; Petit et al. 2017). All these factors are described individually in more depth in Sect. 1.1.3.

Formation of massive stars

One of the open questions about formation and evolution of massive stars is how they are formed. While we have a global idea of how stars are born from the parental clouds, some of the specific details about the case of massive stars are still debated.

Generally speaking, star formation is located within giant molecular clouds (GMCs) in regions that collapse gravitationally, consisting mainly of molecular hydrogen. They represent large clumps of interstellar material that have become over-dense with respect to the surrounding medium, with the cooling capabilities to have the correct density and temperature conditions to form stars ($\sim 10^5$ cm^{-3} and 10-20 K). They contain typically 100-110 $M_\odot$ distributed around bubbles of 50-100 pc (Fukui & Kawamura 2010; Kroupa et al. 2010). Within GMCs, over-dense regions continue to grow and eventually fragment into dense smaller cores where, if the local mass is greater than the associated Jeans mass for the region, star formation takes place. Both high- and low-mass stars are formed at the same time, and the optical depth around this protostellar cores increases, rising the temperature (Zinnecker & Yorke 2007). Finally, the system gets to hydrostatic equilibrium when the radiation pressure exerted by the core compensates the gravitational pull. The collapsed core continues to accrete matter from a disk that has formed around it. A larger protostar is able to accrete a larger amount of additional material from its surroundings, and become a more massive star. The core of the protostar contracts and increases the temperature, reaching hydrogen-burning temperatures. At the moment when hydrogen combustion begins, the object is called a zero-age main sequence (ZAMS) star, onto which accretion of material from the parental cloud could still continue. This ends the period of formation, as the star now has a central energy source that governs the evolution for the remainder of time spent on the main sequence.

Only a few massive stars are formed in comparison to the total number of low mass stars when the parent molecular cloud collapses. Their formation is characterized by an accretion timescale that could be longer than the contrac-

tion timescale, although the details of the formation of individual massive stars is still a matter of debate due to the problem of the strong radiative pressure generated by the luminosity of young massive protostars (Bernasconi & Maeder 1996; Yorke & Sonnhalter 2002; Krumholz et al. 2005). Theory needs to explain the situation where the high-mass star begins to burn hydrogen in its core while still able to accrete material from the parental cloud. For massive stars, this ZAMS star is embedded and optically obscured in the molecular cloud for 15% of their lifetime, even if it is already emitting ultraviolet photons and has created a small Stromgren sphere around it (Churchwell 2002). This means that when the parental cloud is sufficiently dissolved, and the star is visible at wavelengths where the main diagnostics of stellar parameters are concentrated (i.e., the ultraviolet, optical, and although to a lesser extent, the near-infrared; Hanson 1998), it is already somewhat evolved, especially in the case of stars with masses above $\sim$20 $M_{\odot}$ (basically those that evolve as O-type stars from the ZAMS to the end of the main sequence, See Fig. 1.1).

Main sequence and subsequent stages of massive star evolution

All stars spend the majority of their lives on the main-sequence (MS), fusing hydrogen to helium in their cores in a stable state of hydrostatic equilibrium. In the case of massive stars this is done through the carbon–nitrogen–oxygen (CNO) cycle. This nuclear process is characterized by a much higher efficiency than the proton-proton chain cycle occurring in lower mass stars. As a consequence, the CNO cycle reduces considerably the lifetime of the star during the MS and also induces convective and homogeneous mixing in the core (Kippenhahn et al. 2012).

As mentioned above many factors could vary the evolutionary path of massive stars (depicted in Fig. 1.1 as evolutionary tracks of single stars with different initial masses). Mass is the main driver, but the mass-loss by stellar winds, rotation, and binarity can, in addition, significantly affect the amount of fuel available for burning. The stellar winds eject material progressively. The mass of the convective core decreases more rapidly as the star evolves, but due to stellar winds the total mass ratio is higher than in the case without winds. This leads to an evolution at lower luminosities, and therefore wider main-sequence phases for stars with moderate mass-loss. Although rotation decreases as the star evolves in the HR diagram due to the transport of angular momentum produced by an increase of the radius (Ekström et al. 2012), it also could affect the evolution of massive stars. At high initial rotational velocities the evolutionary tracks evolve from the ZAMS towards higher luminosities and temperatures due to an increase of the core size. In addition, binarity can produce mass transfer

between the two companions or they can even merge, modifying abruptly the track. Finally, convection enlarges slightly the lifetime due to the extra amount of material available for fusion, but the CNO-cycle is very efficient and after 4-10 Myr the H available is depleted.

The next stage in the evolution of a massive star starts with the contraction of the inert helium core, a temperature rise, and helium fusion is ignited surrounded by a hydrogen fusing shell. This new energy source causes an expansion in the core that, owing to the mirror principle of shell fusion, results in the expansion of the outer envelope, becoming a supergiant star. This core helium-burning phase of evolution appears in the HR diagram as a come-back of the star to higher-temperatures, which ends with a carbon/oxygen core surrounded by a helium-burning shell, which is in turn surrounded by a hydrogen-burning shell. The situation repeats itself, the inert carbon/oxygen core contracts, heats up, and ignites the core fuel. Massive stars are the only stars which evolve beyond the helium burning phase and thus form elements heavier than oxygen. The cycle of core contraction with new core reactants begins and subsequent neon-, oxygen- and silicon-burning phases follow in the core and shell burning (Woosley et al. 2002). The reactions cease with ^{56}Fe, because its fusion is no longer exothermic. The massive star presents and "onion structure" with an inert iron core surrounded by layers of lighter elements fusing in shells. The outer envelopes and the spectral type of the star does not change significantly during this period due to the short timescale of these fusion reactions (Meynet et al. 2011). The relative abundances of C, N, O in the hot stellar interior change, and possible convective dredge-ups of material during these phases are the reason for the presence of processed CNO material at the stellar surface. These material is then released during stellar outflows and, finally, as supernova ejecta.

Final fate of massive stars

Massive stars end their lives as core-collapse supernovae (CCSN), a violent explosion that origins in the lack of energy generation by the inert iron cores at the end of their nuclear-burning lifetime. This explosion distributes the heavy elements synthesized within massive stars during their nuclear-burning lifetime, plus the new material synthesized during the explosion event. As the temperature reaches 10^{10}K, photons in the core of the star now have enough energy to photo-dissociate iron-group elements into α particles. The increasing density forces electrons into nuclei which merge with protons to create a neutron-rich environment. As densities approach nuclear density, core contraction halts as a result of the repulsive force of the strong interaction (Janka et al. 2012). The

in-falling outer layers crash into the core and the resulting shockwave disrupts the entire star and produces the SNe. Observationally, SNe are broadly classified as type II, type Ib and type Ic based on the presence (II) or absence (I) of hydrogen in their spectra. These events eject fusion products back into the environment, and are believed to produced neutron stars and stellar black holes, and even GRB. In a final poetic circle the surrounding gas is shocked and compressed, triggering more star formation in the environments.

1.1.3 Evolutionary models

Stellar evolutionary models have been developed to explain and predict the physical properties of massive stars along their evolution. The temporal variation of some key parameters (such as, e.g., the $T_{\rm eff}$, radius, luminosity, gravity,...) are then used to build tracks representing the path that stars with different initial masses follow in the HR diagram. Massive stars are born as O and early-B type stars on the ZAMS, after a few million years they evolve to become either a RSG or a WR, depending on the initial mass, passing through the so-called Blue Supergiant (BSG) phase (including O, B, and A-type supergiants), as well as other extreme phases as LBV, or YHG (See Fig. 1.1).

Evolutionary models have many free parameters that can strongly affect the track of a star, even during the MS. It is of paramount importance for many areas within astrophysics to construct and use accurate and reliable models of massive star evolution. All crucial factors for massive stars are being introduced in different ways on one-dimensional hydrodynamic stellar evolution codes. Evolutionary models often rely on various prescriptions to describe the physical processes driving the evolution, and these prescriptions vary significantly in different codes. The most important ones are convection (and its related properties such as overshooting and extension of the convective core), mass-loss, magnetic fields, chemical composition (and the relative abundance of the various species considered in the models), the treatment of rotation and angular momentum transport[5], binarity effects, and of course initial mass (Chiosi & Maeder 1986; Maeder & Meynet 2000a; Martins et al. 2005; Maeder & Meynet 2010; Brott et al. 2011; Ekström et al. 2012). Some of these important factors included in the models are commented in more detail below.

[5]In particular, rotation affects the internal structure, the physical properties (temperature, luminosity), the surface chemical appearance, and the lifetimes of stars.

Stellar winds

The existence of stellar winds in massive stars has been established since the 1960's, when the first rocket UV observations revealed the characteristic P-Cygni signatures of mass-loss in different metallic lines (Morton 1967). Besides radiation (i.e. photons), massive OB stars are also losing particles (i.e. atoms, ions and electrons). Mass-loss effects are crucial for the evolution and final fate of a massive star, since it loses a significant amount of matter[6] from the beginning of their lives, and the momentum and energy expelled always contribute to the dynamics and energetics of the ISM around them (Silich et al. 2001; Oey et al. 2003; Garcia et al. 2011). The strong winds of post-main sequence stages can peel the envelope of the star, leaving a He core and causing strong and broad emission lines in their spectra (WR). Winds are then able to modify the ionizing radiation of hot stars dramatically (Najarro et al. 1996), and they even allow us to study the most luminous stellar objects in distant galaxies, enabling us to obtain important information about their host galaxies (Steidel et al. 1996; Leitherer 1998)

The physical processes driving the stellar winds in stars of different types depend upon the location of the specific star within the HR diagram. In the case of hot massive stars, the theoretical framework was developed by Castor, Abbott & Klein 1975, known as CAK theory via line-driven radiation pressure. The basic mechanism is that hot star winds are driven by strong radiation pressure: the absorption and re-emission of photons by millions of metal lines, transferring photospheric photon momentum to the stellar plasma (Lucy & Solomon 1970; De Loore et al. 1977; Chiosi & Nasi 1978; Chiosi & Maeder 1986; Puls et al. 1996; de Koter et al. 1997; Kudritzki & Puls 2000). This generates a continuous outflow from the external layers of the star. This mechanism works in massive stars, since the luminosity is high and a large number of photons is available, with sufficiently high metallicity, to ensure the presence of enough lines with significant interaction probability.

During the last two decades, the radiation-driven wind theory has been compared with the most reliable mass-loss determinations. In principle, empirical approaches to derive accurate mass-loss rates are severely complicated by the realization that the winds of hot stars are not smooth flows but highly structured or clumped (Hillier 1991; Eversberg et al. 1998; Bouret et al. 2003; Fullerton et al. 2006; Mokiem et al. 2007; Moffat 2008), as expected from theory (Owocki et al. 1988; Cantiello et al. 2009). Finally, the mass-loss recipes arising from first principles are only available for main sequence objects (Vink

[6]For a 60$M_\odot$ main-sequence star the lost mass could be between 3-10 $M_\odot$, depending on the wind-clumping effect.

2000; Vink et al. 2001).

The theory is defined with two global parameters, the amount of mass lost per unit of time (the mass-loss rate, $\dot{M}$) and the velocity of the wind at very large distance from the star (the terminal wind velocity, v_∞).

It is quite clear that the mass-loss rates increase for more massive stars (Puls et al. 2008), and the properties of stellar winds depend on both the number of metal lines available to absorb photon momentum, and on their ability to absorb, i.e. their optical thickness. It is important to know which lines are actually responsible for the acceleration of the winds. As hydrogen and helium only have very few lines in the relevant spectral range in which early-type stars emit most of their radiation, it is mainly lines of metals that are responsible for the line driving, pointing out the importance of a mixture of optically thick and thin lines. Analytic solutions involve force multiplier parameters, α, δ and κ which characterize the outflow (Kudritzki 1980). Of these, α[7] controls the fraction of optically thick/thin lines, κ the number of strong lines, and δ the ionization balance. Theoretical studies have indicated that CNO elements are principal line drivers for the outer, supersonic part of the wind, whilst iron group elements are responsible for the inner, subsonic part (Vink et al. 1999). The former determine the wind velocity, and the latter the mass-loss rate, at least for compositions close to Solar metallicity.

Because these winds are initiated and then continuously accelerated by the absorption of photospheric photons in spectral lines, the terminal velocity v_∞ (corresponding to the maximum velocity of the stellar wind) is reached at very large distances from the star, where the radiative acceleration approaches zero because of the geometrical dilution of the photospheric radiation field.

Rotation

In the past decades, both observational and theoretical developments have clearly shown that stellar rotation affects the evolution of stars as strongly as mass and metallicity (Maeder 1987; Langer 1991; Meynet & Maeder 2000; Heger et al. 2000). All the model outputs (tracks in the HR diagram, lifetimes, surface abundances, nucleosynthetic yields, supernova precursors, etc) are greatly influenced by rotation. It contributes to the transport of angular momentum inside the star and produces a meridional circulation of matter from the poles to the equator (Lee et al. 2016). The chemical composition of the stellar surface is modified by the transport caused by rotation, enhancing the He and N abundances in OB stars (Herrero et al. 1992; Hunter et al. 2008;

[7] This parameter is supposedly generally constant α=0.6 except in extreme cases of low density of the stellar wind.

Morel et al. 2008; Rivero González et al. 2012; Bouret et al. 2013). The phenomenon is known as rotational mixing, and it is more efficient in stars with higher rotation, being able to modify the evolution of the star. During the formation process of all stars, including hot luminous OB stars, the conservation of angular momentum implies that they will commence their Main Sequence life rotating very fast, perhaps close to break-up velocity (Huang & Gies 2006; Ekström et al. 2012).

In addition, at rapid rotation rates the shape of the star could be affected, leading to an oblate shape with a larger equatorial than polar radius and to gravity darkening, affecting the distribution of the effective temperature on the surface. This has an effect on the stellar wind, which is predicted to become aspherical (in this case, prolate, as a result of gravity darkening), and the integrated mass-loss rates might be affected, basically increasing with rotation. The decrease of the effective gravity in fast rotating stars reduces the escape velocity and facilitates the departure of material from the stellar surface by stellar winds (Müller & Vink 2014). Theoretical models predict a dependence of mass-loss on the rotational velocity, even favoring a polar wind due to the change in the shape and the distribution of gravity in the surface. Additionally, the momentum loss in the stellar winds could drastically reduce the apparent rotation during evolution (Packet et al. 1980; Langer & Heger 1998; Ekström et al. 2008; Vink et al. 2010; Brott et al. 2011). However, the current implementation of rotation in one-dimensional codes relies on parametrized formulas, hence the choice of the diffusion coefficients in the formulas has a key impact on the evolution (Meynet et al. 2013).

Multiplicity

Massive stars present a very high degree of multiplicity. Most O- and early B-type stars are found in binaries and multiple systems, and even single field stars are often believed to have been part of a multiple system in the past, then ejected by a supernova kick or by dynamical interaction. In young galactic clusters and associations, between 45% and 75% of the O-type objects have at least one companion detected through either spectroscopy or imaging techniques (Mason et al. 2009; Sana & Evans 2011; Sana et al. 2012), and this rate, corrected from observational biases, could rise the true multiplicity fraction close to 100%. We can thus postulate that the typical end product of massive star formation is not a single star but a multiple system, with at least one and possibly more companions. To ignore the multiplicity of early-type stars is equivalent to neglecting one of their most defining characteristics. Typically, the detected companions have a mass one to five times smaller than the pri-

mary mass and are mostly O and B stars. Because the companion stars are also often of spectral type O, about three-quarters of all O stars will have a strong binary interaction-mass transfer, common envelope evolution or merger episodes, which for about half of them occurs before leaving the main sequence, with decisive effects on the rotational properties (de Mink et al. 2013).

Magnetic field

The nature and role of magnetic fields in massive stars is currently poorly understood. Only roughly 10% of massive stars present magnetic fields strong enough to be detected in current studies (Grunhut et al. 2017), a characteristic that stills needs to be explained. The origin of magnetic fields in main-sequence stars in the upper part of the HR diagram is being debated (Moss 2001; Ferrario et al. 2009; Tutukov & Fedorova 2010; Langer & Kudritzki 2014; Wickramasinghe et al. 2014) and the role that these fields play in stellar evolution is being explored (Maeder & Meynet 2000a; ud-Doula et al. 2009; Briquet et al. 2012; Langer 2012). Magnetic fields have fundamental effects not only on the evolution and properties of massive stars, but also on their rotation (redistributing the angular momentum in the stellar interior), on the structure, dynamics, heating of their radiatively-driven winds, and even lead the stars to end their lives as as exotic objects such as supernova, magnetars (highly magnetised neutron stars), black-holes, or gamma-ray burst (Heger 2012).

From a theoretical point of view, ud-Doula et al. (2009) performed dynamical simulations of magnetically channeled, line-driven winds, and calculated the angular momentum loss and rotational spin-down. The radiative cooling in multi-D models of magnetically confined wind shocks was investigated by ud-Doula et al. (2013), and a magnetic confinement versus rotation classification of massive-star magnetospheres has been presented by Petit et al. (2013).

Link to observational efforts

Due to the interaction of all the aforementioned factors during the lifetime of massive stars and the remarkable sensitivity of some of the physical processes governing the interiors of these extreme objects to these various effects, our theoretical understanding of massive star evolution is still far from being completely settle down.

To serve as an example, Martins & Palacios (2013) compared the HR diagram evolutionary tracks predicted by six different modern stellar evolutionary codes and, while they find a reasonably good agreement between the predictions of the various codes for the main sequence evolution, large differences

are found beyond that point. In the same line, Groh et al. (2014) presented a comparison of the particular effect of changing mass loss recipes for a wide variety of massive stars in various evolutionary stages with the aim of improving the predictions of evolutionary models. He found a large discrepancy in the outcome of the models when altering the mass loss by a mere factor of 2.

These two results highlight the importance of the various assumptions made regarding the input physical ingredients used by the models (overshooting, mass loss, nuclear reaction rates, the presence of magnetic field, etc.), as well as the way in which the various effects affecting massive star evolution are taken into account (e.g. expressions of the diffusion coefficients, treatment of the angular momentum equation, or the behavior of the magnetic field inside the star).

The multi-parameter dependence of massive stars evolution makes it clear that a successful construction of accurate and reliable stellar evolutionary models for massive stars not only requires an adequate implementation in the codes of state-of-the-art knowledge about the physical processes governing the interior of these stellar objects, but also the compilation and analysis of large samples of massive stars in different evolutionary stages. In these regards, the important observational efforts performed by projects such as IACOB, VFTS, MiMeS, or OWN (See Sect. 1.2.1) are opening the window to a new era of study of massive OB-type stars. The wealth of empirical information that will eventually result from these observational projects will help to unveil the impact that parameters in addition to mass, rotation and stellar winds – such as binarity or multiplicity, magnetic fields, or stellar oscillations – have on the physical characteristics, as well as on the evolution of these important astrophysical objects, and provide definitive empirical constraints to the state-of-the-art evolutionary models.

1.2 The IACOB project

We are immersed in the era of large spectroscopic surveys of massive OB-type stars. This enormous observational effort, in combination with the availability of mature stellar atmosphere codes for massive stars (see an extensive list of codes and associated references in Puls et al. 2015), is enabling a considerable – and still on-going – increase in the amount of available information about stellar parameters, and multiplicity in the full OB star domain. The IACOB project, introduced in this section, is producing a remarkable contribution to this new era of massive star research.

1.2.1 Global description: definition and context

The IACOB project (Simón-Díaz et al. 2011a; 2014; 2015) is an ambitious long-term observational project driven by the compilation and scientific exploitation of a large homogeneous optical database of high-resolution multi-epoch spectra of Galactic Northern OB stars. By means of a thorough (qualitative and quantitative) spectroscopic analysis of this unique material, and in combination with data provided by the *Gaia*, *IUE*, and *FUSE* space missions, the project aims to provide an unprecedented empirical overview of the main physical properties of Galactic massive O- and B-type stars. The ultimate objective of the IACOB project is that all this empirical information serves as definitive anchor point for our theories of stellar atmospheres, winds, interiors, and evolution of massive stars.

At present, the IACOB spectroscopic database (last described in Simón-Díaz et al. 2015, see also Chapt. 2) counts on more than 6000 high-resolution spectra of more than 800 stars coming from three different sources: the FIES and HERMES fiber-fed spectrographs attached to the 2.56m Nordic Optical Telescope (NOT) and 1.2m Mercator telescope, respectively, as well as the Hertzsprung-SONG 1m robotic telescope. Some first results of the project can be found in Simón-Díaz et al. (2014, 2017); Godart et al. (2017) and Holgado et al. (2018).

The IACOB project has a clear and focused scientific motivation from the very beginning: improve the situation regarding the state-of-the-art of the field of massive stars by the beginning of the 20th century; this was summarized by S. Simón-Díaz in the following sentence: *In spite of the remarkable advances in the modeling and spectroscopic analysis techniques of massive O and B-type stars in the last two decades, our knowledge of these important (but complex) astrophysical objects has been limited until very recently to conclusions extracted from the analysis of single-epoch medium resolution spectroscopic observations of relatively small samples.*

The IACOB projects perfectly complements the efforts devoted in the last years by other large scale observational spectroscopic studies of massive stars in the Milky Way such as GOSSS (Sota et al. 2011, 2014; Maíz Apellániz et al. 2016; Arias et al. 2016), OWN (Barbá et al. 2010, 2014, 2017), BOB (Morel et al. 2014; Castro et al. 2015, 2017; Przybilla et al. 2016), and MiMeS (Wade et al. 2009, 2016; Martins et al. 2015a; Grunhut et al. 2017) or in nearby Galaxies as VFMS and VFTS (Evans et al. 2005, 2007, 2011; Mokiem et al. 2006, 2007; Hunter et al. 2007, 2008, 2011; Bestenlehner et al. 2011; Sana 2013; Ramírez-Agudelo et al. 2013, 2015, 2017; Walborn et al. 2014; Sabín-Sanjulián et al. 2014, 2017).

The specific objectives of the various projects indicated above are summarized below:

- *The Galactic O-type Star Spectroscopic Survey* (GOSSS[8], P.I. Maíz-Apellániz) aims at performing a homogeneous spectral re-classification of all stars with a previous spectral classification of O or B0, using mid-resolution spectroscopy.
- The main objective of the OWN[9] survey (P.I's Barba & Gamen) is to investigate the multiplicity status of (Southern) Galactic O- and WN-type stars with a high-resolution spectroscopic monitoring program.
- *VLT-FLAMES survey of massive stars* (VFMS, P.I. Smartt), was an unprecedented survey of massive stars with the objective to observe O- and B-type stars in seven clusters distributed over the Galaxy and the Magellanic Clouds to study the role of environment, via stellar rotation and mass-loss, on the evolution of the most massive stars. In total it observed approximately 50 O-type stars and 500 B-type stars.
- *VLT-FLAMES Tarantula Survey* (VFTS, P.I. Evans) was an ESO Large Program to study the properties of an unprecedented number of massive stars in the 30 Doradus star-forming region in the Large Magellanic Cloud (LMC). The motivation of this follow-up survey of VFMS was to investigate rotation, binarity or multiplicity, and wind properties of a large sample of $\sim$ 300 O-type stars during their main-sequence phase with multi-epoch intermediate-resolution optical spectroscopy.
- Finally, the *Magnetism in Massive Stars* (MiMeS, P.I. Wade) and *B fields in OB stars* (BOB, P.I. Morel) surveys concentrated in obtaining high-resolution spectropolarimetric observations of a large number ($\sim$ 500 each) of Galactic early-type stars. Their aim is to compile empirical information about the incidence and properties of magnetic fields in main sequence OBA stars which, ultimately, help to provide a broad physical context for the interpretation and origin of the characteristics of known magnetic B and O stars.

In this context, the IACOB project has a complementary (and very ambitious) objective: namely, performing *a global and homogeneous study of the most complete sample of Galactic OB stars ever studied providing an accurate determination of stellar parameters and abundances through the quantitative spectroscopy analysis of high-quality high-resolution optical spectra, and also*

[8] See more details in Chapt. 2.
[9] See more details in Chapt. 2.

incorporating information about spectroscopic variability. To success in this enterprise, the IACOB project has been subdivided in smaller, more manageable, tasks including:

- the compilation of an outstanding spectroscopic database of Galactic OB-type stars (WP1),
- the quantitative spectroscopic analysis of the sample (WP2 and WP3),
- the comparison of the empirical results with theory and models (WP4),
- the investigation of spectroscopic variability and multiple systems (WP5 and WP6), and finally
- the investigation of the interplay between massive OB stars and the ISM (WP7).

In addition, the global sample of stars has been divided in specific subsamples of stars that require different types of analysis. In brief, this refers to the O-type, early B-type, and B Sgs domain, respectively.

1.2.2 O-type stars in the IACOB project

As indicated in Sect. 1.1.1, O-type stars represent a very important evolutionary phase of massive stars. They portray the initial conditions right after their formation, it is the phase where they spend most of their lifetime, and represent the first stages of the evolution of all very massive objects (LBV, RSG, WR, black holes, etc. See Fig. 1.1). In addition, the fundamental properties of O-type stars are essential for interpreting the spectra of unresolved star-forming regions and of starburst galaxies, and even study the re-ionization epoch of the Universe. Hence, a proper characterization of their physical properties[10] (apart from interesting per-se) is also crucial for many others fields of Astrophysics.

Massive O-type stars present very high luminosities ($L > 10^3 L_{\odot}$), masses (20-100 $M_{\odot}$) and temperatures ($T_{\rm eff}$∼30-50 kK), and their nuclear fuel is quickly exhausted, i.e., they are extremely short-lived (Herrero et al. 2002; Markova 2010). They do not get the chance to move far from their birthplaces in the galactic plane and they are often found in so-called OB-associations: young and very loose "clusters" of stars, containing 10 to 1000 massive O and B-type stars.

In the context of spectral classification O-type stars are subdivided into spectral types (SpT) ranging from O2 to O9.7, and luminosity classes (LC) ranging from dwarfs (V) to supergiants (I) and including intermediate LCs as

[10] A successful achievement of this objective requires not only a large observational effort (See Sect. 1.1.3), but also the development of stellar atmosphere codes (See Sect. 1.3).

bright giants (II), giants (III), and subgiants (IV) (Walborn et al. 2002; Sota et al. 2011; Maíz Apellániz et al. 2015, 2016; Martins 2018).

Traditionally, massive O-type stars have been investigated in the context of single star evolution, however, binarity is increasingly admitted to be an important effect to be taken into account when studying massive O-type stars. In particular, as discussed in Sect. 1.1.3, recent studies have found that 75% of the O stars are found to be in binary systems which components may interact at some point of their evolution with a companion either filling its Roche-lobe, or even merging (Mason et al. 2009; Sana & Evans 2011; Sana et al. 2012; de Mink et al. 2013).

The O-star domain has been a focus of attention for the IACOB project, with the following main objective: *providing a thorough quantitative empirical characterization of the whole O star domain.* To this aim, it was necessary to build the largest possible database of high-resolution spectra of Galactic O-type stars (Simón-Díaz et al. 2015), as well as to develop a battery of semi-automatized tools to perform a homogeneous quantitative spectroscopic analysis of such a large sample of O-type stars in a reasonable amount of time (Simón-Díaz et al. 2011c). Regarding the compilation of spectra, since the observational capabilities of the IACOB project were initially restricted to stars observable from the Northern hemisphere (i.e. from telescopes located in the Canary Islands observatories), we decided to start a collaboration with the complementary Southern high-resolution OWN survey. This allowed us to create a multi-epoch spectroscopic database comprising more than ∼6 000 spectra of more than 400 Galactic O-type stars (see Holgado et al. 2017, and Chapt. 2). This represent *the most complete sample of Galactic O-type stars for which high-resolution, multi-epoch, optical spectroscopy has been obtained.*

The spectroscopic analysis of the complete sample of O-type stars surveyed by the IACOB and OWN projects is the main focus of this thesis (See Sect. 1.4), which eventually aims to complement and extent (by a factor of 5 in number of analyzed stars) the available information about physical parameters in O-type stars from the Milky Way.

1.3 Quantitative spectroscopic analysis of O-type stars

The term "Quantitative spectroscopy" refers to the systematic analysis of observed stellar spectra by means of the comparison with information provided by synthetic spectra generated with adequate stellar atmosphere codes. In the case of O-type stars, quantitative spectroscopy provides the most reliable way to determine accurate and reliable information about stellar parameters (such as $T_{\rm eff}$, $\log g$, $\xi_{\rm t}$) and photospheric abundances.

The optical spectra of O stars are characterized by the presence of strong H lines as well as relatively strong lines from He I and He II. In addition, some weaker absorption lines such as O II-III, Si III-IV, and N III-IV-V, are present, providing a mean to derive abundances, and in certain cases $T_{\rm eff}$. High-resolution spectroscopy is needed in order to extract reliable information about the star from these subtle characteristics of the spectra.

The history of quantitative spectroscopy, from pioneering works by Unsöld & Weidemann (1955) to today, has seen continuous developments to produce more realistic model atmospheres, including a better description of the physical processes that take place in these complex systems, in order to obtain more reliable parameters, and the development in parallel of computing power and faster mathematical algorithms (Puls et al. 2005).

The specific procedure used for the derivation of the stellar parameters in O-type stars has become already standard since the early works by Herrero et al. (1992). While it has been thoroughly described elsewhere (see e.g. Herrero et al. 1992, 2002; Repolust et al. 2004) we briefly describe here the basic ideas. It is based on visual fitting of H Balmer lines and He I and He II lines with synthetic lines previously convolved with the corresponding broadening profiles. Through the He I-II ionization equilibrium the effective temperature can be estimated; the wings of the upper Balmer lines (Hγ, Hδ) are useful for determination of the gravity, and information about the stellar winds is mainly provided by Hα, with additional information provided by the He IIλ4686 and He Iλ5875 diagnostic lines. The stellar atmosphere parameters that can be obtained from the quantitative spectroscopic analysis of the optical spectra of O-type stars are: the effective temperature ($T_{\rm eff}$) , the surface gravity ($\log g$), the microturbulent velocity ($\xi_{\rm t}$), the Helium abundance, the wind strength (inferred from the Mass-loss rate, the stellar radius at the Rosseland optical depth[11], and the terminal velocity), and the exponent of the wind velocity law β (a measure for the flow acceleration). In addition, the rotational velocity $v \sin i$ and macroturbulent velocity $v_{\rm mac}$ are derived from the spectra without using an atmospheric model, as we assume their effect on the profiles. All these parameters (except the radius) can be determined from spectral observations by spectral line fitting of strategic lines with model calculations. Finally, in cases of relatively weak winds, optical spectra are quite insensitive to changes in mass-loss rate, terminal velocity, and β. For these cases UV spectroscopy, more specifically the analysis of the P-Cygni lines, is able to provide more accurate determinations on these parameters. In essence, this is an (iterative) optimization problem, in which one tries to find the optimum fit between ob-

[11] $\tau_{ross} = 2/3$

served and synthetic line profiles, which emerge from the underlying stellar atmosphere model.

A brief of history and state-of-the-art

The consistent explanation of the observations of both lines and continua of luminous hot stars is possible thanks to the numerical techniques that perform extensive NLTE calculations, with the capability to solve the statistical equilibrium and transfer equations simultaneously (Auer & Mihalas 1972; Auer & Heasley 1976). The first studies performing systematic analysis of O-type stars were characterized by samples of relatively small size ($\sim$ 25 stars) and where based on "by-eye" model fitting techniques (Herrero et al. 1992, 2002; Bouret et al. 2003; Repolust et al. 2004; Massey et al. 2004; Markova et al. 2004, 2005; Mokiem et al. 2005; Martins et al. 2005; Markova & Puls 2008; Martins et al. 2012; Bouret et al. 2013; Bestenlehner et al. 2014; Hervé 2015; Mahy et al. 2015). These studies were characterizing the O-type star sample by mean of spectroscopic parameter determination (mainly $T_{\rm eff}$, $\log g$, Helium abundance, $\xi_{\rm t}$). More recently, the improvement both in the atmospheric codes and in the computing capacity, which allowed to improve these codes faster, gave rise to the calculation of abundances by means of optical photospheric lines of H, He and metals (e.g. Rivero González et al. 2011; Martins et al. 2015a,b, 2016; Grin et al. 2017; Cazorla et al. 2017; Carneiro et al. 2018). In addition, the increasing availability of high-quality spectra of much larger samples of O-type stars motivated the advent of several tools for the automatized quantitative spectroscopic analysis (see e.g. Genetic Algorithms (GA), Principal Component Analysis (PCA), and two grid-based automatizations in Mokiem et al. 2005; Urbaneja et al. 2008; Simón-Díaz et al. 2011c; Irrgang et al. 2014, respectively). Numerous studies make use of these more time-efficient automatized fitting process (see, e.g., Simón-Díaz et al. 2011b; Sabín-Sanjulián et al. 2014, 2017; Berlanas et al. 2018), largely increasing the amount of objects studied in them ($\sim$ 70 stars), while the traditional "by-eye" model fitting technique is still used for specific delicate procedures (Markova 2010; Martins et al. 2015a; Markova et al. 2018). For the purposes of this thesis work we have used the IACOB-GBAT automatized tool (Simón-Díaz et al. 2011c) and state-of-the-art model atmospheres computed with FASTWIND code (See below).

Stellar atmosphere codes

As mentioned above, most of our present knowledge about the physical parameters and photospheric abundances of OB-type stars originates from studies

performing quantitative spectroscopy. This knowledge is mainly derived from the detailed study of stellar spectra, which in turn requires adequate stellar atmosphere codes. The outcome of these codes includes, not only the behavior of physical quantities such as pressure, temperature, density, and velocity with depth in the stellar atmosphere, but also a prediction of the emergent spectrum, which is a direct and observable diagnostic of the underlying atmospheric properties. These codes offer us the opportunity to derive rather realistic stellar parameters, including mass-loss rates, wind terminal velocities, and the surface abundance of stars.

The modeling of the atmospheres of massive OB-type stars is a tremendous challenge, mostly because of their intense radiation fields, large sizes, and development of radiatively driven stellar winds. For this purpose sophisticated model atmosphere codes have been developed in the last two decades, e.g., Hubeny & Lanz (1995), Santolaya-Rey et al. (1997), Hillier & Miller (1998), Pauldrach et al. (2001), Gräfener et al. (2002), Hubeny & Lanz (2011), Hubeny & Lanz (2011), Hillier (2012), Rivero González et al. (2012), and Hamann et al. (2009) incorporating as basic ingredients the atomic data, Non-Local Thermodynamic Equilibrium (NLTE), line blanketing, stellar winds, unified model atmospheres and clumping. Overviews of the most used codes for massive stars can be found in Hubeny & Lanz (2011) (TLUSTY), Hillier (2012) (CMFGEN), Puls et al. (2005) see also below (FASTWIND), and Hamann et al. (2009) (PoWR).

The more physics is included, the longer the computation of a single model will take. In a joint collaboration started more than 25 years ago, the massive star groups led by J. Puls (USM, Munich, Germany) and A. Herrero (IAC, Tenerife, Spain), started a project to develop a new and fast code for the NLTE simulation of the atmospheres and winds of O, B and A-type stars: FASTWIND (Fast Analysis of STellar atmospheres with WINDs, Santolaya-Rey et al. 1997, Puls et al. 2005), with the purpose of creating a code sophisticated enough to give an accurate approximation of the real observed spectrum, but at the same time approximate enough to produce a synthetic spectrum within a reasonable computation time.

Due to the shear amount of data to analyze, we consider speed a high priority, and hence choose to use FASTWIND for our purposes. The performance of FASTWIND is perfectly suited for the purposes of this thesis (See Chapt. 3). FASTWIND belongs to the latest generation of unified models, developed for a consistent analysis of stars with extensive atmosphere and the presence of mass outflows. They make some assumptions regarding the physics of the atmosphere still reaching a realistic solution. A detailed description of FASTWIND is beyond the scope of this thesis, but it can be found in the reference papers of FASTWIND (Santolaya-Rey et al. 1997; Puls et al. 2005; Rivero González et al. 2011; Puls

2017) and with some notes on Appendix A.7.

1.4 Aim of thesis and structure

1.4.1 Global objective and specific questions treated in this work

This thesis work is conceived within the framework of the IACOB project (See Sect. 1.2). More specifically, it is part of the work performed in WP1, WP2, WP3, WP4, and in to smaller degree in WP6.

As indicated in Sect. 1.2.2, the main goal of this thesis is the comprehensive empirical characterization of the main physical properties of a large sample of Galactic O-type stars (comprising more than ∼400 targets). *We pursue the compilation of a homogeneous catalog of accurate estimates of stellar and wind parameters for the whole sample of O-type stars surveyed by the IACOB and OWN projects. To this aim, we will use modern semi-automatized tools optimized for the quantitative spectroscopic analysis of large samples of O-type stars (See Chapt. 3), and the high-resolution multi-epoch observations provided by these important spectroscopic surveys (See Chapt. 2).*

The study includes a large number of stars to be able to shed light into the multidependence evolution of the star in various parameters (mass, rotation, mass-loss, binarity, etc.). High-resolution spectroscopy is necessary to detect and analyze subtle spectroscopic features present in the spectra (See Chapt. 2). The availability of more than one spectrum per star will help us to detect spectroscopic binaries as well as to investigate various types of spectroscopic variability phenomena present in these type of stars.

With the resulting catalog of empirical information we will address several topics of interest in the field of massive stars and more specifically those related to the O star domain. These are briefly described below.

Distribution of parameters in the (s)HR diagram

The lack of large systematic analyses is one the main obstacles to improve the general theory of evolution in the upper side of the HR diagram. The use of heterogeneous analysis methods also adds an important uncertainty source that can degrade the results and cause mismatches with theoretical models.

Some of the most complete studies of Galactic O-type stars prior to this work are those of Martins et al. (2015a) or Markova et al. (2018), both with samples of about 70 objects and performing an analysis by the traditional "by-eye" fitting method technique (See Sect. 1.3). In the case of Markova's paper, spectroscopic parameters and nitrogen abundances are derived using two

different atmospheric codes, CMFGEN and FASTWIND. Martins et al., however, derive stellar parameters and abundances for C, N, and O, using only the CMFGEN code. In other galaxies, examples like the work carried out by the VFTS in the LMC has provided stellar parameters for samples of more than 100 O-type stars, using an automatized methodology analogous to ours with extensive grids of FASTWIND models (Sabín-Sanjulián et al. 2017).

With this work, we intend to *provide a general overview of the range of values of spectroscopic parameters in the whole O-type domain, showing the location in the HR diagram (and sHR) of the largest sample of Galactic O-type stars ever studied (more than 300), and evaluating the distributions of their physical properties, e.g. projected rotational velocity, helium abundance, microturbulence, wind-strength parameter, in this evolutionary diagram.* These results are included in Chapters 4, 5, and 6

Calibrations between spectral type/luminosity class and physical properties of O-type stars

The first steps in the determination of an effective temperature scale in the Milky Way were given by Kuiper (1938), who obtained a calibration by assigning ionization temperatures to different spectral types for OBA stars. The effects of the inclusion of different physical processes in the atmosphere models lead to quantitative modifications of the stellar and wind properties of massive stars in general and O stars in particular, especially reducing the effective temperature scale (Vacca et al. 1996; Herrero et al. 2002; Bianchi & Garcia 2002; Repolust et al. 2004; Massey et al. 2004). The most recent calibrations of stellar parameters of O stars as a function of spectral type come from Martins et al. (2005) using the compilation of results from previous spectroscopic studies based on optical diagnostics, and a theoretical scale by using a grid of CMFGEN models. The main improvement from previous ones was the inclusion of line-blanketing and winds in the spherically extended non-LTE atmosphere models.

In this work, new calibrations for the $T_{\rm eff}$ and $\log g$ scales are provided (in Chapt. 4), improving upon previous studies, based on heterogeneously determined parameters from relatively small samples, with the analysis of a larger sample analyzed homogeneously from uniform observations.

The Wind momentum-Luminosity Relationship

The best way to discuss the strengths of stellar winds is in terms of the Wind momentum-Luminosity Relationship (WLR). As a consequence of the Castor,

Abbott & Klein 1975 (CAK) theory, Kudritzki et al. (1992) established a relationship between the modified stellar wind momentum ($D_{\rm mom} = \dot{M} v_\infty R^{0.5}$) and the photon momentum rate meaning that if the wind parameters and the luminosity are known, it is possible to infer the distance to the star. This is established as the WLR:

$$\log D_{\rm mom} = x \log L/L_\odot + \log D_0, \tag{1.1}$$

with x the inverse of the slope of the line-strength distribution function corrected for ionisation effects (α'=α-δ), and D_0 is a constant if the considered objects have the same metallicity and a similar effective number of driving lines (Puls et al. 2000).

The theory of the radiation-driven winds predicts a dependence of the WLR with metallicity, since the strength of the metal lines that propel the stellar wind is proportional to the metal content of the star (Mokiem et al. 2007).

The applicability of this relationship depends very strongly on a good determination of distance. In the case of our Galactic sample, the accuracy in the distance determination is still not enough to precisely assess the WLR. *Making use of our purely spectroscopic analysis of a large sample of Galactic O-type stars, we search and found in this work distance-independent ways to evaluate their wind properties and compare with theoretical predictions.* (See Chapt. 5)

Rotational velocity distribution of O-type stars

Our present knowledge about the distribution of projected rotational velocities ($v \sin i$) in O-type stars in the Milky Way is based in studies by Conti & Ebbets (1977) and Howarth et al. (1997), both of them ignoring the presence of macroturbulence and hence overestimating the measure of the projected rotational velocity. *Our work here supersedes these studies with a larger sample, taking into account macroturbulence effects, and eliminating the binaries in the sample, to extensively study the rotational properties of the Galactic O-type stars evaluating the different scenarios that will explain the present bimodal distribution of velocities.*

In addition, a strong effort has been devoted to evaluate the $v \sin i$ distribution for a large sample of O-type stars in the 30 Doradus region in the LMC (Ramírez-Agudelo et al. 2013, 2015). Our analogous and complementary study in the Galaxy could help to assess the effect of metallicity on the transport and ejection of angular momentum on these extreme objects, expected to change with metallicity due to its interconnection with mass (and hence momentum) loss (Langer 2012). These two topics are treated in Chapt. 6.

Radii, luminosities and masses

The complete characterization of Galactic O-type stars includes the determination of their fundamental parameters (radius, luminosity, and mass). For stars with known distance d (e.g. from the parallax), it is possible to derive the absolute V magnitude M_V. With our methodology, when the absolute V magnitude of the star is provided, IACOB-GBAT is able to provide values and uncertainties for the radius (R), the luminosity (L), and the mass (M), due to its relationship with these fundamental parameters (See Chapt. 3).

In practice, to determine the distance to an individual hot star is no trivial matter, and this represents the greatest difficulty when deriving the physical parameters for Galactic OB stars, especially before the availability of *Gaia* data (Michalik et al. 2015; Gaia Collaboration et al. 2018a). For the objects considered in this thesis we prepare our methodology to use the parallax measurements from the *Gaia* satellite, but also rely on a calibration for M_V as a function of spectral type and luminosity class from Martins et al. (2005) for comparison purposes. (See Chapt. 7). *With the preliminary results for these physical parameters for a subsample of standard stars for spectral classification we evaluate their range of values in the whole O-type domain and compare with the results expected from calibrations for these stars.*

1.4.2 Structure

This work has been structured in three main blocks and they are organized as follows:

- The sample and the observations are described in Chapt. 2, and the tools and techniques for automatic quantitative analyses are presented in detail in Chapt. 3. Here we introduce the selected sample of more than four hundred Galactic O-type stars with optical spectra available in the IACOB+OWN database. We show the strategy followed in the compilation and additional observations made in the process. Then a new grid of FASTWIND stellar models has been created, expanding an already existing one, together with the adequate semi-automatized tools for carrying out a fast and objective quantitative spectroscopic analyses at high resolution. Our methodology consists of an assessment of the variability of the spectra with the multi-epoch observations, and the determination of the stellar and wind properties from the line profile fitting of the best S/N spectra per star to atmosphere models.

- We then present the full spectroscopic characterization, stellar and wind

parameters, of the sample obtained with the techniques already described, first for a suitable subsample of the O-type stars – the standards for spectral classification – in Chapt. 4, and then for the rest of the complete sample of Galactic O stars in Chapt. 5 and Chapt. 6. The first study will provide a general overview of the range of values of spectroscopic parameters in the whole O-type dominion, and help investigate to what extent the standards for spectral classification can be also considered as "standards" in terms of basic stellar parameters. The good-quality results for this statistically meaningful sample were also used to test our procedure, obtaining very satisfying results when compared to alternative analyses using different methods. Then, our study provides a characterization of the massive star population in the Galaxy, locating the stars in the different evolutionary diagrams (Kiel and sHR). New calibrations for the $T_{\rm eff}$ and $\log g$ scale are provided. We explore the wind properties of our sample of stars and compare with theoretical predictions in search of distance-independent ways to evaluate them, and we extensively study the rotational properties of the sample of Galactic O-type stars.

- Finally, Chapt. 7 include the preliminary results for the physical parameter determination (radii, masses, and luminosities) of the sample of standard stars for spectral classification using the *Gaia* DR2 parallaxes. We compare with the results of considering the absolute magnitude calibrations expected for these stars.

All is completed in the end with final remarks, main conclusions, and future work summarized in Chapt. 8. Complementary information is included in the appendixes.

2

Sample definition and spectroscopic observations

The one who reads knows a lot;
but whoever observes knows even more.
Alexandre Dumas

In this chapter we describe the main observational dataset used for this thesis work. This refers to multi-epoch, high resolution spectra of ∼400 Galactic O-type stars gathered in the framework of the IACOB and OWN spectroscopic surveys. Part of these observations were obtained in parallel to the development of this thesis, following some specific requirements of the study presented here.

2.1 Introduction

As stated in Chapter 1, one of the core objectives of this thesis is to produce a catalog of accurate – and homogeneously derived – stellar parameters for a large sample of Galactic massive stars covering the full O-star domain.

The successful achievement of this goal required, as an initial and important step, the compilation of an adequate set of spectroscopic observations. To this aim, we used the Galactic O-Star Catalog (Maíz Apellániz et al. 2013) as basic reference for the sample selection, and performed an exhaustive search for available data in the two modern – high resolution – spectroscopic databases which have resulted from the enormous observational effort devoted by the IACOB and OWN spectroscopic surveys in the last 15 years.

As will be extensively described in this chapter, complementing the observations already available at the beginning of this work (October 2014) with those obtained during the development of the thesis, we have been able to end up with a nearly homogeneous, high quality spectroscopic dataset comprising 2900 spectra for a sample of 415 Galactic O-type stars from both hemispheres.

This chapter starts with a description of the key catalogs and spectroscopic surveys considered in this thesis, and how they have been used. Then, we summarize the process of building the final sample and optimal spectroscopic database, and finally present its global characteristics.

2.2 The Galactic O-Star Catalogue: the starting point

The Galactic O-Star Catalog (GOSC, Maíz Apellániz et al. 2013) is an ambitious project focused in the systematic compilation of as much accurate empirical information as possible regarding these type of objects. At present, the third version of GOSC (GOSCv3) comprises 590 O-type stars. The catalog, which is available through a web interface[1] includes information about coordinates, photometry, and spectral classification, as well as whether a secondary component is detected in the associated GOSSS spectrum (See Sect. 2.3).

The list of stars quoted in GOSCv3 covers a range in B apparent magnitude[2] between $\sim$2 and $\sim$17 (see Figure 2.1) and is already complete up to magnitude $B = 8$ (Maíz Apellániz et al. 2017).

As will be described in Sect. 2.5, GOSC, as a list of all known Galactic O-type stars, has been used as reference guide to build up our final sample of stars and for the compilation of the adequate set of spectroscopic observations.

2.3 The Galactic O-Star Spectroscopic Survey: good quality, but not enough

GOSCv3 also provides access to a high signal-to-noise (S/N) low resolution (R = 2500) spectrum for each of the stars quoted in the catalog. These spectra have been obtained in the framework of the Galactic O-Star Spectroscopic Survey (GOSSS, Maíz Apellániz et al. 2011). GOSSS was started in coordination with GOSC with the purpose of performing a homogeneous re-assessment of the spectral classification of all stars with a previous spectral classification of O or B0 and, since June 2013, it has become the basis for the spectral classification included in GOSC.

[1] http://ssg.iaa.es/en/content/galactic-o-star-catalog/

[2] Approximate B photometry (Tycho-2 or Johnson) quoted as $B_{\rm ap}$ in GOSC.

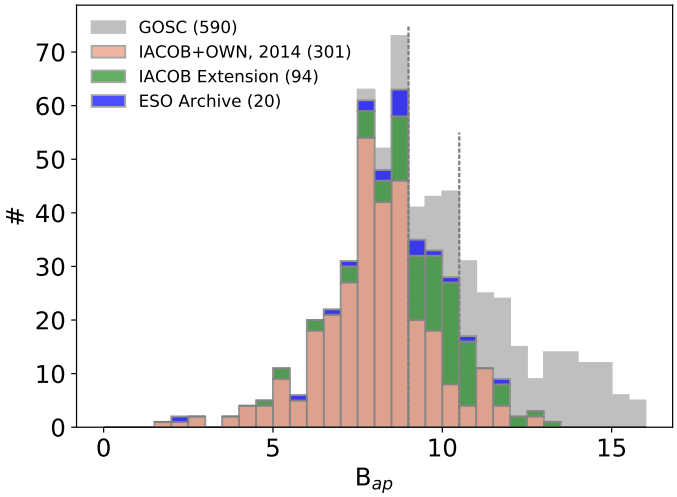

Figure 2.1: B magnitude histogram comparing the GOSC (grey) and IACOB+OWN samples. For the latter, we indicate – using different colors – the stars that were available by the beginning of this thesis (pink), the stars that were compiled in the framework of the IACOB project between 2014 and 2018 (green), and the stars that, not having been surveyed by OWN, count on at least 1 FEROS spectra in the ESO archive (blue).

The quality of the spectra gathered by the GOSSS project is optimal for spectral classification[3]. It has also served for the detection of some new spectroscopic binaries. However, the resolution and wavelength coverage of these spectra were not enough for the purpose of this thesis: namely, the determination of an accurate set of stellar and wind parameters via quantitative spectroscopy. On the one hand, a somewhat larger resolution (R$\geq$15000) is necessary to properly extract information about stellar gravities and rotational velocities in the O-star domain, as well as to better identify spectroscopic binaries[4]. On the other hand, the Hα and O IIIλ5591 lines, two invaluable diagnostic

[3]For a complete and detailed description of the main diagnostic criteria used to perform a qualitative spectral classification in O-type stars see Sota et al. (2011, 2014).

[4]Although we are not initially interested in studying spectroscopic binaries in this thesis, it is important to identify composite spectra to be sure about the reliability of the derived parameters using a single-snapshot spectra.

lines for determining, respectively, mass loss rates and projected rotational velocities in O-type stars (see Chapt. 3), are not included in the GOSSS spectra. These two limitations could be naturally surpassed when considering the spectra gathered by the modern high resolution spectroscopic surveys IACOB and OWN (see Section 2.4.3)

2.4 The IACOB and OWN spectroscopic surveys: the perfect combination

The IACOB and OWN surveys are two ambitious observational projects which (independently and complementarily) have been devoting the last 10 years to compile high-resolution, multi-epoch spectra of Galactic massive O-type stars using small and medium size telescopes in the Canary Islands (Spain), Chile and Argentina. As will be shown in this section, combined together, these two surveys have made available an optimal source of spectroscopic observations for our work.

2.4.1 The IACOB spectroscopic database

As more extensively indicated in Chapt. 1, the IACOB project (Simón-Díaz et al. 2011b,a,c, 2014, 2017) is a long-term observational project which started in 2008 with the main objective of contributing to step forward in our knowledge about the physical properties and evolution of Galactic massive stars. This ambitious project is driven by the compilation and scientific exploitation of a large database of high-resolution multi-epoch spectra of Galactic OB stars: *the IACOB spectroscopic database* (last described in Simón-Díaz et al. 2015).

At present (June 2018) – and after more than 150 nights – the IACOB spectroscopic database counts on 1612 high-resolution spectra for 265 different Northern O stars. These spectra have been ordinarily obtained with the FIES and HERMES spectrographs attached to the Nordic Optical Telescope (NOT, 2.56m) and the Mercator Telescope (1.2m), respectively[5]. Both FIES (Telting et al. 2014) and HERMES (Raskin et al. 2004) are fiber-feb Echelle spectrographs with high resolution capabilities and a complete wavelength coverage of the optical range. In particular, FIES was used in two different settings, depending on the star magnitude, providing spectra with R = 25 000 and 46 000, respectively, in the range 3704-7271 Å. The lower resolution was used for dimmer stars. Regarding HERMES, the instrument provides an even larger

[5]Both telescopes are located in the Observatorio Roque de los Muchachos (La Palma, Spain).

resolution (R = 85 000) and a more extended wavelength coverage (3763-9006 Å) than FIES.

2.4.2 The OWN spectroscopic database

The OWN survey (Barbá et al. 2010, 2014) is a high-resolution spectroscopic monitoring program of (Southern) Galactic O- and WN-type stars. The main objective of this survey, active since 2005, is to contribute to our empirical knowledge of the multiplicity status of Galactic massive stars.

The survey is making use of up to four different telescopes with high-resolution spectrographs at La Silla Observatory, Las Campanas Observatory, Cerro Tololo Inter-American Observatory (Chile), and the Complejo Astronómico El Leoncito (Argentina) (Gamen et al. 2007). So far, it counts with about 7000 spectra for 205 O-type stars (Barbá et al. 2017).

A non negligible percentage of the observations made by the OWN project were obtained with the FEROS instrument in the ESO2.2 telescope. This instrument shares a particularly similar list of characteristics and capabilities with the instruments used for our observations in the IACOB project. In particular, FEROS (Kaufer et al. 1997) is also a fiber-fed Echelle spectrograph providing a resolving power of R = 48 000 in the range 3527-9217 Å.

2.4.3 Why IACOB+OWN is the perfect combination

The combination of spectroscopic observations from the IACOB and OWN surveys resulted in a promising way to achieve our objective of compiling a high quality set of spectroscopic observations to perform a homogeneous, reliable and accurate quantitative spectroscopic analysis of a large sample of Galactic O-type stars, applying the "standard" spectroscopic techniques.

In Fig. 2.2 we show an example of the quality of these spectra. The optical range presents all the necessary diagnostic lines (H, He I, and He II, and O III λ5592) to accurately determine temperature, gravity, projected rotational velocity, macroturbulence, the wind strength parameter, helium abundance, microturbulence, and β, the exponent of the wind law (See Chapt. 3).

The similarity between all the instruments considered (high resolution, Échelle spectrographs with similar resolving power), and the quasi-homogeneous reduction methods allow us to minimize observational effects on the outcome of our spectroscopic study. In particular, we remark that, in spite of the different resolving power provided by the various instruments, for R>25 000 this parameter becomes non-critical for the spectroscopic determination of stellar parameters and for the kind of spectroscopic study performed in this thesis.

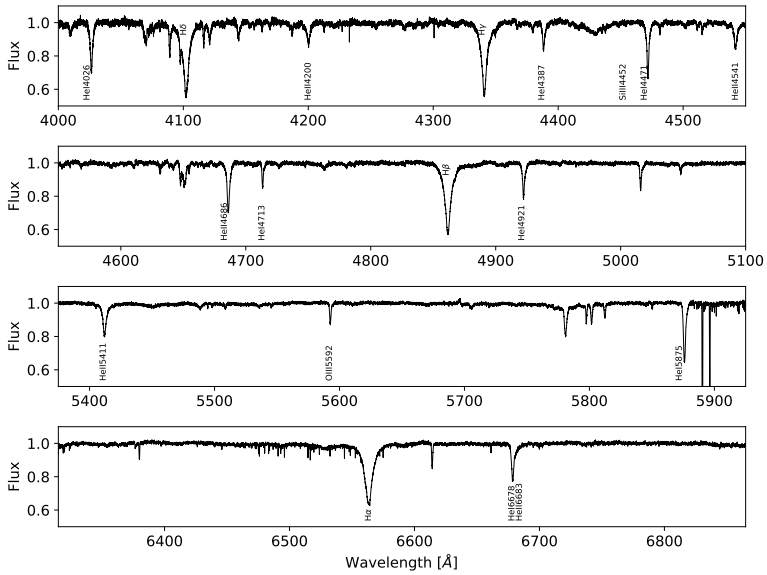

Figure 2.2: Four representative spectral windows of one high-resolution spectrum of HD 46149 (O8.5V) observed with HERMES@Mercator at R∼85 000, from the IACOB+OWN surveys. The main diagnostic lines used in our study are included. The spectra is not corrected from telluric lines.

2.5 Building the sample of spectroscopic observations

Once we convinced ourselves that the combination of FIES, HERMES and FEROS spectra gathered by IACOB and OWN surveys offered us the optimal set of observations for the purposes of our work, we proceed with the identification of the final sample of stars to be investigated and construction of the associated spectroscopic database.

As a first step, we used GOSC as reference guide of all known Galactic O-type stars, and performed an exhaustive search for high-resolution spectra among the lists of stars surveyed by the IACOB and OWN projects[6] by October

[6]The FEROS spectra gathered by the OWN project were kindly provided by R. Barbá. The FIES and HERMES spectra had been mainly obtained by S. Simón-Díaz up to that date.

Table 2.1: Summary of the spectroscopic observations used in this work

Instrument	Resolving power	Range [Å]	# Spectra	# Stars
FIES@NOT2.56m	25 000, 46 000	3750-7250	937	219
HERMES@Mercator1.2m	85 000	3770-9000	675	46
FEROS@ESO2.2m	46 000	3530-9210	1229	244
TOTAL			2900	415*

* after removing stars in common

2014, when this PhD project started. The results from that search are indicated by the pink histogram included in Fig. 2.1. In brief, by that date, at least 1 spectrum for ∼300 O-type stars was already available.

During the development of this thesis we were able to expand this number by means of new NOT and Mercator observing campaigns performed in the context of the IACOB project. The main purpose of these new granted observing time was to extend the number of observed stars toward dimmer targets[7],as well as to increase the number of epochs of stars for which we only had 1 or 2 spectra. The outcome of these campaigns – comprising a total of 94 new stars – is highlighted in green in Fig. 2.1. We remark the importance of these new observations to ensure a higher level of completitude of our final sample of investigated stars when compared with the list of stars quoted in GOSC, especially for luminosity class V stars.

Finally, we used the new phase-3 FEROS data products, available in the ESO archive[8], to search for additional spectra of Southern Galactic O-type stars, including some stars surveyed by the OWN project in observational campaigns posterior to 2014. We found data for 20 new stars (highlighted in blue in Fig. 2.1), and additional spectra for 23 stars with less than 3 epochs in IACOB+OWN.

All unnormalized spectra were obtained with the corresponding pipelines available at each telescope (FIEStool[9], HermesDRS[10], FEROSDRS[11], respectively[12]) and, in a second step, homogeneously normalized and corrected of heliocentric velocity using IDL routines developed in the framework of the IA-

[7]More specifically, we mainly concentrate in those Northern mid- and early-O dwarfs quoted in GOSCv3 with magnitudes up to B = 10.5 mag. The purpose of these new observations was to minimize possible observational biases that could be affecting the sample of stars available at the beginning of this thesis. This is related to the lack of Galactic O-type stars near the ZAMS discussed in Chapter 5.

[8]http://archive.eso.org/wdb/wdb/adp/phase3_spectral/form

[9]http://www.not.iac.es/instruments/fies/fiestool/FIEStool.html

[10]http://www.mercator.iac.es/instruments/hermes/drs/

[11]https://www.eso.org/sci/facilities/lasilla/instruments/feros/tools/DRS.html

[12]Internal consistency checks performed by the IACOB+OWN collaboration have shown

COB project.

2.6 Global characteristics of the final sample and the associated spectroscopic observations

Final sample of stars: characteristics

The final sample of stars comprises 415 targets with spectral types in the range O2 – O9.7 and all luminosity classes. Table 2.1 provides a global overview of the final number of stars (along with the total number of spectra, including multi-epoch observations) that was observed with each of the three instruments.

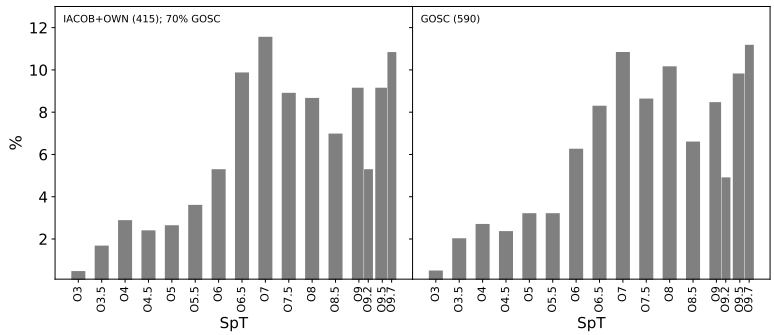

Figure 2.3: Number of stars per spectral type in the IACOB+OWN sample (*left*), and GOSC (*right*). Percentages in the y axis are with respect to the total number in that sample. Percentages in the legend are with respect to the GOSC sample.

The complete list of Galactic O-type stars with available FIES, HERMES or FEROS spectra is presented in Table B.1. In the table, the first four columns quote the name(s) of each star, the spectral classification – following GOSSS –, and the spectral classification of the secondary component in the case of an unresolved GOSC spectrum. The next four columns indicate the B magnitude, and the number of available spectra per instrument. This information is followed by some specific details about the best spectra (one per star) used for the spectroscopic analysis, including the name of the spectrum, the Julian date, and the S/N achieved at $\sim$4500 Å. Finally, the last column in Table B.1

that the dispersion in velocity resulting from the analysis of the interstellar Na I lines when combining FIES, FEROS, and HERMES spectra is below 0.5 km s^{-1}.

is a reference to the table where the spectroscopic parameters of each star are included.

As indicated in Fig. 2.1, the compiled spectroscopic database includes stars with B magnitude in the range of $\approx$ 2 - 12.5. Taking the GOSC as a reference, the IACOB+OWN sample (including the extensions) can be considered 90% complete up to B=9 mag and even 80% complete up to B=10.5 mag.

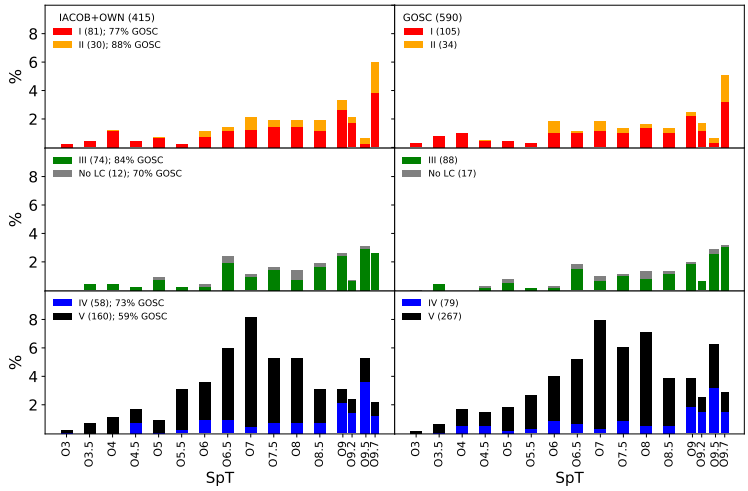

Figure 2.4: Same as figure 2.3 but separated in different luminosity classes. Percentages in the legend are with respect to the GOSC sample of the same luminosity class. No LC corresponds to peculiar stars, Oe and magnetic stars, without an specific luminosity class.

Figures 2.3 and 2.4 present a global summary of the number of stars per spectral type bin comprising the IACOB+OWN sample (left panels) and, for reference purposes, quoted in the GOSCv3 (right). These figures show that our sample is very representative, in terms of spectral type and luminosity class distributions, of all the known Galactic O-type stars.

Generally speaking, our final sample comprises $\sim$ 70% of the stars quoted in GOSCv3. For most luminosity classes, the completitude approaches 75%, except for the dwarf stars, which are almost $\sim$ 60% complete with respect to GOSC (See Fig. 2.4). This is expected from magnitude limitations in our survey, biased towards supergiants stars. Nevertheless, in the figure we see that

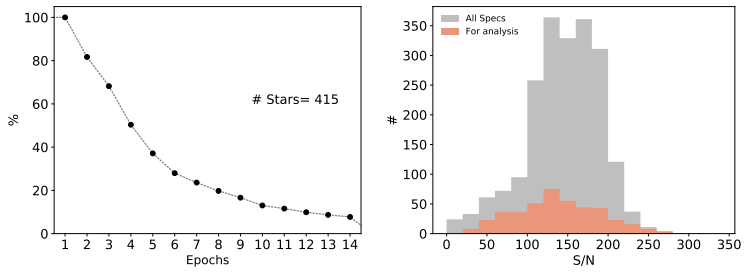

Figure 2.5: (*Left*) Summary of the multi-epoch observations for the IACOB+OWN sample. Each point indicates the percentage of stars having at least that number of observed epochs. (*Right*) S/N of all spectra in the IACOB+OWN database, and the subsample of spectra used for the quantitative spectroscopic analyses (the best spectrum for each star).

our sample of V stars does not present any bias respect to the whole GOSC sample, and therefore it is representative of all known Galactic O V stars.

Number of spectra per target

The left panel of Fig. 2.5 shows a summary of the number of epochs available per star in the IACOB+OWN sample. As expected from the general philosophy of the surveys, we count on more than 2 (3) spectra obtained at different dates for 80% (70%) of the stars in our final sample.

Whenever available, all the multi-epoch spectra per target were used to roughly investigate spectroscopic variability (Sect.3.2), but only the spectrum with the best quality – in terms of signal-to-noise ratio, S/N – was considered for the quantitative spectroscopic analysis leading to the stellar parameters (Sect.3.3).

Exposure time and quality of the spectra in terms of S/N

To serve as a general reference, the exposure time of the FIES, HERMES and FEROS spectra obtained by the IACOB or OWN surveys varies between 100 seconds and 1 hour, with most of the stars having a typical exposure time of less than 15 minutes. Only those stars dimmer than $B = 9$ were exposed between 15 minutes and 1 hour, depending on the B magnitude[13].

[13]We note that 10.5 is the limit in B magnitude to obtain a S/N∼100 high-resolution spectrum of a star in 1 hour with the FIES instrument attached to the NOT2.56m telescope

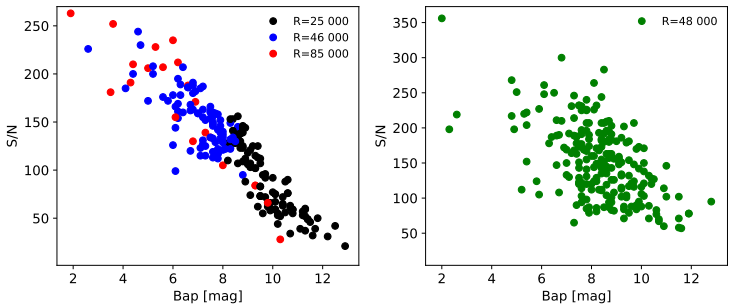

Figure 2.6: S/N achieved for the best spectrum of each star, in relation with the B magnitude and spectral resolution. Results for the IACOB and OWN spectra are included in the left and right panels, respectively.

Concerning the quality of the whole sample, the right panel of Fig. 2.5 depicts the distribution of S/N(@4500 Å) of the complete set of spectra. Most of them (83%) have a measured S/N(@4500 Å) higher than 100, the median of the distribution is ≈150, and the maximum S/N achieved is ≈300. Figure 2.5 also includes for reference the distribution of the S/N (@4500 Å) of the spectra used in the quantitative spectroscopic analysis (i.e. the best spectrum in terms of S/N for each star in the final sample).

The S/N achieved in each best spectrum is related to the exposure time, the B magnitude of the star, and the resolving power of the spectrum. In Fig.2.6 we show how, for the IACOB spectra, the brightest stars appear with larger considered S/N, even when observed at the highest resolution. In the case of OWN spectra, the correlation between S/N an B magnitude has a weaker spread because of the different observing strategy followed by this survey.

2.7 Final remarks

One of the core objectives of this thesis is to produce a catalog of accurate – and homogeneously derived – stellar and wind parameters for a large sample of Galactic massive stars covering the full O-star domain. In this chapter we have explained the process we have followed to end up with the adequate set

using the R = 25 000 fiber (assuming good weather conditions in terms of transparency and seeing).

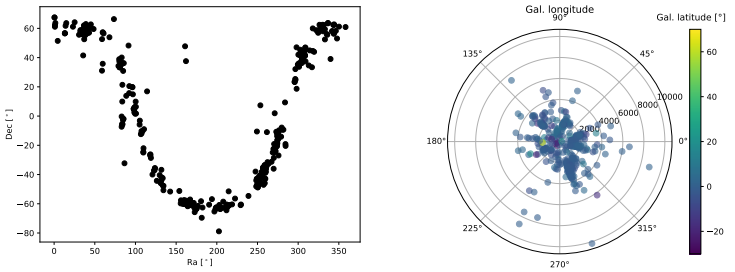

Figure 2.7: *Left* Distribution of the O-type stars sky coordinates in the sample. *Right* Distribution of the O stars in the sample around the Sun. The radial distance is in pc.

of spectroscopic observations needed to successfully reach this ambitious goal. The final spectroscopic database is unique in terms of quantity, quality, and homogeneity.

In this thesis we count on a sample (415 Galactic O-type stars) which is 5-10 times larger than those considered in previous similar studies found in the literature (e.g. Repolust et al. 2004; Martins et al. 2005; Markova & Puls 2008; Martins et al. 2015a). Our sample of stars is highly representative of the sample of all known Galactic O-type stars in terms of spectral type and luminosity class, and include stars from both hemispheres. The left panel of Fig. 2.7 depicts the location of the stars in the RA-DEC diagram. As expected, O-type stars are concentrated in the Galactic plane. The right panel of Fig. 2.7 also presents, for the first time, the radial distribution of the Galactic O-type stars in our sample around the Sun. Distances come from a Bayesian treatment of the parallaxes of the second *Gaia* data release, May 2018 (See Chapt. 7).

For the quantitative spectroscopic analysis of the sample, the data are unbeatable. The number of available diagnostic lines (∼15) and the reached S/N (over 100) are optimal, allowing a homogeneous and unambiguous analysis. Additionally, the multi-epoch and high-resolution character of our spectroscopic database has allowed us to determine with more accuracy the binarity status of the sample (Chapt. 3), supporting a better characterization of the sample.

Finally, we are immersed in the exploitation process of the database. In addition to the type of multiparametric analyses performed in this thesis, these spectra will allow us in the future to study, among other things, abundances and orbital parameters in multiple systems.

3

Spectroscopic and physical characterization of the sample: tools and methodology

Never in my life had I used a tool, but over time, with work, [...] there was nothing that I could not build; especially if I had proper tools.
Robinson Crusoe

In this chapter we summarize the strategy we have followed for determining the stellar properties of our sample of Galactic O-type stars. We first benefit from the availability of multi-epoch observations for a large fraction of the stars in the sample to identify signatures of spectroscopic variability in each investigated target. Then we use the best S/N spectra per star to determine spectroscopic and physical parameters. To this aim, we use a battery of semi-automatized tools – developed in the framework of the IACOB project– based on standard techniques for the quantitative analysis of optical spectra of O-type stars.

3.1 Introduction

This thesis work aims at a thorough and homogeneous spectroscopic characterization of the full sample of O-type stars surveyed by the IACOB and OWN projects. As described in Chapt. 2, the sample includes 415 stars for which more than 2900 multi-epoch spectra were obtained. These numbers encouraged us to define a robust semi-automatized (but supervised) protocol to analyze the

sample. This protocol pursues the achievement of (1) a major objectivity and reproducibility of the spectroscopic analysis of each target, and (2) an optimal homogenization of the results obtained from the analysis of the complete sample. In addition, it allows a straightforward inclusion of new spectra gathered during the development of this work (or in the future).

Figure 3.1 provides a general overview of the strategy we have established to perform the quantitative spectroscopic analysis of each star in the sample. This protocol first includes a rough identification of spectroscopic variability signatures associated with the star (due to, e.g., binarity, pulsations, wind-variability and/or other sources of stellar variability). For this part of the analysis we use the whole set of spectra available (Sect. 3.2 and left part of Fig. 3.1). Then we proceed with the quantitative spectroscopic analysis of the best S/N spectrum for each star. To this aim, we use a battery of IDL semi-automatized tools developed by S. Simón-Díaz (Sect. 3.3 and right-upper part of Fig. 3.1). Finally, the results from the spectroscopic analyses, combined with empirical information about distances, photometry, and extinction from the literature, are used to determine the fundamental parameters of each star (Sect. 3.4 and right-lower part of Fig. 3.1).

In this chapter we describe in more detail all the various steps that define the analysis strategy, as summarized in Figure 3.1. We remark that here, we basically concentrate on the description of the tools and methodology. The results of the analyses are presented in Chapters 4, 5 and 6.

3.2 Spectroscopic variability assessment

Before proceeding with the quantitative spectroscopic analysis of our sample of O-type stars (see Sect. 3.3), we use all the available (multi-epoch) spectra for each star to evaluate whether the considered target presents any signature of spectroscopic variability (related to multitude of known phenomena), or if the spectra present any kind of particular feature in the profile. The number of spectra available for each target is included in Table B.1. The process has two steps. In the first step, more qualitative, we use the whole pool of spectra to visually assign variability flags to each star. In the second step, a quantitative process, we derived radial velocities for all spectra, using the best fitting FASTWIND model (BFM) derived from the IACOB-GBAT analyses (See Sect. 3.3) as reference. The variability of the radial velocity allow us to refine the classification of the stars (1) considered as likely single, (2) presenting line-profile-variability due to, e.g., stellar oscillations, or (3) clearly identified as single-lined spectroscopic binaries.

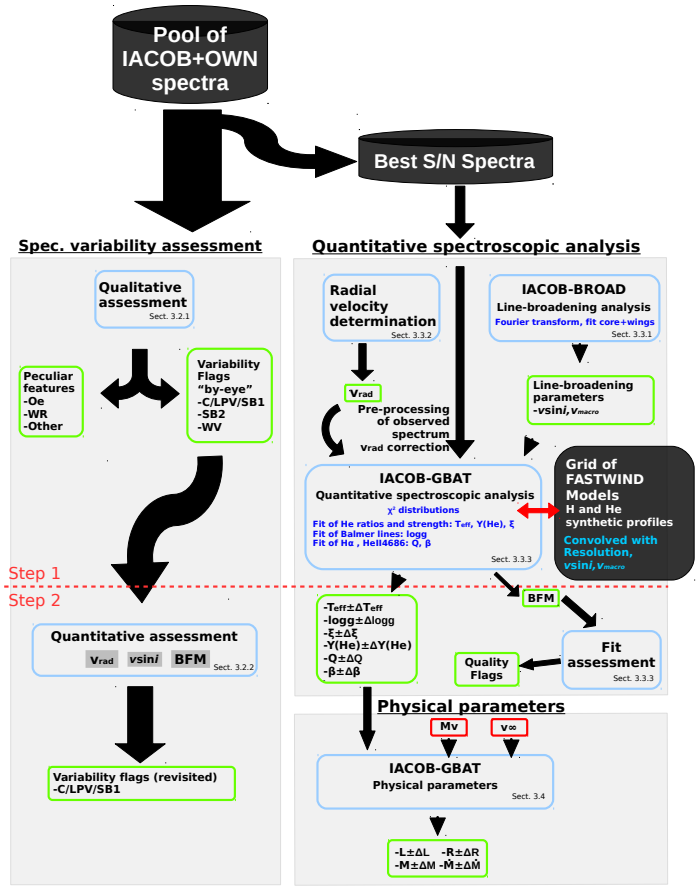

Figure 3.1: Schematic flowchart of the methodology applied in this work.

3.2.1 Visual assessment

In this first iteration, we mainly consider 5 diagnostic lines[1], namely O III λ5592, He I λ4387, Hα, He II λ4686, and He I λ5875. By overplotting all the available spectra per target – zooming into the spectral regions where the diagnostic lines are located – we qualitatively assign one or several of the following flags to each star:

- presumably constant (*C*) star, if we have more than 2 spectra, and we do not visually detect a clear shift in radial velocity (or a variation in the shape of the line profile) in any of the diagnostic lines;
- spectroscopic binary, including cases with one (*SB1*) and two (*SB2*) components detected;
- stars showing clear variability in any of the two main wind-diagnostic lines – Hα and/or He II λ4686 – are marked as wind variable, separating the cases when the lines are in emission (*WVe*) or in absorption (*WVa*);
- line-profile variability (*LPV*), when small variations of the line-profiles – which cannot be clearly assigned to wind variability or binarity effects – are detectable by eye from the inspection of a sufficiently large number of spectra;
- more data (*MD*) needed, when we only count on 1 or 2 spectra and we are not able to assign any of the abovementioned flags.

Some illustrative examples of each of these cases are presented in Figs. 3.2 and 3.3.

3.2.2 Quantitative reassessment of the C/LPV/SB1 cases

In a second iteration, once we have access to the outcome of the IACOB-BROAD and IACOB-GBAT analyses of those stars not identified as *SB2* (see Sects. 3.3.1 and 3.3.3, respectively), we refine the classification of those stars flagged as *C*, *LPV* and *SB1* using a more objective (quantitative) criteria.

In brief, the FASTWIND synthetic spectrum of the IACOB-GBAT best fitting model for each star (convolved with the corresponding $v \sin i$, $v_{\rm mac}$, and R) is used to improve the radial velocity determination of each associated individual

[1] We also include the interstellar Na I $\lambda\lambda$5890, 5895 lines as a sanity check to detect potential instrumental effects and the accuracy of the heliocentric velocity correction.

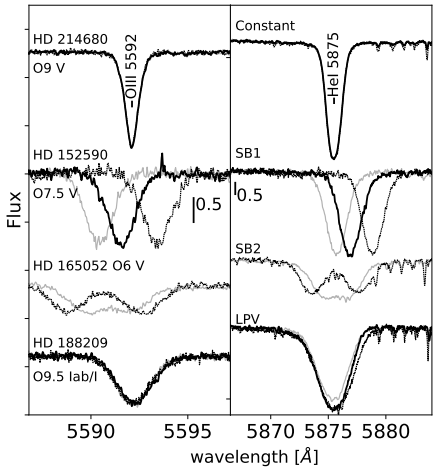

Figure 3.2: Examples of stars flagged as *C*, *SB1*, *SB2* and *LPV* (see Sect. 3.2.1 for explanations). Each star includes three representative spectra (plotted in different tones of grey) to illustrate the variability. Spectra is normalized and the scale is included as a vertical line.

(multi-epoch) spectrum by means of a simple (iterative) cross-correlation technique. To this aim, we consider the following initial set of lines included in the FASTWIND models: He I λ4026, He I λ4387, He I λ4471, He I λ4713, He I λ4922, He I λ5015, He I λ5047, He I λ5875, He II λ4200, He II λ4541, He II λ4686, and He II λ5411. Each line is analyzed separately, and the associated spectral window selected automatically using the corresponding synthetic line. Those lines that are in emission or absent in the observed spectrum are automatically eliminated from the very beginning on a star-by star basis. Then we follow an iterative process by which those lines providing $v_{\rm rad}$ measurements 2 σ larger than the mean of all lines are removed until none is eliminated. Last, final values and associated uncertainties are obtained from the mean and standard deviation of individual $v_{\rm rad}$ measurements acquired from the lines that survive.

By following this method, we determine the radial velocity of all available spectra for each star. We then compute the dispersion – $\sigma(v_{\rm rad})$ – and the peak-to-peak amplitude – $\Delta v_{\rm rad}$ – associated with each set of radial velocity measurements for a given star and, as described below, use these two quantities to re-asses the flags assigned to those targets initially identified as *C*, *LPV*, and

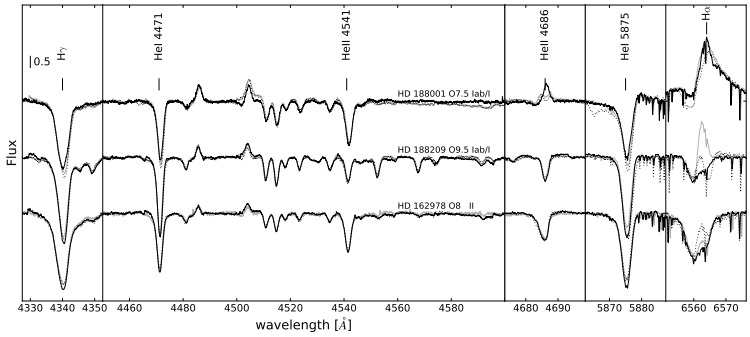

Figure 3.3: Examples of stars showing variability in the wind diagnostic lines (Hα and/or He II λ4686). Each star includes three representative spectra (plotted in different tones of grey) to illustrate the variability. For completeness, we also include other spectral ranges to illustrate if other diagnostic lines also present variability. Spectra is normalized and the scale is included as a vertical line.

SB1. We basically follow two different criteria depending on the projected rotational velocity of the star[2]:

- if $v \sin i \leq 180$ km s^{-1}, we flag those cases with $\Delta v_{\rm rad}$ in the range 5 – 20 km s^{-1} and $\sigma(v_{\rm rad})$ in the range 2.5 – 10 km s^{-1} as *LPV*, while those cases with lower (higher) dispersion were marked as *C* (*SB1*), respectively;
- if $v \sin i > 180$ km s^{-1}, we flag those cases with a ratio $\Delta v_{\rm rad}/v \sin i$ in the range 0.02 – 0.1 and $\sigma(v_{\rm rad})/v \sin i$ in the range 0.01 – 0.05 as *LPV*, while those cases with lower (higher) ratios were marked as *C* (*SB1*), respectively.

Figures 3.4 and 3.5 present a summary of the outcome of this second assessment of spectroscopic variability in those targets initially flagged as *C*/*LPV*/*SB1*. The limiting values of $\Delta v_{\rm rad}$ and $\sigma(v_{\rm rad})$ – or their respective ratios with respect to $v \sin i$ — quoted above are indicated as vertical dotted lines. Interestingly, 55 stars of the sample present a different *C*/*LPV*/*SB1* flag from the originally

[2]This separation between stars with low and high projected rotational velocities accounts from the fact that subtle changes in the shape of the line profile due to, e.g., pulsations, could led to a larger dispersion in the measured (multi-epoch) radial velocities in stars with broad profiles. This situation could be erroneously interpreted as the detection of signatures associated with spectroscopic binarity if not correctly taken into account.

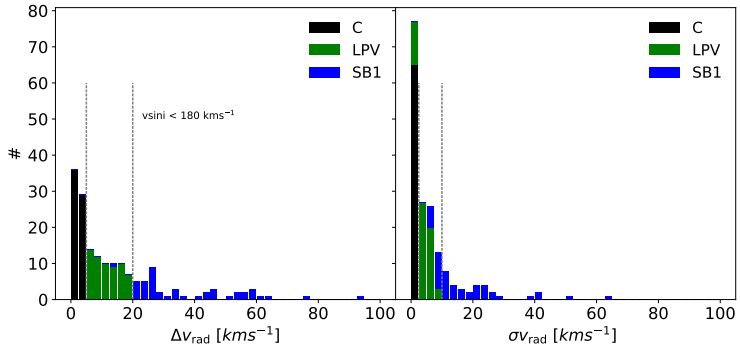

Figure 3.4: Distribution of stars for which the first set of criteria for the quantitative evaluation of the C/LPV/SB1 flag was applied (see notes in Sect. 3.2.1). Only stars with $v \sin i \leq 180$ km s^{-1} are considered in these set of plots.

assigned (17% of the stars considered here[3]), with most cases corresponding to stars where the C flag is transformed to LPV (38 stars), followed by stars where the LPV flag is transformed to SB1 (11 stars). This illustrates the necessity of performing this second step in the spectroscopic variability assessment of each target.

The final outcome from this investigation of spectroscopic variability, along with some notes of the results, can be found in Sects. 4.3 and 5.3 of Chapters 4 and 5, respectively.

3.3 Quantitative spectroscopic analysis

After performing the visual assessment of spectroscopic variability for a given target in our sample of O-type stars, we proceed with the determination of the stellar parameters. We first concentrate on those parameters that can be accurately obtained from the quantitative spectroscopic analysis of the commonly designated *optical part* of the spectrum (i.e. 4 000 – 7 000 Å). These refer to the projected rotational velocity ($v \sin i$) and the amount of non-rotational broadening (aka. macroturbulence, $v_{\rm mac}$) affecting the line-profiles of each star (i.e. the *line-broadening parameters*), plus the *spectroscopic parameters*, namely the effective temperature ($T_{\rm eff}$), surface gravity ($\log g$), wind-strength parameter

[3]Those stars with either C/LPV/SB1 flag and multi-epoch information available.

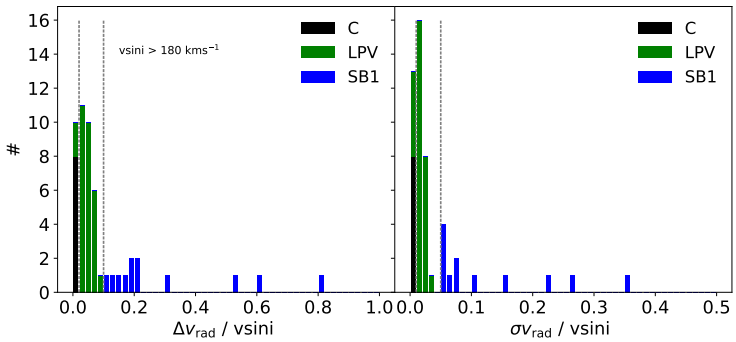

Figure 3.5: Similar as Fig. 3.4, but for stars with a projected rotational velocity larger than 180 km s^{-1} (see notes in Sect. 3.2.1).

(Q), helium abundance ($Y_{\rm He}$), microturbulence ($\xi_{\rm t}$), and the exponent of the wind velocity-law (β).

This section describes the analysis strategy we followed to obtain estimates of the above-mentioned set of parameters (schematically summarized in the upper right part of Fig. 3.1). This analysis is mainly based on the application of two semi-automatized tools designed in the framework of the IACOB project – IACOB-BROAD (Simón-Díaz et al. 2011b) and IACOB-GBAT (Simón-Díaz & Herrero 2014) – to the best S/N spectrum of each considered target.

We remark that not all stars in our sample have been analyzed with these tools. We basically concentrated in those stars labeled[4] as C, $SB1$, LPV and WV (see Sect. 3.2). Those stars presenting in any of their spectra either clear signatures of being a double line spectroscopic binary ($SB2$) or emission lines in accordance with Wolf-Rayet features were not considered for spectroscopic analysis.

3.3.1 Line-broadening parameters: IACOB-BROAD

The line-broadening parameters of each star not identified as SB2[5] in our sample are determined using the IACOB-BROAD tool. As described in Simón-Díaz &

[4]We also analyzed those stars for which we only counted on 1 or 2 spectra (labeled as MD) not detected as $SB2$.

[5]Note: Seven SB2 standard O-type stars were not excluded from the analysis for academic purposes.

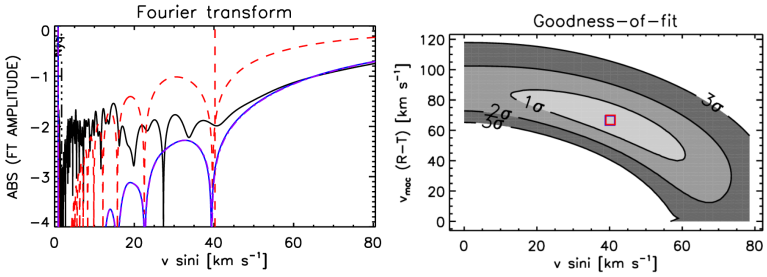

Figure 3.6: Example of part of the graphical output from the iacob-broad tool for the O8.5 IV star HD 46966. *Left* The Fourier transform space of the line. In black the spectrum, in red the FT determination, and in blue the GOF approximation. *Right* The 2D ($v \sin i$ and $v_{\rm mac}$) χ^2-distribution resulting from the GOF analysis of the line. Again in red the FT determination, and in blue the GOF approximation of the minimum of the χ^2-distribution.

Herrero (2014), IACOB-BROAD is based on a combined Fourier transform (FT) + Goodness of fit (GOF) analysis of a specifically selected diagnostic line, chosen by the user. For the sake of homogeneity, we mainly base the analysis on the O III λ5592 line, but have to rely on other alternative metal lines as, e.g., Si III λ4452 or the N V λ4603/20 lines[6] or the N IV λ6380 line in a few cases in which the O III line was weak (Simón-Díaz & Herrero 2014; Markova et al. 2014; Holgado et al. 2018). For some very fast rotators all metal lines appear too diluted to be used, and we have to rely on He I lines.

As shown in Fig. 3.6 (see also Simón-Díaz & Herrero 2014), IACOB-BROAD provides several solutions for the pair of line-broadening parameters. One of them, $v \sin i$(FT), is obtained from the identification of the first zero in the Fourier transform of the line profile[7]. Another two estimates, $v \sin i$(GOF) and $v_{\rm mac}$(GOF), result from the application of a goodness-of-fit technique (see Fig. 3.6). The latter is based on a direct comparison of the observed profile and a grid of synthetic profiles convolved with different values of $v \sin i$ and $v_{\rm mac}$ in which the best fitting profile is obtained by means of a χ^2 optimization.

We used the comparison between $v \sin i$(FT) and $v \sin i$(GOF) as an assessment of the reliability of the results from line-broadening analysis. This comparison allowed us to identify problematic cases that required further con-

[6]Being aware that the N V λ4603/20 lines can be affected by the wind, they were only used if the absence of a strong wind was confirmed.

[7]The Fourier transform technique to determine projected rotational velocities in stars was originally proposed by Carroll (1933). See also Gray (2005) for further notes.

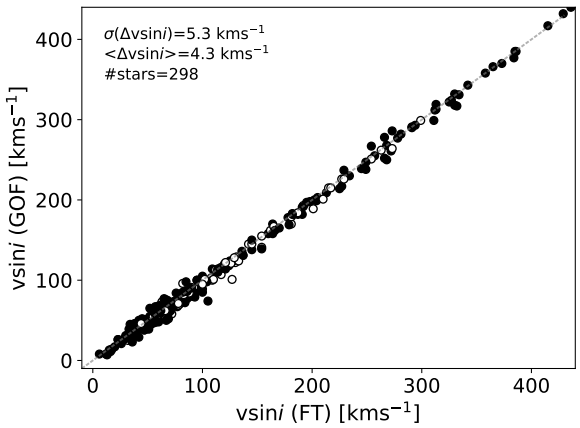

Figure 3.7: Comparison of projected rotational velocities resulting from the FT and GOF analysis strategies incorporated to the IACOB-BROAD tool. Open/filled symbols indicate SB1/likely single stars.

sideration (i.e., those with discrepancies larger than 20 km s^{-1}). See Sect. 4.4.1 for an example of this situation when performing the analysis of the subsample of O-type stars established as standards for spectral classification.

Once the problematic cases were corrected or discarded, we ended up with a set of $v \sin i$(FT) and $v \sin i$(GOF) values that are in fairly good agreement (See Fig. 3.7).

In view of this result, we decided to keep the pair $v \sin i$(GOF) – $v_{\rm mac}$(GOF) for all but a few problematic stars (See Sect. 4.4.1). For the latter, we used $v \sin i$(FT) and the associated $v_{\rm mac}$(FT+GOF)[8] values. The final values $v \sin i$ and $v_{\rm mac}$ considered for the quantitative spectroscopic analysis with IACOB-GBAT (see next Sect.) are quoted in Table B.2, along the selected line, EW and S/N of the diagnostic line used. We also refer the reader to Appendix A for an academic exercise in which we compare results obtained from the use of different diagnostic lines.

[8] $v_{\rm mac}$ obtained from the fit of the line assuming a fixed $v \sin i$ value derived from the FT.

3.3.2 Radial velocities

In parallel to the estimation of the line-broadening parameters, we proceed with the radial velocity correction of the spectra to be analyzed. Apart from the interest of the determination of this quantity ($v_{\rm rad}$) itself, this is a critical step to ensure a reliable quantitative spectroscopic analysis.

We first obtain a rough initial estimate of the radial velocity from direct comparison of the observed location of the core of the He I λ5875 line (identified "by-eye") and its corresponding laboratory wavelength. This value is then used to correct the Doppler shift of the spectrum caused by the star's radial velocity before launching IACOB-GBAT (see Sect. 3.2.2).

After this, in a second iteration, we obtain a new – more objective – estimate of $v_{\rm rad}$ by performing a cross-correlation between the observed spectrum and the synthetic one associated with the best fitting model that arises from the IACOB-GBAT analysis. The methodology used is described in Sect. 3.2.2.

We found that the total number of He I-II lines finally considered is sufficient to compensate for situations like, e.g., the absence of He I lines in early type stars, or the exclusion of the He I λ5875 and He II λ4686 lines when they appear in emission. Indeed, we found that, even in the most complex cases, at least 7 lines are available for the final computation of the radial velocity and its uncertainty.

We note that, following this strategy, we do not intend to provide the most accurate values of $v_{\rm rad}$ that can be extracted from these high-resolution spectra, but to end up with a radial velocity correction good enough for the purpose of the spectroscopic parameter determination. In particular, we consider that the typical uncertainty in $v_{\rm rad}$ (the standard deviation from using all lines) obtained for most of the stars is $\sim$5 km s^{-1}, with a few pathological cases reaching somewhat larger values ($\sim$10 – 25 km s^{-1}).

As a sanity check, in Fig. 3.8 we compare our derived $v_{\rm rad}$ values with $v_{\rm rad}$ values available in SIMBAD for stars in our sample. Roughly 60% of the $v_{\rm rad}$ values gathered come from two main databases: Gontcharov (2006) and Kharchenko et al. (2007). There is in general good agreement (the standard deviation of the differences is $\sim$ 10 km s^{-1}), with the highest discrepancies found in stars for which we have detected clear or likely signatures of binarity in the spectrum.

3.3.3 Spectroscopic parameters: IACOB-GBAT

The next step in the analysis is the determination of the set of spectroscopic parameters that can be obtained from the analysis of the optical part of the

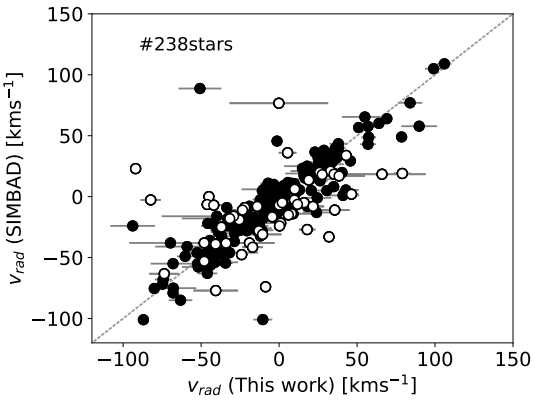

Figure 3.8: Comparison of the $v_{\rm rad}$ values determined in this work with those available in SIMBAD. Open points indicate stars for which we have detected clear or likely signatures of spectroscopic binarity. Lines show the uncertainty of the individual $v_{\rm rad}$ measurements. The dashed line is the 1:1 relationship.

spectra of O-type stars.

The continuously increasing amount of high-quality spectroscopic observations of massive stars provided by different surveys during the last decade has made clear the necessity for semi-automatized tools which allow for the extraction of information on stellar parameters and abundances from large spectroscopic datasets of OB stars in a reasonable computational time. Some notes on various of the techniques proposed can be found in Mokiem et al. (2006); Lefever et al. (2007); Urbaneja et al. (2008); Simón-Díaz et al. (2011c); Castro et al. (2012); Irrgang et al. (2014).

IACOB-GBAT[9] (Simón-Díaz et al. 2011a) is a grid-based automatic tool designed for the quantitative spectroscopic analysis of O-stars. This tool, that is basically an automation of traditional "by-eye" analysis techniques (see, e.g., Herrero et al. 1992, 2002; Repolust et al. 2004), includes an extensive grid of FASTWIND[10] (Santolaya-Rey et al. 1997; Puls et al. 2005; Rivero González et al.

[9] An extensive description of the general structure and philosophy of the IACOB grid-based tool IDL package (IACOB-GBAT) was presented in Simón-Díaz et al. (2011a). Further notes on some of the considerations that must be taken into account when applying the tool to real spectra can be found in Sabín-Sanjulián et al. (2014) and in Appendix A.3.

[10] The stellar atmosphere code used in our analyses (See Appendix A.7 and Sect. 1.3).

2012) models and a variety of IDL programs to handle the observations, perform the analysis by means of a versatile implementation of a χ^2 optimization, and visualize/evaluate the results. It has been developed under the philosophy of being user-friendly, portable, and fast.

In this section, we describe in more detail some pieces of information of interest regarding the IACOB-GBAT analysis of our sample of O-type stars.

Grid of models

As indicated in Simón-Díaz et al. (2011a) IACOB-GBAT offers the user the possibility of selecting among three grids of FASTWIND models computed for different values of metallicity (Z=1, 0.5 and 0.3 $Z_\odot$). In our case, we choose the one corresponding to solar metallicity, since our sample of O-type stars is basically concentrated in the solar neighborhood. This grid, including 6 different free parameters: $T_{\rm eff}$, $\log g$, $Y_{\rm He}$, $\xi_{\rm t}$, $\log Q$, and β [11]; originally comprises 180 000 models.

During the analysis of the IACOB+OWN sample, we found that the lower limit in effective temperature previously considered for the grid of FASTWIND models (25 000 K) was not enough to properly constrain this parameter in late-O supergiants; we hence extended the grid down to 22 000 K. The final ranges and step size considered for each of the six free parameters of the grid are summarized in Table 3.1.

Parameter ranges

In order to optimize the computational time we restrict the range of values of $T_{\rm eff}$ and $\log g$ considered in the IACOB-GBAT analysis using the spectral type and luminosity class calibrations by Martins et al. (2005). We basically use as central values those proposed in Martins' observational calibration and extend the corresponding ranges in these two parameters by $\pm$5 000 K and $\pm$0.4 dex, respectively. In those cases in which the ranges considered in $T_{\rm eff}$ and/or $\log g$ did not allow us to fully sample the lower envelope of the global χ^2 distribution up to χ^2+1 (see Sabín-Sanjulián et al. 2014), we launch again the last part of the analysis[12] of IACOB-GBAT extending a bit further the corresponding ranges. Concerning the other parameters ($\xi_{\rm t}$, $Y_{\rm He}$, $\log Q$, and β) we used the full range available.

[11] The log Q parameter defined in Puls et al. (1996) as $Q = \dot{M}/(v_\infty R)^{1.5}$. The atmospheric material presents a velocity law with a β exponent dependency: $v(r) = v_\infty\,(1 - R_*/r)^\beta$. Here R_* represents the photospheric stellar radius of the star.

[12] See Appendix A.3 and A.4 for a description of the different steps in IACOB-GBAT.

Table 3.1: Parameter space covered by the grid of FASTWIND models at solar metallicity.

Parameter	Range	Step size
$T_{\rm eff}$ [K]	22 000 – 55 000	1 000
$\log g^{\rm a}$ [dex]	2.6 – 4.4	0.1
$\xi_{\rm t}$ [km s^{-1}]	5 – 20	5
$Y_{\rm He}$ [b]	0.06, 0.10, 0.15, 0.20, 0.25, 0.30	Irregular
$\log Q$ [c]	-11.7, -11.9, -12.1, -12.3, -12.5	Irregular
	-12.7, -13.0, -13.5, -14.0, -15.0	
β	0.8 – 1.2	0.2

[a] g in cm s^{-2}
[b] $Y_{\rm He} = N({\rm He})/N({\rm H})$ (by number of atoms)
[c] $Q = \dot{M}/(v_\infty R)^{1.5}$; $\dot{M}$ in $M_\odot\ yr^{-1}$, v_∞ in km s^{-1}, and R in $R_\odot$

Table 3.2: Diagnostic lines used in the IACOB-GBAT spectroscopic analysis

H	He I	He II	He I + He II
Hα	λ4387	λ4200	λ4026
Hβ	λ4471	λ4541	λ6678 + λ6683
Hγ	λ4713	λ4686	
Hδ	λ4922	λ5411	
	λ5875		

Diagnostic lines

Table 3.2 summarizes the complete list of H I and He I-II diagnostic lines considered in the IACOB-GBAT analysis of the IACOB+OWN sample of O-type stars. The lines selected are those traditionally used in the spectroscopic analysis of O-type stars (see, e.g., Herrero et al. 1992; Repolust et al. 2004) plus two more due to our wider wavelength coverage, He I λ5875 and He II λ5411. For the sake of homogeneity, we always use the same set of lines and we give the same initial weight to all of them. Note, however, that IACOB-GBAT follows an automatic iterative strategy to provide weights for the diagnostic lines in the computation of the global χ^2 distribution (See Appendix A.3). This means that not necessarily all diagnostic lines finally have the same weight in the selection of the best fitting model and the final estimation of central values and uncertainties. This iterative process accounts for the quality (in terms of S/N) of the various diagnostic lines and detects those cases where the given lines are

not properly fitting in the final global solution, all this in an automatic and objective manner.

Analysis strategy and outcome of the IACOB-GBAT analysis

Once the range of values for each of the 6 free parameters has been determined and the diagnostic lines selected, we launch IACOB-GBAT for each spectrum. We use the previously derived values of $v \sin i$, $v_{\rm mac}$ and $v_{\rm rad}$ as input parameters, included in Table B.2.

As a first step IACOB-GBAT prompts the user to select the spectral window around each of the lines to be considered in the χ^2 computation. During this pre-processing of the spectra the diagnostic lines can be locally renormalized and nebular lines, blends and cosmic rays eliminated whenever necessary. Then, IACOB-GBAT proceeds to the computation of the global χ^2 distributions and the final results.

IACOB-GBAT provides, as final output, the best fitting model within the considered grid, along with information on central values (or upper/lower limits) for each of the 6 free parameters indicated in Table 3.1 and their associated uncertainties.

In addition, IACOB-GBAT provides the user with two different plots to evaluate the quality of the outcome analysis. These are presented in Fig. 3.9 and Fig. 3.10. The first one depicts the comparison between the observed and the synthetic profiles corresponding to the best fitting model. The second one shows the χ^2 distributions for each of the considered free parameters.

Extra information is included in the right part of Fig. 3.10 concerning the input parameters; the output mean values, uncertainties and best fitting model values; and the location of the star in the HR and spectroscopic HR diagram (defined in Langer & Kudritzki 2014). Whenever extra information about the absolute V magnitude (Mv) and terminal velocities (v_∞) is incorporated to the IACOB-GBAT computation, the tool is also able to provide values, and distributions, for the fundamental parameters (radius, luminosity, spectroscopic mass), as well as for the mass loss rate ($\dot{M}$). We refer the reader to Sect. 3.4 for a more detail information about how this four parameters are computed.

Final supervised assessment of the outcome of IACOB-GBAT

IACOB-GBAT is an automatized tool that has the advantage to provide a complete and objective exploration of the parameter space. However, the outcome of the IACOB-GBAT analysis must not be taken blindly as a valid result without final supervision by the user, as should be for any automatized method. In

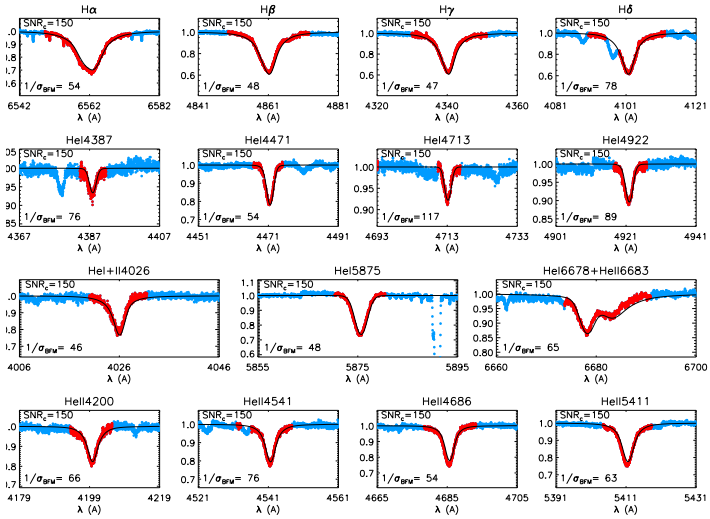

Figure 3.9: An example of the summary plot created by IACOB-GBAT to evaluate the fit quality of the best fitting model. Observed spectra (color dots) and best-fitting synthetic models (black lines) for different H and He lines in the spectrum of the O-type dwarf HD 12993. In each diagnostic line presented the considered/discarded points for the analysis are indicated in red/blue. For this star a S/N∼100 was achieved.

our case, this includes (1) the visual inspection of the χ^2 distributions for each of the parameters considered (See e.g. Fig 3.10) and, more importantly, (2) a final visual assessment of the overall agreement between the proposed best fitting model, adjusted to the resolution and rotational velocity of the star, and the observed spectrum (See an example in Fig 3.9), both outcomes provided by the IACOB-GBAT tool. On the one hand, the former allows us the detection, for example cases in which only upper or lower limits can be obtained, or situations in which a certain parameter cannot be constrained; on the other hand, the visual inspection is a mandatory step to identify cases in which the resulting values for certain (or the whole set of) parameters are not reliable due to, for example, limitations of the grid of FASTWIND models used, or the misidentification of a composite spectrum as if it was associated with a single star.

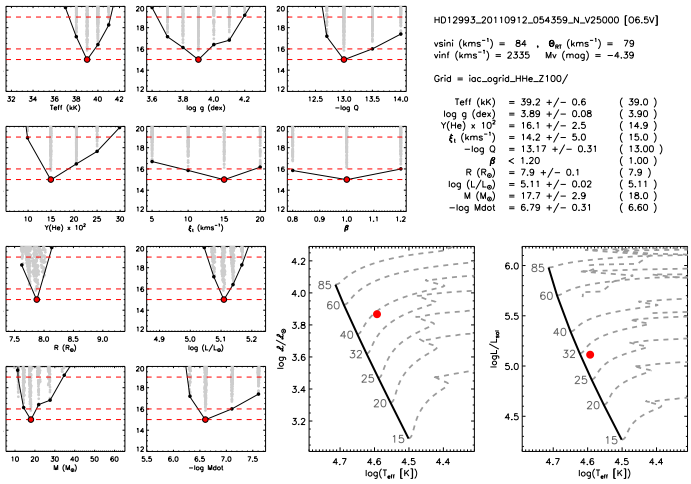

Figure 3.10: An example of the output plot for the χ^2 distributions of one of the stars in this thesis. The panels show the χ^2 distributions of the fitting of the models with respect to the observed spectrum, for the considered parameters. The red point indicates the value of the best fitting model which minimizes the global χ^2. The black curve marks the lower envelope and it is used in combination with the first red dashed line (corresponding to the 1σ confidence level) to provide mean values and uncertainties.

This was done for each of the analyzed spectra. After a careful inspection of the results for all the stars in or sample, we decide to summarize the outcome of each IACOB-GBAT analysis using the following quality flags: (Q1) acceptable fit with no major remarks, (Q2) He II λ4686/Hα appearing in the observed spectrum as an inverse P-Cygni profile or showing a double peak, (Q3) Hα and He II λ4686 not fitting at the same time, (Q4) no He I available to properly constrain the effective temperature of the star. Although the Q2 – Q4 flags are not mutually exclusive, we remark that only one of them was assigned to each individual star, giving priority to Q4 over the other flags and to Q2 over Q3.

Some examples of stars cataloged as Q2 and Q3 are included in Fig. 3.11. For each star, we show the region of the observed spectrum where the He II λ4686 and Hα lines are located along with some FASTWIND synthetic lines used for reference. BD−11 4586 and HD 17603 are two illustrative cases in which

He II λ4686 appears as an inverse P-Cygni profile or a double peak, respectively (i.e., they have been flagged as Q2). The stars HD 24431 and HD 188209 illustrate the situation found in those (58) stars we have flagged as Q3. There is no model in our grid of FASTWIND models producing a simultaneous fit to Hα and He II λ4686. In all cases, we overplot the synthetic profiles corresponding to the best fitting model using both profiles as valid diagnostic lines. This inconsistency is also highlighted in Markova et al. (2018) for 6 O stars, all of them considered Q3 in our study.

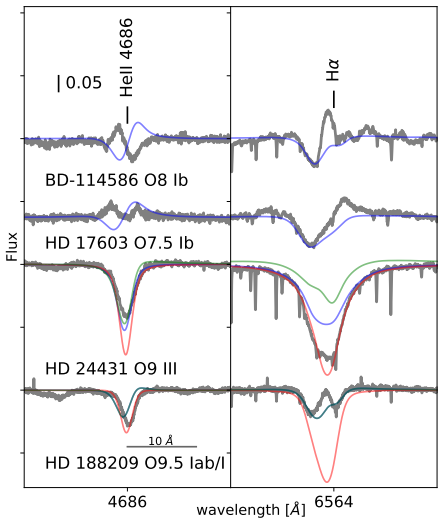

Figure 3.11: Four illustrative examples of stars in which a good fit could not be achieved. Solid blue lines correspond to the synthetic spectra of the best fitting FASTWIND model resulting from the IACOB-GBAT analysis. For HD 24431 and HD 188209 (stars labeled with the Q3 quality flag) we also include the synthetic spectra of two models with different values of the Q parameter (see text for details) where green(red) corresponds to higher (lower) Q, respectively. For HD 188209 green and blue lines are overlapped.

The outcome from this qualitative characterization of the final fit of the each analysis, including its plausible origins and implications, is presented along the results from the quantitative spectroscopic analysis in Chapter 4 and 5.

3.4 Fundamental parameters: IACOB-GBAT + absolute magnitudes

After having obtained six parameters from the purely spectroscopic analysis, the IACOB-GBAT tool has the possibility to be re-launched to obtain additional physical parameters. When the absolute V magnitude of the star is provided IACOB-GBAT is able to provide values and uncertainties for the radius (R), the luminosity (L), and the mass (M). Additionally, if the terminal velocity (v_∞) is included in the analysis, mass-loss rates ($\dot{M}$) are calculated.

The equations that connect the absolute magnitude with these parameters are explained in Kudritzki (1980). They connect the absolute magnitude in the V band[13] and the stellar radius. Then, radius is combined with temperature and gravity to obtain luminosity and mass[14] respectively.

$$\begin{aligned} 5\log R/R_\odot &= 29.57 - M_V + V \\ \log L/L_\odot &= 2\log R/R_\odot + 4\log T_{\rm eff}/T_{\rm eff,\odot} \\ \log M/M_\odot &= 2\log R/R_\odot + \log g/g_\odot \end{aligned} \quad (3.1)$$

The mass loss rate is obtained from the wind-strength parameter ($Q = \dot{M}/(v_\infty R)^{1.5}$). With the terminal velocity v_∞, and the stellar radius R known we derive the mass loss rate $\dot{\rm M}$.

The values and uncertainties are obtained following the χ^2 distributions described in previous section (and in more detail in Appendix A.4), as the rest of the parameters included in FASTWIND models. These χ^2 distributions are included in the graphical output of IACOB-GBAT, Fig. 3.10.

3.5 Additional info gathered from the literature

To complete the analysis and to fully characterize our stars we gather information from different sources.

Spectroscopic binarity and variability

We also have access to the information about variability in Galactic O-type stars compiled by the OWN project in the last years. This independent study (Barbá et al., in prep.) benefits from a much larger number of epochs for most of

[13] The V parameter is obtained from the model as the integral in wavelength of the emergent flux, considering a V-filter function.

[14] This way of determining the mass provide the named spectroscopic mass, as is derived from spectroscopic plus photometric parameters.

the (Southern) stars, including spectra gathered with high-resolution spectrographs at La Silla Observatory, Las Campanas Observatory, Cerro Tololo Inter-American Observatory (Chile), and the Complejo Astronómico El Leoncito (Argentina) (see Gamen et al. 2007). In this case, the following flags were used: *SB1*, *SB2*, *VAR*, *VAR?* and *C*, defined in their work under similar criteria to ours (Barbá et al. 2010).

Magnetic field

Stars considered as magnetic were first catalog as peculiar in our analysis and then, after a thorough search in previous literature of the MiMeS project (Wade et al. 2016; Grunhut et al. 2017), finally cataloged as magnetic O-type stars. We take special aware of stars considered as magnetic. The Magnetism in Massive Stars (MiMeS) Project presents a multidisciplinary strategy to address magnetism in massive stars and it includes a large program of two separate components assessing a large and complete population of hot, massive stars (the Survey Component), and detailed information about the magnetic fields and related physics of individual magnetic-confirmed objects (the Targeted Component).

Photometry and distances

Fundamental parameters, such as the radius (R), the luminosity (L), or the mass (M) require additional information about distances and photometry to be accurately determined. Our methodology provides radii, luminosities, and spectroscopic masses for the stars when their absolute magnitudes are available. We use two different methods to obtain the absolute magnitude.

One of the methods to obtain this magnitude is to infer it from the distance, the visual magnitude, and the extinction. Using Bayesian distances from the *Gaia* DR2 parallaxes of these stars, and the visual magnitude corrected from extinction compiled by GOSC in Maíz Apellániz & Barbá (2018), we were able to obtain the necessary absolute magnitude value.

On a second step, we use the calibrations of absolute magnitude–Spectral type/luminosity class from Martins & Plez (2006).

More details about this can be found in Chapt. 7.

Terminal velocity: v_∞

When including the terminal velocity (v_∞), our methodology is able to provide values and uncertainties for the mass loss rate ($\dot{M}$).

Unable to systematically obtain it from our optical analysis[15] we rely on Howarth et al. (1997) determinations and collect all available values for the stars in our sample.

[15] Is preferably to use UV information, where P-Cygni lines provide accurate determination of this parameter.

4

A benchmark sample: the O-type standard stars for spectral classification

Long is the way of teaching through theories;
brief and effective by means of examples.
Séneca

In this chapter we present results from the quantitative spectroscopic analysis of the sample of ∼130 O stars considered as standards for spectral classification. Our study is based on multi-epoch high-resolution spectra from the on-going large IACOB and OWN spectroscopic surveys, and makes use of modern semi-automatized tools for the quantitative spectroscopic analysis of large samples of O stars. This study serves as a first step towards the homogeneous analysis of the complete combined IACOB+OWN sample of Galactic O-type stars. The content of this chapter has been published in Holgado et al. (2018 A&A, 613, A65).

4.1 Introduction

Once the compilation of a large spectroscopic database of Galactic O-type stars from the IACOB and OWN surveys (see Chapt. 2) was completed, we decided to start with our study using a benchmark sample of targets which could help us to test our methodology. To this aim, we decided to use the recently revised grid of O-type standard stars for spectral classification presented in Maíz Apellániz

et al. (2015).

The analysis of this well-behaved sample has helped us establish a step-by-step protocol (see Chapt. 3), to be followed in the analysis of the more complex whole sample in Chapt. 5. This study has also allowed us to assess the level of agreement between our results, obtained by means of semi-automatized methods, and those provided by more traditional "by-eye" techniques. In particular we evaluate the reliability of our analysis strategy using a subsample of ∼40 stars extensively studied in the literature (Sect. 4.4.3).

In this chapter we present – for the first time in a homogeneous and complete manner – the full set of spectroscopic parameters[1] of the "anchors" of the spectral classification system in the O star domain. We discuss the properties of this particular sample (Sect. 4.5), and review the most recent and commonly used spectral type SpT – $T_{\rm eff}$ and SpT – $\log g$ calibrations for Galactic O-type stars (Sect. 4.6). In addition, we benefit from the multi-epoch character of the IACOB and OWN surveys and present the results from the spectroscopic variability study of this sample (Sect. 4.3).

4.2 Sample and methodology

Walborn & Fitzpatrick (1990) presented the first comprehensive digital atlas of optical spectra for spectral classification of OB stars. It comprised a total of 75 standard objects with spectral types O3 – B3 (– B8 at Ia) that were organized following the Morgan-Keenan (MK) system (and some developments not considered before). The MK classification process takes progressive steps to assign a spectral type: generate a 2-D grid of standard spectra in terms of line ratios to define the different subtypes, compare the unknown spectrum with that grid, and assign the spectral type that most resembles the unknown spectrum. It also allows to qualitative assign anomaly flags or to note discrepancies in the line ratios. Although the classification is discrete, it is possible to interpolate in cases where the observed ratios value are in between two grid points.

Several updates and additions have occurred since this first atlas (see Walborn et al. 2002, and references therein), the last one being developed in the framework of the Galactic O-Star Spectroscopic Survey (GOSSS, Maíz Apellániz et al. 2011; Sota et al. 2011, 2014; Maíz Apellániz et al. 2015, 2016).

We based our work on the O-type stars included in the GOSSS OB2500 v2.0 grid of standard stars[2] as defined in Maíz Apellániz et al. (2015), and included

[1] That can be obtained from the optical spectrum of O-type stars.

[2] We note that the GOSSS project has made available an updated version of the grid of O-type standard stars during the development of this work (Maíz Apellániz et al. 2016), including a few more stars and changes in the spectral classification for three luminosity class

Table 4.1: The OB2500 v2.0 grid of O-type standards for spectral classification (extracted from Maíz Apellániz et al. 2015).

	V	IV	III	II	Ib	Iab/I	Ia
O2						*HD 93129 AaAb*	
O3	*HD 64 568*					Cyg OB2-7	
O3.5	*HD 93 128*		*Pismis 24-17*				
O4	**HD 46 223**		**HD 168 076 AB**			HD 15 570	
	HD 96 715		*HD 93 250 AB*			HD 16 691	
						HD 190 429 A	
O4.5	HD 15 629					HD 14 947	
	HDE 303 308 AB					Cyg OB2-9	
O5	*HDE 319 699*		**HD 168 112**			*CPD -47 2963*	
	HD 46 150		*HD 93 843*				
O5.5	*HD 93 204*					Cyg OB2-11	
						ALS 18 747	
O6	*CPD -59 3600*	*HD 101 190*		HDE 229 196			**HD 169 582**
	HD 42 088						
	HDE 303 311						
O6.5	**HD 167 633**	*HDE 322 417*	HD 190 864	**HD 157 857**			*HD 163 758*
	HD 91 572		*HD 96 946*				
	HD 12 993		*HD 152 723 AaAb*				
			HD 156 738				
O7	*HD 93 146 A*		Cyg OB2-4 A	*HD 94 963*	*HD 69 464*		
	HDE 242 926		*HD 93 160*	*HD 151 515*	HD 193 514		
	HD 91 824						
	HD 93 222						
O7.5	*HD 152 590*		*HD 163 800*	HD 34 656	HD 17 603	HD 192 639	
	HD 35 619			**HD 171 589**	*HD 156 154*	**9 Sge**	
O8	*HD 101 223*	*HD 94 024*	*HDE 319 703*	*63 Oph*	**BD -11 4586**	HD 225 160	*HD 151 804*
	HD 97 848	*HD 135 591*	λ **Ori A**				
	HD 191 978						
O8.5	*HDE 298 429*	**HD 46 966**	*HD 114 737 AB*	*HD 75 211*	*HD 135 241*		*HDE 303 492*
	HD 14 633		HD 218 195 A	HD 207 198			
	HD 46 149						
	HD 57 236						
	Trumpler 14-9						
O9	10 Lac	*HD 93 028*	*HD 93 249 A*	*HD 71 304*	19 Cep	HD 202 124	α Cam
	HD 216 898	*CPD -41 7733*	HD 24 431	τ *CMa AaAb*		*HD 152 249*	
	CPD -59 3551		HD 193 443 AB			HD 210 809	
O9.2	**HD 46 202**	*HD 96 622*	*CPD -35 2105 AB*		*HD 76 968*	*HD 154 368*	*HD 152 424*
	HD 12 323		HD 16 832			*HD 123 008*	
						HD 218 915	
O9.5	AE Aur	HD 192 001	*HD 96 264*	δ **Ori AaAb**		HD 188 209	
	μ Col	*HD 93 027*					
		HD 155 889 AB					
O9.7	υ **Ori**	HD 207 538	HD 189 957	*HD 68 450*	**HD 47 432**	HD 225 146	HD 195 592
			HD 154 405	*HD 153 426*	*HD 154 811*	*μ Nor*	*GS Mus*
			HD 154 643	HD 10 125	*HD 159 147*	*HD 104 565*	
						HD 191 781	

Notes Normal, *italic*, and **bold** typefaces are used for stars with $\delta > +20^{\circ}$, $\delta < -20^{\circ}$, and the equatorial intermediate region, respectively.

here as Table 4.1. It comprises 131 Galactic stars with spectral types in the range O2 – O9.7 (all luminosity classes) from both (northern and southern) hemispheres.

The IACOB+OWN spectroscopic database (see Chapt. 2) includes 1216 spectra for 128 of the 131 standard stars for spectral classification. Most of the stars have more than two spectra, obtained at different epochs (see Chapt. 2). As explained in Chapt. 3, whenever available, all the multi-epoch spectra per target were used to roughly investigate spectroscopic variability, but only the spectrum with best quality – in terms of signal-to-noise ratio, (S/N) – was considered for the quantitative spectroscopic analysis[3] leading to the stellar parameters.

4.3 Spectroscopic variability analysis: results

This section presents the general outcome of the spectroscopic variability assessment for the sample of O-type standard stars for spectral classification. Following the ideas presented in Sect. 3.2 we separate the sample into different groups depending on the type of detected variability. Individual results are presented in Table B.4, and Table 4.2 includes the global summary of the number of stars labeled with the different derived categories (as presented in Sect. 3.2.1).

Table 4.2: Summary of the results in the spectroscopic variability assessment of the sample of standard stars for spectral classification

Variability flag	C$^{(1)}$	LPV$^{(1)}$	SB1$^{(1)}$	SB2$^{(1)}$	MD$^{(1)}$	WV$^{(2)}$
# stars	29	38	28	7	29	40

(1) 128 stars in total.
(2) The WV flag is not exclusive.

We highlight first the standard stars identified as spectroscopic binaries. There are 7 SB2 stars[4] and 28 SB1 stars. This represents ∼30% of this specific subsample of O-type stars, a somewhat lower percentage than the one identified in the whole sample (55%, See Chapt. 5). This difference is understandable under the consideration that standard stars for spectral classification are selected to avoid binarity as much as possible (by definition)[5]. In particular,

III stars that were shifted to luminosity class IV.

[3]This particular subset of spectra can be accessed online via the IACOB webpage: http://www.iac.es/proyecto/iacob/

[4]Two of these SB2 stars were not cataloged as such by the GOSC: HD 57236 and HDE 229196.

[5]They present a very weak second component barely visible even at high-resolution.

the composite spectra of an SB2 is in principle incompatible with the standard category, as the variability in the line-ratios in different epochs provide an unacceptable variable criterion. New standard stars for spectral classification should be found to replace the 7 SB2 stars identified in the sample. Spectral classification depends on spectral, spatial, and/or temporal resolution, and SB2 stars may remain undetected without adequate resolution or temporal coverage. Nevertheless, the majority of the Luminosity class-Spectral type pairs in the grid are covered with more than one star and the presence of the SB2 stars in the sample is not critical.

The stars in this sample flagged as LPV (line-profile-variability), which are $\sim$ 30% of the sample, can be considered as standard stars for spectral classification. In most cases the global shape and equivalent widths of the main diagnostic lines are preserved, particularly in the case of spectra with a resolving power R$\sim$2500-5000, which is the standard resolution in which spectral classification is done.

Concerning the stars flagged as WV (Wind-Variability), $\sim$ 30 %, there are two main effects that may impact our work. The first one refers to the possible impact that variability of the He II λ4686 line could have on the identification of the luminosity class of the star, which in O-type stars mainly depends on the strength of this line in emission or absorption (see, e.g., Table 5 in Sota et al. 2011). The second one is the impact that the variability of Hα and He II λ4686 may have on the stellar and wind parameters associated with a given star.

Concerning the impact on the assigned luminosity class, we have found seven targets in the total sample with clearly detected variability of the He II λ4686 line, all of them plotted in Fig. 4.1 at the original resolution (R$\sim$50000) and degraded to a resolution R$\sim$2500. This variability is almost negligible in four of them when the spectra are degraded to R=2500. For the rest, we have found that the detected variability is not expected to modify the assigned luminosity class when following the spectral classification criteria summarized in Sota et al. (2011).

As an indication of the potential effect of the variability of Hα and He II λ4686 on the derived parameters, we refer the reader to the results presented in Sect. 4.7.2 (see also Markova et al. 2005). In particular Figure 4.11 shows that the effect of Hα and He II λ4686 variability on $T_{\rm eff}$ and $\log g$ is not much larger than the typical uncertainties associated with the determination of these parameters. In any case, one should take into account potential variability in the determined stellar and wind parameters from different single snapshot spectra when comparing results from different studies in the literature (see further notes in Sect. 4.4.3).

The remaining 29 objects for which we had more than 2 spectra are consid-

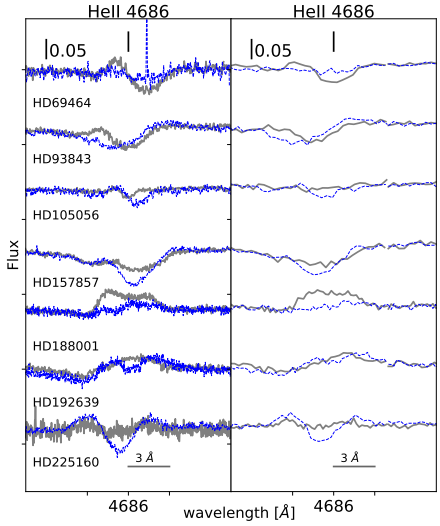

Figure 4.1: Impact of resolving power for stars with very strong variability in He II λ4686. The comparison is between two extreme cases. [Left] Spectra with the original, high resolution. [Right] Spectra downgraded to R=2500 and $\Delta\lambda$ =0.6 Å/pix, the standard resolution used for spectral classification.

ered non-variable (C). In the future, the inclusion of additional epochs to our investigations could modify these classifications.

4.4 Quantitative spectroscopic analysis: results

The results of the IACOB-BROAD and IACOB-GBAT analysis of the 128 O-type standard stars for which we have spectra from the IACOB and/or OWN surveys available can be found in Table B.4. The list of stars is sorted by spectral type and luminosity class[6]. Apart from the derived line-broadening and spectroscopic parameters (and their uncertainties) the table includes the spectral classification of each target, and the flag indicating the quality of the final fit resulting from the IACOB-GBAT analysis (See Sect. 3.3.3).

[6]The table includes the stars for which a reliable determination of the stellar parameters could not be achieved, due to the absence of He I lines (Q4 stars, see Sect. 3.3.3).

In this section we review the methodology of the quantitative spectroscopic analysis described in Chapter 3 for the sample of standard stars for spectral classification. Then we include an overview of the quality flags obtained from the fit, making special emphasis on those aspects that could affect their reliability of the spectral classification (Sect. 4.4.2). Finally, we compare with previous results from the stars in the sample from the literature (Sect. 4.4.3).

4.4.1 IACOB-BROAD analysis: results

As explained in Chapt. 3, we used the IACOB-BROAD tool (Simón-Díaz & Herrero 2014) to determine $v \sin i$ and $v_{\rm mac}$ for each star, mainly relying on the O III λ5592 line. We used the comparison between Fourier transform (FT) + Goodness of fit (GOF) as an assessment of the reliability of the results from the line-broadening analysis, and used alternative spectral lines on problematic cases (i.e., those with discrepancies larger than 20 km s^{-1}). This was the case for thirteen stars, shown in Fig 4.2 and discussed below.

For ten of these targets (indicated in the figure with open squares) we found that the discrepancy between $v \sin i$(FT) and $v \sin i$(GOF) was caused by the combined effect of having a weak O III line and a low S/N spectrum (all these stars have either an early or a late spectral type). The situation improved in all of them when we considered one of the other available diagnostic lines. For illustrative purposes, in the figure we connect the determinations based on the O III line and the alternative diagnostic line

Regarding the remaining three targets with a difference between the two derived values of $v \sin i$ larger than 20 km s^{-1} (see Fig. 4.2) a closer inspection of the IACOB-BROAD graphical output allowed us to identify clear (in one of them, HD 57236) and likely (in the other two, CPD -59 2600 and HDE 298429) signatures of a broad-line secondary component affecting the O III line. In these cases, while the FT is not very much affected, the GOF solution tries to mimic the composite line-profile by increasing $v_{\rm mac}$, hence resulting in a lower $v \sin i$.

As stated in Chapt. 3, the final values considered for the quantitative spectroscopic analysis with IACOB-GBAT (see next section) are the pair $v \sin i$(GOF) – $v_{\rm mac}$(GOF) (which corresponds to 95% of the sample)[7], quoted in Table B.2.

4.4.2 IACOB-GBAT analysis: results

The results from the analysis of the best S/N spectrum of each star includes, along the values and uncertainties of the different parameters, a quality flag that

[7]Except for the three remaining discrepant stars, for which we used $v \sin i$(FT) and the associated $v_{\rm mac}$(FT+GOF).

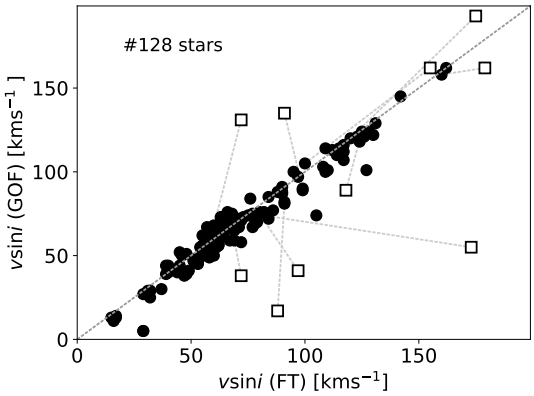

Figure 4.2: Comparison of projected rotational velocities resulting from the FT and GOF analysis strategies incorporated to the IACOB-BROAD tool. Open squares indicate the resulting values for those cases in which the line-broadening analysis of the O III λ5592 line was considered not reliable. Dotted lines connect these results with those obtained from the analysis of the Si III λ4552 or N V λ4603/20 lines.

corresponds to the final individual assessment "by-eye" between the spectrum and the final best fitting model (see Chapt. 3).

Table B.4 presents the quality flag assigned to each of the O-type standard stars, and a summary of the number of stars flagged as Q1-Q4 is included in Table 4.3. A detailed discussion of the plausible cause of the origin of those targets flagged as Q2 and Q3 is presented, together with the results of the IACOB-GBAT analysis of the whole sample, in Chap. 5. As stated above, in this chapter we focus on the effects that these discrepancies between model and observed spectrum could have for the spectral classification.

Table 4.3: Summary of the quality flags for the fit in the analysis of the sample of standard stars

Quality flag	Q1	Q2	Q3	Q4
# stars	75	16	30	7

128 stars in total

The overall agreement between the synthetic spectra associated with the

IACOB-GBAT/FASTWIND best fitting models and the observed spectra is good for most of the analyzed targets, but 46 (Q2+Q3) stars out of the 128 present a particular behavior of the wind diagnostic lines that cannot be reproduced by our grid of spherically symmetric unclumped models. These are potential targets of interest for more detailed investigations of clumpy winds and/or the existence of additional circumstellar emitting components contaminating the wind diagnostic lines (e.g., disks, magnetospheres).

Interestingly, and despite having been selected as standard stars for spectral classification, we have identified 16 stars as Q2 (most of them having luminosity class I or II) with particular spectroscopic features (Hα/He II λ4686 with inverse P-Cygni profile or showing a double peak). This is a clear situation in which He II λ4686 should not be used as diagnostic line for defining the luminosity class of the star. As will be stated in Chapt. 5, these features could be indicating the presence of circumstellar material contaminating the pure stellar (photospheric) spectra. Hence, we keep a warning on these stars as templates for spectral classification.

As for the Q3 stars, in Chapt. 5 we will state that they could be explained due to limitations in the modeling strategy, mainly the absence of wind-clumping on our atmospheric models. In principle they are not affecting the spectral classification, and therefore are not important in the case of the standard stars.

4.4.3 Comparison with previous results

Many of the stars in our sample have been already investigated elsewhere. We present in this section a comparison of our results for the O-type standard stars with those found in the literature with two main purposes. On the one hand, to validate the reliability of our automation of an analysis strategy that has been traditionally performed "by-eye". On the other hand, to identify possible systematic effects resulting from the use of different stellar atmosphere codes, analysis techniques, or specific single snapshot observations.

We concentrate on four parameters ($v \sin i$, $v_{\rm mac}$, $T_{\rm eff}$, and $\log g$) and four of the most recent papers performing quantitative spectroscopic analysis of a relatively large sample of Galactic O-type stars. Specifically, we have found 12, 17, 46, and 36 stars in common with Repolust et al. (2004), Markova et al. (2014), Simón-Díaz & Herrero (2014), and Martins et al. (2015a), respectively.

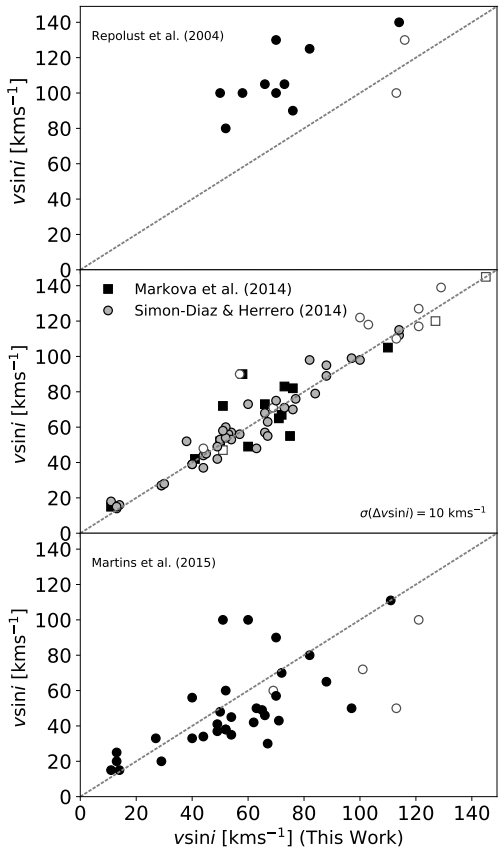

Figure 4.3: Comparison of $v \sin i$ determinations for a sample of stars in common with four reference papers in the literature. Open symbols indicate stars for which we have detected clear or likely signatures of spectroscopic binarity.

Line-broadening parameters ($v \sin i$ and $v_{\rm mac}$)

We start with the comparison of projected rotational velocities in Fig. 4.3. Before proceeding to the discussion of results, we indicate that the values con-

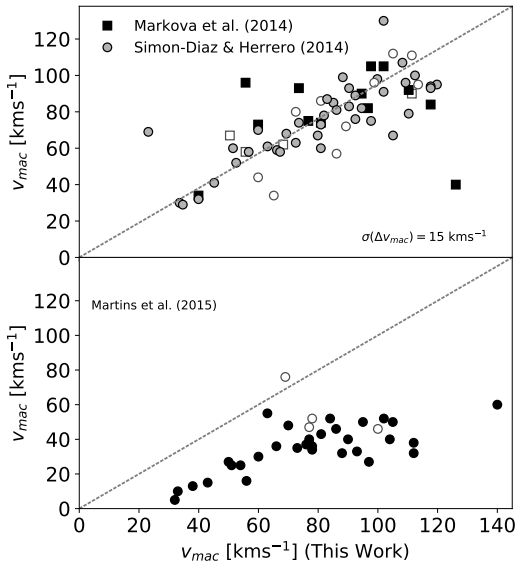

Figure 4.4: Comparison of $v_{\rm mac}$ determinations for a sample of stars in common with three reference papers in the literature. Open symbols indicate stars for which we have detected clear or likely signatures of spectroscopic binarity. See Sect. 4.4.3 for details and discussion.

sidered by Repolust et al. (2004) – top panel – were obtained from the analysis of medium resolution spectra and assuming that rotation is the only source of line-broadening. The other three studies use analysis techniques and spectra of similar quality as in this chapter, with the only difference that Markova et al. (2014) and Simón-Díaz & Herrero (2014) – middle panel – used IACOB-BROAD, while Martins et al. (2015a) – bottom panel – used their own tool to perform the line-broadening analysis. As expected, there is a fairly good agreement between those studies correcting for the effect of macroturbulent broadening, while important discrepancies (up to 50 km s^{-1} in some critical cases) are found with the values provided in Repolust et al. (2004). As stated in, for example, Simón-Díaz & Herrero (2007, 2014) and Markova et al. (2014), the derived values of $v \sin i$ are significantly overestimated in the whole O-type star domain whenever the effects of other broadening agents on the line-profiles are

neglected.

Nine stars present discrepancies in the $v \sin i$ determination larger than 20 km s^{-1} when comparing our results with those from Martins et al. (2015a). Three of them have been identified as spectroscopic binaries in our study. The use of different spectra could explain the discrepancy. For the other six, after checking again the outcome from IACOB-BROAD, we have not found a clear explanation for the disagreement or a reason to modify our results. Indeed, we note that for these stars we find similar values as those previously obtained in Simón-Díaz & Herrero (2014) and Markova et al. (2014) using different spectra.

Figure 4.4 presents a similar comparison but for the case of the macroturbulent velocity. In this case, Repolust et al. (2004) is excluded since they do not consider this parameter in the line-broadening analysis. Again a fairly good agreement is found with Markova et al. (2014) and Simón-Díaz & Herrero (2014) – top panel –, indicating the robustness of the results provided by IACOB-BROAD, even when different spectra are analyzed by different users. The clear disagreement with the values computed by Martins et al. (2015a) can be easily explained if one takes into account the different definition of the macroturbulent profile considered by Martins et al., an isotropic definition (corresponding with a Gaussian profile), and the other three works (a radial-tangential profile). As illustrated in Simón-Díaz & Herrero (2014), for a fixed value of $v \sin i$, a Gaussian-type macroturbulent profile implies a value of $v_{\rm mac}$ ∼65% smaller than when a radial-tangential profile is considered.

We refer the reader to Simón-Díaz & Herrero (2014) for a detailed explanation of the reason why we prefer to use a radial-tangential definition of the macroturbulent broadening profile. In a simple way, they found that the use of a radial-tangential instead of a Gaussian profile tends to more similar values of the $v \sin i$ values obtained for each of the two methods (FT and GOF) implemented in the IACOB-BROAD tool. The work to link this profile to a physical origin is still underway.

From the comparison of results presented in the middle panel of Fig. 4.3 and the top panel of Fig. 4.4, we conclude that the mean uncertainty in $v \sin i$ and $v_{\rm mac}$ associated with the analysis of different single-epoch spectra of the same star is of the order of ∼15 km s^{-1} in both cases. This difference is relevant considering the high resolution spectra (R> 25 000) used in most of these studies (excluding Repolust et al. (2004) with R∼5000), corresponding to limit rotational velocities lower than 12 km s^{-1}.

Effective temperature ($T_{\rm eff}$) and gravity ($\log g$)

Figure 4.5 compares our derived values for $T_{\rm eff}$ and $\log g$ with those determined by Repolust et al. (2004); Markova et al. (2014) and Martins et al. (2015a). Similarly to our work, the first two studies are based on the stellar atmosphere code FASTWIND. In contrast, Martins et al. used CMFGEN (Hillier & Miller 1998; Hillier & Lanz 2001).

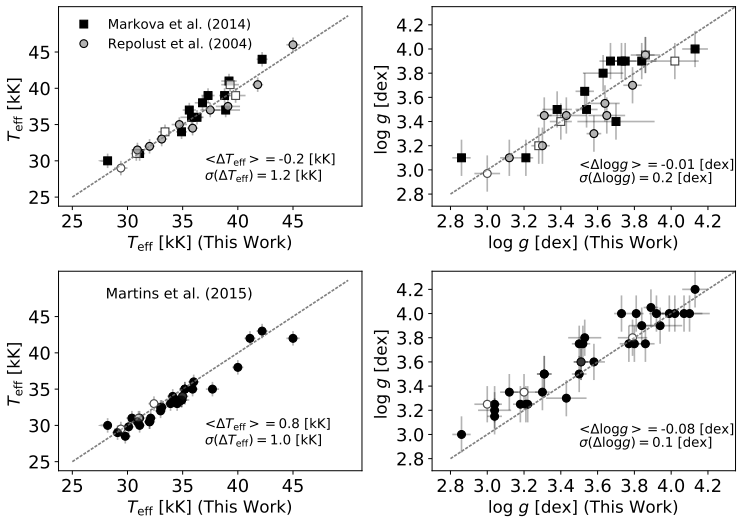

Figure 4.5: Comparison of parameters for stars in common with Repolust et al. (2004) and Markova et al. (2014), FASTWIND studies (Top) and Martins et al. (2015a) – CMFGEN (Bottom). Open symbols indicate stars for which we have detected clear or likely signatures of spectroscopic binarity. The dashed line is the 1:1 relation and each panel shows the mean and standard deviation of differences.

We find good agreement in all cases. These results not only validate our automatized analysis strategy, but also highlight the robustness of the quantitative spectroscopic analyses of O-type stars in the last years – at least regarding the two considered parameters, $T_{\rm eff}$ and $\log g$.

The comparison presented in the top panels indicates that we are basically reproducing the results obtained by Repolust et al. (2004) and Markova et al. (2014), who used the same stellar atmosphere code (FASTWIND) and analysis

strategy as this work, but a more subjective "by-eye" fitting of the main H and He diagnostic lines. The mean values of the differences in $T_{\rm eff}$ and $\log g$ are -200 K and -0.01 dex, respectively, well below the formal uncertainties associated with these parameters (see Table B.4). On the other hand, the standard deviations of the differences are 1200 K and 0.2 dex, respectively. These values, that are somewhat larger than the uncertainties resulting from the IACOB-GBAT analysis (especially for the case of $\log g$, that are of the order of $\pm 0.05-0.10$ dex) indicate that the latter are sometimes too optimistic. Other sources of uncertainty such as those associated with stellar variability, or assumed values for those parameters fixed in the analysis (e.g., $v \sin i$, $v_{\rm mac}$, $\xi_{\rm t}$, v_∞) may have a similar, or even more important effect on the final errors associated with these parameters for a given star. Finally, a correct treatment of the normalization of the spectra is essential for deriving the gravities.

Interestingly, in spite of the different assumptions considered in the set of line-broadening parameters used in the quantitative spectroscopic analysis, we do not find any remarkable difference between the comparison of our results and those by Repolust et al. (2004) and Martins et al. (2015a). This can be interpreted as indirect evidence that the exact parametrization of the global line-broadening (e.g., by means of one –$v \sin i$ – or two parameters – $v \sin i$ and $v_{\rm mac}$, or a different definition of the macroturbulent profile) is not going to critically affect the derived $T_{\rm eff}$ and $\log g$.

When comparing with Martins et al. (2015a) we need to take into account that we are using a similar set of diagnostic lines, but they are using the CMFGEN stellar atmosphere code. A closer inspection of the two bottom panels in Fig. 4.5 indicates that, although there is fair agreement – within the associated derived uncertainties – between results obtained by these two independent works, there seems to be some hints of the existence of a systematic difference in the derived effective temperatures and gravities, with CMFGEN resulting in lower effective temperatures and higher gravities (with mean values of the differences $\sim$800 K and 0.08 dex, respectively). Regarding the gravities, this discrepancy might be attributed to the approximate treatment of the background line opacities in FASTWIND. This could lead to an underestimated radiative acceleration in the upper photosphere and, in consequence, to underestimated gravities (see also Massey et al. 2013). The discrepancy in the derived $T_{\rm eff}$, had already been found previously (see, e.g., Simón-Díaz et al. 2008), who provide some examples. The origin of this discrepancy is rooted in different predictions for the strength of He II λ4200/4541, where CMFGEN provides deeper profiles in the temperature range between 30 to 35 kK, though the corresponding He I profiles match perfectly. Thus far, we have no real explanation for this difference.

Finally, we discuss some of the most discrepant results individually. From

the comparison with Markova et al. (2014) and Repolust et al. (2004), we highlight HD 151804 and HD 193514, two mid O-type supergiants for which differences in $\log g \sim 0.3$ dex are found. HD 151804 is a star with a very strong and variable wind, a fact that could explain the discrepancy in gravities obtained from different snap-shot spectra. HD 193514 has also been labeled as WV; although we do not see clear variability affecting the wings of Hβ and Hγ in our spectra, we cannot discard a similar explanation for this star. From the comparison with Martins et al. (2015a), we highlight HD 30614 (α Cam, $\Delta\log g \sim 0.3$ dex). This is an O9 Ia star that we identified as SB1 and, in addition, for which we measured a $v \sin i \sim 110$ km s^{-1} while Martins et al. (2015a) considered a much lower value for this quantity (50 km s^{-1}) in the spectroscopic analysis. A difference of 60 km s^{-1} in the assumed $v \sin i$ can well explain a difference of 0.3 dex in the derived gravity (with the lower $v \sin i$ implying a higher $\log g$).

4.5 General properties of the sample

In this section we use the results of our homogeneous and automatized spectroscopic analysis to describe the global properties of the sample in terms of $v \sin i$, $T_{\rm eff}$, and $\log g$. For this we construct the histogram distribution of the $v \sin i$ values, and present our results in the Kiel and spectroscopic HR diagrams. We note that all the information used to construct these diagrams, summarized in Table B.4, is directly obtained from the analysis or inspection of the available spectra except for $\log g_{\rm true}$, the gravity corrected from centrifugal acceleration. In this case we used the calibrations presented in Martins et al. (2005), combined with the spectral classification associated with each star to obtain information about the stellar radii, needed to compute the centrifugal correction (Herrero et al. 1992; Repolust et al. 2004).

Despite a short description of results concerning other derived parameters (such as the helium abundance, $Y_{\rm He}$, the microturbulence, $\xi_{\rm t}$, and the wind-strength parameter, $\log Q$) is included in this chapter for completeness. The complete discussion is presented in Chapt. 5 where the results for the whole sample of O-type stars are presented.

4.5.1 $v \sin i$ distribution

This section includes the results from the IACOB-BROAD line-broadening analysis of the sample of O-type standard stars for spectral classification. The seven stars labeled as Q4 (no He I lines available) have not been excluded from the figures and discussion presented in this section, as the $v \sin i$ values are not

expected to be affected. The values of $v \sin i$ for the seven SB2 standard stars are also included in the figures, but must be considered only as upper limits. This makes a total of 128 $v \sin i$ values in the sample.

Figure 4.6 presents the distribution of projected rotational velocities for the sample of O-type standard stars in the form of histogram (left panel) and cumulative distribution (right panel). For comparison purposes, we also show cumulative distribution functions resulting from the line-broadening analysis of the whole sample of Galactic O-type stars, presented in Chap. 5.

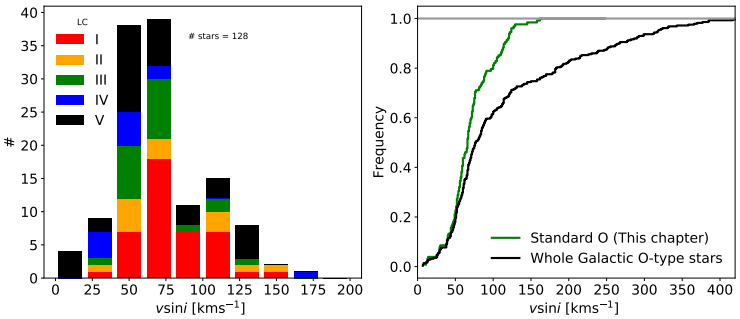

Figure 4.6: [Left] Distribution of $v \sin i$ in the sample of O-type standard stars. Different colors have been assigned to different luminosity classes. [Right] Cumulative histogram of two samples. Green is the standard stars. Black is the whole sample of Galactic O-type stars presented in Chapt. 5. There is one star (HDE 229196, O6 II, $v \sin i \sim 250 \mathrm{km\,s^{-1}}$) which does not appear in the histogram.

The distribution peaks around $40-80$ km s^{-1} and covers a range in $v \sin i$ between ~ 10 and 250 km s^{-1}. More specifically, 95% of the standard stars have $v \sin i < 120 \mathrm{km\,s^{-1}}$.

When we compare the distribution of $v \sin i$ values in the sample of O-type standard stars with the one resulting from the study of the complete sample it becomes clear that the sample of O-type standard for spectral classification is affected by an important selection effect and is not representative of the global spin distribution of Galactic O-type stars. This is, however, not surprising since – almost by definition – these stars are selected among the ones with narrower lines, and hence lower $v \sin i$. Therefore, one has to be very careful when extracting conclusions from the study of this sample, especially in the context of stellar evolution and regarding relative percentages of, for example, fast or slow rotators, detected spectroscopic binaries, or magnetic stars.

Figure 4.6 also shows that there are 27 stars among the list of standard stars with $v \sin i$ values above 120 km s^{-1}. This means that it could happen that a spectroscopic template for a given standard spectral type has broader lines than the star to be classified (even at a resolving power of 2500, in the GOSSS project). It would hence be ideal to try to find new standard stars with a lower $v \sin i$ to replace these 27 stars.

4.5.2 Kiel and spectroscopic HR diagram

This section includes the results from the IACOB-GBAT spectroscopic analysis of the sample of standard stars for spectral classification. The seven stars labeled as Q4 (no He I lines available) have been excluded from the figures and discussion presented in this section, as their $T_{\rm eff}$ values are not properly constrained. The values for the seven SB2 standard stars have not been eliminated from the figures, but properly highlighted as these values are not considered reliable. This makes a total of 121 stars with available values of $T_{\rm eff}$ and $\log g$.

Figure 4.7 presents the location of these 121 stars in the $\log g - T_{\rm eff}$ (Kiel) diagram and the spectroscopic HR (sHR) diagram (Langer & Kudritzki 2014) against the whole sample of Galactic O-type stars, presented in the next chapter. The Geneva non-rotating evolutionary tracks for solar metallicity (Ekström et al. 2012; Georgy et al. 2013) are included for reference purposes (See Appendix A.8 for more in depth description). Additionally, in the right panel of Fig. 4.7, the sample is included with different colors and symbols depending on the luminosity classes. The sample of standard stars is well distributed, covering the same parameter space as the more general sample, between the 20 and 85 $M_\odot$ non-rotating evolutionary tracks. There is lack of standard stars close to the zero age main sequence (ZAMS) above $\sim$25 $M_\odot$, but this feature also appears for the case of the whole sample distribution (see discussion in Sect. 5.6.2). Therefore, the absence of standard stars in this region of the Kiel and sHR diagram does not seem to be related to any bias in the selection of this particular subsample.

4.5.3 Helium abundance

The top panel in Fig. 4.8 shows the distribution of helium abundances of our sample of O-type standard stars in the sHR diagram. We separate the sample in four abundance bins using different symbols and colors. Basically, we consider as stars with normal He abundance those having $Y_{\rm He} = 0.10 \pm 0.02$ (yellow circles) and then distinguish between slightly ($Y_{\rm He} = 0.12 - 0.15$, green triangles) and highly ($Y_{\rm He} > 0.15$, black squares) enriched stars in helium. Finally,

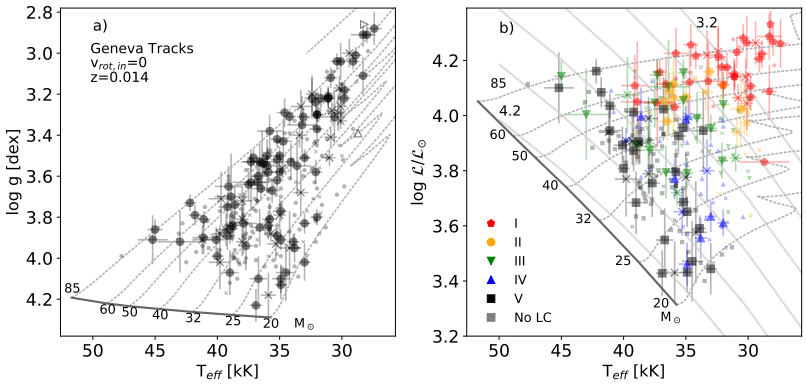

Figure 4.7: Location of 121 O-type standard stars (big symbols) in our sample in the Kiel (left) and spectroscopic HR (right) diagrams, in comparison with the whole sample of Galactic O-type stars (small symbols). Cross symbols indicate stars for which we have detected clear or likely signatures of spectroscopic binarity. Open symbols in left panel are stars for which only upper or lower limits in any of the two parameters used to construct these diagrams ($T_{\rm eff}$ and $\log g$) could be obtained. Right panel uses various colors and symbols to identify different luminosity classes. Individual uncertainties are included as error bars. Evolutionary tracks and position of the ZAMS from the non-rotating, solar metallicity models by Ekström et al. (2012) and Georgy et al. (2013) are included for references. The dotted diagonal lines in the sHR diagram are the isocontours of constant gravity.

the fourth bin comprises stars with helium abundances below the commonly considered baseline for massive stars ($Y_{\rm He} < 0.08$, red pentagons).

We just highlight the following main points regarding helium abundances in the sample of O-type standards for spectral classification:

- More than half of the targets (∼65%) have what we have called normal helium abundances. This subgroup of stars is distributed all around the O star domain. This mean that 35% of the so-called standards stars have anomalous abundances.
- Among the stars with clear He enrichment (∼23%) we mainly find O supergiants and bright giants with masses above ∼40 $M_\odot$, naturally. We note, however, that a similar number of O stars with luminosity classes I and II are found to have normal helium abundances.
- Only six dwarfs and giants have $Y_{\rm He} > 0.12$. Three of them are O dwarfs

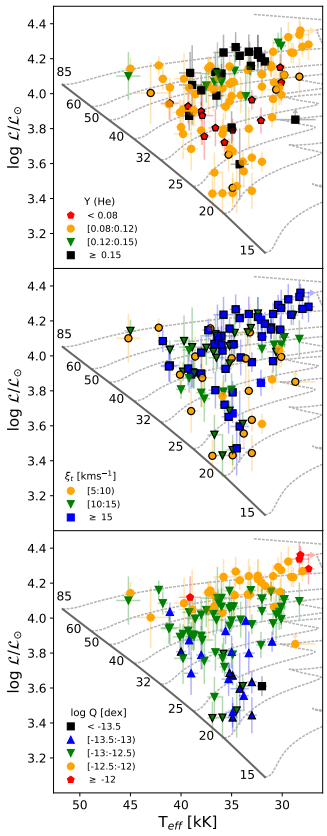

Figure 4.8: Distribution of the helium abundance (top), microturbulence (middle) and wind-strength Q-parameter (bottom) in the sHR diagram. Stars for which it was only possible to obtain upper or lower limits for any of these quantities are indicated by symbols with the border in black. The range in the legend corresponds to the central value in case of a well-determined value, or to the upper or lower limit otherwise.

labeled as SB1. The presence of these enriched stars close to the ZAMS is not easily explicable with the current paradigm of rotational mixing of

single stars.

- Regarding the 15 stars (13% of the full sample) for which the IACOB-GBAT analysis has resulted in He abundances below 0.08, most of them are either giants or relatively evolved dwarfs. The only three O supergiants and bright giants with $Y_{\rm He} < 0.08$ have been found to be spectroscopic binaries, but no clear correlation between binarity signs and low He abundances can be extracted from our study for the stars within the other luminosity classes.

4.5.4 $\xi_{\rm t}$ microturbulence

The middle panel of Fig. 4.8 shows the distribution in the sHR diagram of the values of microturbulence resulting from the IACOB-GBAT analysis of the sample of O-type stars investigated here. As can be seen, we could only determine upper or lower limits for the majority of the targets. However, the diagram already provides a first rough general overview of the behavior of microturbulence in a region of the HR diagram that has been vaguely explored until now. This scenario is very similar to what we found when we analyze the whole sample (Chapt. 5). The comparison between the sample of standard stars and the whole sample provides no extra information, and we leave a deeper analysis on the implications of this parameter for the next chapter with the whole sample results.

4.5.5 Wind-strength Q-parameter

The bottom panel in Fig. 4.8 depicts the distribution of the wind-strength Q-parameter in the sHR diagram. Inspection of this diagram hints a possible positive correlation between $\log Q$ and $\log \mathcal{L}$, which will be studied in depth in Chapter 5 with the whole sample results. Again, this diagram with the O-type standard stars already provides a first rough general overview of the behavior of $\log Q$ in this region of the HR diagram, but we do not see differences between the sample of O-type standard stars and the whole sample. A more detailed discussion of results is then postponed to next chapter.

4.6 SpT–$T_{\rm eff}$ and SpT–$\log g$ calibrations

The calibration of stellar parameters versus spectral type for Galactic O-type stars presented by Martins et al. (2005) (hereafter MSH05) has become a standard reference for the massive star community and also for other related fields

such as, for example, the study of H II regions. This calibration replaced the previous ones based on spectroscopic analyses performed with stellar atmosphere codes that did not take into account non-LTE, wind, and line-blanketing effects (e.g., Vacca et al. 1996). MSH05 provided several recipes connecting the spectral type and luminosity class of a given star with its effective temperature and spectroscopic gravity (along with other parameters). In particular, they used a compilation of the results – available in the literature – from the optical spectroscopic analysis of a sample of Galactic O stars using non-LTE spherically expanding models including line-blanketing to build what they called the observational scale. Despite its novelty and importance, this calibration is based on a heterogeneous set of spectroscopic observations (in terms of quality and resolution), stellar parameter determinations and spectral classifications. In particular, the parameters gathered by MSH05 combine results from Herrero et al. (2002) and Repolust et al. (2004) obtained from FASTWIND, and from Martins et al. (2005), who used CMFGEN. In addition, it relies on a relatively small sample of targets (45 stars distributed among dwarfs, giants, and supergiants).

We compare the SpT–$T_{\rm eff}$ and SpT–$\log g$ calibrations proposed by MSH05 with a much larger sample of stars (114, see below) that (1) have been observed spectroscopically in a homogeneous way, (2) have been analyzed homogeneously with state-of-the-art models and techniques, (3) constitute part of the modern grid of O-type standard stars for spectral classification, and whose spectral classification has been recently reviewed in a homogeneous way by the GOSSS team.

Results are summarized in Fig. 4.9, where we separate the sample in three main blocks by luminosity class: supergiants and bright giants (left, 50 stars), giants (middle, 19 stars), and subgiants and dwarfs (right, 45 stars). The top panel shows the number of stars per spectral type bin in each luminosity class category while the middle and bottom panels present the SpT-$T_{\rm eff}$ and SpT-$\log g$ calibrations, respectively, together with the observational scales proposed by MSH05. Once more, we identify those stars labeled as SB1 with open symbols (SB2 are excluded from these figures). In addition, and similarly to previous figures, we do not include those seven targets labeled as Q4 (see Sect. 3.3.3). As a consequence of the latter, we end up with no targets with spectral types earlier than O3.5 and the number of stars in the spectral type bins O4 and O4.5 are slightly reduced.

We find an overall good agreement with the calibrations presented by MSH05; however, a few points of interest deserve further attention. The most critical one is the systematic offset toward higher $T_{\rm eff}$ (up to $\sim$3 000 K in some cases) that we obtain in the late O-type giants, subgiants and dwarfs with respect

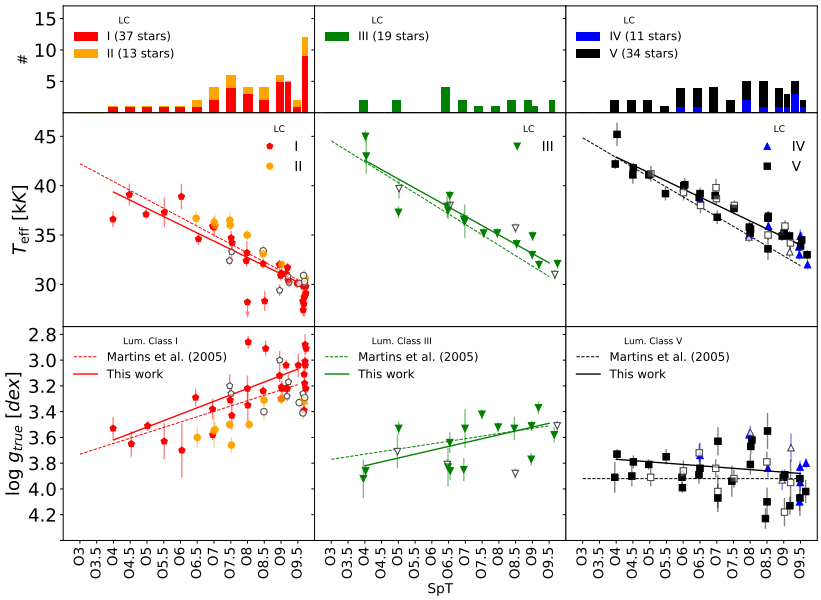

Figure 4.9: SpT–$T_{\rm eff}$ (middle panels) and SpT–log g (bottom panels) calibrations. The global sample is divided by luminosity class groups in columns. Top panels show the number of stars per spectral type bin. The "observational scales" proposed by MSH05 are indicated by dashed lines. Calibrations obtained in this work are solid lines. As in previous figures, open symbols indicate stars for which we have detected clear or likely signatures of spectroscopic binarity. Stars with luminosity class Ia are not considered for the calibrations presented in Table 4.4, and as solid lines in these figures.

to Martins' observational scale. The offset tends to become smaller and even disappears toward the early-type stars. A similar result was already obtained in Simón-Díaz et al. (2014) using a smaller sample of Galactic O-type dwarfs observed in the framework of the IACOB project. The fact that many stars in the O9 spectral type bin have been more recently reclassified as O9.2, O9.5, and O9.7, plus the combined effect of the intrinsic scatter in $T_{\rm eff}$ present in each SpT bin and the low number statistics used to define the observational scale may also have an important impact on the defined calibrations (see a more detailed discussion in Simón-Díaz et al. 2014). Other explanations related to, for

example, discrepancies in the stellar parameters derived using different stellar atmosphere codes or by different people can be ruled out as the main reason of the systematic offset in the late O-type regime in view of the results presented in Fig. 4.5: the agreement between the various studies using FASTWIND is almost perfect, and the mean difference in $T_{\rm eff}$ between our results and those obtained by Martins et al. (2015a) using CMFGEN is ∼900 K. In addition, we note that the observational scales presented in MSH05 were mainly obtained using results from analyses performed by that time with FASTWIND.

In these regards, it is also interesting to see that the scatter in the SpT–$T_{\rm eff}$ and SpT–$\log g$ calibrations discussed in Simón-Díaz et al. (2014) still remains although we are now limiting our sample to the standard stars for spectral classification. This scatter is a natural consequence of the way the spectral classification process is defined (see notes in Sect. 5.5.1) and not necessarily due to caveats related to the classification of O-type stars with intermediate and extreme $v \sin i$ values.

A last point of attention concerns those four late O-type supergiants for which we have obtained values of $\log g_{\rm true}$[8] $\lesssim 2.9$ dex and effective temperatures lower than 28 500 K (see leftmost panels in Fig. 4.9). These stars[9] can be considered as clear outliers from the calibrations. Interestingly, all of them have been classified as Ia, have been flagged as Q2 or Q3 (plus also WV), and are among those targets for which we have obtained the largest values of $\log Q$ (i.e., they have the strongest winds among the analyzed stars). In addition, the derived values of $T_{\rm eff}$ and $\log g$ imply values of the Eddington factor ($\Gamma_{\rm e} = L/L_{\rm Edd}$) close to 0.5. While there is the possibility that late-O stars with luminosity class Ia could form a separated group in the calibrations, given the points above we cannot discount that this result is simply a consequence of the limitations of our analysis strategy for stars approaching the Eddington limit (see further notes in Appendix A.5).

We provide new linear calibrations based on results from the IACOB-GBAT analysis of the standard stars for spectral classification. To obtain them we have discarded all stars for which we have detected clear or likely signatures of spectroscopic binarity. In addition, for the calibrations of supergiant stars, we exclude those stars identified as luminosity class Ia (see notes above).

We find that our SpT – $\log g$ calibration for dwarfs always results in gravities lower than the value proposed by MSH05 ($\log g = 3.9$ dex). However, we remark that assuming a unique value per SpT of this parameter in the O dwarfs is an oversimplified recipe since it actually ranges between 4.2 and 3.5 dex (see also

[8] The gravity corrected from centrifugal acceleration
[9] HD 151804: O8 Iaf, HDE 303492: O8.5 Iaf, HD 105056: ON9.7 Iae, HD 195592: O9.7 Ia.

Table 4.4: Linear fits of the observed data presented in Fig. 4.9. $T_{\rm eff}$ (top) and $\log g$ (bottom) as a function of spectral types (SPT, where, e.g., O9.5 is represented as SPT=9.5) for three luminosity classes.

$$T_{\rm eff}\ [\rm kK] = \begin{cases} -1.66 \times \rm SPT + 46.00 & (\rm I,\ 25\ stars) \\ -1.89 \times \rm SPT + 50.13 & (\rm III,\ 15\ stars) \\ -1.62 \times \rm SPT + 49.38 & (\rm V,\ 25\ stars) \end{cases}$$

$$\log g\ [\rm dex] = \begin{cases} -0.10 \times \rm SPT + 4.02 & (\rm I,\ 25\ stars) \\ -0.06 \times \rm SPT + 4.06 & (\rm III,\ 15\ stars) \\ 0.02 \times \rm SPT + 3.69 & (\rm V,\ 25\ stars) \end{cases}$$

notes in Simón-Díaz et al. 2014). This specific calibration must be handled carefully to avoid misinterpretations. The spectral classification was defined arbitrarily discreet and we are using a linear correspondence with $T_{\rm eff}$.

4.7 Appendix

In this section we present additional studies we perform with the subsample of O-type standard stars, included in Holgado et al. (2018).

4.7.1 The β parameter

As indicated by Puls et al. (1996), the exponent of the wind-velocity law is a crucial parameter for the determination of mass-loss rates. We hence decided to explore the possibility of obtaining information about this parameter, together with the rest of free parameters, by allowing β to vary during the fitting process. Even accounting for the optimal quality of the compiled spectroscopic dataset (in terms of resolution and S/N), we have found that the IACOB-GBAT analysis is not able to provide reliable constraints on this parameter (at least within the considered range of values, i.e., 0.8–1.2). The resulting reduced χ^2 distributions for this parameter are degenerate in ∼40% of the stars in the sample, and only rough upper or lower limits could be found in another ∼50%.

In view of the difficulty of constraining this parameter in more than 90% of the sample, we have make use of the flexibility of the IACOB-GBAT tool to study what is the effect of fixing β to a given value making use of the very well-behaved sample of O-type standard stars for spectral classification. We focus on the effect on the central values and associated uncertainties obtained for the Q-parameter in that case. To this end, we launched the last step of IACOB-GBAT (see Appendix A.3) for all stars, but fixing β to 1, and compared

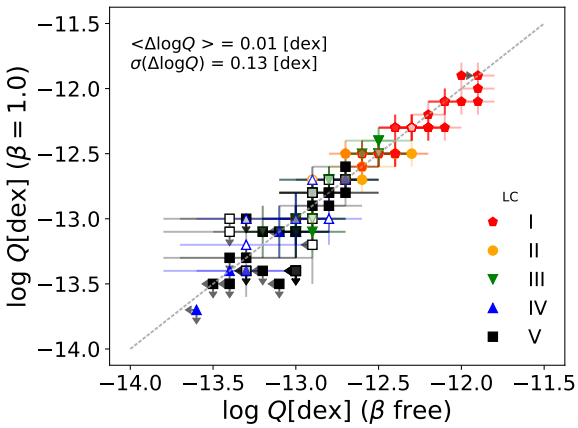

Figure 4.10: Comparison of log Q values derived from the IACOB-GBAT analysis leaving β as a free parameter (x-axis), and fixing this parameter to one (y-axis). The figure includes results for all stars in the standard sample. Different colors and symbols indicate different luminosity classes. Open symbols indicate stars for which we have detected clear or likely signatures of spectroscopic binarity. The dashed line is the 1:1 relation, and we show the mean and standard deviation of differences.

the results with those obtained when leaving β as a free parameter. Results are summarized in Fig. 4.10, in which we separate stars by luminosity class using different symbols and colors. On the one hand, as expected, the uncertainties provided by IACOB-GBAT for the Q-parameter are smaller when β is fixed. The main reason is because in the latter case, the degeneracy between β and log Q is broken. On the other hand, while a certain dispersion ($\sigma = 0.13$ dex) in the difference of values associated with the best fitting model is found (in agreement with previous findings by Puls et al. (1996) for the case of stars with thin winds), there is not a clear correlation between positive and negative differences in the derived log Q values and luminosity class or wind strength.

Therefore, fixing β to 1 seems a reasonable assumption when analyzing large samples of optical spectra of O-type stars in the case a reduction of the computational time is necessary. In our case, however, we make use of the fast-pace analysis of the grid system of FASTWIND+IACOB-GBAT and leave the β parameter range free. This allows degeneracy with the log Q parameter and avoids the necessity to add an additional uncertainty of $\sim 0.15-0.20$ dex to the

formal uncertainties resulting from the fitting process.

4.7.2 On the $T_{\rm eff}$ and $\log g$ dependence on $\log Q$ in Q3 stars

We take advantage of the well-behaved sample of standard O-type stars for spectral classification to study the effects on the wind-strength parameter $\log Q$, $T_{\rm eff}$, and $\log g$ produced by the discrepancy between Hα and He II λ4686 diagnostic lines, the Q3 stars. The standard sample is ideal in terms of stability, and they have been extensively studied in the literature.

As stated above, in the analysis of the stars we found several O-type standard stars for which the best-fitting model and the spectra of the star present a particular discrepancy, the Hα and He II λ4686 diagnostic line were not able to fit at the same time. These are cataloged as Q3 stars. We discuss their possible origin in Chapt. 5. Here, we study the effects that this discrepancy could have in the results. For this, we repeat our analyses two more times, selecting only one of the two diagnostic lines (either Hα or He II λ4686) as our wind-strength indicator, and discarding the other one. This is possible thanks to the versatility of the IACOB-GBAT tool to select and de-select certain diagnostic lines and redo the analysis in seconds. The main results are presented in Table B.3 and, graphically, in Fig. 4.11. We concentrate on the effect on the derived effective temperature and gravity.

The main results of this formal exercise can be summarized as follows:

- At first glance, there is not a clear systematic trend in which one of the two wind diagnostic lines requires a higher value of $\log Q$ to be fitted individually (see, however, Chapt. 5).
- The difference in the extreme $\log Q$ values can be up to 1 dex in some cases
- The standard deviation of the difference in the derived $T_{\rm eff}$ and $\log g$ when fixing $\log Q$ to one of the two extreme values is of the order of the uncertainties associated with these quantities; however, more critical situations, with differences up to 3500 K and 0.2 dex in $T_{\rm eff}$ and $\log g$ respectively, are also found in specific cases.

Globally, even though a more detailed modeling of individual cases – with a simultaneous fit of Hα and He II λ4686 – will help to better constrain the mass loss rates associated with these stars, we can conclude that we do not expect an important effect on the derived effective temperatures and gravities in most cases.

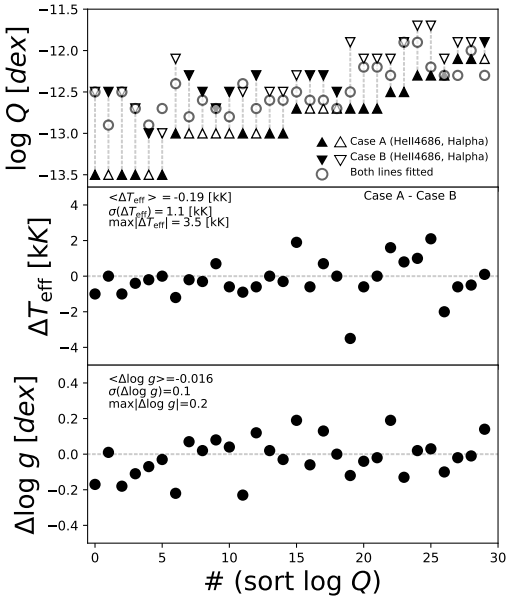

Figure 4.11: Difference in the resulting $T_{\rm eff}$ (middle panel) and $\log g$ (bottom panel) when fixing $\log Q$ to those values needed to fit the He II λ4686 or Hα lines, in the sample of stars labeled as Q3. In the top panel the weaker (stronger) wind is represented by a triangle with the peak up (down). Filled triangles are $\log Q$ obtained from He II λ4686, and open triangles with Hα. Open circles are the values obtained when fitting both lines at the same time automatically. Stars are sorted by increasing minimum $\log Q$ in the horizontal axis. Standard deviation, maximum and mean of the differences also included in the middle and bottom panels.

Nevertheless, the mass-loss, the ultimate purpose of the study of the winds, and the parameter that is characterizing the evolution of the star, is fluctuating in a much lesser extent (Markova et al. 2005). Markova found that the observed variations of Hα typically seen in O supergiants imply changes of $\pm$4% with respect to the mean value of $\dot{M}$ for stars with stronger winds, and of $\pm$16% for stars with weaker winds. The evolutionary models for these stars consider that the average of the mass-loss is conserved despite the variability in the wind-strength.

4.7.3 Q3 stars and clumping

As defined in Chapter 3, and recalled in Section 4.7.2, Q3 stars are those in which a simultaneous fit to Hα and the He II λ4686 could not be achieved with any synthetic spectrum generated from our grid of unclumped FASTWIND models. Since these two lines are the main spectroscopic features in the optical spectra of O-type stars providing information about the wind-strength Q-parameter, we stressed that the values of log Q indicated in Table B.4 should be treated with caution (differences up to 1 dex in log Q can be found in some extreme cases depending on whether we rely on Hα or He II λ4686). In this section, we further evaluate the possibility that the situation found in those stars labeled as Q3 was actually linked to limitations of our spectroscopic analysis using unclumped models.

The main effect of introducing (optically thin) clumping in the modeling of the stellar wind is a global reduction of the derived values of the mass loss rate ($\dot{M}$) by a factor $\sqrt{f_{cl}}$ (see, e.g., Repolust et al. 2004; Puls et al. 2006, 2008; Sundqvist et al. 2014). Concerning the outcome of a quantitative spectroscopic analysis based on the H and He lines in the optical regime, in most cases, the inclusion of clumping in the models only affects the derived value of log Q, but the overall fit-quality barely changes (at least if one assumes a clumping factor that is spatially constant in the wind-line forming region). However, there are also some situations in which Hα and He II λ4686 react differently to clumping. This may help to solve the problem indicated above.

In the O-star domain this was illustrated, for example, in the study of central stars of planetary nebulae with effective temperatures similar to the main sequence O-type stars by Kudritzki & Urbaneja (2006) and Urbaneja et al. (2008). They found that, as expected from theory, below $T_{\rm eff} \approx 37000$ K the effect of clumping on He II λ4686 and Hα lines start to become different, due to the different dependence of opacity on density: below the indicated threshold in $T_{\rm eff}$ He III begins to recombine, and He II λ4686 changes from a ρ^2-dependent line to a ρ-dependent one, while Hα preserves its ρ^2-dependent character. As a result, in stars presenting a clumpy wind in this domain of stellar parameters, the Hα line will require a larger value of log Q than the He II λ4686 line when performing the spectroscopic analysis using unclumped models. With this in mind, we now evaluate the hypothesis that the 30 stars in our sample labeled as Q3 are actually showing observational evidence of having a clumpy wind.

Figure 4.12 depicts the location of all the stars in this subsample in the sHR diagram. As already shown in Figure 4.11, not all of them are consistent with the requirement that Hα needs a larger value of log Q than He II λ4686. Indeed, there are 11 stars clearly showing the opposite. We hence separate

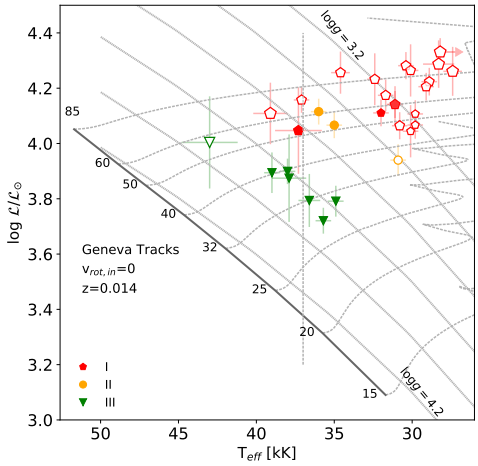

Figure 4.12: Same as right panel in Fig. 4.7, but only for stars with Q3 quality flag. Size depends on the log Q obtained in the automatic analysis. Open (filled) points are stars for which the value of log Q when fitting only the Hα line is larger (smaller) than when fitting He II λ4686. The horizontal line at $T_{\rm eff} = 37$ kK indicates the boundary of the region where clumping in the wind is expected to affect the two wind diagnostic lines differently (see text).

both subgroups in Fig. 4.12, showing both those cases in which log Q(Hα) > log Q(He II λ4686), and those for which the situation is the opposite.

Most of the open symbols are luminosity class I, and they are concentrated in the region ($T_{\rm eff} \lesssim 37000$ K) where clumping in the wind is expected to affect the two main lines differently. The overall fit for all these stars will hence likely improve when including the effect of wind clumping in the analysis. Interestingly, there are five additional stars with luminosity class I and II (filled red and orange symbols) for which IACOB-GBAT provides a larger value of log Q when fitting only the He II λ4686 line. We do not find an obvious explanation at this point, but we notice that all of them have been classified as WVa (variability of H_α in absorption).

Concerning the stars with luminosity class III labeled with the Q3 flag (green triangles), it is interesting to note that the analysis of most of them (seven out of the eight) results in a larger value of log Q when fitting only the He II λ4686 (filled symbols). A closer inspection of this subsample of giant

stars indicates that all of them are located well within the area of the diagram where dwarfs and sub-giants are found (see also left panel in Fig. 4.7). This could mean that these are actually not luminosity class III stars. One possible explanation is that the He II λ4686 is contaminated by an extra source of circumstellar emission not directly connected with the stellar wind. This may be biasing the spectral classification in that direction. Interestingly, these stars are also characterized by having a low value of the helium abundance (as provided by IACOB-GBAT, see Fig. 4.8). This may be alternatively or complementary indicating that we are actually dealing with composite spectra. Indeed, most of these stars are flagged as visual binaries with similar brightness by Sota et al. (2011, 2014).

The only giant star labeled as Q3 and showing the contrary effect is HD 168076 AB. We note that its luminosity class has changed from III to IV in the last GOSSS revision (Maíz Apellániz et al. 2016), and it has been depicted as a binary star in Sana et al. (2006). In addition, this star presents a remarkably strong Hα line in emission while this is not expected for this combination of SpT and LC. This resembles the case of, for example, the O9.7 V star HD 54879[10] (Castro et al. 2015), or the well-known magnetic O-type stars HD 37022 (Stahl et al. 1993; Wade et al. 2006) and HD 191612 (Walborn et al. 2003; Sundqvist et al. 2012), whose spectra also show a strong Hα emission which has been associated with a strong magnetic field.

Concluding, we have provided strong evidence that wind clumping effects are a likely explanation for the behavior of most of the stars labeled as Q3 with luminosity class I and II. These are targets of potential interest for further investigations of wind clumping. In addition, Q3 giants would require a different explanation, possibly associated with the presence of extra sources of circumstellar emission in He II λ4686 or hidden components. Finally, while the Q3 stars that can be explained by the inclusion of clumping in our models can still be regarded as standards for spectral classification, the status of the targets that exhibit possible signatures of contamination in the He II λ4686 line as classification standards should be carefully reviewed.

[10] See Sect. 5.6.3 for this particular result.

5

The complete sample (I): results from the spectroscopic analysis

Genius begins the great works,
but only work ends them.
Joseph Joubert

This chapter present the core of this thesis, the results from the quantitative spectroscopic analysis of the complete sample of Galactic O-type stars surveyed by IACOB and OWN, comprising more than 400 targets. **Following the same approach as the one presented in Chapt. 4 for the case of the grid of O-type standard stars for spectral classification, we use again the complete set of multi-epoch, high-resolution, optical spectra from the abovementioned spectroscopic surveys, and make use of the** IACOB-BROAD **and** IACOB-GBAT **semi-automatized tools, optimized for the quantitative spectroscopic analysis of large samples of O stars.**

5.1 Introduction

As a follow up of the study presented in Chapt. 4, we present here the results of the spectroscopic analysis of the complete sample (of more than 400) Galactic O-type stars surveyed by IACOB and OWN. As described in previous chapter, the grid of O-type stars for spectral classification has been used to establish and test a step-by-step protocol which can be now applied to the complete sample. This chapter includes the results of the spectroscopic variability assessment of the available multi-epoch observations (Sect. 5.3), as well as the outcome

of the IACOB-BROAD and IACOB-GBAT analysis (including all the spectroscopic parameters that can be obtained from the optical part of the spectra, Sect. 5.4). We then describe the general properties of the sample by allocating the stars in the Kiel and the spectroscopic HR diagrams, as well as other diagrams of interest. We present and discuss the distribution of the various derived parameters in those diagrams and use this information to address several questions of interest regarding the empirical characterization of this sample of massive stars. We note that here we only concentrate on those parameters resulting from the quantitative spectroscopic analysis; additional results regarding other stellar parameters, such as radius, mass and luminosity are presented in Chapt. 7.

5.2 Sample and methodology

As described in Chapt. 2, our pool of high-resolution spectra includes 2900 FIES, HERMES, and FEROS spectra for 415 different Galactic O-type stars. This sample of stars represents ∼70% of the Galactic O-type stars known to date (see Sect. 2.2). We highlight that such a large sample of Galactic O-type stars has never been studied before in a homogeneous way, or with such an extensive multi-epoch spectroscopic dataset. Working with such a large number of stars will not only allow us to find general trends in the distribution of the various investigated empirical quantities in the sHR diagram, but also to better identify and understand the outlayers in the distribution.

We refer the reader to Chapt. 3 and Chapt. 4 for a detail description of the methodology and the analysis protocol we have followed for the analysis of this sample of O-type stars. In brief, all the multi-epoch spectra per target have been used to roughly investigate spectroscopic variability (Sect. 5.3), and the spectrum with best quality – in terms of signal-to-noise ratio, (S/N) – was considered for the quantitative spectroscopic analysis[1] leading to the full set of spectroscopic parameters (Sect. 5.4).

5.3 Spectroscopic variability assessment: results

This section presents the information about the empirical characterization of the sample of all O-type stars resulting from the spectroscopic variability assessment. Following the notes presented in Sect. 3.2, one or several of the variability flags indicated in Table 5.1 were assigned to each star in the sample.

[1] In each step of the analysis we include the precise number of stars analyzed because in some cases (for example binaries, or early O-type stars) some of the parameters could not be properly determined.

While details on individual stars are quoted in Tables B.4 and B.5, Table 5.1 presents the global summary of the number of stars comprising each of the groups associated with the various defined variability flags.

Table 5.1: Summary of the results of the spectroscopic variability assessment and the identification of singular spectroscopic features in the complete sample of O-type stars investigated in this thesis

Variability flag	C	LPV	SB1	SB2	MD	WV
# stars	79	91	59	113	99	63
Singular features	Oe	Mag	WR			
# stars	6	10	4			

415 targets in total.
528 O-type stars considering SB2 as double stars.

We remark that stars with more than 3 spectra were always flagged using one or several of the abovementioned categories, depending on the presence of clear spectroscopic signatures of binarity, wind-variability, etc; in addition, stars with less than 3 spectra were always labeled as more data needed (MD). We note however that some of the later could be also already identified as SB2 or SB1 with the available information.

The first two major differentiated groups are the spectroscopic binaries. We identified 113 double-lined systems and 59 single-line spectroscopic binaries (variability in radial velocity unlikely produced by stellar oscillations), labeled as SB2 and SB1 respectively. In total, at least ∼55% (283 out of 528[2] massive stars) of our sample can be considered as part of a multiple system. In parallel, we assigned two different flags related to the spectroscopic variability not originated by binarity effects: Line-Profile-Variability (LPV) and Wind-Variability (WV). We identified 91 LPV stars, and 63 WV stars. Approximately 40% of the whole sample presents this kind of variability in the spectra. Last, 79 stars were found with no clear variation in radial velocity or shape of the line profile, and labeled as C. While we initially consider these 79 stars as likely single, investigations including a larger number of multi-epoch observations may modify this classification, highlighting the binary status of some of them. As a plus in our spectroscopic variability assessment, we could also identify stars showing some peculiar features in the spectrum. In particular, we found 6 Oe stars, 10 stars with a detected magnetic field[3] (see Sect. 5.3.3), and 4 Wolf-Rayet stars.

[2] 528 considering SB2 as double stars.
[3] Magnetic stars were considered as such only when confirmed by the Magnetism in Massive Stars (MiMeS) study (Wade et al. 2016; Grunhut et al. 2017).

5.3.1 Multiplicity

The fraction of massive stars that appears in isolation or in a multiple system has been the object of study in the last years through a series of dedicated papers (Mason et al. 2009; Sana & Evans 2011; Chini et al. 2012; Sana 2013; Sana et al. 2014; Kobulnicky et al. 2014; Sota et al. 2014; Aldoretta et al. 2015; Almeida et al. 2015, 2017; Barbá et al. 2017; Sana 2017). These studies are fundamentally performed using three different observational techniques: spectroscopy, imaging, and interferometry. The final result of the studies of binarity in the massive star domain trough spectroscopy concurs in percentages of massive stars in multiple systems in the Galaxy and the LMC between 50-70%. This percentage is in good agreement with our results from the spectroscopic assessment of binarity in the sample of Galactic O-type stars surveyed by IACOB and OWN, with $\sim 55\%$ of stars in a binary or higher-multiplicity system.

Noteworthy, Sana (2017) reviewed the observational bias and corrections necessary to provide a real estimate of the percentage of stars affected by binary interaction in their life-time. They found that, when empirical information obtained from interferometry is included and the observational biases corrected, the binarity fraction of O-type stars increases up to 91%. This means that, despite our intention to eliminate binary stars from the sample to provide only accurate spectroscopic parameters, there is a percentage of stars that may be still affected by undetected companions.

5.3.2 Line-Profile- and Wind-Variability

From the spectroscopic analysis of the multiple epochs of each star we were able to flag stars with line-profile-variability as LPV or with wind-variability as WV. LPVs can be distinguished from radial velocity variations associated with a SB1 stars because of the different behavior of the shape of the line-profile. The origin of the line-profile variability in the O star domain is not entirely understood, but asteroseismology studies have often related it to high-order mode oscillations (Aerts et al. 2008, 2010, 2014; Simón-Díaz et al. 2010), or surface motions driven by the presence of subsurface convection zones or internal gravity waves (Grassitelli et al. 2015; Aerts et al. 2017).

The detected variability in the wind diagnostic lines is likely related to the intrinsic stochastic nature of the line-driven winds developed in these extreme stars. The opacity fluctuations due to several inhomogeneities in the atmosphere of the star, such as the clumping over-densities (Kudritzki & Puls 2000), or the rotational modulation of large scale wind structures (Puls et al.

2008), are the most likely origin of these variations.

Fullerton et al. (1996) performed a study of the occurrence of line-profile-variability in O-type stars and found (using a limited sample of 30 stars) that 77±16% of the analyzed sample was affected by this type of variability. The study by Fullerton et al. was based on a Temporal-Variance-Spectrum (TVS) system which was able to provide several quantitative measures (signal compare to continuum, equivalent width, etc) using mainly C IV lines and the He II λ5875 line[4]. In our sample of 302 stars, excluding the 113 SB2 stars, only 30% of the stars are labeled as LPV, in strong disagreement with Fullerton's study. The origin of this discrepancy could be double. On the one hand, the sample used in their study is limited to 30 stars, with ∼40% of them having suspected signatures of spectroscopic binarity. On the other hand, our study separates the stars with a line-profile variability detected in the main wind-diagnostic lines (WV stars) from that occurring in purely photospheric lines (LPV). If we add together both categories we end up with 55% of the stars not identified as SB2 having signatures of line-profile variability, which is closer to the study by Fullerton.

5.3.3 Peculiar stars

As explained in Negueruela et al. (2004), Oe stars show emission in the Balmer lines, but not in He II λ4686 or any N III lines. They represent the natural continuation of the Be stars towards higher masses. There is a strong correlation between fast rotation and the Be phenomenon, manifested clearly when examining the Ω/Ω_{crit} factor[5]. Due to the evolution of this ratio for massive (M>15 $M_\odot$) stars, decreasing in their lifetime because of the strong winds (Meynet & Maeder 2000), it is expected a decline in the fractions of Be for spectral types earlier than B0 (Oe stars). The percentage of Be stars between B0-B1 reaches 10−15% (Zorec & Briot 1997), and in our sample we have only 6 Oe stars, which implies a percentage of 1.5−2.5%, depending on whether SB2 stars are considered to compute the total number of stars. The Oe effect is also more scarce towards earlier spectral types. Half of our Oe stars present spectral types later than O8, and all of them are later than O6. This effect has been proposed to come from the presence of the winds disrupting the Oe phenomenon, or the different evolution of angular momentum in fast rotators of moderate and high mass (Meynet & Maeder 2000). In addition, 4 Oe in the sample are cataloged as SB1 stars, and could have been sped up to high rotational velocities because

[4]This line could appear with some emission refill in case of extremely strong winds.

[5]The surface angular velocity as a fraction of the critical breakup velocity. When the factor Ω/Ω_{crit} approach unity the stars develop higher emissions.

of mass transfer (de Mink et al. 2013). The extreme rotation present in Oe stars causes the strong dilution of the metallic diagnostic lines, needed for an accurate determination of the line-broadening parameters (see Sect. 3.3.1), and even of the He I-II ionization balance, from which other spectroscopic parameters such as $T_{\rm eff}$, $\log g$, $Y_{\rm He}$, and $\xi_{\rm t}$ are inferred (Sect. 3.3.3). In some cases the lines may be contaminated by the double-peak emission from a circumstellar disk of material. As a consequence, the parameters obtained from the IACOB-GBAT spectroscopic analysis of Oe stars are considered not valid in most cases, and hence not provided in the tables (see Sect. 5.4).

The spectra of stars affected by a strong magnetic field are normally characterized by the presence of peculiar profiles in magnetic sensitive lines (Howarth et al. 2007; Donati & Landstreet 2009; Martins et al. 2012; Castro et al. 2015). These include, among others, inverse P-Cygni profiles or unexpected strong emission in the wind-related diagnostic lines (and/or even sometimes in photospheric lines). These features are normally not reproducible by our FASTWIND models, and the parameters obtained in the quantitative spectroscopic analysis of 8 of these stars, including one SB2 star, are considered not valid and discarded from the diagrams presented through this thesis (see Table B.5). Dedicated spectroscopic surveys such as MiMeS (Wade et al. 2016) and BOB (Morel et al. 2014) have found that only a small fraction ($\sim$10%) of massive stars exists with strong evidence of magnetic field. The percentage of magnetic stars identified in our sample ($\approx$ 3%, 10 magnetic stars) is much lower than this percentage. We would expect at least to find $\sim$30 magnetic stars in the sample, excluding the SB2. We always use the MiMeS survey (Wade et al. 2016) as a confirmation to label a star as magnetic. Their results yield that 6 (and possibly 3 more), of a more limited sample of 108 O-type stars, present a magnetic field of at least 50 G, obtained with the LSD line-cumulative method (Grunhut et al. 2017). The difference in the percentages of magnetic massive stars between their study and ours could then simply be due to the absence of magnetic detection capabilities in our study, and the absence of many of the plausible magnetic stars in our study in their more limited sample.

Wolf-Rayet (WR) stars are known to be the very advanced stages of the life of massive stars (Conti & Frost 1976) with a faint continuum and strong broad emission lines. Due to the strong winds present in their atmosphere we are unable to construct FASTWIND models to predict their spectra. The 4 WR stars in our sample were discarded for the quantitative spectroscopic analysis.

5.4 Quantitative spectroscopic analysis: results

The results of the quantitative spectroscopic analysis of those 285 stars for which we could obtain meaningful results from the IACOB-BROAD and/or IACOB-GBAT analysis are included in Tables B.4 and B.5. In particular, Table B.4 presents the 128 available O-type standard stars for spectral classification, studied in the previous chapter, and Table B.5 the remaining 157 stars. These tables are complemented with Tables B.6, and B.7, where we list those stars identified as SB2 or WR, respectively.

We note that all the information included in Tables B.4 and B.5 is directly obtained from the analysis or inspection of the available spectra except for $\log g_{\rm true}$, the gravity corrected from centrifugal acceleration. In this case we used the calibrations presented in Martins et al. (2005), combined with the spectral classification associated with each star to obtain information about the stellar radii, needed to compute the centrifugal correction (Herrero et al. 1992; Repolust et al. 2004). In the tables, in addition to the line-broadening and spectroscopic parameters and their associated uncertainties (whenever available), we quote the spectral classification of the stars (following Maíz Apellániz et al. 2016), the flag indicating the quality of the final fit resulting from the quantitative spectroscopic analysis (see Sect. 5.4.2), and the type of variability detected from inspection of the multi-epoch spectra available in the IACOB and OWN surveys (see Sect. 5.3).

Tables B.4 and B.5 are complemented with Figs. C.1 to C.51, where we show, for each of the analyzed spectra, the overall agreement between the best fitting FASTWIND model and the observed spectrum for all diagnostic lines considered in the spectroscopic analysis.

5.4.1 IACOB-BROAD analysis: results

Information about the derived $v \sin i$ and $v_{\rm mac}$ for those stars not identified as SB2 and/or WR can be found in columns 3 and 4 of Tables B.4 and B.5. As explained in Chapt. 3, the IACOB-BROAD tool (Simón-Díaz & Herrero 2014) was used to obtain $v \sin i$ and $v_{\rm mac}$ for each star by means of a combined Fourier transform (FT) + Goodness of fit (GOF) analysis. We rely mostly on the O III λ5592 line (90% cases) and used alternative spectral lines on the case that the comparison between the two methods (FT and GOF) give discrepancies larger than 20 $\rm km\,s^{-1}$ (see Chapt. 6 for more details about the final set of considered diagnostic lines).

As stated in Chapt. 3, the final values considered for the quantitative spectroscopic analysis with IACOB-GBAT (see next section) are the pair $v \sin i - v_{\rm mac}$

quoted in Tables B.4 and B.5.

5.4.2 IACOB-GBAT analysis: results

The complete set of spectroscopic parameters ($T_{\rm eff}$, $\log g$, $Y_{\rm He}$, $\xi_{\rm t}$, plus the associated uncertainties) resulting from the IACOB-GBAT analysis of the 285 stars not identified as SB2 and/or WR can be found in Tables B.4 and B.5. In the last column of these tables we also indicate one of the quality flags described in Sect. 3.3.3 (see also below).

These quality flags are a result of a visual assessment of the final fit between the observed and the best fitting spectrum provided by IACOB-GBAT for each individual analysis, and represents an integral part of our analysis strategy (See Chapt. 3).

Table 5.2: Summary of the results of the IACOB-GBAT spectroscopic analysis

Quality flag	Q1	Q2	Q3	Q4
# stars	167	50	58	10

Table 5.2 presents a summary of the number of stars cataloged with each of these quality flags. As indicated in this Table, we could obtain good fits (Q1) for more than half of the sample (∼60%). In addition, we found that 108 stars present a certain mismatch between the final best fitting FASTWIND models and the observed spectrum that may compromise the calculation of the stellar wind parameters (Q2-Q3). Lastly, for 10 early-type stars IACOB-GBAT did not provide reliable estimates of $T_{\rm eff}$ due to absence of He I lines in the spectra (Q4).

As an initial remark, we warn that labeling a given result from IACOB-GBAT as Q1 does not necessarily imply that the star is single. We have found seven cases where, after obtaining a Q1 fit in the analysis, the multi-epoch study has allowed us to identify the star as SB2. In these cases the analyzed single snapshot spectrum[6] does not show any obvious signature of dealing with a composite spectrum, and the final outcome from IACOB-GBAT (in terms of quality of the global fit) is almost perfect. This reinforces our suggestion to incorporate – as an important ingredient – the information provided by multi-epoch observations to the stellar parameter determination process (See Sect. 3.2).

Q2 were defined as stars showing peculiar double-peak or inverse P-Cygni

[6] We recall that our only criterion to select the spectrum to be analyzed with IACOB-GBAT is having the largest S/N among the available spectra for a given target.

profile in He II λ4686 (See Sect. 3.3.3). The most likely explanation of the observed behavior of the He II λ4686 line in the stars flagged as Q2 is the presence of a stellar disk or other type of emitting material surrounding the star. High rotation, the coupling of the magnetic field and the stellar wind (e.g., Breysacher & François 2000; ud-Doula & Owocki 2002; Martins et al. 2015a; Castro et al. 2017), and/or binary interaction (e.g., Teodoro et al. 2016) can give origin to the occurrence of this type of large scale circumstellar structures. These are two clear situations in which He II λ4686 should not be used as diagnostic line for defining the luminosity class and/or determining the wind-strength Q-parameter (i.e., the mass loss rate) of the star.

Q3 stars are defined as those in which a simultaneous fit to the Hα and He II λ4686 lines cannot be achieved by means of our grid of unclumped models. In these cases, IACOB-GBAT tries to find a compromise between all the diagnostic lines that provide information about the stellar wind (mainly Hα and He II λ4686, but also H$_\beta$ and He I λ5875), and ends up (normally) with an intermediate value of the wind-strength Q-parameter (see Fig. 3.11). There are several effects that could explain this result, all of them related to limitations in the modeling strategy adopted in this work (which is based on spherically symmetric unclumped wind models, see Sect.5.6.3).

Results presented in Tables B.4 and B.5 must be taken with care for stars not flagged as Q1 (good fit). In particular, we note that this table does include the resulting parameters of the IACOB-GBAT analysis for those stars labeled as Q4. These stars are early O-type stars and, as already mentioned elsewhere (e.g., Rivero González et al. 2012), these objects require the use of nitrogen lines to obtain a more reliable effective temperature (and hence the complete set of parameters). Their spectroscopic results are then not considered for the discussion in this chapter, except for the $v \sin i$ and $v_{\rm mac}$ values, which are not affected. Regarding the reliability of the parameters provided in Tables B.4 and B.5 for stars flagged as Q2 or Q3, we refer the reader to notes above and in Sect. 4.4.2.

5.5 General properties of the sample

In this section we use the results of our homogeneous IACOB-BROAD and IACOB-GBAT spectroscopic analysis (summarized in Tables B.4 and B.5, and described in Sects. 5.3 and 5.4) to describe the global properties of the sample. To this aim, we display the results in several diagnostic diagrams. We remark that the stars labeled as Q4 (no He I lines available), the SB2 stars, and 17 peculiar stars (i.e. Wolf-Rayet, Oe, and 7 magnetic stars) have been excluded from the figures. As a consequence, the final sample of stars discussed in this section

comprises 275 targets.

5.5.1 Kiel and spectroscopic HR diagrams

Figure 5.1 presents the location of the sample of 275 O-type stars in the $\log g$ – $T_{\rm eff}$ (Kiel) diagram and the spectroscopic HR (sHR) diagram[7] (Langer & Kudritzki 2014). Both diagrams also include the Geneva non-rotating evolutionary tracks for solar metallicity (Ekström et al. 2012; Georgy et al. 2013) for reference purposes.

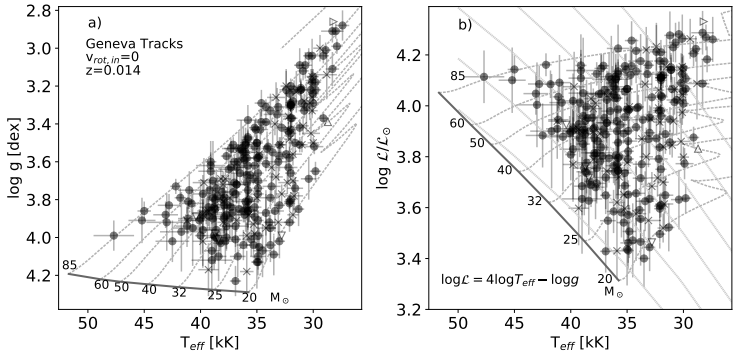

Figure 5.1: Location of 275 of the stars in our sample in the Kiel (*left*) and spectroscopic HR (*right*) diagrams. Cross symbols indicate stars for which we have detected clear or likely signatures of spectroscopic binarity. Open symbols are stars for which only upper or lower limits in any of the two parameters used to construct these diagrams ($T_{\rm eff}$ and $\log g$) could be obtained. Individual uncertainties are included as error bars. Evolutionary tracks and position of the ZAMS from the non-rotating, solar metallicity models by Ekström et al. (2012) and Georgy et al. (2013) are included for references. The dotted diagonal lines in the sHR diagram are the isocontours of constant gravity. We note that neither early O-type stars flagged as Q4, nor peculiar and SB2 stars are included in the figures.

[7]The idea of the sHR diagram (presented in Langer & Kudritzki 2014) is to replace the luminosity (L) with the quantity $\mathcal{L} = T_{\rm eff}^4/g$, which is the inverse of the flux-weighted gravity introduced by Kudritzki et al. (2003). It depends only on those variables that can be directly derived from stellar spectra without knowledge of the stellar distance or the extinction. It presents horizontal stellar evolutionary tracks for massive stars and allows for a direct comparison with the Eddington factor, as $\mathcal{L} \sim \Gamma_e$. This is particularly useful for massive stars, where the Eddington factor is not extremely small anymore and can approach values close to unity.

As already stated elsewhere (see, e.g., Repolust et al. 2004; Markova et al. 2014; Martins et al. 2015a), the O-type stars mostly concentrate between the 20 and 85 $M_\odot$ evolutionary tracks, and are located within the main sequence (if we use non-rotating models as reference).

The expected good coverage of the complete O star domain is challenged by the lack of stars close to the zero age main sequence (ZAMS) above $\sim$25 $M_\odot$. The existence of this empirical gap, already highlighted in several papers dealing with samples of relatively small size, is becoming more and more evident with the increase in the number of O-type stars analyzed spectroscopically (see, e.g., Herrero et al. 1992; Repolust et al. 2004; Martins et al. 2005; Herrero et al. 2007; Simón-Díaz & Herrero 2014; Castro et al. 2014; Sabín-Sanjulián et al. 2017; Holgado et al. 2018). Therefore, the absence of stars in this region of the Kiel and sHR diagram seems to be a general observational characteristic of massive stars. A more detailed discussion of this result, including some notes on several hypotheses of their plausible origin, will be presented in Sect. 5.6.2.

As for the binaries in the sample, the stars which are single-line spectroscopic binaries (cross symbols) are not located in a specific region of the diagrams; instead, they can be found everywhere in the O star domain.

Figure 5.2 shows again the whole sample in the sHR diagram but, this time, color-coded as a function of luminosity class (left panel) and spectral type (right panel). From inspection of the left panel it becomes clear that, in the O star domain, the separation between luminosity classes in the sHR diagram is not defined by strict boundaries but, instead, there are many overlapping regions in which stars with different luminosity classes have similar effective temperatures and gravities.

In addition, the combination of information provided in the two panels of Fig. 5.2 serves us to also illustrate the well-known trends of effective temperature with spectral types and luminosity class, how the various luminosity classes are more clearly separated in terms of stellar parameters in the late O-type star domain, and the intrinsic scatter in $T_{\rm eff}$ and $\log g$ expected for any given combination of spectral type and luminosity class.

The subsample of stars labeled with filled yellow squares in the left panel of Fig. 5.2 are the so-called Vz stars. The Vz phenomenon is a spectroscopic peculiarity defined by a stronger He II 4686 absorption, relative to other He lines, compared to that found in typical class V spectra (Walborn 2009). This spectroscopic feature was originally proposed to be a clear indication of youth, and hence proximity to the ZAMS; however, as thoroughly discussed in Sabín-Sanjulián et al. (2014), the situation is bit more complex. In particular, these authors used a customized grid of FASTWIND models to deliver prediction on the behavior of the O Vz phenomenon as a function of $T_{\rm eff}$, $\log g$, $\log Q$, and

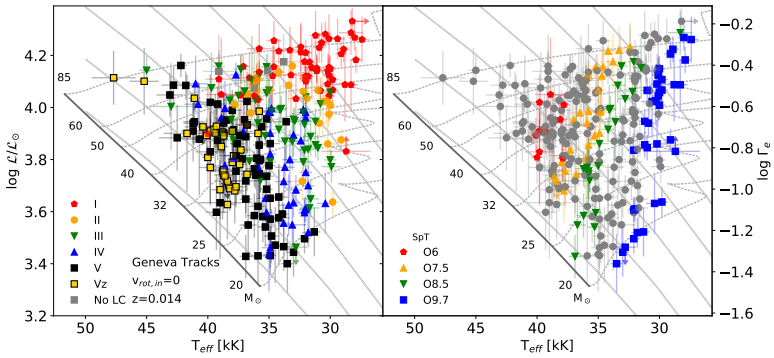

Figure 5.2: Same as right panel of Fig. 5.1, but using various colors and symbols to identify different luminosity classes (left) and specific spectral types (right). The right-hand ordinate axis displays the electron scattering Eddington factor (Γ_e). In this figure we do not differentiate between likely single stars and those targets for which we have detected clear or likely signatures of spectroscopic binarity.

$v \sin i$ and found that specific combinations of these parameters could produce a spectrum with the Vz characteristic, independently of the age or proximity to the ZAMS. Our study reinforces this argument. While O Vz stars should trace the lower boundary of the distribution of O dwarfs in the sHR diagram (if this spectroscopic feature was just and indicator of youth); they are still 0.2 dex away (in $\log g$) from the theoretical ZAMS defined by the Ekström et al. (2012) models.

5.5.2 Line-broadening parameters ($v \sin i$ and $v_{\rm mac}$)

Results from the line broadening analysis of our sample of O-type stars are discussed in this section. As described above, the SB2 stars, and 17 peculiar stars (i.e. Wolf-Rayet, Oe, and 7 magnetic stars) have been excluded from the figures and discussion presented here[8]. On the contrary, the 10 stars of the sample labeled as Q4 could be included in those diagrams in this section that only depend on the line-broadening parameters (e.g. the $v \sin i$ histograms). While the absence of He I lines prevent IACOB-GBAT to properly constraint the effective temperature of the star, the line-broadening parameters could be obtained whenever an adequate diagnostic line was available.

[8]The seven SB2 standard O-type stars evaluated in Chapt. 4 are not excluded.

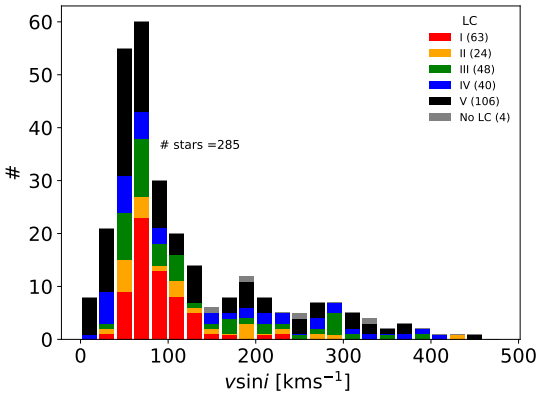

Figure 5.3: Distribution of $v \sin i$ in the sample, excluding stars flagged as SB2 and peculiar stars. Different colors have been assigned to different luminosity classes.

Figure 5.3 presents the distribution of projected rotational velocities of the sample of 285 O-type stars considered in this section in the form of histogram. The sample is divided in the different luminosity classes. Generally speaking, the distribution peaks around 40-80 km s^{-1} and covers a range in $v \sin i$ between ∼10 and 440 km s^{-1}. The main difference between the distribution of projected rotational velocities for the various luminosity class groups refers to the covered range of $v \sin i$ values. Supergiants are mostly concentrated in the 40-150 km s^{-1} range, while dwarfs spread all over the aforementioned range. This difference could be explained by two effects. The limit in the detection of low $v \sin i$ stars among the supergiants could be an artifact of the Fourier analysis method, limited by the higher microturbulence velocities expected for these stars (Simón-Díaz & Herrero 2014). The extended high $v \sin i$ tail in the V class stars can be explained in terms of evolution. Critical velocity for supergiants is intrinsically lower, due to the lower gravity value, and the weaker winds expected for stars lower than 40 $M_\odot$, where the majority of our V stars correspond (see Fig. 5.6, in next section), are not expected to produce a pronounced loss of angular momentum and the subsequent spin down (Vink et al. 2010).

A more extensive discussion of results regarding rotational velocities in our sample of O-type stars can be found in Chapter 6. This section has included

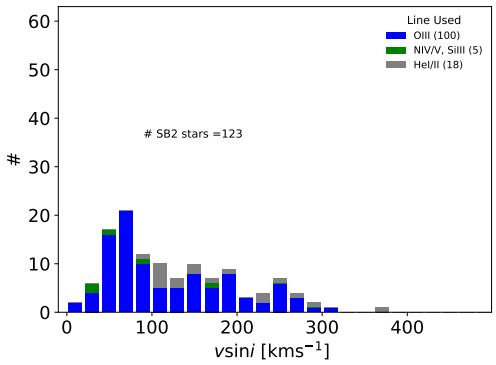

Figure 5.4: $v \sin i$ histogram of the sample of SB2 stars. Different colors are used depending on the diagnostic line used in the line-broadening analysis.

the general description of the whole population excluding the SB2 stars.

A short note on SB2 and peculiar stars

As stated in Sect. 3.3.1, the SB2 stars were not initially considered for the line-broadening analysis. The impossibility to disentangle the two components prevents an accurate determination of the line-broadening parameters in any of the two components of the binary system. Nevertheless, with the purpose of studying the effect of including SB2 $v \sin i$ measures in the results, we determine here for each SB2 star a unique value of the $v \sin i$ measuring one diagnostic line. This is a meaningless measure for either star, but represents an upper limit for the components of the system. The derived $v \sin i$ value comes from considering a pure rotational profile, without considering the broadening component of the *macroturbulence*.

The $v \sin i$ results for the 113 SB2 stars are presented in Fig. 5.4. With this distribution we want to highlight that the inclusion of the $v \sin i$ results for the SB2 stars in any sample will enhance the number of stars with intermediate $v \sin i$ values (100-200 km s^{-1}) as well as the tail of fast rotators with velocities over 200 km s^{-1}.

As a final note, projected rotational velocities for 20 peculiar stars (6 Oe, 4 WR, and 10 magnetic) of the sample are included in table B.5, and in Fig. 5.5 in contrast to the whole sample distribution. Magnetic stars are expected to

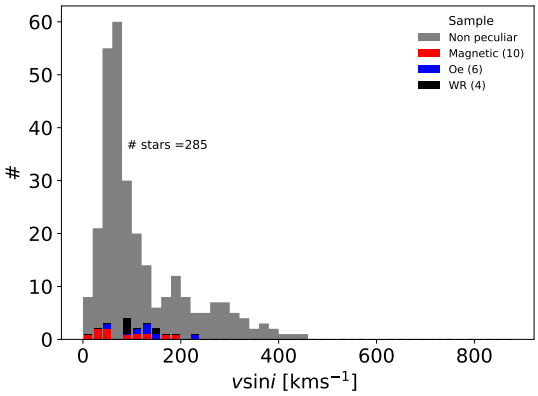

Figure 5.5: Distribution of the $v \sin i$ of peculiar stars in the sample, in comparison with the full sample. Different colors have been assigned to different peculiar stars.

present a distinct $v \sin i$ distribution when compared with the global sample (ud-Doula & Owocki 2002; Grunhut et al. 2017). The coupling between magnetic fields and winds could enhance the mass-loss and induce an extra-braking effect. Regrettably, the number of magnetic stars in our sample is not enough to study them with appropriate statistics as a differentiated subsample.

Line-broadening parameters ($v \sin i$ and $v_{\rm mac}$) in the sHR diagram

Figure 5.6 presents again the location of the 275 O-type stars considered in this section in the sHR diagram. In the left-hand panel the sample is color-coded as a function of $v \sin i$. At first glance there are no clear boundaries in the distribution of stars depending on the $v \sin i$, but the scarcity of very slow or very fast rotators stars above the 32 $M_{\odot}$ evolutionary track is worth noticing. This and other results related to rotation are further discussed in Chapter 6.

In the right panel of Fig. 5.6 the sample is colored as a function of $v_{\rm mac}$. Again, no clear separation between stars in the different $v_{\rm mac}$ bins is found. We only highlight that stars for which the lower values of $v_{\rm mac}$ ($<$50 km s^{-1}) have been derived seems to concentrate below the 32 $M_{\odot}$ evolutionary track, while those stars showing larger values of $v_{\rm mac}$ ($>$100 km s^{-1}) are only found above this track. Our results basically mimic those presented and discussed in Simón-Díaz et al. (2017).

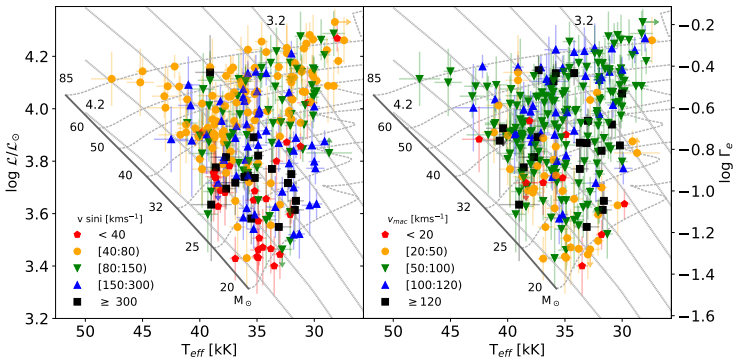

Figure 5.6: Same as right panel of Fig. 5.1, but using various colors and symbols to identify different $v \sin i$ values (left) and $v_{\rm mac}$ values (right).The right-hand ordinate axis displays the electron scattering Eddington factor (Γ_e). In this figure we do not differentiate between likely single stars and those targets for which we have detected clear or likely signatures of spectroscopic binarity.

The extra source of line broadening found in OB stars, here referred as macroturbulence ($v_{\rm mac}$), has been often proposed to be related to the collective broadening effect produced by stellar oscillations (Lucy 1976; Howarth 2004; Aerts et al. 2010). The origin of these oscillations has been suggested to be connected simultaneously to different phenomena. The two main hypothesis are pulsation modes associated with a heat-driven mechanism (Aerts et al. 2014; Simón-Díaz et al. 2017); or surface motions initiated by internal gravity waves or turbulent pressure instabilities in subsurface convection zones or the boundary core-envelope (Grassitelli et al. 2015; Aerts et al. 2017). As pointed out by Simón-Díaz et al. (2017), it is possible that the real origin is a combination of both to some degree. Within the IACOB project, in Simón-Díaz et al. (2017); Godart et al. (2017), $v_{\rm mac}$ empirical results of a sample of O-type stars are compared to the instability strips generated by the heat-driven non-radial modes activated by the $\kappa-mechanism$ in the iron opacity bump. They found that the inclusion of higher degree modes helps to find a better correlation between the $v_{\rm mac}$ results and zones with expected oscillations. In addition, they compare the $v_{\rm mac}$ results with the expected behavior of the turbulent pressure and found a very good correlation between these two quantities for the upper part of the sHR diagram, as already pointed out by Grassitelli et al. (2015).

5.5.3 Helium abundance

CNO and Helium surface abundances in the star are important observables. They trace the evolution of the star when mixing processes, related to rotational effects, are able to dredge-up processed material to the surface (Meynet & Maeder 2000; Hunter et al. 2011; Kudritzki et al. 2003). Our work tracks the observed surface Helium abundance as $Y_{\rm He}$[9]. Classically, both models and observational studies have coincide, with standard values of helium abundance ratio (0.08-0.12) for the majority of stars in the beginning-mid main sequence.

Figure 5.7 shows the distribution of helium abundances of our sample of O-type stars in the sHR diagram. We separate the sample in four abundance bins using different symbols and colors. Basically, we consider as stars with normal He abundance those having $Y_{\rm He} = 0.08 \pm 0.02$ (yellow circles) and then distinguish between slightly ($Y_{\rm He} = 0.12 - 0.15$, green triangles) and highly ($Y_{\rm He} > 0.15$, black squares) enriched stars in helium. Finally, the fourth bin comprises stars with helium abundances below the commonly considered baseline for massive stars ($Y_{\rm He} < 0.08$, red pentagons).

A complementary view is presented in Fig. 5.8, connecting the derived helium abundances with the $v \sin i$ values for each star, and separating the sample in the various luminosity class groups. We highlight the following main points regarding helium abundances in the sample of Galactic O-type stars:

- More than half of the targets have what we have called standard helium abundances. This subgroup of stars is distributed all around the O star domain and covers the whole range of projected rotational velocities.
- Among the stars with clear He enrichment we mainly find O supergiants and bright giants with masses above $\sim$40 $M_\odot$. This is consider the standard enrichment due to evolution. We note, however, that a similar number of O stars with luminosity classes I and II are found to have normal helium abundances.
- Many dwarfs and giants have $Y_{\rm He} > 0.12$, expanding in all the range of $v \sin i$. Only a few of them are O dwarfs labeled as SB1. The presence of these enriched stars close to the ZAMS is not easily explicable with the current paradigm of rotational mixing of single stars.
- Regarding the stars for which the IACOB-GBAT analysis has resulted in He abundances below 0.08, most of them are either slow rotators giants or relatively evolved dwarfs. They present, to some degree, a distribution in

[9] $Y_{\rm He} = N({\rm He})/N({\rm H})$

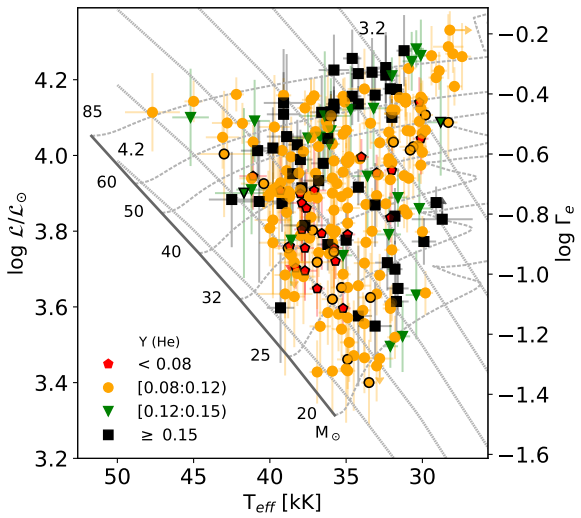

Figure 5.7: Same as right panel of Fig. 5.1, but using various colors and symbols to identify ranges of values of the Helium abundance. The right-hand ordinate axis displays the electron scattering Eddington factor (Γ_e). Stars for which it was only possible to obtain upper or lower limits for the Helium abundance are indicated by symbols with the border in black. The range in the legend corresponds to the central value in case of a well-determined value, or to the upper or lower limit otherwise. In this figure we do not differentiate between likely single stars and those targets for which we have detected clear or likely signatures of spectroscopic binarity.

the sHR diagram. Sometimes, the presence of this low abundances could be a consequence of an undetected companion in the spectra, diluting the He lines in the global spectrum (resulting in lower $Y_{\rm He}$ abundances than expected). The only three O supergiants and bright giants with $Y_{\rm He} < 0.08$ have been found to be spectroscopic binaries.

- The giants in the sample follow the expected behavior of enrichment due to to rotational mixing, which states higher helium abundances for the fastest rotators (Maeder 1987; Langer 1992; Denissenkov 1994; Herrero & Villamariz 1999).

- The giants and dwarfs with He excess and a $v \sin i$ below 100 km s^{-1} could

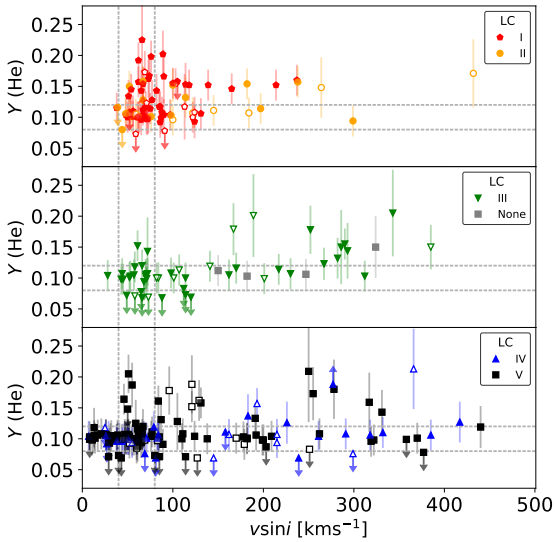

Figure 5.8: Helium abundance as a function of projected rotational velocity for the Galactic O-type stars. Upper and lower limits are represented by arrows. Different colors and shapes represent luminosity classes. Open symbols indicate stars for which we have detected clear or likely signatures of spectroscopic binarity. Dashed gray lines delimit the range of values in $v \sin i$ and $Y_{\rm He}$ in which most of the stars are concentrated: $50-100$ km s^{-1} and $0.08-0.12$, respectively.

be interpreted in different ways, as stated in Sabín-Sanjulián et al. (2017). First, these stars could simply be rotating at higher velocities due to projection effects, a proper deconvolution is not possible for all these stars and such a task is is out of the scope of this work. Second, the enhanced He abundances could indicate a binary origin for these stars, increasing their He abundance by means of mass transfer from a companion (Hunter et al. 2008). Finally, another possibility is that they could be magnetic stars (Schneider et al. 2016). Additionally, the possibility that stellar winds may be the cause for this He excess could be discarded, since such a strong wind should generate a larger He contamination on the surface and strong features in the spectrum, comparable to the situation for WR stars.

5.5.4 Microturbulence

Recent studies link the origin of microtubulence in massive O- and B-type stars to subsurface convection caused by the iron opacity peak (Cantiello et al. 2009). However, the observational assessment of this hypothesis has been exclusively concentrated in the B-star domain. It still needs to be further evaluated in stars with higher masses, like O-type stars. The efforts devoted to investigating and empirically characterizing microturbulence in the O-star domain have been scarce since the works by McErlean et al. (1998); Smith & Howarth (1998) and Villamariz & Herrero (2000). The main reason is probably related to the fact that, in contrast to the case of early B-type stars, the number of metal lines available to determine accurate values of this parameter (e.g., using the curve of growth method) is much more limited in O stars. Some information can be obtained from the study of the He lines; however, as illustrated by the outcome of our IACOB-GBAT spectroscopic analysis, this is a hard task, since one can only obtain lower or upper limits for this parameter in most cases (see Table B.5).

As a consequence, most of the quantitative spectroscopic analyses of O-type stars consider microturbulence as a fixed parameter (see, e.g., Herrero et al. 2002; Repolust et al. 2004; Markova et al. 2014). Only a few works have recently started to leave microturbulence as a free parameter (e.g., Mokiem et al. 2005; Sabín-Sanjulián et al. 2014; Ramírez-Agudelo et al. 2017); however, the quality and wavelength coverage of the spectra considered in those studies are more limited than in our case.

The Fig. 5.9 shows the distribution in the sHR diagram of the values of microturbulence resulting from the IACOB-GBAT analysis of the sample of O-type stars investigated here. For 76% of the stars we were not able to even restraint the ξ_t value using all our grid of values, we could only determine upper or lower limits. This highlights the necessity to extend the range of microturbulence values in our grids (toward higher values) and, in addition, the inherent limitations of the use of He lines for the determination of microturbulence.

As previously outlined by Massey et al. (2013), O stars, particularly supergiants, systematically imply quite a high value of microturbulence. We find that there is a non negligible number of dwarfs in the whole O star domain with relatively high values of microturbulence. This may have important consequences for the reliability of the projected rotational velocities determined using FT techniques, as discussed by Simón-Díaz & Herrero (2014), and might explain why we are still empirically detecting certain thresholds in the measured values of $v \sin i$ for O-type star (See more in Sect. 6.3.2).

We note that the lower values of ξ_t concentrate below the 32 $M_\odot$ evolu-

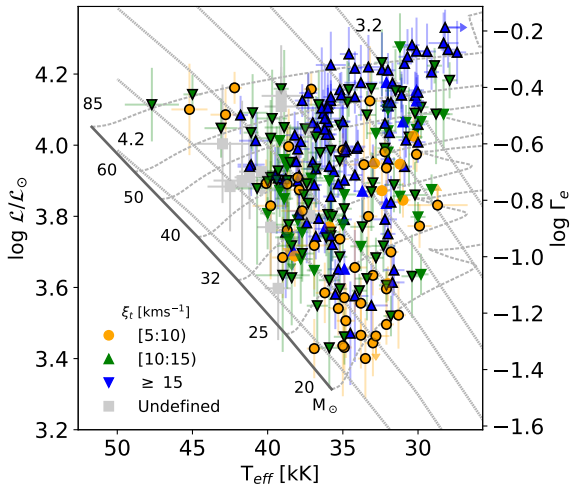

Figure 5.9: Same as right panel of Fig. 5.1, but using various colors and symbols to identify ranges of values of the ξ_t. The right-hand ordinate axis displays the electron scattering Eddington factor (Γ_e). Stars for which it was only possible to obtain upper or lower limits for the Helium abundance are indicated by symbols with the border in black. The range in the legend corresponds to the central value in case of a well-determined value, or to the upper or lower limit otherwise. In this figure we do not differentiate between likely single stars and those targets for which we have detected clear or likely signatures of spectroscopic binarity.

tionary track, but again the sample there presents values in all ranges and a majority of completely undetermined limits results due to degeneration. Interestingly, the vast majority of them are forming the envelope of the distribution which is closer to the ZAMS.

A more detailed investigation of microturbulence in O stars, exploring the availability of other diagnostic lines better suited to obtain more accurate estimations of this parameter is one important line of future work. As indicated by Markova et al. (2018), a proper treatment of turbulence in the modeling of O-type stars might be of ultimate importance for a proper characterization of the density structure of the stellar photosphere.

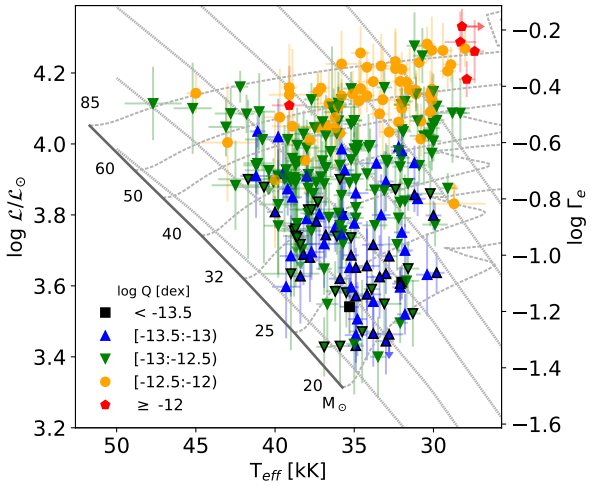

Figure 5.10: Same as right panel of Fig. 5.1, but using various colors and symbols to identify ranges of log Q values. Stars for which it was only possible to obtain upper or lower limits for any this quantity are indicated by symbols with the border in black. The range in the legend corresponds to the central value in case of a well-determined value, or to the upper or lower limit otherwise. In this figure we do not differentiate between likely single stars and those targets for which we have detected clear or likely signatures of spectroscopic binarity.

5.5.5 Wind-strength Q-parameter

Mass-loss crucially affects the evolution and fate of a massive star, while the momentum and energy expelled contribute to the dynamics and energetics of the ISM (Vink et al. 2001; Kudritzki & Puls 2000; Puls et al. 2005; Mokiem et al. 2005; Groh et al. 2013). Stellar winds have pronounced effects on the physics of hot star atmospheres dominating the density distribution and the radiative transfer, and modifying the chemical profile, surface abundances and the spectral energy distribution. Our estimates of O mass-loss rates are obtained from optical line profiles of wind-sensitive diagnostic lines, mainly Hα and He II λ4686, via the wind-strength parameter log Q (See Chapt. 3).

Fig. 5.10 shows the distribution of the wind-strength Q-parameter in the sHR diagram. The figure includes stars for which IACOB-GBAT only provides upper limits for the value of log Q. As expected, these mainly refer to stars

with $\log \mathcal{L}/\mathcal{L}_\odot \lesssim 3.8$ and $\log g > 3.8$ [dex] (i.e., the late O dwarfs). Those stars present very weak winds that only produce very subtle effects on the pure (photospheric) absorption line profiles of Hα and He IIλ4686. We note that the error bars associated with $\log Q$ shown in Fig. 5.10 only reflect the uncertainties in this parameter obtained during the IACOB-GBAT fitting process. Other sources of uncertainties resulting from the discrepancies between the terminal velocities assumed in the grid of FASTWIND models coupled with IACOB-GBAT and the actual values of this parameter for each analyzed target (see notes in Appendix A.5) are not considered. Inspection of this diagram indicates a positive correlation between $\log Q$ and $\log \mathcal{L}$ which will be studied in depth in Sect. 5.6.1.

5.5.6 Line-Profile- and Wind-Variability in the sHR diagram

Figure 5.11 presents the location of the stars from our sample of likely-single and SB1 stars labeled as as Wind-Variable (WV) (55), and stars with Line-Profile-Variability (LPV) (86). LPV stars appear distributed in all the area covered by the general sample of Galactic O-type stars, although the density of the relative distribution of these stars (compared with the global sample) seems to be higher above the 32 $M_\odot$ evolutionary track. The figure also shows a clear concentration of WV stars in the area of supergiants and bright giants. Most of the targets with detected WV correspond to luminosity classes I and II (all spectral types) with a few of them found among early type stars with luminosity classes III, IV, and V. The two WV stars that are separated from the rest, near the 20 $M_\odot$ evolutionary track, are HD 57682 (O9.2 IV) and HD 54879 (O9.7 V). Both have a value of $v \sin i$ extremely low (7 and 8, respectively) and are considered magnetic stars, a plausible explanation for its remarkably strong Hα line in emission, not expected in this region of the HR diagram (Castro et al. 2014).

As discussed in Sect. 5.3, Fullerton et al. (1996) conducted a similar study of the occurrence of line-profile variability in the O star domain, and presented the distribution of 33 O-type stars with variability in the HR diagram, comparing with domains of radial instability for massive stars calculated in Kiriakidis et al. (1993). Their results, like ours, reveal a good agreement with the domains in Kiriakidis et al. (1993), a greater probability of variability in more massive and evolved stars. In particular, the temperature range provided in Kiriakidis et al. (1993) matches greatly with the area covered by our sample of WV stars. However, the comparison of more specific results did not match so perfectly, and Fullerton et al. (1996) also found a pair of less luminous and less massive stars near the ZAMS with signs of variability in an area that Kiriakidis et al.

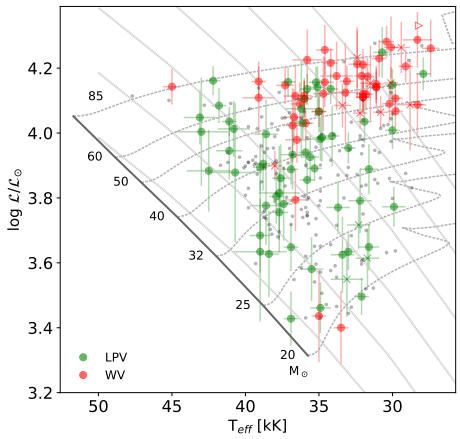

Figure 5.11: Same as right panel of Fig. 5.1 but locating the LPV and WV stars in our sample in comparison with the whole sample of Galactic O-type stars (small symbols).

(1993) could not predict. More recent studies indicate that our WV stars are located in the region where heat-driven p- and g-modes are expected to be efficiently excited (Godart et al. 2017). Meanwhile, the variability detected in stars closer to the ZAMS could be due to other type of stellar oscillations (e.g., turbulent pressure due to sub-surface convection zones, internal gravity waves Grassitelli et al. 2015; Aerts et al. 2017).

5.6 Further results from the spectroscopic analysis

In addition to the description of the general properties of the sample of 415 O-type stars presented in this chapter, we have also used the results of the spectroscopic analysis of the full sample to investigate four other topics of interest in the field of massive stars. Three of them are described in this section. The fourth one, due to its extension and importance, is presented in a separated chapter (see Chapt. 6).

5.6.1 A distance independent test of the Wind-momentum Luminosity Relationship (WLR)

The theory of radiatively-driven winds, based on Castor et al. (1975), predicts that the modified stellar wind momentum ($D_{\rm mom} = \dot{M} v_\infty R^{0.5}$) depends directly on luminosity through the WLR (Vink 2000; Kudritzki & Puls 2000), represented as

$$\log D_{\rm mom} = x \log L/L_\odot + \log D_0, \tag{5.1}$$

where x is defined as $1/\alpha'$ being $\alpha' = \alpha - \delta$[10], and D_0 is a constant if the considered objects have the same metallicity and a similar effective number of driving lines, which, for example, is roughly valid for O-stars as discussed here (Puls et al. 1996, and references therein)[11].

At present, we lack accurate information about distances (and hence R, L, M, and $\dot{M}$) for most stars in our sample (See however Chapt. 7). This limits the possibility to compare our results with those from theory and literature using the conventional WLR. Here we concentrate on the spectroscopic results from the study of the stellar wind properties of the sample and propose two different ways to evaluate our results with respect to previous theoretical and empirical studies, using spectroscopic parameters alone (i.e. no information about distances is needed).

Purely spectroscopic approach to the WLR

Figure 5.10 depicts the distribution of the wind-strength Q-parameter in the sHR diagram. Inspection of this diagram indicates a positive correlation between log Q and log $\mathcal{L}$ which is further confirmed in Fig. 5.12. We note the use of a different color coding in each of the two related figures. While in Fig. 5.10 symbols are colored following various ranges of increasing log Q, the different colors are used in Fig. 5.12 to separate the various luminosity classes. As in previous figures, open symbols correspond to stars for which we have identified clear or likely signatures of spectroscopic binarity. In addition, as stated in Sect. 5.5.5, error bars associated with log Q only reflect the uncertainties in this parameter obtained during the IACOB-GBAT fitting process. Additional sources of uncertainty, like the terminal velocities assumed in the grid of FASTWIND models are not considered (see Appendix A.5).

[10] α' corresponds to the slope of the line-strength distribution function (α), corrected for ionization effects (δ) (Puls et al. 1996).

[11] Indeed, Eq.5.1 would contain an additional mass dependence if x was quite different from 3/2.

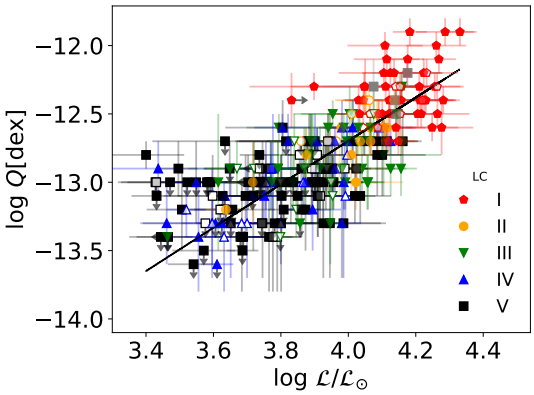

Figure 5.12: Distribution of the O-type stars in our sample in the log Q-log $\mathcal{L}$ diagram (which could be considered as a purely spectroscopic proxy of the WLR, see text and Appendix A.6). Upper and lower limits are represented by arrows. Different colors and symbols represent luminosity classes. Open symbols indicate stars for which we have detected clear or likely signatures of spectroscopic binarity. The solid line represents the linear regression of the values, excluding stars marked with an open symbol and/or an arrow.

In the following, we show how the diagram presented in Fig. 5.12 can be used as a distance-independent test of the WLR in the O-star domain, and as an alternative way to compare observational results and predictions by the theory of radiatively driven winds using only parameters obtained from the spectroscopic analysis of optical spectra. Basically, we replace the two spectroscopic parameters[12] (log Q and log $\mathcal{L}$) into the WLR.

By considering Eq. 5.1 and the definition of $D_{\rm mom}$, Q, and $\mathcal{L}$, we can obtain the following expression[13].

$$\log Q = x \log \mathcal{L} + \frac{3}{4} \log \frac{M}{R} + f(x, M), \tag{5.2}$$

where $f(x, M)$ depends on x, M, and several constants, and its mass dependence vanishes if $x \approx 2$.

Since M/R is not changing too much over the considered region of the

[12] As a reminder we repeat here the definition of both parameters: $Q = \dot{M}/(v_\infty R)^{2/3}$, $\mathcal{L} = T_{eff}^4/g$.
[13] See the various steps required to transform Eq. 5.1 into Eq. 5.2 in Appendix A.6.

HR diagram, $\log(M/R)$ varies between 0.2 and 0.8 in the Geneva non-rotating evolutionary tracks for solar metallicity, a roughly linear correlation between $\log Q$ and $\log \mathcal{L}$ is expected, with x being the slope. We remark, however, that this is not as exact as the WLR, since the term M/R is indeed varying.

We then applied a method of orthogonal least squares to perform a linear regression of the data presented in Fig. 5.12, to obtain the parameter x, corresponding to $1/\alpha$'. We took into account errors in both axes individually but not their correlation, as that treatment is not simple and we do not expect a major effect. We excluded from the regression stars with clear or likely signatures of spectroscopic binarity, and also those stars for which only upper or lower limits in $\log Q$ could be obtained. The final sample to perform the linear regression comprised 175 O-type stars. We found a slope value of 1.59±0.17, which is in fairly good agreement with the range of values of x (=1.51 – 2.18) provided by Herrero et al. (2002), and in particular concordance with Mokiem et al. (2007) (x = 1.86±0.20 without considering clumping correction). Taking into account uncertainties, our value of x is in agreement with studies providing lower values of x, hence higher values of α', $\alpha' \approx 0.63\pm0.07$. Regarding the current paradigm, the acceleration arising from optically thick and from all lines[14] is very similar to the theoretically predicted value (x = 1.826) in Vink (2000); Puls et al. (2000).

A previous similar approach with B Supergiants

Markova & Puls (2008) presented an analogous work as the one described above using only parameters that can be derived spectroscopically (i.e, no previous knowledge about distances needed) to study the theoretically suggested bistability jump of mass loss (Vink 2000). In their case, they used a sample of Galactic B Supergiants (B Sgs)[15] and define a new, distance-independent parameter Q' as:

$$Q' = Q g_{eff} (v_\infty)^{1/2} \tag{5.3}$$

where the parameter g_{eff} is defined as $g_{eff} = g(1-\Gamma)$.

Note that to obtain this parameter is necessary to include the value of the terminal velocity (v_∞). This parameter is not accurately derived from the optical part of the spectrum (See Sect. 3.5).

[14] As $x = 1/\alpha$, and α can be interpreted as the ratio of the acceleration from optically thick lines to the one provided by the totality of the lines (Puls et al. 2000).

[15] They used an heterogeneous sample that comes from Markova et al. (2004); Crowther et al. (2006) and Lefever et al. (2007).

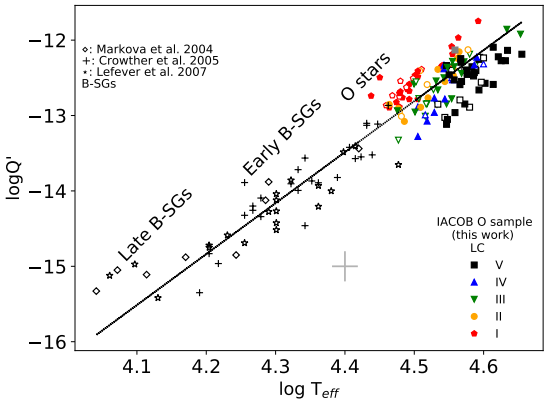

Figure 5.13: Extended version of the log Q' vs log $T_{\rm eff}$ diagram presented in Markova & Puls (2008, their Fig. 13), including not only their sample of B Sgs but also our sample of O-type stars. Colors in O stars depend on luminosity class. The gray cross shows the typical uncertainties for these results.

Then they obtain, starting from the WLR (Eq. 5.1) and using the definition of the Q' parameter (Eq. 5.3), a relationship between the Q' parameter an the effective temperature ($T_{\rm eff}$):

$$\log Q' = 4x \log T_{\rm eff} + f'(x) \tag{5.4}$$

When they plotted the distribution of their empirical measurements in a log Q' vs log $T_{\rm eff}$ diagram, they did not found any discontinuity in this relationship. We construct this diagram again in Fig. 5.13, now also including those stars in our O sample with available[16] values of v_∞ and reliable results from the IACOB-GBAT analysis (117 stars). Even with the inclusion of the new sample of O stars the trend present in the B Sgs domain continues, with no clear sign of an abrupt shift on the slope. The later B Sgs appear to be separated from the general trend, but more data are required to assure the presence of this discontinuity.

We applied a linear regression to the whole sample of O stars and B Sgs, obtaining a value for the parameter x, useful to compare again with observational results and predictions from the theory of radiatively-driven winds. We

[16] We compiled values for our sample of stars from dedicated studies (Howarth et al. 1997).

took into account errors in both axes individually but not their correlation, and exclude from the regression stars with signatures of spectroscopic binarity, and those stars with only upper or lower limits in $\log Q$. The final sample to perform the linear regression is comprised of 137 O and Bsgs stars.

Our final value (x=1.68±0.05) is in good agreement with our previous determination using the $\log Q$ vs $\log \mathcal{L}$ diagram (previous section), and marginally consistent with the results obtained in Markova & Puls (2008) for B Supergiants alone.

5.6.2 On the absence of stars close to the ZAMS

When presenting the distribution of O-type stars in the sHR diagram (see Fig. 5.1, in Sect. 5.5.1) it became evident that there is a lack of stars near the ZAMS above the 32 $M_\odot$ evolutionary track. There is clear offset between the theoretical and empirical ZAMS, which increases with mass. This divergence between theory and observations have been encountered before with different working samples, and many solutions to explain this lack of observed stars close to the commonly accepted "theoretical" location of the ZAMS have been proposed (Herrero et al. 2007; Castro et al. 2014; Haemmerlé et al. 2016). This feature appears to be independent of metallicity, as is also present in a large sample of massive stars studied in the LMC (Sabín-Sanjulián et al. 2017), where they note a lack of stars younger than 1 Myr in their sample between the ZAMS, the 1 Myr isochrone and the 30 and 100 $M_\odot$ stellar tracks in the HR diagram.

Among the possible explanations, we highlight (1) extreme scarcity of high-mass stars in this region of the HR diagram due to the fast evolution of massive stars during their early phases (Garmany et al. 1982; Schneider et al. 2018) (2) observational limitations, with the possibility that very young massive stars could be still embedded in their birth cocoon, hampering its detection and hence study in the optical range (e.g., Yorke 1986; Hanson 1998; Castro et al. 2014) and (3) theoretical considerations about how pre main-sequence objects connect with their main-sequence evolution (e.g., Bernasconi & Maeder 1996; Behrend & Maeder 2001; Herrero et al. 2007; Haemmerlé et al. 2016).

The hypothesis considering that the evolution of these stars is so fast that indeed we would not expect that part of the diagram to be populated could be assessed with a deeper study involving the IMF and comparing different regions of the sHR diagram between the 1 and 10 Myr isochrones. This is out of the scope of this work and, while we cannot exclude this bias effect, the complete absence of stars near the upper end of the theoretical ZAMS lines might also be related to the fact that such young massive stars are likely still embedded

in their birth clouds. We decide then to focus[17] on the second explanation and evaluate the possibility that the sample could present an observable bias lacking the youngest and most obscured stars.

To avoid the possibility of an observational bias we started a new observing project to obtain spectra for the faintest-earlier O-type stars still not observed in the IACOB and OWN sample. The youngest stars could be still embedded in their birth cocoons and therefore extinguished in V and B magnitudes. This potential liability was the reason to extend the maximum magnitude of the observed stars in the IACOB sample from B=9 to B=10.5. As stated in Chapt. 2, the GOSC was used to determine the most interesting targets to assess this possible limitation: 94 new mid- and early-O dwarfs with magnitudes in GOSCv3 up to B = 10.5 mag. In Fig. 5.14 we highlight their position in the sHR diagram. The new results are not filling the void of stars next to the ZAMS. Indeed, many of them are found among the youngest stars in the sample, delineating the empiric distribution, but in general they present an spread distribution covering most of the space the sHR diagram.

This could mean that, in fact, there are no real massive stars with those parameters, considering that our sample represents 70% of the stars in GOSC (See Fig. 2.1). An empirical result like this presents an important challenge to the actual formation and evolution theories of massive stars. Nevertheless, Fig. 2.1 also shows that there are still many stars without spectroscopic parameters determined at magnitudes dimmer that B = 10. Despite this, a dimmer star does not univocally represent a more obscured/reddened star, as it could be that this star in particular is further away from us. A very promising next step is to be able to observe and analyze stars in the process of formation or very recently formed, making use of infrared observations, capable of penetrating thick layers of material and dust.

In our study we are constantly using the sHR diagram instead of the HR due to our lack of accurate distance values to derive luminosities (see more in depth in Chapt. 7). The differences and possible caveats between these two diagrams are discussed in Langer & Kudritzki (2014), but for this particular topic of stars near the ZAMS the results are completely analogous, as can be seen in studies using the HR diagram with similar results (Sabín-Sanjulián et al. 2017; Schneider et al. 2018), and our preliminary results in the HR diagram presented in Sect. 7.3.4.

The additional possibility that the star formation could have ceased (See e.g., Sabín-Sanjulián et al. 2017; Schneider et al. 2018) due to strong local feedback from supermassive star formation is not reasonable for our sample, as

[17] Due to the expertise and possibilities of our working group.

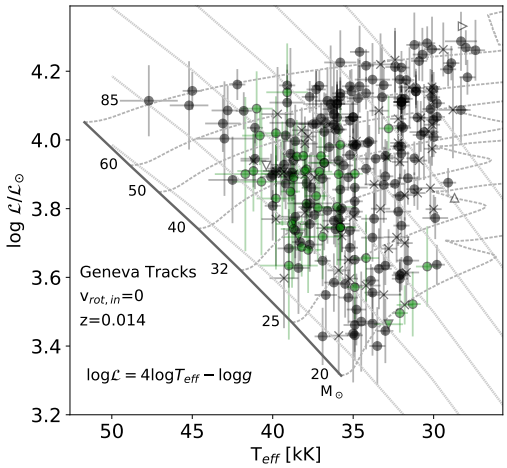

Figure 5.14: Same as right panel of Fig. 5.1 but green points indicate dimmer (magnitudes up to B = 10.5) stars observed during this thesis in order to eliminate possible observational bias. The lack of stars near the ZAMS for masses above the 32 $M_\odot$ evolutionary track is not cover by the inclusion of the new 94 observed dwarfs stars (See text).

the Galactic sample is not confined to an specific area of the Galaxy or cluster.

A pioneering study of the dearth of very young stars among the most massive ones is Herrero et al. (2007). Besides commenting on the possibility that this is an effect caused by the inclusion of line-blanketing in the new atmospheric codes, they consider many alternative options, such as the possibility that their sample lacks stars belonging to really young clusters (< 1 Myr), or that the observational results are defining a real empirical ZAMS, while the theoretical ZAMS needs to be corrected towards cooler temperatures. This last explanation has been explored before by Bernasconi & Maeder (1996) and Norberg & Maeder (2000) considering that the current paradigm of a constant rate of accretion is not able to reproduce the empirical data. With this in mind, we have been working with our sample to study the kind of behavior that the accretion rate needs to have in the pre main-sequence models to be able to achieve the empirical ZAMS that we obtain (Haemmerle et al. in prep.). Our preliminary results show that a decreasing rate of accretion with mass could be able to reconcile observations and evolutionary models and hydrodynam-

ical simulations, and this could be explained by UV and radiation feedback (Haemmerle priv. comm.).

Last, we note that the presence of the gap has been mainly outlined up to now by studies making use of FASTWIND models (Castro et al. 2014; Sabín-Sanjulián et al. 2017; Holgado et al. 2018), but is also present in multi-code studies (Schneider et al. 2018). If we account for the systematic differences in $T_{\rm eff}$ and $\log g$ found when comparing FASTWIND and CMFGEN models (see Fig. 4.5), $\log \mathcal{L}$ might roughly decrease by 0.12 dex. Would this correction in $\log \mathcal{L}$ be really needed, the gap could be reduced. However, the lower values of $T_{\rm eff}$ required by the CMFGEN analysis would move again the stars away from the predicted ZAMS.

5.6.3 Q3 stars and clumping revisited

In Sect. 4.7.3 we evaluated the Q3 stars in the sample of O-type standard for spectral classification. Our inability to find a simultaneous fit to both the Hα and He II λ4686 lines was linked to limitations in our spectroscopic analysis using unclumped FASTWIND models. We provided strong evidence that most of the stars labeled as Q3 with luminosity class I and II could be likely explained by wind clumping effects. In addition, we showed that these giants labeled as Q3 may need an alternative explanation, such as, e.g., the presence of extra sources of circumstellar emission in He II λ4686, or hidden stellar components. This section presents an extension of this study including the Q3 obtained in the spectroscopic analysis of the whole sample of Galactic O-type stars, almost doubling the sample.

As stated in Sect. 4.7.3, there are particular combinations of $T_{\rm eff}$ and $\log g$ in the O-star domain where Hα and He II λ4686 react differently to clumping (Kudritzki & Urbaneja 2006; Urbaneja et al. 2008), with the Hα line requiring a larger value of $\log Q$ than the He II λ4686 line when performing the spectroscopic analysis using unclumped models. We use this to assess if the Q3 stars could be explained by clumpy winds.

In Fig. 5.15 we show the location in the sHR diagram of all Q3 stars, separating those where Hα needs a larger/smaller/equal value of $\log Q$ than He II λ4686. In comparison with Fig. 4.12 this sample presents more luminosity classes, and a particular set of stars where both lines give raise to the same value of $\log Q$ when analyzed separately. These stars with equal values of $\log Q$ appear in a narrow band of the diagram (between the 40 $M_\odot$ and 60 $M_\odot$ Geneva evolutionary tracks) and are able to compensate the fit of the particular diagnostic line with the same $\log Q$ by a small but perceptible offsets on the rest of the spectroscopic parameters ($T_{\rm eff}$ $\sim$0.3 [kK] and $\log g$ $\sim$0.06 [dex]).

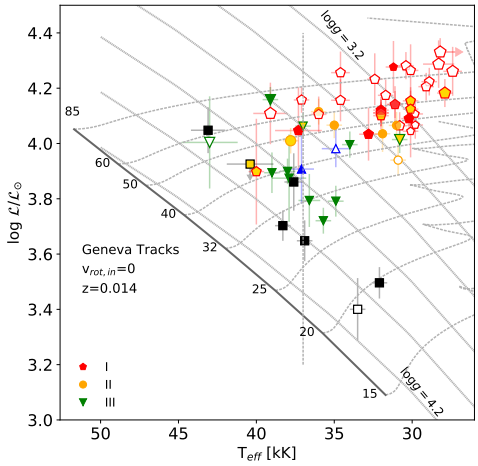

Figure 5.15: Same as right panel in Fig. 5.1, but only for stars with Q3 quality flag. Size depends on the log Q obtained in the automatic analysis. Open (filled) points are stars for which the value of log Q when fitting only the Hα line is larger (smaller) than when fitting He II λ4686. The horizontal line at $T_{\rm eff} = 37$ kK indicates the boundary of the region where clumping in the wind is expected to affect the two wind diagnostic lines differently (see Sect. 4.7.3).

In general, the conclusions are very similar to those obtained using only the standard O-type stars, with most of the luminosity class I and II stars with open symbols (clumping explanation), and the rest (now luminosity class III, IV, and even V) with filled symbols (not explained by clumping) except for two particular cases: the giant star HD 168076 AB discussed in Sect. 4.7.3, and the dwarf star HD 54879.

The only dwarf star labeled as Q3 and with a stronger wind arising from the fit of only the Hα line, in accordance to clumping effects, is HD 54879. This star exhibits a remarkably strong Hα line in emission when this is not expected for this combination of SpT and LC. Notably, this star has been found to be the most strongly magnetic, non-variable single O-star detected to date (Castro et al. 2015).

6

Rotational velocities of Galactic O-type stars

As long as the world is turning and spinning,
we're gonna be dizzy and make mistakes.
Mel Brooks

In this chapter we make use of the results from the quantitative spectroscopic analysis of the complete sample of Galactic O-type stars surveyed by IACOB and OWN – presented in previous chapters – to perform a more detailed study of the rotational properties of these massive stellar objects. We present and discuss the global $v \sin i$ distribution resulting from the analysis of 298 likely single and SB1 stars. We use the derived $T_{\rm eff}$ and $\log g$ for 275 of these stars to present and discuss the distribution of $v \sin i$ values in the sHR diagram. The chapter also includes a brief description of the main predictions – regarding rotational velocities – by two state-of-the-art evolutionary models for single stars, as well as from population synthesis simulations of massive stars including binary interaction. We use these theoretical scenarios as a guideline to evaluate the empirical dependence of $v \sin i$ on mass and evolution in the O-type domain.

6.1 Introduction

All stars are affected by rotation during their whole life. Most of the angular momentum acquired by the stars in the formation process comes from the collapse of the progenitor cloud (Bodenheimer 1995; Zinnecker & Yorke 2007; Rosen et al. 2012). In the proto-stellar phase, huge amounts of angular momen-

tum are ejected into the medium by different means (Mestel 1965; Krumholz 2009; Larson 2010). Despite this, at the time of the start of the main sequence phase 10% of the initial angular momentum presented in the cloud is still in the star (Hartmann & Stauffer 1989; Huang et al. 2010). This momentum, and how it is modified along the lifetime of the star, will mark the whole evolution of the stellar object.

Rotation is known to play a fundamental role in the evolution of massive stars (see, e.g., reviews by Maeder & Meynet 2000b; Langer 2012). Rotation was found to be behind the important discrepancies between model predictions and observations found by several pioneering empirical studies measuring surface abundances in massive stars (see Maeder & Meynet 1995, and references therein).

Stellar rotation affects the global physical characteristics and the evolution of massive stars in many different ways. Fast rotation can induce internal mixing in the star, providing the stellar core with fresh material from the outer layers (Maeder & Meynet 2000a; Heger et al. 2000; Yoon & Langer 2005; Brott et al. 2011; Potter et al. 2012; Ekström et al. 2012). As a consequence, stellar rotation can drastically modify the amount of time a massive star spends in the main sequence, its post-main-sequence evolution and, ultimately, the nature of its final remnant after the supernova explosion (Maeder & Meynet 2000a; Georgy et al. 2009). In extreme cases, a very high initial rotation velocity may even lead to chemically homogeneous evolution (Maeder 1980; Brott et al. 2011). In addition, this rotational mixing is capable to bring processed material from the interior of the star to the stellar surface (Meynet 1992; Langer et al. 1997; Heger et al. 2000; Hunter et al. 2007).

From a physical point of view, fast rotation can distort the geometry of the star along the rotation axis, transforming the sphere into an oblate spheroid, with a smaller radius in the rotation poles (Collins 1963, 1966). The distortion effect have an overall impact on the stellar surface gravity (e.g. since the stellar radius at the pole gets shorter than in the equator, the surface gravity is larger in the poles than in the equator). This makes the effective temperature of the star hotter in the poles than in the equator (von Zeipel 1924). In addition, mass-loss is enhanced in the fast spinning material near the equator, with large localized ejections of material that could even form a disk.

In view of the critical importance of rotation in massive star evolution, this parameter is presently included as a key ingredient in the most commonly used stellar evolutionary codes (e.g., Ekström et al. 2012; Brott et al. 2011). Using these codes, the Geneva and Bonn group have made available to the community grids of models for the massive star domain considering a range in initial rotational velocities of up to $350-400\,\mathrm{km\,s^{-1}}$. Those maximum velocities

correspond to ∼40 % of the critical velocity of the stars[1].

Investigating and characterizing the initial rotation distribution of a given population of stars is of special interest because [1] stellar rotation rates at birth are an impression of the star formation process (Maeder & Meynet 2000a) and [2] this initial distribution will mark the subsequent evolution of the stellar population. In the case of stars with masses above $\sim 20\ M_{\odot}$, this task implies the study of rotational velocities (or, actually, projected rotational velocities, $v \sin i$) in a large-enough sample of O-type stars. However, in this endeavor we must also take into account possible evolutionary effects when inferring the initial distribution from the observed one.

As massive stars evolve, they are expected to modify their surface rotational velocities due to different processes. In the case of single stars, the principle of angular momentum conservation, combined with the increase of stellar radius and mass loss due to the winds, dominate the evolution of the surface rotational velocity which decreases monotonically (Maeder & Meynet 2000a, and references therein). Magnetic fields are also able to additionally spin down these stars (ud-Doula & Owocki 2002). In this sense, single stars do not have ways of accelerating themselves, on the contrary they are expected to slowly spin down. However, for stars in binary systems the stellar spin of the individual components can be also modified by tidal effects and/or mass transfer, or even a merging process (de Mink et al. 2013, and references therein).

Tidal interaction in close binaries, where the separation between the stars is comparable to the stellar radii, tends to accelerate one component. The orbital period is forced to remain constant and stars are kept in corotation. As the primary star expands, its rotational velocity gradually increases. All this could produce $v \sin i$ values over 200 $\mathrm{km\,s^{-1}}$, and it is even possible that all very rapidly rotating massive stars origin from binary interaction (Langer et al. 2008). Such binary evolution products are expected to appear as single stars because the mass donor has lost so much mass that the effect of RV variations in the new main star are below any practical detection limit, or because of a large increase in the period of the system, or because there is no longer a binary system due to merging or the as a consequence of a supernova explosion (de Mink et al. 2013).

Before the first years of the 20th century, all studies of rotational velocities in relatively large samples of O-type stars found an interesting result: the stars

[1]The critical velocity is defined as the rotational velocity above which the star is not able to survive, because the material escapes the gravity forces. Despite the parental cloud contains enough angular momentum to accelerate all protostars up to critical rotation (Larson 2010), some studies argue that gravitational torques prohibit a star from rotating above ∼50% of its critical speed during formation (Lin et al. 2011).

for which a low value of $v \sin i$ was determined were extremely scarce (Conti & Ebbets 1977; Penny 1996; Howarth et al. 1997). This was not expected given the fact that, statistically, a certain percentage of these stars should be seen close to pole on (i.e., $\sin i \sim 0$). This result was explained by hypothesizing the presence of an extra source of line-broadening that was called "macroturbulence"[2]. The $v \sin i$ measurements in all these works could not disentangle the effect of rotation from that of the *macroturbulence* in the line-broadening analysis . This problem was claimed to be solved when we had access to better quality observations (in terms of S/N and resolution) and Fourier techniques were applied in the line-broadening analysis (see, e.g, Simón-Díaz & Herrero 2007, 2014, and references therein); however, we still miss a complete reassessment of the works presented by the abovementioned authors.

In view of the caveats of previous studies in this regard we decided to use the outcome from our line-broadening analysis of the full sample of O-type stars surveyed by IACOB and OWN to review our empirical knowledge about stellar rotation in Galactic massive stars on the main sequence. This study supersedes and extends the works by Conti & Ebbets (1977); Penny (1996); Howarth et al. (1997), as well as serves as a complement to the study performed by the VLT-FLAMES Tarantula Survey in the 30 Doradus region of the Large Magellanic Cloud (Ramírez-Agudelo et al. 2013, 2015; Sabín-Sanjulián et al. 2017). In this chapter, we present the $v \sin i$ histogram results separated for different subclasses, making use of our multi-epoch study. Additionally, we use the $T_{\rm eff}$ and $\log g$ estimates to present the distribution of $v \sin i$ in the sHR diagram. We expect the distribution of rotational velocities of a massive star population to change as a function of stellar evolution due to single evolution and binary interactions, and decide to study the $v \sin i$ behavior and evolution from the comparison of subsamples in different regions of the sHR diagram.

6.2 Sample and methodology

To provide a modern empirical assessment of rotational velocities in Galactic O-type stars we used the 239 likely-single stars[3] and the 59 SB1 identified among the O-type stars surveyed by the IACOB and OWN projects (see Chapt. 5 and Tables B.4 and B.5). Throughout this chapter we use three basic quantities resulting from our quantitative spectroscopic analysis (see Chapt. 3) to construct

[2]The name *macroturbulence* is only kept along this text for historical reasons, as it is discarded that this additional broadening is related to large-scale turbulent motions (Simón-Díaz et al. 2010).

[3]This number includes 6 Oe and 7 Magnetic single-lined stars in the sample without IACOB-GBAT results.

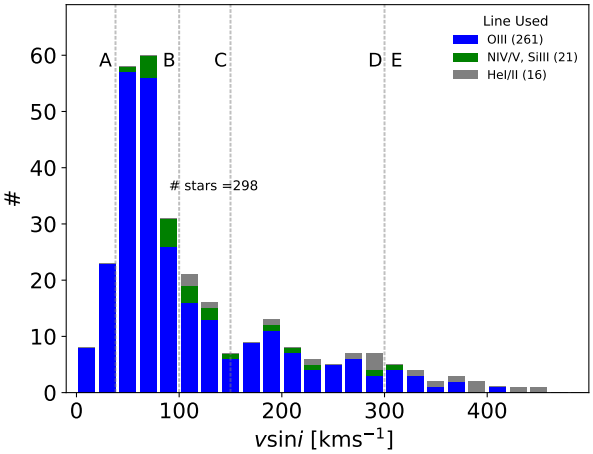

Figure 6.1: $v \sin i$ histogram of the complete sample of likely-single (239) and SB1 (59) O-type stars considered in this work. Different colors are used depending on the diagnostic line used in the line-broadening analysis. (See Table 6.1). $v \sin i$ ranges marked with letters "A" to "E" are used in Fig. 6.8.

updated distributions of projected rotational velocities, and to evaluate the distribution of the global sample (and different subsamples) in the spectroscopic HR diagram; namely $T_{\rm eff}$, $\log g$, and $v \sin i$.

Table B.1 summarizes the various diagnostic lines used to obtain measurements of $v \sin i$ in the whole sample of analyzed stars[4].

Table 6.1: Summary of the diagnostic lines used in the line-broadening analysis of our sample of IACOB+OWN spectra

Diagnostic line	O III	Si III	N V	N IV	He I	Total
likely-single+SB1	261	10	10	1	16	298
likely-single	210	7	9	1	12	239
SB1	51	3	1	-	4	59

O III=O III λ5592, Si III=Si III λ4452, N V=N V λ4603/20, N IV=N IV λ6380

[4]A comparison of the results using different diagnostic lines available in the same stars are included in Appendix A.2.

Figure 6.1 depicts the distribution of projected rotational velocities of the likely-single and SB1 stars in the sample, colored by the different diagnostic lines used in the IACOB-BROAD analysis. As can be noticed from the info provided in Table 6.1, we were able to use the O IIIλ5592 line for the vast majority of the stars. Only for 37 stars the O III line was not strong enough in the spectra to be used as diagnostic line, and hence we needed to use an alternative metal line or a He I line. We note that, although the use of a He I line may present caveats in the case of slow rotators (see Appendix A.2), all the stars for which we needed to use a He I line have a $v \sin i$ value above $\sim$100 km s^{-1}, and hence the effect of Stark broadening in the determination of $v \sin i$ becomes almost negligible. In summary, for 95% of the sample the analysis is made with a metallic line, and in 88% of the sample the O IIIλ5592 line has been chosen.

6.3 Distribution of projected rotational velocities in Galactic O-type stars

In this section we present several histograms and cumulative distribution functions of projected rotational velocities for the 298 Galactic O-type stars studied in this work. These include the global sample as well as specific subsamples separating likely single and SB1 stars. We also compare our resulting distributions with those provided by previous studies of O-type stars to see how our work is contributing to update and improve them. Finally, we present and discuss the distribution of our $v \sin i$ results in the sHR diagram.

6.3.1 $v \sin i$ histogram

Figure 6.1 depicts the $v \sin i$ distribution of those stars labeled as likely-single and SB1 in our sample. As found by previous works (see, e.g., Conti & Ebbets 1977; Ramírez-Agudelo et al. 2013) the distribution shows a bimodal character, presenting a slow velocity peak with $v \sin i$ values around $\sim$80 km s^{-1}, and a tail of fast rotators reaching 450 km s^{-1}.

Although it was initially attributed to undetected extra-broadening and normal evolution processes (Conti & Ebbets 1977), more recent studies propose that this bimodal distribution can be explained by the effect of binary interaction during massive star evolution (de Mink et al. 2013).

Figure. 6.2 presents again the same distribution, but separating the stars for which we have detected clear or suspicious signatures of being a single lined spectroscopic binary (SB1) from those we considered as likely-single (C).

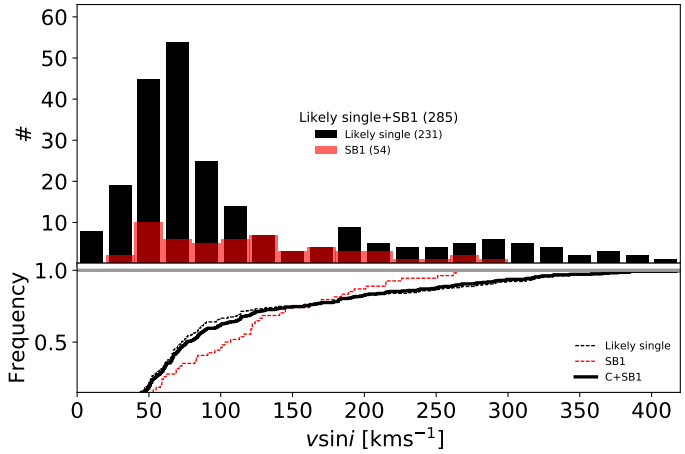

Figure 6.2: $v \sin i$ histogram (up) and cumulative histogram (down) for the likely-single and SB1 subsample, separated by detected binarity status.

This time, and in the following section, we complement the histogram with the associated cumulative distribution function.

We highlight the lack of SB1 stars in the fast rotators tail, as they completely disappear for $v \sin i > 300$ km s^{-1}. The lower panel of Figure 6.2 shows the cumulative histogram of both samples (C/SB1), and the combined one. The distribution of likely single stars is very similar to the combined one, meaning that they are clearly dominating the distribution. On the contrary, the comparison of the C and SB1 samples highlight clear differences. In particular, the SB1 sample presents a similar percentage of slow ($v \sin i < 100$ km s^{-1}) and intermediate-rotators ($v \sin i$ =100-200 km s^{-1}), there is no clear peak in the slow part, and they lack stars above 300 km s^{-1}. Present-day studies argue that ∼90% of massive O-type stars will evolve as interacting binaries at some point of their lifetime (Sana et al. 2012). The missing SB1 stars in the tail of fast rotators could be supporting de Mink et al. (2013) scenario, arguing that these stars have evolved into mergers or are apparently-single post-mass-transfer stars (see Sect. 6.1 and further discussion in Sect. 6.4.1).

Comparison with previous studies

The main studies presenting the distribution of projected rotational velocities in a large sample of O-type stars before our work are those of Conti & Ebbets (1977), Penny (1996), Howarth et al. (1997), and Ramírez-Agudelo et al. (2013, 2015). In this section we compare our results with those obtained by three of these studies. First, we compare our results with Conti & Ebbets (1977) and Howarth et al. (1997), hereafter CE77 and H97, two reference studies of rotational velocities in Galactic O-type stars which included the line-broadening characterization of 200 and 252 targets, respectively. Then, we compare our distribution with that obtained by Ramírez-Agudelo et al. (2013) from a sample of 216 likely-single O-type stars in the 30 Doradus region of the Large Magellanic Cloud.

Comparison with Conti & Ebbets (1977) and Howarth et al. (1997)

Figures 6.3 and 6.4 present the comparison (in the form of a histogram –upper panel– and a cumulative distribution function –lower panel–) of the $v \sin i$ distribution resulting from our study and the work by CE77 and H97, respectively. CE77 considered a cross-correlation method using models as templates to derive the $v \sin i$ values from optical spectra; similarly, H97 used the whole IUE ultraviolet spectra and a cross-correlation method, using one star (HD 191423) as template, to derive the $v \sin i$ values. The methodology and the resolving power of the spectra, of approximately $17 \mathring{A} mm^{-1}$ in both studies, did not allow them to separate between rotation and *macroturbulence*. As stated in Simón-Díaz & Herrero (2014), this resulted in an overestimation of the derived $v \sin i$ of up to $\sim$45 km s^{-1} in stars rotating slower than 120 km s^{-1} (depending on the amount of *macroturbulence* broadening affecting the diagnostic lines).

As expected from the abovementioned argument, in both of their $v \sin i$ distributions (Figs. 6.3 and 6.4) the low-velocity peak appears centered in larger values of $v \sin i$ ($\sim$100-120 km s^{-1}) compared to ours. Figs. 6.5 and 6.6 present the comparison of the individual $v \sin i$ values resulting from the IACOB-BROAD analysis of the IACOB/OWN spectra for stars in common with CE77 (193) and H97 (177), respectively[5]. There is a general good agreement in the fast rotation regime (>150 km s^{-1}) but, as explained above, because of their inability to separate the non-rotational component from the global line-broadening, in both diagrams their $v \sin i$ determinations are systematically larger than ours in the low $v \sin i$ regime.

[5]We note that C77 and H97 could derive values for the 2 components of 51 and 25 SB2 systems, respectively.

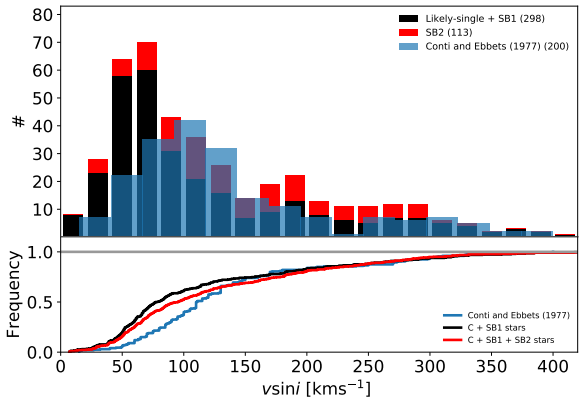

Figure 6.3: $v \sin i$ histogram (up) and cumulative histogram (down) for Conti & Ebbets (1977) sample and our sample. They include results for our sample of Galactic single/SB1 O-type stars (black), and SB2 stars (red).

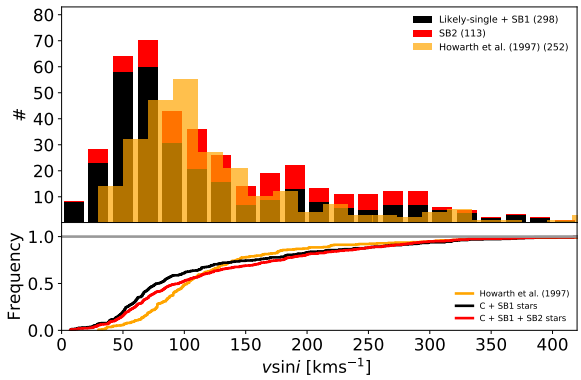

Figure 6.4: $v \sin i$ histogram (up) and cumulative histogram (down) for Howarth et al. (1997) sample and our sample. They include results for our sample of Galactic single/SB1 O-type stars (black), and SB2 stars (red).

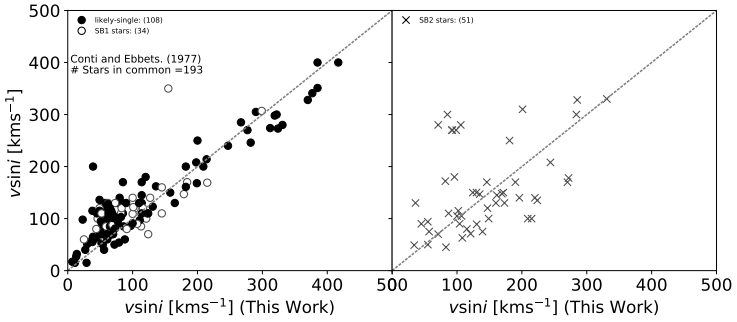

Figure 6.5: Comparison of $v \sin i$ determinations for stars in common with Conti & Ebbets (1977). Open symbols indicate stars with clear or likely signatures of single-line spectroscopic binarity. Crosses indicate signatures of double-line spectroscopic binarity.

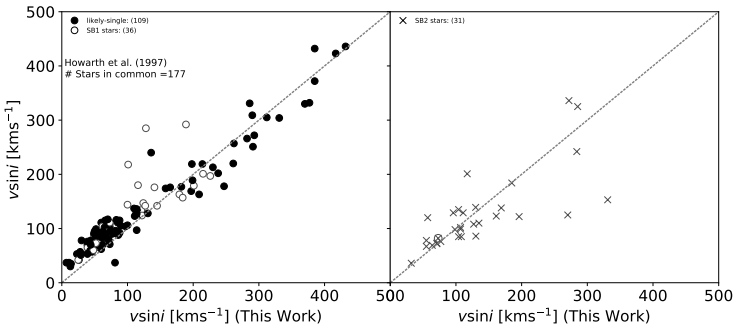

Figure 6.6: Comparison of $v \sin i$ determinations for stars in common with Howarth et al. (1997). Open symbols indicate stars with clear or likely signatures of single-line spectroscopic binarity. Crosses indicate signatures of double-line spectroscopic binarity.

In the right-hand panels of Figs.6.5 and 6.6, we also include the comparsion between derived $v \sin i$ values for stars identified in this thesis work as SB2, but for which CE77 and H97 only provided one estimation of the projected rotational velocity. As explained in Chapt.5, we obtained an upper limit for the $v \sin i$ values of 113 Galactic O-type SB2 stars as an academic exercise to study the contamination effect of including them in the whole sample[6]. Including undetected SB2 stars in the distribution could enhance the number of stars of intermediate and fast-rotators (See Chapt. 5). However in Fig. 6.3, we draw the cumulative distribution of our sample including the $v \sin i$ values of the SB2 stars, and we see how their effect is not enough to reconcile CE77 results with ours.

In conclusion, our study represents an advance with respect to the works by Conti & Ebbets (1977) and Howarth et al. (1997) in three main aspects:

- Our sample is larger, 1.5 times the one considered by CE77.
- The availability of multi-epoch spectra has allowed us to identify and highlight the SB1 stars, and eliminate the SB2 stars contaminating the sample.
- The higher resolution of our spectroscopic dataset has allowed us disentangle the *macroturbulence* broadening component and obtain more accurate $v \sin i$ determinations.

Comparison with Ramírez-Agudelo et al. (2013)

Figure 6.7 presents the histogram and the associated cumulative histogram with the $v \sin i$ distribution obtained by (Ramírez-Agudelo et al. 2013, RA13) for a sample of 216 likely-single stars O-type in the 30 Doradus region, of the Large Magellanic Cloud. This is a representative distribution of $v \sin i$ values for stars in a different metallicity environment ($Z_{\rm LMC} \sim 0.5 Z_{\odot}$). Their $v \sin i$ values are derived using the same methodology as our work, separating the macroturbulent broadening contamination. However, the lower resolving power (R∼8000) and more limited wavelength coverage of their spectra imposed some caveats in the line-broadening characterization of their sample of stars. For example, their resolution implied that below 40 km s^{-1} any $v \sin i$ determination was uncertain. In addition, their reduced wavelength range force them to rely in almost all cases to He I and He II lines (which are not optimal lines to determine $v \sin i$ in O-type stars, see Appendix A.2).

[6] We remind that this $v \sin i$ value is considered as purely rotation, without considering the *macroturbulence* broadening component, and only represents an upper limit, as it is affected by the presence of two blended lines.

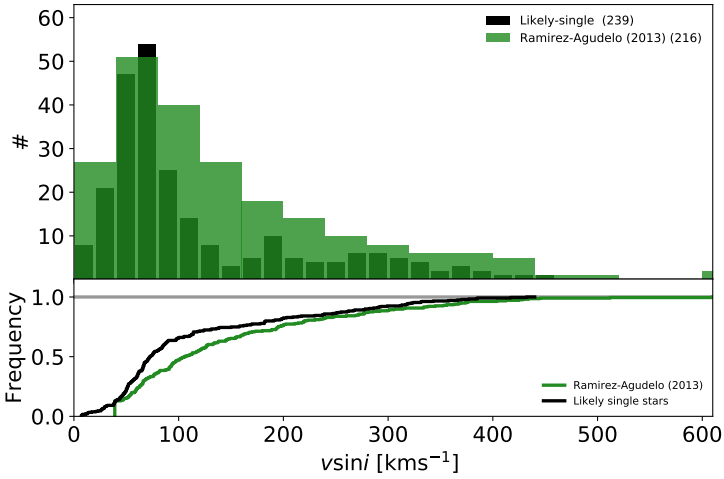

Figure 6.7: $v \sin i$ histogram (up) and cumulative histogram (down) for Ramírez-Agudelo et al. (2013) and our sample. It includes the results for our sample of Galactic likely-single O-type stars (black).

The main expected difference with respect to the Galactic case is that, at lower metallicities, the O-type stars are characterized by developing weaker winds (Vink 2000; Mokiem et al. 2007). This reduces the amount of angular momentum that the star loses through the wind, which would finally produce a $v \sin i$ distribution with a higher average speed, and a possible greater extreme rotation than in the Galactic case.

While the latter effect can be actually identified when comparing both distributions (the fast-rotators tail of RA13 distribution reach up[7] to 600 km s^{-1}), no clear conclusions can be extracted in the low-velocity peak (below ∼40 km s^{-1}, or even ∼100 km s^{-1} in some cases) due to the limitations affecting the $v \sin i$ measurements of the RA13 distribution.

[7]Note that this is not an effect of including SB2 stars, enhancing the number of fast rotators, as their sample only includes the likely-single O-type stars.

6.3.2 Distribution of $v \sin i$ in the sHR diagram

The works by CE77 and H97 offered us a good opportunity to learn about the global $v \sin i$ distribution of Galactic O-type star using large enough samples. Despite these studies also presented a comparison of results associated with different sub-samples of stars (e.g. separating by the stars by broad luminosity or spectral type classes), they could not provide any meaningful information about the distribution of the $v \sin i$ values in the HR diagram. Some work in this direction was presented by Markova et al. (2018); however, their sample of O-type stars was limited to 53 targets. In this section, we benefit from our thorough quantitative spectroscopic analysis of the full sample of O-type stars surveyed by IACOB and OWN to drive scientific advance in these regards compared to state-of-the-art studies. We make use of the results of our quantitative spectroscopic analysis ($T_{\rm eff}$ and $\log g$) along the $v \sin i$ results to construct an sHR diagram.

In Fig. 6.8, the sample of likely-single/SB1 stars is presented in the sHR diagram. We exclude those with no He I line available (Q4 stars, see Sect. 3.3.3) and the peculiar stars (Oe and Magnetic). This leaves 275 stars included in all panels of Fig. 6.8. We also include in each panel the Geneva non-rotating evolutionary tracks for solar metallicity (Ekström et al. 2012; Georgy et al. 2013), for reference purposes.

The first panel shows the full sample of stars color-coded as a function of luminosity class. This panel is included as a reference, to provide the reader with the distribution of the different luminosity classes in the sHR diagram. In each of the other five panels comprising Fig. 6.8, we include again the full sample of 275 targets but highlighting those cases having a $v \sin i$ in a specific range. The various considered ranges in $v \sin i$ have been selected to separate the main components of the bimodal $v \sin i$ distribution (see Fig. 6.1).

Below, we describe the main highlights that can be extracted from inspection of the various panels in Fig. 6.1, also providing the particular reasons to select each of abovementioned boundaries.

- In panel A we highlight 31 stars with $v \sin i$ <40 km s^{-1}, the slowest rotators in the sample. This boundary has been selected to coincide with the left wing of the low-velocity peak of the bimodal distribution (see Fig. 6.1). In the sHR diagram, these stars are practically absent above the 32 $M_{\odot}$ evolutionary track. This is an unexpected result, since we are considering projected rotational velocities. The random distribution of the inclination angle i is incompatible with the absence of slow rotators in any particular region of the diagram. This gives the impression that

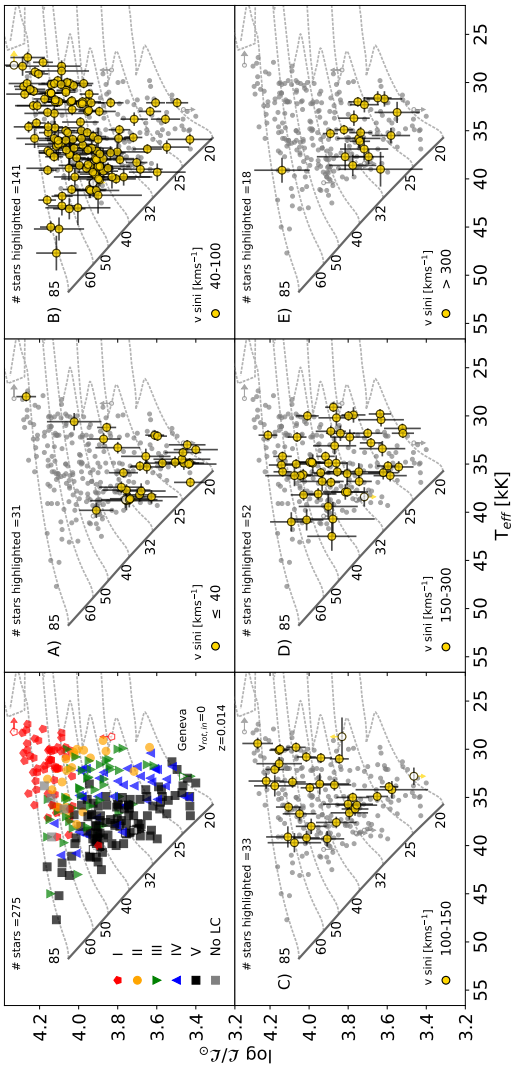

Figure 6.8: Location of the 275 stars in the sample with reliable spectroscopic parameters in the spectroscopic HR diagram ($\mathcal{L}$=4log$T_{\rm eff}$-log$g_{\rm true}$). Open points represent stars with upper or lower limits in $T_{\rm eff}$ or log g. Evolutionary tracks and position of the ZAMS from the non-rotating, solar metallicity models by Ekström et al. (2012); Georgy et al. (2013) are included as references. In the first panel we use colors and symbols to identify different luminosity classes. In panels marked A to E the stars are highlighted (gold) depending on specific ranges of their $v \sin i$ value. For the marked stars individual uncertainties are included as error bars.

something is limiting the determination of low $v \sin i$ values above the 40 $M_\odot$ evolutionary track.

With respect to methodology limitations, we note that due to the high-quality of our data in terms of resolution R>25000, our limit in the $v \sin i$ determination corresponds to $\sim$12 km s^{-1}. While the origin of this imposed limit is then not clear, Simón-Díaz & Herrero (2014) proposed that this could be due to the effect of microturbulence on the determination of $v \sin i$ below a certain value of this quantity (see also notes in Gray 2005). In these regards it is interesting to remember that in Sect. 5.5.4 we found some empirical hints of the occurrence of positive correlation between microturbulence and luminosity (actually between ξ_t and log $\mathcal{L}$) in the O-star domain (see also Fig. 5.7).

- In panel B we highlight 141 stars with $v \sin i$ in the range 40-100 km s^{-1}. This range represents the main peak of the bimodal distribution, including approximately 50% of the sample. Although these stars are distributed everywhere in the diagram, we highlight two interesting results that drew our attention: (1) the relative density of stars with this characteristic is larger above the 40 $M_\odot$ evolutionary track, and (2) all the very-hot massive stars ($T_{\rm eff}$ >42 kK) are included in this group.

- In panel C we highlight 33 stars with $v \sin i$ in the range 100-150 km s^{-1}. This range represents the right wing of the main peak of the bimodal distribution (see Fig. 6.1). The distribution of these stars in the sHR diagram is very similar to that of the stars highlighted in panel B, with the difference that they do not appear at any point close to the ZAMS.

- In panel D we highlight 52 stars with $v \sin i$ in the range 150-300 km s^{-1}. This range represents the intermediate-rotators in the sample. It corresponds to the first half of the tail of the bimodal distribution. These stars are distributed throughout the O stars domain in the sHR digram. Interestingly, most of the stars at the end of the main sequence below the 40 $M_\odot$ evolutionary track are included in this group.

- In panel E we highlight the 18 stars with $v \sin i$ values over 300 km s^{-1}. We note that the boundary between stars in groups D and E was selected because we found that stars with $v \sin i$ above 300 km s^{-1} are mainly concentrated in an specific region of the diagram. In particular, all stars but one in group E are found below the 40 $M_\odot$ evolutionary track. The lone star with higher luminosity is HD 14442, an O5 star with no luminosity

class for which we only count with one spectra. In the next section we will discuss the plausible binary origin of these stars (de Mink et al. 2013).

In summary, the principal result that comes up from the inspection of Fig. 6.8 is that the slowest-rotators (<40 $\mathrm{km\,s^{-1}}$, panel A) and the very fast rotators (>300 $\mathrm{km\,s^{-1}}$, panel E) in the sample appear concentrated in a very specific region of the diagram (below the 32 $\mathrm{M_\odot}$ evolutionary track). The rest of stars are distributed in a more homogeneous way, covering the entire diagram.

6.4 $v \sin i$ dependence on mass and evolution

In this section we investigate how the distribution of projected rotational velocities in the O star domain depends on mass and evolutionary state. To this aim, we separate the complete sample of 275 stars in four subsamples covering two mass ranges and two regions of the sHR diagram (roughly) corresponding to the first and second half of the main sequence (see Fig. 6.12). The results of this study, as well as the reason of the selection of the specific boundaries separating the four subsamples, are further explained and discussed in Sect. 6.4.2. But, before, we present a brief summary of the main predictions resulting from two state-of-the-art evolutionary models for single stars (Ekström et al. 2012; Brott et al. 2011) and from the population synthesis computations performed by de Mink et al. (2013) taking into account the effect of binary interaction during the evolution of massive stars.

6.4.1 Two theoretical scenarios describing the spin rate evolution in O-type stars

Single-star rotating evolutionary models: Figures 6.9 and 6.10 depict the evolution of the equatorial rotational velocity (using gravity as a proxy of time) of stars with three different masses as predicted by the evolutionary models including rotation of Brott et al. (2011) and Ekström et al. (2012), respectively. In both cases, we include the tracks corresponding to two different sets of initial rotational velocities: $v_{\mathrm{eq,ini}} \sim$200 and 300 $\mathrm{km\,s^{-1}}$ for Brott (aka. Bonn) models, and $v_{\mathrm{eq,ini}} = 20$ and 40% of the critical velocity for Ekström (aka. Geneva) models.

The information presented in Figs. 6.9 and Fig. 6.10 allow us to briefly summarize the main points to take into account when interpreting our empirical results regarding the distribution of projected rotational velocities in the sHR diagram in the context of single-star evolution:

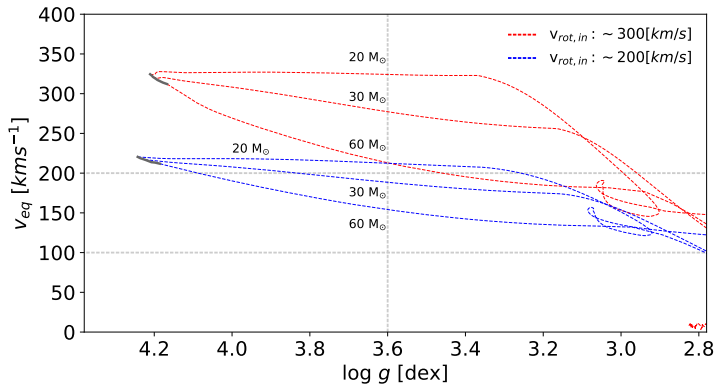

Figure 6.9: v_{eq} evolution predicted by Bonn evolutionary models with initial rotation ∼ 200-300 km s^{-1} (Brott et al. 2011). Gravity has been used as a proxy for stellar evolution.

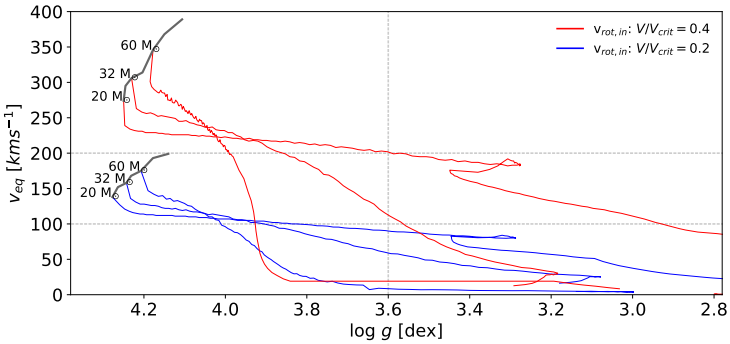

Figure 6.10: v_{eq} evolution predicted by Geneva evolutionary models with initial rotation 20/40% of the critical velocity (Ekström et al. 2012; Georgy et al. 2013). Gravity has been used as a proxy for stellar evolution.

- Single massive stars always slow down their rotational speeds during the main sequence.
- Stellar winds become an efficient mechanism to transport angular momentum out of the star only above a certain mass (M>30–40 $M_{\odot}$).

- At the end of the main-sequence, massive stars suffer from a quick expansion that produces a minor deceleration of the surface velocity.

- Bonn and Geneva models predict a different evolution of the spin rate of massive stars during the main sequence.

The latter difference is just a consequence of the treatment of the angular momentum transport in the stellar interior by the two evolutionary codes. On the one hand, Bonn models treat the angular momentum transport including magnetic fields (caused by a Spruit-Tayler dynamo, see Brott et al. 2011 and references therein), resulting in a quasi solid-body rotation that produced a extremely efficient angular momentum transport from the core to the surface. This compensates for the angular momentum loss by stellar winds, allowing the Bonn models to retain a high surface velocity throughout its main-sequence evolution. Geneva models, on the other hand, do not include magnetic fields and include angular momentum advection from meridional circulation, which may transport angular momentum from the envelope inwards (Ekström et al. 2012). A direct consequence of this different treatment is that angular velocity losses are small in the Bonn models and very large in the Geneva models, producing a set of Bonn models rotating (at the surface) faster than the Geneva counterparts.

As a final remark, we want to highlight that magnetic fields have been suggested to be able to additionally spin down significantly massive stars (ud-Doula & Owocki 2002); however, this must be considered as a secondary effect when interpreting the general distribution of projected rotational velocities in the O star domain since the percentage of O-type stars holding a strong magnetic field is only 10% (Wade et al. 2016; Grunhut et al. 2017).

Population synthesis with binary interaction: In the case of binary systems, the evolution of the spin rate of each individual component is affected by several additional effects. For example, in close binaries, the tidal interaction synchronize rotation and orbit, and hence the stars in these binary systems could experience modifications in the individual spin rates (either increasing or decreasing the equatorial velocities depending on the specific case). Also, mass (and momentum) transfer ocurring after Roche-lobe overflow can spin up the initially less massive star up to very high rotational velocities[8].

[8] In addition, after Roche-lobe overflow (∼10 Myr.) the secondary star in the system would experience an increase in luminosity and speed, due to mass-transfer, that would transform the appearance of the system to a fast younger single object.

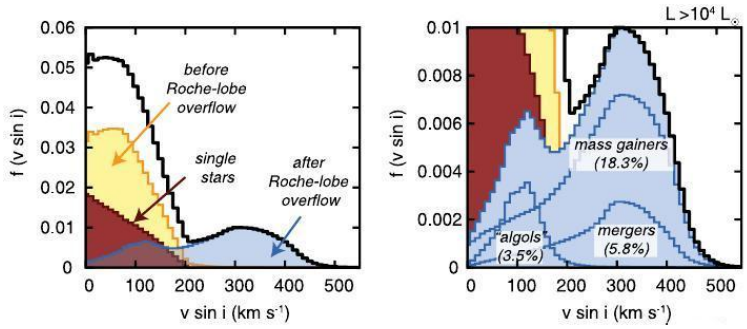

Figure 6.11: Projected rotation rate distribution for a simulated population of main-sequence stars assuming continuous star formation and different effects on the $v \sin i$, including binary interactions (de Mink et al. 2013). Panels show the full distribution function and a zoom-in highlighting the contribution of the various binary products.

Figure 6.11 shows the $v \sin i$ distribution resulting from a simulated population of main-sequence massive binary stars (de Mink et al. 2013). The study by de Mink assumes a constant star formation rate, with initial values of rotation always below 200 km s^{-1}. Interestingly, the simulations create a population of massive stars with high rotational rates that merges with the main slow-peak component. As expected, this tail of fast rotators is mainly a product of mergers and secondary stars spun up by mass (and momentum) transfer.

6.4.2 Interpretation of the empiric distribution of $v \sin i$ in the sHR diagram

As stated above, we now separate the global results in four subsamples to provide some hints on the empirical distribution of $v \sin i$ as a function of mass and evolutionary status. To this aim, we consider two ranges of masses and divide the sample between stars in the first and second half of the main-sequence. Particularly, the stars are divided by mass estimate from their position in the sHR diagram. The limit selected is the 40 $M_\odot$ evolutionary track, as stars with M>40 $M_\odot$ are expected to develop winds strong enough to significantly affect the angular momentum evolution of the stars (see Figs. 6.9 and 6.10). For the evolutionary status, gravity is here considered a proxy of evolution. We divide the sample using $\log g$=3.6 dex as a boundary roughly separating the first and second half, respectively, of the O-star main-sequence.

Fig 6.12 present our empiric results for 275 stars separated in these four sub-

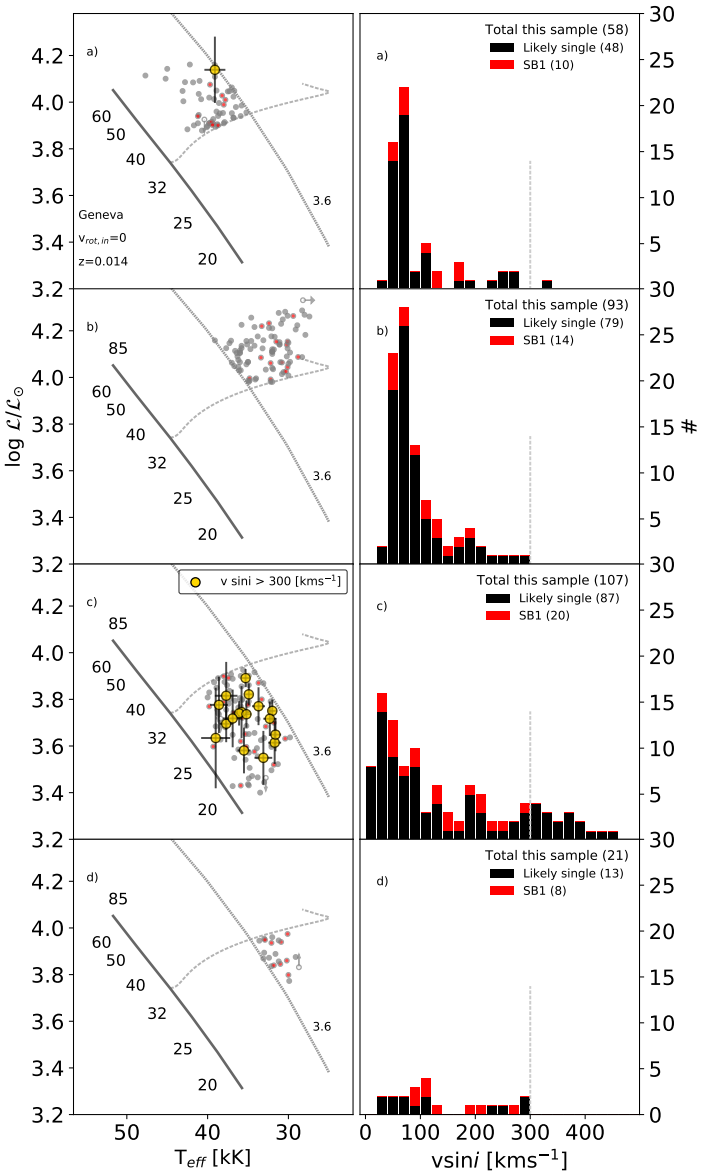

Figure 6.12: Distribution in the sHR diagram and $v \sin i$ histogram of the 275 stars in the sample with reliable spectroscopic parameters. Each row corresponds to a specific region of the sHR diagram, separating stars above or below the 40 $M_\odot$ Geneva evolutionary track, and left or right of the $\log g$=3.6 [dex] value. Each sample is divided in likely-single (black) or SB1 (red) stars. Very fast rotators ($v \sin i$ >300 km s^{-1}) are highlighted in yellow.

samples, showing the location in the sHR diagram and their respective $v \sin i$ histogram. Likely-single and SB1 stars are indicated in black and red, respectively. In addition, in all panels, we highlight those stars having a $v \sin i$>300 km s^{-1} as we note that they are restricted to a very specific region of the sHR diagram (see Fig. 6.8 and notes in Sect. 6.3.2).

The four top panels, marked as "a" and "b", represent the most massive stars (located above the 40 $M_{\odot}$ evolutionary track in the sHR diagram). The stars in the group "a" can be considered as progenitors of the stars in group "b". Equivalently, the $v \sin i$ distribution of group "a" is expected to become the $v \sin i$ distribution of the group "b" by the effect of stellar evolution. The system is analogous for the bottom panels, including those stars below the 40 $M_{\odot}$ evolutionary track (group "c" is a progenitor sample of group "d").

We now proceed to evaluate these results in the context of the theoretical scenarios presented in previous section.

Interpretation of results in the context of single-star evolution:

A direct comparison of the empirical distribution of $v \sin i$ values against the expected behavior of this parameter as predicted by the single-star rotating evolutionary models rise several points of interest, briefly summarized here:

- In the upper part of the diagram (M>40 $M_{\odot}$), the relative percentage of stars with intermediate values of $v \sin i$ (100-150 km s^{-1}) appears to not strongly decrease with evolution (from panels "a" to panels "b"). This is in contrast with the predictions resulting from Geneva models –an accused decrease in the $v \sin i$– but in fair agreement with the more moderated spin down characterizing the Bonn models (see Figs. 6.10 and 6.9). To further explore on the magnitude of the difference between the samples comprising groups "a" and "b", we perform a Kuiper test (Kuiper 1960) that evaluates the possibility that these two subsamples are representative of the same original population. From the results of this test we found a 66% probability that these two samples are randomly produced from the same parent distribution.

- In the lower part of the sHR diagram (M<40 $M_{\odot}$) the proportion of intermediate and fast rotators (100-300 km s^{-1}) is much larger than in the upper part. In the case of the Bonn evolutionary code, the large slow-peak would not be reproducible if we consider that stars are born with $v \sin i$ values between 200-300 km s^{-1}, because the stars are not able to spin down significantly during the main-sequence evolution. Regarding Geneva models, this caveat is not present.

- Regarding the very fast rotators, as we already indicated in Sect. 6.3.2, they are mainly concentrated below the 40 $M_{\odot}$ evolutionary track. Now, we can also note how they disappear above the $\log g$=3.6 dex threshold. Naively, this could be linked to the fact that fastest-rotators are the very young newborns stars that still maintain a very fast initial rotation rate (as rotation in a star tends only to decelerate) but the fact that these stars are not concentrated very close to the ZAMS evidence against this possibility. All this makes the explanation of the behavior of the very fast rotators in the context of single-star evolution very challenging, and maybe related to binary interaction (see below).

To sum up; while the $v \sin i$ distribution for the more massive stars (M>40 $M_{\odot}$) appears to not change (spin down) drastically as the stars evolve, in accordance with Bonn models, the $v \sin i$ distribution of the less massive stars (M<40 $M_{\odot}$) presents a more evident evolution, with the fastest-rotators disappearing. The latter is more in accordance with Geneva's evolutionary tracks. This problem to reconcile observations and models was already pointed out by Markova et al. (2018) study, using 53 Galactic O-type stars and the Geneva and Bonn set of models. They found that neither set of models was able to represent their distribution appropriately, when considering only the expected behavior of the $v \sin i$ evolution included in single-star rotating evolutionary models.

Interpretation of results in the context of binary evolution:

The interpretation of our empiric results with only the single-evolutionary models leave us with an unsatisfactory explanation, but this changes if we reconsider the origin of the fastest-rotators and attribute their existence to binary interaction. By introducing binary interaction in a population synthesis study, de Mink et al. (2013) found that the tail of fast-rotators ($v \sin i$ above 200 $\mathrm{km\,s^{-1}}$) could be the product of mass-transfer or even merger situations. With enough time, the binary interactions produce a larger number of faster rotators, explaining the very fast-rotators ($v \sin i$ above 300 $\mathrm{km\,s^{-1}}$) that appear in our sample.

In addition, our lack of SB1 stars in the very fast-rotators tail (see Fig. 6.2) is predicted by population synthesis computations including interacting binaries. As stated in sect. 6.3.1, all our very fast-rotators are identified as likely-single stars. If we assume that there is no reason why the stars born in binary systems present a different (slower) initial distribution of $v \sin i$ values, the lack of SB1 stars in the tail of fast rotators supports the hypothesis that the stars in the high-velocity tail are actually post-interaction products of binaries, and

originally single stars are not born with spins faster than 200 $\mathrm{km\,s^{-1}}$. This prediction is included in de Mink et al. (2013) study. This argument was also used to explain a similar situation for the $v \sin i$ distribution of stars in 30 Doradus in Ramírez-Agudelo et al. (2013), where their extra-galactic sample also presents very fast-rotators, and most of them appear as single stars.

Similarly to our study, most of fast-rotators in the Ramírez-Agudelo et al. (2013) sample appear as late-O spectral types (O6-O9) dwarfs. This can be explained if we consider that these stars come from a mass transfer or merger process involving less massive stars (B-type stars). The same processes in O-stars would produce more massive final objects with larger luminosities, and therefore stronger stellar winds. The resulting massive object then quickly loses angular momentum and spins down from extreme rotational speeds (de Mink et al. 2013).

A final note on the initial distribution of rotational velocities:

The initial rotation is a influential input condition for the evolutionary models of massive stars and provides a very decisive constraint in star formation theories. We note that deriving true birth distribution of massive stars directly from observations is difficult, but with our results we could establish a qualitative limit in their initial rotational rate.

If the majority of massive stars are only able to lose between the 10-20% of their rotation rate from the initial rate, the bulk of the massive stars would need to be born with rotation rates closer to $\sim$120 $\mathrm{km\,s^{-1}}$ in order to generate the observed distribution (Fig. 6.1). This corresponds to an initial rotation of $\sim$20% of the critical velocity.

From the two last panels of Fig 6.8 (D and E) we see how the faster rotators of our sample are distributed in the sHR diagram. They do not represent the majority of the sample and the very fastest rotators ($v \sin i$>300 $\mathrm{km\,s^{-1}}$) only appear in a certain area of the diagram, below the 40 $M_{\odot}$ evolutionary track. The majority of the sample, in panel B, present lower values of $v \sin i$, and it is concentrated above the 40 $M_{\odot}$ evolutionary track.

These are strong arguments against the use of very high initial velocities in the evolutionary models ($\sim$40% of the critical velocity, or 300 $\mathrm{km\,s^{-1}}$), especially for masses above 40 $M_{\odot}$. This situation for the Galactic O-type stars is in accordance with the results obtained in the LMC in Ramírez-Agudelo et al. (2013). They found that the majority of their sample of O-type stars were rotating at $\sim$20% of the critical velocity, and this is only possible with moderated initial velocities ($\sim$25-30% of the critical).

A word of caution regarding rotational mixing: Rotational mixing theories suggest a surface enrichment for stars above a certain threshold of $v \sin i$ (Meynet & Maeder 2000; Heger et al. 2000). In the interpretation that the faster rotators in massive stars samples are only the product of binary interaction, we must advice caution when calibrating rotational mixing theories, as the result of mass transfer or mixing in merger products could mimic the metal enhancement due to rotational mixing. The on-going work on the multi-epoch analyses of the sample of stars with $v \sin i$>200 km s^{-1} would help on this matter.

7

The complete sample (II): parallaxes and fundamental parameters

The distance is nothing
when one has a motive.
Jane Austen

In this chapter we first perform a thorough assessment of the available information on parallaxes for our complete sample of Galactic O-type stars. We evaluate, in terms of quantity and accuracy, the improvement from the *Hipparcos-Tycho* catalog to the recent second data release by the *Gaia* mission (*Gaia*-DR2). Then, following the same approach as the one presented in Chapt. 4, we use the grid of O-type standard stars for spectral classification as a benchmark sample to evaluate the accuracy of the radii, luminosities, and spectroscopic masses resulting from the combination of the parallaxes provided by *Gaia*-DR2 and the results from our IACOB-GBAT spectroscopic analysis.

7.1 Introduction

The complete empirical characterization of the physical properties of the sample of O-type stars investigated in this thesis requires to complement the set of parameters that can be directly obtained from the quantitative spectroscopic analysis (see Chapt. 5) with information about the stellar radii (R), luminosities (L), and spectroscopic masses ($M_{\rm sp}$). A reliable empirical determination of these three important parameters necessarily requires to have access to accurate information about distances (d) to each of the considered stars (or,

alternatively, about the individual absolute magnitudes, M_V).

The *Gaia* mission, launched in December 2013, was envisaged as a unique opportunity to improve the landscape of available information about distances to massive OB stars provided by the previous large astrometric space mission: *Hipparcos*. The development of this thesis work was hence planned to timely connect with the second data release of *Gaia* (Gaia-DR2, Gaia Collaboration et al. 2018a; Lindegren et al. 2018; Luri et al. 2018). However, as will be indicated along this Chapter, although *Gaia* will certainly end up providing very valuable and accurate information about the distances to a large percentage of the stars in our sample, we will have to wait to *Gaia*-DR3 (planned for the first half of 2021) to complement our catalog of empirical information about the largest sample of Galactic O-type stars investigated to date with meaningful information about radii, luminosities and spectroscopic masses.

Despite the present limitations of the second data release of *Gaia* (see Section 7.2), we decided to use the available information about parallaxes to evaluate the reliability of the derived distances, as well as to investigate the potential impact on the estimated absolute magnitudes, radii, luminosities and spectroscopic masses (Sect. 7.3). To this aim, we concentrate on what we have defined as our benchmark sample: the grid of O-type standard stars for spectral classification (see Chapt. 4).

As indicated in Chapt. 3, once the value of the absolute magnitude is included as input in IACOB-GBAT, the code automatically allows us to quickly infer values and uncertainties for the radius, luminosity, and spectroscopic mass of each studied star. In Sect. 7.3.1, we use two different methods to infer the absolute magnitude of our benchmark sample of stars: (a) the Bayesian calculation of the distance from the *Gaia*-DR2 parallaxes provided by Bailer-Jones et al. (2018), combined with the apparent V magnitude corrected from extinction, from Maíz Apellániz & Barbá (2018), and (b) the SpT/LC$-M_V$ calibrations presented in Martins & Plez (2006).

Both sets of M_V values are then used in Sect. 7.3.3 to obtain the corresponding estimates for the radii, luminosities, and masses. There, we also compare our resulting values of M_V, R, log$L$ and M_{sp} with those that can be inferred from the available calibrations of these parameters with SpT and LC. Finally, the distribution of stars in the HR diagram is presented in Sect. 7.3.4, and compared with the one extensively presented along this thesis in the sHR diagram.

7.2 Distances to Galactic O-type stars: From Tycho to *Gaia* DR2

7.2.1 Parallaxes: From Tycho to *Gaia*

Astrometric measurements (source positions, proper motions, and parallaxes) are made by repeatedly determining the direction to a source on the sky and modeling the change of direction to the source as a function of time as a combination of its motion through space (as reflected in its proper motion and radial velocity) and the motion of the observing platform (Earth, *Gaia*, etc.) around the Sun.

Historically, the first large astrometric survey providing galactic parallaxes is The Hipparcos and Tycho Catalog (ESA 1997). Tycho refers to the various catalogs built from the observations provided by the star mapper instrument of the *Hipparcos* satellite (Perryman et al. 1997; Hoeg et al. 1997). The original Tycho-1 Catalog, almost complete up to V = 11.5, gave positions and parallaxes for about 1 million stars. The later reduction of the astrometric data (van Leeuwen 2007), correcting inaccuracies in the along-scan attitude reconstruction, claims accuracies for stars brighter than magnitude[1] Hp = 8 to be in the range of 0.09 to 0.19 mas, comparing to open cluster studies.

We searched for available information about parallaxes for our initial sample of 415 Galactic O-type stars in the Tycho catalog and found values for 152 objects. Figure 7.1 presents a normalized cumulative distribution function of the nominal relative error in parallax for these stars as a reference for its accuracy. As we will see in Sect. 7.2.3 a large relative error of the parallax measure represents an important caveat in the determination of the distance.

The next big revolution came with the first data release by the *Gaia* mission (*Gaia*-DR1, September 2016) with astrometric results –based on observations collected by the *Gaia* satellite during the first 14 months of its operational phase– for more than 1 billion stars brighter than magnitude[2] G$\sim$ 20.7. Multiple observations of a given star over several years are crucial for a successful disentanglement of the effects of stellar parallax and proper motion. *Gaia*-DR1 is only able to provide complete astrometric single-star solutions – including proper motions and parallaxes – by incorporating positional information from the earlier *Hipparcos* and Tycho-2 catalogs[3] (Høg et al. 2000; van Leeuwen 2007). This intermediate solution was proposed by Michalik et al. (2015) and

[1] Hp$\sim$V in this context.
[2] $G \sim B$ in this context.
[3] The parallaxes from the *Hipparcos* catalog and the proper motions from the *Hipparcos* and Tycho-2 catalog were not used, only positions.

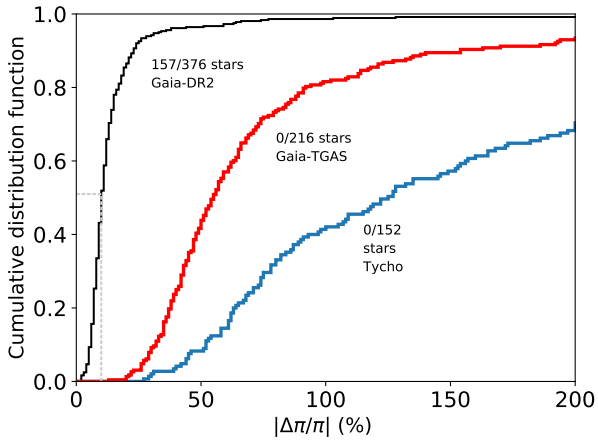

Figure 7.1: Cumulative histogram of the nominal relative error in parallax of the Galactic O-type sample of stars stars with parallax values available for each of the different astrometric catalogs: Tycho, *Gaia*-TGAS, and *Gaia* DR2. Each catalog shows the total number of stars with parallax value available and those with less than 10% relative error, marked also with a vertical dotted line in the graph.

called *TGAS: The Tycho-Gaia astrometric solution.*

TGAS benefits from the ∼24 yr time difference between *Hipparcos* and *Gaia* to improve the proper motions and, for example, detect long-period astrometric binaries. For about two million bright stars (V∼ 11.5) they are able to obtain positions, parallaxes, and proper motions up to Hipparcos-type precision or better (0.09 to 0.19 mas). However, TGAS has an important caveat, since the primary data set lacks the bright stars (G<6) not nominally observed by *Gaia* due to saturation and calibrations limitations (Martín-Fleitas et al. 2014; Michalik et al. 2015; Lindegren et al. 2016; Sahlmann et al. 2016).

We found 216 Galactic O-type stars from our sample with available parallaxes values in TGAS. The associated information is incorporated to Fig. 7.1. The improvement from Tycho to TGAS is clear, with a larger number of stars with available values and a decrease in the mean relative error. Unfortunately, TGAS was not yet good enough for the purposes of this thesis, since many of the stars in our sample were missing and, from those included in the catalog, non of them has a relative error in parallax better than 20%.

It is important to emphasize the provisional nature of the astrometric results in the first data release of *Gaia*. The processing for a given data release starts with a task that groups individual *Gaia* observations and links them to sources on the sky (see Fabricius et al. 2016; Lindegren et al. 2018). The observations are linked to known sources, or sources are newly "created" from the clustering of the observations around a celestial position where previously no source was known to exist. Severe limitations were set by the short time period on which the solution is based, and the circumstance that the processing of the raw data – including cross-matching of sources – had not yet benefited from improved astrometry and the new optical reference frame to be determined entirely from *Gaia* data, independent of the *Hipparcos* reference frame, in subsequent data releases. In comparison with external data, they found good agreement on a global level, with differences generally compatible with the accuracy errors. However, there are clear indications of systematic differences at the level of ∼0.2 mas, mainly depending on color and position on the sky (e.g., 9% of systematic errors in the distance for OB stars according to Bobylev & Bajkova 2018). Nevertheless, TGAS offered the opportunity to perform a full-sky analysis providing an important early scientific validation of the *Gaia* instrument, calibration, and data processing at sub-mas level much earlier than previously anticipated.

The second data release of *Gaia* (*Gaia* DR2, May 2018) contains results for 1693 million sources in the G magnitude range 3 to 21 based on observations[4] collected by the *Gaia* satellite during the first 22 months of its operational phase. *Gaia*-DR2 represents a major advance with respect to *Gaia* DR1 in terms of completeness[5], performance, and richness of the data products. It gives five-parameter astrometric solutions of 1332 million sources, with formal uncertainties ranging from about 0.02 mas to 2 mas in parallax. For sources with G $\sim$ 12 mag –such data were included already in the first release– the present results are generally more accurate and fully independent of the *Hipparcos* and Tycho catalog.

Because the observational time baseline for *Gaia* DR2 is sufficiently long to define a very accurate celestial reference frame (Gaia-CRF2)[6], as described in Gaia Collaboration et al. (2018b), parallax and proper motion can be derived based solely on the *Gaia* observations alone, without the necessity of the Tycho Astrometric Solution. In addition, the algorithm that carries out the

[4] Although stars with G∼6 generally have inferior astrometry due to calibration issues (Martín-Fleitas et al. 2014; Sahlmann et al. 2016; Lindegren et al. 2018).

[5] Essentially complete between G = 12-17.

[6] *Gaia* DR2 contains the positions and proper motions for about half a million identified quasars.

grouping and linking was much improved at the beginning of the processing for *Gaia* DR2, giving better results in dense areas. For *Gaia* DR2 the source list was created essentially from scratch, unlike *Gaia* DR1, based directly on the detections and using a cluster analysis algorithm that takes into account a possible linear motion of the source. The source list for *Gaia* DR2 is therefore much cleaner and of higher angular resolution, resulting in an improved astrometry. This reflects in a great number of objects for which the source-identifier changed with respect to the *Gaia* DR1. At magnitudes brighter than G $\sim$ 16 some 80–90 % of the sources changed source identifier. At G $\sim$ 18 mag this reduces to some 20 %, going down to zero source identifier changes G $\sim$ 20 mag. The source list is expected to be already stable, with minimum change expected between *Gaia* DR2 and *Gaia* DR3.

In Fig. 7.1 we show the total of 376 Galactic O-type stars from our sample with available parallaxes values in *Gaia* DR2 in a normalized cumulative distribution function of the nominal relative error in parallax. There is again a clear improvement of the situation from *Gaia* DR1 to DR2, with a representative increase of objects with available parallax, but especially a decrease in the mean relative error.

This is already discussed in Fig. 7 of Gaia Collaboration et al. (2018a) depicting the parallax uncertainties in *Gaia* DR2 as a function of G compared to the uncertainties quoted for *Gaia* DR1. In addition, they show the expected end-of-mission parallax performance predicted after the commissioning of *Gaia*, noticing how the performance for *Gaia* DR2 is still limited by calibration uncertainties for sources brighter than G $\sim$ 14. Nevertheless, *Gaia* DR2 still represents an early data release based on only a limited amount (less than two years) of input data, partly inadequate calibrations, and an incomplete understanding of the behavior of the spacecraft, payload, and instruments. These shortcomings manifest themselves as systematic errors which, although much reduced in size from *Gaia* DR1 to *Gaia* DR2, will remain a limiting factor in scientific uses of the data, in particular at the bright end of the survey and, for example, for distant samples. In the following subsections we first analyze the characteristics and quality of these paralactic measures and then make use of distances inferred through Bayesian calculations from these results.

7.2.2 Parallaxes: *Gaia* DR2

In this section we evaluate the sample of O-type stars with available *Gaia* DR2 parallaxes values, as well as the parallax values themselves. We establish the completeness, possible limitations, and known errors for these measurements.

Firstly, we want to note that *Gaia* DR2 represents the largest parallax cat-

alog ever produced and contains parallaxes of faint objects observed relatively few times and of extragalactic objects. For many of such objects the value of the parallax listed in the catalog may be negative. As explained in Luri et al. (2018) the presence of negative parallaxes is a natural consequence of the way the *Gaia* observations are described in terms of a linearised astrometric source model, with the parameters of the model solved through a least-squares process. Hence negative parallaxes represent perfectly valid measurements and can be included in analyses of the *Gaia* DR2 data.

Figure 7.2 depicts a histogram with the B magnitudes of our sample of Galactic O-type stars with a value (positive or negative) of parallax available in *Gaia* DR2. Comparing with the complete sample, included in the figure as a background distribution in gray, we see how this sample is very representative of the complete sample.

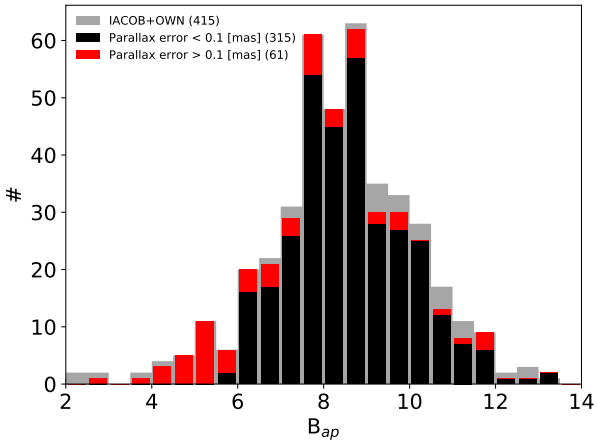

Figure 7.2: B magnitude histogram showing the number of Galactic O-type stars in the IACOB+OWN sample with available parallax value in the *Gaia* DR2 catalog. Black/red color indicates a nominal absolute error in parallax as provided by *Gaia* DR2 below/above 0.1 mas.

The astrometric uncertainties listed in *Gaia* DR2 are derived from the formal uncertainties resulting from the astrometric data treatment. Although the measurement principle of *Gaia* should give absolute parallaxes, the results for quasars very clearly indicate a global zero point of about -0.03 mas (Gaia Col-

laboration et al. 2018a). In addition, strong correlated errors (or systematics) exist on spatial scales of 1 deg up to 0.1 mas correlated to celestial position, source color, and source magnitude. This can be seen as unphysical patterns in the parallax maps of high-density areas around the Galactic center, clearly related to *Gaia*'s scanning law with its precessional motion of about 1 deg per revolution (Lindegren et al. 2018). For this reason, Fig. 7.2 highlights the stars that present an absolute error in the measurement greater than 0.1 mas, already at the same level of the correlated positional systematics. Interestingly most of the stars brighter than $B \sim 6$ present an error of these characteristics.

The use of physical CCD gates in the observation of the brightest stars to prevent saturation (see description in Kohley et al. 2012), limits the photon number and, unfortunately, generates separate calibration procedures for each gate, altering the centroiding precision acquisition. This can be seen in Lindegren et al. (2018) where they show that the quadratic difference in parallax amounts to about 0.3, 0.25, and 0.15 mas for G = 6-12, 12-13, and G>13, respectively[7]. Below $G < 6$ there is an extremely strong rise of the error caused by uncalibrated CCD saturation (Lindegren et al. 2018). A main task in preparation for future *Gaia* data releases is to improve these calibrations and hence reduce these differences.

For all these reasons, we decided to work with the whole sample of parallax results, but always highlighting the stars with unreliable parallaxes, i.e., brighter than $B = 6$ and/or with an absolute error in the parallax at the same level as the systematic (0.1 mas). The complete compilation of these parallaxes is included in Table B.8.

7.2.3 Distances: *Gaia* DR2

With the precise positions, proper motions, and parallaxes for an unprecedented number of Galactic O-type stars from the *Gaia* DR2 catalog we want to proceed with the inference of astrophysical quantities, a task that is less trivial than it appears, especially when parallaxes are involved. For the vast majority of stars in the second *Gaia* data release, especially in the case of large relative errors, reliable distances cannot be obtained by the naive inversion of the parallax.

A correct inference procedure must instead be used to account for the non-linearity of the transformation and the asymmetry of the resulting probability distribution, otherwise, the effects of the observational errors in the parallaxes can potentially lead to strong biases. Estimating distances is an inference problem in which the use of prior assumptions is unavoidable. Here we provide

[7] This includes the correction of an initial bug in the reduction of the data presented in Appendix A of Lindegren et al. (2018).

insight in this matter and compile distances obtained from proper Bayesian calculations.

The direct inversion of the parallax method presents serious drawbacks as we are forced to dispose of non-positive parallaxes (the removal of the targets with negative parallaxes could bias the results, see Luri et al. 2018), and it has a very high variance. Furthermore, as shown in Bailer-Jones (2015), the inversion of the parallax rapidly becomes significantly biased for values with relative error over 10%, providing non-Gaussian distributions, with the mode estimator de-aligned relative to the true distance value, and a long tail towards large values of distance (Smith & Eichhorn 1996). Other types of truncations in the sample, e.g., removing all the parallaxes with a relative error above a given threshold can strongly affect the properties of the sample, as stars at short distances are favored with respect to distant stars (Luri et al. 2018). The main recommendation is thus to always treat the derivation of physical parameters from astrometric data when using parallaxes as an inference problem, preferably with a full Bayesian approach.

A full treatment of this Bayesian calculation was given in Bailer-Jones (2015), who investigated and considered the properties of various priors and estimators. They reached to the conclusion that the best, and most uninformative, prior is the exponentially decreasing space density (EDSD) prior[8], using as estimator the mode, which is significantly closer to the true value than the other estimators, and as measure of uncertainty the highest density interval (HDI).

The EDSD is a weak distance prior that varies smoothly as a function of Galactic longitude and latitude according to a Galaxy model[9] with a single length scale parameter and decreasing asymptotically to zero at infinite distance. This length scale parameter, obtained by fitting to a three-dimensional model of the Galaxy as seen by *Gaia*, varies smoothly and realistically as function of Galactic longitude and latitude. The mode is found analytically by solving a cubic equation.

The HDI is the span of the distance that encloses the region of highest posterior probability density, defined by the lower and upper bounds, r_{lo} and r_{hi}, respectively, and is unique if the posterior is unimodal. Conceptually, the HDI can be found by lowering a horizontal line over the distribution until the integral of the curve contained by the intersection points is equal to 0.6827 (corresponding to percentiles 5% and 95%). While this prior (and estimator)

[8] Any uniform prior in distance or with a sharp cut-off are shown to give very poor distance estimates.

[9] It uses a chemo-dynamical model to simulate the Galaxy over the entire sky.

overcomes many of the problems that others present, the choice of prior (and estimator) always has a significant impact on the inferred distances.

Although more precise distances can be estimated for a subset of the stars using additional data (such as photometry), our goal is to use purely geometric distance estimates, independent of assumptions, as the ones provided in the Bailer-Jones et al. (2018) catalog. The results for our sample are compiled and included in Table B.8.

By using an inference approach, they can infer meaningful distances even from non-positive parallaxes, with estimators that degrade gracefully as the data quality degrades, and with credible intervals that grow with the observational uncertainties until they reach the typical scales of the prior when the observations are non-informative. In the limit of precise parallaxes, say better than about 10% in relative error, the prior has little impact on the resulting distance estimates, and already at relative error 25% the posterior is almost indistinguishable from the prior (Bailer-Jones et al. 2018). In addition, a noisy inverse parallax can extend to arbitrarily large distances, something that the prior constrains.

Figure 7.3 compares the distance estimates for our sample of Galactic O-type stars from Bailer-Jones et al. (2018) with those obtained from a naive parallax inversion. The figure shows the tendency of inverse parallax to extend to larger distances, something already depict in a comparison with the whole *Gaia* DR2 sample in Bailer-Jones et al. (2018).

Finally, and to get an general idea of the distribution of these stars in the solar environment, Fig. 7.4 presents the radial distribution around the Sun of our sample of the Galactic O-type stars, using the distances obtained in the Bayesian calculation of Bailer-Jones et al. (2018). In the figure are marked with an $\times$ the stars that we have considered to have unreliable parallaxes, following the criteria of the previous section ($B < 6$, or absolute error of the parallax $>$ 0.1 mas). The great majority of the sample (80%) is closer than 4 kpc, and the latitude of the majority (shown with the color) indicates that they are grouped –as expected– around the galactic thick disk ($\pm 20°$). Interestingly, closer than 1 kpc most of the stars have unreliable parallax values.

7.3 Fundamental parameters of Galactic O-type stars

The complete empirical characterization of any star requires the determination of the fundamental parameters (radii, luminosities, and masses) in addition to the spectroscopic parameters ($v \sin i$, $T_{\rm eff}$, $\log g$, $Y_{\rm He}$, $\log Q$, $\xi_{\rm t}$). Although this thesis initially envisaged as one important objective the determination of the former three parameters for all the likely-single and SB1 O-type stars in the

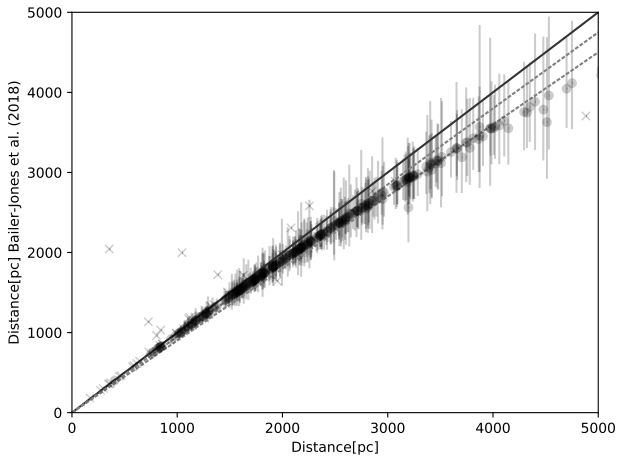

Figure 7.3: Distance comparison between the naive parallax inversion and the Bayesian distance inference using *Gaia* DR2 from Bailer-Jones et al. (2018) for the Galactic O-type stars in the IACOB+OWN sample. Crosses mark the stars with unreliable parallax measures (see text). Solid black line is the 1:1 relation, and dashed lines represent a 5% and 10% error respectively.

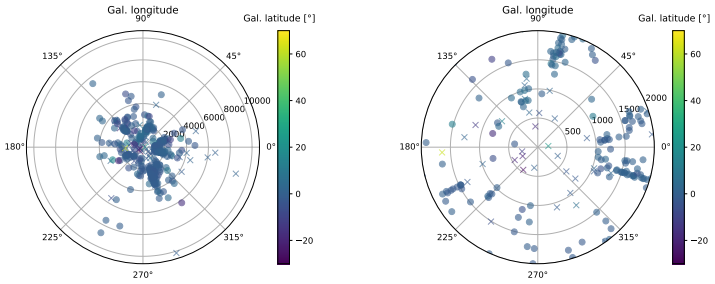

Figure 7.4: *Left* Distribution of the Galactic O-type stars in the IACOB+OWN sample around the Sun with Bayesian *Gaia* DR2 distance results from Bailer-Jones et al. (2018). 0° is the direction to the Galactic center. The radial distance is in pc. Crosses mark the stars with unreliable parallax measures (see text). *Right* Zoom to the innermost 2 kpc.

IACOB+OWN sample, the reliability and accuracy of the parallaxes provided in *Gaia*-DR2 were somewhat poorer than we expected. In view of this, and given the timeline of this thesis, we hence decided to basically concentrate, as a first step, in those stars comprising what we have defined as our benchmark sample (see Chapt. 4): the grid of O-type standards for spectral classification.

From the 128 standard stars for which we could obtain spectroscopic parameters (see Chapt. 4 and Table B.4), all but one have a parallax in *Gaia* DR2[10]. Of these, 18 targets have unreliable parallaxes according to the criteria established in previous section ($B < 6$, or absolute error of the parallax > 0.1 mas). These 18 stars are included along the various diagrams presented in this section, but highlighted using different symbols than the other ones.

7.3.1 Absolute magnitude

As a first step, we compiled information about the visual magnitude corrected from extinction (V_0) for our stars from Maíz Apellániz & Barbá (2018). Then we combine these values with the set of distances presented in Sect. 7.2 to determine the absolute V magnitude:

$$M_V = V_0 + 5 - 5log(d)$$

We also compute estimates for the associated uncertainties repeating the process but using the upper and lower limit values in distance provided by Bailer-Jones et al. (2018) (see previous section). Generally speaking, the resulting uncertainties in M_V are of the order of 0.17 mag for most of the stars in the sample, except for those targets with B brighter than ∼6, for which a much larger error is obtained (∼0.7 mag). We note that the uncertainties associated with the apparent visual magnitudes are generally negligible when compared with those associated with the distance estimation following the strategy described above.

The resulting values and uncertainties, quoted in Table B.9, are also presented in Fig. 7.5 as a function of SpT. In this figure, the sample is separated by luminosity class. Stars labeled as SB1 are highlighted using open symbols. In addition, as indicated above, we use cross symbols to highlight those stars with an unreliable parallax. The figure also includes the SpT – M_V calibrations[11] by (Martins & Plez 2006, MP06).

[10] HD 36486 does not have parallax in *Gaia* DR2, surely because of its high brightness.

[11] In Martins & Plez (2006), synthetic photometry for UBVJHK magnitudes was computed from the grid of atmosphere models presented by Martins et al. (2005), with bolometric corrections derived as a function of $T_{\rm eff}$ and the flux from the emergent SED. The obtained calibrations of the V magnitudes as a function of spectral type were in good agreement with previous calibrations (smaller than 0.5 mag) although systematically smaller.

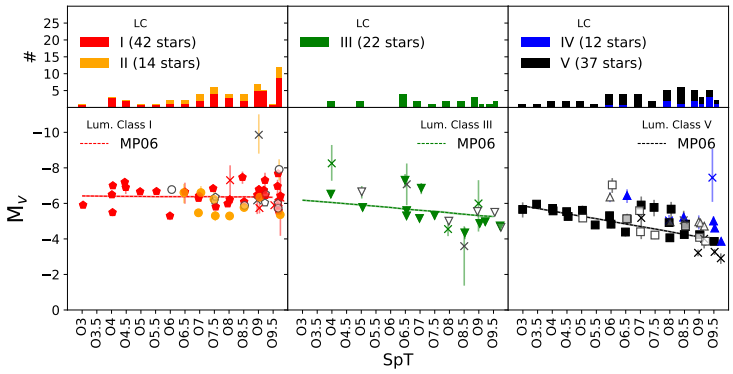

Figure 7.5: Results from the M_V determination for the 127 standard O-type stars for spectral classification with parallax information in *Gaia* DR2. The global sample is divided by luminosity class groups in columns. Top panels show the number of stars per spectral type bin. The synthetic photometry calibrations proposed by Martins & Plez (2006) (and errors) are indicated by dashed lines (and shadows). Open symbols indicate stars for which we have detected clear or likely signatures of spectroscopic binarity, and crosses represent stars with unreliable parallax values (See text). The *Y-axis* of the lower panels is inverted to have brighter stars on the upper part. These results are then used to derive radii and luminosities, presented in the similar Fig 7.7.

The agreement between our empirical (individual) determination of M_V and the one obtained from MP06 calibration is, in general, relatively good. The mean value of the differences is –0.17 mag, of the same magnitude as the associated uncertainties, and the standard deviation is 0.7 mag. Interestingly, the stars that deviate the most are among the ones with parallaxes considered as unreliable (marked with a × symbol). If we exclude those problematic cases, the mean and standard deviation of the differences are then –0.10 and 0.5 mag, respectively.

Although the calibration by MP06 provides a single value of M_V for each SpT/LC combination, reality is that a certain scatter is expected in this type of calibrations. This is because, as we see in Fig. 5.2, the spectral types and luminosity classes are distributed in boxes in the sHR diagram rather than exact points. Due to the possible valid range in log L of, say approximately 0.2 dex, we calculate that the magnitude can vary in:

$$M_V = -2.5 \log L;\ \Delta M_V = -2.5 \cdot 0.2 = 0.5\ mag$$

for each SpT/LC combination.

In addition, the empirically obtained absolute magnitude may present contamination from an unresolved companion. In that case, the star under study would appear brighter than it actually is by the following amount:

$$\Delta M_{\rm V} = -2.5 \log \frac{F_1 + F_2}{F_1}$$

The maximum effect will occur when the secondary component has the same flux as the primary (i.e., $F_2 = F_1$). In that case,

$$\Delta M_{\rm V} = -2.5 \log 2 \approx -0.75 \;\; mag$$

Hence, an unresolved binary system with two stars of similar magnitudes will have a magnitude 0.75 brighter than it should be if it is assumed to be an isolated target.

7.3.2 Two test cases: HD 36861 (O8 III) and HD 46150 (O5 V)

We are now ready to re-launch IACOB-GBAT, including the information about absolute V magnitude, in order to determine the radii, luminosities, and masses – as well as the associated uncertainties – for all stars in our benchmark sample.

At this point, we must note that the uncertainties provided by IACOB-GBAT for R, $\log L$, and $M_{\rm sp}$, are due exclusively to the propagation of errors in $T_{\rm eff}$ and $\log g$, since only one value of $M_{\rm V}$ is considered every time the second step of IACOB-GBAT is launched.

In order to illustrate the extra-effect on the estimation of the central values and uncertainties associated with R, $\log L$, and $M_{\rm sp}$ when a given uncertainty in $M_{\rm V}$ is considered, we decided to perform an academic exercise using two stars in our sample: HD 36861, a very bright ($B < 6$) O8 III with an unreliable parallax[12]; and HD 46150, an O5 V star with an intermediate distance and a parallax considered accurate.

To this aim, we launched IACOB-GBAT considering several different values of $M_{\rm V}$; namely. those computed using: (1) The central value of the distance provided by Bailer-Jones et al. (2018), (2/3) the upper/lower limit values of the Bailer-Jones et al. (2018) calculation, (4) the expected magnitude from Martins & Plez (2006) calibrations, and (5) the distance from the naive inversion of the parallax. The results are summarized in Table 7.1.

As can be seen in the table, the absolute magnitudes are greatly influenced ($\sim$0.35 mag) by considering the different (central, maximum, or minimum) distances from Bailer-Jones et al. (2018). At the same time, in the case of the star

[12]The bright limit in *Gaia*-DR2 parallaxes is $B = 6$. See Sect. 7.2.2 and Luri et al. (2018).

Table 7.1: Fundamental parameters derived from the different M_V magnitudes considered for the two test case stars. Quoted errors in R, log L, and M_{sp} correspond to the IACOB-GBAT formal uncertainties (where ΔM_V=0).

Star	Origin[c]	Distance [pc]	M_V[a]	R [$R_\odot$]	log $L/L_\odot$	M_{sp}[$M_\odot$]
HD 36861	BJ18c	279	-4.55	9.1±0.1	5.06±0.02	9.8±2.5
O8 III	BJ18max	335	-4.95	10.9±0.1	5.22±0.02	14.0±2.4
B[a]=3.6	BJ18min	238	-4.21	7.8±0.2	4.92±0.02	7.4±1.8
T_{eff}=35.2±0.5 kK	$1/\pi$	271	-4.49	8.9±0.1	5.03±0.02	9.4±1.5
$log\mathcal{L}$=4.06±0.05	MP06	...	-5.47	13.9±0.2	5.42±0.02	23.6±2.4
HD 46150	BJ18c	1544	-5.61	13.4±0.1	5.66±0.02	42.7±3.9
O5 V	BJ18max	1771	-5.91	15.4±0.1	5.78±0.02	57.0±6.1
B[a]=6.9	BJ18min	1368	-5.34	11.9±0.2	5.56±0.02	34.0±3.6
T_{eff}=41.1±0.5 kK	$1/\pi$	1697	-5.58	13.9±0.1	5.69±0.02	45.8±4.2
$log\mathcal{L}$=4.03±0.05	MP06	...	-5.27	11.5±0.1	5.53±0.02	31.4±3.4

[a] B and M_V in [mag]
[b] $\mathcal{L}:={T_{eff}}^4/g$
[c] BJ18c/BJ18max/BJ18min: Bailer-Jones et al. (2018) central, maximum, and minimum distance values.
MP06: Martins & Plez (2006).

with an unreliable parallax (HD 36861), the Martins & Plez (2006) magnitude calibration is very different (1 mag). For the other star (HD 46150) the calibration magnitude is also outside the range of values derived with Bailer-Jones distances, but relatively close to the resulting value obtained from using the smaller distance (only 0.06 mag). It is worthwhile noticing the good agreement between the calculations obtained from using the Bailer-Jones central value and those obtained with distance as the naive inversion of the parallax. This confirms that for many stars this simple approach does not deviate too much from a more accurate inference, making evident the high quality of the *Gaia* DR2 data.

The uncertainty in the magnitude is propagated into the rest of the physical parameters derived from it. The different distances provided by Bailer-Jones et al. (2018) imply changes of 10%, 0.2 dex, and up to 15% in the derived R, log$L$ and M_{sp}, respectively. This variation due to the uncertainty in the distance/magnitude is greater than the one associated with the formal error of the IACOB-GBAT analysis (i.e. resulting from the propagation of uncertainties in T_{eff} and $\log g$).

For both stars, the resulting values of radius, luminosity and spectroscopic mass obtained when considering the absolute magnitude proposed in MP06 calibration are very different from the rest, making clear the importance of a good approximation to the real absolute magnitude when constructing any type of calibration.

The right panel of Fig. 7.6 shows an HR diagram with the location of the

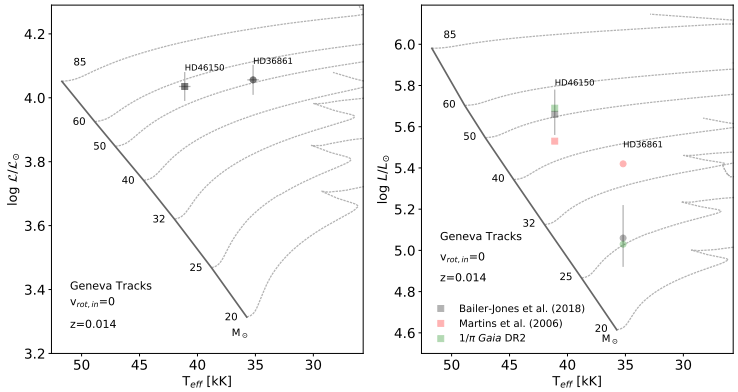

Figure 7.6: Results from the purely spectroscopic analysis (*Left*) and fundamental parameter results (*Right*) for the two test case stars. The spectroscopic results are presented in the sHR diagram ($\mathcal{L}:=T_{\rm eff}{}^4/{\rm g}$). The fundamental parameters are shown in the HR diagram, where colors come from the different $M_{\rm V}$ considered. The errors depict for the Bailer-Jones determination are inferred from their maximum and minimum limits. Evolutionary tracks and position of the ZAMS from the non-rotating, solar metallicity models by Ekström et al. (2012) and Georgy et al. (2013) are included as reference in both cases.

two test stars corresponding to the various solutions indicated in Table 7.1. For comparative purposes, left panel of Fig. 7.6 shows the position of the two stars in the sHR diagram used so far in this thesis. These diagrams can be used to infer the so-called evolutionary mass ($M_{\rm ev}$) using the position of a given star in each of the diagrams and a given set of evolutionary tracks as reference (see examples in Herrero et al. 2002; Sabín-Sanjulián et al. 2017; Schneider et al. 2014). A general view of the HR diagram shows that in the case of the star with a parallax considered as reliable (HD 46150) the difference between the different luminosity determinations is not great, and the evolutionary mass would be around 50 $M_{\odot}$. For the star with unreliable parallax (HD 36861) there is a difference in luminosities so great that the evolutionary mass could vary much more, between 25 and 35 $M_{\odot}$. When compared with the results that would be obtained from the sHR diagram, only the star HD 46150 presents a coherent evolutionary mass, $\sim$55$M_{\odot}$, and clearly the star HD 36861 would present a very discrepant value, 50 $M_{\odot}$.

Finally, an extensive literature exist comparing the evolutionary mass ($M_{\rm ev}$) with that obtained from the spectroscopic analysis ($M_{\rm sp}$), with a recurrent in-

coherent result classically called the "mass discrepancy" (Herrero et al. 1992, 2002; Massey et al. 2005; Evans et al. 2005; Sabín-Sanjulián et al. 2017; Schneider et al. 2014).

In our case, compared to the mass values in the table (the $M_{\rm sp}$), the star HD 36861 presents a wide mass range (between 7-23 $M_{\odot}$) but very far from both the HR and the sHR $M_{\rm ev}$ possibilities. Note that the only good agreement appears between the $M_{\rm sp}$ of the determination with Martins calibrations and the $M_{\rm ev}$ from considering the *Gaia* data, but in this case the luminosity that is inferred from the *Gaia* data (∼5.0) is quite far from the calibration expected by Martins (∼5.4, see next section). The HD 46150 star has a wide $M_{\rm sp}$ range (31-57 $M_{\odot}$) that closely resembles the $M_{\rm ev}$ values that could be inferred in both the HR and the sHR. The "mass discrepancy" is not due to the uncertainties in $M_{\rm V}$, for if we change $M_{\rm V}$, we change both the spectroscopic and the evolutionary masses in the same sense (Martins & Plez 2006).

7.3.3 Radii, luminosities and masses: comparison with calibrations

This section presents the results for the radii, luminosities, and spectroscopic masses of the 127 stars comprising the grid of O-type standard stars for spectral classification. We present two sets of computations. We first consider the $M_{\rm V}$ derived from the distances estimated by Bailer-Jones et al. (2018) using *Gaia*-DR2 parallaxes. Then, for comparison purposes, we repeat the calculations using the absolute magnitudes indicated in the SpT/LC calibrations by Martins & Plez (2006).

Physical parameters from *Gaia*-DR2-BJ18 distances

The corresponding results are included in Table B.9, along with the name and spectral classification of each star, distance and dereddened magnitude used for the analysis, and quality flag of the IACOB-GBAT analysis (See Sect. 3.3.3). This table include the results for 7 stars labeled as Q4 (No He I is available to constrain the $T_{\rm eff}$, See Sect. 3.3.3), although they have been systematically eliminated from the figures since the $T_{\rm eff}$ intervenes in the methodology to derive the fundamental parameters (Sect. 3.4).

Figure 7.7 shows our results of R and L, separated in LC, comparing with Martins et al. (2005) calibrations with spectral classification expected for these parameters. It shows some interesting results:

- The figure shows the stars with a parallax considered unreliable (Sect. 7.2.2) as an ×. These clearly present, in many cases, an evident discrepancy with the calibrations, in addition to disproportionate errors.

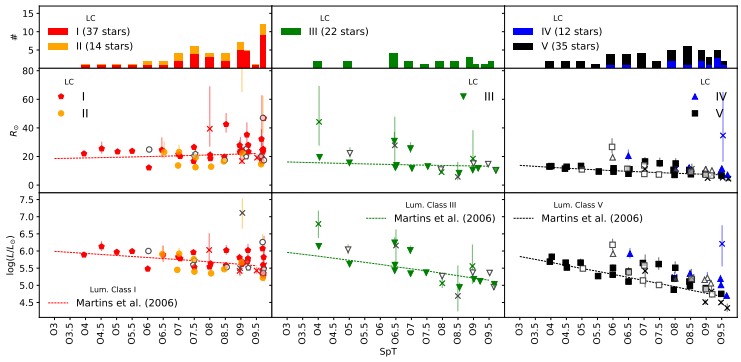

Figure 7.7: Radii and luminosities results for 120 standard O-type stars for spectral classification with parallax information in *Gaia* DR2. 7 Q4 O-type stars (no He I visible) are not included in this figure. Values and error bars are derived from absolute magnitudes obtained with distance values and limits from Bailer-Jones et al. (2018). The sample is divided by luminosity class groups in columns. Top panels are the number of stars per spectral type bin. As in previous figures, open symbols indicate stars for which we have detected clear or likely signatures of spectroscopic binarity, and crosses represent stars with unreliable parallax values (See Sect. 7.2.2). The "observational scales" calibrations for radius and luminosity proposed by Martins et al. (2005) are indicated by dashed lines.

- The figure shows the stars with signs of binarity as open points. As we have commented in the previous section, the absolute magnitude can be contaminated up to -0.75 mag by the companion star and, propagating the error, could produce errors of +40% in R and +0.3 dex in log L. However, that represents extreme cases of SB2 binaries. The stars included here with signs of binarity are mostly SB1, where the contamination has a much lower effect.

- The rest of the stars, with no evident problem, seem to adapt to the trend of the calibrations, although with a large dispersion. The errors derived from considering the range of distances given by Bailer-Jones et al. (2018) often remains far below that dispersion.

- Finally, a particular case are late supergiants, with two of them (HDE 303492: O8.5 Iaf, and HD 195592: O9.7 Ia) separating a lot from calibrations (R >40 $R_\odot$). The Ia stars have already been presented as problematic when considering the calibrations of spectral classification with temper-

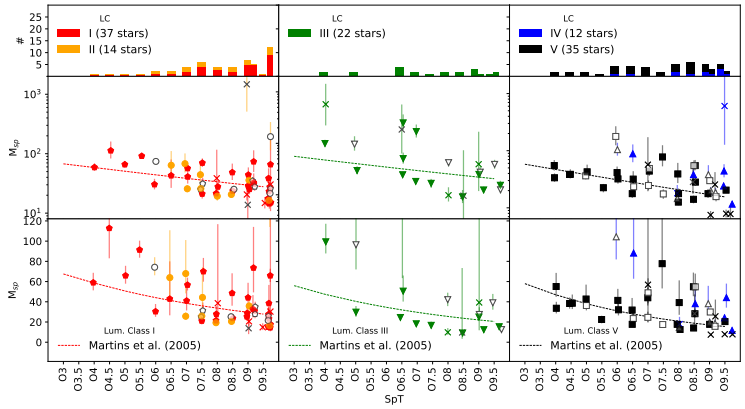

Figure 7.8: M_{sp} results for 120 standard O-type stars for spectral classification with parallax information in *Gaia* DR2. 7 Q4 O-type stars (no He I visible) are not included in this figure. Values and error bars are derived from absolute magnitudes obtained with distance values and limits from Bailer-Jones et al. (2018). The sample is divided by luminosity class groups in columns. Top panels are the number of stars per spectral type bin. Second row is in a logarithmic scale to show the large outliers. As in previous figures, open symbols indicate stars for which we have detected clear or likely signatures of spectroscopic binarity, and crosses represent stars with unreliable parallax values (See Sect. 7.2.2). The "observational scale" mass calibration proposed by Martins et al. (2005) is indicated by dashed lines.

ature and gravity (see Sect. 4.6). Again the strong winds, characterized by large values of log Q, may be showing that these stars really present themselves as a differentiated group in the calibration, or is simply a limitation of our analysis strategy for stars with very strong winds (see further notes in Appendix A.5).

As we have already commented several times throughout this thesis, the mass is a critical parameter in the characterization of a star, hence, an accurate estimation of this parameter is crucial in the understanding of massive stars. In this case, our determination of the mass from the radius and the gravity, as explained in Chapt. 3, is called spectroscopic mass (M_{sp}), because it is derived from parameters inferred from the spectrum.

Figure 7.8 shows our results for M_{sp}, separated in various LC, comparing with the expected calibrations for these values. The results to highlight are the following:

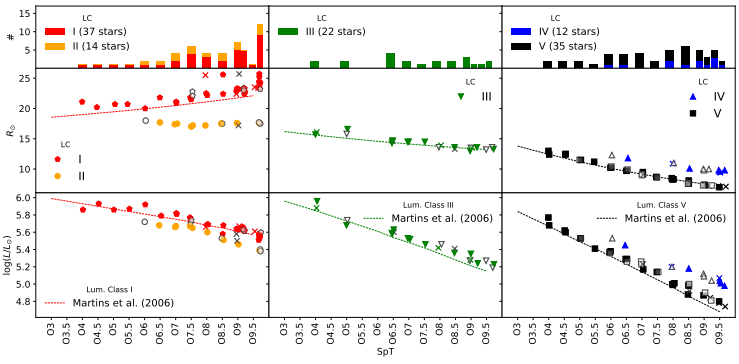

Figure 7.9: Same as Fig. 7.7 but considering absolute magnitudes from Martins et al. (2005) calibrations.

- The scatter is very large, with some outliers with really impossible values (M_{sp}>1000 $M_\odot$), although these outliers are stars with parallaxes considered unreliable, marked as an ×. (Sect. 7.2.2).
- The errors, obtained from the distance limits of Bailer-Jones, are considerable (±20%), and again the stars with parallaxes considered unreliable are the ones with the highest errors (±25%, but up to 200% in some cases).
- Some of the stars with binarity signs have masses higher than expected by their calibration. The contamination produced by a second component in the spectrum can cause an increase in the determination of gravity, due to blending in the wings of the Balmer lines, the spectroscopic feature used for $\log g$ determination (see, e.g., Herrero et al. 2002; Sabín-Sanjulián et al. 2017). In addition, altering the absolute magnitude in -0.75 mag (due to the presence of a second identical component, see previous section), could end up in values of the inferred mass doubling the original value.

Physical parameters from M_V–SpT/LC calibrations

In a second step, we determine again the parameters R and L, considering in this case the M_V of its SpC calibration in Martins & Plez (2006). Included in

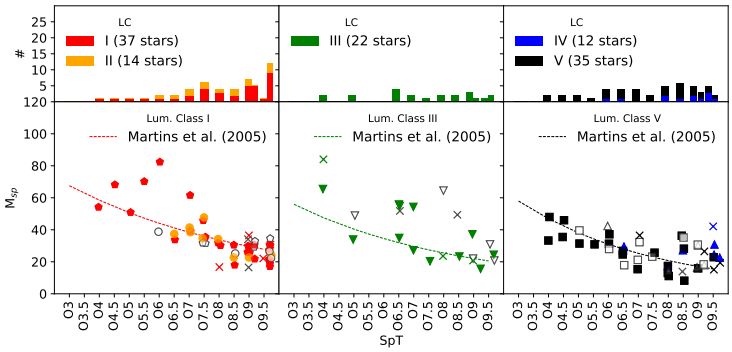

Figure 7.10: Same as Fig. 7.7 but considering absolute magnitudes from Martins et al. (2005) calibrations.

Fig. 7.8 we can see that the results follow the trend expected by Martins et al. (2005) calibrations, including the stars with non-reliable parallaxes, as in this case they are not used. Inspecting the figure in more detail we can highlight that:

- Two late Sgs appear with a radius greater than expected (R >25 $R_\odot$) and again they are the late Ia stars HDE 303492: O8.5 Iaf, and HD 195592: O9.7 Ia. In addition, Another late Sg Ia star (HD 105056: ON9.7 Iae) appear with a large radius $R = 24$ $R_\odot$.
- Both giants and late dwarfs present luminosities somewhat greater than those expected by the calibration. If we look at Fig. 4.9 with the calibrations of SpC with $T_{\rm eff}$ we note how our results (and our new derived calibrations) for these stars present a general trend of higher temperatures (about 2000-3000 K for giants-dwarfs) with respect to Martins'. Because the luminosity determination depends on the $T_{\rm eff}$, this difference would suppose a systematic difference of +0.12 dex log L, in accordance with what we see in the figure[13].

In a final check, we again determine the $M_{\rm sp}$ parameter, considering in this case the $M_{\rm V}$ of its SpC calibration (Martins & Plez 2006). The results are

[13]On top of this, the uncertainty in log L is also influenced by the radius uncertainty, with differences up to an additional ±0.14 dex (Repolust et al. 2004).

presented in Fig. 7.10, with a very large dispersion in comparison with (Martins et al. 2005) SpC calibration for the mass. Our methodology, dependent on the $\log g$, drags the dispersion in gravity calibrations –evident for these stars in Fig. 4.9 (Chapt. 4)– into our calculation of $M_{\rm sp}$.

A typical uncertainty of 0.1 dex in the determination of the $\log g$ (See Sect. 5.5.1), propagates into an error of at least 20% in the mass determination (Eq. 3.1). On top of this, we must add the uncertainty caused by the determination of the radius, influenced by distance. All this translates into a present limitation when it comes to an accurate determination of the spectroscopic mass (20-30%).

7.3.4 (s)HR diagram

As we have done in the test case (Sect. 7.3.2), having the luminosity of these stars allows us to place them in the HR diagram. So far in the thesis, we have been using the sHR diagram, since it can be constructed from pure spectroscopic analysis, without the need for a distance value. The sHR diagram, presented in Langer & Kudritzki (2014), is analogous to the HR diagram in many aspects. Both are used for similar things, mainly: evaluating the evolution scenarios by placing the stars in them using derived parameters; and inferring the so-called evolutionary masses (and ages) by comparing the position of the stars with the evolutionary tracks (and isochrones). In this section we present the results for the sub-sample of O-type standard stars of spectral classification in both diagrams, we compare their peculiarities and contrast their differences.

As commented above, the sHR diagram use only the variables directly derived from stellar spectra, i.e, surface gravity and effective temperature, without knowledge of the stellar distance. The parameter $\mathcal{L}{:=}{T_{\rm eff}}^4/{\rm g}$, used to built this diagram, is the inverse of the "flux-weighted gravity" defined by Kudritzki et al. (2003), and has a direct dependence on the Eddington factor (Γ_e), a measure of how close a star is to its maximum luminosity (Castro et al. 2014). Lines of constant $\log g$ can be drawn as straight lines in the sHR diagram, whereas this is not possible in the HR diagram, as two stars with the same surface temperature and luminosity that have different masses occupy the same location in the HR diagram, but their radii must be different, altering their $\log g$. In addition, the HR diagram requires a calculation of the absolute magnitude, either through distance (very imprecise so far in the galactic case) or from calibrations. A positive aspect of the HR diagram is its independence from gravity, a parameter in which a considerable uncertainty still exists (Massey et al. 2013). In either case a reliable determination of $T_{\rm eff}$ is critical when studying the po-

sition of the stars with the earliest spectral types in these diagrams, as a range of effective temperatures spanning 50 000 K to 55 000 K could produce a span in evolutionary masses from 70 $M_\odot$ to 150 $M_\odot$ (Sabín-Sanjulián et al. 2017).

We show the position of the stars studied in this section, the grid of O-type standards for spectral classification, in each of these two diagrams in Fig. 7.11. 120 stars are depicted, marking the stars with parallaxes considered unreliable and those with signs of spectroscopic binarity. The main features are:

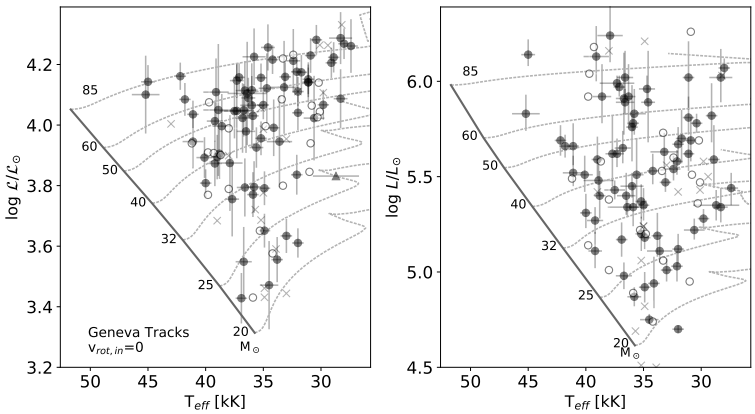

Figure 7.11: Location of 120 stars, the subsample of O-type standards stars for spectral classification, in the spectroscopic HR (*Left*) and HR diagram (*Right*). sHR results come from the IACOB-GBAT analysis (Sect. 5.5.1), included as triangles when only upper or lower limits in any of the two parameters used to construct these diagrams ($T_{\rm eff}$ and $\log g$) could be obtained. Luminosity values and errors in the HR diagram come from the absolute magnitude ($M_{\rm V}$) range inferred from the Bailer-Jones et al. (2018) determination of the distance. Cross symbols indicate stars with unreliable parallax value (See Sect. 7.2.2), and open points stars for which we have detected clear or likely signatures of spectroscopic binarity. Evolutionary tracks and position of the ZAMS from the non-rotating, solar metallicity models by Ekström et al. (2012) and Georgy et al. (2013) are included as reference in both cases. The 7 Q4 O-type standard stars (no He I visible) are not included in this figure.

- In both diagrams, the zone that the sample covers is similar, although in the sHR diagram they seem to accumulate near the evolutionary tracks of higher masses, corresponding with lower gravities[14]. This is especially

[14] As the star evolves away from the ZAMS towards lower temperatures, its gravity decreases and its stellar luminosity increases.

visible with the presence of many relatively evolved stars with masses below the 32 $M_{\odot}$ evolutionary track in the HR diagram, but not in the sHR.

- There is an absence of stars very close to the ZAMS above the 32 $M_{\odot}$ evolutionary track in both diagrams, but in the HR diagram there are some stars with $\sim$30 $M_{\odot}$ close to the ZAMS that do not exist in the sHR diagram. This same feature was already discussed with a sample of O-type V and IV stars in VFTS, arguing a possible underestimation of the gravity as its origin (Sabín-Sanjulián et al. 2017).

- O-type stars with unreliable parallax values appear in the sHR in a plausible location, but in HR they appear with impossible low luminosities, in the area of the early B-type stars.

The jump from the sHR to the HR diagram has not solved the problem with the absence of O-type stars very close to the ZAMS, discussed in Sect. 5.6.2. In addition, both diagrams present a considerable discrepancy when inferring evolutionary masses[15], using one or the other diagram. Finally, the stars considered to have unreliable parallaxes values are the stars with larger alterations, with respect to evolutionary tracks, when considering one or the other diagram. This is a clear sign that their *Gaia* distances are still an unreliable source.

[15]Evolutionary masses are estimated by interpolating between evolutionary tracks in the different diagrams.

8

Summary, conclusions and future work

The work that is never started
is the one that takes longer to complete
J. R. R. Tolkien

This last chapter summarizes the main results, present highlights reached on the research done in the framework of this thesis, and provide some opportunities for further continuation of this work.

O stars represent a fundamental phase in the zoo of massive stars. They ionize the material around them and flood their environment with processed material via strong stellar winds and supernova explosions. On top of the mass-loss, factors such as rotation and multiplicity have become key processes to understand their evolution. A better understanding of these complex objects requires a better empirical characterization of their physical properties, something that can only be obtained through extensive quantitative analysis of large datasets. Despite this, there was still no study in the Galaxy that provided homogeneous results from a quantitative spectroscopic analysis of a sample of Galactic O stars comprising more than a hundred targets. This has been the main purpose of this thesis, the quantitative spectroscopic and physical empirical characterization of an unprecedented sample of 415 Galactic O-type stars. This last chapter summarizes these results, present conclusions on the research done in the framework of this thesis, and provide some opportunities for further

continuation of this work.

A crucial part of the work has been the compilation of a homogeneous database of optical spectroscopic observations of Galactic O stars. The main spectroscopic observations used during this thesis come from the extensive databases gathered in the framework of the IACOB and OWN spectroscopic surveys. The IACOB-OWN collaboration –established by the beginning of this thesis– has allowed us to work with an optimal source of spectroscopic data for the purpose of our work, with observations taken with very similar criteria, from both the Northern and the Southern hemisphere. In addition to spectra already available at the beginning, several new observational campaigns and compilation of data in the ESO-FEROS archive have been carried out during the development of the thesis. This has allowed us to add 114 extra O-type stars to the initial sample. These observations were aimed at extending the number of observed stars in the sample to dimmer targets. In total, in this study we have used 2900 spectra of 415 Galactic O-type stars. The high-quality (average S/N∼150, and resolution R>25000), homogeneity, and multi-epoch characteristic –2 (3) spectra for 80% (70%) of the stars–, are ideal to provide statistically meaningful results for the parameters derived in the analysis.

The strategy analysis follows two steps. The multi-epoch spectra allowed us to evaluate, in a first step, the spectroscopic variability of these stars. Then, we performed a detailed spectroscopic analysis of the stars in the sample not identified as SB2 or WR using the best spectrum for each star in terms of S/N. To cope with the large amount of targets, we made use of the semi-automated (but supervised) tools for the quantitative spectroscopic analysis IACOB-BROAD (Simón-Díaz & Herrero 2014) and IACOB-GBAT (Simón-Díaz et al. 2011b), developed in the framework of the IACOB project. First, the IACOB-BROAD program uses a combination of the Fourier transform method and a profile-fitting of a single photosperic diagnostic line (O III λ5592 in 90% cases) to derive $v \sin i$ and $v_{\rm mac}$, separating the effect of these two line-broadening effects.

Then, with IACOB-GBAT we performed a detailed line fitting procedure to the high-resolution spectra of these stars to derive the stellar atmosphere and wind parameters of this sample that could be inferred from the optical part of the spectrum. We have followed the standard "Spectroscopy synthesis method" procedure (ionization balances, Balmer wings) for the quantitative spectroscopic analysis at high resolution (R>25000) to derive the photosperic parameters (Herrero et al. 1992), and wind parameters are fixed thanks to its effect in the Hα profile and the He IIλ 4686 line (Puls et al. 1996). The program calculates in a fast, objective, and reproducible way, values and uncertainties for $T_{\rm eff}$, $\log g$, $Y_{\rm He}$, $\xi_{\rm t}$, and $\log Q$. In the IACOB-GBAT grid-based fitting process we use a total number of 15 H and He I-II diagnostic lines of the spectrum,

a χ^2 optimization-method, and the emergent synthetic spectra of a grid of FASTWIND atmosphere models, specifically extended for this study. Finally, an individualized review of the visual outcome of the IACOB-GBAT fit was made "by-eye" in each star to assess the reliability of the results, or identify possible caveats in the adjustment.

The optical spectra of a sample of 415 O-type stars in the Milky Way have been analyzed. The stars in the sample cover spectral types from O2 to O9.7, all luminosity classes, and do not belong to any specific Galactic cluster. This represents the largest sample of O stars with spectroscopically determined parameters in the Galaxy, 5-10 times larger than those considered in previous similar studies (e.g. Repolust et al. 2004; Martins et al. 2005; Markova & Puls 2008; Martins et al. 2015a). In comparison with GOSC –a catalog intended to include all known Galactic O-type stars– our sample represents 70% of the stars included in the latest version of GOSC. From the multi-epoch variability assessment, we found that 55% of the sample shows signs of binarity, 113 SB2 stars and 59 SB1. In parallel, variability appears in lines related to the stellar wind in 63 WV stars, or in purely photospheric lines in 91 LPV stars. In addition, the catalog also encloses exotic stars: 6 Oe and 4 WR have been detected, and there are 10 stars considered magnetic in the sample.

Two line-broadening parameters ($v \sin i$ and $v_{\rm mac}$) values were obtained for 285 likely-single and SB1 O-type stars. The result of the combined analysis, using two different techniques (Fourier transform and profile-fitting), indicates that in 99% of the results $v \sin i$ and $v_{\rm mac}$ are determined without degeneracy. From the results of the visual evaluation of the IACOB-GBAT analyses, we found that the majority (60%) presents a high level of agreement (Q1), 108 present some mismatch between the observed spectrum and the best fitting FASTWIND model that could compromise the calculation of the stellar wind parameters (Q2-Q3), and finally, 10 stars with spectral types in the range O2-O4 in which the lack of He I limits the correct inference of the $T_{\rm eff}$ (Q4). Removing these Q4 stars, we were able to produce a catalog of accurate –and homogeneously derived– stellar and wind parameters for 275 Galactic O-type stars.

In addition to the description of the general properties of the sample, we have also used the results of the analysis of the full sample of Galactic O-type stars to investigate other topics of interest in the field of massive stars. The main highlights from these studies are quoted below.

O-type standard stars for spectral classification:

From the catalog of Galactic O stars presented, we selected and analyzed a benchmark subsample –the grid of O-type standard stars for spectral classification–

to assess the level of agreement between our results, and those provided by more traditional "by-eye" techniques, and to establish a step-by-step protocol to be followed in the analysis of the complete combined IACOB+OWN sample of Galactic O-type stars. In brief:

- We count on 1216 spectra for 128 of the 131 stars that are included in the revision of the grid of O-type standards for spectral classification presented in Maíz Apellániz et al. (2015).
- Thanks to the availability of multi-epoch spectroscopic observations for all stars in the sample we could identify 7 double-line spectroscopic binaries (SB2) stars, all with a very faint secondary component. It would be advisable to find alternative stars to replace these targets as standard stars, even though at the resolution of spectral classification (R∼2500-5000) the effect is negligible.
- There are 16 stars that show the Hα/He II λ4686 spectral line with an inverse P-Cygni profile or showing a double peak (Q2), possibly related to the presence of circumstellar material contaminating the pure stellar (photospheric) spectra. This is a clear situation in which He II λ4686 should not be used as diagnostic line for defining the luminosity class of the star.
- We have made a comparative study of our results for this subsample in four parameters ($v \sin i$, $v_{\rm mac}$, $T_{\rm eff}$, and $\log g$), with previous results in the literature (Repolust et al. 2004; Markova et al. 2014; Simón-Díaz & Herrero 2014; Martins et al. 2015a). The comparison of values of $v \sin i$ and $v_{\rm mac}$ showed an overall good agreement, except in cases where the methodology was different (they did not separate the *macroturbulence* broadening component or defined its profile differently). For $T_{\rm eff}$ and $\log g$ there are small differences in the mean values of the differences compared to other studies using the atmospheric code FASTWIND (-200 K and -0.01 dex, respectively), and somewhat larger (800 K and -0.08 dex) when compared to other studies using the CMFGEN code. In the latter there is also a systematic shift, with CMFGEN resulting in lower effective temperatures and higher gravities, a result already highlighted comparing results directly from models (Massey et al. 2013). The consistency between the results for these parameters validate the reliability of our analysis automation.
- We present a full spectroscopic characterization, stellar and wind parameters, of the benchmark subsample of O-type standard stars obtained

with the techniques already described to provide a general overview of how the standards for spectral classification can be also considered as "standards" in terms of basic stellar parameters. We have performed a differential study by comparing the spectroscopic properties of the stars in the standard grid and the complete sample of Galactic O-type stars surveyed by the IACOB and OWN, by locating them in the $v \sin i$ histogram, Kiel, and sHR diagrams. The sample of O-type standard stars for spectral classification is affected by an important selection effect, by the definition of a "standard" star, and the $v \sin i$ values are in general lower than in the complete sample. In addition, there are 27 standard stars with $v \sin i$ values above 120 km s^{-1} that, ideally, should be replaced by new candidates. In the Kiel and sHR diagram the sample of standard stars is representative of the parameter space covered by the more general sample.

- We have investigated the behavior of $T_{\rm eff}$ and $\log g$ with SpT/LC for the subsample of standard O-type stars for spectral classification in order to, firstly, contrast our IACOB-GBAT results with the currently widely used calibration by Martins et al. (2005) (MSH05) and, secondly, construct new linear $T_{\rm eff}$ and $\log g$ calibrations as a function of SpT/LC for Galactic O-type stars. From the comparison, we highlight a few points of interest: (1) Our SpT – $\log g$ calibration for dwarfs always results in gravities lower than the value proposed by MSH05 ($\log g = 3.9$ dex), however, assuming a unique value per SpT in the O dwarfs is an oversimplified recipe (see also notes in Simón-Díaz et al. 2014); (2) there is a systematic offset toward higher $T_{\rm eff}$ (by up to $\sim$3 000 K) in the late O-type giants, subgiants and dwarfs with respect to MSH05; (3) the scatter in the SpT–$T_{\rm eff}$ and SpT–$\log g$ calibrations discussed in Simón-Díaz et al. (2014) still exists even for our sample of standard stars for spectral classification, and is proposed to appear as a natural consequence of the way the spectral classification process is defined. We have used 114 standard stars, after discarding all stars for which we have detected clear or likely signatures of spectroscopic binarity and the supergiants identified as luminosity class Ia, to provide the most complete calibrations for the MW in terms of homogeneity and number of stars to date. Our sample covers spectral types from O2 to O9.7, with a statistically significant number of stars for most spectral types (although stars with spectral types earlier than O4 are scarce).

- We have found that, even accounting for the optimal quality of our spectroscopic dataset, the IACOB-GBAT analysis is not able to provide reliable

constraints of the exponent of the wind law (β) with our available parameter range (i.e., 0.8 –1.2 km s^{-1}). To avoid degeneracy with the log Q parameter we leave the β parameter free in our analyses, but do not provide values or uncertainties for it.

- We study the effects on the wind-strength parameter log Q, $T_{\rm eff}$, and log g produced by the discrepancy that appears in some stars (Q3) between Hα and He II λ4686 diagnostic lines by repeating the analysis fitting alternatively only one or the other line. Our results manifest that the effect on $T_{\rm eff}$ and log g is negligible in most cases, although critical situations exists with differences up to 3500 K and 0.2 dex, and even one case of a extreme shift of 1 dex in log Q.

The complete sample of Galactic O-type stars:

We have extended our investigation to the whole sample of Galactic O-type stars surveyed by IACOB and OWN. Besides the general results included in the summary of this chapter, other points of interest to be highlighted from the analysis of the complete sample are:

- We count on 2900 FIES, HERMES, and FEROS spectra for 415 different Galactic O-type stars. This sample of stars represents ∼70% of the Galactic O-type stars known to date.

- From the multi-epoch variability study we identified 113 double-lined systems and 59 single-line spectroscopic binaries. This constitutes ∼55% of the investigated sample, in accordance to studies of binarity percentages of massive stars in the Galaxy and the LMC (50-70%).

- We identified 91 stars showing line-profile-variability in photospheric lines (LPV), and 63 stars presenting variability in the main wind diagnostic lines (WV). Together they make up 55% of the stars not identified as SB2, in mild agreement with previous studies of LPV occurrence in O-type stars using more limited samples (Fullerton et al. 1996).

- We provide the line-broadening and/or spectroscopic characterization, stellar and wind parameters, for 285 Galactic O-type stars. The largest sample of Galactic O-type stars spectroscopically investigated to date. Some stars showing peculiar features in the spectrum could not been properly analyzed since the FASTWIND models were not able to reproduce these features.

- The Q2 characteristic, found for 50 O-type stars, is tentatively linked to the presence of a stellar disk or other type of emitting material surrounding the star. The Q3 stars in the sample (58) are investigated to understand its connection to limitations in the modeling strategy adopted in this work based on unclumped wind models.

- The study of the superficial distribution of helium in our stars and their current $v \sin i$ results shows inconclusive results of an obvious product of rotational mixing.

- For 76% of the stars our analysis strategy was not able to accurately constraint the microturbulence (ξ_t), and we could only determine upper or lower limits.

A distance independent test of the WLR:

As a by-product of this study, we were able to investigate one particular topic of interest in the field of massive stars, namely, to obtain a distance-independent analogy to the wind-momentum luminosity relationship (WLR). In brief:

- We use atmospheric and wind parameters for 275 Galactic O-type stars investigated in our work and propose two different ways to evaluate our results with respect to previous theoretical and empirical studies, using spectroscopic parameters alone. Both ways yield highly consistent results, and agree well with the theory of radiatively driven winds

- We propose an alternative way to compare observational results and predictions by the WLR using only parameters obtained from the spectroscopic analysis of optical spectra. We replace two spectroscopic parameters[1] ($\log Q$, $\log \mathcal{L}$) into the WLR and obtain a linear relationship between them. From a linear regression of the 175 likely-single stars with an accurate $\log Q$ determination in the analysis, we obtain the slope as x=1.59±0.17, corresponding to[2] $1/\alpha$'. This value is in fairly good agreement with the range of values of x ($1.51-2.18$) provided by Herrero et al. (2002). Regarding the current paradigm, the acceleration arising from optically thick and from all lines is very similar to the theoretically predicted value ($x = 1.826$) in Vink (2000); Puls et al. (2000).

[1] Defined as $\mathcal{L} = T_{\rm eff}^4/g$ in Langer & Kudritzki (2014).
[2] α' is the slope of the line-strength distribution function, corrected for ionization effects Mokiem et al. (2007).

- Markova & Puls (2008) presented an analogous work using a sample of Galactic B Supergiants. With alike distance limitations to ours, they define a new distance-independent parameter[3] Q' which presents a linear relationship with $T_{\rm eff}$ once substituted into the classical WLR. We reconstruct this diagram again in Fig. 5.13 including 117 O-type stars in our sample with available v_∞ and perform a linear regression of the results. We obtain a value for the parameter x=1.68±0.05, in good agreement with our previous distance-free determination.

On the absence of stars close to the ZAMS:

With the results of the IACOB-GBAT spectroscopic analysis of 275 stars we built the sHR diagram and find a lack of stars near the theoretical ZAMS above the 32 $M_\odot$ evolutionary track. This result has been documented before and appears to be independent of metallicity. Regarding this:

- To avoid the possibility that our sample lacks the youngest and more massive stars, still embedded in their birth cocoon (Yorke 1986; Hanson 1998; Castro et al. 2014), we extended our sample towards dimmer stars and obtain spectra for 94 new mid- and early-O dwarfs with magnitudes in GOSCv3 of up to $B = 10.5$ mag. In total, the new sample represents 70% of the stars in GOSC. Despite this, the results for the new stars were not able to reconcile observations and evolutionary models. This represents an important drawback on the actual formation and evolution theories of massive stars.

- The other investigated possibility is that observational results are defining a real empirical ZAMS (Bernasconi & Maeder 1996; Behrend & Maeder 2001; Herrero et al. 2007; Haemmerlé et al. 2016). A work by Haemmerle et al. (in prep.) –using our results for the spectroscopic analysis of O-type stars surveyed by IACOB and OWN – deepens on the necessary pre main-sequence conditions, related to mass rate of accretion, that could lead to a corrected new theoretical ZAMS in accordance with our empirical results.

Relationship between Q3 stars and clumping:

The Q3 characteristic, the inability to obtain a simultaneous fit to Hα and the He II λ4686, was found for 58 stars in the sample. We make use of the IACOB-GBAT spectroscopic analysis for these stars to evaluate a plausible origin coupled to the use of unclumped FASTWIND models. There are specific situations in which Hα and He II λ4686 react differently to clumping. Those cases in which Hα needs a larger/smaller value of log Q than He II λ4686, we

[3] $Q'=Qg_{eff}(v_\infty)^{1/2}$

could consider that wind clumping effects are a likely/unlikely explanation for the behavior of stars labeled as Q3. Most of the Q3 stars with luminosity class I and II are included in the former group, but Q3 stars with luminosity class III would require a different explanation, possibly associated with the presence of extra sources of circumstellar emission in He II λ4686 or hidden components.

Rotational velocities of Galactic O-type stars:

The results for the $v \sin i$ of a sample of 298 likely single and SB1 stars Galactic O-type stars have been presented. It represents the largest sample of $v \sin i$ results for Galactic O-type stars derived homogeneously and from high-resolution observations to-date. These results have been used to study the distribution and evolution of the $v \sin i$ for massive stars, and to compare with the single and binary channels of $v \sin i$ evolution. The main results included:

- Our $v \sin i$ distribution represents a step forward with respect to previous works by being a larger sample, excluding SB2 binaries, and with a proper disentanglement of the *macroturbulence* broadening component from the real $v \sin i$ value.
- The histogram of the $v \sin i$ values presents the expected bimodal distribution (Conti & Ebbets 1977). Interestingly, the tail of fast rotators presents fewer SB1 stars than the rest of the distribution, indicating a possible origin in the effect of binary interaction during massive star evolution (de Mink et al. 2013).
- In the sHR diagram, both the very slow-rotators ($v \sin i$<40 km s^{-1}) and the very fast-rotators ($v \sin i$>300 km s^{-1}) appear concentrated in the lower part of the diagram. The rest are distributed homogeneously.
- We divide the sample into four subsamples separating the more massive and less massive O stars (M above or below 40 $M_{\odot}$), in the first or the second half of the main sequence, as depicted in the sHR diagram. For the more massive stars (M>40 $M_{\odot}$), the $v \sin i$ results show very little difference between stars in the first or the second half (evolution). This is in marginal agreement with Bonn evolutionary models expected behavior of the $v \sin i$ but it is not expected by the Geneva evolutionary code. The less massive stars (M<40 $M_{\odot}$) present a larger number of fast-rotators than the early-type stars. Bonn models with initial rotation 200-300 km s^{-1} would not be able to spin down enough to reproduce the $v \sin i$ distribution resulted from the analysis of these less massive stars, but Geneva models could.

- The localized presence of the very fast rotators ($v \sin i$>300 km s^{-1}), and the absence of SB1 stars in the very fast-rotators tail could all be explained with de Mink et al. (2013) study of population synthesis simulations including binary interaction. The SB1 stars are absent in the tail of fast rotators because these are post-interaction binaries where the companion has transfer mass and momentum, becoming a less luminous object.

- In general, the majority of these stars present low $v \sin i$ values (< 100 km s^{-1}). In order to generate the observed distribution massive stars would need to be born with rotation rates closer to ∼120 km s^{-1}. These are strong arguments against the use of very high initial velocities in the evolutionary models (∼40% of the critical velocity, or 300 km s^{-1}), especially for masses above 40 $M_{\odot}$.

Fundamental parameters of Galactic O-type stars with Gaia:
The main results from this study are:

- We compile for our whole sample of Galactic O-type stars *Gaia*-DR2 parallaxes as well as distances inferred by Bailer-Jones et al. (2018). Our sample of O-type stars is distributed around the closest ∼4 kpc to the Sun. We evaluate its precision (in therms of relative uncertainty), and its comparison with the naive inverse determination. The new parallaxes are a step forward from the previous TGAS data-release in terms of number of objects (100 targets more), but especially in terms of accuracy (errors from 0.2 mas to ∼0.03 mas). Bright stars (G<6) present problems in the parallax determination (Lindegren et al. 2018) and, along stars with large parallax errors (>0.1 mas), provide discrepant results when determining the rest of physical parameters. The difference between the Bayesian inference of the distance with respect to the naive inverse calculation is imperceptible for our stars closer than 2 kpc, but the results tend to differ beyond that point, with systematic smaller distances for the Bayesian calculations. In addition, the use of a prior is imperative in order to make reasonable distance estimates in case of negative parallaxes and when the fractional parallax errors are larger than about 10%.

- For the stars in the grid of O-type standard stars for spectral classification we use the compiled distances, and dereddened visual magnitudes from Maíz Apellániz & Barbá (2018) of Galactic O-type stars, to determine the absolute V magnitude. The derived absolute magnitudes are compared with those quoted in the SpT/LC–$M_{\rm V}$ calibrations by Martins &

Plez (2006). The effect of the allowed range in distances produce an uncertainty in the magnitude very small most of the times ($\sim \pm 0.17$ mag), except for the cases marked as unreliable parallaxes ($\sim \pm 0.7$ mag). In addition, stars with plausible photometric contamination due to binarity could appear up to 0.75 magnitudes brighter.

- The results for the physical parameters (radii, luminosities and spectroscopic masses) of the sample of O-type standard stars for spectral classification have been obtained by means of classical techniques. It represents the larger sample of Galactic O-type stars with homogeneous quantitative analysis from high-resolution observations to-date. We have used the absolute magnitudes derived from the Bailer-Jones distances, and the expected magnitudes from the Martins & Plez (2006) calibration. Both results have been compared with the calibrations expected for these parameters with respect to spectral classification from Martins et al. (2005). Again, stars with unreliable parallax are the most discrepant outliers. The dispersion of the results with respect to the calibration is not explained by the distance indetermination. When considering the absolute magnitude from the calibration, systematically larger luminosities appear for late giants and dwarfs possibly due to the equivalent shift in the $T_{\rm eff}$ calibration found in Chapt.4. The spectroscopic mass results present a large scatter, even when considering the $M_{\rm V}$ from Martins & Plez (2006) calibrations. The origin could be both the effect of the distance indetermination, here with a stronger influence, and the typical $\log g$ uncertainty (0.1 dex), that could alter the mass determination up to 20%.

- Finally, we have constructed the most complete HR diagram of a Galactic sample using *Gaia*-DR2 data. We have evaluated the distribution of our sample, and we have compared it with the analogous sHR diagram that we have been using throughout the rest of the thesis. The general results are similar in both diagrams: equivalent area covered, and a lack of O-type stars near the ZAMS. Nevertheless, differences appear: the sample groups in higher masses in the sHR diagram, and some stars appear closer to the ZAMS in th HR diagram below the 32 $M_{\odot}$ evolutionary track.

In conclusion, the *Gaia* results for our stars seem to have some limitations with large distances and especially for bright stars. The comparisons with physical parameters calibrations indicate some dispersion not explained by the available range in distance. The mass, still depending on the limited accuracy of the gravity determination, is the most affected. The shift from sHR to HR has not eliminated the gap of O-type stars near the ZAMS.

FUTURE WORK**:**

Future work with the O-type sample will include a long-term and high-precision time series investigation of the detected spectroscopic variability (along the lines of, e.g., Fullerton et al. 1996, Martins et al. 2015a) and to characterize the orbital and physical characteristics of those stars identified as spectroscopic binaries in more detail, including spectra from other related surveys such as OWN, CAFÉ-BEANS and the ESO archives. In addition to the purely quantitative spectroscopic analysis, our plan includes to incorporate information about parallaxes (distances) from the *Gaia* Data Release 2 (DR2, Lindegren et al. 2018), allowing us to determine spectroscopic masses, radii and luminosities for the whole sample. Finally, the full characterization will include a detail determination of photosperic abundances of C, N, and O, for the whole sample of likely single and SB1 stars. Our ultimate objective is to produce a homogeneous and statistically significant empirical overview of physical parameters and abundances of Galactic O-type stars and, eventually, use these results to assess theoretical predictions for the early phases of massive stars evolution, as well as provide empirical constraints to some of the free parameters considered in these models. All this work with the O sample should be repeated in a similar way with the B stars in the IACOB+OWN sample, in a future complementary thesis work.

A

Notes on the analysis

In this appendix, we further elaborate some details of the quantitative spectroscopic analysis that have not been included in the bulk of the text because of their technical character. We also provide a brief summary of the main characteristics of the stellar atmosphere codes and the evolutionary models used throughout the thesis.

A.1 Notes on the IACOB-BROAD tool

As described in Simón-Díaz & Herrero (2014), IACOB-BROAD is a specifically designed tool, based on a combined Fourier transform (FT) + Goodness of fit (GOF) technique, that has been used in this thesis (See Sect. 3.3.1) for the determination of the line-broadening parameters (i.e. projected rotational velocity $-v \sin i-$ and the amount of non-rotational broadening $-v_{\rm mac}-$). The IACOB-BROAD tool is available at the IACOB project webpage[1], along a quick reference guide to start using it.

The analysis is based on a selected single diagnostic line. Before starting the combined FT+GOF analysis, the tool allows for a individual selection and pre-processing of the line profile (e.g., renormalization of the local continuum, clipping part of the line-profile to eliminate nebular contamination). This is shown in Fig A.1, in the upper left-hand panel, as the darker highlighted region of the spectra. The two methods are completely independent, and results for both are provided simultaneously at the end of IACOB-BROAD calculations. The whole set of calculations for one line-profile are completed in ∼10 minutes.

The Fourier transform technique is based on the identification of the first zero in the Fourier transform of the highlighted region of the line-profile, and

[1] http://www.iac.es/proyecto/iacob/pages/tools/iacob-tools.php

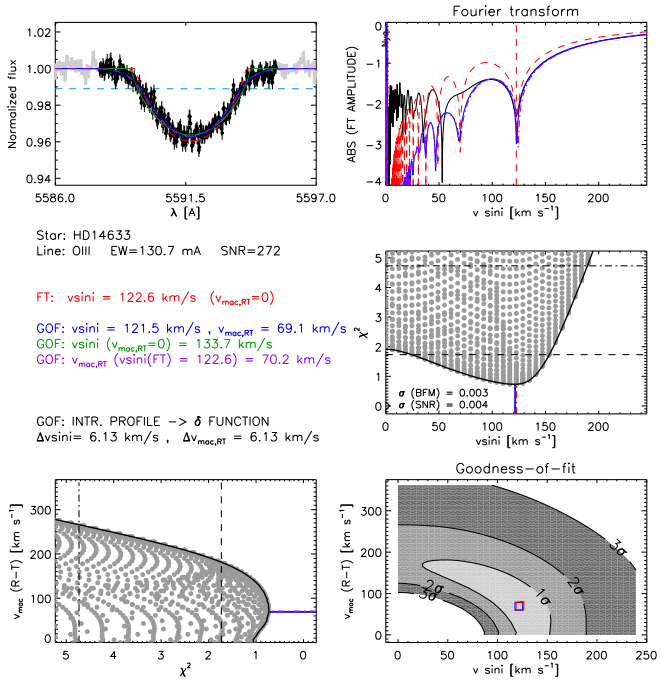

Figure A.1: Example of graphical output from the IACOB-BROAD tool for the O8.5 V star HD 14633. Five main graphical results are presented: (a) the line profile (upper left); (b) the FT of the line (upper right); and (c) 2D χ^2 -distributions resulting from the GOF analysis (lower right) and their projections (middle and lower left). See text for more detailed explanations.

the direct translation of the associated frequency (σ_1) into the corresponding projected rotational velocity via the formula

$$\frac{\lambda}{c} v \sin i \, \sigma_1 = 0.660$$

where λ is the central line wavelength and c is the velocity of light.

The goodness-of-fit (GOF) technique is based on a simple line-profile fitting in which the intrinsic profile (a delta in our methodology) is convolved with

the various considered/investigated line-broadening profiles (using a systematic grid of values) and compared with the observed profile using a χ^2 formalism. In our case, the rotation profile is semicircular, by Doppler effect, and the macroturbulence is represented by a radial-tangential profile[2].

The tool presents a graphical output of the results (Fig. A.1). It includes five main graphical results (a) the line profile (upper left); (b) the FT of the line (upper right); and (c) 2D χ^2-distributions resulting from the GOF analysis (lower right) and their projections (above and to the left). In addition, the following information is provided in the same figure:

1. the $v \sin i$ corresponding to the first zero of the FT;
2. the $v \sin i$ and macroturbulent velocity resulting from the GOF, assuming both are free parameters;
3. the $v \sin i$ resulting from the GOF, when the macroturbulent velocity is fixed to zero (i.e., this result assumes that the full broadening is due to rotation and is directly comparable with previous studies not accounting from the extra-broadening);
4. the $v_{\rm mac}$ resulting from the GOF when the $v \sin i$ is fixed to the value corresponding to the first zero of the FT;

From the IACOB-BROAD analyses we obtain two independent measurements of the $v \sin i$, resulting from either the Fourier transform $v \sin i$(FT) or the Goodness of fit $v \sin i$(GOF), whose comparison is used as a consistency check. The program is also able to provide uncertainties for the case of the GOF analysis that we have decided not to use in this thesis.

A.2 Comparison of diagnostic lines in the line-broadening analysis

The use of Helium lines in the line-broadening analysis of O-type stars is a well-known caveat for the accurate determination of $v \sin i$ in these stellar objects. This is related to the non-negligible contribution and limited accuracy modeling of the Stark-broadening to the global shape of the line-profiles, expected to be negligible when rotation clearly dominates the profile, but critical for slow rotators.

[2]The reasons to select the radial-tangencial profile are discussed in Simón-Díaz & Herrero (2014)

To test the effect of using He lines in the $v \sin i$ determination of some of the stars in our sample (see Sect. 6.2), we performed an academic exercise in which we obtain additional $v \sin i$ values to 118 O-type stars previously analyzed using a metal line, but using a He I or He II line instead. Panels in Fig. A.2 include the $v \sin i$(GOF) results obtained with a metal diagnostic line with respect to results obtained with He I and He II lines respectively.

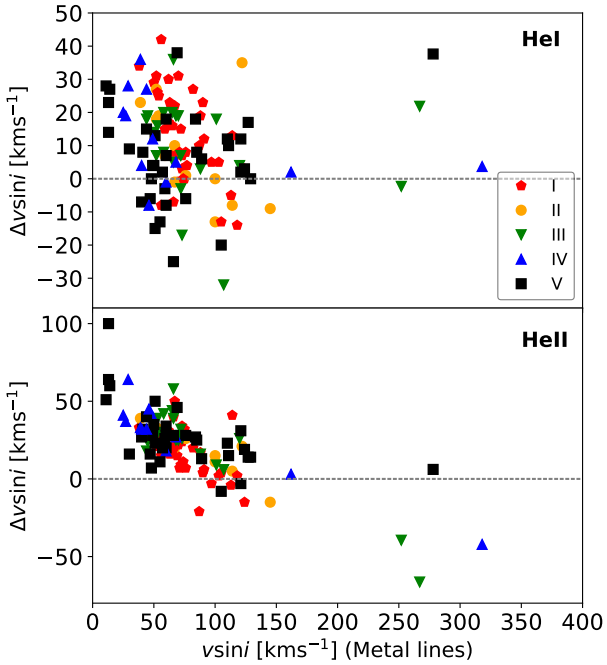

Figure A.2: Differences of $v \sin i$ results using a metal line or He I(top)/He II(bottom) lines. Color and shape depends on luminosity class.

In the comparison with the analysis using He I lines, the discrepancies are larger below 100 km s^{-1}. In the comparison with the results using He II lines we found a similar discrepancy. For the slow rotators He II provides $v \sin i$ values up to 100 km s^{-1} larger. We conclude that, as expected, the effect of using

He lines, especially He II lines, for the line-broadening analysis of stars with $v \sin i$<100 km s^{-1} is not negligible. This result is in agreement with Ramírez-Agudelo et al. (2013) and Simón-Díaz & Herrero (2007).

As a final remark, our analysis of faster rotators using He II lines provide lower values of $v \sin i$, by 70 km s^{-1} in some cases, compared to the analyses with metal lines. This may be related with the distortion effect in fast-rotators that produce He II lines coming from a different region (poles) of the star.

A.3 IACOB-GBAT tool

As presented in Simón-Díaz et al. (2011a), IACOB-GBAT is a grid-based automatic IDL tool that has been used in this thesis for the quantitative spectroscopic analysis of O-stars (See Sect. 3.3.3). The program is available by means of a direct request to its author (Sergio Simón-Díaz).

For better understanding of the information presented in Sect. 3.3.3 and Appendix A.4, we are going to review the four main steps that define the IACOB-GBAT tool, including the new updates incorporated for this work, and present a schematic flowchart of the methodology applied in the IACOB-GBAT tool in Fig A.3:

1. *Providing the input information to* IACOB-GBAT*:* In this first step, the user provides the observed spectrum to be analyzed, as well as all the information required for the spectroscopic analysis. This refers to the resolving power of the spectrum, the line-broadening parameters of the star, the metallicity of the grid of FASTWIND models to be used, the range of values for the various free parameters and, last, the set of H/He lines to be considered.

2. *Pre-processing of the spectra:* This step allows the user to select the spectral window around each line to be considered in the χ^2 computation and also includes the possibility to (a) correct the spectrum from radial velocity, (b) locally renormalize the diagnostic lines whenever necessary, and (d) clip part of the line to eliminate nebular lines, blends and cosmic rays.

3. *Line-by-line χ^2 computation:* In this third step, IACOB-GBAT computes and stores the individual χ^2 per considered diagnostic line for each combination of the 6 free parameters within the established range per parameter. This step lasts between a few minutes and less than 1 hour depending on the number of lines and the considered range in the free parameters.

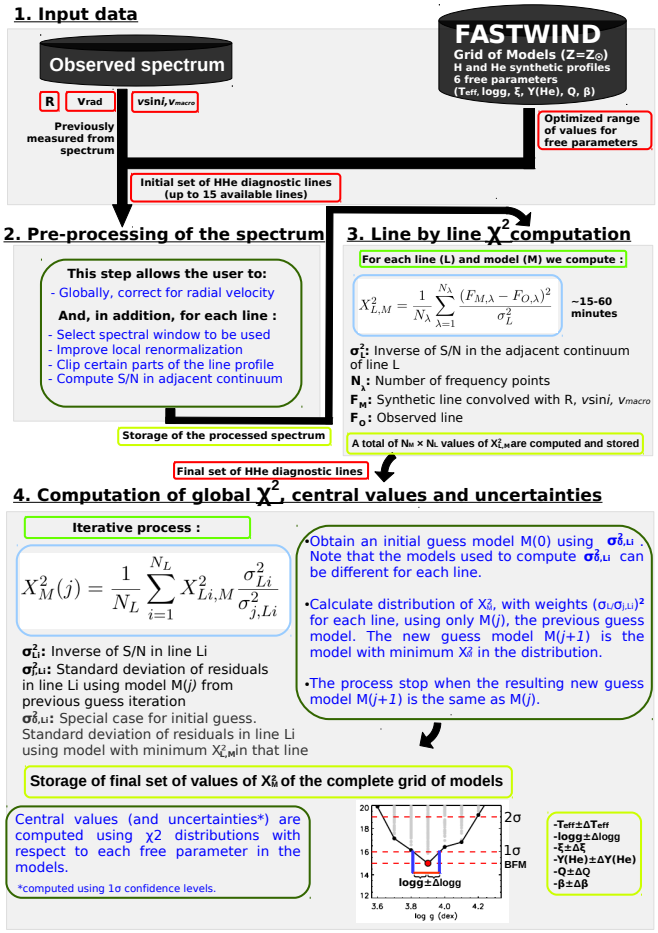

Figure A.3: Schematic flowchart of the methodology applied in the IACOB-GBAT tool.

4. *Global χ^2 computation and final results:* In this final step, IACOB-GBAT uses the information stored in the previous step to iteratively compute

the global χ^2 distribution and provide estimations for the central values (or upper/lower limits) and associated uncertainties for each of the free parameters of the grid. In addition, if empirical values for the absolute visual magnitude ($M_{\rm v}$) and terminal velocity of the wind (v_∞) are provided, IACOB-GBAT will also compute and provide results for the stellar radius (R), luminosity (L), spectroscopic mass ($M_{\rm sp}$) and mass loss rate ($\dot{M}$). No more than 1 minute is needed to run this step.

The last three steps can be launched independently, with the only condition that a given step requires previous steps to be performed before. This provides a great versatility to the tool. The final set of lines considered for the spectroscopic analysis can be decided by the user depending on the observed wavelength range, as well as other (more subjective) reasons based on, e.g., previous knowledge about the reliability of the available diagnostic lines or cosmic rays affecting the part of the observed spectrum. The tool also includes the possibility to establish an initial set of lines for which the line-by-line χ^2 computation is performed (*Step 3*) and then exclude some of these lines for the computation of the global χ^2 distribution and the estimation of the final parameters and uncertainties (*Step 4*). This possibility allows the user to evaluate in a few seconds the effect of including/excluding some of the initially considered diagnostic lines on the resulting stellar parameters.

A.4 Update in the IACOB-GBAT tool

The main changes incorporated in IACOB-GBAT in the context of this thesis include (1) an iterative strategy implemented in the last steps of the tool to provide – in an automatic and objective way – weights to the diagnostic lines during the computation of the final χ^2 distribution, and (2) how the central values and uncertainties for the 6 free parameters are computed from this final χ^2 distribution.

As indicated above, the tool starts (in *Step 3*) computing the quantity $X^2_{L,M}$ for each considered line (L) and every model (M) in the subgrid

$$X^2_{L,M} = \frac{1}{N_\lambda} \sum_{\lambda=1}^{N_\lambda} \frac{(F_{M,\lambda} - F_{O,\lambda})^2}{\sigma_L^2} \tag{A.1}$$

where $F_{M,\lambda}$ and $F_{O,\lambda}$ are the normalized fluxes corresponding to the synthetic and observed spectrum, respectively; $\sigma_L = (\mathrm{S/N})^{-1}$ account for the S/N of the line; and N_λ is the number of frequency points in the line.

All the quantities computed in *Step 3* (a total of $N_M \times N_L$ values of $X^2_{L,M}$, where N_M and N_L are the number of models and lines, respectively) are then stored before proceeding with the computation of the global χ^2 distribution. As indicated above, this saves a considerable amount of time in case the effect of using different strategies to combine the individual $X^2_{L,M}$ quantities to obtain this final χ^2 distribution wants to be evaluated.

Under ideal conditions (e.g., for a perfect model), $X^2_{L,M}$ corresponds to a reduced χ^2. However, as indicated in Simón-Díaz et al. (2011c), this situation is unlikely reached in the analysis of real spectra. Therefore, the $X^2_{L,M}$ values need to be corrected to account for possible deficiencies in the fitting process. In its present version, IACOB-GBAT proceed as follows. First, it identifies the model $M(0, L_i)$ which results in the minimum value of $X^2_{L,M}$ for line L_i ($i = 1$, N_L). At this point, it is important to stress that the model $M(0, L_i)$ may be different for each of the considered lines. Subsequently, as an initial guess and for each model, IACOB-GBAT computes the quantity

$$X^2_M(0) = \frac{1}{N_L} \sum_{i=1}^{N_L} X^2_{Li,M} \frac{\sigma^2_{Li}}{\sigma^2_{0,Li}} \tag{A.2}$$

where $\sigma_{0,Li}$ is defined as the standard deviation of the residuals of line L_i using the corresponding synthetic line from model $M(0, L_i)$. In this way, the code obtains a first global χ^2 distribution using more realistic estimations of the quantities σ^2_L per line (i.e., taking into account other sources of uncertainties in the profile fitting procedure apart from the noise in the observed spectrum).

Then, the code starts an iterative process in which, once the model in the grid resulting in the minimum value of X^2_M is identified – $M(j)$ –, a new quantity, again for all models,

$$X^2_M(j) = \frac{1}{N_L} \sum_{i=1}^{N_L} X^2_{Li,M} \frac{\sigma^2_{Li}}{\sigma^2_{j,Li}} \tag{A.3}$$

is computed, where now $\sigma_{j,Li}$ is defined as the standard deviation of the residuals of line L_i using the corresponding synthetic line from model $M(j)$. We note that, in this case, the same model in the grid is considered to compute the quantities $\sigma_{j,Li}$.

The process is repeated until convergence, i.e., when the best fitting model in one iteration is the same as the previous one. This is normally achieved in less than 10 iterations. Following this strategy, a lower weight is automatically and objectively given (in each iteration) to those lines which result in a worse fitting compared to the rest of lines.

Table A.1: Reference models used for the determination of the effect of v_∞ in the analysis. In all models $Y_{\rm He}$ and β were fixed to 0.10 and 1.0, respectively.

Model	$T_{\rm eff}$ [K]	$\log g$ [dex]	$\log Q$ [dex]	v_∞ [km s^{-1}]
D11	35000	4.0	13.0	3014
D12	35000	4.0	13.5	3014
D21	40000	4.0	13.0	3054
D22	40000	4.0	13.5	3054
D31	45000	4.0	13.0	3002
D32	45000	4.0	13.5	3002
S11	30000	3.5	12.1	2428
S12	30000	3.5	12.5	2428
S21	35000	3.5	12.1	2265
S22	35000	3.5	12.5	2265
S31	40000	3.5	12.1	1915
S32	40000	3.5	12.5	1915

Last, once the final X^2_M distribution is obtained, central values and uncertainties (or upper/lower limits) are computed as described here. In Fig. 3.10 we represent the χ^2 distributions comparing observed spectrum and FASTWIND model for each of the evaluated parameters. In each panel the 1σ and 2σ confidence levels are plotted. The 1σ is used to derive mean values and uncertainties. The final stellar parameters are computed using only the models located within the 1σ levels on each χ^2 distribution. The central value of the crossing points of the envelope with the 1σ level is considered the mean value, the uncertainty is the symmetric distance to each crossing point. This process provides a perfect representation of the 1σ level of confidence as the range of valid models in each particular case. As a final remark, the IACOB-GBAT tool is able to identify degeneracies in the χ^2 distribution (when the envelope of the best models is not crossing the 1σ confidence level) and provides upper or lower limits considering the opposite point where it cross the 1σ line.

A.5 On the effect of v_∞ in the determination of the wind-strength Q-parameter

The IACOB-GBAT tool follows a grid-based analysis strategy in which all the information about the stellar wind properties is condensed in the wind-strength Q parameter, defined as $Q = \dot{M}/(v_\infty R)^{1.5}$, which is the optical-depth invariant

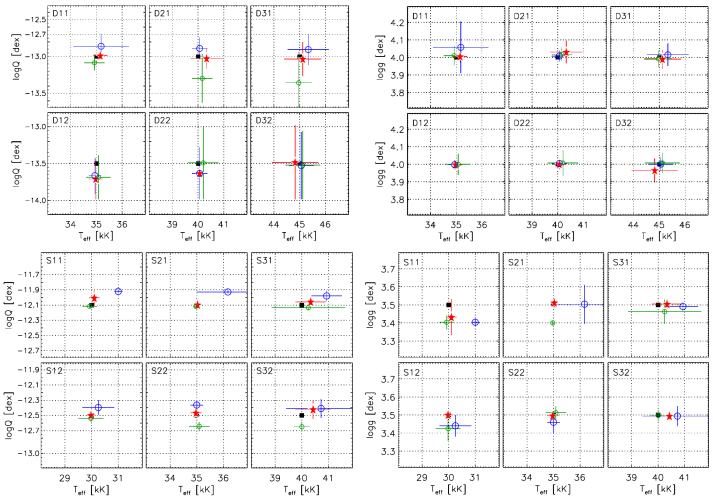

Figure A.4: Results of the IACOB-GBAT analysis of mock models presented in Table A.1. Horizontal and vertical dotted lines indicate the values considered in the grid of FASTWIND models. Black squares indicate the input parameters of the models. The other three symbols indicate the results of the IACOB-GBAT analysis (central values + associated 1-σ uncertainties) for each set of 3 models with the same ($T_{\rm eff}$, $\log g$, $\log Q$, $Y_{\rm He}$, $\xi_{\rm t}$ and β), but different values of v_∞ (see text for explanation). Namely, red star: same v_∞ as the one in the grid of FASTWIND models coupled with IACOB-GBAT ($v_{\infty,\rm grid}$); large blue circle: $v_\infty = 1.3\ v_{\infty,\rm grid}$; small green circle: $v_\infty = 0.7\ v_{\infty,\rm grid}$.

for ρ^2-dependent opacities such as Hα. As indicated in Table 3.1, this is one of the six free parameters that were considered to build the grid of FASTWIND models coupled with the automatized analysis tool. Details about the specific values of v_∞, R, and $\dot{M}$ that were considered in each model within the grid are provided in Simón-Díaz et al. (2011c). Basically, for each pair ($T_{\rm eff}$, $\log g$) in the grid a radius was assumed following the Martins et al. (2005) calibrations. This radius and the scaling relation $v_\infty \approx 2.65 v_{esc}$(Kudritzki & Puls 2000) were then considered to compute the terminal velocity. Last, the value of $\dot{M}$ was obtained from Q, v_∞, and R, for all the different values of Q indicated in Table 3.1.

This analysis strategy assumes that the effect on the line profiles of different combinations of v_∞, R, and $\dot{M}$ producing the same value of Q is small whenever the assumed values of R and v_∞ do not depart very much from the actual

values. While this has been already tested in the case of R (Puls et al. 1996), this statement has not been formally evaluated for the case of the terminal velocity.

By comparing the values of v_∞ that would be inferred for the stars in our sample following the strategy mentioned above with those empirically obtained by Howarth et al. (1997), we have found that the mean difference in the ratio between the assumed and measured terminal velocities is 0.95 with an associated standard deviation of 0.25.

To evaluate the effect of a difference of 30% in terminal velocity on the derived Q, we computed a set of FASTWIND models with fixed stellar parameters (comprising 12 different combinations of the parameters $T_{\rm eff}$, $\log g$ and log Q, see Table A.1) and three different combinations of $\dot{M}$ and v_∞ providing the same value of Q. Basically, apart from the 12 reference models (which adopt the same values of v_∞ as those in the grid of FASTWIND models coupled with IACOB-GBAT), we computed another 24 models in which the terminal velocity was changed by $\pm$30% and the mass-loss rates where modified accordingly while keeping the same values of R and log Q as in the reference models.

All the synthetic spectra associated with these 36 models (convolved with a $v \sin i = 60$ km s^{-1} and degraded to a S/N=200) were then analyzed with IACOB-GBAT. The main results regarding $T_{\rm eff}$, $\log g$, and log Q are summarized in Fig. A.4. We basically found that a 30% difference in v_∞ leads to a maximum variation in log Q of 0.15 dex, where larger values of this parameter are obtained for the models with increased terminal velocity. This uncertainty is on the order of (or a bit larger than) the uncertainty in log Q associated with the fitting process for values of the wind-strength Q-parameter typical of supergiants (log Q > -12.7), but negligible when compared with the accuracy reached in the case of dwarfs, which is $\gtrsim$0.25 dex. The rest of the parameters are barely affected (differences up to 500 K in $T_{\rm eff}$ and 0.05 dex in $\log g$) except for very specific cases where differences up to 1000 K and 0.1 dex, respectively, have been found. In particular, we remark the very good agreement between the output of the IACOB-GBAT and the input values for those cases in which v_∞=$v_{\infty,grid}$. This demonstrate the strength of our automatized analysis strategy.

A.6 On the linear dependency between log Q and log $\mathcal{L}$

In Sect. 5.6.1 we introduced a distance-independent version of the wind-momentum luminosity relationship in the O-star domain. This section provides more details about how this relationship is obtained from the WLR.

We start from the wind-momentum luminosity relationship:

$$\log D_{\rm mom} = x \log L + D_0. \tag{A.4}$$

By considering the following definitions:

$$\mathcal{L} := T_{eff}^4/g = L/4\pi\sigma_{\rm B}GM \tag{A.5}$$

$$D_{\rm mom} := \dot{M} v_\infty R^{1/2} \tag{A.6}$$

$$Q := \dot{M}/(v_\infty R)^{3/2} \tag{A.7}$$

Equation A.4 can be also expressed as:

$$\log(\dot{M} v_\infty R^{1/2}) = x \log \mathcal{L} + x \log(4\pi\sigma_{\rm B}G) + x \log M + D_0 \tag{A.8}$$

or, equivalently:

$$\log(Q v_\infty^{5/2} R^2) = x \log \mathcal{L} + x \log(4\pi\sigma_{\rm B}G) + x \log M + D_0. \tag{A.9}$$

If now we assume the scaling relationship between v_∞ and $v_{\rm esc}$:

$$v_\infty = \eta v_{\rm esc} \tag{A.10}$$

with $\eta \sim 2.65$ (Kudritzki & Puls 2000) and

$$v_{\rm esc} = (2GM(1-\Gamma)/R)^{1/2} \tag{A.11}$$

we end up with the following:

$$\log(Q\eta^{5/2}(2G(1-\Gamma))^{5/4}(M/R)^{5/4}R^2) = x \log \mathcal{L} + x \log(4\pi\sigma_{\rm B}G) + x \log M + D_0 \tag{A.12}$$

Regrouping and isolating $\log Q$:

$$\log Q = x \log \mathcal{L} + \frac{3}{4}\log\frac{M}{R} + (x-2)\log M - \frac{5}{4}\log(2\eta^2 G(1-\Gamma)) + x \log(4\pi\sigma_{\rm B}G) + D_0. \tag{A.13}$$

Since $x \approx 2$, the term involving $\log M$ is negligible, and when we perform a linear regression to the data as presented in Fig. 5.12, the slope provides us with a rough estimation of the parameter x. As explained in the main text, with this approach we are able to obtain the slope of the WLR without the need of information about distances. Finally, we note that, compared to the classic WLR, a larger scatter is expected in this relationship due to the rest of the terms that are not exactly constant but depend on M or M/R.

A.7 FASTWIND

FASTWIND (Fast Analysis of STellar atmospheres with WINDs, see Santolaya-Rey et al. 1997; Puls et al. 2005; Rivero González et al. 2012) is the stellar atmosphere code used in this work. The current version (v10.1) of the code obtains a consistent atmosphere structure with spherical geometry in in the photosphere, reproducing the plane-parallels and hydrostatic models with modest unclumped winds. It is capable of calculate an optical and IR spectra of OB stars in $\sim$ 15 minutes. The code was developed with the particular intention to provide relatively fast results, with very accurate profiles determination of certain species, using the vast majority rest of the lines as background effects.

FASTWIND utilizes the thermal balance of electrons in the line forming regions and in the optically thin part of the outer atmosphere to enable a fast calculation of a consistent temperature structure. This equation accounts for all important bound-bound and bound-free interactions, but also the free-free absorption/emission and radiative ionisation/recombination. For larger optical depths, in the lower atmosphere, a flux-correction method is applied, which calculates the temperature stratification from the condition of flux conservation. The flux conservation is used as an independent tool to check the consistency of the models throughout the complete atmosphere, usually with results better than 1%.

Another FASTWIND approach to speed up the process, saving computational effort, is the distinction between two groups of chemical elements, the explicit elements and the background elements. The former are calculated with high precision with a co-moving frame (CMF) transport for the line transitions. These will be used as diagnostics in the spectral line synthesis and in our O-type stars analyses are the hydrogen (H) and helium (He). For the background elements, the line-blocking effects in the emergent spectrum is treated in an approximate, via the Sobolev approximation (Sobolev 1960), by using suitable mean values for the corresponding line opacities

A.8 Evolutionary models

Along this thesis we use evolutionary tracks from two families of state-of-the-art evolutionary codes.

The Geneva evolutionary models grid used here was published in Ekström et al. (2012); Georgy et al. (2013). It presents solar reference chemical composition base on Asplund et al. (2005) (Z=0.014) and OPAL radiative opacities from Iglesias & Rogers (1996). It follows the Schwarzschild criterion to define the convective regions and include classical overshoot at the convective core edge of $\alpha_{over} = 0.1$, adopted to reproduce the main-sequence width in the range 1.35-9M $_{\odot}$. For the mass loss it follows different prescriptions including de Jager et al. (1988); Vink (2000); Crowther et al. (2002), and scaled for the rotating models. In our case we are using grid of models with different initial rotation distribution, adjusting the transport of angular momentum rotational-mixing as described in Meynet & Maeder (1997). Magnetic fields are not included.

The thesis use three different Geneva evolutionary models sets[3] with three different initial rotation rates for the stars: absence of rotation, 20% of the critical rate, and 40% of the critical rate.

The Bonn evolutionary models (Brott et al. 2011) are a a dense grid of evolutionary tracks and isochrones of rotating massive main-sequence stars. They provide three grids with different initial compositions tailored to compare with early OB stars in the Small and Large Magellanic Clouds and in the Galaxy, based on the solar abundances by Asplund et al. (2005). They use the Ledoux criterion to determine the extension of the convective regions, and a 16 $M_{\odot}$ model at LMC metallicity is used to calibrate the classical overshooting parameter. Mass loss is included following a combination of prescriptions or recipes that are specific for each evolutionary phase of massive stars. In particular for winds of early O and B-type stars Vink (2000); Vink et al. (2001) is implemented, scaled to the v_{∞} in the case of rotating models. The effects of centrifugal acceleration on the stellar structure is considered according to Kippenhahn et al. (1970), and transport of angular momentum and chemical species is treated in a diffusive way calibrating on VLT-FLAMES observations. In addition to that, the action of magnetic fields is included through the Tayler-Spruit dynamo (Spruit 2002), affecting the transport of angular momentum.

Each Bonn grid covers masses ranging from 5 to 60 $M_{\odot}$ and initial rotation rates between 0 and about 600 $\mathrm{km\,s^{-1}}$. In this thesis we use three different

[3]Available from the Syclist platform in obswww.unige.ch/Recherche/evol/-Database-

sets[4] including initial rotation rates of 0, 200, and 300 $\mathrm{km\,s^{-1}}$.

[4]Available at ftp://cdsarc.u-strasbg.fr/pub/cats/J/A+A/530/A115/

B

Tables

In this appendix we tabulate all the results from the analysis and additional data compiled for our sample of Galactic O-type stars.

Table B.1: Complete list of stars considered in this work.

They are separated in two groups. The first part of the table includes stars sorted by HD number when available. The second group comprises those stars that do not have an HD number, sorted alphabetically. Columns 1 to 6 come directly from GOSC, the name(s) of each star, spectral classification, the secondary component in the unresolved spectrum, and the B magnitude. Then, the number of available spectra per instrument (N:FIES , M:HERMES, F:FEROS,) (columns 6 to 8). Finally, specific details about the spectra used for the spectroscopic analysis: name (indicating star, date, instrument, and resolution), Julian date, and S/N, and a reference to the table with the spectroscopic parameters obtained in the analysis (columns 9 to 12).

Name	Alt. name	SpT LC	secondary	B_{ap}	N	M	F	Best S/N spectrum in IACOB+OWN	HJD -2450000	S/N 4500 Å	Ref. Table
HD 108	HD 108	O8 fp-var	.	7.5	4	0	0	HD108_20100908_230933_N_V46000	55448.4	166	B.5
HD 1337	AO Cas	O9.2 II	.	6.0	11	0	0	HD1337_20121223_214853_N_V46000	56285.4	178	B.6
HD 10125	HD 10 125	O9.7 II	.	8.7	3	0	0	HD10125_20110115_232529_N_V25000	55577.5	123	B.4
HD 12323	HD 12 323	ON9.2 V	.	8.8	2	0	0	HD12323_20121225_225051_N_V25000	56287.5	109	B.4
HD 15137	HD 15 137	O9.5 II-IIIn	.	7.9	3	0	0	HD15137_20091113_034656_N_V46000	55148.6	146	B.6
HD 12993	HD 12 993	O6.5 V((f))_Nstr	.	9.2	3	0	0	HD12993_20110912_054359_N_V25000	55816.7	125	B.4
HD 13022	HD 13 022	O9.7 II-III	.	9.1	2	0	0	HD13022_20110912_034420_N_V25000	55816.6	107	B.5
HD 13268	HD 13 268	ON8.5 IIIn	.	8.3	3	0	0	HD13268_20110112_201716_N_V25000	55574.3	153	B.5
HD 13745	HD 13 745	O9.7 II(n)	.	8.0	3	0	0	HD13745_20110910_015932_N_V46000	55814.5	129	B.5
HD 14434	HD 14 434	O5.5 IVnn(f)p	.	8.7	3	0	0	HD14434_20110911_043935_N_V25000	55815.7	138	B.5
HD 14442	HD 14 442	O5 n(f)p	.	9.6	1	0	0	HD14442_20161229_225242_N_V25000	57752.4	95	B.5
HD 14947	HD 14 947	O4.5 If	.	8.5	3	0	0	HD14947_20081108_231044_N_V46000	54779.5	133	B.4
HD 14633 AaAb	HD 14 633	ON8.5 V	.	7.2	3	1	0	HD14633_20091113_024720_N_V46000	55148.6	187	B.4
HD 15558	HD 15 558 A	O4.5 III(f)	.	8.4	9	0	0	HD15558_20081106_231616_N_V46000	54777.5	134	B.6
HD 15570	HD 15 570	O4 If	.	8.8	3	0	0	HD15570_20081107_004909_N_V46000	54777.5	95	B.4
HD 15629	HD 15 629	O4.5 V((fc))	.	8.8	3	0	8	HD15629_20110913_020206_N_V25000	55817.6	123	B.4
HD 15642	HD 15 642	O9.5 II-IIIn	.	8.6	3	0	0	HD15642_20110911_033543_N_V25000	55815.6	107	B.5
HD 16429	HD 16 429 A	O9 II-III(n)_Nwk	.	8.5	3	0	0	HD16429_20100909_051728_N_V46000	55448.7	130	B.6
HD 16691	HD 16 691	O4 If	.	9.1	3	0	0	HD16691_20110913_032931_N_V25000	55817.7	104	B.4
HD 16832	HD 16 832	O9.2 III	.	9.3	2	0	0	HD16832_20110912_045551_N_V25000	55816.7	102	B.4
HD 17505	HD 17 505 A	O6.5+O8 III+Vn(f)	.	7.7	7	0	0	HD17505_20100908_061729_N_V46000	55447.8	159	B.6
HD 17520	HD 17 520 A	O8 V	.	9.1	3	0	0	HD17520_20110911_041817_N_V25000	55815.6	121	B.4
HD 17603	HD 17 603	O7.5 Ib(f)	.	9.1	2	0	0	HD17603_20110114_215807_N_V25000	55576.4	103	B.4
HD 18326	HD 18 326	O6.5 V((f))z	O9/B0V:	8.3	3	0	0	HD18326_20110115_230402_N_V46000	55577.5	132	B.6
HD 18409	HD 18 409	O9.7 Ib	.	8.8	2	0	0	HD18409_20110113_195319_N_V25000	55575.3	125	B.5
HD 19820	CC Cas	O8.5 III(n)((f))	.	7.6	3	0	0	HD19820_20121225_223239_N_V46000	56287.4	156	B.6
HD 24431	HD 24 431	O9 III	.	7.2	4	0	0	HD24431_20081109_032702_N_V46000	54779.7	163	B.4
HD 24534	X Per	O9.5: npe	.	7.1	3	0	0	HD24534_20110115_192813_N_V46000	55577.3	123	B.5
HD 24912	xi Per	O7.5 III(n)((f))	.	4.1	20	0	0	HD24912_20081109_012026_N_V46000	54779.5	185	B.5
HD 28446 A	1 Cam A	O9.7 IIn	.	6.0	3	1	0	HD28446A_20091113_003939_N_V46000	55148.5	126	B.5
HD 30614	alpha Cam	O9 Ia	.	4.3	8	15	0	HD30614_20111109_033231_M_V85000	55874.7	191	B.4
HD 34078	AE Aur	O9.5 V	.	6.2	5	1	0	HD34078_20081109_012706_N_V46000	54779.6	154	B.4
HD 34656	HD 34 656	O7.5 II(f)	.	6.9	4	58	0	HD34656_20131218_234051_M_V85000	56645.5	171	B.4
HD 35619	HD 35 619	O7.5 V((f))	.	8.8	5	0	0	HD35619_20110913_041546_N_V25000	55817.7	139	B.4

Table B.1: continued.

Name	Alt. name	SpT LC	secondary	B_{ap}	N	M	F	Best S/N spectrum in IACOB+OWN	HJD -2450000	S/N 4500 Å	Ref. Table
HD 35921	LY Aur A	O9.5 II	.	7.3	4	0	0	HD35921_20091112_002003_N_V46000	55147.5	152	B.6
HD 36483	HD 36 483	O9.5 IV(n)	.	8.6	4	0	0	HD36483_20110913_043711_N_V25000	55817.6	129	B.5
HD 36486 AaAb	delta Ori AaA	O9.5 IINwk	.	2.3	3	7	2	HD36486_20090501_231005_F_V48000	54953.5	198	B.4
HD 36512	upsilon Ori	O9.7 V	.	4.4	3	1	0	HD36512_20111109_032351_M_V85000	55874.6	210	B.4
HD 36861 A	lambda Ori	O8 III((f))	.	3.6	50	124	0	HD36861_20140211_200754_M_V85000	56700.3	252	B.4
HD 36879	HD 36 879	O7 V(n)((f))	.	7.8	3	0	0	HD36879_20081109_020337_N_V46000	54779.5	158	B.5
HD 37022	theta^1 Ori CaCb	O7 Vp	.	5.2	5	0	3	HD37022_20081108_055255_N_V46000	54778.7	208	B.5
HD 37041	theta^2 Ori A	O9.5 IVp	.	5.0	7	0	8	HD37041_20091112_042416_N_V46000	55147.6	172	B.6
HD 37043	iota Ori	O9 IIIvar	.	2.6	9	1	6	HD37043_20091110_015505_N_V46000	55145.5	226	B.6
HD 37366	HD 37 366 A	O9.5 IV	.	7.7	3	0	0	HD37366_20110910_044910_N_V46000	55814.7	129	B.6
HD 37468 AB	sigma Ori AaAbB	O9.7 III	.	4.4	38	0	6	HD37468AB_20081106_054721_N_V46000	54776.8	200	B.6
HD 37737	HD 37 737	O9.5 II-III(n)	.	8.4	6	0	0	HD37737_20130129_214159_N_V25000	56322.4	130	B.5
HD 37742	zeta Ori AaAb	O9.2 IbNwk_var	.	1.9	31	96	8	HD37742_20131030_064651_M_V85000	56595.7	263	B.5
HD 37743	zeta Ori B	O9.5 II-III(n)	.	3.5	0	1	0	HD37743_20131218_024355_M_V85000	56644.6	181	B.5
HD 38666	mu Col	O9.5 V	.	4.9	0	0	5	HD38666_20090503_231437_F_V48000	54955.5	198	B.4
HD 39680	HD 39 680	O6 V:[n]pe_var	.	7.9	4	0	0	HD39680_20121224_031527_N_V46000	56285.6	139	B.5
HD 41161	HD 41 161	O8 Vn	.	6.7	4	0	0	HD41161_20081109_030049_N_V46000	54779.6	168	B.5
HD 41997	HD 41 997	O7.5 Vn((f))	.	8.8	3	0	0	HD41997_20110913_051707_N_V25000	55817.7	146	B.5
HD 42088	HD 42 088	O6 V((f))z	.	7.6	3	1	0	HD42088_20110116_013309_N_V46000	55577.6	160	B.4
HD 44811	HD 44 811	O7 V(n)z	.	8.6	3	0	0	HD44811_20110913_055938_N_V25000	55817.7	137	B.5
HD 45314	PZ Gem	O9: npe	.	6.7	5	0	0	HD45314_20110114_230558_N_V46000	55576.4	120	B.5
HD 46056	HD 46 056	O8 Vn	.	8.4	3	0	1	HD46056_20130129_003033_N_V25000	56321.5	141	B.5
HD 46106	HD 46 106	O9.7 III(n)	.	8.1	3	0	0	HD46106_20130128_223200_N_V46000	56321.4	122	B.6
HD 46149	HD 46 149	O8.5 V	.	7.8	3	0	2	HD46149_20121224_025709_N_V46000	56285.6	142	B.4
HD 46150	HD 46 150	O5 V((f))z	.	6.9	15	2	2	HD46150_20081108_020753_N_V46000	54778.6	182	B.4
HD 46202	HD 46 202	O9.2 V	.	8.7	4	0	0	HD46202_20130130_002935_N_V25000	56322.5	138	B.4
HD 46223	HD 46 223	O4 V((f))	.	7.5	5	1	1	HD46223_20081107_050512_N_V46000	54777.7	160	B.4
HD 46485	HD 46 485	O7 V((f))n_var?	.	8.6	3	0	0	HD46485_20110913_053847_N_V25000	55817.7	156	B.5
HD 46573	HD 46 573	O7 V((f))z	.	8.3	3	0	0	HD46573_20121224_040337_N_V46000	56285.6	122	B.5
HD 46966	HD 46 966	O8.5 IV	.	7.1	3	38	0	HD46966_20091112_011937_N_V46000	55147.6	185	B.4
HD 47129	HD 47 129	O8 fp_var	.	6.1	5	0	0	HD47129_20121224_035006_N_V46000	56285.7	144	B.6
HD 47432	HD 47 432	O9.7 Ib	.	6.4	3	1	0	HD47432_20091112_032247_N_V46000	55147.6	160	B.4
HD 47839	15 Mon AaAb	O7 V((f))z_var	.	4.6	5	0	0	HD47839_20091110_025831_N_V46000	55145.6	244	B.5
HD 48099	HD 48 099	O5.5 V((f))z	O9V	6.3	3	0	0	HD48099_20091112_031457_N_V46000	55147.6	178	B.6
HD 48279	HD 48 279 A	O8.5 VNstr_var?	.	8.0	3	0	1	HD48279_20121224_033329_N_V46000	56285.6	134	B.5
HD 5005 A	HD 5005 A	O4 V((fc))	.	8.6	3	0	0	HD5005A_20100910_045224_N_V46000	55449.7	145	B.5
HD 5005 C	HD 5005 C	O8.5 V(n)	.	8.9	1	0	0	HD5005C_20130129_203700_N_V25000	56322.3	112	B.5
HD 5005 D	HD 5005 D	O9.2 V	.	9.7	1	0	0	HD5005D_20161028_223703_N_V25000	57690.4	72	B.5
HD 52266	HD 52 266	O9.5 IIIn	.	7.2	2	0	3	HD52266_20110115_014505_N_V46000	55576.5	131	B.5

Table B.1: continued.

Name	Alt. name	SpT	LC	secondary	B_{sp}	N	M	F	Best S/N spectrum in IACOB+OWN	HJD -2450000	S/N 4500 Å	Ref. Table
HD 52533	HD 52 533 A	O8.5	IVn	.	7.6	2	0	1	HD52533_20090501_232857_F_V48000	54953.4	191	B.5
HD 53975	HD 53 975	O7.5	Vz	.	6.4	3	0	1	HD53975_20091112_040202_N_V46000	55147.6	207	B.5
HD 54662	HD 54 662 AB	O7	Vz_var?	.	6.8	3	0	4	HD54662_20091110_053426_N_V46000	55145.7	191	B.6
HD 54879	HD 54 879	O9.7	V	.	7.6	2	0	5	HD54879_20121226_033157_N_V46000	56287.6	146	B.5
HD 55879	HD 55 879	O9.7	III	.	5.8	4	2	3	HD55879_20121224_041714_N_V46000	56285.6	172	B.5
HD 5689	HD 5689	O7	Vn((f))	.	9.5	1	0	0	HD5689_20161029_030818_N_V25000	57690.6	73	B.5
HD 57060	29 CMa	O7	Iafp-var	.	4.8	3	0	2	HD57060_20090505_005603_F_V48000	54956.5	217	B.6
HD 57061	tau CMa AaAb	O9	II	.	4.8	3	1	5	HD57061_20110321_015810_F_V48000	55641.6	268	B.4
HD 57236	HD 57 236	O8.5	V	.	8.9	2	0	4	HD57236_20121224_043200_N_V25000	56285.7	109	B.4
HD 57682	HD 57 682	O9.2	IV	.	6.2	3	0	2	HD57682_20121226_040502_N_V46000	56287.6	195	B.5
HD 60848	BN Gem	O8:	V:pe	.	6.7	3	0	0	HD60848_20110116_044117_N_V46000	55577.7	162	B.5
HD 64315	HD 64 315 AB	O5.5	V	.	10.1	5	0	1	HD64315_20070419_005559_F_V48000	54209.5	171	B.6
HD 64568	HD 64 568	O3	V((f*))z	.	9.5	0	0	3	HD64568_20080607_230926_F_V48000	54625.5	181	B.4
HD 66811	zeta Pup	O4	I(n)fp	.	2.0	0	0	7	HD66811_20110323_021313_F_V48000	55643.6	356	B.5
HD 68450	HD 68 450	O9.7	II	.	6.4	0	0	4	HD68450_20090503_001401_F_V48000	54954.5	187	B.4
HD 69106	HD 69 106	O9.7	IIn	.	7.0	0	0	1	HD69106_20060104_044914_F_V48000	53739.7	133	B.6
HD 69464	HD 69 464	O7	Ib(f)	.	9.1	0	0	8	HD69464_20080608_231326_F_V48000	54626.5	152	B.4
HD 71304	HD 71 304	O9	II	.	8.8	0	0	2	HD71304_20090503_002457_F_V48000	54954.5	163	B.4
HD 73882	NX Vel AB	O8.5	IV	.	8.0	0	0	7	HD73882_20110212_054245_F_V48000	55604.7	112	B.5
HD 74194	LM Vel	O8.5	Ib-II(f)p	.	7.8	0	0	20	HD74194_20090502_013746_F_V48000	54953.5	240	B.5
HD 74920	HD 74 920	O7.5	IVn((f))	.	7.6	0	0	1	HD74920_20041224_044455_F_V48000	53363.7	177	B.5
HD 75211	HD 75 211	O8.5	II((f))	.	7.9	0	0	4	HD75211_20120519_235311_F_V48000	56067.5	184	B.4
HD 75222	HD 75 222	O9.7	Iab	.	7.8	0	0	5	HD75222_20150405_010826_F_V48000	57117.5	141	B.5
HD 75759	HD 75 759 AB	O9	V	.	6.1	0	0	6	HD75759_20090503_012654_F_V48000	54954.5	248	B.6
HD 76341	HD 76 341	O9.2	IV	.	7.5	0	0	4	HD76341_20110323_024223_F_V48000	55643.6	121	B.5
HD 76556	HD 76 556	O6	IV(n)((f))p	.	8.6	0	0	4	HD76556_20080609_235952_F_V48000	54627.5	141	B.5
HD 76968	HD 76 968	O9.2	Ib	.	7.2	0	0	5	HD76968_20080513_001447_F_V48000	54599.5	231	B.4
HD 89137	HD 89 137	ON9.7	II(n)	.	7.9	0	0	3	HD89137_20110517_012116_F_V48000	55698.5	79	B.5
HD 90087	HD 90 087	O9.2	III(n)	.	7.8	0	0	4	HD90087_20110214_022932_F_V48000	55606.6	98	B.5
HD 90273	HD 90 273	ON7	V((f))	.	9.2	0	0	1	HD90273_20041222_045853_F_V48000	53361.7	115	B.5
HD 91572	HD 91 572	O6.5	V((f))z	.	8.3	0	0	5	HD91572_20080609_010335_F_V48000	54626.5	193	B.4
HD 91651	HD 91 651	ON9.5	IIIn	.	8.8	0	0	9	HD91651_20110516_005321_F_V48000	55697.5	101	B.5
HD 91824	HD 91 824	O7	V((f))z	.	8.1	0	0	9	HD91824_20070419_012940_F_V48000	54209.6	264	B.4
HD 92206 A	HD 92 206 A	O6	V((f))z	.	8.3	0	0	21	HD92206A_20080515_004900_F_V48000	54601.5	149	B.6
HD 92206 B	HD 92 206 B	O6	V((f))	.	9.3	0	0	9	HD92206B_20120520_003745_F_V48000	56067.5	202	B.6
HD 92206 C	HD 92 206 C	O8	V(n)z	B0:V	9.1	0	0	8	HD92206C_20070419_015218_F_V48000	54209.6	156	B.6
HD 92504	HD 92 504	O8.5	V(n)	.	8.4	0	0	4	HD92504_20080610_003438_F_V48000	54627.5	155	B.5
HD 93027	HD 93 027	O9.5	IV	.	8.7	0	0	2	HD93027_20090502_015334_F_V48000	54953.6	180	B.4
HD 93028	HD 93 028	O9	IV	.	8.3	0	0	7	HD93028_20080514_015221_F_V48000	54600.6	168	B.4

Table B.1: continued.

Name	Alt. name	SpT	LC	secondary	B_{sp}	N	M	F	Best S/N spectrum in IACOB+OWN	HJD -2450000	S/N 4500 Å	Ref. Table
HD 93128	HD 93 128	O3.5	V((fc))z	.	9.2	0	0	3	HD93128_20150403_033259_F_V48000	57115.7	186	B.4
HD 93129 AaAb		O2	If*	.	7.8	0	0	12	HD93129A_20150405_023412_F_V48000	57117.6	225	B.4
HD 93129 B	HD 93 129 B	O3.5	V((f))z	.	9.0	0	0	1	HD93129B_20150403_025102_F_V48000	57115.6	181	B.5
HD 93130	HD 93 130	O6.5	III(f)	.	8.4	0	0	6	HD93130_20090504_013947_F_V48000	54955.5	111	B.6
HD 93146 A	HD 93 146 A	O7	V((f))	.	8.4	0	0	8	HD93146_20080514_020823_F_V48000	54600.6	244	B.4
HD 93160 AB	HD 93 160	O7	III((f))	.	8.2	0	0	4	HD93160_20150402_042354_F_V48000	57114.7	232	B.4
HD 93161 A	HD 93 161 A	O7.5	V	.	8.6	0	0	3	HD93161A_20040505_234101_F_V48000	53131.4	135	B.6
HD 93161 B	HD 93 161 B	O6.5	IV((f))	.	8.7	0	0	1	HD93161B_20040606_235743_F_V48000	53132.5	184	B.5
HD 93162	HD 93 162	O2.5	If*/WN6	OB	8.5	0	0	28	HD93162_20090331_015614_F_V48000	54921.6	283	B.6
HD 93204	HD 93 204	O5.5	V((f))	.	8.5	0	0	3	HD93204_20080609_015400_F_V48000	54626.6	180	B.4
HD 93205	HD 93 205	O3.5	V((f))	O8V	7.8	0	0	4	HD93205_20090502_033748_F_V48000	54953.7	207	B.6
HD 93206	QZ Car AaAc	O9.7	Ibn	.	7.0	0	0	5	HD93206_20120521_025659_F_V48000	56068.6	150	B.6
HD 93222 AB	HD 93 222	O7	V((f))	.	8.8	0	0	3	HD93222_20110214_050447_F_V48000	55606.7	191	B.4
HD 93249 A	HD 93 249	O9	III	.	8.5	0	0	11	HD93249_20090502_003412_F_V48000	54953.5	192	B.4
HD 93250 AB	HD 93 250	O4	IV(fe)	.	7.9	0	0	4	HD93250_20120521_014809_F_V48000	56068.6	207	B.4
HD 93343	HD 93 343	O8	V	.	9.8	0	0	8	HD93343_20150402_044100_F_V48000	57114.7	170	B.6
HD 93403	HD 93 403	O5.5	III(fc)_var	.	7.5	0	0	2	HD93403_20090505_021204_F_V48000	54956.6	177	B.6
HD 93521	HD 93 521	O9.5	IIInn	.	6.8	22	0	0	HD93521_20121226_045343_N_V46000	56287.7	180	B.5
HD 93632	HD 93 632	O5	If_var	.	8.7	0	0	2	HD93632_20110323_055431_F_V48000	55643.7	157	B.5
HD 93843	HD 93 843	O5	III(fc)	.	7.3	0	0	4	HD93843_20150403_055036_F_V48000	57115.7	246	B.4
HD 94024	HD 94 024	O8	IV	.	8.8	0	0	8	HD94024_20080515_011756_F_V48000	54601.6	183	B.4
HD 94370	HD 94 370 A	O7	(n)fp	.	8.4	0	0	7	HD94370_20150402_053237_F_V48000	57114.7	184	B.5
HD 94963	HD 94 963	O7	II(f)	.	7.1	0	0	3	HD94963_20070421_040533_F_V48000	54211.7	192	B.4
HD 96264	HD 96 264	O9.5	III	.	7.5	0	0	5	HD96264_20110321_053854_F_V48000	55641.7	151	B.4
HD 96622	HD 96 622	O9.2	IV	.	9.1	0	0	4	HD96622_20080513_011335_F_V48000	54599.6	159	B.4
HD 96670	HD 96 670 AB	O8.5	(n)fp_var	.	7.9	0	0	7	HD96670_20090503_042422_F_V48000	54954.6	87	B.6
HD 96715	HD 96 715	O4	V((f))z	.	8.4	0	0	2	HD96715_20150403_052702_F_V48000	57115.7	182	B.4
HD 96917	HD 96 917	O8	Ib(n)(f)	.	7.2	0	0	4	HD96917_20110213_081641_F_V48000	55605.8	164	B.5
HD 96946	HD 96 946	O6.5	III(f)	.	8.7	0	0	5	HD96946_20120520_033905_F_V48000	56067.7	163	B.4
HD 97166	HD 97 166	O7.5	IV((f))	O9III:	8.0	0	0	13	HD97166_20070421_051914_F_V48000	54211.7	160	B.6
HD 97253	HD 97 253 AB	O5	III(f)	.	7.4	0	0	2	HD97253_20090504_021148_F_V48000	54955.5	178	B.5
HD 97434	HD 97 434	O7.5	III(n)((f))	.	8.2	0	0	3	HD97434_20150402_055328_F_V48000	57114.7	171	B.5
HD 97848	HD 97 848	O8	V	.	8.7	0	0	2	HD97848_20090502_041114_F_V48000	54953.7	210	B.4
HD 99546	HD 99 546	O7.5	V((f))_Nstr	.	8.2	0	0	1	HD99546_20041225_061416_F_V48000	53364.8	129	B.5
HD 99897	HD 99 897	O6.5	IV((f))	.	8.5	0	0	1	HD99897_20070527_035741_F_V48000	54247.6	152	B.5
HD 100213	TU Mus	O8	V(n)	.	8.4	0	0	1	HD100213_20090503_045502_F_V48000	54954.7	207	B.6
HD 101131	HD 101 131 AB	O5.5	V((f))	O8:V	7.4	0	0	2	HD101131_20110214_064950_F_V48000	55606.8	187	B.6
HD 101190 AaAb	HD 101 190	O6	IV((f))	.	7.8	0	0	3	HD101190_20110321_032654_F_V48000	55641.7	226	B.4
HD 101191	HD 101 191	O8	V	.	8.5	0	0	4	HD101191_20070421_044639_F_V48000	54211.7	207	B.5

Table B.1: continued.

Name	Alt. name	SpT	LC	secondary	B_{ap}	N	M	F	Best S/N spectrum in IACOB+OWN	HJD -2450000	S/N 4500 Å	Ref. Table
HD 101205	HD 101 205 AB	O7	II:(n)	.	6.6	0	0	3	HD101205_20080514_032347_F_V48000	54600.6	147	B.6
HD 101223	HD 101 223	O8	V	.	8.9	0	0	5	HD101223_20040508_231307_F_V48000	53134.5	126	B.4
HD 101298	HD 101 298	O6.5	IV((f))	.	8.1	0	0	6	HD101298_20120520_043018_F_V48000	56067.6	144	B.5
HD 101413	HD 101 413 AB	O8	V	.	8.6	0	0	5	HD101413_20150405_050130_F_V48000	57117.7	163	B.5
HD 101436	HD 101 436	O6.5	V((f))	.	7.7	0	0	8	HD101436_20080515_020341_F_V48000	54601.6	169	B.6
HD 101545 AaAb	HD 101 545 AaAb	O9.2	II	.	7.5	0	0	2	HD101545A_20090505_051248_F_V48000	54956.7	129	B.5
HD 102415	HD 102 415	ON9	IV:nn	.	9.4	0	0	3	HD102415_20080513_042228_F_V48000	54599.6	101	B.5
HD 104565	HD 104 565	OC9.7	Iab	.	9.6	0	0	1	HD104565_20080513_024739_F_V48000	54599.6	121	B.4
HD 105056	GS Mus	ON9.7	Iae	.	7.4	0	0	6	HD105056_20090502_044058_F_V48000	54953.7	188	B.4
HD 105627	HD 105 627	O9	III	.	8.2	0	0	5	HD105627_20110321_061139_F_V48000	55641.7	124	B.5
HD 110360	HD 110 360	ON7	V	.	9.5	0	0	2	HD110360_20110516_031504_F_V48000	55697.6	117	B.5
HD 112244	HD 112 244	O8.5	Iab(f)p	.	5.4	0	0	12	HD112244_20110516_035623_F_V48000	55697.6	204	B.5
HD 113904 B	theta Mus B	O9	III	.	7.5	0	0	2	HD113904B_20090505_060747_F_V48000	54956.7	120	B.5
HD 114737 AB	HD 114 737	O8.5	III	.	8.4	0	0	4	HD114737_20150405_051825_F_V48000	57117.7	173	B.4
HD 114886	HD 114 886 AaAb	O9	III	.	7.5	0	0	8	HD114886_20150405_053037_F_V48000	57117.7	123	B.6
HD 115071	HD 115 071	O9.5	III	.	8.2	0	0	1	HD115071_20090502_051155_F_V48000	54953.7	81	B.6
HD 115455	HD 115 455	O8	III(((f)))	.	8.2	0	0	14	HD115455_20060819_232241_F_V48000	53967.4	149	B.6
HD 116852	HD 116 852	O8.5	II-III(((f)))	.	8.4	0	0	2	HD116852_20080513_035626_F_V48000	54599.6	135	B.5
HD 117490	HD 117 490	ON9.5	IIInn	.	8.9	0	0	10	HD117490_20150403_063845_F_V48000	57115.7	108	B.5
HD 117797	HD 117 797	O7.5	fp	.	9.7	0	0	4	HD117797_20150405_055828_F_V48000	57117.7	124	B.5
HD 117856	HD 117 856	O9.7	II-III	.	7.6	0	0	9	HD117856_20110515_061235_F_V48000	55696.7	114	B.6
HD 118198	HD 118 198	O9.7	III	.	8.7	0	0	2	HD118198_20080513_054748_F_V48000	54599.7	94	B.5
HD 120521	HD 120 521	O7.5	Ib(f)	.	8.8	0	0	2	HD120521_20120520_062307_F_V48000	56067.7	126	B.5
HD 120678	HD 120 678	O9.5	Ve	.	8.1	0	0	11	HD120678_20110322_092507_F_V48000	55642.9	160	B.5
HD 123008	HD 123 008	ON9.2	Iab	.	9.2	0	0	2	HD123008_20080514_040321_F_V48000	54600.7	132	B.4
HD 123056	HD 123 056	O9.5	IV(n)	.	8.3	0	0	9	HD123056_20120521_063705_F_V48000	56068.7	112	B.5
HD 123590	HD 123 590 AB	O8	Vz	.	8.4	0	0	21	HD123590_20080513_050255_F_V48000	54599.7	143	B.6
HD 124314	HD 124 314 AaAb	O6+O9.2	IV(((f))+IV(n)	.	7.5	0	0	15	HD124314_20070420_072345_F_V48000	54210.8	173	B.6
HD 124979	HD 124 979	O7.5	IV(n)(((f)))	.	8.6	0	0	6	HD124979_20150404_035200_F_V48000	57116.6	145	B.5
HD 125206	HD 125 206 AB	O9.7	IVn	.	8.5	0	0	6	HD125206_20090502_053255_F_V48000	54953.7	87	B.6
HD 125241	HD 125 241	O8.5	Ib(f)	.	8.8	0	0	4	HD125241_20150402_074924_F_V48000	57114.8	143	B.4
HD 130298	HD 130 298	O6.5	III(n)(f)	.	9.7	0	0	10	HD130298_20080514_042531_F_V48000	54600.6	148	B.5
HD 135240	delta Cir AaAbAc	O7	IV(((f)))	B	5.2	0	0	3	HD135240_20090502_063326_F_V48000	54953.7	112	B.6
HD 135591	HD 135 591	O8	IV(((f)))	.	5.4	0	0	3	HD135591_20070420_073310_F_V48000	54210.8	222	B.4
HD 148546	HD 148 546	O9	Iab	.	8.0	0	0	4	HD148546_20080513_060555_F_V48000	54599.7	120	B.5
HD 148937	HD 148 937 AaAb	O6	f?p	.	7.8	0	0	22	HD148937_20070420_074115_F_V48000	54210.8	167	B.5
HD 149038	mu Nor	O9.7	Iab	.	5.0	0	0	28	HD149038_20090525_045827_F_V48000	54976.7	251	B.4
HD 149404	HD 149 404	O8.5	Iab(f)p	.	5.9	0	0	1	HD149404_20090504_052931_F_V48000	54955.7	227	B.6
HD 149452	HD 149 452	O9	IVn	.	9.6	0	0	2	HD149452_20120520_070844_F_V48000	56067.8	88	B.5

Table B.1: continued.

Name	Alt. name	SpT LC	secondary	B_{ap}	N	M	F	Best S/N spectrum in IACOB+OWN	HJD -2450000	S/N 4500 Å	Ref. Table
HD 149757	zeta Oph	O9.2 IVnn	.	2.6	10	0	3	HD149757_20090504_050358_F_V48000	54955.7	219	B.5
HD 150135	HD 150 135 AaAb	O6.5 V((f))z	.	7.5	0	0	19	HD150135_20060822_001512_F_V48000	53969.5	232	B.6
HD 150136	HD 150 136 AaAb	O3.5-4 III(f*)	O6IV	6.1	0	0	11	HD150136_20120620_043915_F_V48000	56098.7	261	B.6
HD 150574	HD 150 574	ON9 III(n)	.	8.7	0	0	1	HD150574_20080513_061845_F_V48000	54599.7	87	B.5
HD 150958	HD 150 958 AB	O6.5 Ia(n)f	.	7.9	0	0	11	HD150958_20150402_092649_F_V48000	57114.8	190	B.6
HD 151003	HD 151 003 AB	O8.5 III	.	7.6	0	0	4	HD151003_20110515_075138_F_V48000	55696.8	122	B.6
HD 151018	HD 151 018	O9 Ib	.	9.3	0	0	1	HD151018_20080515_033828_F_V48000	54601.6	84	B.5
HD 151515	HD 151 515	O7 II(f)	.	7.3	0	0	2	HD151515_20070419_072807_F_V48000	54976.9	65	B.4
HD 151804	HD 151 804	O8 Iaf	.	5.3	0	0	2	HD151804_20150404_050304_F_V48000	57116.7	220	B.4
HD 152003	HD 152 003	O9.7 IabNwk	.	7.4	0	0	2	HD152003_20120521_074209_F_V48000	56068.8	90	B.5
HD 152147	HD 152 147	O9.7 IbNwk	.	7.8	0	0	4	HD152147_20080515_040719_F_V48000	54601.7	196	B.4
HD 152200	HD 152 200	O9.7 IV(n)	.	8.4	0	0	4	HD152200_20040506_062054_F_V48000	53131.8	112	B.5
HD 152218	HD 152 218	O9 IV	.	7.8	0	0	5	HD152218_20110518_062956_F_V48000	55699.7	85	B.6
HD 152219	HD 152 219	O9.5 III(n)	.	7.8	0	0	7	HD152219_20040506_093100_F_V48000	53131.9	155	B.6
HD 152233	HD 152 233 AaAb	O6 II(f)	.	6.8	0	0	9	HD152233_20120521_043009_F_V48000	56068.6	210	B.5
HD 152246	HD 152 246 AaAb	O9 IV	.	8.1	0	0	10	HD152246_20150403_084035_F_V48000	57115.8	124	B.6
HD 152247	HD 152 247 AaAb	O9.2 III	.	7.6	0	0	7	HD152247_20090504_094829_F_V48000	54955.9	103	B.5
HD 152248	HD 152 248 AaAb	O7 Iabf	O7Ib(f)	6.3	0	0	3	HD152248_20090504_093900_F_V48000	54955.9	178	B.6
HD 152249	HD 152 249	OC9 Iab	.	6.6	0	0	19	HD152249_20090504_092636_F_V48000	54955.9	189	B.4
HD 152314	HD 152 314 AaAb	O9 IV	.	8.2	0	0	4	HD152314_20090525_064042_F_V48000	54976.7	86	B.6
HD 152386	HD 152 386	O6: Iafpe	.	8.6	0	0	4	HD152386_20120520_074320_F_V48000	56067.8	119	B.7
HD 152405	HD 152 405	O9.7 II	.	7.3	0	0	8	HD152405_20120521_055904_F_V48000	56068.8	168	B.4
HD 152408	HD 152 408	O8: Iafpe	.	5.9	0	0	15	HD152408_20040502_075650_F_V48000	53127.8	105	B.7
HD 152424	HD 152 424	OC9.2 Ia	.	6.7	0	0	5	HD152424_20150405_074548_F_V48000	57117.8	190	B.4
HD 152590	HD 152 590	O7.5 Vz	.	8.6	0	0	10	HD152590_20090525_052211_F_V48000	54976.7	196	B.4
HD 152623	HD 152 623 AaAbB	O7 V(n)((f))	.	7.5	0	0	2	HD152623_20080513_080116_F_V48000	54599.8	143	B.5
HD 152723	AaAb	O6.5 III(f)	.	7.6	0	0	13	HD152723_20080515_043624_F_V48000	54601.7	225	B.4
HD 153426	HD 153 426	O8.5 III	.	7.6	0	0	6	HD153426_20120521_060858_F_V48000	56068.7	94	B.6
HD 153919	HD 153 919	O6 Iafcp	.	6.8	0	0	2	HD153919_20090503_063316_F_V48000	54954.8	300	B.6
HD 154368	HD 154 368	O9.2 Iab	.	6.6	0	0	5	HD154368_20090504_065633_F_V48000	54955.8	211	B.4
HD 154643	HD 154 643	O9.7 III	.	7.4	0	0	5	HD154643_20080514_081212_F_V48000	54600.8	163	B.4
HD 154811	HD 154 811	OC9.7 Ib	.	7.3	0	0	2	HD154811_20080514_082138_F_V48000	54600.9	189	B.4
HD 155756	HD 155 756	O9 Ibp	.	9.8	0	0	2	HD155756_20080514_082917_F_V48000	54600.8	84	B.5
HD 155775	HD 155 775	O9.7 III(n)	.	6.7	0	0	2	HD155775_20060510_102012_F_V48000	53865.9	108	B.6
HD 155806	HD 155 806 AB	O7.5 V((f))(e)	.	6.1	0	1	2	HD155806_20110617_003322_M_V85000	55729.5	155	B.5
HD 155889	AB	O9.5 IV	.	7.0	0	0	5	HD155889_20120620_051117_F_V48000	56098.7	169	B.4
HD 155913	HD 155 913	O4.5 Vn((f))	.	8.7	0	0	9	HD155913_20060818_000814_F_V48000	53965.5	182	B.5
HD 156154	HD 156 154	O7.5 Ib(f)	.	8.7	0	0	4	HD156154_20070420_082005_F_V48000	54210.9	195	B.4
HD 156292	HD 156 292	O9.7 III	.	7.8	0	0	8	HD156292_20090503_061911_F_V48000	54954.7	120	B.6

Table B.1: continued.

Name	Alt. name	SpT LC	secondary	B_{op}	N	M	F	Best S/N spectrum in IACOB+OWN	HJD -2450000	S/N 4500 Å	Ref. Table
HD 156738 AB	HD 156 738	O6.5 III(f)	.	10.6	0	0	2	HD156738_20110517_070459_F_V48000	55698.8	77	B.4
HD 157857	HD 157 857	O6.5 II(f)	.	8.0	2	0	3	HD157857_20110911_201644_N_V46000	55816.3	121	B.4
HD 158186	HD 158 186	O9.2 V	.	7.1	0	0	8	HD158186_20080514_091754_F_V48000	54600.8	130	B.6
HD 159176	HD 159 176	O7 V((f))	O7V((f))	5.8	0	0	2	HD159176_20110517_104345_F_V48000	55698.9	124	B.5
HD 161853	HD 161 853	O8 V(n)z	B	8.1	0	0	4	HD161853_20090505_063717_F_V48000	54956.7	226	B.6
HD 162978	63 Oph	O8 II((f))	.	6.2	2	1	4	HD162978_20110828_205502_N_V46000	55802.4	161	B.4
HD 163758	HD 163 758	O6.5 Iafp	.	7.3	0	0	3	HD163758_20120520_102704_F_V48000	56067.9	214	B.4
HD 163800	HD 163 800	O7.5 III((f))	.	7.3	2	1	1	HD163800_20110829_203034_N_V46000	55803.4	125	B.4
HD 163892	HD 163 892	O9.5 IV(n)	.	7.6	2	0	10	HD163892_20110907_202704_N_V46000	55812.3	113	B.5
HD 164019	HD 164 019	O9.5 IVp	.	9.5	0	0	1	HD164019_20080608_075144_F_V48000	54625.8	79	B.5
HD 164438	HD 164 438	O9.2 IV	.	7.8	2	0	5	HD164438_20080514_092403_F_V48000	54600.8	131	B.5
HD 164492	HD 164 492 A	O7.5 Vz	.	7.6	2	0	0	HD164492_20110829_212004_N_V46000	55803.3	133	B.5
HD 164794	9 Sgr AB	O4 V((f))	.	6.5	2	1	6	HD164794_20090505_103135_F_V48000	54956.9	250	B.5
HD 164816	HD 164 816	O9.5 V	.	7.1	2	0	2	HD164816_20110829_204542_N_V46000	55803.3	115	B.6
HD 165052	HD 165 052	O6 Vz	O8Vz	7.0	4	0	2	HD165052_20110829_201802_N_V46000	55803.4	159	B.6
HD 165174	HD 165 174	O9.7 IIn	.	6.1	4	0	0	HD165174_20110907_222610_N_V46000	55812.4	99	B.5
HD 165246	HD 165 246	O8 V(n)	.	7.9	2	0	12	HD165246_20110829_213907_N_V46000	55803.4	133	B.5
HD 165921	HD 165 921	O7 V(n)z	B0:V:	7.5	3	0	1	HD165921_20110829_210228_N_V46000	55803.3	134	B.6
HD 166546	HD 166 546	O9.5 IV	.	7.3	1	0	3	HD166546_20100909_204628_N_V46000	55449.3	115	B.5
HD 166734	HD 166 734	O7.5 Iabf	.	9.5	2	0	0	HD166734_20110912_210924_N_V25000	55817.4	83	B.5
HD 167263	16 Sgr AaAb	O9.5 III	.	6.1	4	0	2	HD167263_20100907_204037_N_V46000	55447.3	166	B.6
HD 167264	15 Sgr	O9.7 Iab	.	5.4	2	1	7	HD167264_20090525_083224_F_V48000	54976.8	152	B.5
HD 167633	HD 167 633	O6.5 V((f))	.	8.4	2	0	1	HD167633_20110910_222422_N_V25000	55815.4	153	B.4
HD 167659	HD 167 659	O7 II-III(f)	.	7.6	2	0	2	HD167659_20070526_100517_F_V48000	54246.9	197	B.5
HD 167771	HD 167 771	O7 III((f))	O8III	6.6	4	0	1	HD167771_20100907_205624_N_V46000	55447.4	186	B.6
HD 167971	MY Ser AaAb	O8 Iaf(n)	O4/5	8.9	0	0	6	HD167971_20150404_100108_F_V48000	57116.9	156	B.6
HD 168075	HD 168 075	O6.5 V((f))	.	9.2	2	0	11	HD168075_20080514_071331_F_V48000	54600.8	134	B.6
HD 168076 AB	HD 168 076	O4 IV(f)	.	9.2	2	0	2	HD168076_20120521_081558_F_V48000	56068.9	151	B.4
HD 168112 AB	HD 168 112	O5 IV(f)	.	9.9	1	0	10	HD168112_20060820_011745_F_V48000	53967.6	173	B.4
HD 168137 AaAb	HD 168 137	O8 Vz	.	10.0	0	0	9	HD168137_20060509_075740_F_V48000	53864.8	106	B.6
HD 168461	HD 168 461	O7.5 V((f))_Nstr	.	10.2	1	0	0	HD168461_20170601_001025_N_V25000	57905.5	44	B.5
HD 168504	HD 168 504	O7.5 V(n)z	.	9.7	0	0	1	HD168504_20040705_055920_F_V48000	53191.8	116	B.5
HD 168941	HD 168 941	O9.5 IVp	.	9.4	0	0	2	HD168941_20090504_080947_F_V48000	54955.8	104	B.5
HD 169582	HD 169 582	O6 Iaf	.	9.3	1	0	1	HD169582_20090525_100844_F_V48000	54976.9	71	B.4
HD 171589	HD 171 589	O7.5 II(f)	.	8.5	2	0	1	HD171589_20110912_204533_N_V25000	55817.4	138	B.4
HD 172175	HD 172 175	O6.5 I(n)fp	.	10.0	0	0	1	HD172175_20070527_083116_F_V48000	54247.8	116	B.5
HD 173010	HD 173 010	O9.7 Ia+var	.	10.0	0	0	2	HD173010_20120619_090148_F_V48000	56097.8	88	B.5
HD 173783	HD 173 783	O9 Iab	.	9.8	0	0	1	HD173783_20090503_094026_F_V48000	54954.9	90	B.5
HD 175514	HD 175 514	O7 V(n)((f))z	B	9.2	0	0	2	HD175514_20150512_073023_F_V48000	57154.8	102	B.6

Table B.1: continued.

Name	Alt. name	SpT LC	secondary	B_{sp}	N	M	F	Best S/N spectrum in IACOB+OWN	HJD -2450000	S/N 4500 Å	Ref. Table
HD 175754	HD 175 754	O8 II(n)(((f))p	.	6.9	2	1	4	HD175754_20110517_102018_F_V48000	55698.9	172	B.5
HD 175876	HD 175 876	O6.5 III(n)(f)	.	6.8	4	0	6	HD175876_20100908_202812_N_V46000	55448.3	188	B.5
HD 186980	HD 186 980	O7.5 III(((f))	.	7.5	3	1	0	HD186980_20100808_045738_N_V46000	55416.7	161	B.5
HD 188001	9 Sge	O7.5 Iabf	.	6.2	21	71	0	HD188001_20110620_013133_M_V85000	55732.6	212	B.4
HD 188209	HD 188 209	O9.5 Iab	.	5.6	23	89	0	HD188209_20130603_054038_M_V85000	56446.7	207	B.4
HD 189957	HD 189 957	O9.7 III	.	7.8	2	0	0	HD189957_20100909_213830_N_V46000	55449.4	122	B.4
HD 190429 A	HD 190 429	O4 If	.	7.3	2	1	0	HD190429_20110615_020805_M_V85000	55727.6	139	B.4
HD 190864	HD 190 864	O6.5 III(f)	.	8.0	2	0	0	HD190864_20100908_234450_N_V46000	55448.5	137	B.4
HD 191201	HD 191 201 A	O9.5+O9.7 III+III	.	7.8	3	0	0	HD191201_20100623_005948_N_V46000	55370.5	117	B.6
HD 191423	HD 191 423	ON9 II-IIInn	.	8.2	3	0	0	HD191423_20110829_012427_N_V25000	55802.5	110	B.5
HD 191612	HD 191 612	O8 f?p-var	.	8.0	2	0	0	HD191612_20100909_212050_N_V46000	55449.3	140	B.5
HD 191781	HD 191 781	ON9.7 Iab	.	10.3	0	1	0	HD191781_20110619_224718_M_V85000	55732.5	28	B.4
HD 191978	HD 191 978	O8 V	.	8.2	2	1	0	HD191978_20110829_022107_N_V25000	55802.6	128	B.4
HD 192001	HD 192 001	O9.5 IV	.	8.6	2	0	0	HD192001_20110911_232147_N_V25000	55816.5	134	B.4
HD 192281	HD 192 281	O4.5 IV(n)(f)	.	7.9	3	0	0	HD192281_20100808_051701_N_V46000	55416.7	152	B.5
HD 192639	HD 192 639	O7.5 Iabf	.	7.5	7	2	0	HD192639_20110615_041736_M_V85000	55727.7	134	B.4
HD 193322	HD 193 322 AaAb	O9 IV(n)	.	6.8	3	0	0	HD193322_20091110_213548_N_V46000	55146.4	163	B.6
HD 193443 AB	HD 193 443	O9 III	.	8.3	1	1	0	HD193443_20100623_011844_N_V46000	55370.6	123	B.4
HD 193514	HD 193 514	O7 Ib(f)	.	7.8	2	0	0	HD193514_20110910_000224_N_V46000	55814.5	112	B.4
HD 193595	HD 193 595	O7 V((f))	.	9.1	1	0	0	HD193595_20170601_044741_N_V25000	57905.7	74	B.5
HD 193682	HD 193 682	O4.5 IV((f))	.	8.9	1	0	0	HD193682_20170601_052757_N_V25000	57905.7	88	B.5
HD 194649 AB	HD 194 649 AB	O6.5 V((f))	.	10.6	1	0	0	HD194649AB_20170602_003246_N_V25000	57906.5	76	B.6
HD 195592	HD 195 592	O9.7 Ia	.	8.0	1	1	0	HD195592_20110618_003043_M_V85000	55730.5	105	B.4
HD 198846	Y Cyg	O9.5 IV	.	7.2	5	0	0	HD198846_20101024_212345_N_V46000	55494.4	127	B.6
HD 199579	HD 199 579	O6.5 V((f))z	.	6.0	26	0	0	HD199579_20130829_004031_M_V85000	56533.5	235	B.5
HD 201345	HD 201 345	ON9.2 IV	.	7.6	3	0	0	HD201345_20100909_210331_N_V46000	55449.3	148	B.5
HD 202124	HD 202 124	O9 Iab	.	8.0	3	0	0	HD202124_20101024_221756_N_V46000	55494.4	129	B.4
HD 202214	HD 202 214 AaAb	O9.5 IV	.	6.6	1	7	0	HD202214_20110617_052848_M_V85000	55729.7	188	B.5
HD 203064	68 Cyg	O7.5 IIIn((f))	.	5.0	3	17	0	HD203064_20110616_044516_M_V85000	55728.7	206	B.5
HD 204827	HD 204 827 AaAb	O9.5 IV	.	9.3	3	0	0	HD204827_20110829_010631_N_V25000	55802.6	102	B.6
HD 206183	HD 206 183	O9.5 IV-V	.	7.5	2	0	0	HD206183_20100808_041510_N_V46000	55416.6	154	B.5
HD 206267	HD 206 267 AaAb	O6.5 V((f))	O9/B0V	6.2	5	0	0	HD206267_20101024_191624_N_V46000	55494.3	169	B.6
HD 207198	HD 207 198	O8.5 II((f))	.	6.3	15	38	0	HD207198_20091111_193521_N_V46000	55147.3	189	B.4
HD 207538	HD 207 538	O9.7 IV	.	7.6	1	1	0	HD207538_20100716_035701_N_V46000	55393.7	119	B.4
HD 209339	HD 209 339	O9.7 IV	B1:V:	6.8	3	1	0	HD209339_20121026_201224_M_V85000	56227.3	130	B.5
HD 209481	14 Cep	O9 IV(n)-var	.	5.6	6	3	0	HD209481_20091111_235954_N_V46000	55147.5	176	B.6
HD 209975	19 Cep	O9 Ib	.	5.2	42	38	0	HD209975_20091111_190418_N_V46000	55147.3	200	B.4
HD 210809	HD 210 809	O9 Iab	.	7.6	3	1	0	HD210809_20100908_232632_N_V46000	55448.5	150	B.4
HD 210839	lambda Cep	O6.5 I(n)fp	.	5.3	25	17	0	HD210839_20111108_215240_M_V85000	55874.4	228	B.5

Table B.1: continued.

Name	Alt. name	SpT LC	secondary	B_{sp}	N	M	F	Best S/N spectrum in IACOB+OWN	HJD -2450000	S/N 4500 Å	Ref. Table
HD 213023 A	HD 213 023 A	O7.5 Vz	.	9.9	5	0	0	HD213023A_20171119_193455_N_V25000	58077.3	66	B.6
HD 214680	10 Lac	O9 V	.	4.7	33	1	0	HD214680_20081107_210248_N_V46000	54778.4	230	B.4
HD 215835	DH Cep	O5.5 V((f))	O6V(((f))	8.9	3	0	0	HD215835_20110912_013004_N_V25000	55816.6	144	B.6
HD 216532	HD 216 532	O8.5 V(n)	.	8.5	3	0	0	HD216532_20110911_015716_N_V25000	55815.5	128	B.5
HD 216898	HD 216 898	O9 V	.	8.5	3	0	0	HD216898_20110911_023348_N_V25000	55815.6	132	B.4
HD 217086	HD 217 086	O7 Vnn((f))z	.	8.3	4	0	0	HD217086_20121225_202151_N_V46000	56287.3	149	B.5
HD 218195 A	HD 218 195	O8.5 IIINstr	.	8.7	3	0	0	HD218195_20110911_031217_N_V25000	55815.6	130	B.4
HD 218915	HD 218 915	O9.2 Iab	.	7.2	4	0	0	HD218915_20100716_043411_N_V46000	55393.7	155	B.4
HD 225146	HD 225 146	O9.7 Iab	.	9.0	3	0	0	HD225146_20121225_213415_N_V25000	56287.4	106	B.4
HD 225160	HD 225 160	O8 Iabf	.	8.5	3	0	0	HD225160_20110114_201920_N_V25000	55576.4	138	B.4
HD 226868	Cyg X-1	O9.7 Iabp_var	.	9.7	5	0	0	HD226868_20110913_000626_N_V25000	55817.5	92	B.5
HD 227018	HDE 227 018	O6.5 V((f))z	.	9.4	1	0	0	HDE227018_20170601_030325_N_V25000	57905.6	62	B.5
HD 227245	HDE 227 245	O7 V((f))z	.	10.3	1	0	0	HDE227245_20170601_034327_N_V25000	57905.6	52	B.5
HD 227465	HDE 227 465	O7 V((f))	.	10.7	1	0	0	HDE227465_20170602_042407_N_V25000	57906.6	61	B.5
HD 228759	HDE 228 759	O6.5 V(n)((f))z	O8:II:	10.1	1	0	0	HDE228759_20170602_013835_N_V25000	57906.7	75	B.6
HD 228766	HDE 228 766	O4 If*	O8:II:	9.8	0	6	0	HDE228766_20171030_202755_M_V85000	58057.3	66	B.6
HD 228841	HDE 228 841	O6.5 Vn((f))	.	9.5	2	0	0	HD228841_20110909_225750_N_V25000	55814.4	112	B.5
HD 228854	HDE 228 854	O6 IVn_var	O5Vnvar	9.5	1	0	0	HDE228854_20170602_000933_N_V25000	57906.5	73	B.6
HD 229196	HDE 229 196	O6 II(f)	.	9.4	2	0	0	HD229196_20110912_003950_N_V25000	55816.5	113	B.4
HD 229202	HDE 229 202	O7.5 V(n)(((f))	.	10.4	1	0	0	HDE229202_20170602_011626_N_V25000	57906.6	63	B.6
HD 229232	HDE 229 232	O4 Vn(((f))	.	10.4	1	0	0	HD229232_20161028_211623_N_V25000	57690.3	72	B.5
HD 237211	HDE 237 211	O9 Ib	.	9.5	3	0	0	HD237211_20110116_002922_N_V25000	55577.5	107	B.5
HD 242908	HDE 242 908	O4.5 V(n)((fc))z	.	9.3	0	8	0	HD242908_20121027_035934_M_V85000	56227.7	84	B.6
HD 242926	HDE 242 926	O7 Vz	.	9.7	2	0	0	HD242926_20161029_034457_N_V25000	57690.7	96	B.4
HD 242935 A	HDE 242 935 A	O6.5 V((f))z	.	9.8	1	0	0	HD242935_20161029_015032_N_V25000	57690.5	62	B.5
HD 256725 A	HDE 256 725 A	O5 V((fc))	.	10.1	3	0	0	HD256725_20110115_040003_N_V25000	55576.6	75	B.5
HD 298429	HDE 298 429	O8.5 V	.	10.3	0	0	1	HD298429_20110213_061413_F_V48000	55605.8	71	B.4
HD 303308 AB	HDE 303 308	O4.5 V((fc))	.	8.6	0	0	3	HD303308_20090502_023316_F_V48000	54953.6	209	B.4
HD 303311	HDE 303 311	O6 V((f))z	.	9.1	0	0	1	HD303311_20070419_034639_F_V48000	54209.7	148	B.4
HD 303492	HDE 303 492	O8.5 Iaf	.	9.4	0	0	4	HD303492_20080513_005333_F_V48000	54599.5	179	B.4
HD 305523	HDE 305 523	O9 II-III	.	8.6	0	0	1	HD305523_20090503_033852_F_V48000	54954.6	104	B.5
HD 305525	HDE 305 525	O5.5 V((f))z	O7.5V+B	10.7	0	0	1	HD305525_20120520_030436_F_V48000	56067.6	67	B.5
HD 305532	HDE 305 532	O6.5 V((f))z	.	10.5	0	0	1	HD305532_20110515_003522_F_V48000	55696.5	127	B.5
HD 305619	HDE 305 619	O9.7 II	.	9.9	0	0	1	HD305619_20080513_002944_F_V48000	54599.5	95	B.5
HD 308813	HDE 308 813	O9.7 IV(n)	.	9.3	0	0	5	HD308813_20050521_013624_F_V48000	53511.6	88	B.5
HD 313846	HDE 313 846	O7: Iafpe	.	10.7	0	0	7	HD313846_20120501_081326_F_V48000	56048.8	70	B.7
HD 319699	HDE 319 699	O5 V((fc))	.	10.3	0	0	4	HD319699_20070419_093144_F_V48000	54209.9	132	B.4
HD 319702	HDE 319 702	O8 III	.	11.0	0	0	5	HD319702_20150402_085257_F_V48000	57114.9	102	B.4
HD 319703 A	HDE 319 703 A	O7 V((f))	O9.5V	11.9	0	0	6	HD319703A_20090502_081857_F_V48000	54953.9	78	B.6

Table B.1: continued.

Name	Alt. name	SpT	LC	secondary	B_{ap}	N	M	F	Best S/N spectrum in IACOB+OWN	HJD -2450000	S/N 4500 Å	Ref. Table
HD 319718 A	Pismis 24-1 AB	O3.5	III(f*)	.	12.8	0	0	3	HD319718A_20080515_051204_F_V48000	54601.7	95	B.6
HD 322417	HDE 322 417	O6.5	IV((f))	.	10.9	0	0	5	HD322417_20080515_031709_F_V48000	54601.6	114	B.4
HD 323110	HDE 323 110	ON9	Ia	.	10.9	0	0	1	HD323110_20150404_083053_F_V48000	57116.8	60	B.6
HD 326329	HDE 326 329	O9.7	V	.	8.8	0	0	3	HD326329_20090717_030916_F_V48000	55029.6	94	B.5
HD 326331	HDE 326 331	O8	IVn((f))	.	7.6	0	0	6	HD326331_20080513_080849_F_V48000	54599.8	231	B.5
HD 326775	HDE 326 775	O6.5	V(n)((f))z	.	11.6	0	0	3	HD326775_20150404_073109_F_V48000	57116.8	57	B.5
HD 338916	HDE 338 916	O7.5	Vz	.	10.8	1	0	0	HDE338916_20170602_035916_N_V25000	57906.6	59	B.5
HD 338931	HDE 338 931	O6	III(f)	.	9.8	0	1	0	HDE338931_20171112_192321_N_V25000	58070.3	66	B.5
HD 344777	HDE 344 777	O7.5	Vz	.	10.2	1	0	0	HDE344777_20170601_021111_N_V25000	57905.5	55	B.5
HD 344784	HDE 344 784 A	O6.5	V((f))z	.	9.9	1	0	0	HD344784_20161028_214433_N_V25000	57690.4	58	B.5
ALS 2063	ALS 2063	O5	If$_p$	.	11.5	0	0	9	ALS2063_20040505_011931_F_V48000	53130.6	102	B.7
ALS 4880	ALS 4880	O6	V((f))	.	11.3	1	0	0	ALS4880_20170601_012645_N_V25000	57905.5	37	B.5
ALS 7833	ALS 7833	O8	Vz	.	10.4	1	0	0	ALS7833_20161029_051933_N_V25000	57690.7	64	B.5
ALS 8272	ALS 8272	O7	V((f))	B0III-V	11.8	4	0	0	ALS8272_20171003_055943_N_V25000	58029.7	50	B.6
ALS 8294	ALS 8294	O7	V(n)z	.	10.7	1	0	0	ALS8294_20161230_052039_N_V25000	57752.7	34	B.5
ALS 12 320	ALS 12 320	O7	IV((f))	.	11.2	1	0	0	ALS12320_20171118_220228_N_V25000	58076.4	53	B.6
ALS 12 370	ALS 12 370	O6.5	Vnn((f))	.	10.5	4	0	0	ALS12370_20171002_233240_N_V25000	58029.4	88	B.5
ALS 12 619	ALS 12 619	O7	V((f))z	.	11.3	1	0	0	ALS12619_20171119_000737_N_V25000	58076.5	52	B.5
ALS 12 688	ALS 12 688	O5.5	V(n)((fc))	B	11.3	1	0	0	ALS12688_20171004_040942_N_V25000	58030.6	60	B.6
ALS 15 210	ALS 15 210	O3.5	If*_Nwk	.	11.5	0	0	1	ALS15210_20110515_014935_F_V48000	55696.5	71	B.5
ALS 18 747	ALS 18 747	O5.5	Ifc	.	13.2	0	0	0	...	...	0	No table
BD -10 4682	BD -10 4682	O7	Vn((f))	.	10.2	1	0	0	BD-104682_20170601_003238_N_V25000	57905.5	53	B.5
BD -11 4586	BD -11 4586	O8	Ib(f)	.	10.4	0	0	2	BD-114586_20070527_073741_F_V48000	54247.8	128	B.4
BD -13 4927	BD -13 4927	O7	II(f)	.	10.4	0	0	6	BD-134927_20070526_092756_F_V48000	54246.9	120	B.5
BD -14 5014	BD -14 5014	O7.5	V(n)((f))	.	11.1	1	0	0	BD-145014_20170602_024845_N_V25000	57906.6	39	B.6
BD -14 5040	BD -14 5040	O5.5	V(n)((f))	.	11.5	1	0	0	BD-145040_20170602_031044_N_V25000	57906.5	46	B.5
BD -16 4826	BD -16 4826	O5.5	V((f))z	.	10.6	0	0	1	BD-164826_20150405_093726_F_V48000	57117.9	83	B.6
BD +33 1025 A	BD +33 1025 A	O7.5	V(n)z	.	10.7	1	0	0	BD+331025_20161029_022841_N_V25000	57690.6	63	B.5
BD +36 4145	BD +36 4145	O8.5	V(n)	.	9.6	2	0	0	BD+364145_20171118_192318_N_V25000	58076.3	55	B.5
BD +39 1328	BD +39 1328	O8.5	Iab(n)(f)	.	10.4	1	0	0	BD+391328_20161029_055939_N_V25000	57690.7	65	B.5
BD +45 3216 A	BD +45 3216 A	O5	V((f))z	.	10.0	1	0	0	BD+453216A_20170602_020157_N_V25000	57906.5	92	B.6
BD +55 2840	BD +55 2840	O7.5	V(n)	.	10.6	3	0	0	BD+552840_20171003_013302_N_V25000	58029.5	90	B.6
BD +60 134	BD +60 134	O5.5	V(n)((f))	.	11.3	3	0	0	BD+60134_20171002_025128_N_V25000	58028.6	59	B.5
BD +60 261	BD +60 261	O7.5	III(n)((f))	.	9.0	3	0	0	BD+60261_20110912_025532_N_V25000	55816.6	118	B.5
BD +60 497	BD +60 497	O6.5	V((f))	O8/B0V	9.4	3	0	0	BD+60497_20110912_040819_N_V25000	55816.7	125	B.6
BD +60 498	BD +60 498	O9.7	II-III	.	10.5	1	0	0	BD+60498_20171120_015502_N_V25000	58077.5	56	B.5
BD +60 499	BD +60 499	O9.5	V	.	10.8	1	0	0	BD+60499_20161029_001830_N_V25000	57690.5	55	B.5
BD +60 501	BD +60 501	O7	V(n)((f))z	.	10.1	1	0	0	BD+60501_20161028_233526_N_V25000	57690.4	67	B.5
BD +60 513	BD +60 513	O7	Vn	.	9.9	1	0	0	BD+60513_20161028_230520_N_V25000	57690.4	60	B.5

Table B.1: continued.

Name	Alt. name	SpT	LC	secondary	B_{sp}	N	M	F	Best S/N spectrum in IACOB+OWN	HJD -2450000	S/N 4500 Å	Ref. Table
BD+60 586	BD +60 586 A	O7	Vz	.	8.8	3	0	0	BD+60586_20110913_024725_N_V25000	55817.6	143	B.5
BD+60 2522	BD +60 2522	O6.5	(n)fp	.	9.1	3	0	0	BD+602522_20110912_032100_N_V25000	55816.6	104	B.5
BD+60 2635	BD +60 2635	O6	V((f))	.	10.6	5	0	0	BD+602635_20171002_034308_N_V25000	58028.6	76	B.5
BD+61 411	BD +61 411 A	O6.5	V((f))z	.	11.2	1	0	0	BD+61411_20161229_233500_N_V25000	57752.4	57	B.5
BD+62 424	BD +62 424	O6.5	V(n)((f))	.	9.3	3	0	0	BD+62424_20110912_043319_N_V25000	55816.6	115	B.5
BD+62 2078	BD +62 2078	O7	V((f))z	.	10.8	2	0	0	BD+622078_20171003_004742_N_V25000	58029.5	59	B.5
BD+66 1675	BD +66 1675	O7.5	Vz	.	10.1	3	0	0	BD+661675_20171002_012436_N_V25000	58028.5	59	B.6
CPD-26 2716	CPD-26 2716	O6.5	Iabf	.	10.1	0	0	5	CPD-262716_20070526_235156_F_V48000	54247.5	138	B.5
CPD-28 2561	CPD-28 2561	O6.5	f?p	.	10.1	0	0	12	CPD-282561_20080609_231237_F_V48000	54627.5	150	B.5
CPD-35 2105 AaAb	CPD-35 2105	O9.2	III	.	10.2	0	0	0	...	...	0	No table
CPD-41 7721 A	CPD-41 7721 A	O9.7	V:(n)	.	8.8	0	0	1	CPD-417721A_20040509_060240_F_V48000	53134.8	83	B.5
CPD-41 7733	CPD-41 7733	O9	IV	.	7.9	0	0	5	CPD-417733_20040505_042329_F_V48000	53130.7	174	B.4
CPD-47 2963 AB	CPD-47 2963	O5	Ifc	.	9.7	0	0	5	CPD-472963_20070419_002543_F_V48000	54209.5	207	B.4
CPD-54 6791 AB	CPD-54 6791 AB	O9.5	V	.	11.5	0	0	1	CPD-546791_20090504_024958_F_V48000	54955.6	58	B.5
CPD-58 2611	CPD-58 2611	O6	V((f))z	.	9.9	0	0	1	CPD-582611_20070527_014252_F_V48000	54247.5	142	B.5
CPD-59 2551	CPD-59 2551	O9	V	.	9.2	0	0	2	CPD-592551_20100507_002325_F_V48000	55323.5	113	B.4
CPD-59 2600	CPD-59 2600	O6	V((f))	.	8.8	0	0	7	CPD-592600_20150405_030555_F_V48000	57117.6	203	B.4
CPD-59 2635	CPD-59 2635	O8	V(n)	O9.5V	9.5	0	0	2	CPD-592635_20080608_234308_F_V48000	54626.4	132	B.6
CPD-59 2636	CPD-59 2636 AB	O8	V	.	10.1	0	0	1	CPD-592636_20080609_001123_F_V48000	54626.5	103	B.6
CPD-59 2641	CPD-59 2641	O6	V((fc))	.	9.5	0	0	3	CPD-592641_20080610_013438_F_V48000	54627.5	154	B.6
CPD-59 5634	CPD-59 5634	O9.2	Ib	.	10.3	0	0	2	CPD-595634_20080515_024853_F_V48000	54601.6	89	B.5
CYG OB2-4 A	Cyg OB2-4 A	O7	III((f))	.	11.6	1	0	0	CYGOB2-4_20160429_004947_N_V25000_G	57507.5	32	B.4
CYG OB2-7	Cyg OB2-7	O3	If*	O8Vz	12.2	1	0	0	CYGOB2-7_20160429_014211_N_V25000_G	57507.6	31	B.4
CYG OB2-9	Cyg OB2-9	O4.5	If	.	12.9	1	0	0	CYGOB2-9_20160429_023433_N_V25000_G	57507.6	21	B.4
CYG OB2-11	Cyg OB2-11	O5.5	Ifc	.	11.7	1	0	0	CYGOB2-11_20160429_032645_N_V25000_G	57507.6	39	B.4
Herschel 36	Herschel 36	O7:	V	.	11.0	0	0	22	HERSCHEL36_20080515_054510_F_V48000	54601.7	146	B.6
LS III +46 11	LS III +46 11	O3.5	If*	O3.5If*	12.5	3	2	0	LSII+4611_20110915_234039_N_V25000	55820.4	42	B.6
LS III +46 12	LS III +46 12	O4.5	IV(f)	.	11.4	1	0	0	LSII+4612_20170602_022441_N_V25000	57906.6	49	B.6
MY CAM	MY Cam	O5.5	V(n)	O6.5V(n)	10.0	1	0	0	MY-CAM_20161029_044455_N_V25000	57690.7	77	B.6
Pismis 24-17	Pismis 24-17	O3.5	III(f*)	.	13.3	0	0	0	...	...	0	No table
Trumpler 14-9	Trumpler 14-9	O8.5	V	.	10.1	0	0	2	TRUMPLER14-9_20100510_005721_F_V48000	55326.5	121	B.4
V572 CAR	V572 Car	O7.5	V(n)	B0V(n)	8.9	0	0	1	V572CAR_20041226_064652_F_V48000	53365.7	82	B.6
V747 CEP	V747 Cep	O5.5	V(n)((f))	.	11.4	5	0	0	V747CEP_20171004_005249_N_V25000	58030.5	49	B.6

Table B.2: Individual input parameters for the spectroscopic analysis.

				$v_{\rm rad}$		IACOB-BROAD					
Name	SpT	LC	Spec. Used	This work	Literat.	Line	S/N	EW	$v \sin i$(FT)	$v \sin i$(GOF)	$v_{\rm mac}$(GOF)
ALS 4880	O6	V((f))	ALS4880_20170601_012645_N_V25000	17±9	...	O III λ5592	93	249	93	84	89
ALS 7833	O8	Vz	ALS7833_20161029_051933_N_V25000	-36±5	-32	O III λ5592	158	271	100	85	104
ALS 8294	O7	V(n)z	ALS8294_20161230_052039_N_V25000	-24±2	...	O III λ5592	67	195	67	50	87
ALS 12370	O6.5	Vnn((f))	ALS12370_20171002_233240_N_V25000	-100±25	...	He I λ4471	75	526	436	440	130
ALS 12619	O7	V((f))z	ALS12619_20171119_000737_N_V25000	-47±2	...	O III λ5592	100	233	26	21	43
ALS 15210	O3.5	If*_Nwk	ALS15210_20110515_014935_F_V48000	-17±7	...	N V λ4603	93	49	85	98	4
BD -10 4682	O7	Vn((f))	BD-104682_20170601_003238_N_V25000	8±19	...	O III λ5592	111	390	358	358	15
BD -11 4586	O8	Ib(f)	BD-114586_20070527_073741_F_V48000	21±4	...	O III λ5592	60	365	75	74	68
BD -13 4927	O7	II(f)	BD-134927_20070526_092756_F_V48000	19±5	15	O III λ5592	176	377	104	98	78
BD -14 5040	O5.5	V(n)((f))	BD-145040_20170602_031044_N_V25000	-11±12	...	O III λ5592	97	312	268	268	106
BD +33 1025 A	O7.5	V(n)z	BD+331025_20161029_022841_N_V25000	20±6	...	O III λ5592	121	200	178	178	10
BD +36 4145	O8.5	V(n)	BD+364145_20171118_192318_N_V25000	-36±3	...	O III λ5592	111	314	205	203	33
BD +39 1328	O8.5	Iab(n)(f)	BD+391328_20161029_055939_N_V25000	-74±2	-71	O III λ5592	170	128	89	90	37
BD +60 134	O5.5	V(n)((f))	BD+60134_20171002_025128_N_V25000	-93±14	-24	O III λ5592	123	224	268	250	133
BD +60 2522	O6.5	...(n)fp	BD+602522_20110912_032100_N_V25000	-18±13	-26	O III λ5592	223	347	249	247	62
BD +60 261	O7.5	III(n)((f))	BD+60261_20110912_025532_N_V25000	-63±7	-85	O III λ5592	211	274	166	162	92
BD +60 2635	O6	V((f))	BD+602635_20171002_034308_N_V25000	-49±3	...	O III λ5592	114	207	49	51	73
BD +60 498	O9.7	II-III	BD+60498_20171120_015502_N_V25000	-10±6	-100	Si III λ4452	52	103	121	114	40
BD +60 499	O9.5	V	BD+60499_20161029_001830_N_V25000	-45±2	-22	O III λ5592	127	126	20	17	38
BD +60 501	O7	V(n)((f))z	BD+60501_20161028_233526_N_V25000	-47±10	-47	O III λ5592	141	252	191	182	87
BD +60 513	O7	Vn	BD+60513_20161028_230520_N_V25000	-51±7	...	O III λ5592	128	285	313	319	17
BD +60 586	O7	Vz	BD+60586_20110913_024725_N_V25000	-60±5	-49	O III λ5592	260	148	40	38	77
BD +61 411	O6.5	V((f))z	BD+61411_20161229_233500_N_V25000	-41±4	-41	O III λ5592	133	176	42	29	98
BD +62 2078	O7	V((f))z	BD+622078_20171003_004742_N_V25000	-14±1	...	O III λ5592	139	216	39	38	38
BD +62 424	O6.5	V(n)((f))	BD+62424_20110912_043319_N_V25000	-33±2	-9	O III λ5592	191	216	58	60	65
CPD -26 2716	O6.5	Iabf	CPD-262716_20070526_235156_F_V48000	89±11	57	O III λ5592	220	300	154	139	138
CPD -41 7721 A	O9.7	V:(n)	CPD-417721A_20040509_060240_F_V48000	-25±10	...	O III λ5592	319	95	191	191	66
CPD -41 7733	O9	IV	CPD-417733_20040505_042329_F_V48000	-92±1	23	O III λ5592	265	231	62	56	71
CPD -47 2963 AB	O5	Ifc	CPD-472963_20070419_002543_F_V48000	24±9	-13	O III λ5592	152	233	77	67	110
CPD -54 6791	O9.5	V	CPD-546791_20090504_024958_F_V48000	-39±1	-26	O III λ5592	170	175	30	31	39
CPD -58 2611	O6	V((f))z	CPD-582611_20070527_014252_F_V48000	0±1	...	O III λ5592	142	214	51	39	73
CPD -59 2551	O9	V	CPD-592551_20100507_002325_F_V48000	-7±5	...	O III λ5592	193	181	128	124	92
CPD -59 2600	O6	V((f))	CPD-592600_20150405_030555_F_V48000	-45±3	...	O III λ5592	127	157	127	101	136
CPD -59 5634	O9.2	Ib	CPD-595634_20080515_024853_F_V48000	-43±2	...	O III λ5592	188	264	60	48	102
CYG OB2-4 A	O7	III((f))	CYGOB2-4_20160429_004947_N_V25000_G	-11±7	-6	O III λ5592	98	361	84	72	105
CYG OB2-7	O3	If*	CYGOB2-7_20160429_014211_N_V25000_G	-13±9	-27	N V λ4603	35	559	80	75	126
CYG OB2-9	O4.5	If	CYGOB2-9_20160429_023433_N_V25000_G	-40±35	-16	He I λ5875	94	362	117	112	82
CYG OB2-11	O5.5	Ifc	CYGOB2-11_20160429_032645_N_V25000_G	-25±6	-27	O III λ5592	119	218	68	75	85

Notes: EW in [mÅ]; $v_{\rm rad}$, $v \sin i$, and $v_{\rm mac}$ in [km s^{-1}]

Table B.2: continued.

Name	SpT	LC	Spec. Used	$v_{\rm rad}$		IACOB-BROAD					$v_{\rm mac}$(GOF)
				This work	Literat.	Line	S/N	EW	$v \sin i$(FT)	$v \sin i$(GOF)	
HD 108	O8	...fp_var	HD108_20100908_230933_N_V46000	-73±9	-63	O III λ5592	322	228	44	46	86
HD 10125	O9.7	II	HD10125_20110115_232529_N_V25000	-48±5	-38	O III λ5592	264	146	130	122	125
HD 12323	ON9.2	V	HD12323_20121225_225051_N_V25000	-17±6	-41	O III λ5592	167	92	126	121	82
HD 12993	O6.5	V((f))_Nstr	HD12993_20110912_054359_N_V25000	-87±2	-101	O III λ5592	197	175	76	84	79
HD 13022	O9.7	II-III	HD13022_20110912_034420_N_V25000	-49±3	-56	Si III λ4452	153	207	98	98	131
HD 13268	ON8.5	IIIn	HD13268_20110112_201716_N_V25000	-106±5	-126	He I λ4471	178	795	291	290	102
HD 13745	O9.7	II(n)	HD13745_20110910_015932_N_V46000	-12±10	-21	O III λ5592	231	188	195	197	57
HD 14434	O5.5	IVnn(f)p	HD14434_20110911_043935_N_V25000	-33±29	-17	O III λ5592	246	266	415	417	144
HD 14442	O5	...n(f)p	HD14442_20161229_225242_N_V25000	-36±12	...	He I λ4471	86	392	327	324	45
HD 14633	ON8.5	V	HD14633_20091113_024720_N_V46000	-34±4	-38	O III λ5592	272	131	123	121	69
HD 14947	O4.5	If	HD14947_20081108_231044_N_V46000	-44±12	-56	O III λ5592	281	76	109	114	22
HD 15570	O4	If	HD15570_20081107_004909_N_V46000	-41±9	-24	N V λ4603	158	95	91	81	115
HD 15629	O4.5	V((fc))	HD15629_20110913_020206_N_V25000	-68±14	-55	O III λ5592	254	153	80	76	64
HD 15642	O9.5	II-IIIn	HD15642_20110911_033543_N_V25000	-31±18	-46	O III λ5592	235	148	273	286	104
HD 16691	O4	If	HD16691_20110913_032931_N_V25000	-59±20	-41	N V λ4603	133	184	160	158	88
HD 16832	O9.2	III	HD16832_20110912_045551_N_V25000	-25±1	...	O III λ5592	230	206	53	45	70
HD 17603	O7.5	Ib(f)	HD17603_20110114_215807_N_V25000	-25±5	...	O III λ5592	247	302	108	103	108
HD 18409	O9.7	Ib	HD18409_20110113_195319_N_V25000	-44±7	-42	O III λ5592	251	197	137	131	102
HD 24431	O9	III	HD24431_20081109_032702_N_V46000	-4±1	-8	O III λ5592	302	238	54	49	81
HD 24534	O9.5:	...npe	HD24534_20110115_192813_N_V46000	-240±189	-50	He I λ4387	140	270	229	226	104
HD 24912	O7.5	III(n)((f))	HD24912_20081109_012026_N_V46000	55±14	65	O III λ5592	358	297	234	230	82
HD 30614	O9	Ia	HD30614_20111109_033231_M_V85000	10±5	6	O III λ5592	248	298	112	113	77
HD 34078	O9.5	V	HD34078_20081109_012706_N_V46000	51±3	56	O III λ5592	261	132	15	13	32
HD 34656	O7.5	II(f)	HD34656_20131218_234051_M_V85000	-12±1	-5	O III λ5592	185	232	57	67	77
HD 35619	O7.5	V((f))	HD35619_20110913_041546_N_V25000	0±3	-1	O III λ5592	210	211	44	40	60
HD 36483	O9.5	IV(n)	HD36483_20110913_043711_N_V25000	-9±14	6	O III λ5592	257	149	164	158	74
HD 36486	AaAb	IINwk	HD36486_20090501_231005_F_V48000	36±5	18	O III λ5592	186	184	109	100	94
HD 36512	O9.7	V	HD36512_20111109_032351_M_V85000	16±2	17	O III λ5592	230	76	17	13	33
HD 36861	A	O8 III((f))	HD36861_20140211_200754_M_V85000	34±1	33	O III λ5592	320	322	45	52	77
HD 36879		O7 V(n)((f))	HD36879_20081109_020337_N_V46000	28±13	26	O III λ5592	241	259	213	209	40
HD 37022		O7 Vp	HD37022_20081108_055255_N_V46000	29±5	23	O III λ5592	325	103	36	23	68
HD 37737	O9.5	II-III(n)	HD37737_20130129_214159_N_V25000	21±7	-8	O III λ5592	255	202	210	201	95
HD 37742	O9.2	IbNwk_var	HD37742_20131030_064651_M_V85000	27±5	18	O III λ5592	511	245	121	122	97
HD 37743	O9.5	II-III(n)	HD37743_20131218_024355_M_V85000	26±4	13	O III λ5592	246	237	114	112	112
HD 38666	O9.5	V	HD38666_20090503_231437_F_V48000	106±4	109	O III λ5592	150	139	114	111	56
HD 39680	O6	V:[n]pe_var	HD39680_20121224_031527_N_V46000	66±27	18	He I λ4471	156	197	102	101	31
HD 41161	O8	Vn	HD41161_20081109_030049_N_V46000	-23±14	-16	O III λ5592	203	221	334	331	6
HD 41997	O7.5	Vn((f))	HD41997_20110913_051707_N_V25000	-31±12	-18	O III λ5592	273	251	263	262	38
HD 42088	O6	V((f))z	HD42088_20110116_013309_N_V46000	15±1	23	O III λ5592	206	232	58	49	76

Notes: EW in [mÅ] ; $v_{\rm rad}$, $v \sin i$, and $v_{\rm mac}$ in [km s^{-1}]

Table B.2: continued.

Name	SpT	LC	Spec. Used	$v_{\rm rad}$ This work	$v_{\rm rad}$ Literat.	IACOB-BROAD Line	S/N	EW	$v \sin i$(FT)	$v \sin i$(GOF)	$v_{\rm mac}$(GOF)
HD 44811	O7	V(n)z	HD44811_20110913_055938_N_V25000	-3±4	10	O III λ5592	232	218	23	26	43
HD 45314	O9:	...npe	HD45314_20110114_230558_N_V46000	-120±266	-25	Si III λ4452	173	60	129	128	4
HD 46056	O8	Vn	HD46056_20130129_003033_N_V25000	24±17	21	O III λ5592	253	308	373	370	103
HD 46149	O8.5	V	HD46149_20121224_025709_N_V46000	23±3	36	O III λ5592	266	145	37	30	49
HD 46150	O5	V((f))z	HD46150_20081108_020753_N_V46000	37±10	31	O III λ5592	287	110	60	60	112
HD 46202	O9.2	V	HD46202_20130130_002935_N_V25000	34±1	28	O III λ5592	257	132	16	11	38
HD 46223	O4	V((f))	HD46223_20081107_050512_N_V46000	38±5	43	O III λ5592	231	129	59	51	112
HD 46485	O7	V((f))n_var?	HD46485_20110913_053847_N_V25000	20±16	14	O III λ5592	219	342	325	322	100
HD 46573	O7	V((f))z	HD46573_20121224_040337_N_V46000	45±3	29	O III λ5592	204	212	65	77	81
HD 46966	O8.5	IV	HD46966_20091112_011937_N_V46000	36±4	39	O III λ5592	279	171	40	40	66
HD 47432	O9.7	Ib	HD47432_20091112_032247_N_V46000	64±4	60	O III λ5592	272	144	97	97	63
HD 47839	O7	V((f))z_var	HD47839_20091110_025831_N_V46000	29±4	22	O III λ5592	307	208	43	43	67
HD 48279	O8.5	VNstr_var?	HD48279_20121224_033329_N_V46000	40±2	19	O III λ5592	201	163	137	131	74
HD 5005A	O4	V((fc))	HD5005A_20100910_045224_N_V46000	-31±3	...	O III λ5592	165	142	69	52	79
HD 5005C	O8.5	V(n)	HD5005C_20130129_203700_N_V25000	-40±9	...	O III λ5592	136	218	202	200	59
HD 5005D	O9.2	V	HD5005D_20161028_223703_N_V25000	-34±2	...	O III λ5592	164	154	32	32	57
HD 52266	O9.5	IIIn	HD52266_20110115_014505_N_V46000	30±6	5	O III λ5592	209	129	254	267	52
HD 52533	O8.5	IVn	HD52533_20090501_232857_F_V48000	0±31	76	He I λ4713	285	160	299	299	107
HD 53975	O7.5	Vz	HD53975_20091112_040202_N_V46000	5±5	36	O III λ5592	225	241	181	179	45
HD 54879	O9.7	V	HD54879_20121226_033157_N_V46000	27±2	34	O III λ5592	198	57	6	8	8
HD 55879	O9.7	III	HD55879_20121224_041714_N_V46000	28±2	32	O III λ5592	284	119	32	28	61
HD 5689	O7	Vn((f))	HD5689_20161029_030818_N_V25000	-79±6	...	O III λ5592	133	257	257	255	76
HD 57061	O9	II	HD57061_20110321_015810_F_V48000	43±3	33	O III λ5592	229	252	62	57	85
HD 57236	O8.5	V	HD57236_20121224_043200_N_V25000	79±5	19	O III λ5592	165	172	29	5	72
HD 57682	O9.2	IV	HD57682_20121226_040502_N_V46000	24±2	24	O III λ5592	259	122	13	7	34
HD 60848	O8:	V:pe	HD60848_20110116_044117_N_V46000	42±8	5	He I λ4471	169	311	136	136	123
HD 64568	O3	V((f*))z	HD64568_20080607_230926_F_V48000	84±7	77	N V λ4603	162	104	77	75	53
HD 66811	O4	I(n)fp	HD66811_20110323_021313_F_V48000	-12±5	-23	N V λ4603	340	125	198	198	12
HD 68450	O9.7	II	HD68450_20090503_001401_F_V48000	35±2	36	O III λ5592	126	186	48	39	77
HD 69464	O7	Ib(f)	HD69464_20080608_231326_F_V48000	57±5	43	O III λ5592	119	271	79	73	105
HD 71304	O9	II	HD71304_20090503_002457_F_V48000	25±2	32	O III λ5592	93	256	58	52	100
HD 73882	O8.5	IV	HD73882_20110212_054245_F_V48000	33±8	21	O III λ5592	273	198	145	145	58
HD 74194	O8.5	Ib-II(f)p	HD74194_20090502_013746_F_V48000	9±6	-2	O III λ5592	331	314	187	184	49
HD 74920	O7.5	IVn((f))	HD74920_20041224_044455_F_V48000	9±8	...	O III λ5592	239	266	291	291	16
HD 75211	O8.5	II((f))	HD75211_20120519_235311_F_V48000	26±5	20	O III λ5592	120	275	142	145	53
HD 75222	O9.7	Iab	HD75222_20150405_010826_F_V48000	69±3	64	Si III λ4452	279	135	84	86	65
HD 76341	O9.2	IV	HD76341_20110323_024223_F_V48000	28±2	26	O III λ5592	279	216	48	51	93
HD 76556	O6	IV(n)((f))p	HD76556_20080609_235952_F_V48000	25±9	28	O III λ5592	259	202	245	239	86
HD 76968	O9.2	Ib	HD76968_20080513_001447_F_V48000	-22±2	-9	O III λ5592	108	195	58	53	65

Notes: EW in [mÅ] ; $v_{\rm rad}$, $v \sin i$, and $v_{\rm mac}$ in [km s^{-1}]

Table B.2: continued.

Name	SpT	LC	Spec. Used	$v_{\rm rad}$		IACOB-BROAD					$v_{\rm mac}$(GOF)
				This work	Literat.	Line	S/N	EW	$v \sin i$(FT)	$v \sin i$(GOF)	
HD 89137	ON9.7	II(n)	HD89137_20110517_012116_F_V48000	-2±9	-17	Si III λ4452	231	266	249	238	33
HD 90087	O9.2	III(n)	HD90087_20110214_022932_F_V48000	-1±9	-2	He I λ4713	200	309	294	293	64
HD 90273	ON7	V((f))	HD90273_20041222_045853_F_V48000	-1±1	-5	O III λ5592	187	208	52	55	55
HD 91572	O6.5	V((f))z	HD91572_20080609_010335_F_V48000	-2±3	...	O III λ5592	150	213	58	60	57
HD 91651	ON9.5	IIIn	HD91651_20110516_005321_F_V48000	-10±12	-31	He I λ4387	149	365	201	189	242
HD 91824	O7	V((f))z	HD91824_20070419_012940_F_V48000	6±4	-15	O III λ5592	144	198	48	51	48
HD 92504	O8.5	V(n)	HD92504_20080610_003438_F_V48000	-28±5	-30	O III λ5592	243	208	183	182	63
HD 93027	O9.5	IV	HD93027_20090502_015334_F_V48000	-3±1	...	O III λ5592	113	139	53	46	66
HD 93028	O9	IV	HD93028_20080514_015221_F_V48000	-37±4	-25	O III λ5592	109	195	32	25	55
HD 93128	O3.5	V((fc))z	HD93128_20150403_033259_F_V48000	4±4	...	O III λ5592	231	49	61	58	56
HD 93129AaAb	O2	If*	HD93129A_20150405_023412_F_V48000	8±6	-14	N V λ4620	275	457	117	116	142
HD 93129B	O3.5	V((f))z	HD93129B_20150403_025102_F_V48000	1±4	...	O III λ5592	223	71	72	66	62
HD 93146 A	O7	V((f))	HD93146_20080514_020823_F_V48000	-17±1	...	O III λ5592	171	220	59	60	67
HD 93160 AB	O7	III((f))	HD93160_20150402_042354_F_V48000	-21±3	-16	O III λ5592	291	131	120	120	64
HD 93161 B	O6.5	IV((f))	HD93161B_20040506_235743_F_V48000	-15±4	...	O III λ5592	236	208	89	81	101
HD 93204	O5.5	V((f))	HD93204_20080609_015400_F_V48000	-4±2	...	O III λ5592	148	210	114	110	93
HD 93222 AB	O7	V((f))	HD93222_20110214_050447_F_V48000	-3±2	...	O III λ5592	129	308	46	50	90
HD 93249 A	O9	III	HD93249_20090502_003412_F_V48000	-7±3	...	O III λ5592	113	221	61	55	72
HD 93250 AB	O4	IV(fc)	HD93250_20120521_014809_F_V48000	0±10	-3	O III λ5592	196	96	79	70	84
HD 93521	O9.5	IInn	HD93521_20121226_045343_N_V46000	9±17	-14	He I λ4471	187	993	386	385	192
HD 93632	O5	If_var	HD93632_20110323_055431_F_V48000	-5±4	...	O III λ5592	193	143	86	86	47
HD 93843	O5	III(fc)	HD93843_20150403_055036_F_V48000	-10±6	-9	O III λ5592	279	212	57	58	120
HD 94024	O8	IV	HD94024_20080515_011756_F_V48000	33±4	...	O III λ5592	87	281	162	162	52
HD 94370	O7	...(n)fp	HD94370_20150402_053237_F_V48000	-1±10	...	O III λ5592	248	288	182	182	91
HD 94963	O7	II(f)	HD94963_20070421_040533_F_V48000	0±4	-3	O III λ5592	131	332	66	76	92
HD 96264	O9.5	III	HD96264_20110321_053854_F_V48000	32±2	-33	O III λ5592	114	124	32	29	65
HD 96622	O9.2	IV	HD96622_20080513_011335_F_V48000	29±2	...	O III λ5592	233	191	39	39	61
HD 96715	O4	V((f))z	HD96715_20150403_052702_F_V48000	-27±3	-27	N V λ4603	219	99	69	59	86
HD 96917	O8	Ib(n)(f)	HD96917_20110213_081641_F_V48000	-5±4	2	O III λ5592	270	308	170	165	77
HD 96946	O6.5	III(f)	HD96946_20120520_033905_F_V48000	-7±5	11	O III λ5592	125	163	71	72	58
HD 97253	O5	III(f)	HD97253_20090504_021148_F_V48000	0±9	1	O III λ5592	308	170	67	70	105
HD 97434	O7.5	III(n)((f))	HD97434_20150402_055328_F_V48000	-27±5	-20	O III λ5592	223	288	227	217	114
HD 97848	O8	V	HD97848_20090502_041114_F_V48000	-4±1	-7	O III λ5592	125	275	49	41	77
HD 99546	O7.5	V((f))_Nstr	HD99546_20041225_061416_F_V48000	-4±1	-4	O III λ5592	224	243	42	50	60
HD 99897	O6.5	IV((f))	HD99897_20070527_035741_F_V48000	-6±1	-3	O III λ5592	220	299	55	50	94
HD 101190AaAb	O6	IV((f))	HD101190_20110321_032654_F_V48000	-14±6	-8	O III λ5592	181	93	58	49	74
HD 101191	O8	V	HD101191_20070421_044639_F_V48000	0±2	5	O III λ5592	235	285	145	138	101
HD 101223	O8	V	HD101223_20040508_231307_F_V48000	3±1	9	O III λ5592	315	238	54	55	63
HD 101298	O6.5	IV((f))	HD101298_20120520_043018_F_V48000	3±1	1	O III λ5592	229	220	68	71	69

Notes: EW in [mÅ] ; $v_{\rm rad}$, $v \sin i$, and $v_{\rm mac}$ in [km s^{-1}]

Table B.2: continued.

Name	SpT	LC	Spec. Used	$v_{\rm rad}$ This work	$v_{\rm rad}$ Literat.	IACOB-BROAD Line	S/N	EW	$v \sin i$(FT)	$v \sin i$(GOF)	$v_{\rm mac}$(GOF)
HD 101413	O8	V	HD101413_20150405_050130_F_V48000	0±3	1	O III λ5592	188	206	90	80	91
HD 101545AaAb	O9.2	II	HD101545A_20090505_051248_F_V48000	-2±3	0	O III λ5592	241	186	49	44	79
HD 102415	ON9	IV:nn	HD102415_20080513_042228_F_V48000	-24±25	...	He I λ4471	139	896	365	366	162
HD 104565	OC9.7	Iab	HD104565_20080513_024739_F_V48000	-22±6	-11	O III λ5592	96	270	55	56	116
HD 105056	ON9.7	Iae	HD105056_20090502_044058_F_V48000	5±2	-9	O III λ5592	161	147	58	56	46
HD 105627	O9	III	HD105627_20110321_061139_F_V48000	46±4	2	O III λ5592	211	215	154	141	122
HD 110360	ON7	V	HD110360_20110516_031504_F_V48000	-25±4	-19	O III λ5592	146	115	82	96	86
HD 112244	O8.5	Iab(f)p	HD112244_20110516_035623_F_V48000	35±4	18	O III λ5592	266	288	133	124	80
HD 113904B	O9	III	HD113904B_20090505_060747_F_V48000	-16±5	...	O III λ5592	198	227	88	84	83
HD 114737AB	O8.5	III	HD114737_20150405_051825_F_V48000	-105±4	...	O III λ5592	251	237	72	58	83
HD 116852	O8.5	II-III((f))	HD116852_20080513_035626_F_V48000	-38±4	-47	O III λ5592	178	272	114	114	69
HD 117490	ON9.5	IIInn	HD117490_20150403_063845_F_V48000	-3±16	...	He I λ4471	177	829	342	343	135
HD 117797	O7.5	...fp	HD117797_20150405_055828_F_V48000	-20±12	-25	O III λ5592	213	372	145	150	80
HD 118198	O9.7	III	HD118198_20080513_054748_F_V48000	-16±2	...	O III λ5592	201	146	43	43	56
HD 120521	O7.5	Ib(f)	HD120521_20120520_062307_F_V48000	-44±5	-36	O III λ5592	150	257	95	100	95
HD 120678	O9.5	Ve	HD120678_20110322_092507_F_V48000	-39±58	...	O III λ5592	242	71	154	155	84
HD 123008	ON9.2	Iab	HD123008_20080514_040321_F_V48000	-12±2	-32	O III λ5592	69	259	55	62	94
HD 123056	O9.5	IV(n)	HD123056_20120521_063705_F_V48000	-40±11	-39	O III λ5592	248	121	192	193	26
HD 124979	O7.5	IV(n)((f))	HD124979_20150404_035200_F_V48000	-74±5	-68	O III λ5592	191	386	272	261	54
HD 125241	O8.5	Ib(f)	HD125241_20150402_074924_F_V48000	-37±6	-47	O III λ5592	65	335	124	118	95
HD 130298	O6.5	III(n)(f)	HD130298_20080514_042531_F_V48000	-8±3	-74	O III λ5592	210	180	165	167	85
HD 135591	O8	IV((f))	HD135591_20070420_073310_F_V48000	0±2	-3	O III λ5592	127	274	58	60	60
HD 148546	O9	Iab	HD148546_20080513_060555_F_V48000	-52±3	-55	O III λ5592	254	311	82	85	95
HD 148937	O6	...f?p	HD148937_20070420_074115_F_V48000	-41±14	-53	O III λ5592	331	91	46	39	76
HD 149038	O9.7	Iab	HD149038_20090525_045827_F_V48000	7±4	6	O III λ5592	137	198	57	52	90
HD 149452	O9	IVn	HD149452_20120520_070844_F_V48000	-50±13	88	O III λ5592	193	318	330	318	120
HD 149757	O9.2	IVnn	HD149757_20090504_050358_F_V48000	-5±12	-9	He I λ4471	285	845	385	385	94
HD 150574	ON9	III(n)	HD150574_20080513_061845_F_V48000	-41±11	...	O III λ5592	235	228	266	252	172
HD 151018	O9	Ib	HD151018_20080515_033828_F_V48000	-39±2	-48	O III λ5592	276	257	61	67	65
HD 151515	O7	II(f)	HD151515_20070419_072807_F_V48000	-22±1	-9	O III λ5592	59	265	64	67	98
HD 151804	O8	Iaf	HD151804_20150404_050304_F_V48000	-46±6	-63	O III λ5592	291	308	66	72	73
HD 152003	O9.7	IabNwk	HD152003_20120521_074209_F_V48000	-20±4	-28	O III λ5592	224	239	52	65	83
HD 152147	O9.7	IbNwk	HD152147_20080515_040719_F_V48000	-13±5	-28	O III λ5592	104	202	90	91	64
HD 152200	O9.7	IV(n)	HD152200_20040506_062054_F_V48000	-40±14	-77	O III λ5592	318	101	227	226	21
HD 152233	O6	II(f)	HD152233_20120521_043009_F_V48000	-29±3	-16	O III λ5592	243	154	66	62	105
HD 152247	O9.2	III	HD152247_20090504_094829_F_V48000	-4±3	-16	O III λ5592	297	234	83	82	96
HD 152249	OC9	Iab	HD152249_20090504_092636_F_V48000	-21±2	-24	O III λ5592	132	354	72	71	70
HD 152405	O9.7	II	HD152405_20120521_055904_F_V48000	0±3	-7	O III λ5592	129	187	67	59	61
HD 152424	OC9.2	Ia	HD152424_20150405_074548_F_V48000	-24±3	-47	O III λ5592	86	353	61	59	66

Notes: EW in [mÅ] ; $v_{\rm rad}$, $v \sin i$, and $v_{\rm mac}$ in [km s^{-1}]

Table B.2: continued.

Name	SpT	LC	Spec. Used	$v_{\rm rad}$ This work	$v_{\rm rad}$ Literat.	IACOB-BROAD Line	S/N	EW	$v \sin i$(FT)	$v \sin i$(GOF)	$v_{\rm mac}$(GOF)
HD 152590	O7.5	Vz	HD152590_20090525_052211_F_V48000	-45±2	0	O III λ5592	114	286	52	48	56
HD 152623	O7	V(n)((f))	HD152623_20080513_080116_F_V48000	-41±7	-7	O III λ5592	294	207	88	83	138
HD 152723 AaAb	O6.5	III(f)	HD152723_20080515_043624_F_V48000	2±5	-5	O III λ5592	350	184	63	73	100
HD 154368	O9.2	Iab	HD154368_20090504_065633_F_V48000	11±3	3	O III λ5592	91	279	64	65	78
HD 154643	O9.7	III	HD154643_20080514_081212_F_V48000	18±5	-27	O III λ5592	103	177	110	101	78
HD 154811	OC9.7	Ib	HD154811_20080514_082138_F_V48000	-23±4	-24	Si III λ4452	250	158	125	124	62
HD 155756	O9	Ibp	HD155756_20080514_082917_F_V48000	-7±2	...	O III λ5592	210	383	62	62	99
HD 155806	O7.5	V((f))(e)	HD155806_20110617_003322_M_V85000	5±3	11	O III λ5592	221	208	56	49	103
HD 155889 AB	O9.5	IV	HD155889_20120620_051117_F_V48000	3±4	7	O III λ5592	118	122	29	27	51
HD 155913	O4.5	Vn((f))	HD155913_20060818_000814_F_V48000	10±9	488	O III λ5592	235	113	266	278	0
HD 156154	O7.5	Ib(f)	HD156154_20070420_082005_F_V48000	2±4	-4	O III λ5592	106	300	64	62	102
HD 156738 AB	O6.5	III(f)	HD156738_20110517_070459_F_V48000	-2±14	-2	O III λ5592	128	162	69	65	103
HD 157857	O6.5	II(f)	HD157857_20110911_201644_N_V46000	57±5	57	O III λ5592	191	226	115	114	69
HD 159176	O7	V((f))	HD159176_20110517_104345_F_V48000	8±5	10	O III λ5592	257	267	116	114	90
HD 162978	O8	II((f))	HD162978_20110828_205502_N_V46000	-9±5	-12	O III λ5592	258	219	55	54	86
HD 163758	O6.5	Iafp	HD163758_20120520_102704_F_V48000	-45±5	-48	O III λ5592	196	282	82	76	87
HD 163800	O7.5	III((f))	HD163800_20110829_203034_N_V46000	1±3	4	O III λ5592	252	383	59	53	107
HD 163892	O9.5	IV(n)	HD163892_20110907_202704_N_V46000	35±9	-11	O III λ5592	205	202	215	215	53
HD 164019	O9.5	IVp	HD164019_20080608_075144_F_V48000	-26±3	-27	O III λ5592	202	219	62	69	62
HD 164438	O9.2	IV	HD164438_20080514_092403_F_V48000	0±3	-24	O III λ5592	208	217	55	55	94
HD 164492	O7.5	Vz	HD164492_20110829_212004_N_V46000	-5±1	0	O III λ5592	226	240	33	39	54
HD 164794	O4	V((f))	HD164794_20090505_103135_F_V48000	9±3	10	O III λ5592	301	105	71	62	95
HD 165174	O9.7	IIn	HD165174_20110907_222610_N_V46000	38±16	17	O III λ5592	182	203	273	264	175
HD 165246	O8	V(n)	HD165246_20110829_213907_N_V46000	16±9	...	O III λ5592	233	259	254	251	39
HD 166546	O9.5	IV	HD166546_20100909_204628_N_V46000	1±1	2	O III λ5592	297	184	47	38	73
HD 167264	O9.7	Iab	HD167264_20090525_083224_F_V48000	11±3	-6	Si III λ4452	425	231	78	71	69
HD 167633	O6.5	V((f))	HD167633_20110910_222422_N_V25000	-48±3	-53	O III λ5592	287	215	131	129	106
HD 167659	O7	II-III(f)	HD167659_20070526_100517_F_V48000	16±4	15	O III λ5592	295	240	76	71	84
HD 168076 AB	O4	IV(f)	HD168076_20120521_081558_F_V48000	18±14	25	N v λ4603	164	100	60	68	101
HD 168112 AB	O5	IV(f)	HD168112_20060820_011745_F_V48000	16±5	-5	O III λ5592	127	274	117	107	78
HD 168461	O7.5	V((f))_Nstr	HD168461_20170601_001025_N_V25000	5±6	...	O III λ5592	131	306	192	192	30
HD 168504	O7.5	V(n)z	HD168504_20040705_055920_F_V48000	20±2	5	O III λ5592	171	276	64	61	89
HD 168941	O9.5	IVp	HD168941_20090504_080947_F_V48000	99±5	105	O III λ5592	228	240	88	83	101
HD 169582	O6	Iaf	HD169582_20090525_100844_F_V48000	1±13	-9	O III λ5592	122	169	69	66	97
HD 171589	O7.5	II(f)	HD171589_20110912_204533_N_V25000	20±16	19	O III λ5592	232	265	95	100	86
HD 172175	O6.5	I(n)fp	HD172175_20070527_083116_F_V48000	24±9	-1	O III λ5592	207	262	229	237	69
HD 173010	O9.7	Ia+var	HD173010_20120619_090148_F_V48000	78±2	49	O III λ5592	183	318	55	61	88
HD 173783	O9	Iab	HD173783_20090503_094026_F_V48000	57±4	48	O III λ5592	224	344	100	89	90
HD 175754	O8	II(n)((f))p	HD175754_20110517_102018_F_V48000	-1±5	-11	O III λ5592	213	326	187	182	121

Notes: EW in [mÅ] ; $v_{\rm rad}$, $v \sin i$, and $v_{\rm mac}$ in [km s^{-1}]

Table B.2: continued.

Name	SpT	LC	Spec. Used	$v_{\rm rad}$		IACOB-BROAD					$v_{\rm mac}$(GOF)
				This work	Literat.	Line	S/N	EW	$v \sin i$(FT)	$v \sin i$(GOF)	
HD 175876	O6.5	III(n)(f)	HD175876_20100908_202812_N_V46000	0±13	6	O III λ5592	278	326	281	282	70
HD 186980	O7.5	III((f))	HD186980_20100808_045738_N_V46000	-3±1	2	O III λ5592	204	345	63	61	83
HD 188001	O7.5	Iabf	HD188001_20110620_013133_M_V85000	19±5	13	O III λ5592	219	320	63	69	100
HD 188209	O9.5	Iab	HD188209_20130603_054038_M_V85000	-1±3	-8	O III λ5592	201	225	57	54	93
HD 189957	O9.7	III	HD189957_20100909_213830_N_V46000	38±4	39	O III λ5592	193	155	90	88	54
HD 190429 A	O4	If	HD190429_20110615_020805_M_V85000	-16±4	-18	N V λ4603	138	181	99	90	113
HD 190864	O6.5	III(f)	HD190864_20100908_234450_N_V46000	-12±4	-2	O III λ5592	271	276	58	66	90
HD 191423	ON9	II-IIInn	HD191423_20110829_012427_N_V25000	-69±26	-38	He I λ4471	214	840	429	432	108
HD 191612	O8	...f?p-var	HD191612_20100909_212050_N_V46000	-25±18	-27	O III λ5592	272	124	34	45	60
HD 191781	ON9.7	Iab	HD191781_20110619_224718_M_V85000	-8±6	-13	Si III λ4452	26	204	100	105	48
HD 191978	O8	V	HD191978_20110829_022107_N_V25000	-10±1	-17	O III λ5592	296	265	60	57	82
HD 192001	O9.5	IV	HD192001_20110911_232147_N_V25000	-38±1	-27	O III λ5592	245	150	39	44	57
HD 192281	O4.5	IV(n)(f)	HD192281_20100808_051701_N_V46000	-34±4	-54	He I λ4471	166	260	278	277	43
HD 192639	O7.5	Iabf	HD192639_20110615_041736_M_V85000	-7±5	-7	O III λ5592	168	297	91	82	95
HD 193443 AB		O9 III	HD193443_20100623_011844_N_V46000	-16±4	-17	O III λ5592	319	247	65	66	140
HD 193514	O7	Ib(f)	HD193514_20110910_000224_N_V46000	-20±4	-20	O III λ5592	265	282	73	73	84
HD 193595	O7	V((f))	HD193595_20170601_044741_N_V25000	-13±1	-19	O III λ5592	163	209	38	46	61
HD 193682	O4.5	IV(f)	HD193682_20170601_052757_N_V25000	-52±5	-46	O III λ5592	233	152	182	183	90
HD 195592	O9.7	Ia	HD195592_20110618_003043_M_V85000	-11±2	-27	O III λ5592	172	178	47	38	100
HD 199579	O6.5	V((f))z	HD199579_20130829_004031_M_V85000	-46±2	-6	O III λ5592	235	215	58	52	90
HD 201345	ON9.2	IV	HD201345_20100909_210331_N_V46000	21±3	19	O III λ5592	300	137	93	79	89
HD 202124	O9	Iab	HD202124_20101024_221756_N_V46000	-33±6	-24	O III λ5592	242	276	88	88	114
HD 202214	O9.5	IV	HD202214_20110617_052848_M_V85000	-19±4	-16	O III λ5592	252	79	28	26	36
HD 203064	O7.5	IIIn((f))	HD203064_20110616_044516_M_V85000	41±10	1	O III λ5592	259	275	312	312	66
HD 206183	O9.5	IV-V	HD206183_20100808_041510_N_V46000	-19±1	-7	O III λ5592	286	91	12	8	29
HD 207198	O8.5	II((f))	HD207198_20091111_193521_N_V46000	-23±4	-17	O III λ5592	388	327	58	52	97
HD 207538	O9.7	IV	HD207538_20100716_035701_N_V46000	-22±1	-14	O III λ5592	288	82	31	29	50
HD 209339	O9.7	IV	HD209339_20121026_201224_M_V85000	-23±4	-20	O III λ5592	222	101	88	84	78
HD 209975	O9	Ib	HD209975_20091111_190418_N_V46000	-6±3	-12	O III λ5592	289	261	60	50	104
HD 210809	O9	Iab	HD210809_20100908_232632_N_V46000	-68±1	-79	O III λ5592	274	277	63	70	105
HD 210839	O6.5	I(n)fp	HD210839_20111108_215240_M_V85000	-67±14	-75	O III λ5592	286	287	225	214	146
HD 214680	O9	V	HD214680_20081107_210248_N_V46000	-11±1	-10	O III λ5592	415	181	17	14	43
HD 216532	O8.5	V(n)	HD216532_20110911_015716_N_V25000	-13±5	-28	O III λ5592	244	207	204	199	54
HD 216898	O9	V	HD216898_20110911_023348_N_V25000	1±3	-21	O III λ5592	248	177	45	44	57
HD 217086	O7	Vnn((f))z	HD217086_20121225_202151_N_V46000	-19±16	-16	O III λ5592	270	301	384	377	40
HD 218195 A	O8.5	IIINstr	HD218195_20110911_031217_N_V25000	-26±1	-27	O III λ5592	253	245	40	44	78
HD 218915	O9.2	Iab	HD218915_20100716_043411_N_V46000	-80±1	-75	O III λ5592	247	223	60	63	88
HD 225146	O9.7	Iab	HD225146_20121225_213415_N_V25000	-39±4	-29	O III λ5592	206	100	71	67	88
HD 225160	O8	Iabf	HD225160_20110114_201920_N_V25000	-38±5	-45	O III λ5592	241	250	86	77	103

Notes: EW in [mÅ]; $v_{\rm rad}$, $v \sin i$, and $v_{\rm mac}$ in [km s^{-1}]

Table B.2: continued.

Name	SpT	LC	Spec. Used	$v_{\rm rad}$ This work	$v_{\rm rad}$ Literat.	IACOB-BROAD Line	S/N	EW	$v \sin i$(FT)	$v \sin i$(GOF)	$v_{\rm mac}$(GOF)
HD 226868	O9.7	Iabp_var	HD226868_20110913_000626_N_V25000	-82±6	-2	O III λ5592	211	144	100	95	70
HD 227018	O6.5	V((f))z	HDE227018_20170601_030325_N_V25000	16±2	20	O III λ5592	161	247	60	61	78
HD 227245	O7	V((f))z	HDE227245_20170601_034327_N_V25000	0±3	-13	O III λ5592	127	276	55	47	71
HD 227465	O7	V((f))	HDE227465_20170602_042407_N_V25000	7±4	...	O III λ5592	108	220	61	61	79
HD 228841	O6.5	Vn((f))	HD228841_20110909_225750_N_V25000	-51±10	-57	O III λ5592	204	287	332	317	130
HD 229196	O6	II(f)	HD229196_20110912_003950_N_V25000	-19±16	-38	O III λ5592	210	223	262	248	25
HD 229232	O4	V:n((f))	HD229232_20161028_211623_N_V25000	-46±13	...	N IV λ6380	136	478	313	313	46
HD 237211	O9	Ib	HD237211_20110116_002922_N_V25000	-28±3	-36	O III λ5592	173	193	47	51	82
HD 242926	O7	Vz	HD242926_20161029_034457_N_V25000	18±10	-8	O III λ5592	194	191	99	89	52
HD 242935 A	O6.5	V((f))z	HD242935_20161029_015032_N_V25000	3±3	5	O III λ5592	126	141	32	29	64
HD 256725 A	O5	V((fc))	HD256725_20110115_040003_N_V25000	28±1	38	O III λ5592	110	108	69	67	38
HD 28446A	O9.7	IIn	HD28446A_20091113_003939_N_V46000	-6±19	...	Si III λ4452	197	178	311	299	0
HD 298429	O8.5	V	HD298429_20110213_061413_F_V48000	25±5	20	O III λ5592	156	267	105	74	117
HD 303308 AB	O4.5	V((fc))	HD303308_20090502_023316_F_V48000	0±8	-1	O III λ5592	168	117	84	85	67
HD 303311	O6	V((f))z	HD303311_20070419_034639_F_V48000	-5±3	...	O III λ5592	118	229	51	47	61
HD 303492	O8.5	Iaf	HD303492_20080513_005333_F_V48000	35±2	8	O III λ5592	75	256	90	87	55
HD 305523	O9	II-III	HD305523_20090503_033852_F_V48000	0±3	...	O III λ5592	363	260	57	57	78
HD 305525	O5.5	V((f))z	HD305525_20120520_030436_F_V48000	-26±11	...	O III λ5592	125	183	69	66	139
HD 305532	O6.5	V((f))z	HD305532_20110515_003522_F_V48000	-1±1	45	O III λ5592	137	209	48	51	53
HD 305619	O9.7	II	HD305619_20080513_002944_F_V48000	-10±2	4	O III λ5592	238	231	58	48	94
HD 308813	O9.7	IV(n)	HD308813_20050521_013624_F_V48000	-23±10	-11	Si III λ4452	184	134	217	215	10
HD 319699	O5	V((fc))	HD319699_20070419_093144_F_V48000	-38±3	...	O III λ5592	211	117	78	69	76
HD 319702	O8	III	HD319702_20150402_085257_F_V48000	8±2	...	O III λ5592	64	252	69	66	50
HD 322417	O6.5	IV((f))	HD322417_20080515_031709_F_V48000	-6±3	...	O III λ5592	84	280	67	68	100
HD 326329	O9.7	V	HD326329_20090717_030916_F_V48000	-21±3	...	O III λ5592	196	85	88	87	39
HD 326331	O8	IVn((f))	HD326331_20080513_080849_F_V48000	-30±7	...	O III λ5592	338	430	330	332	100
HD 326775	O6.5	V(n)((f))z	HD326775_20150404_073109_F_V48000	10±5	...	O III λ5592	120	294	181	170	108
HD 338916	O7.5	Vz	HDE338916_20170602_035916_N_V25000	-2±1	7	O III λ5592	116	251	23	26	45
HD 338931	O6	III(f)	HDE338931_20171112_192321_N_V25000	-41±8	...	O III λ5592	163	218	164	170	9
HD 344777	O7.5	Vz	HDE344777_20170601_021111_N_V25000	17±2	...	O III λ5592	141	331	56	47	103
HD 344784	O6.5	V((f))z	HD344784_20161028_214433_N_V25000	13±3	5	O III λ5592	133	191	58	65	70
Trumpler14-9	O8.5	V	TRUMPLER14-9_20100510_005721_F_V48000	-1±1	...	O III λ5592	187	183	66	66	41

Notes: EW in [mÅ] ; $v_{\rm rad}$, $v \sin i$, and $v_{\rm mac}$ in [km s^{-1}]

Table B.3: Spectroscopic parameters for the sample of standard stars labeled as Q3 (Hα and He II λ4686 II not fitting at the same time).

For each star we include three lines. The first one refers to the parameters obtained from the conventional analysis, i.e., fitting all diagnostic H/He lines. The other two lines are the parameters obtained by forcing to fit either Hα or He II λ4686, respectively, and still fitting the other diagnostic lines at the same time. Columns include: Name, spectral type and luminosity classification, multi-epoch annotation, line forced in the fitting, effective temperature, gravity, wind strength parameter (without uncertainties for the forced cases), helium abundance, and microturbulence.

Name	SpT	LC	Notes	mass-loss diagnostic	$T_{\rm eff}$ [kK]	$\log g$ [dex]	$\log Q$ [dex]	$Y_{\rm He}$ [dex]	ξ_t [km s^{-1}]
HD 10125	O9.7	II	SB1	both lines	30.9±0.5	3.38±0.06	-12.7±0.1	0.11±0.03	>16
				He II λ4686	<30.4	<3.23	-13.5	>0.10	11±4
				Hα	<30.4	<3.26	-13.0	>0.09	13±3
HD 14947	O4.5	Iab/I f	LPV,WVe	both lines	39.1±1.1	3.64±0.11	-12.0±0.1	0.15±0.04	5.0-19.9
				He II λ4686	39.0±1.0	3.64±0.11	-12.1	0.15±0.04	5.0-19.9
				Hα	39.5±0.9	3.65±0.09	-11.9	0.15±0.03	<16
HD 47432	O9.7	Ib	LPV,WVe	both lines	29.1±0.5	3.01±0.05	-12.5±0.1	0.10±0.03	>19
				He II λ4686	28.1±0.5	<2.84	-13.5	>0.13	10±3
				Hα	29.1±0.5	3.01±0.05	-12.5	0.10±0.03	>19
HD 76968	O9.2	Ib	SB1,WVe	both lines	30.8±0.5	3.28±0.05	-12.5±0.1	0.10±0.03	12±6
				He II λ4686	31.9±0.5	>3.43	-12.7	<0.09	>14
				Hα	30.0±0.5	<3.24	-12.3	>0.25	<10
HD 104565	O9.7	Iab/I	MD1	both lines	28.9±0.5	3.00±0.05	-12.2±0.1	0.10±0.03	>14
				He II λ4686	29.0±0.5	<2.98	-12.7	0.12±0.03	>9
				Hα	<29.0	<3.00	-12.1	0.11±0.03	>18
HD 105056	O9.7	Ia e	LPV,WVe	both lines	27.4±0.6	2.86±0.08	-12.0±0.1	0.11±0.03	>16
				He II λ4686	28.0±0.5	2.71±0.05	-12.5	0.23±0.02	<8
				Hα	27.2±0.5	2.84±0.10	-11.9	0.11±0.03	>18
HD 123008	O9.2	Iab/I	WVe,MD2	both lines	31.7±0.5	3.21±0.06	-12.2±0.1	0.19±0.03	>18
				He II λ4686	31.2±0.5	<3.15	-12.7	0.17±0.03	>15
				Hα	31.8±0.5	3.19±0.05	-12.1	0.20±0.02	>18
HD 149038	O9.7	Iab/I	WVe,MD2	both lines	29.8±0.5	3.18±0.05	-12.6±0.1	<0.11	>10
				He II λ4686	29.2±0.5	3.12±0.05	-13.0	0.10±0.03	10±3
				Hα	29.5±0.6	3.15±0.08	-12.5	0.10±0.03	13±6
HD 151804	O8	Ia f	WVa	both lines	<28.2	2.83±0.05	-11.9±0.1	0.10±0.03	>17
				He II λ4686	30.2±0.6	2.84±0.05	-12.3	>0.26	<12
				Hα	<28.1	2.81±0.05	-11.7	0.10±0.03	>17
HD 152147	O9.7	Ib Nwk	SB1	both lines	30.1±0.5	3.24±0.10	-12.6±0.1	<0.08	14±6
				He II λ4686	30.0±0.5	3.22±0.10	-13.0	<0.07	10±3
				Hα	30.0±0.5	3.20±0.05	-12.5	<0.07	11±3
HD 154368	O9.2	Iab/I	WVe,MD2	both lines	30.4±0.5	3.03±0.05	-12.4±0.1	0.14±0.03	>16
				He II λ4686	<29.4	<2.84	-13.0	0.20±0.02	>18
				Hα	30.3±0.5	3.07±0.10	-12.5	0.14±0.03	>18
HD 154811	O9.7	Ib	LPV,WVe	both lines	29.8±0.5	3.18±0.05	-12.7±0.1	0.09±0.03	14±5
				He II λ4686	<29.3	<3.07	-13.5	0.10±0.03	<12
				Hα	29.7±0.5	3.18±0.05	-12.7	0.09±0.03	14±5
HD 163758	O6.5	Ia fp	LPV,WVe	both lines	34.6±0.6	3.28±0.08	-12.3±0.1	0.20±0.03	>15
				He II λ4686	34.8±0.5	3.29±0.05	-12.1	0.16±0.03	>15
				Hα	35.4±0.6	3.31±0.05	-11.9	>0.20	>18
HD 168076 AB	O4	III (f)	LPV	both lines	43.0±1.8	3.92±0.16	-12.5±0.2	<0.09	5.0-19.9
				He II λ4686	42.7±1.2	3.86±0.10	-12.7	<0.09	5.0-19.9
				Hα	46.2±1.7	3.98±0.08	-11.9	0.14±0.04	5.0-19.9
HD 188001	O7.5	Iab/I f	SB1,WVe	both lines	32.4±0.5	3.19±0.09	-12.2±0.1	0.18±0.03	>14
				He II λ4686	34.0±0.5	3.42±0.07	-12.5	0.11±0.03	>14
				Hα	32.4±0.6	3.23±0.07	-12.1	0.11±0.03	>16
HD 188209	O9.5	Iab/I	LPV,WVe	both lines	30.1±0.5	3.03±0.10	-12.5±0.1	0.14±0.03	>19
				He II λ4686	29.1±0.5	<2.85	-13.5	0.21±0.02	>13
				Hα	30.1±0.5	3.03±0.10	-12.5	0.14±0.03	>19
HD 202124	O9	Iab/I	WVe	both lines	31.1±0.5	3.20±0.06	-12.4±0.1	0.11±0.03	>18
				He II λ4686	29.0±0.5	2.80±0.05	-13.0	0.20±0.02	15±3
				Hα	30.2±0.5	3.02±0.05	-12.1	0.15±0.03	>19
HDE 303492	O8.5	Ia f	LPV,WVe	both lines	28.3±1.0	2.86±0.07	-11.9±0.1	0.10±0.03	>17
				He II λ4686	29.1±0.5	2.82±0.05	-12.3	0.19±0.02	>13
				Hα	28.1±0.5	2.80±0.05	-11.7	0.26±0.03	>12
CPD -47 2963 AB	O5	Iab/I fc	LPV	both lines	37.1±0.5	3.51±0.05	-12.3±0.1	0.11±0.03	>8

Table B.3: continued.

Name	SpT LC	Notes	mass-loss diagnostic	$T_{\rm eff}$ [kK]	$\log g$ [dex]	$\log Q$ [dex]	$Y_{\rm He}$ [dex]	ξ_t [km s^{-1}]
			He IIλ4686	37.1±0.5	3.51±0.05	-12.3	0.11±0.03	>8
			Hα	39.1±0.5	3.61±0.05	-12.1	0.11±0.03	>8
HD 24431	O9 III	C	both lines	34.9±0.5	3.77±0.06	-12.9±0.2	<0.07	>18
			Hα	34.9±0.5	3.70±0.05	-13.5	<0.07	15±3
			He IIλ4686	34.9±0.5	3.69±0.05	-12.5	<0.07	>19
HD 34656	O7.5 II (f)	LPV,WVa	both lines	36.0±0.5	3.50±0.05	-12.6±0.1	0.16±0.03	>18
			Hα	36.0±0.5	3.50±0.05	-12.7	0.16±0.03	>18
			He IIλ4686	36.6±0.6	3.56±0.07	-12.3	0.21±0.03	>18
HD 93160 AB	O7 III ((f))	LPV,WVa	both lines	36.6±0.7	3.84±0.10	-12.6±0.1	<0.07	<18
			Hα	37.0±0.5	3.86±0.07	-13.0	<0.07	<9
			He IIλ4686	37.3±0.6	3.84±0.08	-12.5	<0.07	5.0-19.9
HD 96946	O6.5 III (f)	LPV	both lines	39.0±0.5	3.86±0.08	-12.8±0.3	0.11±0.03	<16
			Hα	39.0±0.5	3.89±0.05	-13.0	0.10±0.03	<10
			He IIλ4686	39.2±0.5	3.82±0.06	-12.3	0.11±0.03	>14
HD 114737 AB	O8.5 III	SB1	both lines	35.7±0.5	3.88±0.05	-12.9±0.2	<0.07	>16
			Hα	35.5±0.7	3.81±0.12	-13.5	<0.07	<11
			He IIλ4686	35.7±0.5	3.88±0.05	-13.0	<0.07	>16
HD 152723 AaAb	O6.5 III (f)	SB1,WVa	both lines	38.0±0.5	3.81±0.05	-12.7±0.1	<0.07	>16
			Hα	38.4±0.6	3.83±0.07	-13.0	<0.07	<13
			He IIλ4686	39.0±0.5	3.71±0.05	-12.3	0.10±0.03	>9
HD 156738 AB	O6.5 III (f)	MD1	both lines	37.9±1.1	3.83±0.16	-12.8±0.2	<0.08	>7
			Hα	37.4±1.0	3.79±0.15	-13.0	<0.08	<16
			He IIλ4686	38.0±1.5	3.75±0.20	-12.5	<0.12	5.0-19.9
HD 162978	O8 II ((f))	WVa	both lines	35.0±0.5	3.50±0.05	-12.7±0.1	0.10±0.03	>16
			Hα	34.9±0.5	3.50±0.05	-13.0	0.10±0.03	13±4
			He IIλ4686	34.2±0.5	3.42±0.05	-12.7	0.10±0.03	>16
HD 209975	O9 Ib	LPV,WVa	both lines	32.0±0.5	3.30±0.05	-12.7±0.1	0.10±0.03	15±3
			Hα	32.0±0.5	3.30±0.05	-12.7	0.10±0.03	15±3
			He IIλ4686	32.0±0.5	3.30±0.05	-12.5	0.10±0.03	15±3
HD 218915	O9.2 Iab/I	WVe	both lines	31.1±0.5	3.21±0.05	-12.6±0.1	0.10±0.03	>19
			Hα	31.0±0.5	3.20±0.05	-12.7	0.10±0.03	>19
			He IIλ4686	30.3±0.5	<3.07	-12.3	0.10±0.03	>19
CYG OB2-11	O5.5 Iab/I fc	C	both lines	37.3±1.5	3.63±0.15	-12.3±0.1	0.11±0.03	5.0-19.9
			Hα	39.7±0.9	>3.73	-12.1	0.12±0.03	5.0-19.9
			He IIλ4686	>39.6	>3.59	-11.9	>0.15	>12

Table B.4: Spectroscopic parameters for the sample of O-type standard stars, presented in Holgado et al. (2018). The last columns of the table also include information about the quality of the best fitting model resulting from the IACOB-GBAT/FASTWIND analysis and about detected spectroscopic binarity/variability.

Columns include: Name, spectral type and luminosity classification, projected rotational velocity and macroturbulence used in the analysis, effective temperature, gravity, rotational corrected gravity, helium abundance, microturbulence and wind strength parameter, derived from spectra. Errors are the maximum between half of the step in the grid and the formal error from the IACOB-GBAT results. As noted in Appendix A.5 the log Q is affected by an additional uncertainty of up to 0.15 dex, due to the adopted v_∞ scaling, that it is not included here. Finally, this table provides the quality flag (Sect. 5.4), and multi-epoch annotation from this work (Sect. 4.3) and the OWN project (priv comm.).

Name	SpT	LC	$v \sin i$ [km s^{-1}]	$v_{\rm mac}$ [km s^{-1}]	$T_{\rm eff}$ [kK]	$\log g$ [dex]	$\log g_{\rm true}$ [dex]	$Y_{\rm He}$ [dex]	ξ_t [km s^{-1}]	$\log Q$ [dex]	qual. flag	Notes	OWN Notes
HD 93129 AaAb	O2	I f*	116	142	*45.6±1.1*	*3.88±0.10*	*3.89±0.10*	*0.1±0.03*	*5.0-19.9*	*-12.0±0.1*	Q4	SB1	VAR
CYG OB2-7	O3	I f*	75	126	*50.3±1.8*	*4.09±0.14*	*4.09±0.13*	*>0.14*	*5.0-19.9*	*-12.1±0.1*	Q4	C	.
HD 190429 A	O4	I f	90	113	36.6±0.8	3.52±0.10	3.53±0.09	0.17±0.04	<10	-12.1±0.1	Q1	WVe	.
HD 15570	O4	I f	81	115	*40.2±0.8*	*3.63±0.07*	*3.63±0.06*	*0.1±0.03*	*>13*	*-11.9±0.1*	Q4	C	.
HD 16691	O4	I f	158	88	*>39.7*	*>3.72*	*>3.74*	*0.21±0.07*	*5.0-19.9*	*>-12.1*	Q4	LPV	.
HD 14947	O4.5	I f	114	22	39.1±1.1	3.64±0.11	3.65±0.10	0.15±0.04	5.0-19.9	-12.0±0.1	Q3	LPV, WVe	.
CYG OB2-9	O4.5	I f	112	82	*40.1±1.0*	*3.91±0.10*	*3.92±0.10*	*0.11±0.03*	*5.0-19.9*	*-12.2±0.1*	Q4	C	.
CPD -47 2963 AB	O5	I f c	67	110	37.1±0.5	3.51±0.05	3.51±0.04	0.11±0.03	>8	-12.3±0.1	Q3	LPV	.
CYG OB2-11	O5.5	I f c	75	85	37.3±1.5	3.63±0.15	3.63±0.14	0.11±0.03	5.0-19.9	-12.3±0.1	Q3	C	.
HD 169582	O6	Ia f	66	97	38.9±1.3	3.70±0.22	3.70±0.21	0.23±0.07	>13	-12.3±0.2	Q1	MD2	VAR
HDE 229196	O6	II (f)	248	25	36.8±1.0	3.50±0.11	3.60±0.08	0.1±0.03	<8	-12.4±0.1	Q1	SB2	.
HD 163758	O6.5	Ia fp	76	87	34.6±0.6	3.28±0.08	3.29±0.07	0.2±0.03	>15	-12.3±0.1	Q3	LPV, WVe	VAR
HD 157857	O6.5	II (f)	114	69	36.7±0.7	3.58±0.08	3.60±0.08	0.13±0.03	>15	-12.4±0.1	Q1	WVa	VAR?
HD 69464	O7	Ib (f)	73	105	35.8±1.0	3.37±0.09	3.38±0.08	0.16±0.03	>16	-12.4±0.1	Q2	LPV, WVa	SB1
HD 193514	O7	Ib (f)	73	84	35.9±0.5	3.58±0.05	3.58±0.04	0.1±0.03	>18	-12.4±0.1	Q2	WVa	.
HD 94963	O7	II (f)	76	92	36.3±0.6	3.54±0.07	3.54±0.06	0.1±0.03	>16	-12.6±0.2	Q2	WVa	C
HD 151515	O7	II (f)	67	98	36.0±1.0	3.55±0.14	3.55±0.13	0.13±0.04	>17	-12.6±0.1	Q1	MD2	C
HD 188001	O7.5	Iab f	69	100	32.4±0.5	3.19±0.09	3.20±0.09	0.17±0.03	>14	-12.2±0.1	Q3	SB1, WVe	.
HD 192639	O7.5	Iab f	82	95	34.7±0.7	3.42±0.12	3.43±0.11	0.14±0.03	>14	-12.4±0.1	Q2	WVe	.
HD 156154	O7.5	Ib (f)	62	102	34.2±0.5	3.31±0.05	3.31±0.04	0.16±0.03	>17	-12.5±0.1	Q2	LPV, WVa	VAR
HD 17603	O7.5	Ib (f)	103	108	33.3±0.8	3.24±0.09	3.26±0.08	0.15±0.03	>18	-12.4±0.1	Q2	SB1	.
HD 171589	O7.5	II (f)	100	86	36.5±0.8	3.65±0.07	3.66±0.06	0.15±0.03	>15	-12.6±0.1	Q1	LPV, WVa	.
HD 34656	O7.5	II (f)	67	77	36.0±0.5	3.50±0.05	3.50±0.04	0.16±0.03	>18	-12.6±0.1	Q3	LPV, WVa	.
HD 151804	O8	Ia f	72	73	<28.2	2.83±0.05	2.86±0.05	0.1±0.03	>17	-11.9±0.1	Q3	WVa	VAR
HD 225160	O8	Iab f	77	103	33.2±1.2	3.34±0.15	3.35±0.14	0.13±0.03	>10	-12.2±0.1	Q2	WVe	.
BD -11 4586	O8	Ib (f)	74	68	32.4±0.6	3.21±0.11	3.22±0.10	0.17±0.04	>16	-12.4±0.1	Q2	LPV, WVe	C
HD 162978	O8	II ((f))	54	86	35.0±0.5	3.50±0.05	3.50±0.04	0.1±0.03	>16	-12.7±0.1	Q3	WVa	VAR
HDE 303492	O8.5	Ia f	87	55	28.3±1.0	2.86±0.07	2.91±0.06	0.1±0.03	>17	-11.9±0.1	Q3	LPV, WVe	VAR?
HD 125241	O8.5	Ib (f)	118	95	32.1±0.5	3.21±0.05	3.24±0.04	0.15±0.03	15±4	-12.1±0.1	Q2	LPV, WVe	VAR?

Notes: C:Constant, LPV:Line profile variability, WV:Wind variable. $g_{true} = g + g_{cent}$, $g_{cent} \approx \frac{(V_{rot} \sin i)^2}{R_*}$
For the Q4 stars the results in italics are not reliable (See Sect. 5.4).

Table B.4: continued.

Name	SpT LC	$v \sin i$ [km s^{-1}]	$v_{\rm mac}$ [km s^{-1}]	$T_{\rm eff}$ [kK]	$\log g$ [dex]	$\log g_{\rm true}$ [dex]	$Y_{\rm He}$ [dex]	ξ_t [km s^{-1}]	$\log Q$ [dex]	qual. flag	Notes	OWN Notes
HD 75211	O8.5 II ((f))	145	53	33.4±0.6	3.35±0.07	3.40±0.06	0.11±0.03	>15	-12.5±0.1	Q2	SB1,WVa	SB1
HD 207198	O8.5 II ((f))	52	97	33.1±0.5	3.31±0.05	3.31±0.04	0.15±0.03	>13	-12.7±0.1	Q1	LPV,WVa	.
HD 30614	O9 Ia	113	77	29.4±0.6	2.94±0.08	3.00±0.07	0.12±0.05	>18	-12.3±0.1	Q2	SB1,WVe	.
HD 152249	OC9 Iab	71	70	31.1±0.5	3.20±0.05	3.21±0.04	0.1±0.03	>11	-12.5±0.1	Q2	LPV,WVe	VAR?
HD 202124	O9 Iab	88	114	31.1±0.5	3.20±0.06	3.22±0.06	0.11±0.03	>18	-12.4±0.1	Q3	WVe	.
HD 210809	O9 Iab	70	105	30.9±0.5	3.11±0.06	3.12±0.05	0.12±0.03	>18	-12.4±0.1	Q2	LPV,WVe	.
HD 209975	O9 Ib	50	104	32.0±0.5	3.30±0.05	3.30±0.04	0.1±0.03	15±3	-12.7±0.1	Q3	LPV,WVa	C
HD 71304	O9 II	52	100	32.0±0.5	3.30±0.05	3.30±0.04	0.11±0.03	>17	-12.7±0.1	Q1	C,MD2	C
HD 57061 AaAb	O9 II	57	85	33.0±0.5	3.50±0.05	3.50±0.04	<0.07	13±6	-12.7±0.1	Q1	SB2,WVe	.
HD 152424	OC9.2 Ia	59	66	30.2±0.5	3.16±0.07	3.17±0.06	<0.07	>17	-12.3±0.1	Q2	SB1	.
HD 218915	O9.2 Iab	63	88	31.1±0.5	3.21±0.05	3.22±0.04	0.1±0.03	>19	-12.6±0.1	Q3	WVe	C
HD 154368	O9.2 Iab	65	78	30.4±0.5	3.03±0.05	3.04±0.04	0.14±0.03	>16	-12.4±0.1	Q3	WVe	C
HD 123008	ON9.2 Iab	62	94	31.7±0.5	3.21±0.06	3.22±0.05	0.19±0.03	>18	-12.2±0.1	Q3	WVe,MD2	C
HD 76968	O9.2 Ib	53	65	30.8±0.5	3.28±0.05	3.28±0.04	0.1±0.03	12±6	-12.5±0.1	Q3	SB1,WVe	SB1
HD 188209	O9.5 Iab	54	93	30.1±0.5	3.03±0.10	3.04±0.09	0.14±0.03	>19	-12.5±0.1	Q3	LPV,WVe	.
HD 36486 AaAb	O9.5 II Nwk	100	94	30.1±0.5	3.31±0.05	3.33±0.04	0.1±0.03	<7	-12.9±0.2	Q1	SB1	B
HD 105056	ON9.7 Ia e	56	46	27.4±0.6	2.86±0.08	2.88±0.08	0.11±0.03	>16	-12.0±0.1	Q3	LPV,WVe	.
HD 195592	O9.7 Ia	38	100	28.0±0.5	2.91±0.05	2.91±0.04	0.12±0.03	>16	-12.1±0.1	Q2	MD2	.
HD 149038	O9.7 Iab	52	90	29.8±0.5	3.18±0.05	3.18±0.04	<0.11	>10	-12.6±0.1	Q3	WVe	C
HD 225146	O9.7 Iab	67	88	28.3±0.6	3.10±0.10	3.11±0.09	>0.1	14±4	-12.6±0.1	Q1	LPV,WVe	.
HD 104565	OC9.7 Iab	56	116	28.9±0.5	3.00±0.05	3.01±0.04	0.1±0.03	>14	-12.2±0.1	Q3	MD1	VAR?
HD 191781	ON9.7 Iab	105	48	28.7±2.0	<3.37	<3.39	<0.16	>9	-12.4±0.2	Q1	MD1	.
HD 154811	OC9.7 Ib	124	62	29.8±0.5	3.18±0.05	3.22±0.04	0.09±0.03	14±5	-12.7±0.1	Q3	LPV,WVe	C
HD 152147	O9.7 Ib Nwk	91	64	30.1±0.5	3.24±0.10	3.26±0.09	<0.08	14±6	-12.6±0.1	Q3	SB1	.
HD 47432	O9.7 Ib	97	63	29.1±0.5	3.01±0.05	3.04±0.04	0.1±0.03	>19	-12.5±0.1	Q3	LPV,WVe	.
HD 68450	O9.7 II	39	77	30.6±0.9	3.31±0.14	3.31±0.13	<0.12	>12	-13.0±0.2	Q1	C	C
HD 10125	O9.7 II	122	125	30.9±0.5	3.38±0.06	3.41±0.05	0.11±0.03	>16	-12.7±0.1	Q3	SB1	.
HD 152405	O9.7 II	59	61	30.3±0.5	3.28±0.10	3.29±0.09	0.1±0.03	8±3	-12.9±0.2	Q1	SB1	.
HD 93250 AB	O4 IV (fc)	70	84	45.0±0.6	3.86±0.06	3.86±0.05	0.11±0.03	>13	-12.5±0.2	Q1	WVa	C
HD 168076 AB	O4 IV (f)	68	101	43.0±1.8	3.92±0.16	3.92±0.15	<0.09	5.0-19.9	-12.5±0.2	Q3	LPV	C
HD 93843	O5 III (fc)	58	120	37.3±0.6	3.53±0.06	3.53±0.05	0.12±0.03	>16	-12.5±0.1	Q2	WVa	C
HD 168112 AB	O5 IV (f)	107	78	39.7±1.0	3.70±0.14	3.71±0.13	0.11±0.03	>13	-12.5±0.2	Q1	SB1	.
HD 152723 AaAb	O6.5 III (f)	73	100	38.0±0.5	3.81±0.05	3.81±0.04	<0.07	>16	-12.7±0.1	Q3	SB1,WVa	.
HD 96946	O6.5 III (f)	72	58	39.0±0.5	3.86±0.08	3.86±0.07	0.11±0.03	<16	-12.8±0.3	Q3	LPV	.
HD 156738 AB	O6.5 III (f)	65	103	37.9±1.1	3.83±0.16	3.83±0.15	<0.08	>7	-12.8±0.2	Q3	MD2	C
HD 190864	O6.5 III (f)	66	90	37.5±0.9	3.64±0.09	3.64±0.08	0.12±0.03	>13	-12.7±0.1	Q1	C	.
HD 93160 AB	O7 III ((f))	120	64	36.6±0.7	3.84±0.10	3.85±0.09	<0.07	<18	-12.6±0.1	Q3	LPV,WVa	VAR
CYG OB2-4 A	O7 III ((f))	72	105	36.4±1.7	3.52±0.16	3.53±0.15	0.14±0.06	>16	-12.8±0.3	Q1	C	.
HD 163800	O7.5 III ((f))	53	107	35.2±0.5	3.42±0.05	3.42±0.04	0.1±0.03	>18	-12.9±0.2	Q1	LPV	VAR?

Notes: C:Constant, LPV:Line profile variability, WV:Wind variable. $g_{true} = g + g_{cent}$, $g_{cent} \approx \frac{(V_{rot} \sin i)^2}{R_*}$
For the Q4 stars the results in italics are not reliable (See Sect. 5.4).

Table B.4: continued.

Name	SpT LC	$v \sin i$ [km s^{-1}]	$v_{\rm mac}$ [km s^{-1}]	$T_{\rm eff}$ [kK]	$\log g$ [dex]	$\log g_{\rm true}$ [dex]	$Y_{\rm He}$ [dex]	ξ_t [km s^{-1}]	$\log Q$ [dex]	qual. flag	Notes	OWN Notes
HDE 319702	O8 III	66	50	36.3±0.7	3.96±0.15	3.96±0.14	<0.08	<13	-12.9±0.2	Q1	SB2	.
HD 36861 A	O8 III((f))	52	77	35.2±0.5	3.52±0.05	3.52±0.04	0.1±0.03	>11	-13.0±0.2	Q1	C	. .
HD 114737 AB	O8.5 III	58	83	35.7±0.5	3.88±0.05	3.88±0.04	<0.07	>16	-12.9±0.2	Q3	SB1	. .
HD 218195 A	O8.5 III Nstr	44	78	34.1±0.5	3.53±0.10	3.53±0.09	0.11±0.03	>18	-13.0±0.2	Q1	LPV	. .
HD 93249 A	O9 III	55	72	32.8±0.5	3.50±0.09	3.50±0.08	0.1±0.03	<10	-13.1±0.2	Q1	SB2	SB2
HD 24431	O9 III	49	81	34.9±0.5	3.77±0.06	3.77±0.05	<0.07	>18	-12.9±0.2	Q3	C	. .
HD 193443 AB	O9 III	66	140	33.0±0.5	3.50±0.05	3.51±0.04	<0.07	>17	-13.0±0.2	Q1	LPV	. .
HD 16832	O9.2 III	45	70	32.0±0.5	3.37±0.06	3.37±0.05	0.1±0.03	15±3	-12.9±0.2	Q1	C,MD2	. .
HD 96264	O9.5 III	29	65	33.1±1.0	3.67±0.16	3.67±0.15	<0.07	<7	-13.0±0.2	Q1	SB2	SB2
HD 154643	O9.7 III	101	78	31.0±0.5	3.49±0.05	3.51±0.04	0.1±0.03	9±3	-13.2±0.2	Q1	SB1	. .
HD 189957	O9.7 III	88	54	32.1±0.5	3.57±0.07	3.58±0.06	<0.07	15±3	-13.0±0.2	Q1	C	. .
HD 64568	O3 V ((f*))z	75	53	*46.9±1.0*	*3.93±0.07*	*3.93±0.06*	*0.1±0.03*	*5.0-19.9*	*-12.8±0.3*	Q4	C	C
HD 93128	O3.5 V ((fc))z	58	56	*49.3±2.2*	*4.09±0.17*	*4.09±0.16*	*0.1±0.03*	*> 10*	*-12.7±0.2*	Q4	C,MD2	C
HD 46223	O4 V ((f))	51	112	42.2±0.5	3.73±0.05	3.73±0.04	0.1±0.03	>9	-12.7±0.2	Q1	LPV	VAR
HD 96715	O4 V ((f))z	59	86	45.2±1.2	3.91±0.13	3.91±0.12	0.13±0.04	>9	-12.8±0.3	Q1	MD2	C
HD 15629	O4.5 V ((fc))	76	64	41.8±0.5	3.79±0.06	3.79±0.05	0.1±0.03	>16	-12.7±0.1	Q1	LPV	.
HDE 303308 AB	O4.5 V ((fc))	85	67	41.1±0.9	3.90±0.09	3.90±0.08	<0.07	<17	-12.7±0.2	Q1	LPV	C
HDE 319699	O5 V ((fc))	69	76	41.2±0.8	3.91±0.08	3.91±0.07	0.1±0.03	<16	-12.7±0.2	Q1	SB1	.
HD 46150	O5 V ((f))z	60	112	41.1±0.5	3.81±0.05	3.81±0.04	0.1±0.03	<12	-13.1±0.2	Q1	LPV	VAR
HD 93204	O5.5 V ((f))	110	93	39.2±0.7	3.73±0.06	3.75±0.06	0.1±0.03	12±6	-12.7±0.2	Q1	C	C
HD 101190 AaAb	O6 IV ((f))	49	74	39.8±0.5	3.88±0.05	3.88±0.04	0.1±0.03	<15	-12.9±0.2	Q1	SB1	SB1
HDE 303311	O6 V ((f))z	47	61	40.1±0.7	3.91±0.07	3.91±0.06	0.11±0.03	>8	-13.0±0.2	Q1	MD1	C
CPD -59 2600	O6 V ((f))z	127	106	39.3±0.8	3.84±0.09	3.86±0.08	<0.07	<18	-12.8±0.2	Q1	SB1	SB1
HD 42088	O6 V ((f))z	49	76	40.0±0.5	3.99±0.05	3.99±0.04	0.1±0.03	12±4	<-13.2	Q1	C	. .
HDE 322417	O6.5 V ((f))z	68	100	38.6±0.8	3.74±0.11	3.74±0.10	0.1±0.03	>5	-12.7±0.2	Q1	LPV	. .
HD 91572	O6.5 V ((f))z	60	57	38.8±0.5	3.84±0.09	3.84±0.08	0.09±0.03	<16	-12.9±0.2	Q1	LPV	VAR
HD 167633	O6.5 V ((f))	129	106	38.0±0.8	3.69±0.08	3.72±0.07	0.16±0.03	<15	-12.9±0.2	Q1	SB1	VAR
HD 12993	O6.5 V ((f))_Nstr	84	79	39.2±0.6	3.89±0.08	3.89±0.07	0.16±0.03	14±5	-13.2±0.3	Q1	C	.
HD 93222 AB	O7 V ((f))z	50	90	36.8±0.7	3.63±0.12	3.63±0.11	0.11±0.03	>12	-12.9±0.2	Q1	WVa	C
HD 91824	O7 V ((f))z	51	48	39.8±0.9	4.02±0.14	4.02±0.13	0.1±0.03	5.0-19.9	-12.9±0.2	Q1	SB1	SB1
HD 93146 A	O7 V ((f))	60	67	38.7±0.6	3.84±0.08	3.84±0.07	0.09±0.03	<14	-12.9±0.2	Q1	SB1	SB1
HDE 242926	O7 V z	89	52	39.0±0.7	4.07±0.12	4.07±0.11	0.09±0.03	<8	-13.4±0.4	Q1	MD2,LPV	. .
HD 152590	O7.5 V z	48	56	38.0±0.5	3.92±0.08	3.92±0.07	0.1±0.03	12±6	-13.4±0.4	Q1	SB1	. .
HD 35619	O7.5 V ((f))	40	60	37.7±0.6	3.94±0.13	3.94±0.12	<0.07	15±3	-13.0±0.2	Q1	LPV	. .
HD 135591	O8 IV ((f))	60	60	35.0±0.5	3.58±0.05	3.58±0.04	0.1±0.03	<8	-13.0±0.2	Q1	C	C
HD 94024	O8 IV	162	52	34.8±0.5	3.49±0.06	3.56±0.05	0.11±0.03	>18	-12.8±0.2	Q1	SB1	SB1
HD 97848	O8 V	41	77	35.6±0.6	3.67±0.07	3.67±0.06	0.1±0.03	<15	-13.3±0.4	Q1	LPV,MD2	C
HD 101223	O8 V	55	63	35.2±0.5	3.62±0.05	3.62±0.05	0.1±0.03	<12	-13.0±0.2	Q1	C	C
HD 191978	O8 V	57	82	35.8±0.6	3.81±0.09	3.81±0.08	0.1±0.03	11±5	<-13.0	Q1	C	.

Notes: C:Constant, LPV:Line profile variability, WV:Wind variable. $g_{true} = g + g_{cent}$, $g_{cent} \approx \frac{(V_{rot} \sin i)^2}{R_*}$
For the Q4 stars the results in italics are not reliable (See Sect. 5.4).

Table B.4: continued.

Name	SpT	LC	$v \sin i$ [km s^{-1}]	$v_{\rm mac}$ [km s^{-1}]	$T_{\rm eff}$ [kK]	$\log g$ [dex]	$\log g_{\rm true}$ [dex]	$Y_{\rm He}$ [dex]	ξ_t [km s^{-1}]	$\log Q$ [dex]	qual. flag	Notes	OWN Notes
HD 46966	O8.5	IV	40	66	35.9±0.5	3.84±0.08	3.84±0.07	0.1±0.03	10±3	-13.0±0.2	Q1	C	.
HDE 298429	O8.5	V	105	80	33.6±1.1	3.51±0.15	3.55±0.14	0.13±0.05	>8	-13.3±0.4	Q1	MD1	C
HD 46149	O8.5	V	30	49	36.9±0.5	4.23±0.09	4.23±0.08	0.09±0.03	<8	<-13.0	Q1	LPV	.
Trumpler 14-9	O8.5	V	66	41	36.7±0.7	4.10±0.11	4.10±0.11	0.11±0.03	<14	-13.0±0.3	Q1	C,MD2	.
HD 57236	O8.5	V	29	62	37.3±1.0	>3.94	>3.94	<0.09	<14	<-12.9	Q1	SB2	VAR
HD 14633 AaAb	ON8.5	V	121	69	35.0±0.5	3.76±0.09	3.79±0.08	0.15±0.03	10±3	-13.4±0.4	Q1	SB1	.
HD 93028	O9	IV	25	55	35.3±0.7	3.93±0.09	3.93±0.08	<0.12	<15	-13.3±0.4	Q1	SB1	SB1
CPD–41 7733	O9	IV	56	71	34.2±0.5	3.65±0.07	3.66±0.07	<0.07	15±3	-13.0±0.2	Q1	SB2	.
CPD–59 2551	O9	V	124	92	34.9±0.5	3.89±0.05	3.91±0.05	0.1±0.03	16±3	<-13.3	Q1	C,MD2	.
HD 214680	O9	V	14	43	35.2±0.5	3.89±0.05	3.89±0.04	0.1±0.03	<12	<-13.5	Q1	C	.
HD 216898	O9	V	44	57	35.9±0.6	4.18±0.12	4.18±0.11	0.1±0.03	<10	<-13.0	Q1	SB1	.
HD 96622	O9.2	IV	39	61	33.3±0.6	3.68±0.12	3.68±0.11	0.1±0.03	<8	-13.3±0.3	Q1	SB1	SB1
HD 46202	O9.2	V	11	38	34.9±0.5	4.13±0.08	4.13±0.07	0.1±0.03	<7	<-13.1	Q1	C	.
HD 12323	ON9.2	V	121	82	34.2±0.9	3.93±0.20	3.95±0.18	0.19±0.05	<16	<-13.3	Q1	SB1,MD2	.
HD 93027	O9.5	IV	46	66	33.8±0.5	3.95±0.08	3.95±0.07	0.1±0.03	<9	-13.4±0.4	Q1	C,MD2	C
HD 192001	O9.5	IV	44	57	33.0±0.5	3.83±0.06	3.83±0.05	0.1±0.03	<7	<-13.1	Q1	LPV	.
HD 155889 AB	O9.5	IV	27	51	34.9±0.7	4.10±0.08	4.10±0.07	<0.09	<12	-13.3±0.3	Q1	LPV	VAR?
HD 38666	O9.5	V	111	56	33.9±0.5	3.90±0.05	3.92±0.04	0.11±0.03	<12	<-13.0	Q1	C	C
HD 34078	O9.5	V	13	32	34.5±0.8	4.07±0.15	4.07±0.14	0.12±0.03	<16	<-13.0	Q1	C	.
HD 207538	O9.7	IV	29	50	32.0±0.5	3.80±0.05	3.80±0.04	0.1±0.03	10±3	<-13.6	Q1	C	.
HD 36512	O9.7	V	13	33	33.0±0.5	4.02±0.10	4.02±0.09	0.1±0.03	<7	<-13.4	Q1	C	.

Notes: C:Constant, LPV:Line profile variability, WV:Wind variable. $g_{true} = g + g_{cent}$, $g_{cent} \approx \frac{(V_{rot} \sin i)^2}{R_*}$
For the Q4 stars the results in italics are not reliable (See Sect. 5.4).

Table B.5: Spectroscopic parameters for the bulk of the sample, excluding the standards stars. The last columns of the table also include information about the quality of the best fitting model resulting from the IACOB-GBAT/FASTWIND analysis and about detected spectroscopic binarity/variability.

The stars are separated in two groups. The first part of the table includes those stars for which the analysis has been successful for both the line-broadening and the spectroscopic fit (see Sect. 5.4). The second part includes 13 peculiar stars (Oe, and Mag). They have reliable values of $v \sin i$ and *macroturbulence* but the spectroscopic fit was not possible. Columns include: Name, spectral type and luminosity classification, projected rotational velocity and macroturbulence used in the analysis, effective temperature, gravity, rotational corrected gravity, helium abundance, microturbulence and wind strength parameter, derived from spectra. Errors are the maximum between half of the step in the grid and the formal error from the IACOB-GBAT results. As noted in Appendix A.5 the log Q is affected by an additional uncertainty of up to 0.15 dex, due to the adopted v_∞ scaling, that it is not included here. Finally, this table provides the quality flag (Sect. 5.4), and multi-epoch annotation from this work (Sect. 5.3) and the OWN project (priv comm.).

Name	SpT	LC	$v \sin i$ [km s^{-1}]	$v_{\rm mac}$ [km s^{-1}]	$T_{\rm eff}$ [kK]	log g [dex]	log $g_{\rm true}$ [dex]	$Y_{\rm He}$ [dex]	ξ_t [km s^{-1}]	log Q [dex]	qual. flag	Notes	OWN Notes
ALS 15210	O3.5 If*_Nwk		98	4	42.4±1.6	3.68±0.05	3.69±0.05	0.1±0.03	>10	-12.2±0.1	Q4	MD1	.
HD 93632	O5 If_var		86	47	40.0±0.5	3.90±0.20	3.90±0.19	0.09±0.03	>13	-12.3±0.1	Q3	C	C
HD 14442	O5 ...n(f)p		324	45	39.1±1.3	3.62±0.13	..	0.15±0.05	5.0-19.9	-12.4±0.1	Q2	MD1	.
HD 152233	O6 II(f)		62	105	37.8±0.5	3.69±0.05	3.69±0.04	0.1±0.03	>16	-12.5±0.1	Q3	SB1	.
CPD -26 2716	O6.5 Iabf		139	138	36.0±0.5	3.48±0.07	3.51±0.06	0.15±0.03	>18	-12.2±0.1	Q3	LPV	VAR
HD 172175	O6.5 I(n)fp		237	69	36.2±0.5	3.51±0.06	3.58±0.05	0.16±0.03	>17	-12.4±0.1	Q2	MD1	VAR
HD 210839	O6.5 I(n)fp		214	146	35.8±0.5	3.39±0.06	3.47±0.04	0.15±0.03	>17	-12.2±0.1	Q2	LPV	.
BD +60 2522	O6.5 ...(n)fp		247	62	36.2±1.1	3.55±0.14	..	0.11±0.03	>17	-12.3±0.2	Q2	LPV	.
BD -13 4927	O7 II(f)		98	78	36.0±0.5	3.50±0.06	3.51±0.05	0.1±0.03	>18	-12.6±0.1	Q2	LPV,WVa	C
HD 94370	O7 ...(n)fp		182	91	35.1±0.5	3.43±0.06	..	0.1±0.03	>18	-12.5±0.1	Q2	LPV	.
HD 120521	O7.5 Ib(f)		100	95	34.6±0.6	3.37±0.08	3.39±0.07	0.15±0.03	>15	-12.4±0.1	Q3	LPV,WVe,MD2	VAR?
HD 117797	O7.5 ...fp		150	80	33.8±1.1	3.33±0.09	..	0.11±0.03	>16	-12.2±0.1	Q2	LPV,WVe	VAR
HD 175754	O8 II(n)(((f))p		182	121	34.2±0.5	3.31±0.05	3.39±0.04	0.15±0.03	>18	-12.4±0.1	Q2	LPV	VAR
HD 96917	O8 Ib(n)(f)		165	77	32.0±0.5	3.12±0.05	3.20±0.04	0.15±0.03	>19	-12.3±0.1	Q2	LPV,WVe	.
BD +39 1328	O8.5 Iab(n)(f)		90	37	32.8±0.6	3.41±0.10	3.42±0.09	0.1±0.03	15±4	-12.5±0.1	Q3	MD1	.
HD 112244	O8.5 Iab(f)p		124	80	31.5±0.7	3.19±0.13	3.23±0.11	0.11±0.03	>14	-12.3±0.1	Q2	SB1,WVe	.
HD 74194	O8.5 Ib-II(f)p		184	49	32.2±0.5	3.27±0.06	3.36±0.04	0.11±0.03	>17	-12.4±0.1	Q2	SB1,WVe	SB1
HD 148546	O9 Iab		85	95	32.0±0.5	3.29±0.05	3.30±0.04	0.12±0.03	>15	-12.3±0.1	Q3	LPV,WVe	VAR
HD 151018	O9 Ib		67	65	32.0±0.5	3.30±0.05	3.31±0.04	0.15±0.03	12±5	-12.5±0.1	Q3	MD1,WVe	C
HD 155756	O9 Ib_p		62	99	32.0±0.5	3.29±0.05	3.29±0.04	0.1±0.03	>18	-12.5±0.1	Q3	MD2,WVe	C
HD 173783	O9 Iab		89	90	31.2±0.5	3.06±0.10	3.09±0.09	0.2±0.04	13±5	-12.6±0.2	Q3	MD1	C
HD 237211	O9 Ib		51	82	30.7±0.6	3.09±0.08	3.09±0.07	0.13±0.03	>18	-12.6±0.1	Q1	LPV	.
CPD-59 5634	O9.2 Ib		48	102	31.8±0.5	3.28±0.05	3.28±0.04	0.1±0.03	>18	-12.7±0.1	Q1	MD2,WVa	C
HD 101545 AaAb	O9.2 II		44	79	31.9±0.5	3.37±0.07	3.37±0.06	<0.08	>15	-12.7±0.1	Q3	LPV,MD1	VAR
HD 37742	O9.2 Ib Nwk_var		122	97	30.1±0.5	3.11±0.05	3.15±0.04	0.1±0.03	16±3	-12.5±0.2	Q3	SB1,WVe,Mag	C
HD 167264	O9.7 Iab		71	69	28.8±0.9	3.13±0.14	3.14±0.13	<0.12	>12	-12.6±0.1	Q1	SB1,WVa	.
HD 13745	O9.7 II(n)		197	57	30.0±0.5	3.16±0.08	3.29±0.05	0.11±0.03	>17	-12.8±0.3	Q2	LPV	.
HD 152003	O9.7 Iab Nwk		65	83	30.1±0.5	3.17±0.07	3.18±0.06	0.1±0.03	15±3	-12.5±0.1	Q3	MD2	C

Notes: C:Constant, LPV:Line profile variability, WV:Wind variable. $g_{true} = g + g_{cent}$, $g_{cent} \approx \frac{(V_{rot} \sin i)^2}{R_*}$

Table B.5: continued.

Name	SpT LC	$v \sin i$ [km s^{-1}]	$v_{\rm mac}$ [km s^{-1}]	$T_{\rm eff}$ [kK]	$\log g$ [dex]	$\log g_{\rm true}$ [dex]	$Y_{\rm He}$ [dex]	ξ_t [km s^{-1}]	$\log Q$ [dex]	qual. flag	Notes	OWN Notes
HD 173010	O9.7 Ia+ var	61	88	27.9±0.5	2.98±0.05	2.99±0.04	0.1±0.03	<12	-11.9±0.1	Q3	LPV,MD2	C
HD 18409	O9.7 Ib	131	102	30.0±0.5	3.10±0.05	3.15±0.04	0.11±0.03	>17	-12.7±0.1	Q1	LPV	.
HD 75222	O9.7 Iab	86	65	30.2±0.5	3.20±0.06	3.22±0.05	0.12±0.03	>14	-12.5±0.1	Q3	LPV,WVe	VAR?
HD 305619	O9.7 II	48	94	31.0±0.5	3.29±0.05	3.29±0.04	0.11±0.03	15±3	-12.7±0.1	Q3	MD1	C
HD 28446A	O9.7 II n	299	0	29.8±0.5	3.52±0.08	3.65±0.05	0.09±0.03	14±5	<-13.2	Q1	C	.
HD 89137	ON9.7 II (n)	238	33	29.1±0.5	3.21±0.05	3.37±0.03	0.16±0.03	14±3	-12.8±0.2	Q2	C	C
HD 165174	O9.7 II n	264	175	30.2±0.8	3.28±0.13	3.45±0.08	0.15±0.05	>13	<-12.7	Q2	SB1	.
HD 97253	O5 III (f)	70	105	39.1±0.5	3.60±0.05	3.60±0.04	0.1±0.03	>15	-12.3±0.1	Q3	LPV,WVa,MD2	C
HDE 338 931	O6 III (f)	170	9	38.1±0.6	3.72±0.10	3.76±0.09	0.12±0.03	>15	-12.5±0.1	Q2	MD1	.
HD 130298	O6.5 III (n)(f)	167	85	38.2±0.6	3.65±0.07	3.69±0.06	0.18±0.04	>16	-12.7±0.1	Q1	SB1	.
HD 175876	O6.5 III (n)(f)	282	70	36.1±0.6	3.43±0.06	3.59±0.04	0.13±0.03	>18	-12.6±0.1	Q2	LPV	VAR
HD 167659	O7 II-III (f)	71	84	37.0±0.5	3.60±0.05	3.60±0.04	0.1±0.03	>19	-12.7±0.1	Q3	C	VAR?
BD +60 261	O7.5 III (n)((f))	162	92	35.0±0.5	3.44±0.07	3.50±0.06	0.1±0.03	>18	-12.6±0.1	Q2	LPV	.
HD 186980	O7.5 III ((f))	61	83	35.8±0.5	3.48±0.05	3.48±0.04	0.15±0.03	>16	-12.9±0.2	Q1	C	.
HD 203064	O7.5 III n((f))	312	66	35.3±0.5	3.53±0.05	3.69±0.03	0.1±0.03	>17	-12.7±0.2	Q2	LPV	.
HD 97434	O7.5 III (n)((f))	217	114	34.8±0.5	3.47±0.10	3.57±0.07	0.11±0.03	>17	-12.6±0.1	Q2	LPV	C
HD 24912	O7.5 III (n)((f))	230	82	35.9±0.5	3.59±0.05	3.67±0.04	0.11±0.03	>18	-12.6±0.1	Q2	LPV	.
HD 116852	O8.5 II-III ((f))	114	69	34.0±0.5	3.49±0.05	3.52±0.04	<0.07	>18	-12.7±0.1	Q3	MD2	C
HD 13268	ON8.5 III n	290	102	34.2±0.5	3.43±0.07	3.61±0.04	0.15±0.03	>17	-12.9±0.3	Q1	C	.
HD 105627	O9 III	141	122	33.7±0.6	3.60±0.09	3.63±0.08	0.12±0.03	15±5	-12.9±0.2	Q1	SB1	.
HD 305523	O9 II-III	57	78	32.2±0.5	3.44±0.06	3.44±0.05	0.1±0.03	<7	-12.9±0.2	Q1	MD1	C
HD 113904B	O9 III	84	83	32.9±0.5	3.50±0.05	3.51±0.04	0.1±0.03	9±3	-13.0±0.2	Q1	SB1,MD2	.
HD 150574	ON9 III (n)	252	172	33.1±0.9	3.46±0.14	3.60±0.10	0.18±0.04	>14	-12.9±0.3	Q2	MD1	VAR
HD 191423	ON9 II-III nn	432	108	32.3±0.8	3.44±0.12	3.71±0.06	0.17±0.06	>13	-13.0±0.3	Q2	LPV	.
HD 152247	O9.2 III	82	96	32.1±0.5	3.47±0.07	3.48±0.06	0.1±0.03	<8	-12.9±0.2	Q1	SB1	.
HD 90087	O9.2 III (n)	293	64	31.6±0.6	3.38±0.09	3.50±0.07	0.14±0.04	>11	-12.7±0.2	Q2	LPV	VAR
HD 37743	O9.5 II-III (n)	112	112	30.8±0.5	3.29±0.05	3.33±0.04	<0.08	>17	-12.5±0.1	Q3	MD1	.
HD 15642	O9.5 II-III n	286	104	29.9±0.8	3.29±0.08	3.52±0.04	0.15±0.06	>10	-13.0±0.3	Q2	LPV	.
HD 37737	O9.5 II-III (n)	201	95	30.0±0.5	3.40±0.05	3.50±0.03	0.1±0.03	14±4	<-13.4	Q1	SB1	.
HD 52266	O9.5 III n	267	52	32.2±0.8	3.49±0.13	3.63±0.09	0.12±0.03	>15	-12.9±0.2	Q2	LPV	C
HD 93521	O9.5 III nn	385	192	31.7±0.8	3.54±0.14	3.78±0.08	0.15±0.04	>16	-13.0±0.5	Q2	LPV	.
HD 117490	ON9.5 III nn	343	135	31.6±0.7	3.54±0.10	3.74±0.06	0.2±0.07	>18	<-12.9	Q1	LPV	VAR
HD 91651	ON9.5 III n	189	242	31.8±0.8	3.48±0.08	3.56±0.06	0.2±0.07	>17	-12.7±0.2	Q2	SB1	.
HD 13022	O9.7 II-III	98	131	30.0±0.5	3.20±0.05	3.24±0.04	0.11±0.03	>17	-13.0±0.2	Q1	C	.
HD 55879	O9.7 III	28	61	31.2±0.5	3.51±0.05	3.51±0.04	0.1±0.03	12±4	<-13.3	Q1	C	C
HD 118198	O9.7 III	43	56	31.2±0.5	3.42±0.05	3.42±0.04	0.1±0.03	9±4	-13.3±0.3	Q1	C	C
BD +60 498	O9.7 II-III:	114	40	32.8±0.9	>3.99	>3.99	0.1±0.03	<7	<-13.4	Q1	MD1	.
HD 93129B	O3.5 V ((f))z	66	62	47.7±1.8	3.99±0.09	3.99±0.08	0.1±0.03	>14	-12.7±0.1	Q1	MD1	C
HD 164794	O4 V ((f))	62	95	43.1±1.1	3.88±0.08	3.88±0.07	0.1±0.03	>12	-12.7±0.1	Q3	LPV	SB2
HD 5005 A	O4 V ((fc))	52	79	42.8±1.0	3.83±0.07	3.83±0.06	0.1±0.03	>9	-12.8±0.3	Q1	C	.

Notes: C:Constant, LPV:Line profile variability, WV:Wind variable. $g_{true} = g + g_{cent}$, $g_{cent} \approx \frac{(V_{rot} \sin i)^2}{R_*}$

Table B.5: continued.

Name	SpT LC	$v \sin i$ [km s^{-1}]	$v_{\rm mac}$ [km s^{-1}]	$T_{\rm eff}$ [kK]	$\log g$ [dex]	$\log g_{\rm true}$ [dex]	$Y_{\rm He}$ [dex]	ξ_t [km s^{-1}]	$\log Q$ [dex]	qual. flag	Notes	OWN Notes
HD 229232	O4 V:n((f))	313	46	42.9±2.2	3.67±0.13	3.81±0.09	>0.14	5.0-19.9	-12.6±0.3	Q4	MD2	.
HD 155913	O4.5 V n((f))	278	0	42.5±1.5	3.96±0.13	4.02±0.11	0.18±0.05	5.0-19.9	-12.7±0.2	Q1	LPV	VAR
HD 192281	O4.5 IV (n)(f)	277	43	40.8±1.1	3.73±0.09	3.82±0.072	>0.19	<16	-12.6±0.2	Q2	LPV	.
HD 193682	O4.5 IV (f)	183	90	41.0±1.0	3.71±0.11	3.75±0.10	0.14±0.04	>11	-12.6±0.1	Q1	MD1	.
HD 256725 A	O5 V ((fc))	67	38	41.2±1.0	3.94±0.12	3.94±0.11	0.12±0.03	5.0-19.9	-13.1±0.3	Q1	C	.
BD -14 5040	O5.5 V (n)((f))	268	106	40.4±2.3	3.88±0.28	3.96±0.23	0.11±0.04	5.0-19.9	<-12.7	Q4	MD1	.
BD +60 134	O5.5 V (n)((f))	250	133	40.7±1.8	3.88±0.24	3.95±0.20	0.21±0.08	>10	<-12.7	Q1	LPV	.
HD 14434	O5.5 IV nn(f)p	417	144	38.6±1.1	3.78±0.17	3.96±0.11	0.13±0.03	>10	-12.9±0.4	Q2	LPV	.
HD 305525	O5.5 V ((f))z	66	139	40.4±1.5	>3.89	>3.89	<0.11	5.0-19.9	-13.0±0.3	Q3	MD1	.
ALS 4880	O6 V ((f))	84	89	39.8±1.2	3.96±0.20	3.96±0.20	0.1±0.03	>8	-13.0±0.3	Q1	MD1	.
BD +60 2635	O6 V ((f))	51	73	39.8±0.9	3.77±0.10	3.77±0.10	0.2±0.03	>14	-13.1±0.2	Q1	C	.
CPD -58 2611	O6 V ((f))z	39	73	39.8±0.8	3.88±0.09	3.88±0.08	0.11±0.03	>12	-13.0±0.3	Q1	MD1	C
HD 76556	O6 IV (n)((f))p	239	86	37.9±0.5	3.84±0.10	3.90±0.08	<0.07	>17	-12.6±0.1	Q2	LPV	VAR
ALS 12370	O6.5 V nn((f))	440	130	39.0±1.8	3.93±0.31	4.12±0.20	0.12±0.03	>13	<-12.7	Q1	LPV	.
BD +61 411	O6.5 V ((f))z	29	98	38.8±1.0	3.99±0.19	3.99±0.18	<0.09	<18	<-12.9	Q1	MD1	.
BD +62 424	O6.5 V (n)((f))	60	65	38.7±0.7	3.80±0.11	3.80±0.10	0.1±0.03	14±4	-12.9±0.2	Q1	C	.
HD 101298	O6.5 IV ((f))	71	69	38.9±0.5	3.79±0.05	3.79±0.04	0.1±0.03	13±4	-12.7±0.1	Q1	C	C
HD 199579	O6.5 V ((f))z	52	90	39.5±0.8	3.86±0.08	3.86±0.07	0.09±0.03	>17	-13.1±0.2	Q1	SB1	.
HD 93161 B	O6 IV (n)((f))p	81	101	37.1±0.8	3.75±0.12	3.76±0.12	<0.07	13±6	-12.7±0.1	Q3	MD1	.
HD 99897	O6.5 IV ((f))	50	94	37.7±0.5	3.57±0.05	3.57±0.04	0.1±0.03	>19	-12.7±0.1	Q1	MD1	C
HDE 227018	O6.5 V ((f))z	61	78	38.7±0.8	3.85±0.15	3.85±0.15	0.09±0.03	>7	-13.0±0.3	Q1	MD1	.
HD 228841	O6.5 V n((f))	317	130	37.7±1.4	3.72±0.19	3.88±0.13	0.16±0.05	>9	<-12.7	Q1	LPV	.
HD 242935 A	O6.5 V ((f))z	29	64	38.7±0.9	>3.98	>3.98	<0.07	<9	<-13.0	Q1	MD1	.
HD 305532	O6.5 V ((f))z	51	53	39.3±0.8	3.84±0.08	3.84±0.07	0.11±0.03	>13	-12.9±0.2	Q1	MD1	C
HD 326775	O6.5 V (n)((f))z	170	108	39.4±1.3	3.83±0.16	3.87±0.14	0.1±0.03	>15	-12.9±0.2	Q1	SB1	.
HD 344784	O6.5 V ((f))z	65	70	38.9±0.6	3.90±0.07	3.90±0.06	0.09±0.03	10±4	-13.1±0.2	Q1	MD1	.
HD 47839	O7 V ((f))z_var	43	67	38.3±0.5	4.02±0.06	4.02±0.05	<0.07	15±3	-13.0±0.2	Q3	C	.
ALS 12619	O7 V ((f))z	21	43	38.2±0.7	4.03±0.08	4.03±0.08	0.11±0.03	10±3	<-13.4	Q1	MD1	.
ALS 8294	O7 V (n)z	50	87	41.7±1.9	3.97±0.22	3.97±0.21	<0.15	5.0-19.9	<-12.7	Q1	MD1	.
BD -10 4682	O7 V n((f))	358	15	36.9±1.2	3.74±0.17	3.94±0.11	<0.1	>9	-13.1±0.4	Q1	MD1	.
BD +60 501	O7 V (n)((f))z	182	87	37.9±0.8	3.85±0.13	3.89±0.11	0.1±0.03	<16	<-13.0	Q1	MD1	.
BD +60 513	O7 V n	319	17	35.8±1.0	3.67±0.16	3.86±0.10	0.1±0.03	<14	-13.0±0.3	Q1	MD1	.
BD +60 586	O7 V z	38	77	38.4±0.7	4.10±0.14	4.10±0.13	0.1±0.03	<11	<-13.1	Q1	LPV	.
BD +62 2078	O7 V ((f))z	38	38	38.7±0.8	4.00±0.14	4.00±0.14	0.1±0.03	12±4	<-13.0	Q1	C	.
HD 152623	O7 V (n)((f))	83	138	37.4±0.7	3.78±0.11	3.79±0.10	0.1±0.03	<12	-12.9±0.2	Q1	SB1,MD2	.
HD 159176	O7 V ((f))	114	90	37.6±0.6	3.81±0.11	3.83±0.10	<0.07	>15	-12.9±0.2	Q3	LPV,MD2	.
HD 193595	O7 V ((f))	46	61	37.9±0.5	3.79±0.06	3.79±0.06	0.16±0.03	>16	-13.0±0.2	Q1	MD1	.
HD 217086	O7 V nn((f))z	377	40	37.7±0.8	3.81±0.12	4.00±0.07	<0.08	>14	-13.1±0.3	Q1	C	.
HD 36879	O7 V (n)((f))	209	40	36.9±0.5	3.69±0.05	3.77±0.04	0.1±0.03	>18	-12.7±0.2	Q2	LPV	.

Notes: C:Constant, LPV:Line profile variability, WV:Wind variable. $g_{true} = g + g_{cent}$, $g_{cent} \approx \frac{(V_{rot} \sin i)^2}{R_*}$

Table B.5: continued.

Name	SpT LC	$v \sin i$ [km s^{-1}]	$v_{\rm mac}$ [km s^{-1}]	$T_{\rm eff}$ [kK]	$\log g$ [dex]	$\log g_{\rm true}$ [dex]	$Y_{\rm He}$ [dex]	ξ_t [km s^{-1}]	$\log Q$ [dex]	qual. flag	Notes	OWN Notes
HD 44811	O7 V (n)z	26	43	37.4±0.6	3.90±0.12	3.90±0.11	0.11±0.03	<16	<-13.3	Q1	LPV	.
HD 46485	O7 V ((f))n_var?	322	100	36.1±0.7	3.71±0.07	3.88±0.04	0.1±0.03	<13	<-13.0	Q1	C	.
HD 46573	O7 V ((f))z	77	81	36.8±0.8	3.71±0.11	3.72±0.10	0.11±0.03	>18	-12.9±0.2	Q1	LPV	.
HD 5689	O7 V n((f))	255	76	36.8±1.0	3.56±0.15	3.72±0.10	0.17±0.04	>15	-12.9±0.3	Q1	MD1	.
HDE 227245	O7 V ((f))z	47	71	38.0±0.7	3.80±0.07	3.80±0.07	0.1±0.03	>10	-13.1±0.3	Q1	MD1	.
HDE 227465	O7 V ((f))	61	79	37.2±1.0	3.87±0.15	3.87±0.15	<0.12	5.0-19.9	-13.1±0.3	Q1	MD1	.
HD 110360	ON7 V	96	86	39.3±0.9	4.17±0.15	4.17±0.14	0.18±0.04	5.0-19.9	-13.1±0.3	Q1	SB1,MD2	.
HD 90273	ON7 V ((f))	55	55	38.5±0.8	3.77±0.10	3.78±0.10	0.19±0.04	>13	-12.9±0.2	Q1	MD1	.
BD +33 1025 A	O7.5 V (n)z	178	10	38.4±1.0	>3.98	>4.01	0.1±0.03	<13	<-13.0	Q1	MD1	.
HD 12979	O7.5 IV (n)((f))	261	54	34.9±0.9	3.39±0.09	3.58±0.05	0.1±0.03	>16	-12.6±0.2	Q3	LPV	VAR
HD 164492	O7.5 V z	39	54	38.6±0.6	4.00±0.11	4.00±0.10	0.1±0.03	12±6	<-13.0	Q1	C	C
HD 168461	O7.5 V ((f))_Nstr	192	30	36.0±1.2	3.75±0.19	3.81±0.16	0.11±0.03	>11	-12.6±0.2	Q2	MD1	.
HD 168504	O7.5 V (n)z	61	89	37.3±0.7	3.83±0.07	3.84±0.07	0.1±0.03	>12	<-13.0	Q1	MD1	.
HD 41997	O7.5 V n((f))	262	38	35.8±0.5	3.59±0.08	3.75±0.05	0.11±0.03	>19	-12.8±0.1	Q1	LPV	.
HD 53975	O7.5 V z	179	45	36.8±0.5	3.87±0.07	3.91±0.06	0.09±0.03	>16	<-13.3	Q1	SB1	.
HD 74920	O7.5 IV n((f))	291	16	34.9±0.5	3.45±0.08	3.66±0.05	0.11±0.03	>17	-12.7±0.2	Q2	MD1	.
HD 99546	O7.5 V ((f))Nstr	50	60	37.0±0.5	3.70±0.05	3.71±0.05	0.11±0.03	>17	-12.9±0.2	Q1	MD1	.
HDE 338 916	O7.5 V z	26	45	37.8±0.8	4.02±0.12	4.02±0.12	0.11±0.03	11±3	<-13.4	Q1	MD1	.
HDE 344777	O7.5 V z	47	103	35.8±0.8	3.62±0.12	3.62±0.12	0.1±0.03	>13	-13.3±0.4	Q1	MD1	.
ALS 7833	O8 V z	85	104	35.9±1.2	3.70±0.14	3.71±0.13	0.1±0.03	11±5	<-13.0	Q1	MD1	.
HD 101191	O8 V	138	101	35.7±0.9	3.77±0.14	3.80±0.12	0.1±0.03	<14	-13.3±0.5	Q1	C	.
HD 101413	O8 V	80	91	36.9±0.5	4.01±0.08	4.01±0.07	<0.07	14±3	-12.9±0.2	Q3	LPV	.
HD 165246	O8 V (n)	251	39	35.9±0.7	3.91±0.09	3.99±0.07	<0.08	>11	<-13.2	Q1	SB1	.
HD 41161	O8 V n	331	6	35.2±0.6	3.59±0.09	3.84±0.05	0.14±0.04	>9	<-12.8	Q1	C	.
HD 46056	O8 V n	370	103	35.5±0.8	3.81±0.15	4.01±0.09	0.1±0.03	<16	<-13.0	Q1	LPV	.
HD 326331	O8 IV n((f))	332	100	34.9±0.5	3.51±0.07	3.74±0.04	0.11±0.03	>15	-12.7±0.2	Q2	C	VAR
BD +36 4145	O8.5 V (n)	203	33	35.8±0.9	3.78±0.18	3.86±0.15	<0.09	>17	-13.3±0.4	Q1	MD2	.
HD 216532	O8.5 V (n)	199	54	35.3±0.6	4.00±0.08	4.04±0.07	0.1±0.03	<7	<-13.6	Q1	C	.
HD 48279	O8.5 V Nstr_var?	131	74	36.2±0.7	3.83±0.07	3.86±0.06	0.16±0.03	16±4	-13.4±0.4	Q1	C	C
HD 5005C	O8.5 V (n)	200	59	36.2±0.6	4.00±0.09	4.04±0.08	0.1±0.03	<8	<-13.0	Q1	MD1	.
HD 52533	O8.5 IV n	299	107	35.2±0.5	3.9±0.06	3.98±0.05	<0.08	<12	-13.3±0.3	Q1	SB1	.
HD 92504	O8.5 V (n)	182	63	34.9±0.8	3.61±0.05	3.70±0.04	0.1±0.03	15±3	-13.2±0.2	Q1	C	C
HD 73882	O8.5 IV	145	58	35.8±0.6	3.83±0.11	3.85±0.10	<0.07	<13	-13.0±0.3	Q1	SB1	VAR
HD 149452	O9 IV n	318	120	33.7±0.8	3.51±0.12	3.73±0.07	0.11±0.03	>14	-12.9±0.2	Q1	LPV,MD2	C
HD 102415	ON9 IV: nn	366	162	33.1±1.1	3.73±0.16	3.92±0.10	0.21±0.07	<17	<-13.0	Q1	LPV	VAR
HD 164438	O9.2 IV	55	94	32.2±0.5	3.42±0.05	3.43±0.04	0.09±0.03	<12	-13.1±0.2	Q1	SB1	SB1
HD 5005 D	O9.2 V	32	57	34.9±0.5	3.99±0.10	3.99±0.09	0.1±0.03	<10	<-13.5	Q1	MD1	.
HD 57682	O9.2 IV	7	34	35.0±0.5	4.13±0.15	4.13±0.14	0.1±0.03	>7	-12.9±0.2	Q1	C,WVe,Mag	C
HD 76341	O9.2 IV	51	93	33.0±0.5	3.57±0.09	3.57±0.08	0.1±0.03	<14	-13.2±0.3	Q1	C	C
HD 149757	O9.2 IV nn	385	94	32.0±0.5	3.5±0.05	3.66±0.04	0.11±0.03	>18	-13.1±0.2	Q1	C	VAR

Notes: C:Constant, LPV:Line profile variability, WV:Wind variable. $g_{true} = g + g_{cent}$, $g_{cent} \approx \frac{(V_{rot} \sin i)^2}{R_*}$

Table B.5: continued.

Name	SpT LC	$v \sin i$ [km s^{-1}]	$v_{\rm mac}$ [km s^{-1}]	$T_{\rm eff}$ [kK]	$\log g$ [dex]	$\log g_{\rm true}$ [dex]	$Y_{\rm He}$ [dex]	ξ_t [km s^{-1}]	$\log Q$ [dex]	qual. flag	Notes	OWN Notes
HD 201345	ON9.2 IV	79	89	33.8±0.7	3.79±0.07	3.79±0.06	0.12±0.03	12±6	<-13.1	Q1	C	. .
BD+60 499	O9.5 V	17	38	34.2±0.8	3.87±0.13	3.87±0.12	0.11±0.03	<9	<-13.2	Q1	MD1	. C
CPD-54 6791	O9.5 V	31	39	34.8±0.6	4.05±0.11	4.05±0.10	0.1±0.03	<9	-13.2±0.3	Q1	MD1	
HD 123056	O9.5 IV (n)	193	26	31.8±0.5	3.63±0.09	3.70±0.07	0.16±0.03	<8	-13.3±0.4	Q1	SB1	. .
HD 163892	O9.5 IV (n)	215	53	32.8±0.5	3.69±0.07	3.77±0.05	0.09±0.03	<13	<-13.3	Q1	SB1	SB1
HD 164019	O9.5 IV p	69	62	32.0±0.5	3.44±0.08	3.45±0.07	<0.08	>17	-12.9±0.2	Q1	MD1	C
HD 166546	O9.5 IV	38	73	32.4±0.6	3.56±0.09	3.56±0.08	0.1±0.03	9±3	<-13.0	Q1	C	C
HD 168941	O9.5 IV p	83	101	32.0±0.5	3.41±0.06	3.43±0.05	0.1±0.03	12±4	-13.3±0.4	Q1	MD2	C
HD 202214	O9.5 IV-V	26	36	32.1±0.5	3.82±0.05	3.82±0.04	0.1±0.03	<8	-13.3±0.4	Q1	C	. .
HD 206183	O9.5 IV-V	8	29	33.8±0.5	4.04±0.10	4.04±0.09	0.1±0.03	<10	<-13.4	Q1	C	
HD 36483	O9.5 IV (n)	158	74	33.4±0.8	3.83±0.13	3.86±0.11	<0.11	<14	<-13.3	Q1	LPV	. . .
CPD-41 7721 A	O9.7 V: (n)	191	66	31.3±0.5	3.77±0.11	3.85±0.09	0.13±0.03	<9	<-13.0	Q1	MD1	
HD 152200	O9.7 IV (n)	226	21	30.4±0.7	3.57±0.14	3.69±0.11	0.13±0.03	<10	-13.4±0.4	Q1	SB1	. . .
HD 209339	O9.7 IV	84	78	32.1±0.5	3.80±0.05	3.81±0.04	0.11±0.03	<12	<-13.3	Q1	C	
HD 54879	O9.7 V	8	8	33.5±0.5	4.09±0.12	4.09±0.11	<0.1	<6	-12.8±0.1	Q3	C,Oe?,WVe?	C
HDE 308813	O9.7 IV (n)	215	10	31.8±0.5	3.81±0.06	3.88±0.05	0.11±0.03	<11	-13.2±0.2	Q3	SB1	. .
HDE 326329	O9.7 V	87	39	32.1±0.5	3.91±0.05	3.92±0.05	0.13±0.03	<10	-12.9±0.2	Q3	LPV	
HD 66811	O4 I (n)fp	198	12	...	...	...	...	...	...	Mag	Onfp,Mag	VAR
HD 148937	O6 ...f?p	39	76	...	...	...	...	...	...	Mag	Mag,SB2?	VAR
CPD-28 2561	O6.5 ...f?p	169	94	...	...	...	...	...	...	Mag	Mag-WR-WVa	VAR
HD 108	O8 ...fp_var	46	86	...	...	...	...	...	...	Mag	SB1,WVe,Mag	
HD 191612	O8 ...f?p_var	45	60	...	...	...	...	...	...	Mag	LPV,WVe,Mag	. . .
HD 45314	O9: ... npe	128	4	...	...	...	...	...	...	Oe	Oe,SB1	. . .
HD 24534	O9.5: ...npe	226	104	...	...	...	...	...	...	Oe	Oe,SB1	. . .
HD 220608	O9.7 Iab p_var	95	70	...	...	...	...	...	...	Mag	SB1,Mag,BH	. . .
HD 39680	O6 V: [n]pe_var	101	31	...	...	...	...	...	...	Oe	Oe,SB1	. . .
HD 37022	O7 V p	23	68	...	...	...	...	...	...	Mag	LPV,WVe,Mag	
HD 155806	O7.5 V ((f))(e)	49	103	...	...	...	...	...	...	Oe	Oe	C
HD 60848	O8: V: pe	136	123	...	...	...	...	...	...	Oe	Oe,LPV	
HD 120678	O9.5 V e	155	84	...	...	...	...	...	...	Oe	Oe,SB1	VAR

Notes: C:Constant, LPV:Line profile variability, WV:Wind variable. $g_{true} = g + g_{cent}$, $g_{cent} \approx \frac{(V_{rot} \sin i)^2}{R_*}$

Table B.6: Stars in the sample with double-line spectroscopic features

Columns include: Name, spectral type and luminosity classification, and spectral classification of the secondary component in the unresolved spectrum (as stated in GOSSS). Finally, this table provides a multi-epoch annotation from the OWN project (priv comm.).

Name	SpT LC	Companion	OWN Notes	Name	SpT LC	Companion	OWN Notes
HD 93162	O2.5 If*/WN6	OB	SB2	HDE 228 854	O6 IV n_var	O5Vnvar	.
LS III +46 11	O3.5 If*	O3.5If*	.	HDE 228 854	O6 IV n_var	O5Vnvar	.
HD 228 766	O4 If	O8:II:	.	HD 165052	O6 V z	O8Vz	.
HD 153919	O6 Ia fcp	.	VAR	HD 165052	O6 V z	O8Vz	VAR?
HD 150958	O6.5 Ia (n)f	.	.	HD 92206B	O6 V ((f))z	.	.
HD 152248	O7 Iab f	O7Ib(f)	.	HD 92206A	O6 V ((f))z	.	.
HD 101205	O7 II: (n)	.	.	HD 124314	O6+O9.2 IV+IV (n)((f))+(n)	.	.
HD 57060	O7 Ia fp_var	.	.	HD 150135	O6.5 V ((f))z	.	.
HD 166734	O7.5 Iab f	.	.	HD 150135	O6.5 V ((f))z	.	.
HD 166734	O7.5 Iab f	.	.	HD 101436	O6.5 V ((f))	.	.
HD 47129	O8 ...fp_var	.	.	HD 101436	O6.5 V ((f))	.	Mag
HD 167971	O8 Ia f(n)	O4/5	.	HD 168075	O6.5 V ((f))	.	.
HD 96670	O8.5 ...(n)fp_var	.	.	HD 206267	O6.5 V ((f))	O9/B0V	.
HD 149404	O8.5 Iab (f)p	.	.	HDE 228 759	O6.5 V (n)((f))z	.	.
HD 323110	ON9 Ia	.	.	HD 194 649 AB	O6.5 V ((f))	.	.
HD 1337	O9.2 II	.	.	BD +60 497	O6.5 V ((f))z	O8/B0V	.
HD 35921	O9.5 II	.	.	HD 18326	O6.5 V ((f))z	O9/B0V:	.
HD 93206	O9.7 Ib n	.	.	HD 135240	O7 IV ((f))	B	.
HD 69106	O9.7 II n	.	.	HD 319703A	O7 V ((f))	O9.5V	C
HD 150136	O3.5-4 III (f*)	O6IV	.	HD 319703A	O7 V ((f))	O9.5V	C
HDE 319718 A	O3.5 III (f*)	.	.	HD 165921	O7 V (n)z	B0:V:	.
HD 15558	O4.5 III (f)	.	.	HD 54662	O7 V z_var?	.	SB2
HD 93403	O5.5 III (fc)_var	.	.	Herschel 36	O7: V	.	.
HD 93130	O6.5 III (f)	.	.	HD 175514	O7 V (n)((f))z	B	.
HD 17505	O6.5+O8 III+V n(f)+...	.	.	ALS 12320	O7 IV ((f))	.	.
HD 167771	O7 III ((f))	O8III	.	ALS 8272	O7 V ((f))	B0III-V	.
HD 167771	O7 III ((f))	O8III	.	HDE 229 202	O7.5 V (n)((f))	.	.
HD 115455	O8 III ((f))	.	.	HD 93161 A	O7.5 V z	.	.
HD 151003	O8.5 III	.	.	BD +66 1675	O7.5 V z	.	.
HD 19820	O8.5 III (n)((f))	.	.	BD +66 1675	O7.5 V z	.	.
HD 153426	O8.5 III	.	.	HD 97166	O7.5 IV ((f))	O9III:	.
HD 37043	O9 III var	.	.	HD 213 023 A	O7.5 V z	.	.
HD 16429	O9 II-III (n)_Nwk	.	.	BD -14 5014	O7.5 V (n)((f))	.	.
HD 114886	O9 III	.	.	BD +55 2840	O7.5 V (n)	.	.
HD 15137	O9.5 II-III n	.	.	V572 CAR	O7.5 V (n)	B0V(n)	.
HD 167263	O9.5 III	.	.	CPD -59 2635	O8 V (n)	O9.5V	.
HD 152219	O9.5 III (n)	.	.	HD 161853	O8 V (n)z	B	.
HD 115071	O9.5 III	.	.	HD 100213	O8 V (n)	.	.

Table B.6: continued.

Name	SpT LC	Companion	OWN Notes	Name	SpT LC	Companion	OWN Notes
HD 156292	O9.7 III	.	.	HD 123590	O8 V z	.	.
HD 191201	O9.5+O9.7 III+III...+...	.	.	HD 123590	O8 V z	.	.
HD 191201	O9.5+O9.7 III+III...+...	.	.	HD 92206 C	O8 V (n)z	B0:V	.
HD 155775	O9.7 III (n)	.	.	HD 17520	O8 V	.	.
HD 46106	O9.7 III (n)	.	.	HD 93343	O8 V	.	SB2
HD 117856	O9.7 II-III	.	.	CPD -59 2636	O8 V	.	.
HD 374685AB	O9.7 III	.	.	HD 168137 AaAb	O8 V z	.	.
HD 93205	O3.5 V ((f))	O8V	.	HD 209481	O9 IV (n)_var	B1:V:	.
HD 242908	O4.5 V (n)((fc))z	.	.	HD 152218	O9 IV (n)	.	.
HD 242908	O4.5 V (n)((fc))z	.	.	HD 193322	O9 IV (n)	.	.
LS III +4612	O4.5 IV (f)	.	.	HD 152314	O9 IV	.	.
BD +45 3216 A	O5 V ((f))z	.	.	HD 75759	O9 V	.	.
HD 215835	O5.5 V ((f))	O6V((f))	.	HD 152246	O9 IV	.	.
HD 48099	O5.5 V ((f))z	O9V	.	HD 158186	O9.2 V	.	.
BD -16 4826	O5.5 V ((f))z	.	.	HD 37041	O9.5 IV p	.	.
HD 64315	O5.5 V	.	.	HD 37366	O9.5 IV	.	.
MY CAM	O5.5 V (n)	O6.5V(n)	.	HD 198846	O9.5 IV	.	.
HD 101131	O5.5 V ((f))	O8:V	.	HD 164816	O9.5 V	.	.
ALS 12688	O5.5 V (n)((fc))	B	.	HD 204827	O9.5 IV	.	.
V747 CEP	O5.5 V (n)((f))	.	.	HD 125206	O9.7 IV n	.	VAR
CPD -59 2641	O6 V ((fc))	.	.				

Table B.7: Stars in the sample without a satisfactory fit from the line-broadening and the spectroscopic analysis. The lines from the Balmer series appear in strong emission.

Name	SpT LC	Notes	OWN Notes
ALS 2063	O5 Ifp	Iafpe/WR	VAR?
HD 152386	O6: Ia fpe	Iafpe/WR	VAR
HD 313846	O7: Ia fpe	WR	C
HD 152408	O8: Ia fpe	Iafpe/WR	C

Table B.8: Complete list of stars considered in this work with available *Gaia* DR2 parallaxes.

They are separated in two groups. The first part of the table includes stars sorted by HD number when available. The second group comprises those stars that do not have an HD number, sorted alphabetically. Columns 1 and 3 come directly from GOSC, the name(s) of each star, spectral classification, and the B magnitude. Then, the parallax value from *Gaia* DR2 database (column 4). Columns 5, 6 , and 7 are the Bayesian calculation of the distance from Bailer-Jones et al. (2018), and its lower and upper limits. Final columns are the Galactic longitude and latitude from SIMBAD (columns 8 and 9).

Name	SpT	LC	B_{ap}	*Gaia* DR2 π	BJ18 distance [pc]			l	b
			[mag]	[mas]	c	min	max	[º]	[º]
HD 108	O8	fp_var	7.5	0.385±0.034	2418	2230	2640	72.99	1.43
HD 1337	O9.2	II	6	0.552±0.098	1702	1445	2060	117.59	-11.09
HD 10125	O9.7	II	8.7	0.019±0.058	7417	5700	9878	128.29	1.82
HD 12323	ON9.2	V	8.8	0.356±0.044	2569	2302	2903	132.91	-5.87
HD 15137	O9.5	II-III n	7.9	0.27±0.05	3190	2743	3789	137.46	-7.58
HD 12993	O6.5	V ((f))_Nstr	9.2	0.386±0.045	2398	2159	2695	133.11	-3.4
HD 13022	O9.7	II-III	9.1	0.413±0.047	2258	2034	2535	132.91	-2.57
HD 13268	ON8.5	III n	8.3	0.591±0.047	1616	1500	1750	133.96	-4.99
HD 13745	O9.7	II (n)	8	0.441±0.053	2121	1902	2394	134.58	-4.96
HD 14434	O5.5	IV nn(f)p	8.7	0.391±0.047	2365	2122	2668	135.08	-3.82
HD 14442	O5	n(f)p	9.6	0.256±0.034	3449	3080	3912	134.21	-1.32
HD 14947	O4.5	I f	8.5	0.265±0.048	3307	2845	3931	135	-1.74
HD 14633 AaAb	ON8.5	V	7.2	0.198±0.127	2739	2139	3614	140.78	-18.2
HD 15558	O4.5	III (f)	8.4	0.466±0.086	2043	1715	2516	134.72	0.92
HD 15570	O4	I f	8.8	0.399±0.035	2340	2159	2554	134.77	0.86
HD 15629	O4.5	V ((fc))	8.8	0.458±0.035	2057	1917	2218	134.77	1.01
HD 15642	O9.5	II-III n	8.6	0.241±0.041	3551	3097	4146	137.09	-4.73
HD 16429	O9	II-III (n)_Nwk	8.5	-0.209±0.384	3566	2150	5858	135.68	1.15
HD 16691	O4	I f	9.1	0.44±0.043	2130	1944	2355	137.73	-2.73
HD 16832	O9.2	III	9.3	0.417±0.042	2232	2037	2468	138	-2.88
HD 17505	O6.5+O8	III+V n(f)	7.7	0.361±0.033	2564	2358	2807	137.19	0.9
HD 17520	O8	V	9.1	-2.801±0.975	3495	2018	5797	137.22	0.88
HD 17603	O7.5	Ib (f)	9.1	0.389±0.045	2379	2145	2669	138.77	-2.08
HD 18326	O6.5	V ((f))z	8.3	0.421±0.038	2222	2047	2429	138.03	1.5
HD 18409	O9.7	Ib	8.8	0.394±0.039	2369	2164	2615	137.12	3.46
HD 19820	O8.5	III (n)((f))	7.6	0.733±0.034	1314	1257	1377	140.12	1.54
HD 24431	O9	III	7.2	1.216±0.085	808	754	869	148.84	-0.71
HD 24534	O9.5:	npe	7.1	1.234±0.056	792	758	829	194.07	-5.88
HD 24912	O7.5	III (n)((f))	4.1	1.379±1.431	1134	529	2276	160.37	-13.11
HD 28446 A	O9.7	II n	6	1.297±0.091	759	709	817	151.91	3.95
HD 30614	O9	Ia	4.3	1.369±0.33	758	579	1084	144.07	14.04
HD 34078	O9.5	V	6.2	2.464±0.066	401	391	412	172.08	-2.26
HD 34656	O7.5	II (f)	6.9	0.401±0.09	2340	1902	3012	170.04	0.27
HD 35619	O7.5	V ((f))	8.8	0.285±0.065	3114	2563	3931	173.04	-0.09
HD 36483	O9.5	IV (n)	8.6	0.775±0.117	1270	1095	1509	172.29	1.88
HD 36512	O9.7	V	4.4	3.361±0.423	301	265	349	210.44	-20.98
HD 36861 A	O8	III ((f))	3.6	3.689±0.545	279	238	335	195.05	-12
HD 36879	O7	V (n)((f))	7.8	0.448±0.054	2095	1874	2372	185.22	-5.89
HD 37022	O7	V p	5.2	2.707±0.332	373	329	429	336.37	-0.22
HD 37041	O9.5	IV p	5	2.215±0.275	453	400	522	209.05	-19.37
HD 37366	O9.5	IV	7.7	0.501±0.1	1918	1582	2422	177.63	-0.11
HD 37737	O9.5	II-III (n)	8.4	0.459±0.096	2068	1697	2626	173.46	3.24
HD 38666	O9.5	V	4.9	2.148±0.162	462	429	500	237.29	-27.1
HD 39680	O6	V: [n]pe_var	7.9	0.296±0.062	3009	2514	3718	202.51	17.52
HD 41161	O8	V n	6.7	0.628±0.058	1520	1395	1667	164.97	12.89
HD 41997	O7.5	V n((f))	8.8	0.463±0.053	2041	1837	2295	194.15	-1.98
HD 42088	O6	V ((f))z	7.6	0.575±0.059	1663	1508	1852	190.04	0.48
HD 44811	O7	V (n)z	8.6	0.19±0.059	4049	3283	5173	192.4	3.21
HD 45314	O9:	npe	6.7	1.209±0.047	809	779	841	163.08	-17.14
HD 46056	O8	V n	8.4	0.656±0.06	1469	1345	1617	206.34	-2.25
HD 46106	O9.7	III (n)	8.1	0.597±0.087	1622	1409	1909	206.2	-2.09
HD 46149	O8.5	V	7.8	0.656±0.068	1472	1332	1644	206.22	-2.04

Notes: *: BJ18c/BJ18min/BJ18max: Bailer-Jones et al. (2018) central, minimum, and maximum distance values.

Table B.8: continued.

Name	SpT	LC	B_{ap}	*Gaia* DR2 π	BJ18 distance [pc]			l	b
			[mag]	[mas]	c	min	max	[º]	[º]
HD 46150	O5	V ((f))z	6.9	0.626±0.079	1544	1368	1770	206.31	-2.07
HD 46202	O9.2	V	8.7	0.741±0.145	1347	1100	1730	206.31	-2
HD 46223	O4	V ((f))	7.5	0.576±0.053	1663	1522	1831	206.44	-2.07
HD 46485	O7	V ((f))n_var?	8.6	0.553±0.07	1735	1536	1989	206.9	-1.84
HD 46573	O7	V ((f))z	8.3	0.647±0.058	1488	1365	1635	208.73	-2.63
HD 46966	O8.5	IV	7.1	0.55±0.071	1742	1541	2001	205.81	-0.55
HD 47129	O8	fp_var	6.1	0.658±0.094	1477	1285	1733	205.87	-0.31
HD 47432	O9.7	Ib	6.4	0.387±0.07	2412	2041	2935	210.03	-2.11
HD 47839	O7	V ((f))z_var	4.6	-0.784±0.624	3216	1875	5348	202.94	2.2
HD 48099	O5.5	V ((f))z	6.3	0.522±0.058	1822	1642	2043	206.21	0.8
HD 48279	O8.5	V Nstr_var?	8	0.523±0.082	1833	1579	2179	210.41	-1.17
HD 5005 A	O4	V ((fc))	8.6	0.339±0.05	2668	2346	3085	123.12	-6.24
HD 5005 C	O8.5	V (n)	8.9	0.292±0.043	3032	2673	3493	123.12	-6.24
HD 5005 D	O9.2	V	9.7	0.358±0.049	2547	2254	2922	123.12	-6.25
HD 52266	O9.5	III n	7.2	0.645±0.049	1489	1386	1608	219.13	-0.68
HD 52533	O8.5	IV n	7.6	0.516±0.063	1844	1644	2098	216.85	0.8
HD 53975	O7.5	V z	6.4	0.802±0.051	1208	1136	1289	225.68	-2.32
HD 54662	O7	V z_var?	6.8	0.855±0.08	1142	1042	1262	224.17	-0.78
HD 54879	O9.7	V	7.6	0.863±0.052	1125	1061	1196	225.55	-1.28
HD 55879	O9.7	III	5.8	0.989±0.054	985	934	1042	224.73	0.35
HD 5689	O7	V n((f))	9.5	0.311±0.033	2930	2665	3251	123.86	0.75
HD 57060	O7	Ia fp_var	4.8	0.677±0.158	1508	1164	2126	237.82	-5.37
HD 57061 AaAb	O9	II	4.8	-5.445±0.965	5500	3236	8970	238.18	-5.54
HD 57236	O8.5	V	8.9	0.406±0.042	2311	2100	2568	235.64	-4.02
HD 57682	O9.2	IV	6.2	0.806±0.052	1201	1128	1284	224.41	2.63
HD 60848	O8:	V: pe	6.7	0.313±0.084	2561	2127	3170	209.01	-19.38
HD 64315	O5.5	V	10.1	-0.054±0.072	7507	5684	10064	243.16	0.36
HD 64568	O3	V ((f*))z	9.5	0.137±0.039	5392	4492	6654	243.14	0.71
HD 68450	O9.7	II	6.4	0.637±0.042	1507	1416	1611	254.47	-2.02
HD 69106	O9.7	II n	7	0.774±0.051	1250	1174	1337	254.52	-1.33
HD 69464	O7	Ib (f)	9.1	0.213±0.033	4046	3553	4684	253.61	-0.3
HD 71304	O9	II	8.8	0.354±0.038	2620	2373	2922	261.75	-3.77
HD 73882	O8.5	IV	8	2.886±0.451	357	302	437	260.18	0.64
HD 74194	O8.5	Ib-II (f)p	7.8	0.424±0.03	2212	2071	2372	264.04	-1.95
HD 74920	O7.5	IV n((f))	7.6	0.348±0.036	2649	2412	2934	265.29	-1.95
HD 75211	O8.5	II ((f))	7.9	0.555±0.038	1715	1608	1838	263.95	-0.47
HD 75222	O9.7	Iab	7.8	0.367±0.037	2513	2292	2779	258.29	4.18
HD 75759	O9	V	6.1	0.963±0.061	1011	951	1078	262.8	1.25
HD 76341	O9.2	IV	7.5	0.749±0.076	1292	1172	1438	263.54	1.52
HD 76556	O6	IV (n)((f))p	8.6	0.471±0.033	2000	1873	2146	267.58	-1.63
HD 76968	O9.2	Ib	7.2	0.427±0.036	2199	2033	2395	270.23	-3.37
HD 89137	ON9.7	II (n)	7.9	0.259±0.039	3416	3004	3950	279.69	4.45
HD 90087	O9.2	III (n)	7.8	0.312±0.041	2946	2615	3369	285.16	-2.13
HD 90273	ON7	V ((f))	9.2	0.308±0.035	2957	2673	3307	284.18	-0.25
HD 91572	O6.5	V ((f))z	8.3	0.37±0.055	2513	2191	2940	285.52	-0.05
HD 91651	ON9.5	III n	8.8	0.517±0.045	1844	1698	2017	286.55	-1.72
HD 91824	O7	V ((f))z	8.1	0.429±0.044	2190	1991	2432	285.7	0.07
HD 92206 A	O6	V ((f))z	8.3	0.273±0.038	3289	2908	3777	286.22	-0.17
HD 92206 B	O6	V ((f))	9.3	0.324±0.031	2833	2603	3107	286.23	-0.17
HD 92504	O8.5	V (n)	8.4	0.358±0.046	2581	2297	2943	285.92	0.99
HD 93027	O9.5	IV	8.7	0.262±0.036	3426	3031	3933	287.61	-1.13
HD 93028	O9	IV	8.3	0.284±0.053	3194	2701	3890	287.64	-1.19
HD 93128	O3.5	V ((fc))z	9.2	0.289±0.029	3145	2874	3471	287.4	-0.58
HD 93129 AaAb	O2	I f*	7.8	0.323±0.032	2841	2600	3131	287.41	-0.57
HD 93129 B	O3.5	V ((f))z	9	0.382±0.033	2438	2253	2656	287.41	-0.57
HD 93130	O6.5	III (f)	8.4	0.359±0.037	2587	2354	2870	287.57	-0.86
HD 93146 A	O7	V ((f))	8.4	0.288±0.039	3156	2799	3612	287.67	-1.05
HD 93160 AB	O7	III ((f))	8.2	0.251±0.039	3549	3101	4140	287.44	-0.59
HD 93161 A	O7.5	V	8.6	0.258±0.042	3460	3003	4071	287.44	-0.59
HD 93161 B	O6.5	IV ((f))	8.7	0.325±0.038	2828	2543	3183	287.44	-0.59

Notes: *: BJ18c/BJ18min/BJ18max: Bailer-Jones et al. (2018) central, minimum, and maximum distance values.

Table B.8: continued.

Name	SpT LC	B_{ap}	*Gaia* DR2 π	BJ18 distance [pc]			l	b
		[mag]	[mas]	c	min	max	[º]	[º]
HD 93162	O2.5 If*/WN6	8.5	0.476±0.033	1985	1860	2126	287.51	-0.71
HD 93204	O5.5 V((f))	8.5	0.449±0.038	2102	1943	2287	287.57	-0.71
HD 93205	O3.5 V((f))	7.8	0.372±0.039	2503	2272	2784	287.57	-0.71
HD 93206	O9.7 Ib n	7	0.908±0.102	1083	970	1227	287.67	-0.94
HD 93222 AB	O7 V((f))	8.8	0.34±0.036	2718	2470	3019	287.74	-1.02
HD 93249 A	O9 III	8.5	0.294±0.034	3096	2792	3472	287.41	-0.36
HD 93250 AB	O4 IV(fc)	7.9	0.363±0.03	2555	2369	2771	287.51	-0.54
HD 93343	O8 V	9.8	0.369±0.034	2521	2316	2765	287.64	-0.68
HD 93403	O5.5 III(fc)_var	7.5	-0.428±0.101	10170	7610	13600	287.54	-0.34
HD 93521	O9.5 III nn	6.8	0.513±0.123	1644	1376	2017	183.14	62.15
HD 93632	O5 If_var	8.7	0.374±0.033	2485	2291	2715	288.03	-0.87
HD 93843	O5 III(fc)	7.3	0.381±0.035	2448	2253	2680	288.24	-0.9
HD 94024	O8 IV	8.8	0.307±0.036	2962	2668	3326	287.34	1.27
HD 94370	O7 (n)fp	8.4	0.313±0.041	2918	2597	3327	288.01	0.63
HD 94963	O7 II(f)	7.1	0.227±0.044	3883	3279	4736	289.76	-1.81
HD 96264	O9.5 III	7.5	0.315±0.032	2915	2656	3228	290.4	-0.8
HD 96622	O9.2 IV	9.1	0.349±0.03	2647	2446	2884	290.09	0.57
HD 96670	O8.5 (n)fp_var	7.9	0.249±0.034	3577	3170	4096	290.2	0.4
HD 96715	O4 V((f))z	8.4	0.278±0.032	3254	2937	3643	290.27	0.33
HD 96917	O8 Ib(n)(f)	7.2	0.197±0.042	4257	3598	5175	289.28	3.06
HD 96946	O6.5 III(f)	8.7	0.309±0.04	2964	2634	3385	290.73	-0.34
HD 97166	O7.5 IV((f))	8	0.315±0.036	2907	2620	3261	290.67	0.19
HD 97253	O5 III(f)	7.4	0.266±0.04	3372	2954	3920	290.79	0.09
HD 97434	O7.5 III(n)((f))	8.2	0.363±0.035	2558	2339	2820	291.04	-0.15
HD 97848	O8 V	8.7	0.182±0.045	4496	3723	5613	290.74	1.53
HD 99546	O7.5 V((f))_Nstr	8.2	0.246±0.042	3585	3102	4235	292.33	1.68
HD 99897	O6.5 IV((f))	8.5	0.407±0.035	2302	2128	2506	293.61	-1.28
HD 100213	O8 V(n)	8.4	0.422±0.039	2230	2044	2451	294.81	-4.14
HD 101131	O5.5 V((f))	7.4	0.38±0.073	2489	2076	3096	294.78	-1.62
HD 101190 AaAb	O6 IV((f))	7.8	0.297±0.039	3073	2730	3509	294.78	-1.49
HD 101191	O8 V	8.5	0.344±0.05	2701	2364	3144	294.84	-1.68
HD 101205	O7 II:(n)	6.6	0.351±0.135	2765	1921	4528	294.85	-1.65
HD 101223	O8 V	8.9	0.368±0.038	2527	2298	2805	294.81	-1.49
HD 101298	O6.5 IV((f))	8.1	0.369±0.034	2519	2317	2760	294.94	-1.69
HD 101413	O8 V	8.6	0.53±0.044	1797	1662	1956	295.03	-1.71
HD 101436	O6.5 V((f))	7.7	0.326±0.103	2890	2147	4269	295.04	-1.71
HD 101545 AaAb	O9.2 II	7.5	0.377±0.051	2477	2188	2849	294.88	-0.81
HD 102415	ON9 IV:nn	9.4	0.458±0.027	2058	1946	2184	295.3	0.45
HD 104565	OC9.7 Iab	9.6	0.151±0.037	5180	4353	6334	296.51	4.02
HD 105056	ON9.7 Ia e	7.4	0.316±0.033	2907	2646	3223	298.94	-7.06
HD 105627	O9 III	8.2	0.394±0.04	2375	2162	2632	298.15	-0.1
HD 110360	ON7 V	9.5	0.424±0.037	2212	2041	2415	301.8	2.2
HD 112244	O8.5 Iab(f)p	5.4	0.857±0.192	1195	933	1650	303.55	6.03
HD 113904 B	O9 III	7.5	0.337±0.043	2749	2448	3133	304.67	-2.49
HD 114737 AB	O8.5 III	8.4	1.244±0.419	963	575	2683	305.41	-0.82
HD 114886	O9 III	7.5	0.957±0.579	1998	874	4857	305.52	-0.83
HD 115071	O9.5 III	8.2	0.476±0.038	1987	1845	2153	305.76	0.15
HD 115455	O8 III((f))	8.2	0.441±0.047	2137	1934	2385	306.06	0.22
HD 116852	O8.5 II-III((f))	8.4	0.044±0.056	6213	4936	7988	304.88	-16.13
HD 117490	ON9.5 III nn	8.9	0.472±0.044	2004	1835	2205	307.88	1.66
HD 117797	O7.5 fp	9.7	0.23±0.033	3817	3381	4374	307.86	0.04
HD 117856	O9.7 II-III	7.6	0.39±0.038	2397	2189	2646	307.77	-0.87
HD 118198	O9.7 III	8.7	0.355±0.043	2610	2338	2951	307.96	-1.22
HD 120521	O7.5 Ib(f)	8.8	0.187±0.043	4395	3681	5403	310.73	3.42
HD 120678	O9.5 V e	8.1	0.402±0.039	2324	2126	2561	352.59	2.87
HD 123008	ON9.2 Iab	9.2	0.21±0.038	4114	3539	4894	311.01	-2.8
HD 123056	O9.5 IV(n)	8.3	0.638±0.048	1505	1402	1624	312.17	1.03
HD 123590	O8 V z	8.4	0.504±0.037	1881	1757	2023	311.95	-1
HD 124314	O6+O9.2 IV+IV(n)((f))+(n)	7.5	0.553±0.036	1722	1619	1839	312.67	-0.42
HD 124979	O7.5 IV(n)((f))	8.6	0.293±0.047	3105	2691	3660	316.4	9.08

Notes: *: BJ18c/BJ18min/BJ18max: Bailer-Jones et al. (2018) central, minimum, and maximum distance values.

Table B.8: continued.

Name	SpT	LC	B_{ap}	*Gaia* DR2 π	BJ18 distance [pc]			l	b
			[mag]	[mas]	c	min	max	[º]	[º]
HD 125206	O9.7	IV n	8.5	0.421±0.043	2227	2024	2473	313.45	-0.03
HD 125241	O8.5	Ib (f)	8.8	0.414±0.034	2261	2095	2454	313.54	0.14
HD 130298	O6.5	III (n)(f)	9.7	0.324±0.036	2831	2564	3157	318.77	2.77
HD 135240	O7	IV ((f))	5.2	1.556±0.169	642	577	724	319.69	-2.91
HD 135591	O8	IV ((f))	5.4	1.197±0.168	839	728	991	320.13	-2.64
HD 148546	O9	Iab	8	0.339±0.068	2752	2287	3436	343.38	7.15
HD 148937	O6	f?p	7.8	0.881±0.046	1101	1047	1161	255.98	-4.71
HD 149038	O9.7	Iab	5	1.187±0.436	1031	607	2777	339.38	2.51
HD 149404	O8.5	Iab (f)p	5.9	0.76±0.165	1333	1054	1801	340.54	3.01
HD 149452	O9	IV n	9.6	0.726±0.049	1329	1246	1424	337.46	0.03
HD 149757	O9.2	IV nn	2.6	5.829±1.023	181	148	234	6.28	23.59
HD 150135	O6.5	V ((f))z	7.5	0.872±0.066	1117	1038	1209	336.71	-1.57
HD 150136	O3.5-4	III (f*)	6.1	0.944±0.12	1049	925	1210	336.71	-1.57
HD 150574	ON9	III (n)	8.7	0.392±0.06	2390	2075	2810	339	-0.2
HD 151003	O8.5	III	7.6	0.548±0.045	1740	1610	1892	342.72	2.41
HD 151018	O9	Ib	9.3	0.476±0.046	1988	1815	2197	339.51	-0.41
HD 151515	O7	II (f)	7.3	0.596±0.044	1607	1498	1732	342.81	1.7
HD 151804	O8	Ia f	5.3	0.614±0.213	1714	1165	3005	343.62	1.94
HD 152003	O9.7	Iab Nwk	7.4	0.506±0.059	1882	1688	2126	343.33	1.41
HD 152147	O9.7	Ib Nwk	7.8	0.565±0.074	1702	1502	1961	343.15	1.1
HD 152200	O9.7	IV (n)	8.4	0.65±0.068	1486	1344	1660	343.42	1.22
HD 152218	O9	IV	7.8	0.499±0.049	1903	1735	2107	343.53	1.28
HD 152219	O9.5	III (n)	7.8	0.644±0.084	1507	1329	1738	343.39	1.18
HD 152233	O6	II (f)	6.8	0.557±0.049	1714	1578	1874	343.48	1.22
HD 152246	O9	IV	8.1	0.683±0.049	1411	1317	1520	344.03	1.67
HD 152247	O9.2	III	7.6	0.515±0.056	1850	1671	2069	343.61	1.3
HD 152248	O7	Iab f	6.3	0.589±0.058	1630	1484	1809	343.46	1.18
HD 152249	OC9	Iab	6.6	0.484±0.055	1962	1765	2207	343.45	1.16
HD 152314	O9	IV	8.2	0.62±0.052	1549	1431	1688	343.52	1.14
HD 152386	O6:	Ia fpe	8.6	-2.239±0.246	8850	6455	12067	344.08	1.49
HD 152405	O9.7	II	7.3	0.47±0.055	2018	1809	2280	344.56	1.89
HD 152408	O8:	Ia fpe	5.9	0.446±0.108	2155	1703	2899	75.19	0.96
HD 152424	OC9.2	Ia	6.7	0.779±0.05	1242	1167	1327	343.36	0.89
HD 152590	O7.5	V z	8.6	0.611±0.061	1575	1431	1750	344.84	1.83
HD 152623	O7	V (n)((f))	7.5	-8.418±1.246	4496	2694	7231	344.62	1.61
HD 152723 AaAb	O6.5	III (f)	7.6	0.06±0.336	3485	2032	5996	344.81	1.61
HD 153426	O8.5	III	7.6	0.462±0.051	2049	1848	2298	347.14	2.38
HD 153919	O6	Ia fcp	6.8	0.549±0.064	1749	1563	1983	347.75	2.17
HD 154368	O9.2	Iab	6.6	0.822±0.049	1180	1114	1254	349.97	3.22
HD 154643	O9.7	III	7.4	0.933±0.084	1050	961	1157	350.54	3.19
HD 154811	OC9.7	Ib	7.3	0.849±0.047	1142	1083	1209	341.06	-4.22
HD 155756	O9	Ib p	9.8	0.274±0.057	3306	2746	4128	342.57	-4.39
HD 155775	O9.7	III (n)	6.7	0.877±0.065	1110	1034	1198	348.8	0.15
HD 155806	O7.5	V ((f))(e)	6.1	1.006±0.131	990	868	1151	196.96	1.52
HD 155889 AB	O9.5	IV	7	-0.249±0.934	4039	1911	7572	352.5	2.67
HD 155913	O4.5	V n((f))	8.7	0.77±0.061	1259	1167	1367	345.29	-2.61
HD 156154	O7.5	Ib (f)	8.7	0.638±0.058	1511	1385	1661	351.22	1.36
HD 156292	O9.7	III	7.8	0.545±0.07	1763	1560	2026	345.35	-3.08
HD 156738 AB	O6.5	III (f)	10.6	0.267±0.048	3374	2878	4060	351.18	0.48
HD 157857	O6.5	II (f)	8	0.252±0.065	3547	2832	4681	12.97	13.31
HD 158186	O9.2	V	7.1	0.94±0.064	1039	973	1114	355.91	1.6
HD 159176	O7	V ((f))	5.8	-0.807±0.351	6646	3993	10748	355.67	0.05
HD 161853	O8	V (n)z	8.1	0.782±0.077	1249	1134	1389	358.43	-1.88
HD 162978	O8	II ((f))	6.2	0.907±0.088	1082	984	1201	4.54	0.3
HD 163758	O6.5	Ia fp	7.3	0.258±0.066	3568	2805	4840	355.36	-6.1
HD 163800	O7.5	III ((f))	7.3	0.812±0.08	1203	1093	1337	7.05	0.69
HD 163892	O9.5	IV (n)	7.6	0.69±0.064	1403	1284	1547	7.15	0.62
HD 164019	O9.5	IV p	9.5	0.178±0.08	4766	3385	7390	1.91	-2.62
HD 164438	O9.2	IV	7.8	0.807±0.069	1205	1110	1318	10.35	1.79
HD 164492	O7.5	V z	7.6	0.638±0.087	1529	1337	1785	7	-0.25

Notes: *: BJ18c/BJ18min/BJ18max: Bailer-Jones et al. (2018) central, minimum, and maximum distance values.

Table B.8: continued.

Name	SpT LC	B_{ap}	*Gaia* DR2 π	BJ18 distance [pc]			l	b
		[mag]	[mas]	c	min	max	[º]	[º]
HD 164794	O4 V((f))	6.5	0.851±0.095	1155	1036	1305	6.01	-1.21
HD 164816	O9.5 V	7.1	0.844±0.07	1155	1066	1260	6.06	-1.2
HD 165052	O6 V z	7	0.784±0.046	1235	1167	1312	6.12	-1.48
HD 165174	O9.7 II n	6.1	0.901±0.074	1083	1001	1181	29.27	11.29
HD 165246	O8 V(n)	7.9	0.501±0.113	1971	1561	2653	6.4	-1.56
HD 165921	O7 V(n)z	7.5	0.908±0.056	1072	1009	1143	6.94	-2.1
HD 166546	O9.5 IV	7.3	0.613±0.099	1596	1360	1927	10.36	-0.92
HD 167263	O9.5 III	6.1	0.48±0.248	2307	1391	4597	10.76	-1.58
HD 167264	O9.7 Iab	5.4	1.161±0.135	857	763	976	10.46	-1.74
HD 167633	O6.5 V((f))	8.4	0.525±0.064	1823	1623	2077	14.34	-0.07
HD 167659	O7 II-III(f)	7.6	0.604±0.079	1605	1414	1853	12.2	-1.27
HD 167771	O7 III((f))	6.6	0.52±0.05	1832	1674	2024	12.7	-1.13
HD 167971	O8 Ia f(n)	8.9	0.492±0.11	1976	1581	2612	18.25	1.68
HD 168075	O6.5 V((f))	9.2	0.533±0.071	1802	1588	2079	16.94	0.84
HD 168076 AB	O4 IV(f)	9.2	-2.135±0.556	5061	3142	7951	16.94	0.84
HD 168112 AB	O5 IV(f)	9.9	0.384±0.063	2437	2097	2900	18.44	1.62
HD 168137 AaAb	O8 V z	10	0.488±0.074	1961	1698	2315	16.97	0.76
HD 168461	O7.5 V((f))_Nstr	10.2	0.577±0.059	1664	1511	1852	18.57	1.25
HD 168504	O7.5 V(n)z	9.7	0.443±0.082	2152	1803	2658	17.03	0.35
HD 168941	O9.5 IV p	9.4	0.402±0.079	2393	1973	3030	5.82	-6.31
HD 169582	O6 Ia f	9.3	0.571±0.06	1680	1521	1876	21.33	1.2
HD 171589	O7.5 II(f)	8.5	0.446±0.057	2127	1884	2440	18.65	-3.09
HD 172175	O6.5 I(n)fp	10	0.441±0.054	2146	1911	2445	24.53	-0.85
HD 173010	O9.7 Ia+ var	10	0.221±0.048	3961	3286	4947	23.73	-2.49
HD 173783	O9 Iab	9.8	0.294±0.059	3125	2602	3891	24.18	-3.34
HD 175514	O7 V(n)((f))z	9.2	0.783±0.053	1237	1158	1326	41.71	3.38
HD 175754	O8 II(n)((f))p	6.9	0.453±0.057	2102	1867	2404	16.39	-9.92
HD 175876	O6.5 III(n)(f)	6.8	0.364±0.071	2607	2158	3280	15.28	-10.58
HD 186980	O7.5 III((f))	7.5	0.472±0.041	2010	1851	2197	67.39	3.66
HD 188001	O7.5 Iab f	6.2	0.534±0.048	1786	1641	1957	56.48	-4.33
HD 188209	O9.5 Iab	5.6	0.668±0.073	1450	1306	1628	80.99	10.09
HD 189957	O9.7 III	7.8	0.483±0.044	1966	1802	2163	77.43	6.17
HD 190429 A	O4 If	7.3	0.46±0.035	2054	1914	2217	72.59	2.61
HD 190864	O6.5 III(f)	8	0.489±0.03	1936	1827	2059	72.47	2.02
HD 191201	O9.5+O9.7 III+III	7.8	0.107±0.243	4065	2410	7012	72.75	1.78
HD 191423	ON9 II-III nn	8.2	0.605±0.037	1584	1493	1686	78.64	5.37
HD 191612	O8 f?p_var	8	0.47±0.036	2010	1872	2168	245.44	-0.1
HD 191781	ON9.7 Iab	10.3	0.318±0.03	2890	2653	3171	81.18	6.61
HD 191978	O8 V	8.2	0.673±0.039	1428	1351	1514	77.87	4.25
HD 192001	O9.5 IV	8.6	0.548±0.038	1738	1628	1863	78.53	4.66
HD 192281	O4.5 IV(n)(f)	7.9	0.751±0.033	1284	1231	1342	77.12	3.4
HD 192639	O7.5 Iab f	7.5	0.385±0.034	2418	2233	2635	74.9	1.48
HD 193322	O9 IV(n)	6.8	1.011±0.155	988	845	1186	78.1	2.78
HD 193443 AB	O9 III	8.3	0.722±0.468	1722	942	3568	76.15	1.28
HD 193514	O7 Ib(f)	7.8	0.522±0.03	1815	1718	1923	77	1.8
HD 193595	O7 V((f))	9.1	0.562±0.037	1693	1593	1808	76.86	1.62
HD 193682	O4.5 IV(f)	8.9	0.582±0.037	1640	1544	1748	75.92	0.82
HD 195592	O9.7 Ia	8	0.574±0.03	1659	1578	1748	82.36	2.96
HD 198846	O9.5 IV	7.2	0.576±0.043	1656	1543	1788	77.25	-6.23
HD 199579	O6.5 V((f))z	6	1.063±0.059	918	870	972	85.7	-0.3
HD 201345	ON9.2 IV	7.6	0.314±0.055	2879	2472	3433	78.44	-9.54
HD 202124	O9 Iab	8	0.304±0.033	2977	2705	3307	87.29	-2.66
HD 202214	O9.5 IV	6.6	2.82±1.237	2044	397	4940	98.52	7.99
HD 203064	O7.5 III n((f))	5	1.703±0.18	587	528	660	87.61	-3.84
HD 204827	O9.5 IV	9.3	0.773±0.093	1269	1127	1451	99.17	5.55
HD 206183	O9.5 IV-V	7.5	0.957±0.033	1016	982	1051	98.89	3.4
HD 206267	O6.5 V((f))	6.2	0.895±0.236	1190	854	1941	99.29	3.74
HD 207198	O8.5 II((f))	6.3	0.976±0.053	999	947	1056	103.14	6.99
HD 207538	O9.7 IV	7.6	1.194±0.028	818	800	837	101.6	4.67
HD 209339	O9.7 IV	6.8	1.184±0.03	825	805	846	104.58	5.87

Notes: *: BJ18c/BJ18min/BJ18max: Bailer-Jones et al. (2018) central, minimum, and maximum distance values.

Table B.8: continued.

Name	SpT LC	B_{ap}	*Gaia* DR2 π	BJ18 distance [pc]			l	b
		[mag]	[mas]	c	min	max	[º]	[º]
HD 209481	O9 IV (n)_var	5.6	0.908±0.104	1084	968	1232	102	2.18
HD 209975	O9 Ib	5.2	1.165±0.146	857	756	988	104.87	5.39
HD 210809	O9 Iab	7.6	0.231±0.035	3747	3303	4318	99.85	-3.13
HD 210839	O6.5 I (n)fp	5.3	1.62±0.127	612	567	665	103.83	2.61
HD 213023 A	O7.5 V z	9.9	0.978±0.037	994	958	1033	107.73	5.2
HD 214680	O9 V	4.7	2.788±0.232	358	330	392	96.65	-16.98
HD 215835	O5.5 V ((f))	8.9	0.308±0.035	2943	2663	3285	107.07	-0.9
HD 216532	O8.5 V (n)	8.5	1.332±0.03	735	719	752	109.65	2.68
HD 216898	O9 V	8.5	1.191±0.033	820	799	843	109.93	2.39
HD 217086	O7 V nn((f))z	8.3	1.174±0.028	831	812	851	110.22	2.72
HD 218195 A	O8.5 III Nstr	8.7	0.63±0.093	1532	1330	1804	109.31	-1.79
HD 218915	O9.2 Iab	7.2	0.124±0.047	5131	4217	6404	108.06	-6.89
HD 225146	O9.7 Iab	9	0.289±0.032	3110	2821	3463	117.23	-1.24
HD 225160	O8 Iab f	8.5	0.294±0.037	3061	2740	3461	117.44	-0.14
HD 226868	O9.7 Iab p_var	9.7	0.422±0.032	2229	2077	2405	117.93	1.25
HD 227018	O6.5 V ((f))z	9.4	0.475±0.033	1993	1866	2138	71.58	2.87
HD 227245	O7 V ((f))z	10.3	0.625±0.026	1531	1473	1594	72.17	2.62
HD 227465	O7 V ((f))	10.7	0.163±0.029	5093	4411	6004	70.73	1.21
HD 228759	O6.5 V (n)((f))z	10.1	0.574±0.027	1659	1587	1738	79.01	3.62
HD 228766	O4 I f*	9.8	0.455±0.03	2068	1946	2207	309.91	-0.69
HD 228841	O6.5 V n((f))	9.5	0.583±0.028	1637	1565	1716	76.6	1.68
HD 228854	O6 IV n_var	9.5	0.544±0.03	1745	1656	1844	74.54	0.2
HD 229196	O6 II (f)	9.4	0.52±0.031	1823	1722	1937	78.76	2.07
HD 229202	O7.5 V (n)((f))	10.4	0.494±0.03	1912	1806	2032	78.19	1.63
HD 229232	O4 V: n((f))	10.4	0.5±0.027	1891	1797	1995	77.4	0.93
HD 237211	O9 Ib	9.5	0.189±0.036	4420	3794	5268	147.14	2.97
HD 242908	O4.5 V (n)((fc))z	9.3	0.223±0.052	3785	3149	4695	173.47	-1.66
HD 242926	O7 V z	9.7	0.049±0.428	2957	1697	5127	173.65	-1.74
HD 242935 A	O6.5 V ((f))z	9.8	0.429±0.114	2206	1721	3016	173.58	-1.67
HD 256725 A	O5 V ((fc))	10.1	0.222±0.067	3628	2920	4689	192.31	3.36
HD 298429	O8.5 V	10.3	0.445±0.035	2115	1967	2287	274.47	-0.25
HD 303308 AB	O4.5 V ((fc))	8.6	0.407±0.039	2302	2104	2539	287.59	-0.61
HD 303311	O6 V ((f))z	9.1	0.252±0.029	3552	3211	3970	287.49	-0.54
HD 303492	O8.5 Ia f	9.4	0.199±0.036	4283	3694	5076	288.05	0.4
HD 305523	O9 II-III	8.6	0.346±0.033	2675	2449	2945	287.66	-0.9
HD 305525	O5.5 V ((f))z	10.7	0.205±0.159	3704	2419	6121	287.79	-0.71
HD 305532	O6.5 V ((f))z	10.5	0.274±0.034	3301	2958	3731	287.78	-0.84
HD 305619	O9.7 II	9.9	0.327±0.03	2815	2594	3077	288.22	-0.96
HD 308813	O9.7 IV (n)	9.3	0.189±0.039	4485	3794	5452	294.79	-1.61
HD 313846	O7: Ia fpe	10.7	0.313±0.041	2938	2605	3365	289.77	-1.22
HD 319699	O5 V ((fc))	10.3	0.581±0.041	1646	1540	1767	351.32	0.92
HD 319702	O8 III	11	0.62±0.05	1550	1436	1684	351.35	0.61
HD 319703 A	O7 V ((f))	11.9	-0.048±0.136	6004	4041	9077	351.03	0.65
HD 322417	O6.5 IV ((f))	10.9	0.351±0.063	2641	2242	3200	345.26	1.47
HD 323110	ON9 Ia	10.9	0.63±0.063	1531	1392	1700	349.65	-0.67
HD 326329	O9.7 V	8.8	0.684±0.051	1408	1312	1519	343.46	1.17
HD 326331	O8 IV n((f))	7.6	0.616±0.045	1556	1451	1677	343.49	1.14
HD 326775	O6.5 V (n)((f))z	11.6	0.524±0.065	1826	1622	2086	345.01	-0.3
HD 338916	O7.5 V z	10.8	0.492±0.039	1926	1788	2086	61.47	0.38
HD 338931	O6 III (f)	9.8	0.462±0.039	2044	1891	2223	61.19	-0.14
HD 344777	O7.5 V z	10.2	0.516±0.04	1842	1712	1993	59.41	0.11
HD 344784	O6.5 V ((f))z	9.9	1.735±0.138	572	529	622	59.4	-0.15
ALS 2063	O5 I fp	11.5	0.443±0.262	2581	1486	5256	341.11	-0.94
ALS 4880	O6 V ((f))	11.3	0.459±0.046	2060	1875	2283	18.32	1.87
ALS 7833	O8 V z	10.4	0.287±0.04	3143	2783	3603	146.25	3.12
ALS 8272	O7 V ((f))	11.8	0.19±0.055	4259	3445	5477	168.75	1
ALS 8294	O7 V (n)z	10.7	0.356±0.056	2590	2244	3053	173.61	-1.72
ALS 12320	O7 IV ((f))	11.2	0.249±0.029	3554	3217	3966	102.98	-0.76
ALS 12370	O6.5 V nn((f))	10.5	0.167±0.036	4787	4089	5731	103.05	-1.41

Notes: *: BJ18c/BJ18min/BJ18max: Bailer-Jones et al. (2018) central, minimum, and maximum distance values.

Table B.8: continued.

Name	SpT LC	B_{ap}	*Gaia* DR2 π	BJ18 distance [pc]			l	b
		[mag]	[mas]	c	min	max	[º]	[º]
ALS 12619	O7 V ((f))z	11.3	0.412±0.028	2266	2130	2421	107.18	-0.95
ALS 12688	O5.5 V (n)((fc))	11.3	0.186±0.029	4465	3961	5102	107.42	-2.87
ALS 15210	O3.5 I f*_Nwk	11.5	0.394±0.03	2367	2206	2553	287.52	-0.71
BD -10 4682	O7 V n((f))	10.2	0.506±0.054	1883	1703	2103	20.24	1.01
BD -11 4586	O8 Ib (f)	10.4	0.573±0.046	1670	1548	1812	19.08	2.14
BD -13 4927	O7 II (f)	10.4	0.616±0.063	1563	1417	1741	16.98	0.85
BD -14 5040	O5.5 V (n)((f))	11.5	0.61±0.036	1570	1484	1666	16.9	-1.12
BD -16 4826	O5.5 V ((f))z	10.6	0.568±0.043	1682	1565	1818	15.26	-0.73
BD +60 498	O9.7 II-III .	10.5	0.453±0.065	2087	1828	2428	134.63	0.99
BD +60 499	O9.5 V	10.8	0.353±0.051	2609	2293	3022	134.64	1
BD +60 501	O7 V (n)((f))z	10.1	0.424±0.03	2209	2068	2369	134.71	0.94
BD +61 411	O6.5 V ((f))z	11.2	0.394±0.057	2372	2079	2755	133.84	1.17
CPD -26 2716	O6.5 Iab f	10.1	0.043±0.032	8738	7147	10910	243.82	0.14
CPD -28 2561	O6.5 . f?p	10.1	0.199±0.042	4214	3570	5106	7.36	-0.85
CPD -41 7721 A	O9.7 V: (n)	8.8	0.636±0.048	1509	1406	1629	343.44	1.17
CPD -41 7733	O9 IV	7.9	0.557±0.049	1716	1580	1877	343.46	1.17
CPD -47 2963 AB	O5 I fc	9.7	0.547±0.037	1740	1633	1863	267.98	-1.36
CPD -54 6791	O9.5 V	11.5	0.165±0.11	4197	2954	6358	327.56	-0.83
CPD -58 2611	O6 V ((f))z	9.9	0.313±0.027	2929	2711	3183	287.39	-0.59
CPD -59 2551	O9 V	9.2	0.312±0.03	2937	2690	3232	287.67	-1.05
CPD -59 2600	O6 V ((f))	8.8	0.166±0.038	4925	4125	6058	287.6	-0.74
CPD -59 2635	O8 V (n)	9.5	0.464±0.036	2036	1895	2200	287.64	-0.68
CPD -59 2641	O6 V ((fc))	9.5	0.439±0.034	2141	1994	2312	287.64	-0.65
CPD -59 5634	O9.2 Ib	10.3	0.233±0.038	3754	3277	4381	315.37	-0.08
CYG OB2-4 A	O7 III ((f))	11.6	0.67±0.036	1431	1359	1511	80.22	1.02
CYG OB2-7	O3 I f*	12.2	0.625±0.03	1529	1462	1603	80.24	0.8
CYG OB2-9	O4.5 I f	12.9	0.601±0.033	1586	1507	1675	80.17	0.76
CYG OB2-11	O5.5 I fc	11.7	0.581±0.027	1639	1569	1714	80.57	0.83
Herschel 36	O7: V	11	0.902±0.219	1170	869	1778	5.97	-1.17
MY CAM	O5.5 V (n)	10	0.133±0.079	4774	3568	6703	146.27	3.14
Trumpler 14-9	O8.5 V	10.1	0.431±0.036	2183	2018	2376	287.4	-0.58
V572 CAR	O7.5 V (n)	8.9	0.243±0.037	3645	3199	4226	287.59	-0.69
V747 CEP	O5.5 V (n)((f))	11.4	1.016±0.031	958	930	987	118.2	5.09

Notes: *: BJ18c/BJ18min/BJ18max: Bailer-Jones et al. (2018) central, minimum, and maximum distance values.

Table B.9: Fundamental physical parameters derived for the sample of O-type standard stars using the Bailer-Jones et al. (2018) distance values, and limits, to the stars.

Columns include: Name, spectral type and luminosity classification, dereddened magnitud compiled from Maíz Apellániz & Barbá (2018), and ranges for absolute V magnitude, radius, luminosity, and spectroscopic mass. The last column is the analysis quality flag (Sect. 5.4).

Name	SpT LC	V0 [mag]	M_V range [mag]	R range [$R_\odot$]	log L range [$L_\odot$]	M_{sp} range [$M_\odot$]	qual. flag
HD 93129 AaAb	O2 I f*	4.83	$-7.44^{-0.21}_{+0.19}$	$29.5^{+3.0}_{-2.5}$	$6.55^{+0.08}_{-0.08}$	$737.0^{+156.6}_{-118.0}$	Q4
CYG OB2-7	O3 I f*	5.01	$-5.91^{-0.1}_{+0.1}$	$13.9^{+0.7}_{-0.6}$	$6.05^{+0.04}_{-0.04}$	$94.9^{+8.6}_{-8.3}$	Q4
HD 190429 A	O4 I f	5.07	$-6.49^{-0.17}_{+0.15}$	$22.0^{+1.8}_{-1.5}$	$5.89^{+0.07}_{-0.06}$	$59.0^{+9.7}_{-7.7}$	Q1
HD 15570	O4 I f	4.84	$-7.0^{-0.19}_{+0.18}$	$26.4^{+2.4}_{-2.0}$	$6.21^{+0.08}_{-0.07}$	$106.1^{+19.6}_{-14.6}$	Q4
HD 16691	O4 I f	6.15	$-5.49^{-0.22}_{+0.2}$	$13.0^{+1.3}_{-1.2}$	$5.63^{+0.09}_{-0.08}$	$41.1^{+9.3}_{-6.8}$	Q4
HD 14947	O4.5 I f	5.7	$-6.9^{-0.38}_{+0.33}$	$25.5^{+4.9}_{-3.6}$	$6.13^{+0.16}_{-0.13}$	$112.8^{+47.6}_{-29.8}$	Q3
CYG OB2-9	O4.5 I f	3.81	$-7.19^{-0.12}_{+0.11}$	$28.4^{+1.6}_{-1.4}$	$6.27^{+0.05}_{-0.05}$	$243.8^{+30.9}_{-23.1}$	Q4
CPD -47 2963 AB	O5 I fc	4.54	$-6.66^{-0.15}_{+0.14}$	$23.4^{+1.7}_{-1.3}$	$5.97^{+0.06}_{-0.05}$	$65.9^{+9.7}_{-8.0}$	Q3
CYG OB2-11	O5.5 I fc	4.4	$-6.68^{-0.1}_{+0.09}$	$23.8^{+1.1}_{-1.1}$	$5.99^{+0.04}_{-0.04}$	$91.4^{+9.1}_{-7.8}$	Q3
HD 169582	O6 Ia f	5.83	$-5.3^{-0.24}_{+0.22}$	$12.2^{+1.4}_{-1.2}$	$5.48^{+0.1}_{-0.08}$	$30.4^{+7.4}_{-5.3}$	Q1

Table B.9: continued.

Name	SpT	LC	V0 [mag]	M_V range [mag]	R range [$R_\odot$]	log L range [$L_\odot$]	M_{sp} range [$M_\odot$]	qual. flag
HD 229196	O6	II (f)	4.53	$-6.78^{-0.13}_{+0.12}$	$24.9^{+1.5}_{-1.5}$	$6.0^{+0.06}_{-0.05}$	$74.2^{+9.9}_{-8.0}$	Q1
HD 163758	O6.5	Ia fp	6.12	$-6.64^{-0.66}_{+0.52}$	$24.6^{+8.8}_{-5.3}$	$5.89^{+0.27}_{-0.21}$	$42.9^{+37.1}_{-16.3}$	Q3
HD 157857	O6.5	II (f)	6.14	$-6.61^{-0.6}_{+0.49}$	$23.1^{+7.4}_{-4.6}$	$5.91^{+0.24}_{-0.19}$	$63.9^{+46.9}_{-23.2}$	Q1
HD 69464	O7	Ib (f)	6.61	$-6.43^{-0.32}_{+0.28}$	$21.6^{+3.4}_{-2.6}$	$5.83^{+0.13}_{-0.11}$	$41.0^{+13.7}_{-9.6}$	Q2
HD 193514	O7	Ib (f)	5	$-6.29^{-0.13}_{+0.12}$	$20.1^{+1.2}_{-1.0}$	$5.78^{+0.05}_{-0.04}$	$56.7^{+7.2}_{-5.5}$	Q2
HD 94963	O7	II (f)	6.34	$-6.61^{-0.43}_{+0.37}$	$23.1^{+5.0}_{-3.7}$	$5.92^{+0.17}_{-0.15}$	$67.9^{+33.2}_{-19.6}$	Q2
HD 151515	O7	II (f)	5.56	$-5.47^{-0.16}_{+0.15}$	$13.7^{+1.1}_{-0.9}$	$5.45^{+0.07}_{-0.06}$	$25.7^{+3.9}_{-3.2}$	Q1
HD 188001	O7.5	Iab f	5.12	$-6.14^{-0.2}_{+0.18}$	$20.4^{+1.9}_{-1.6}$	$5.6^{+0.08}_{-0.07}$	$25.1^{+5.2}_{-3.9}$	Q3
HD 192639	O7.5	Iab f	5.08	$-6.84^{-0.19}_{+0.17}$	$26.5^{+2.5}_{-2.0}$	$5.96^{+0.07}_{-0.07}$	$70.0^{+13.4}_{-10.1}$	Q2
HD 156154	O7.5	Ib (f)	5.09	$-5.81^{-0.21}_{+0.19}$	$16.7^{+1.7}_{-1.4}$	$5.53^{+0.09}_{-0.07}$	$21.1^{+4.3}_{-3.5}$	Q2
HD 17603	O7.5	Ib (f)	5.52	$-6.36^{-0.25}_{+0.23}$	$21.9^{+2.6}_{-2.1}$	$5.73^{+0.1}_{-0.09}$	$31.3^{+8.0}_{-5.9}$	Q2
HD 171589	O7.5	II (f)	6.34	$-5.3^{-0.3}_{+0.26}$	$12.5^{+1.9}_{-1.4}$	$5.4^{+0.12}_{-0.1}$	$25.9^{+8.2}_{-5.6}$	Q1
HD 34656	O7.5	II (f)	5.61	$-6.23^{-0.55}_{+0.45}$	$19.4^{+5.7}_{-3.6}$	$5.76^{+0.22}_{-0.18}$	$44.3^{+29.9}_{-15.1}$	Q3
HD 151804	O8	Ia f	3.87	$-7.3^{-1.22}_{+0.84}$	$39.4^{+29.7}_{-12.5}$	$6.03^{+0.49}_{-0.33}$	$38.6^{+78.2}_{-20.2}$	Q3
HD 225160	O8	Iab f	6.22	$-6.21^{-0.27}_{+0.24}$	$21.0^{+2.8}_{-2.2}$	$5.63^{+0.1}_{-0.1}$	$27.8^{+7.9}_{-5.4}$	Q2
BD -11 4586	O8	Ib (f)	5.13	$-5.98^{-0.18}_{+0.16}$	$18.6^{+1.7}_{-1.2}$	$5.54^{+0.07}_{-0.06}$	$21.4^{+3.7}_{-2.9}$	Q2
HD 162978	O8	II ((f))	4.88	$-5.29^{-0.23}_{+0.21}$	$12.9^{+1.4}_{-1.1}$	$5.35^{+0.09}_{-0.08}$	$19.3^{+4.6}_{-3.1}$	Q3
HD 303492	O8.5	Ia f	5.69	$-7.47^{-0.37}_{+0.32}$	$42.5^{+7.9}_{-5.8}$	$6.02^{+0.15}_{-0.13}$	$48.5^{+19.7}_{-12.4}$	Q3
HD 125241	O8.5	Ib (f)	5.68	$-6.1^{-0.18}_{+0.17}$	$19.8^{+1.6}_{-1.5}$	$5.58^{+0.06}_{-0.07}$	$23.7^{+4.0}_{-3.4}$	Q2
HD 75211	O8.5	II ((f))	5.29	$-5.88^{-0.15}_{+0.14}$	$17.5^{+1.2}_{-1.1}$	$5.53^{+0.06}_{-0.06}$	$25.2^{+3.7}_{-3.1}$	Q2
HD 207198	O8.5	II ((f))	4.23	$-5.77^{-0.12}_{+0.12}$	$16.6^{+0.9}_{-0.9}$	$5.47^{+0.05}_{-0.05}$	$20.6^{+2.4}_{-2.2}$	Q1
HD 30614	O9	Ia	3.23	$-6.17^{-0.78}_{+0.58}$	$23.5^{+10.2}_{-5.5}$	$5.5^{+0.31}_{-0.23}$	$13.8^{+14.3}_{-5.8}$	Q2
HD 152249	OC9	Iab	4.68	$-6.78^{-0.26}_{+0.23}$	$27.8^{+3.6}_{-2.8}$	$5.81^{+0.11}_{-0.09}$	$44.1^{+14.7}_{-8.4}$	Q2
HD 202124	O9	Iab	6.03	$-6.34^{-0.23}_{+0.21}$	$23.1^{+2.7}_{-2.1}$	$5.62^{+0.09}_{-0.09}$	$25.3^{+5.9}_{-4.5}$	Q3
HD 210809	O9	Iab	6.39	$-6.47^{-0.31}_{+0.27}$	$24.4^{+3.8}_{-2.8}$	$5.69^{+0.12}_{-0.11}$	$28.8^{+9.5}_{-6.3}$	Q2
HD 209975	O9	Ib	3.93	$-5.74^{-0.31}_{+0.27}$	$16.8^{+2.6}_{-2.0}$	$5.42^{+0.13}_{-0.11}$	$20.6^{+6.8}_{-4.3}$	Q3
HD 71304	O9	II	5.74	$-6.35^{-0.24}_{+0.21}$	$22.3^{+2.5}_{-2.2}$	$5.67^{+0.09}_{-0.09}$	$35.8^{+8.4}_{-6.6}$	Q1
HD 57061 AaAb	O9	II	3.84	$-9.86^{-1.06}_{+1.15}$	$110.3^{+69.6}_{-45.3}$	$7.11^{+0.42}_{-0.46}$	$1472.0^{+2430.9}_{-961.6}$	Q1
HD 152424	OC9.2	Ia	3.93	$-6.54^{-0.14}_{+0.14}$	$25.5^{+1.9}_{-1.5}$	$5.69^{+0.06}_{-0.05}$	$35.0^{+5.1}_{-4.1}$	Q2
HD 218915	O9.2	Iab	6.25	$-7.3^{-0.48}_{+0.43}$	$35.2^{+8.7}_{-6.3}$	$6.02^{+0.19}_{-0.17}$	$73.6^{+40.5}_{-24.3}$	Q3
HD 154368	O9.2	Iab	3.62	$-6.74^{-0.13}_{+0.13}$	$28.0^{+1.8}_{-1.5}$	$5.78^{+0.05}_{-0.05}$	$31.0^{+4.3}_{-3.1}$	Q3
HD 123008	ON9.2	Iab	6.62	$-6.45^{-0.38}_{+0.33}$	$23.4^{+4.5}_{-3.2}$	$5.7^{+0.15}_{-0.13}$	$32.8^{+13.8}_{-8.4}$	Q3
HD 76968	O9.2	Ib	5.67	$-6.04^{-0.18}_{+0.17}$	$19.9^{+1.7}_{-1.5}$	$5.51^{+0.07}_{-0.07}$	$27.8^{+5.0}_{-4.1}$	Q3
HD 188209	O9.5	Iab	4.91	$-5.9^{-0.25}_{+0.23}$	$19.2^{+2.3}_{-1.9}$	$5.43^{+0.1}_{-0.09}$	$14.8^{+3.9}_{-2.8}$	Q3
HD 105056	ON9.7	Ia e	6.17	$-6.15^{-0.22}_{+0.2}$	$23.7^{+2.5}_{-2.2}$	$5.44^{+0.08}_{-0.09}$	$14.5^{+3.2}_{-2.6}$	Q3
HD 195592	O9.7	Ia	3.42	$-7.68^{-0.11}_{+0.11}$	$46.8^{+2.4}_{-2.3}$	$6.07^{+0.05}_{-0.04}$	$65.9^{+6.8}_{-6.3}$	Q2
HD 149038	O9.7	Iab	3.74	$-6.32^{-2.15}_{+1.15}$	$23.2^{+39.6}_{-9.5}$	$5.58^{+0.86}_{-0.46}$	$30.3^{+191.7}_{-19.5}$	Q3
HD 225146	O9.7	Iab	6.61	$-5.86^{-0.23}_{+0.21}$	$19.6^{+2.2}_{-1.8}$	$5.34^{+0.1}_{-0.08}$	$17.6^{+4.2}_{-3.5}$	Q1
HD 104565	OC9.7	Iab	7.15	$-6.42^{-0.44}_{+0.38}$	$25.2^{+5.5}_{-4.1}$	$5.59^{+0.18}_{-0.15}$	$23.2^{+11.3}_{-6.3}$	Q3
HD 191781	ON9.7	Iab	6.49	$-5.82^{-0.2}_{+0.19}$	$19.2^{+1.9}_{-1.6}$	$5.35^{+0.08}_{-0.08}$	$27.5^{+5.6}_{-11.6}$	Q1
HD 154811	OC9.7	Ib	4.71	$-5.58^{-0.12}_{+0.12}$	$16.6^{+0.9}_{-0.9}$	$5.28^{+0.05}_{-0.05}$	$15.1^{+1.9}_{-1.1}$	Q3
HD 152147	O9.7	Ib Nwk	5.14	$-6.02^{-0.31}_{+0.27}$	$20.1^{+3.1}_{-2.3}$	$5.47^{+0.13}_{-0.11}$	$25.9^{+8.5}_{-5.1}$	Q3
HD 47432	O9.7	Ib	4.95	$-6.97^{-0.43}_{+0.36}$	$32.2^{+5.9}_{-4.9}$	$5.82^{+0.17}_{-0.14}$	$38.5^{+18.2}_{-10.8}$	Q3
HD 68450	O9.7	II	5.53	$-5.36^{-0.14}_{+0.14}$	$14.6^{+1.0}_{-0.8}$	$5.22^{+0.06}_{-0.05}$	$16.4^{+2.5}_{-1.8}$	Q1
HD 10125	O9.7	II	6.44	$-7.91^{-0.62}_{+0.57}$	$47.0^{+15.6}_{-10.8}$	$6.26^{+0.24}_{-0.23}$	$193.5^{+147.7}_{-79.5}$	Q3
HD 152405	O9.7	II	5.8	$-5.73^{-0.26}_{+0.24}$	$17.4^{+2.2}_{-1.8}$	$5.36^{+0.1}_{-0.1}$	$21.5^{+5.8}_{-4.3}$	Q1
HD 93250 AB	O4	IV (fc)	5.51	$-6.52^{-0.18}_{+0.16}$	$19.5^{+1.6}_{-1.4}$	$6.14^{+0.08}_{-0.06}$	$99.3^{+17.9}_{-11.5}$	Q1
HD 168076 AB	O4	IV (f)	5.27	$-8.25^{-0.98}_{+1.03}$	$44.2^{+25.2}_{-16.6}$	$6.79^{+0.39}_{-0.41}$	$574.0^{+859.4}_{-351.3}$	Q3
HD 93843	O5	III (fc)	6.17	$-5.77^{-0.2}_{+0.18}$	$15.6^{+1.5}_{-1.3}$	$5.62^{+0.08}_{-0.07}$	$29.7^{+6.1}_{-4.5}$	Q2
HD 168112 AB	O5	IV (f)	5.28	$-6.65^{-0.38}_{+0.33}$	$22.3^{+4.2}_{-3.1}$	$6.04^{+0.15}_{-0.13}$	$96.4^{+40.9}_{-24.4}$	Q1

Table B.9: continued.

Name	SpT LC	V0 [mag]	M_V range [mag]	R range [$R_\odot$]	log L range [$L_\odot$]	M_{sp} range [$M_\odot$]	qual. flag
HD 152723 AaAb	O6.5 III (f)	5.64	$-7.07^{-1.18}_{+1.17}$	$27.8^{+20.1}_{-11.6}$	$6.16^{+0.47}_{-0.47}$	$185.8^{+383.3}_{-122.4}$	Q3
HD 96946	O6.5 III (f)	6.77	$-5.59^{-0.29}_{+0.26}$	$13.8^{+1.9}_{-1.6}$	$5.59^{+0.12}_{-0.1}$	$50.5^{+15.5}_{-10.3}$	Q3
HD 156738 AB	O6.5 III (f)	5.34	$-7.3^{-0.4}_{+0.34}$	$30.8^{+6.3}_{-4.5}$	$6.24^{+0.16}_{-0.14}$	$249.4^{+115.2}_{-67.6}$	Q3
HD 190864	O6.5 III (f)	6.14	$-5.3^{-0.13}_{+0.13}$	$12.3^{+0.8}_{-0.7}$	$5.43^{+0.05}_{-0.05}$	$24.5^{+3.5}_{-2.7}$	Q1
HD 93160 AB	O7 III ((f))	5.9	$-6.85^{-0.33}_{+0.29}$	$25.6^{+4.4}_{-3.1}$	$6.02^{+0.14}_{-0.11}$	$169.3^{+62.8}_{-39.7}$	Q3
CYG OB2-4 A	O7 III ((f))	5.63	$-5.15^{-0.12}_{+0.11}$	$11.7^{+0.7}_{-0.5}$	$5.34^{+0.04}_{-0.05}$	$18.2^{+1.8}_{-1.9}$	Q1
HD 163800	O7.5 III ((f))	5.08	$-5.32^{-0.23}_{+0.21}$	$13.0^{+1.5}_{-1.2}$	$5.37^{+0.09}_{-0.09}$	$16.7^{+3.7}_{-3.0}$	Q1
HD 319702	O8 III	5.95	$-5.0^{-0.18}_{+0.17}$	$10.9^{+1.0}_{-0.7}$	$5.27^{+0.07}_{-0.07}$	$42.1^{+6.9}_{-6.4}$	Q1
HD 36861 A	O8 III ((f))	2.67	$-4.55^{-0.4}_{+0.34}$	$9.1^{+1.8}_{-1.3}$	$5.06^{+0.16}_{-0.14}$	$9.8^{+4.2}_{-2.4}$	Q1
HD 114737 AB	O8.5 III	6.33	$-3.59^{-2.22}_{+1.12}$	$5.8^{+10.4}_{-2.4}$	$4.69^{+0.89}_{-0.45}$	$9.6^{+63.8}_{-6.2}$	Q3
HD 218195 A	O8.5 III Nstr	6.59	$-4.34^{-0.35}_{+0.31}$	$8.4^{+1.5}_{-1.1}$	$4.94^{+0.14}_{-0.13}$	$9.1^{+3.3}_{-2.2}$	Q1
HD 93249 A	O9 III	6.91	$-5.55^{-0.25}_{+0.22}$	$15.1^{+1.8}_{-1.6}$	$5.37^{+0.1}_{-0.09}$	$27.5^{+7.1}_{-5.3}$	Q1
HD 24431	O9 III	4.67	$-4.87^{-0.16}_{+0.15}$	$10.6^{+0.8}_{-0.7}$	$5.18^{+0.06}_{-0.06}$	$24.9^{+3.8}_{-3.3}$	Q3
HD 193443 AB	O9 III	5.18	$-6.0^{-1.58}_{+1.31}$	$18.5^{+19.9}_{-8.4}$	$5.56^{+0.63}_{-0.52}$	$39.3^{+128.8}_{-27.5}$	Q1
HD 16832	O9.2 III	6.78	$-4.97^{-0.22}_{+0.2}$	$11.8^{+1.2}_{-1.1}$	$5.12^{+0.08}_{-0.08}$	$12.4^{+2.0}_{-1.7}$	Q1
HD 96264	O9.5 III	6.82	$-5.5^{-0.22}_{+0.2}$	$14.7^{+1.6}_{-1.2}$	$5.36^{+0.09}_{-0.08}$	$39.0^{+8.8}_{-6.8}$	Q1
HD 154643	O9.7 III	5.46	$-4.65^{-0.21}_{+0.19}$	$10.4^{+1.0}_{-0.9}$	$4.95^{+0.09}_{-0.07}$	$12.5^{+2.1}_{-1.8}$	Q1
HD 189957	O9.7 III	6.74	$-4.73^{-0.21}_{+0.19}$	$10.5^{+1.1}_{-0.9}$	$5.03^{+0.08}_{-0.08}$	$15.3^{+3.4}_{-2.2}$	Q1
HD 64568	O3 V ((f*))z	8	$-5.66^{-0.46}_{+0.4}$	$12.7^{+3.0}_{-2.2}$	$5.85^{+0.18}_{-0.16}$	$50.2^{+26.5}_{-15.3}$	Q4
HD 93128	O3.5 V ((fc))z	6.53	$-5.96^{-0.21}_{+0.2}$	$14.3^{+1.4}_{-1.3}$	$6.03^{+0.08}_{-0.08}$	$100.5^{+20.6}_{-16.9}$	Q4
HD 46223	O4 V ((f))	5.53	$-5.58^{-0.21}_{+0.19}$	$13.0^{+1.4}_{-1.1}$	$5.69^{+0.08}_{-0.08}$	$33.6^{+6.4}_{-5.1}$	Q1
HD 96715	O4 V ((f))z	6.84	$-5.72^{-0.25}_{+0.22}$	$13.3^{+1.7}_{-1.2}$	$5.83^{+0.1}_{-0.09}$	$55.1^{+13.5}_{-10.2}$	Q1
HD 15629	O4.5 V ((fc))	6.03	$-5.53^{-0.16}_{+0.15}$	$12.8^{+1.1}_{-0.8}$	$5.66^{+0.06}_{-0.06}$	$38.3^{+6.0}_{-5.1}$	Q1
HD 303308 AB	O4.5 V ((fc))	6.55	$-5.26^{-0.21}_{+0.2}$	$11.5^{+1.2}_{-1.0}$	$5.52^{+0.09}_{-0.07}$	$38.6^{+8.6}_{-5.8}$	Q1
HD 319699	O5 V ((fc))	5.91	$-5.18^{-0.15}_{+0.14}$	$11.0^{+0.8}_{-0.7}$	$5.49^{+0.06}_{-0.06}$	$36.3^{+5.6}_{-4.8}$	Q1
HD 46150	O5 V ((f))z	5.33	$-5.61^{-0.3}_{+0.26}$	$13.4^{+2.0}_{-1.5}$	$5.66^{+0.12}_{-0.1}$	$42.7^{+14.3}_{-8.7}$	Q1
HD 93204	O5.5 V ((f))	6.83	$-4.79^{-0.18}_{+0.17}$	$9.5^{+0.8}_{-0.7}$	$5.27^{+0.07}_{-0.07}$	$22.5^{+3.7}_{-3.8}$	Q1
HD 101190 AaAb	O6 IV ((f))	6.08	$-6.36^{-0.29}_{+0.26}$	$19.4^{+2.7}_{-2.2}$	$5.92^{+0.12}_{-0.1}$	$104.3^{+33.4}_{-22.4}$	Q1
HD 303311	O6 V ((f))z	7.45	$-5.3^{-0.24}_{+0.22}$	$11.8^{+1.4}_{-1.1}$	$5.51^{+0.1}_{-0.09}$	$41.4^{+11.4}_{-7.1}$	Q1
CPD -59 2600	O6 V ((f))	6.42	$-7.04^{-0.45}_{+0.38}$	$26.7^{+6.1}_{-4.4}$	$6.18^{+0.18}_{-0.15}$	$177.6^{+90.4}_{-53.2}$	Q1
HD 42088	O6 V ((f))z	6.27	$-4.83^{-0.23}_{+0.21}$	$9.4^{+1.1}_{-0.8}$	$5.31^{+0.1}_{-0.08}$	$32.1^{+7.9}_{-5.6}$	Q1
HD 322417	O6.5 IV ((f))	5.67	$-6.44^{-0.42}_{+0.36}$	$20.5^{+4.4}_{-3.1}$	$5.92^{+0.17}_{-0.14}$	$88.2^{+40.6}_{-25.4}$	Q1
HD 91572	O6.5 V ((f))z	6.88	$-5.12^{-0.34}_{+0.3}$	$11.1^{+1.9}_{-1.4}$	$5.4^{+0.13}_{-0.12}$	$31.8^{+12.0}_{-7.7}$	Q1
HD 167633	O6.5 V ((f))	6.17	$-5.14^{-0.28}_{+0.25}$	$11.4^{+1.5}_{-1.3}$	$5.38^{+0.11}_{-0.1}$	$23.4^{+7.1}_{-4.7}$	Q1
HD 12993	O6.5 V ((f))_Nstr	7.51	$-4.39^{-0.25}_{+0.23}$	$7.9^{+0.9}_{-0.8}$	$5.11^{+0.1}_{-0.09}$	$17.7^{+4.5}_{-2.8}$	Q1
HD 93222 AB	O7 V ((f))	6.26	$-5.91^{-0.23}_{+0.21}$	$16.5^{+1.8}_{-1.5}$	$5.65^{+0.09}_{-0.08}$	$44.0^{+9.9}_{-7.7}$	Q1
HD 91824	O7 V ((f))z	7.3	$-4.4^{-0.23}_{+0.21}$	$7.8^{+0.9}_{-0.7}$	$5.14^{+0.09}_{-0.08}$	$24.6^{+5.6}_{-4.3}$	Q1
HD 93146 A	O7 V ((f))	6.91	$-5.59^{-0.29}_{+0.26}$	$13.8^{+2.0}_{-1.5}$	$5.58^{+0.12}_{-0.1}$	$48.9^{+14.3}_{-10.4}$	Q1
HD 242926	O7 V z	7.17	$-5.18^{-1.19}_{+1.21}$	$11.3^{+8.3}_{-4.8}$	$5.42^{+0.48}_{-0.48}$	$56.9^{+115.6}_{-37.4}$	Q1
HD 152590	O7.5 V z	6.77	$-4.22^{-0.23}_{+0.21}$	$7.4^{+0.8}_{-0.7}$	$5.01^{+0.09}_{-0.09}$	$17.5^{+3.5}_{-3.1}$	Q1
HD 35619	O7.5 V ((f))	6.69	$-5.78^{-0.51}_{+0.42}$	$15.3^{+3.9}_{-2.8}$	$5.62^{+0.2}_{-0.17}$	$77.7^{+47.0}_{-24.5}$	Q1
HD 135591	O8 IV ((f))	4.58	$-5.04^{-0.36}_{+0.31}$	$11.4^{+2.1}_{-1.5}$	$5.24^{+0.15}_{-0.12}$	$18.0^{+7.1}_{-3.9}$	Q1
HD 94024	O8 IV	7.4	$-4.96^{-0.25}_{+0.23}$	$11.1^{+1.3}_{-1.2}$	$5.2^{+0.1}_{-0.09}$	$14.5^{+3.5}_{-2.7}$	Q1
HD 97848	O8 V	7.59	$-5.68^{-0.48}_{+0.41}$	$15.1^{+3.7}_{-2.6}$	$5.51^{+0.19}_{-0.16}$	$39.2^{+22.0}_{-12.1}$	Q1
HD 101223	O8 V	7.1	$-4.92^{-0.23}_{+0.21}$	$10.7^{+1.2}_{-1.0}$	$5.2^{+0.09}_{-0.09}$	$17.7^{+4.1}_{-3.7}$	Q1
HD 191978	O8 V	6.71	$-4.06^{-0.13}_{+0.12}$	$7.1^{+0.4}_{-0.4}$	$4.87^{+0.05}_{-0.05}$	$12.6^{+1.6}_{-1.5}$	Q1
HD 46966	O8.5 IV	5.98	$-5.22^{-0.3}_{+0.27}$	$12.2^{+1.8}_{-1.4}$	$5.34^{+0.12}_{-0.1}$	$38.1^{+13.6}_{-7.1}$	Q1
HD 298429	O8.5 V	6.8	$-4.83^{-0.17}_{+0.16}$	$10.6^{+0.8}_{-0.8}$	$5.11^{+0.07}_{-0.06}$	$14.1^{+2.3}_{-2.1}$	Q1
HD 46149	O8.5 V	6.14	$-4.7^{-0.24}_{+0.22}$	$9.3^{+1.1}_{-0.8}$	$5.17^{+0.09}_{-0.09}$	$54.9^{+14.0}_{-9.4}$	Q1
Trumpler 14-9	O8.5 V	7.45	$-4.25^{-0.18}_{+0.17}$	$7.6^{+0.7}_{-0.5}$	$4.98^{+0.07}_{-0.07}$	$28.2^{+5.1}_{-3.9}$	Q1

Table B.9: continued.

Name	SpT	LC	V0 [mag]	M_V range [mag]	R range [$R_\odot$]	log L range [$L_\odot$]	M_{sp} range [$M_\odot$]	qual. flag
HD 57236	O8.5	V	7.09	$-4.73^{-0.23}_{+0.21}$	$9.4^{+1.1}_{-0.8}$	$5.19^{+0.09}_{-0.08}$	$54.8^{+13.1}_{-9.6}$	Q1
HD 14633 AaAb	ON8.5	V	7.14	$-5.05^{-0.6}_{+0.54}$	$11.4^{+3.6}_{-2.5}$	$5.24^{+0.24}_{-0.21}$	$28.3^{+19.0}_{-10.7}$	Q1
HD 93028	O9	IV	7.56	$-4.96^{-0.43}_{+0.36}$	$10.9^{+2.4}_{-1.6}$	$5.22^{+0.17}_{-0.15}$	$38.1^{+17.7}_{-10.8}$	Q1
CPD -41 7733	O9	IV	6.28	$-4.9^{-0.19}_{+0.18}$	$10.9^{+0.9}_{-0.9}$	$5.16^{+0.08}_{-0.07}$	$19.8^{+3.4}_{-3.2}$	Q1
CPD -59 2551	O9	V	8.1	$-4.24^{-0.21}_{+0.19}$	$7.9^{+0.7}_{-0.7}$	$4.92^{+0.08}_{-0.08}$	$17.7^{+3.7}_{-2.8}$	Q1
HD 214680	O9	V	4.55	$-3.22^{-0.19}_{+0.18}$	$4.9^{+0.4}_{-0.4}$	$4.51^{+0.08}_{-0.07}$	$7.5^{+1.3}_{-1.1}$	Q1
HD 216898	O9	V	5.49	$-4.09^{-0.06}_{+0.06}$	$7.2^{+0.2}_{-0.2}$	$4.89^{+0.02}_{-0.03}$	$29.9^{+1.7}_{-1.5}$	Q1
HD 96622	O9.2	IV	7.4	$-4.72^{-0.19}_{+0.17}$	$10.2^{+0.9}_{-0.8}$	$5.06^{+0.07}_{-0.07}$	$18.5^{+3.8}_{-2.6}$	Q1
HD 46202	O9.2	V	6.64	$-4.01^{-0.54}_{+0.44}$	$7.1^{+2.0}_{-1.3}$	$4.82^{+0.22}_{-0.17}$	$25.6^{+16.6}_{-9.1}$	Q1
HD 12323	ON9.2	V	8.18	$-3.87^{-0.26}_{+0.24}$	$6.7^{+0.9}_{-0.6}$	$4.74^{+0.11}_{-0.09}$	$15.7^{+4.5}_{-2.7}$	Q1
HD 93027	O9.5	IV	7.67	$-5.01^{-0.3}_{+0.27}$	$11.5^{+1.7}_{-1.3}$	$5.19^{+0.12}_{-0.11}$	$44.1^{+13.9}_{-9.9}$	Q1
HD 192001	O9.5	IV	6.59	$-4.61^{-0.15}_{+0.14}$	$9.8^{+0.7}_{-0.7}$	$5.01^{+0.06}_{-0.06}$	$24.1^{+3.5}_{-3.3}$	Q1
HD 155889 AB	O9.5	IV	5.58	$-7.45^{-1.36}_{+1.63}$	$34.7^{+30.5}_{-18.3}$	$6.21^{+0.54}_{-0.66}$	$605.9^{+1533.6}_{-478.9}$	Q1
HD 38666	O9.5	V	5.05	$-3.27^{-0.17}_{+0.16}$	$5.2^{+0.4}_{-0.4}$	$4.5^{+0.07}_{-0.06}$	$7.9^{+1.4}_{-1.1}$	Q1
HD 34078	O9.5	V	4.16	$-3.86^{-0.06}_{+0.06}$	$6.7^{+0.1}_{-0.2}$	$4.75^{+0.03}_{-0.02}$	$20.4^{+1.3}_{-1.2}$	Q1
HD 207538	O9.7	IV	5.7	$-3.86^{-0.05}_{+0.05}$	$7.1^{+0.1}_{-0.2}$	$4.7^{+0.02}_{-0.02}$	$11.6^{+0.5}_{-0.3}$	Q1
HD 36512	O9.7	V	4.49	$-2.91^{-0.32}_{+0.28}$	$4.5^{+0.7}_{-0.5}$	$4.34^{+0.13}_{-0.11}$	$7.8^{+2.5}_{-1.3}$	Q1

C

Figures

Comparison plots showing observed spectra and best fitting model for the main diagnostic lines used in the IACOB-GBAT analysis of the sample of Galactic O-type stars.

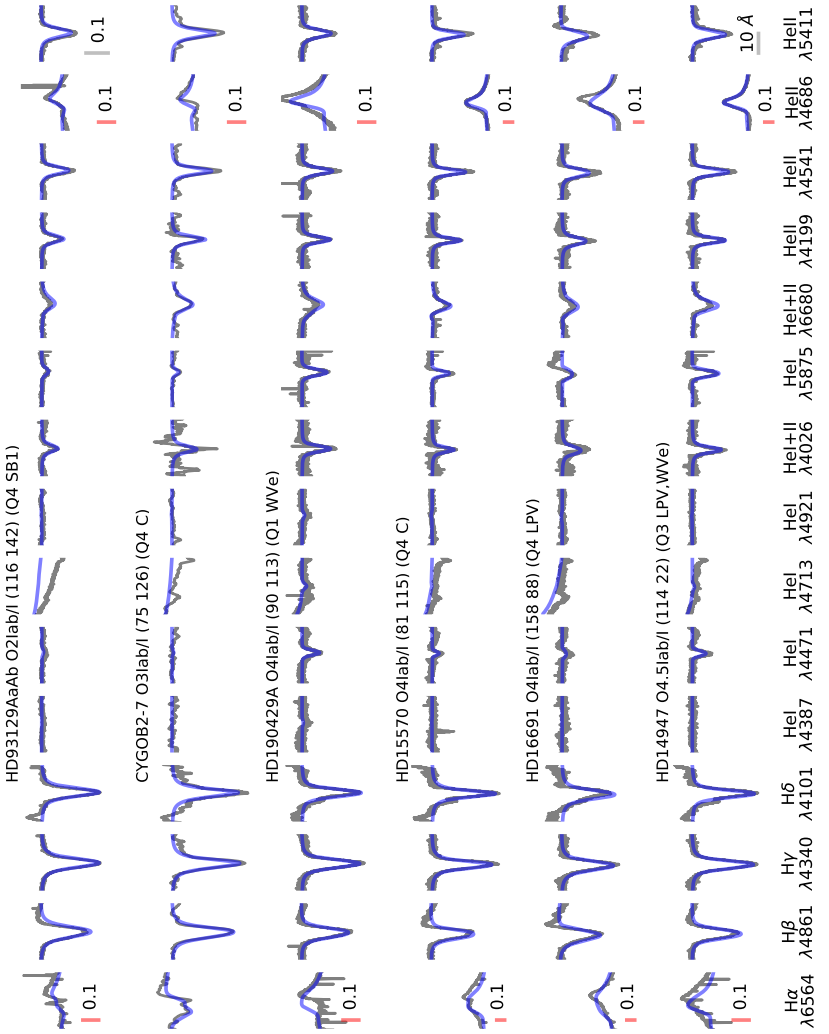

Figure C.1: Observed spectra (gray) and best fitting model (blue) comparison for the main diagnostic lines. The FASTWIND synthetic spectra of the best fitting model has been convolved with the corresponding resolution, $v \sin i$, and $v_{\rm mac}$. The sample is sorted following Tables B.4 and B.5. Each star is labeled with its name and spectral class, $v \sin i$ and $v_{\rm mac}$ values, the quality flag and notes on binarity. The scale is the same for all lines except those marked with a red scale.

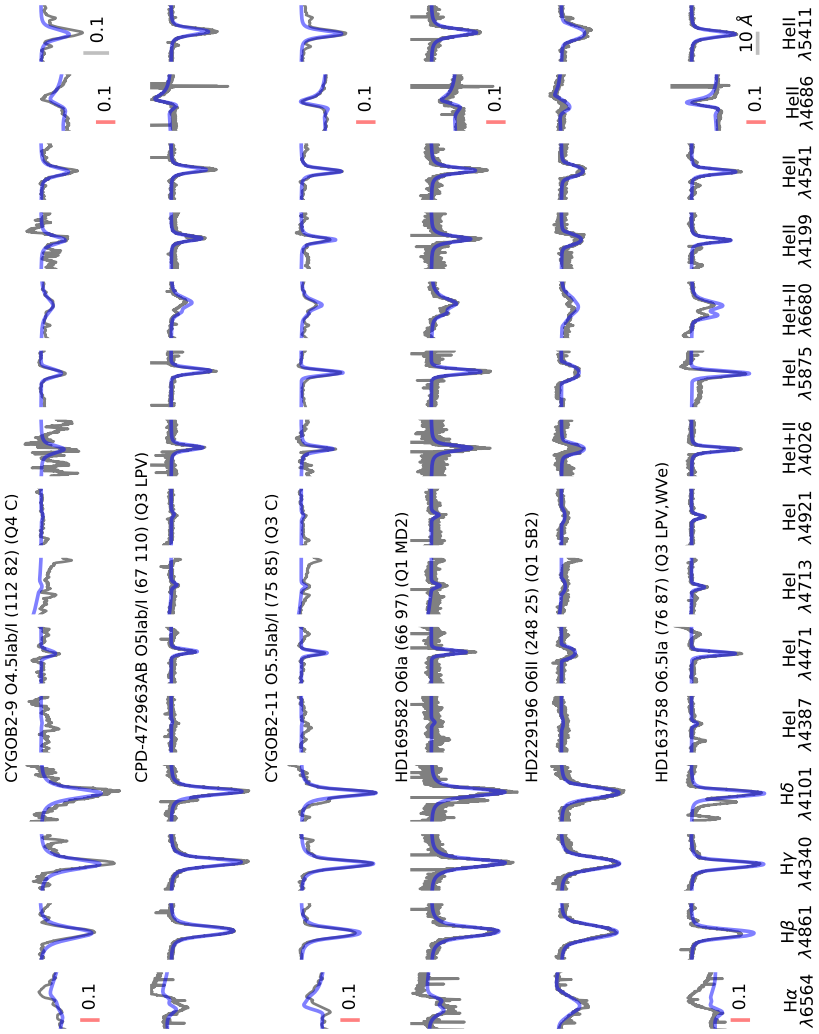

Figure C.2: Same as Fig. C.1.

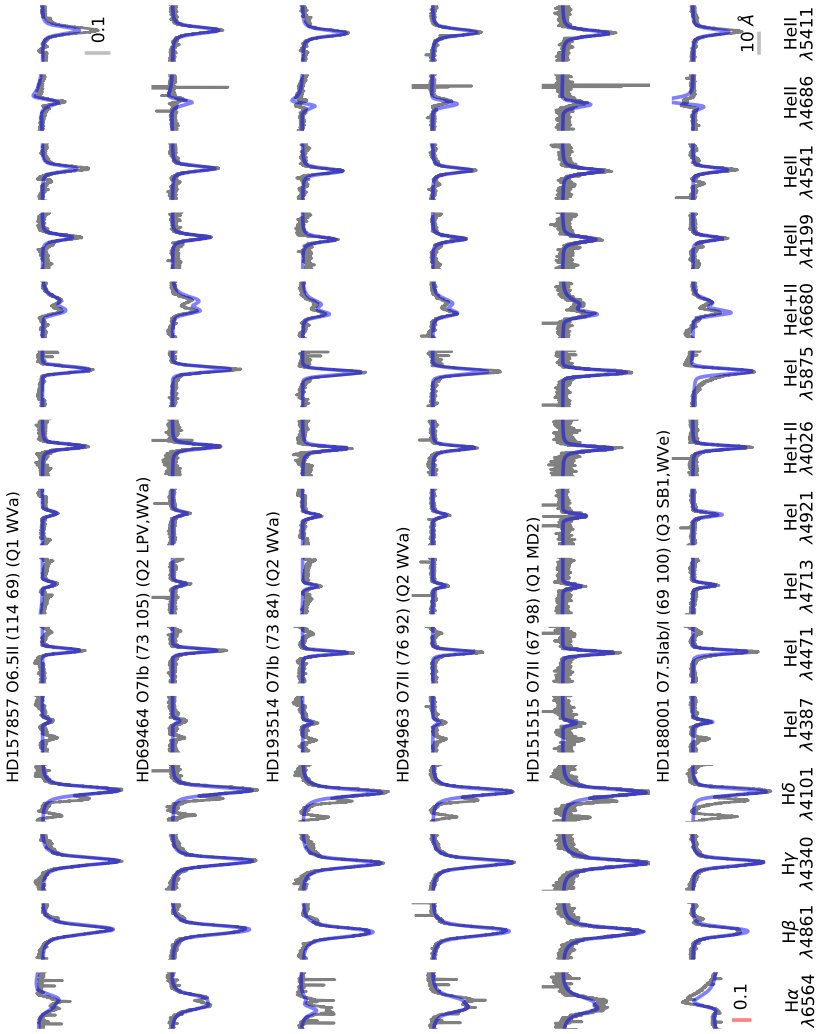

Figure C.3: Same as Fig. C.1.

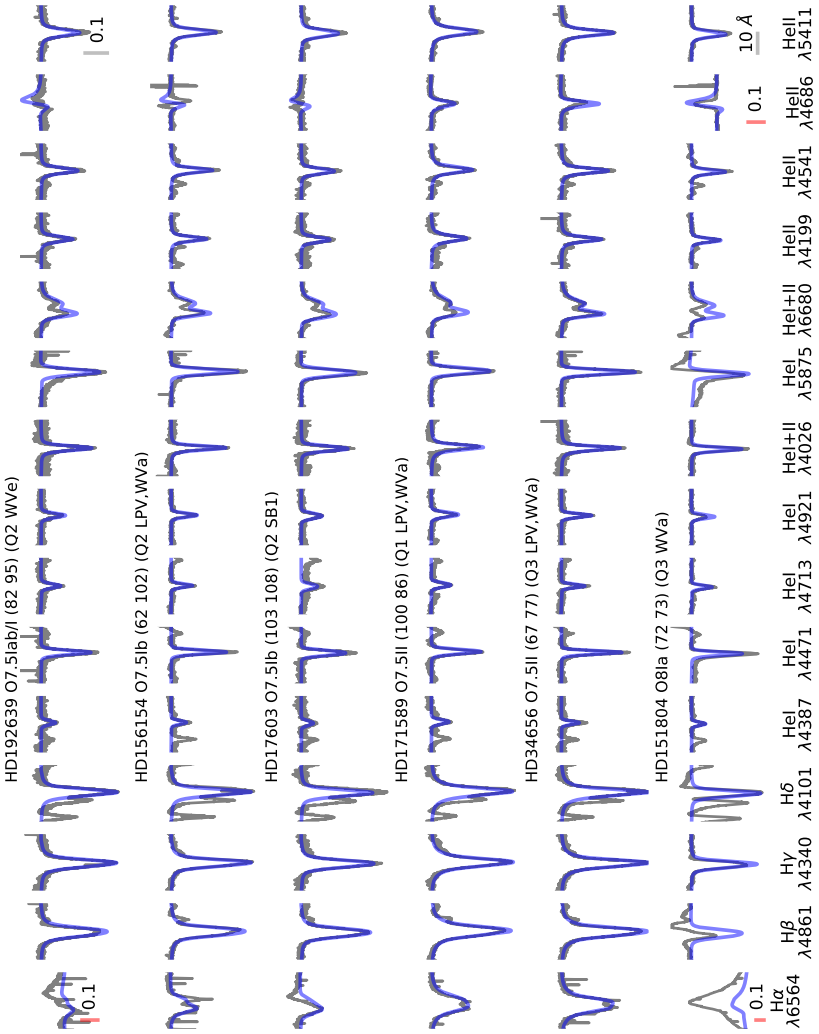

Figure C.4: Same as Fig. C.1.

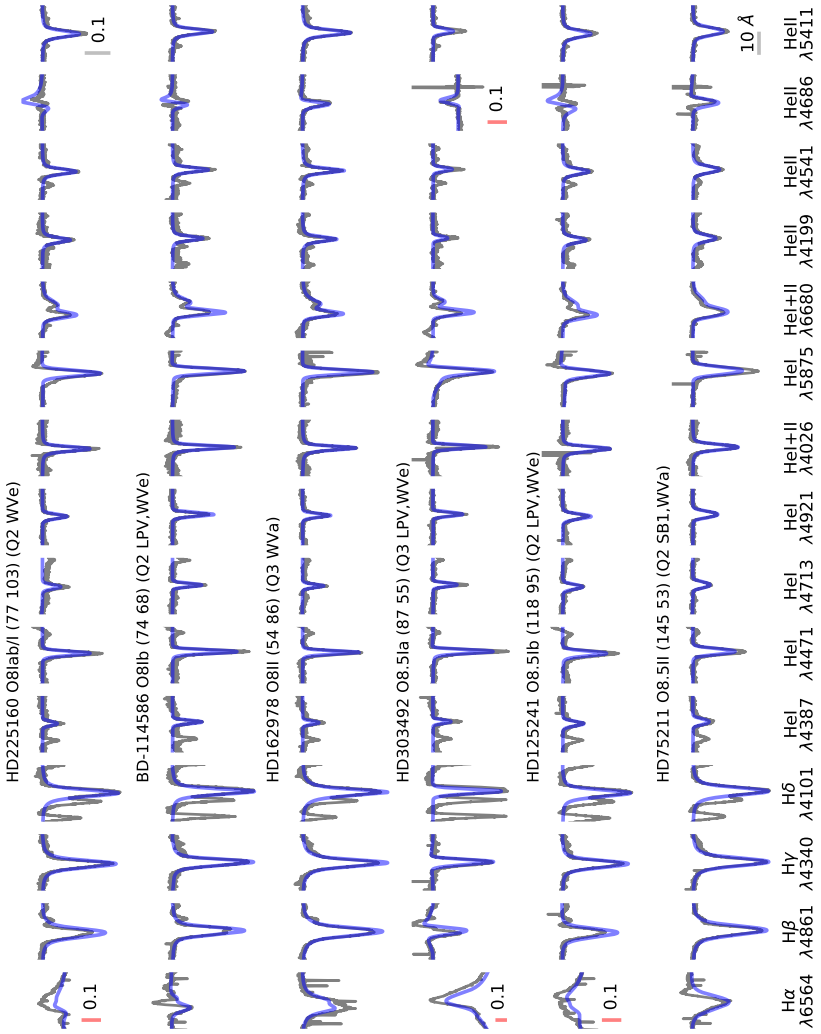

Figure C.5: Same as Fig. C.1.

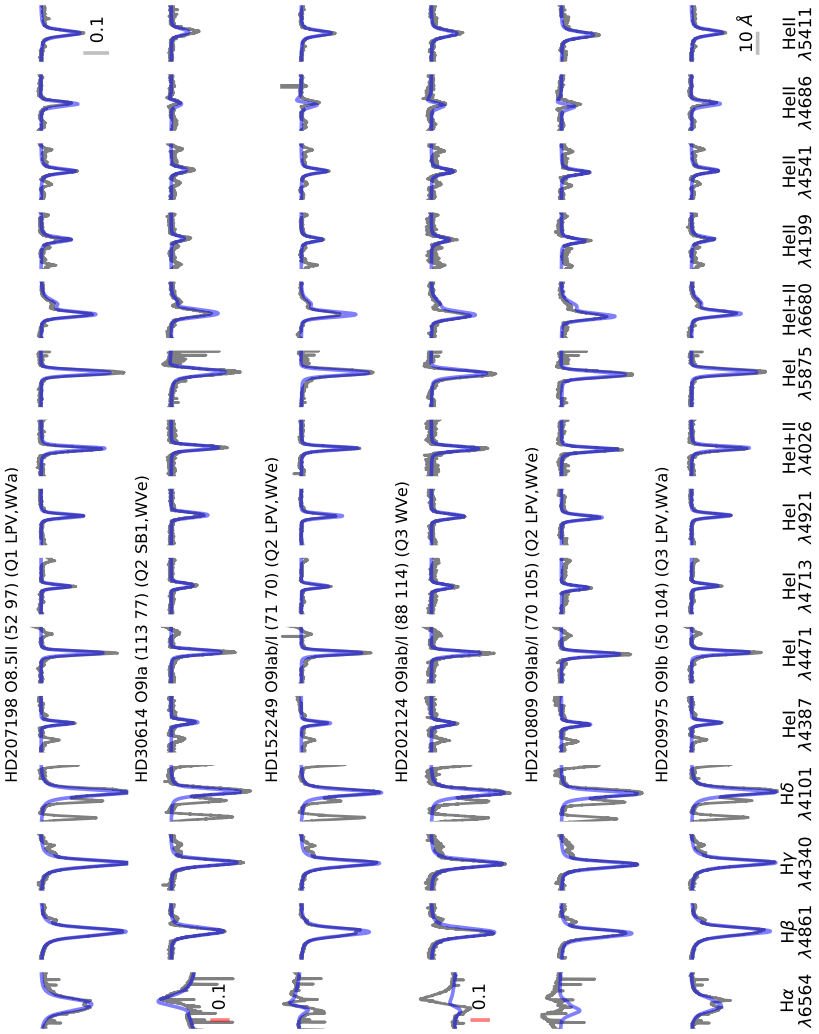

Figure C.6: Same as Fig. C.1.

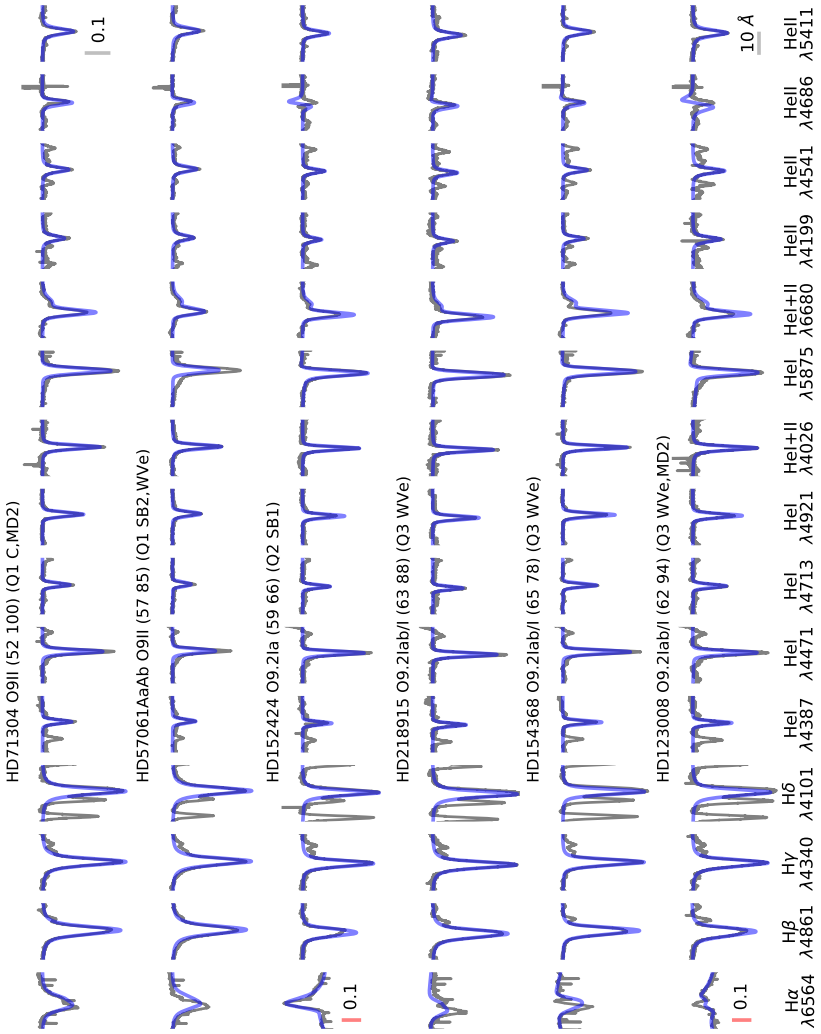

Figure C.7: Same as Fig. C.1.

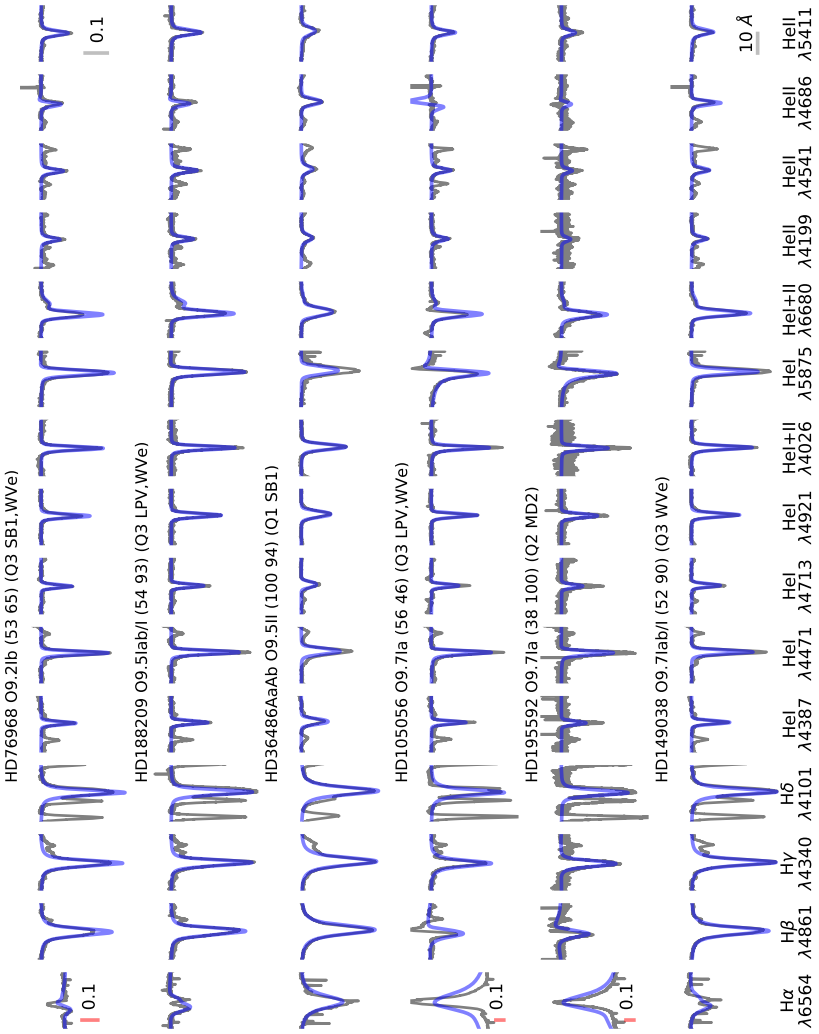

Figure C.8: Same as Fig. C.1.

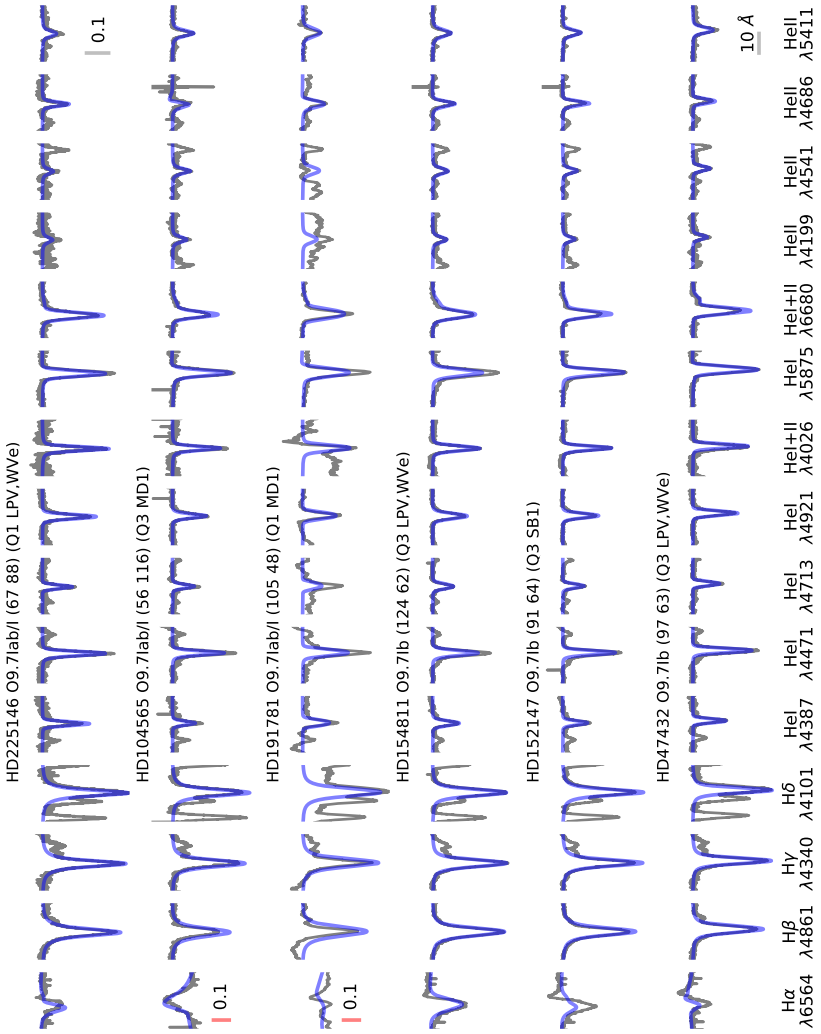

Figure C.9: Same as Fig. C.1.

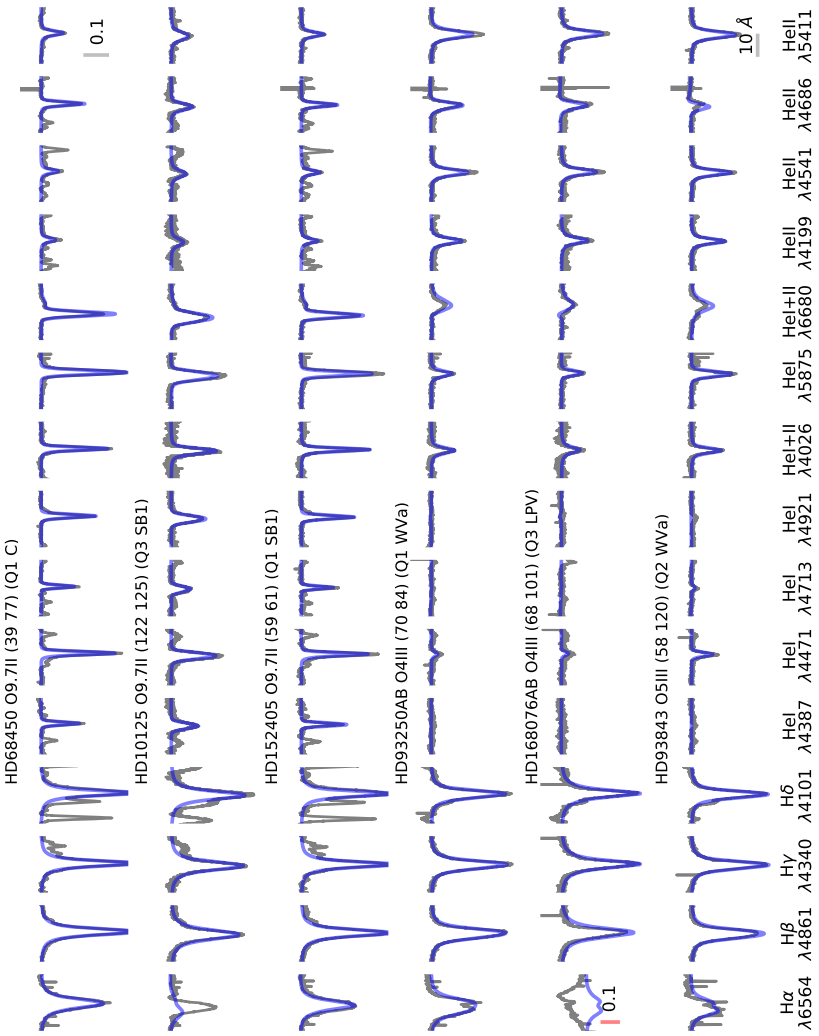

Figure C.10: Same as Fig. C.1.

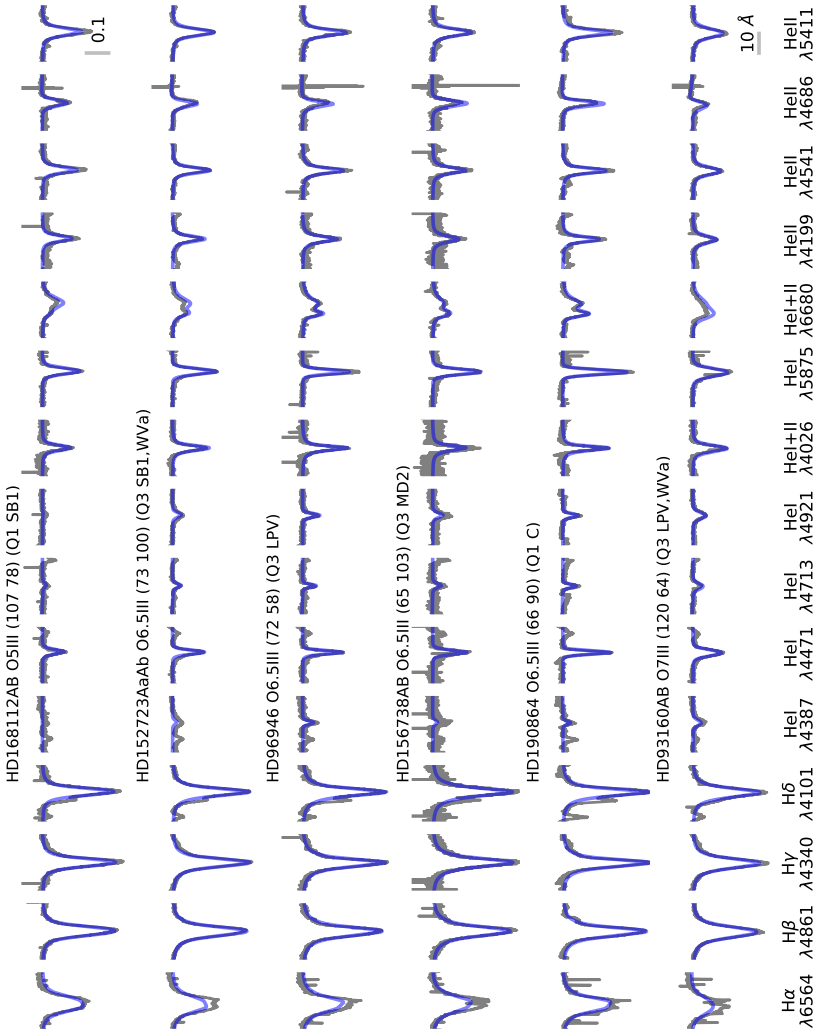

Figure C.11: Same as Fig. C.1.

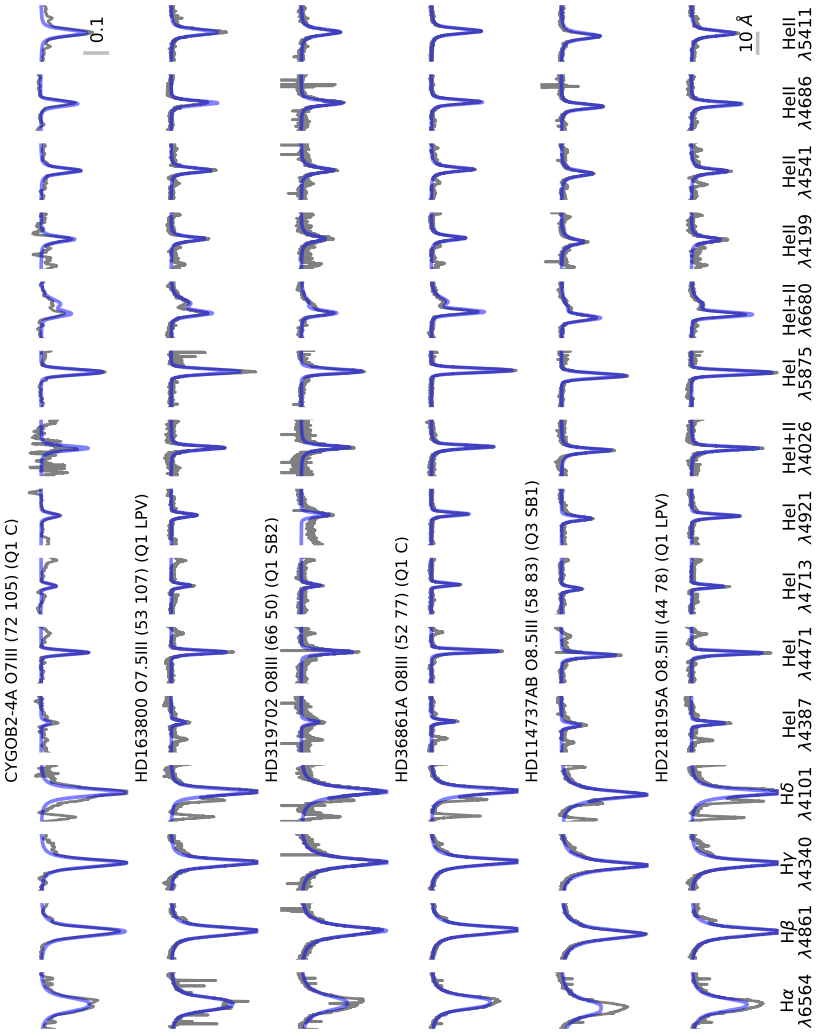

Figure C.12: Same as Fig. C.1.

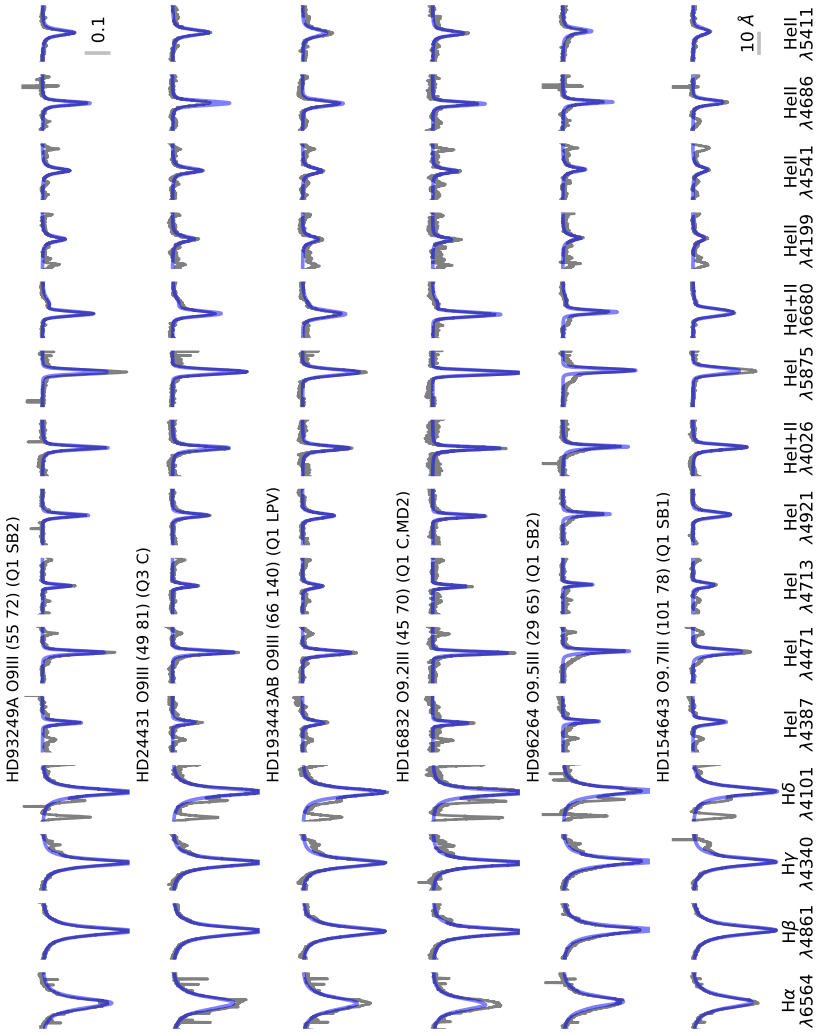

Figure C.13: Same as Fig. C.1.

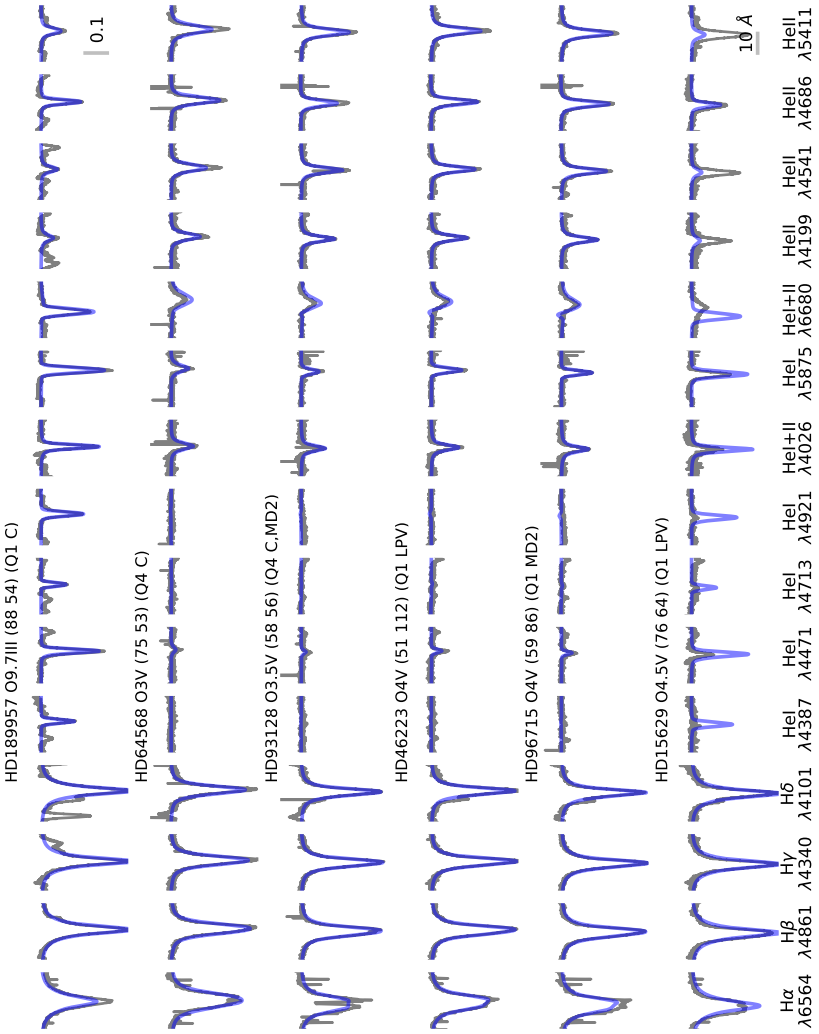

Figure C.14: Same as Fig. C.1.

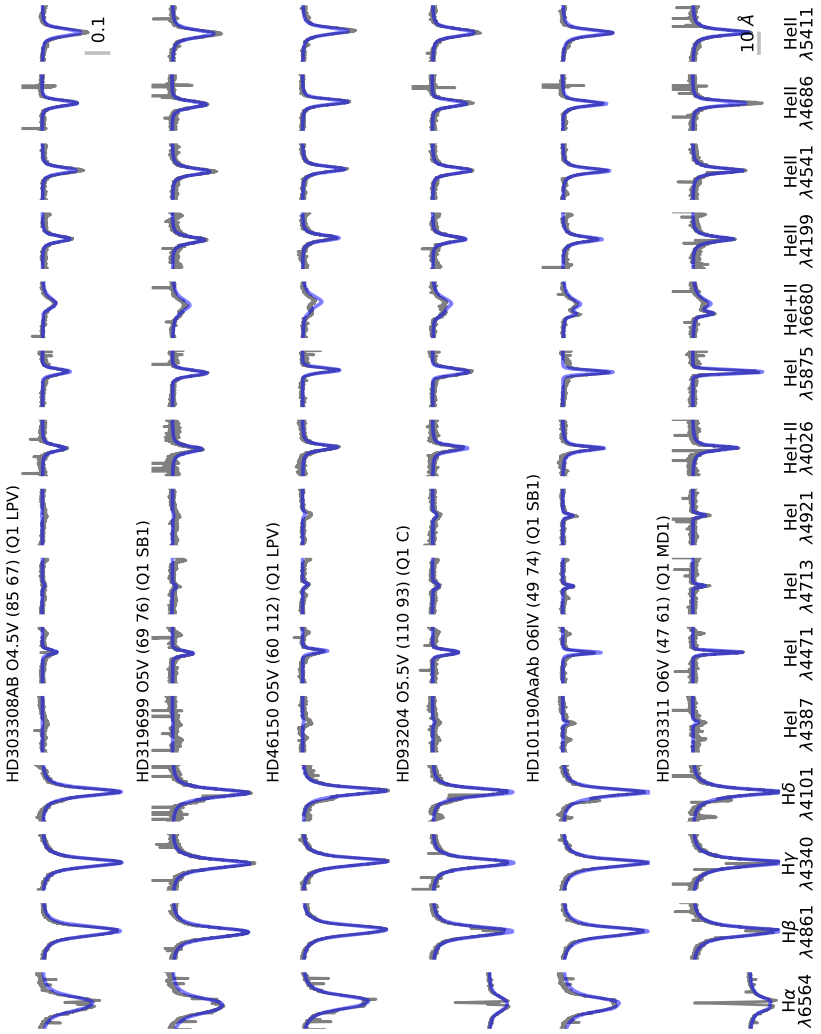

Figure C.15: Same as Fig. C.1.

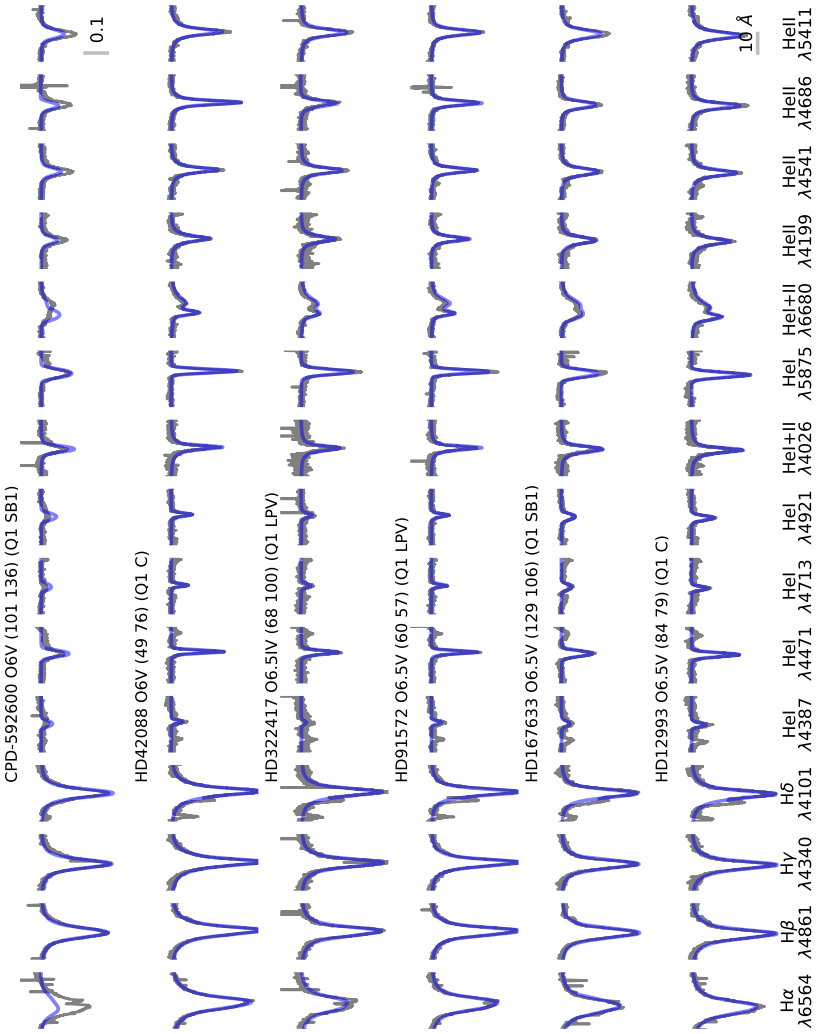

Figure C.16: Same as Fig. C.1.

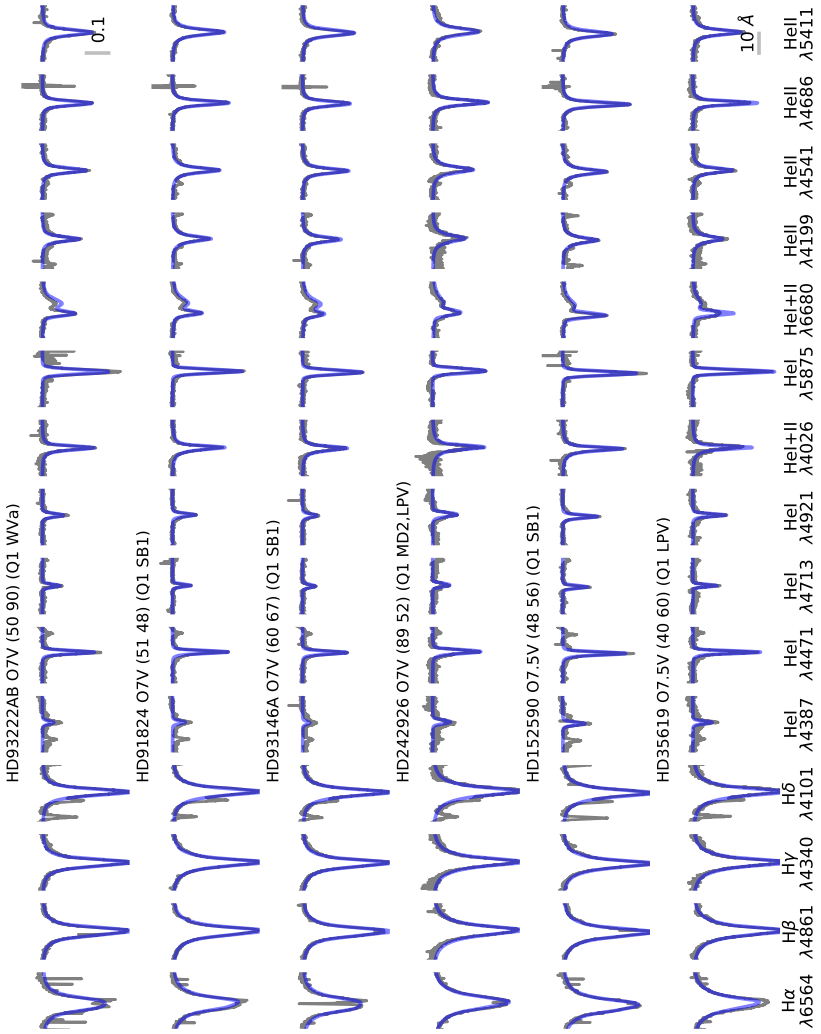

Figure C.17: Same as Fig. C.1.

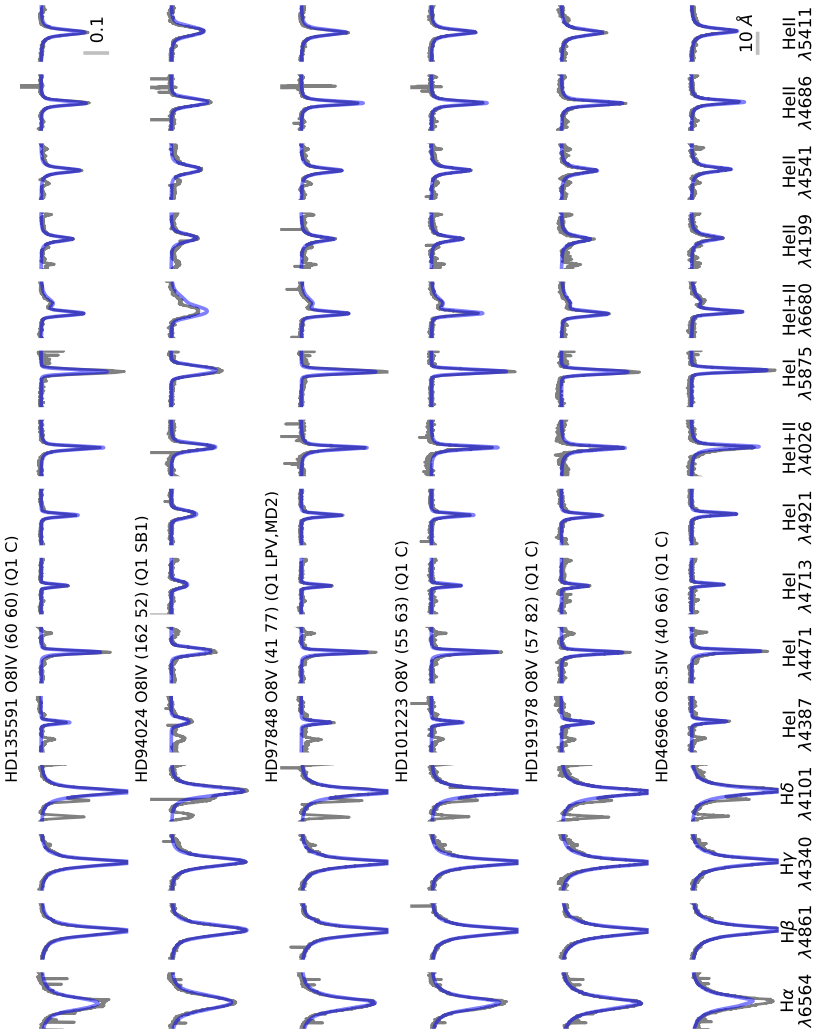

Figure C.18: Same as Fig. C.1.

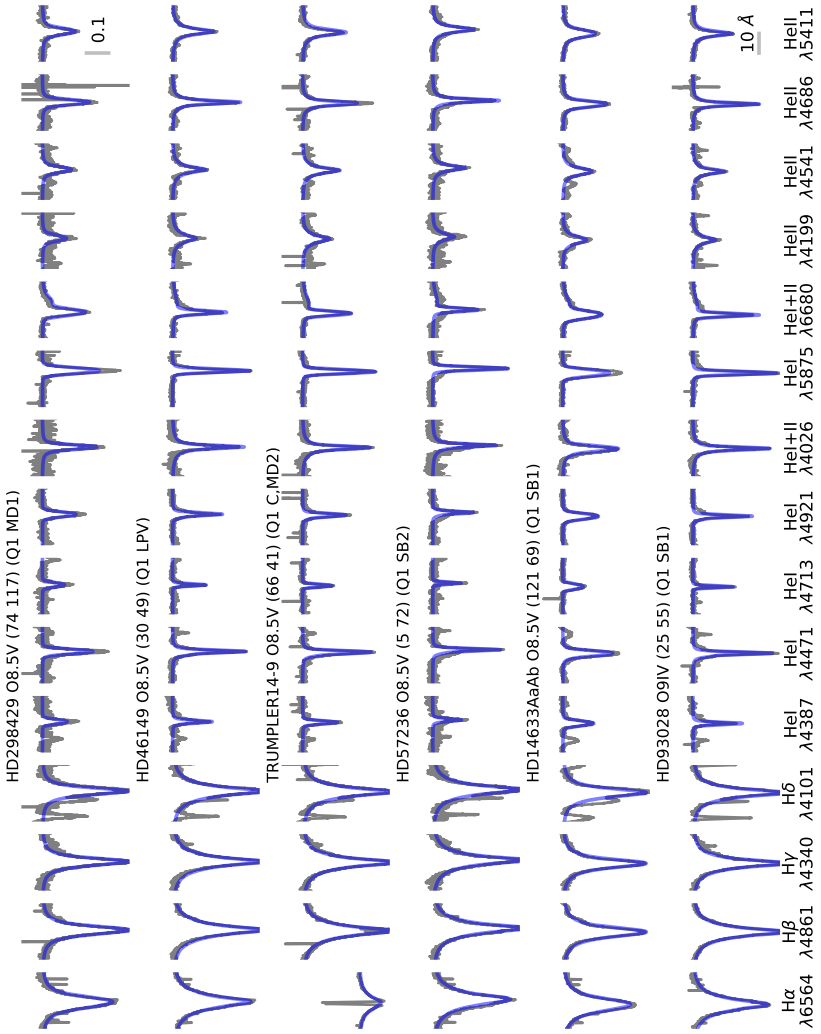

Figure C.19: Same as Fig. C.1.

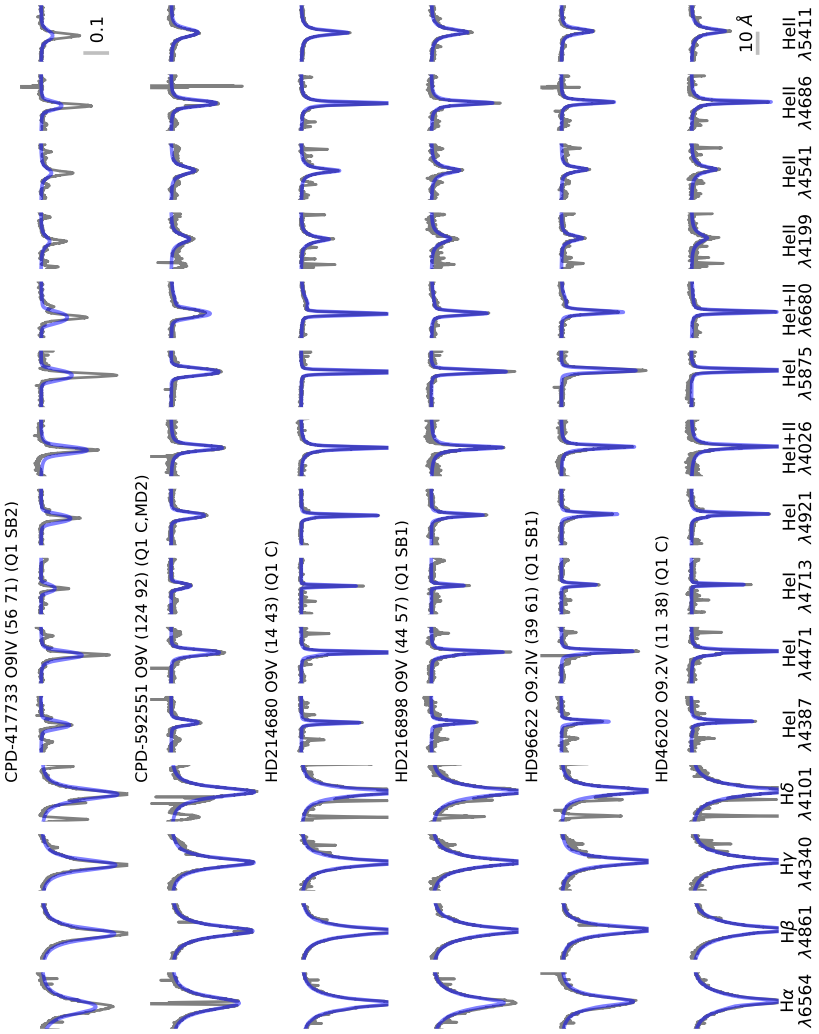

Figure C.20: Same as Fig. C.1.

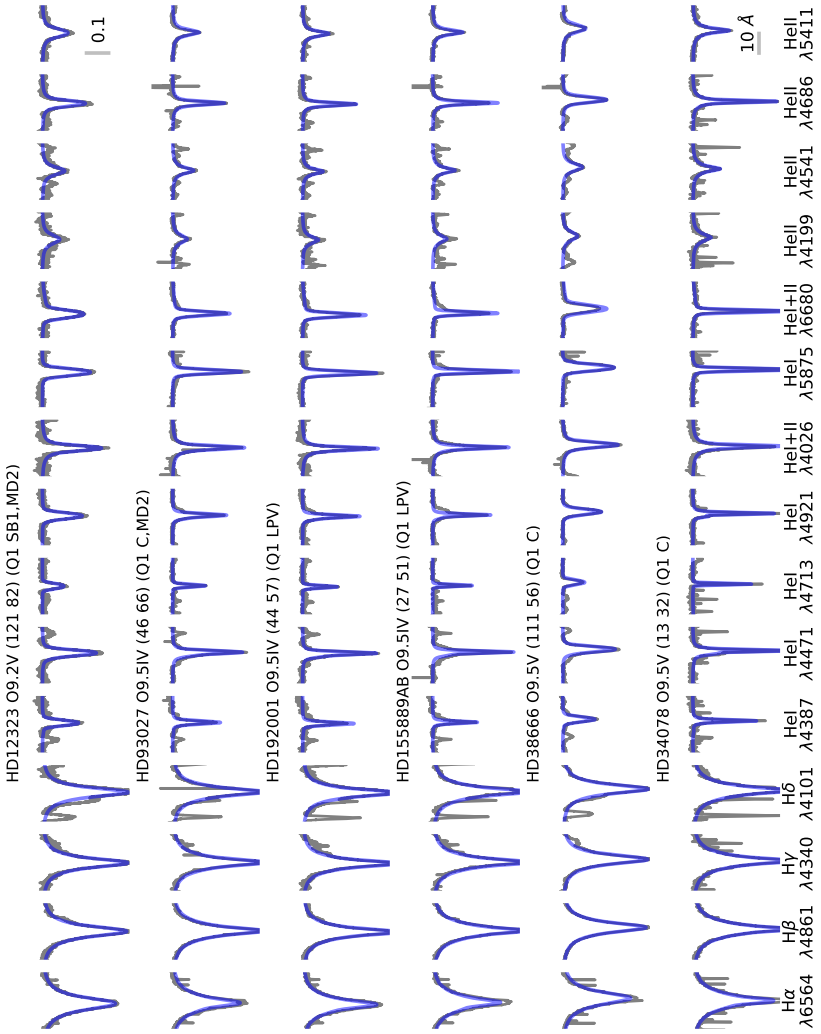

Figure C.21: Same as Fig. C.1.

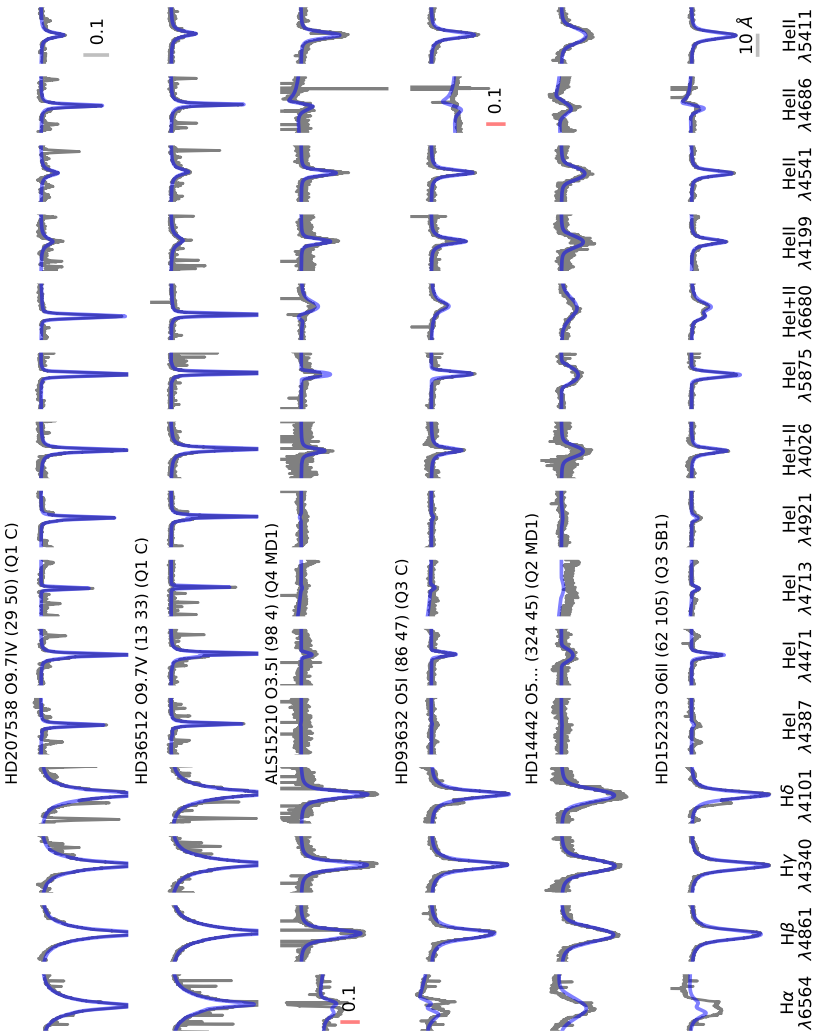

Figure C.22: Same as Fig. C.1.

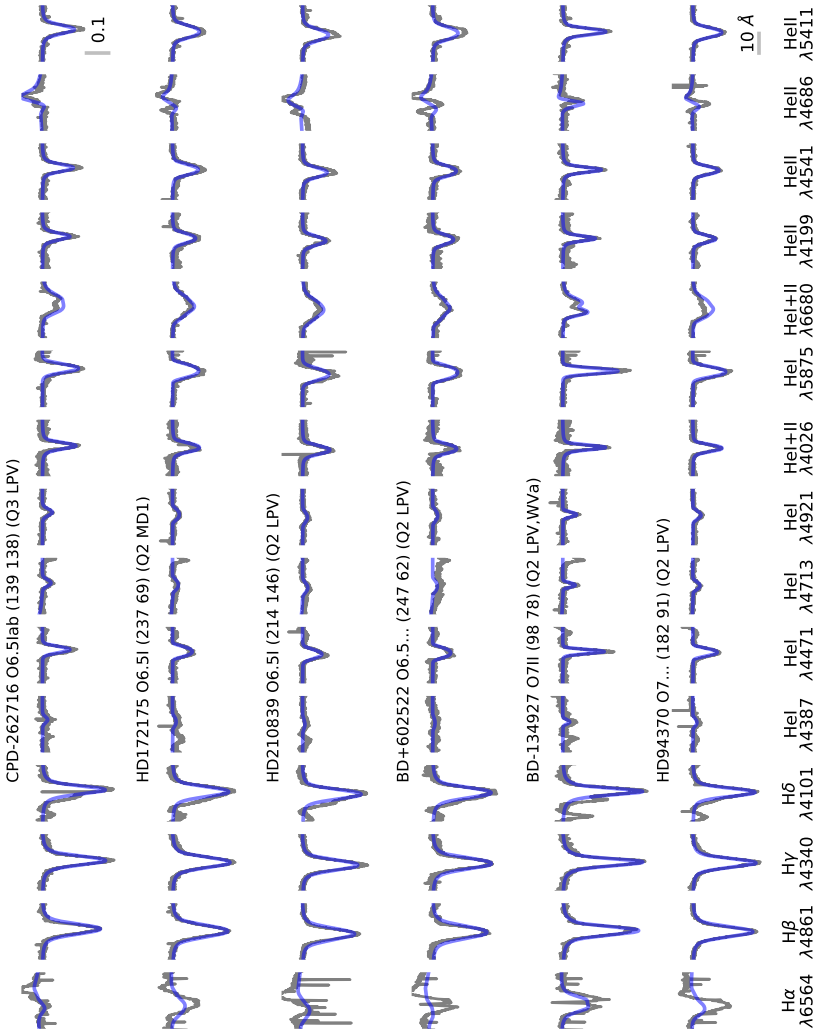

Figure C.23: Same as Fig. C.1.

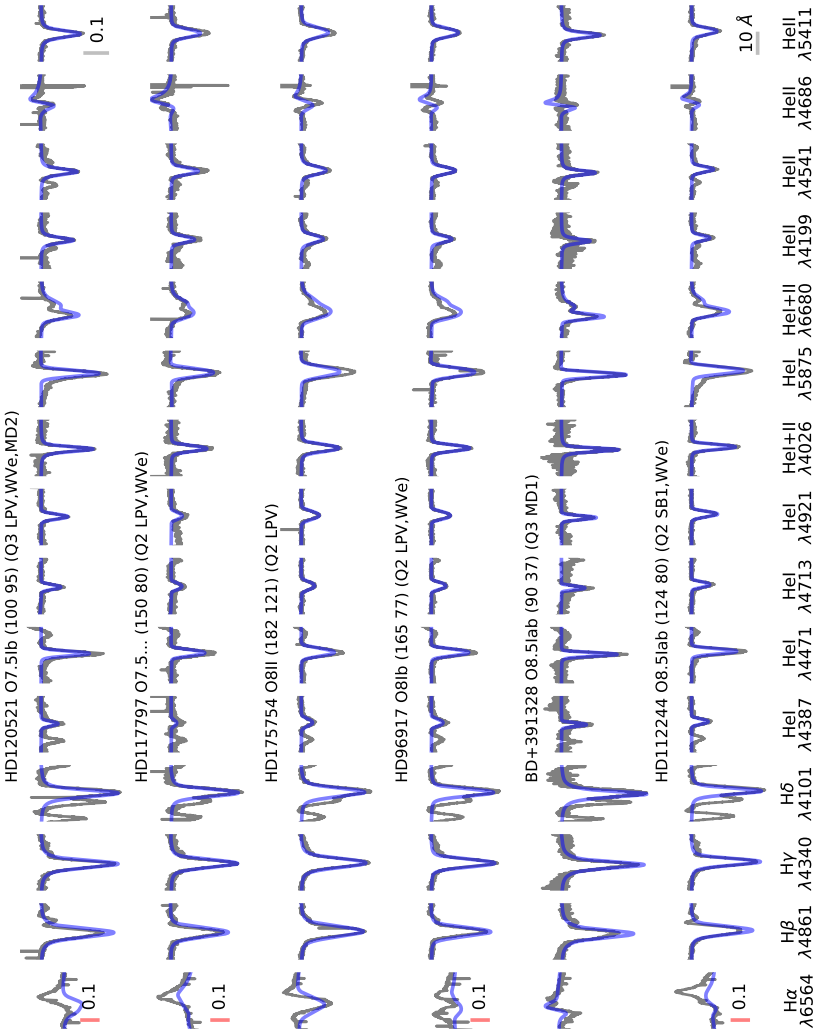

Figure C.24: Same as Fig. C.1.

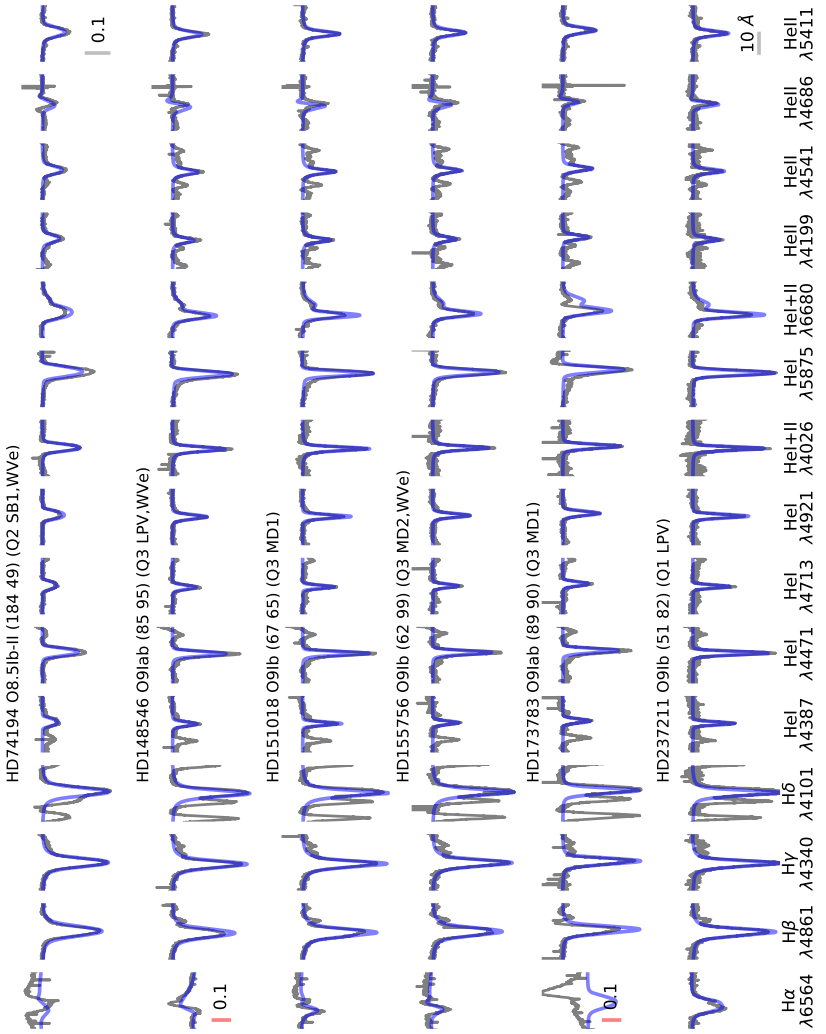

Figure C.25: Same as Fig. C.1.

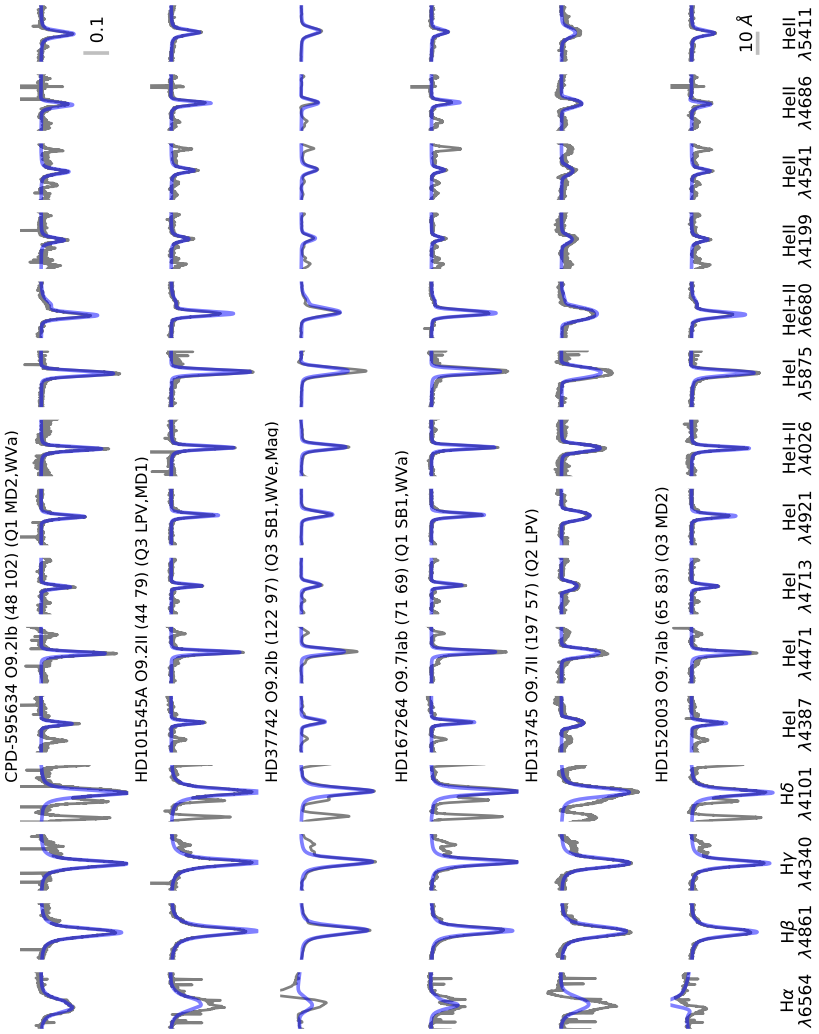

Figure C.26: Same as Fig. C.1.

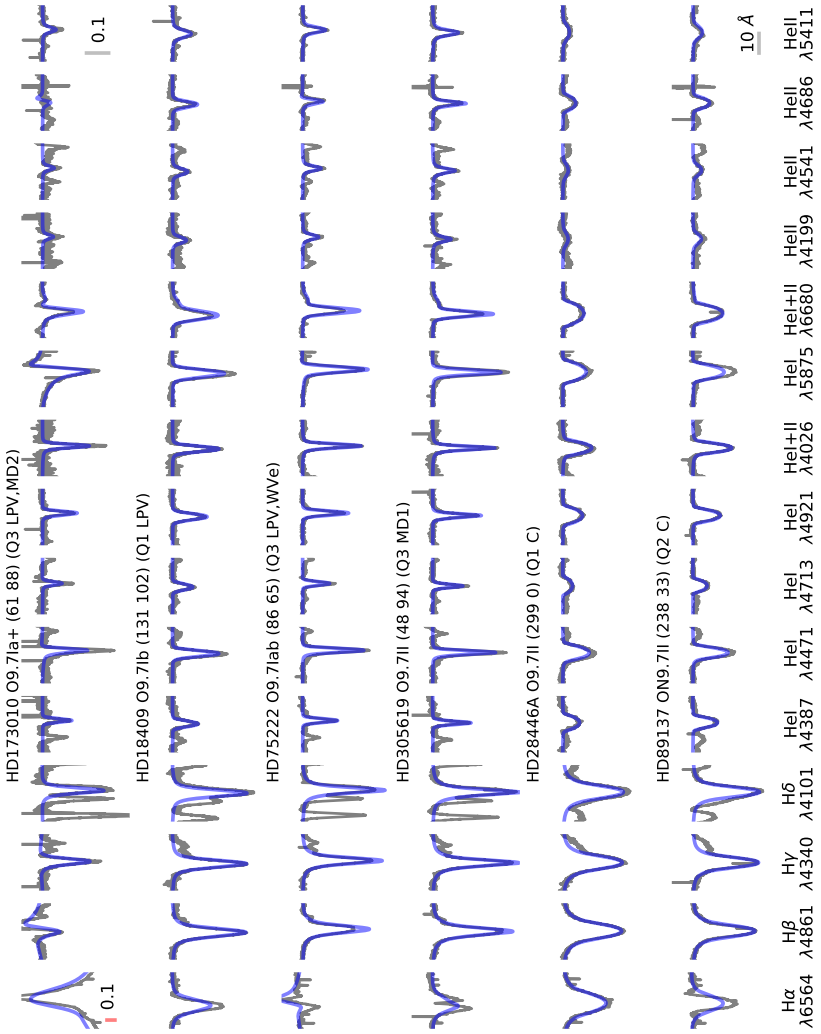

Figure C.27: Same as Fig. C.1.

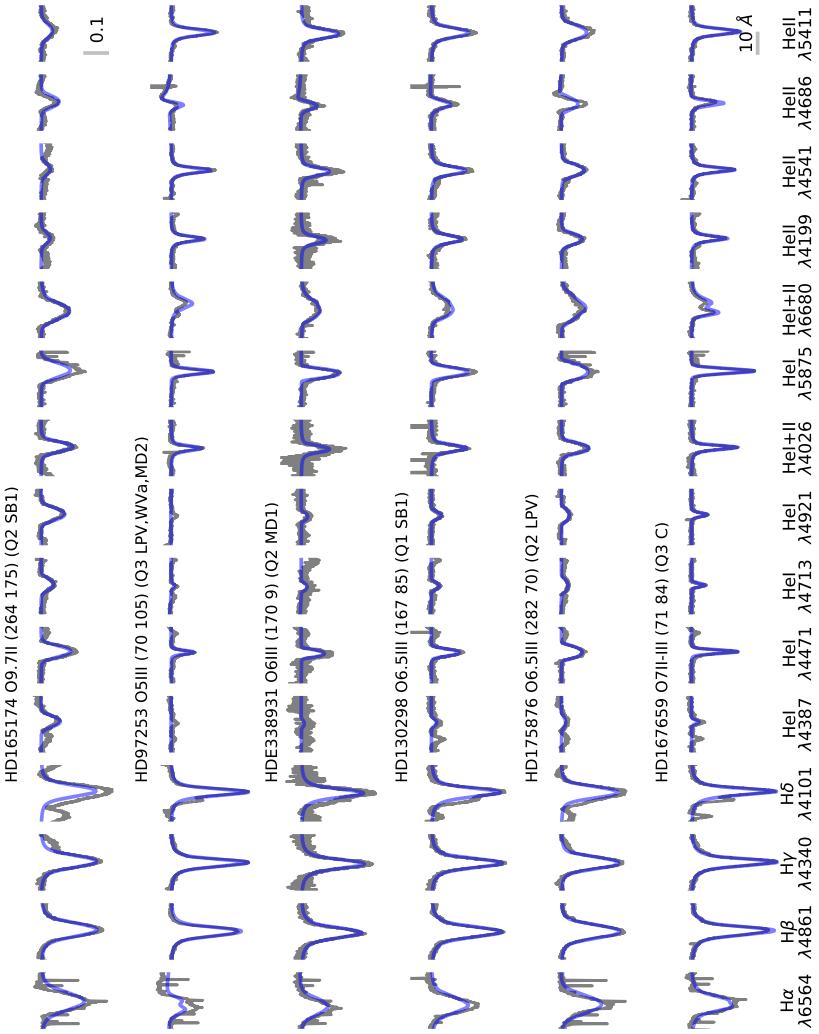

Figure C.28: Same as Fig. C.1.

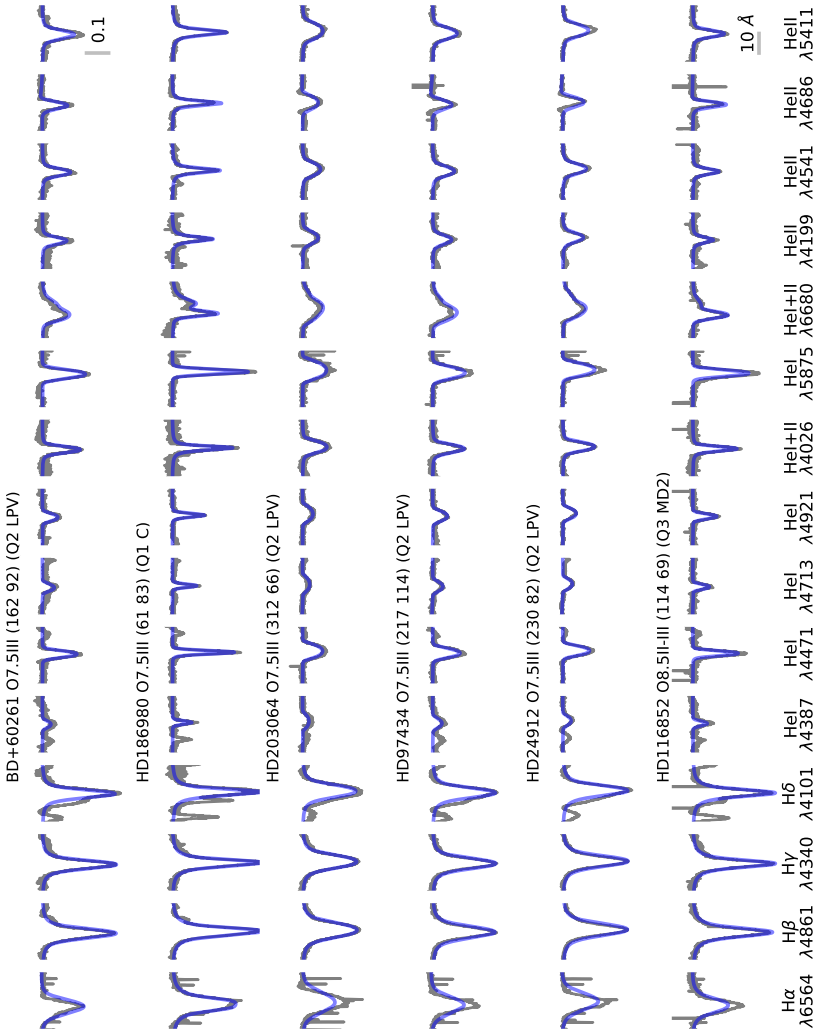

Figure C.29: Same as Fig. C.1.

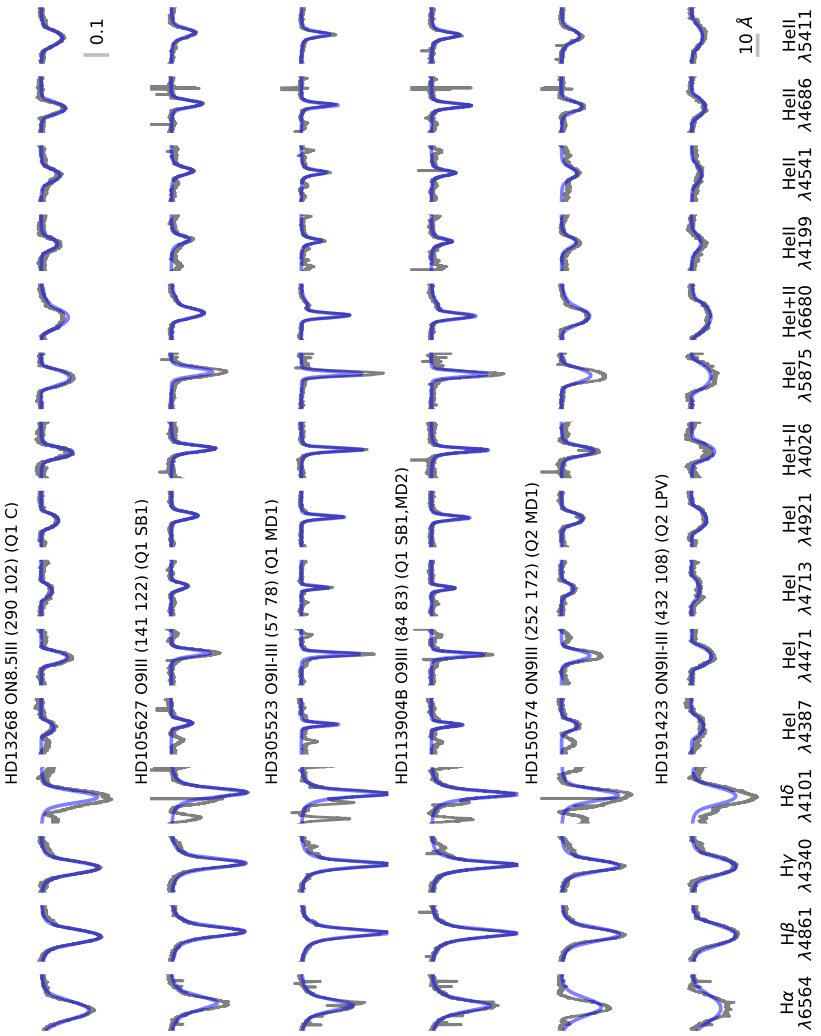

Figure C.30: Same as Fig. C.1.

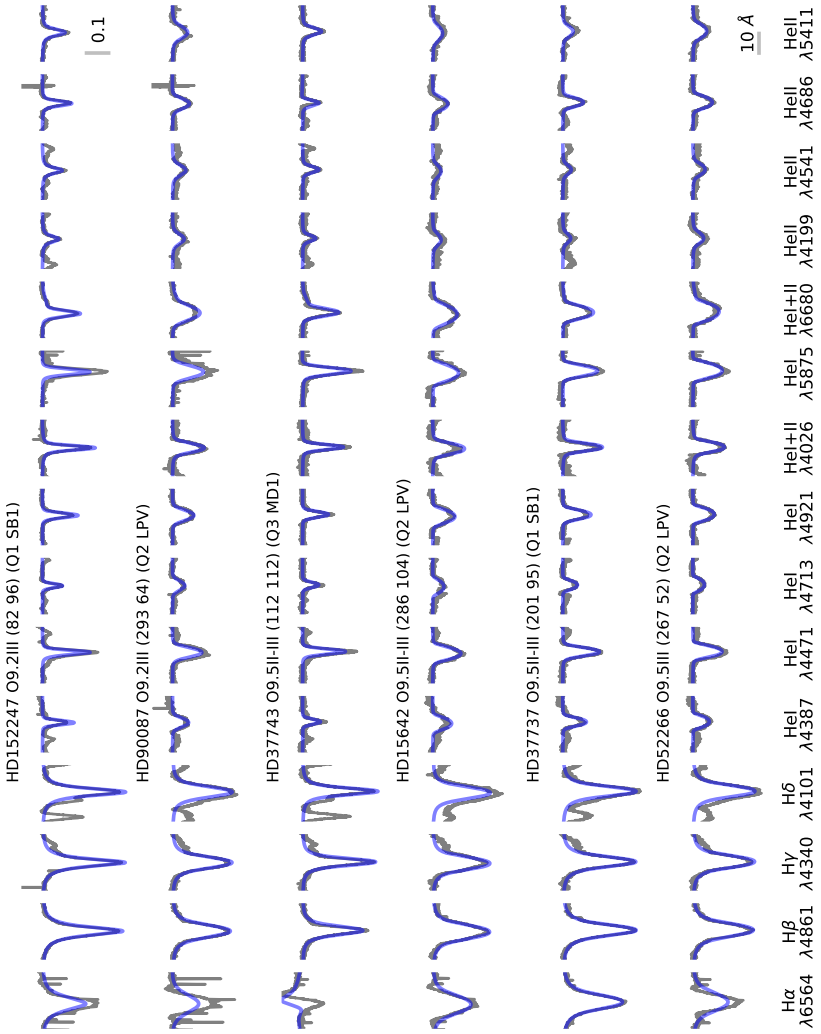

Figure C.31: Same as Fig. C.1.

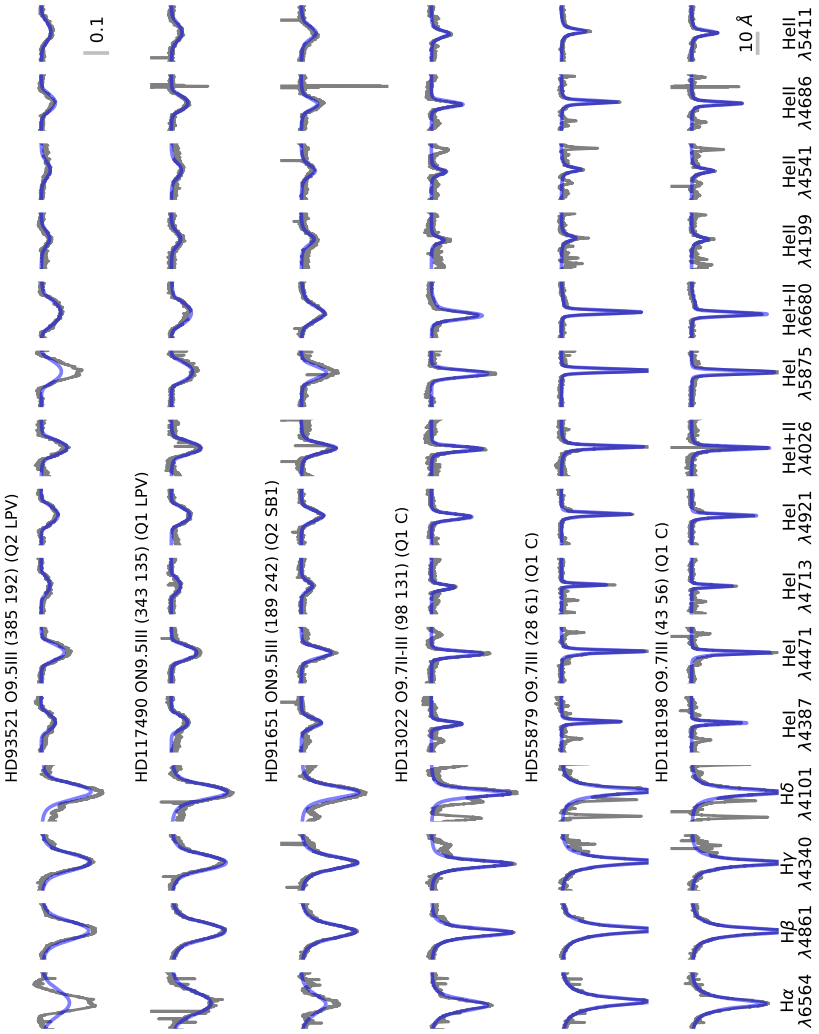

Figure C.32: Same as Fig. C.1.

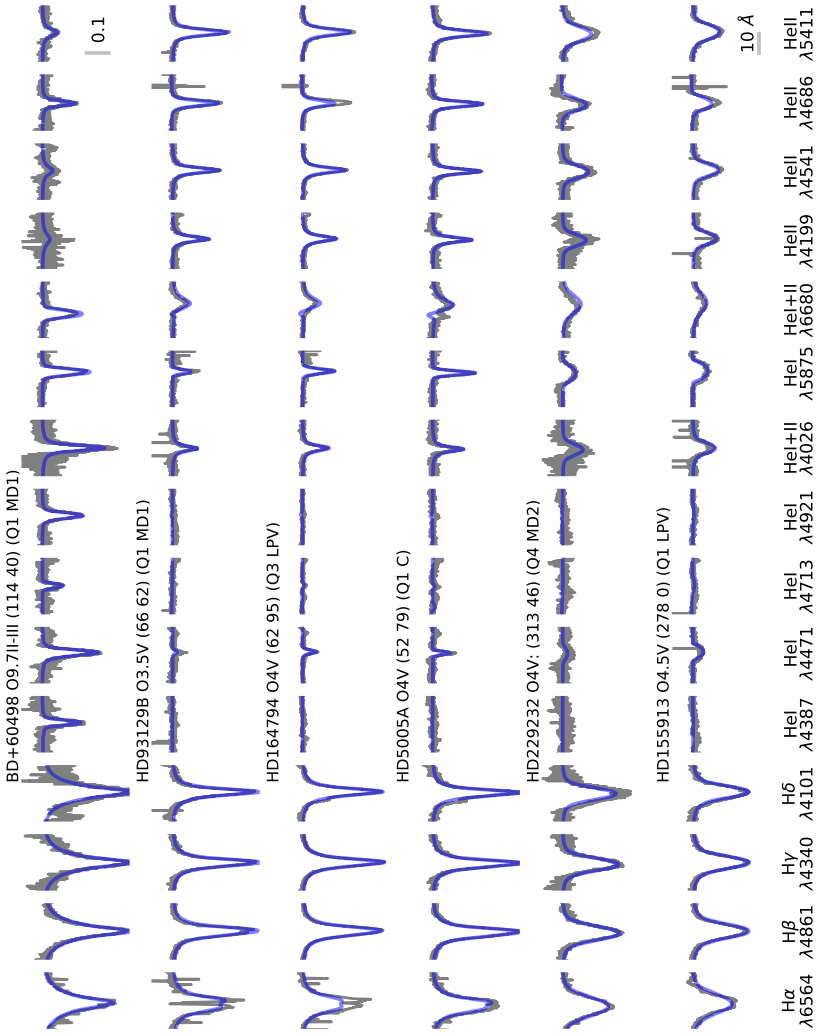

Figure C.33: Same as Fig. C.1.

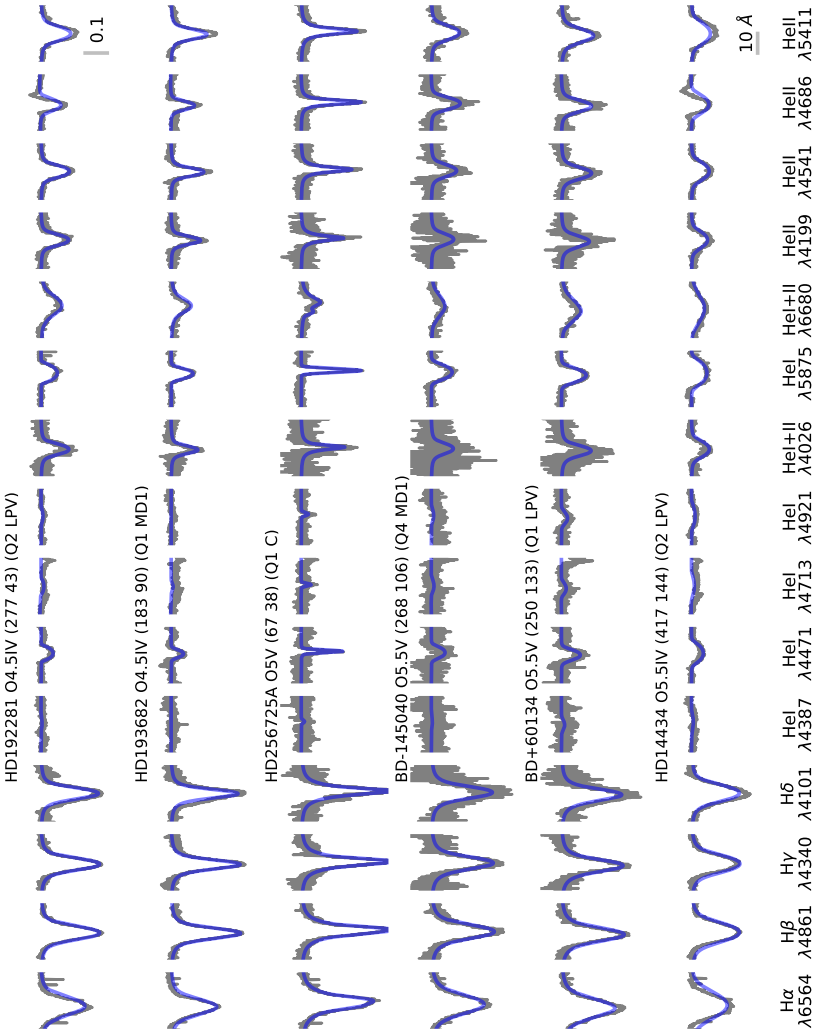

Figure C.34: Same as Fig. C.1.

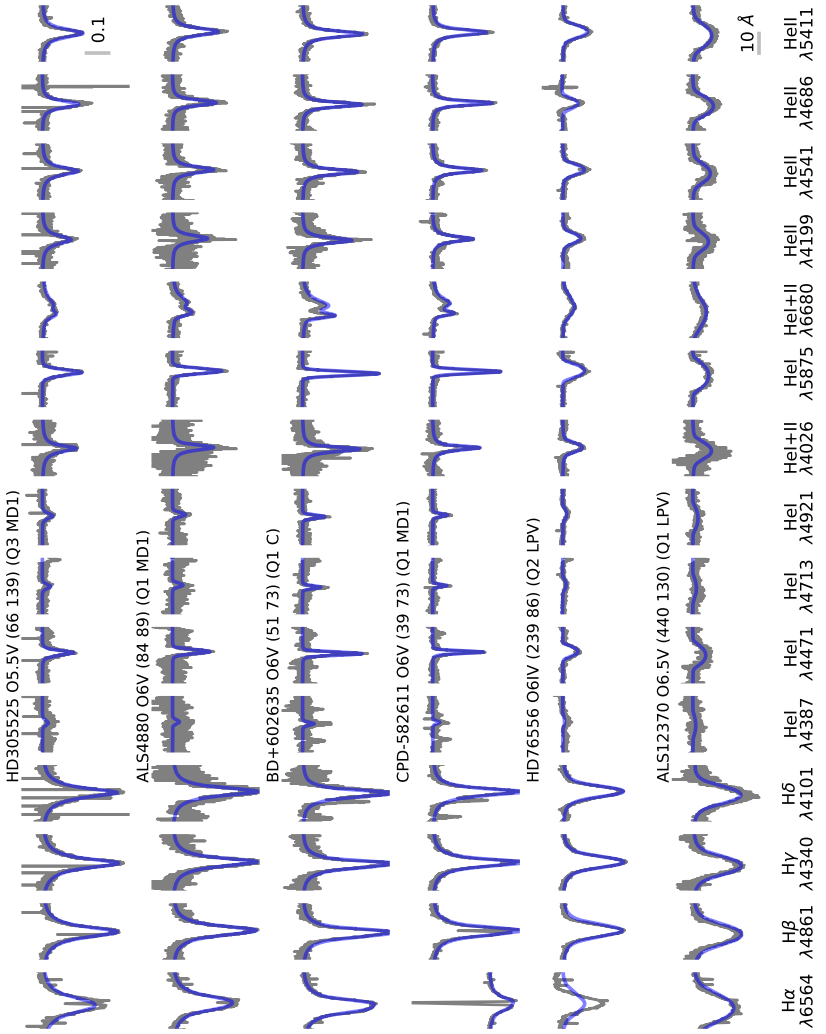

Figure C.35: Same as Fig. C.1.

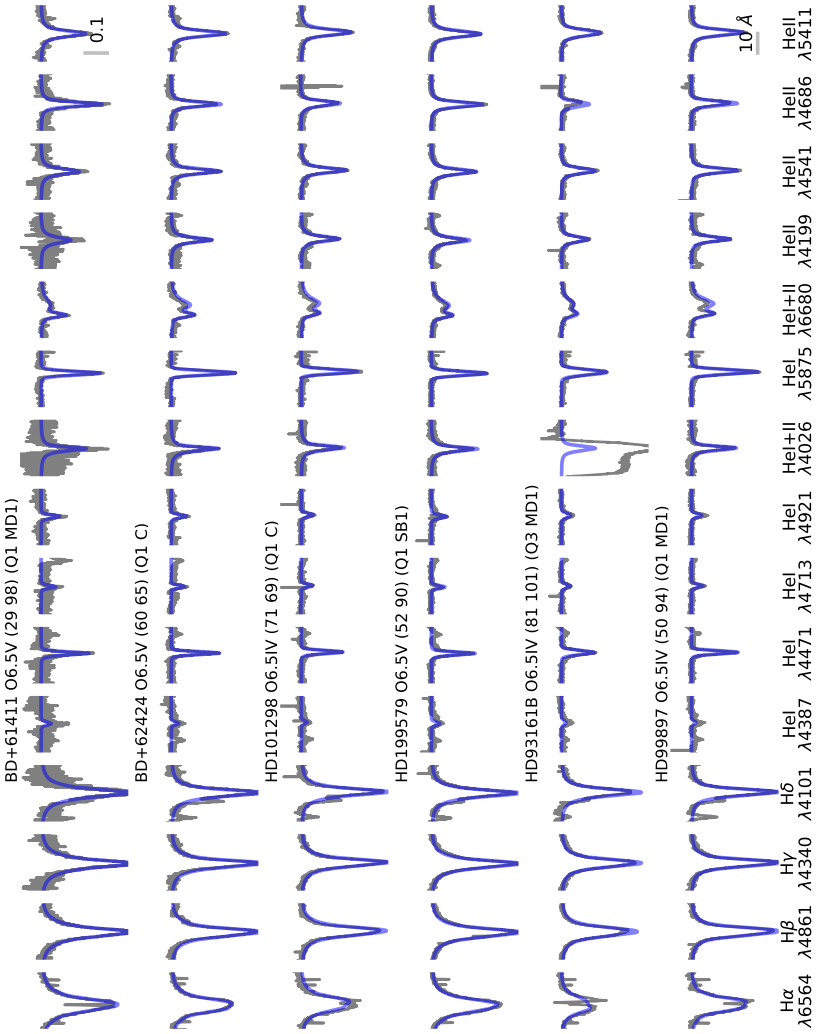

Figure C.36: Same as Fig. C.1.

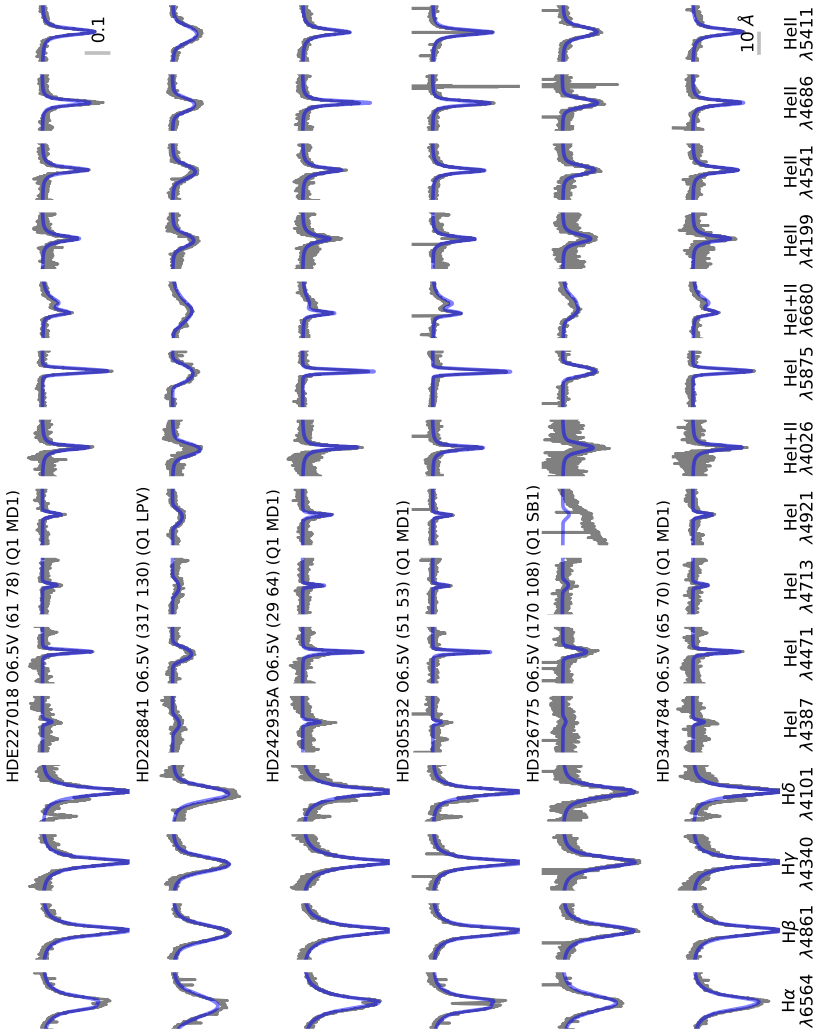

Figure C.37: Same as Fig. C.1.

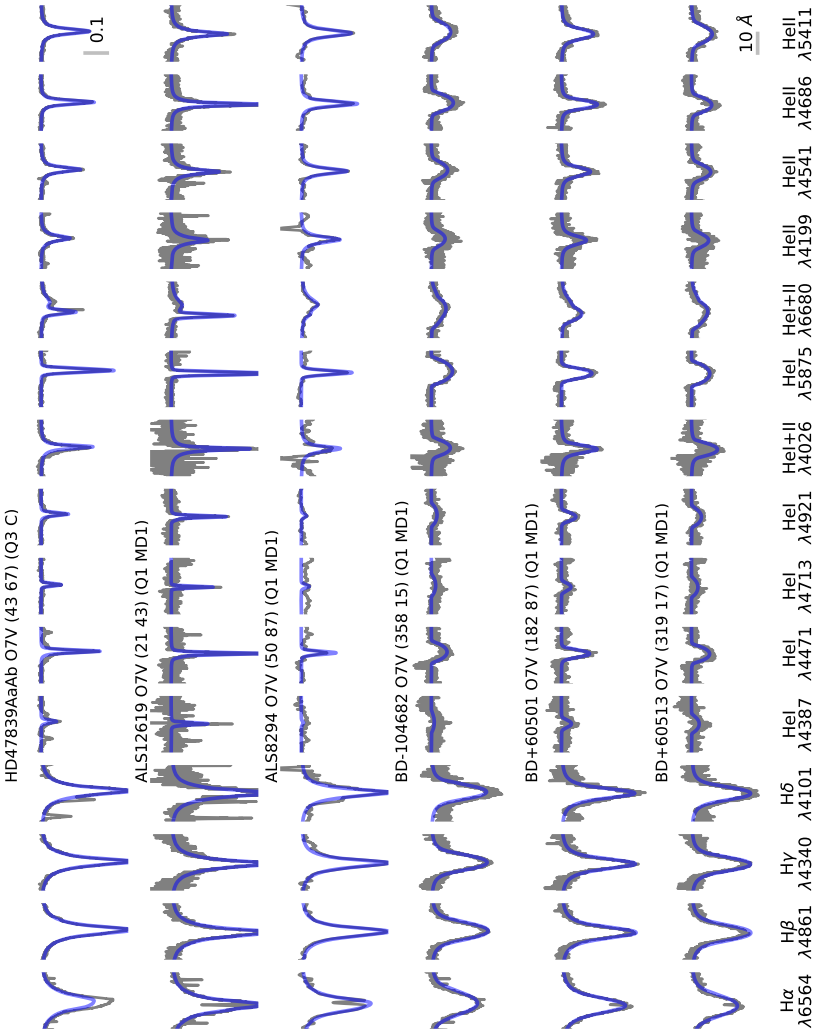

Figure C.38: Same as Fig. C.1.

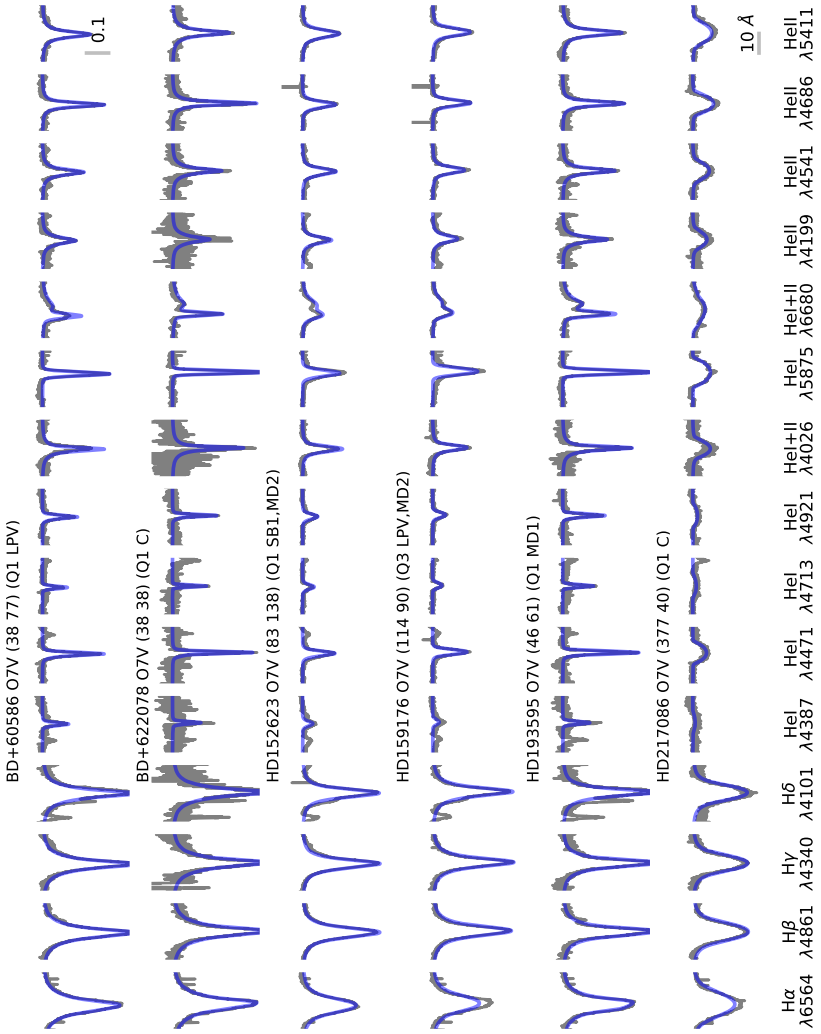

Figure C.39: Same as Fig. C.1.

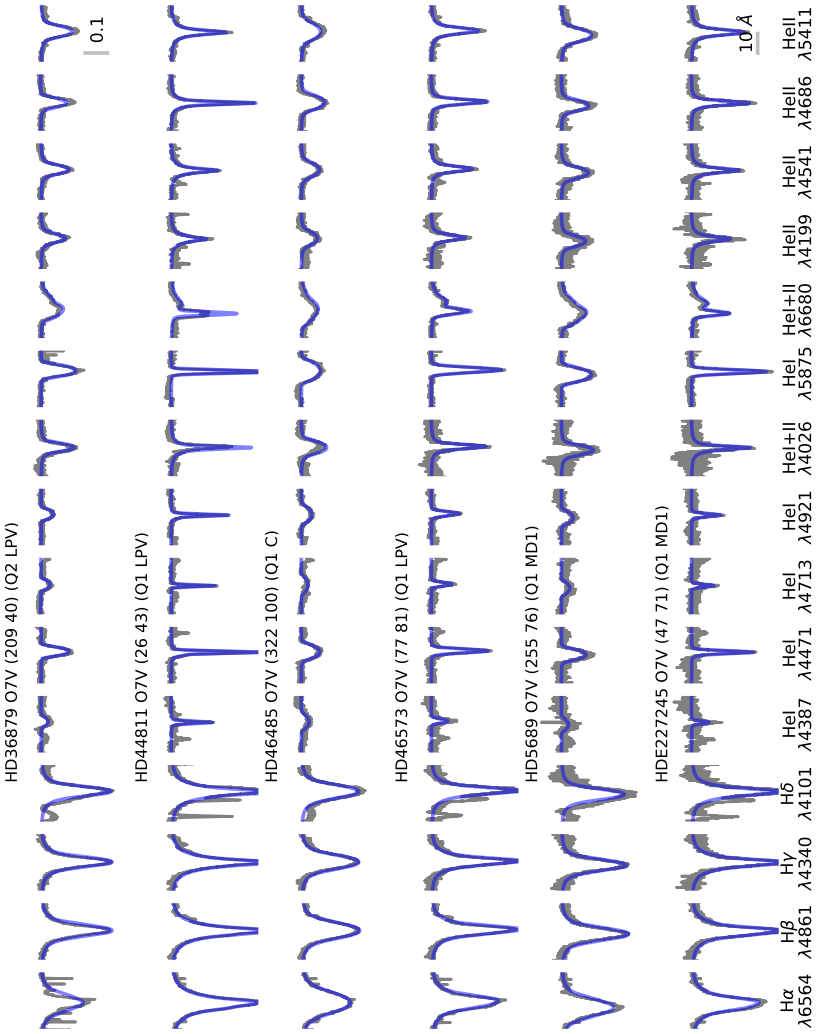

Figure C.40: Same as Fig. C.1.

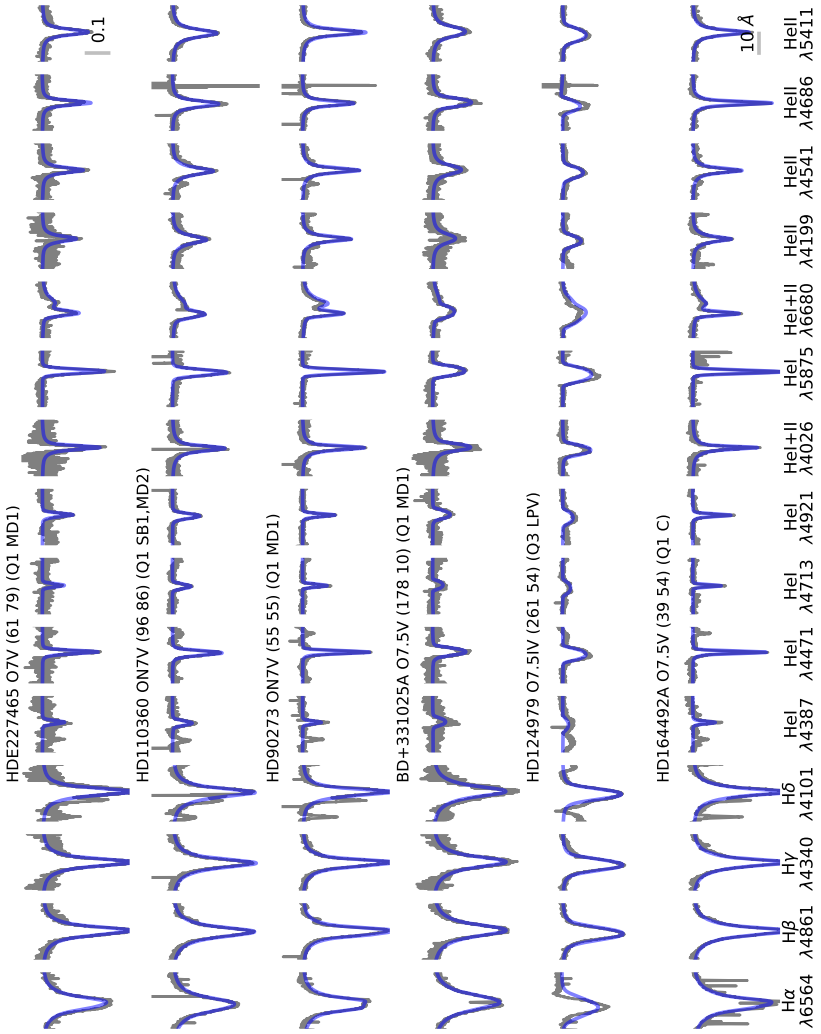

Figure C.41: Same as Fig. C.1.

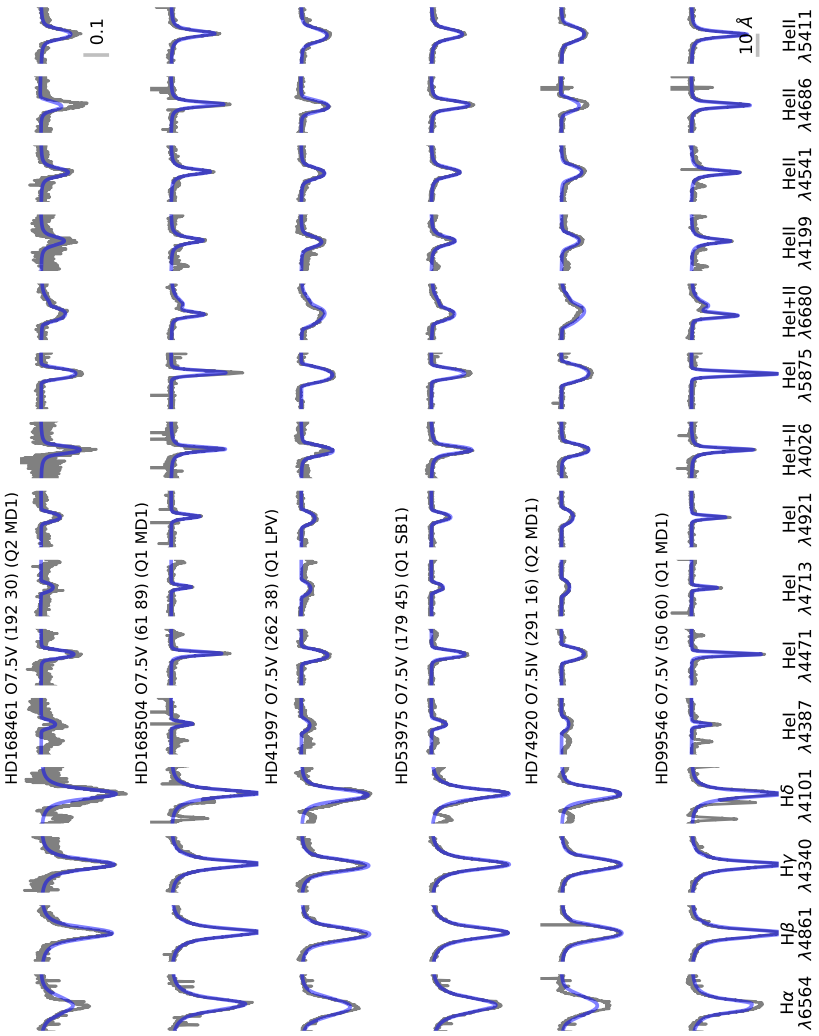

Figure C.42: Same as Fig. C.1.

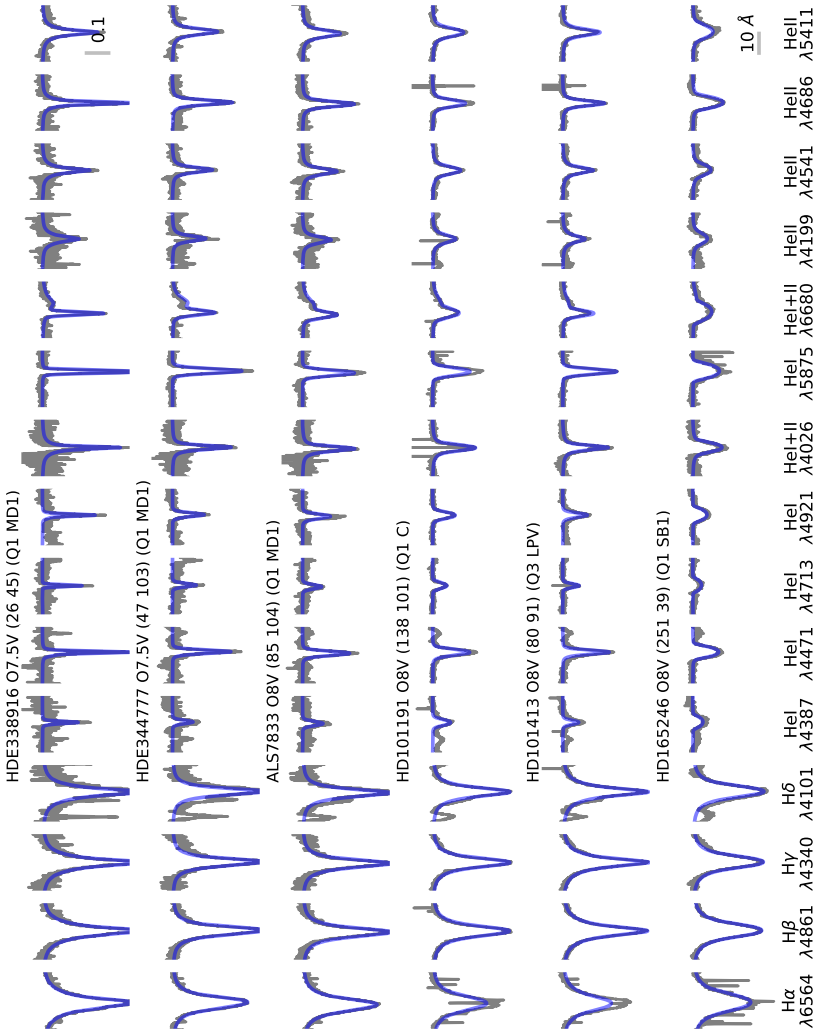

Figure C.43: Same as Fig. C.1.

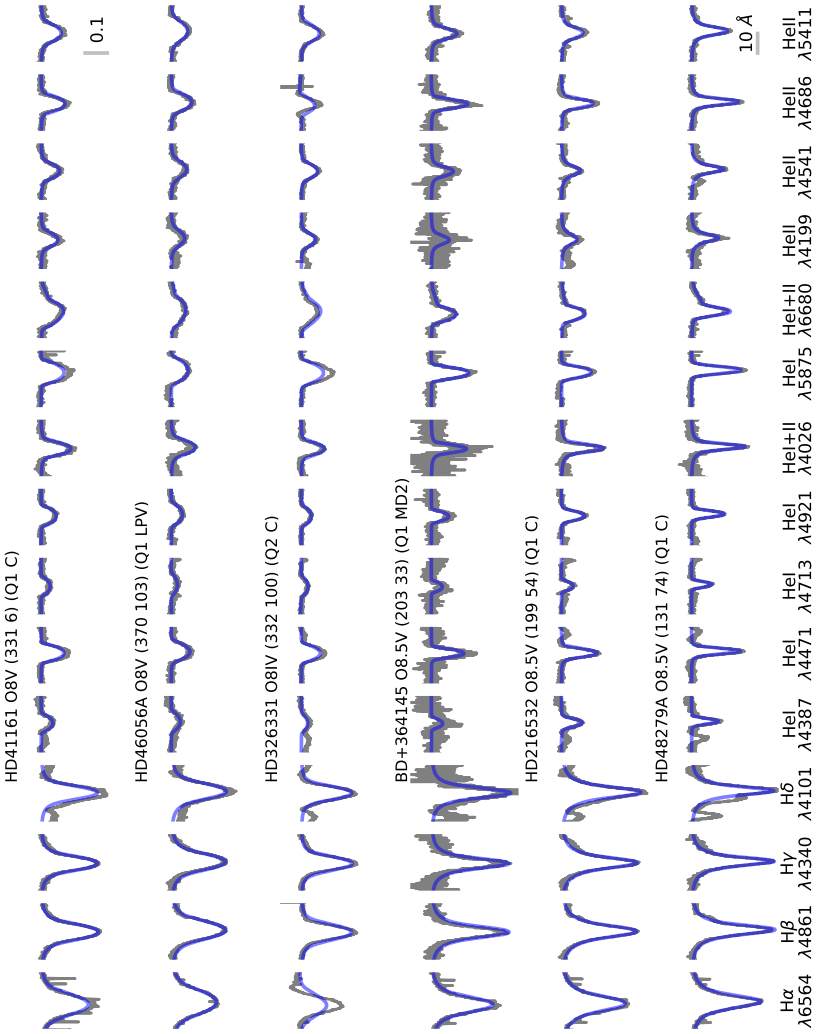

Figure C.44: Same as Fig. C.1.

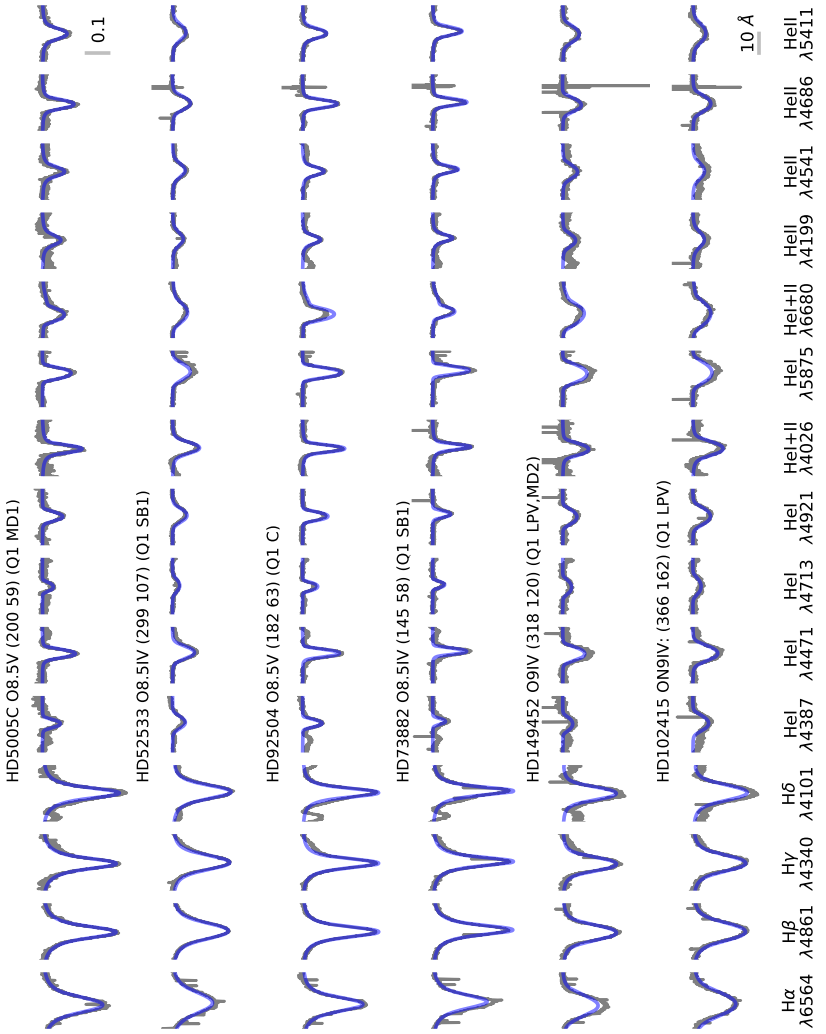

Figure C.45: Same as Fig. C.1.

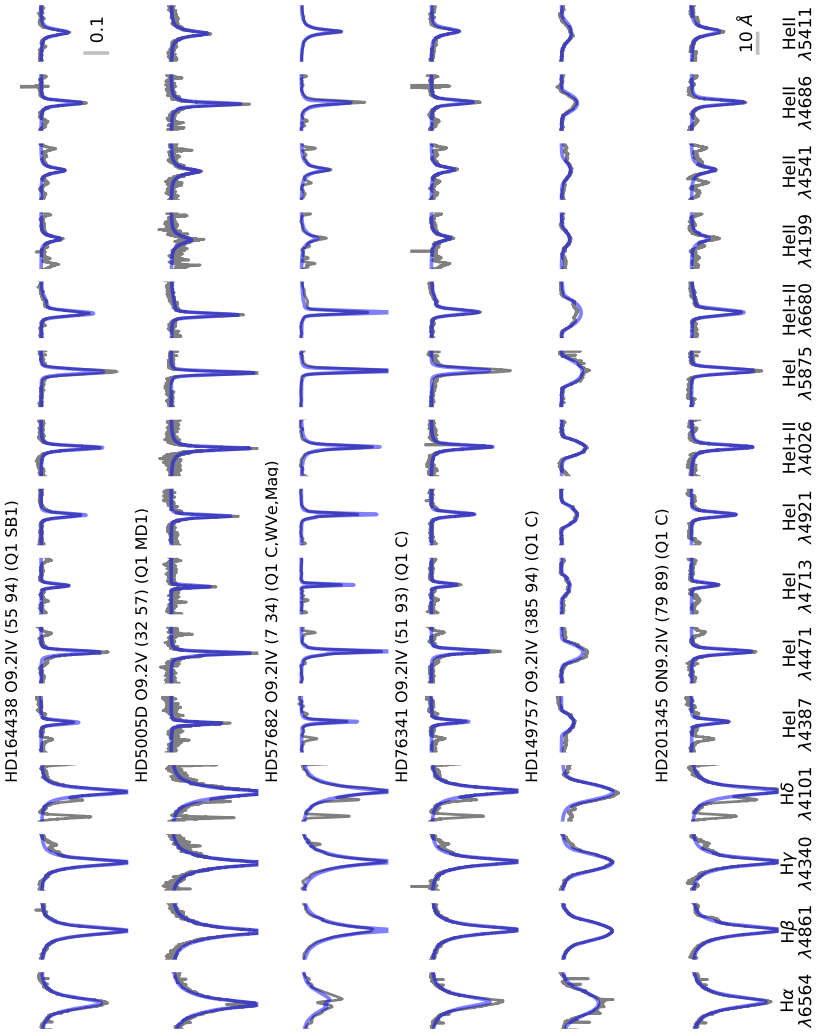

Figure C.46: Same as Fig. C.1.

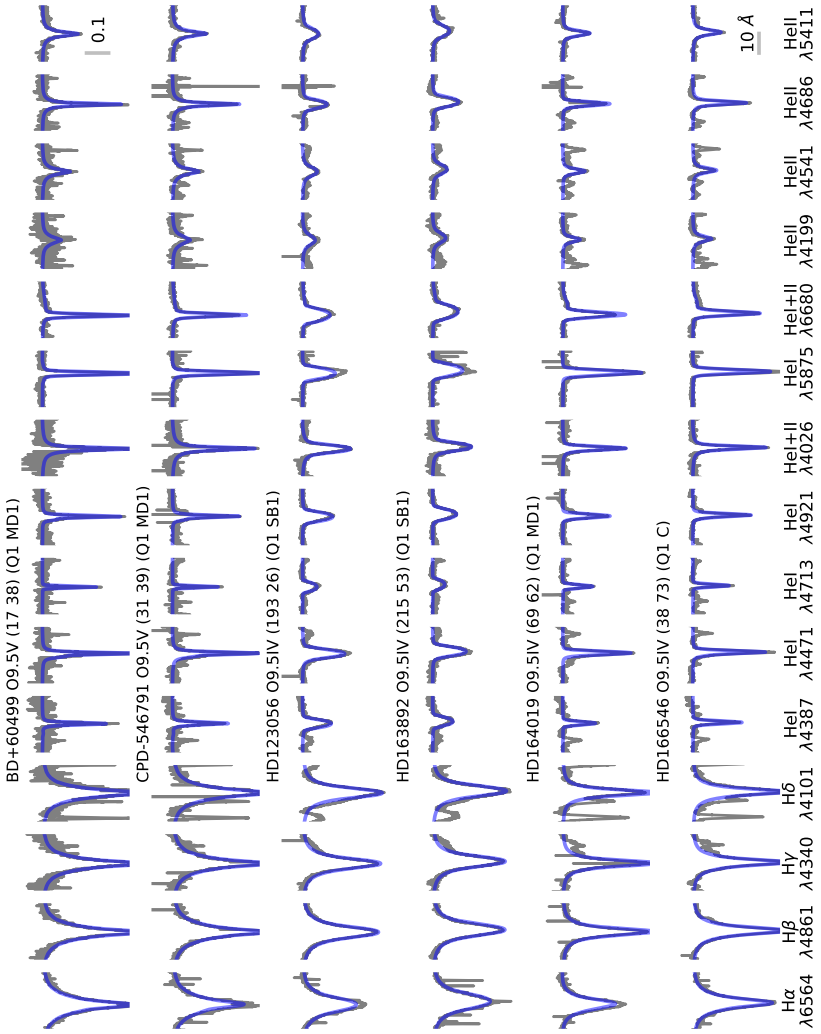

Figure C.47: Same as Fig. C.1.

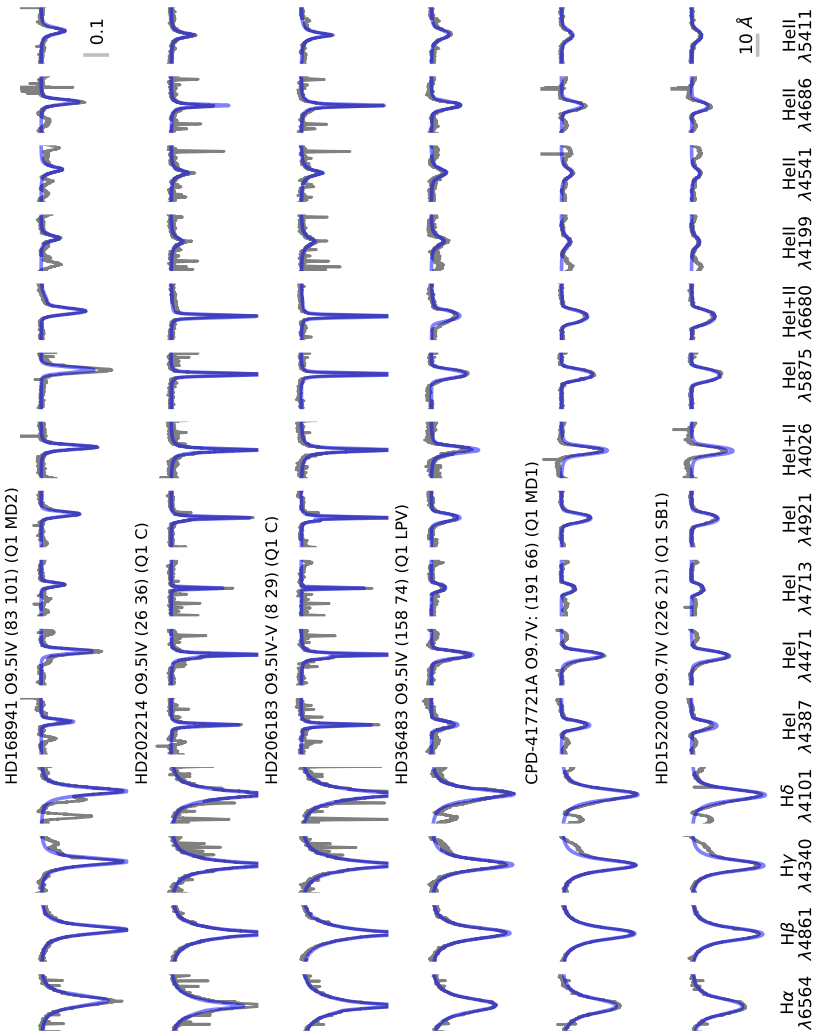

Figure C.48: Same as Fig. C.1.

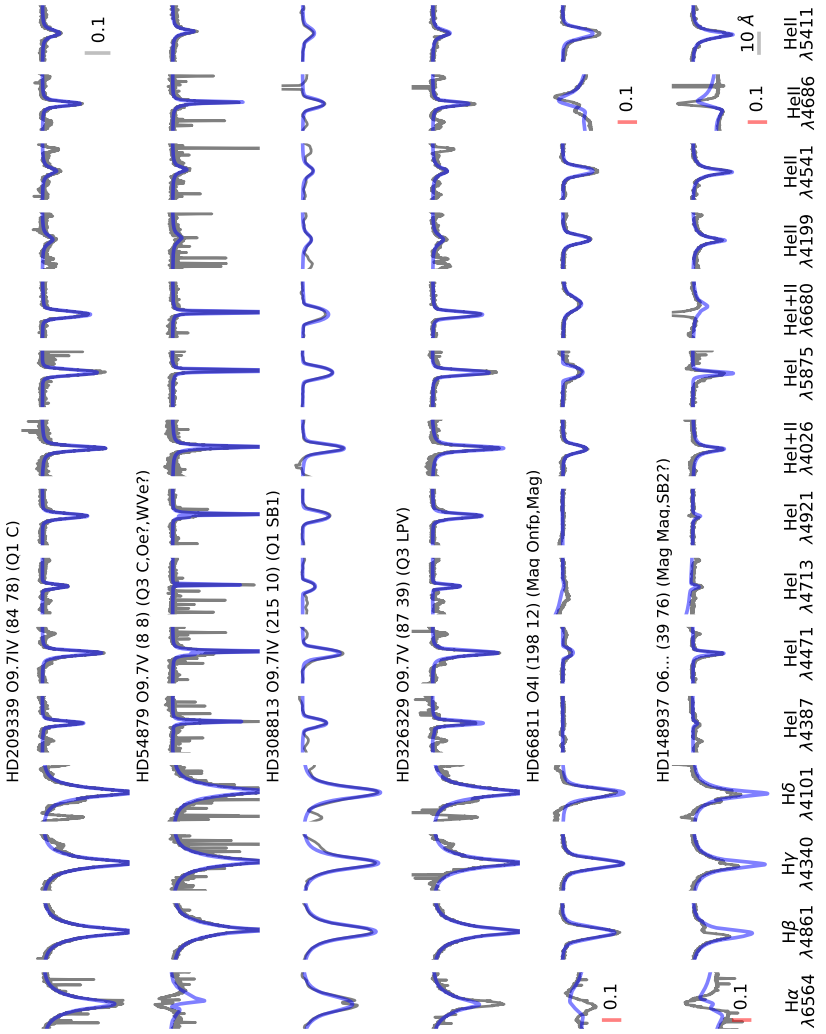

Figure C.49: Same as Fig. C.1.

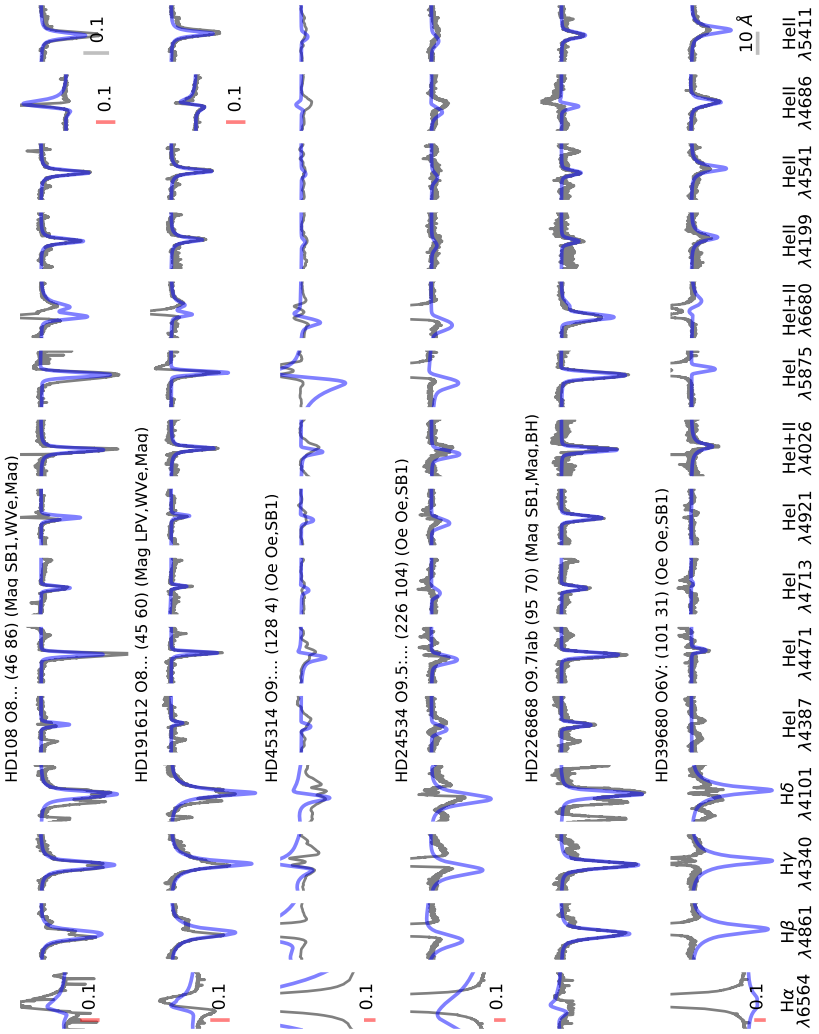

Figure C.50: Same as Fig. C.1.

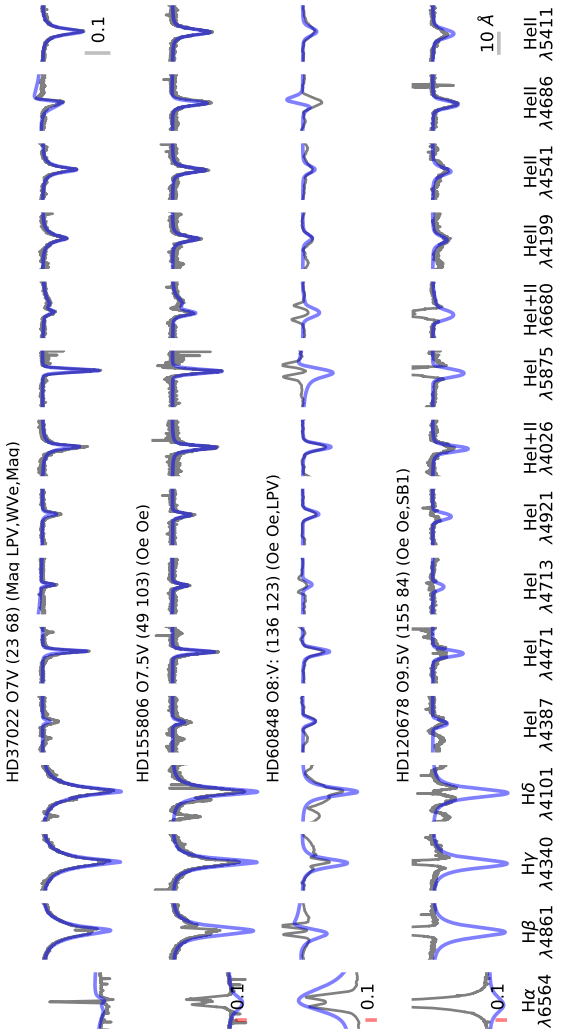

Figure C.51: Same as Fig. C.1.

Bibliography

Abbott, B. P., Abbott, R., Abbott, T. D., et al. 2016, Living Reviews in Relativity, 19, 1

Aerts, C., Christensen-Dalsgaard, J., Cunha, M., & Kurtz, D. W. 2008, Sol. Phys., 251, 3

Aerts, C., Christensen-Dalsgaard, J., & Kurtz, D. W. 2010, Asteroseismology

Aerts, C., Simón-Díaz, S., Groot, P. J., & Degroote, P. 2014, A&A, 569, A118

Aerts, C., Símon-Díaz, S., Bloemen, S., et al. 2017, A&A, 602, A32

Aldoretta, E. J., Caballero-Nieves, S. M., Gies, D. R., et al. 2015, AJ, 149, 26

Almeida, L. A., Sana, H., de Mink, S. E., et al. 2015, ApJ, 812, 102

Almeida, L. A., Sana, H., Taylor, W., et al. 2017, A&A, 598, A84

Arias, J. I., Walborn, N. R., Diaz, S. S., et al. 2016, VizieR Online Data Catalog, 515

Asplund, M., Grevesse, N., & Sauval, A. J. 2005, in Astronomical Society of the Pacific Conference Series, Vol. 336, Cosmic Abundances as Records of Stellar Evolution and Nucleosynthesis, ed. T. G. Barnes, III & F. N. Bash, 25

Auer, L. H., & Heasley, J. N. 1976, ApJ, 205, 165

Auer, L. H., & Mihalas, D. 1972, ApJS, 24, 193

Bailer-Jones, C. A. L. 2015, PASP, 127, 994

Bailer-Jones, C. A. L., Rybizki, J., Fouesneau, M., Mantelet, G., & Andrae, R. 2018, AJ, 156, 58

Barbá, R., Gamen, R., Arias, J. I., et al. 2014, in Revista Mexicana de Astronomia y Astrofisica, vol. 27, Vol. 44, Revista Mexicana de Astronomia y Astrofisica Conference Series, 148–148

Barbá, R. H., Gamen, R., Arias, J. I., et al. 2010, in Revista Mexicana de Astronomia y Astrofisica, vol. 27, Vol. 38, Revista Mexicana de Astronomia y Astrofisica Conference Series, 30–32

Barbá, R. H., Gamen, R., Arias, J. I., & Morrell, N. I. 2017, in IAU Symposium, Vol. 329, The Lives and Death-Throes of Massive Stars, ed. J. J. Eldridge, J. C. Bray, L. A. S. McClelland, & L. Xiao, 89–96

Behrend, R., & Maeder, A. 2001, A&A, 373, 190

Berlanas, S. R., Herrero, A., Comerón, F., et al. 2018, A&A, 612, A50

Bernasconi, P. A., & Maeder, A. 1996, A&A, 307, 829

Bestenlehner, J. M., Vink, J. S., Gräfener, G., et al. 2011, A&A, 530, L14

Bestenlehner, J. M., Gräfener, G., Vink, J. S., et al. 2014, A&A, 570, A38

Bianchi, L., & Garcia, M. 2002, ApJ, 581, 610

Bobylev, V. V., & Bajkova, A. T. 2018, ArXiv e-prints, arXiv:1801.08521

Bodenheimer, P. 1995, ARA&A, 33, 199

Bouret, J.-C., Lanz, T., Hillier, D. J., et al. 2003, ApJ, 595, 1182

Bouret, J.-C., Lanz, T., Martins, F., et al. 2013, A&A, 555, A1

Bresolin, F., Crowther, P. A., & Puls, J., eds. 2008, IAU Symposium, Vol. 250, Massive Stars as Cosmic Engines

Breysacher, J., & François, P. 2000, A&A, 361, 231

Briquet, M., Neiner, C., Aerts, C., et al. 2012, MNRAS, 427, 483

Bromm, V., Ferrara, A., & Heger, A. 2009, First stars: formation, evolution and feedback effects, ed. G. Chabrier (Cambridge University Press), 180

Brott, I., de Mink, S. E., Cantiello, M., et al. 2011, A&A, 530, A115

Cantiello, M., Langer, N., Brott, I., et al. 2009, A&A, 499, 279

Carneiro, L. P., Puls, J., & Hoffmann, T. L. 2018, A&A, 615, A4

Carroll, J. A. 1933, MNRAS, 93, 478

Castor, J. I., Abbott, D. C., & Klein, R. I. 1975, ApJ, 195, 157

Castro, N., Fossati, L., Langer, N., et al. 2014, A&A, 570, L13

Castro, N., Urbaneja, M. A., Herrero, A., et al. 2012, A&A, 542, A79

Castro, N., Fossati, L., Hubrig, S., et al. 2015, A&A, 581, A81

—. 2017, A&A, 597, L6

Cazorla, C., Nazé, Y., Morel, T., et al. 2017, A&A, 604, A123

Chini, R., Hoffmeister, V. H., Nasseri, A., Stahl, O., & Zinnecker, H. 2012, MNRAS, 424, 1925

Chiosi, C., & Maeder, A. 1986, ARA&A, 24, 329

Chiosi, C., & Nasi, E. 1978, Ap&SS, 56, 431

Churchwell, E. 2002, ARA&A, 40, 27

Collins, II, G. W. 1963, ApJ, 138, 1134

—. 1966, ApJ, 146, 914

Conti, P. S. 1975, Memoires of the Societe Royale des Sciences de Liege, 9, 193

Conti, P. S., & Ebbets, D. 1977, ApJ, 213, 438

Conti, P. S., & Frost, S. A. 1976, in BAAS, Vol. 8, Bulletin of the American Astronomical Society, 340

Conti, P. S., Garmany, C. D., & Massey, P. 1984, in BAAS, Vol. 16, Bulletin of the American Astronomical Society, 948

Crowther, P., & Smartt, S. 2007, Astronomy and Geophysics, 48, 1.35

Crowther, P. A., Caballero-Nieves, S. M., Castro, N., & Evans, C. J. 2017, in IAU Symposium, Vol. 329, The Lives and Death-Throes of Massive Stars, ed. J. J. Eldridge, J. C. Bray, L. A. S. McClelland, & L. Xiao, 292–296

Crowther, P. A., Hillier, D. J., Evans, C. J., et al. 2002, ApJ, 579, 774

Crowther, P. A., Lennon, D. J., & Walborn, N. R. 2006, A&A, 446, 279

de Jager, C., Nieuwenhuijzen, H., & van der Hucht, K. A. 1988, A&AS, 72, 259

de Koter, A., Heap, S. R., & Hubeny, I. 1997, ApJ, 477, 792

De Loore, C., De Greve, J. P., & Lamers, H. J. G. L. M. 1977, A&A, 61, 251

de Mink, S. E., Langer, N., Izzard, R. G., Sana, H., & de Koter, A. 2013, ApJ, 764, 166

Denissenkov, P. A. 1994, A&A, 287, 113

Donati, J.-F., & Landstreet, J. D. 2009, ARA&A, 47, 333

Ekström, S., Meynet, G., Chiappini, C., Hirschi, R., & Maeder, A. 2008, A&A, 489, 685

Ekström, S., Georgy, C., Eggenberger, P., et al. 2012, A&A, 537, A146

Elmegreen, B. G., & Lada, C. J. 1977, ApJ, 214, 725

Elmegreen, D. M., & Elmegreen, B. G. 1980, AJ, 85, 1325

ESA, ed. 1997, ESA Special Publication, Vol. 1200, The HIPPARCOS and TYCHO catalogues. Astrometric and photometric star catalogues derived from the ESA HIPPARCOS Space Astrometry Mission

Evans, C., Taylor, W., Sana, H., et al. 2011, The Messenger, 145, 33

Evans, C. J., Lennon, D. J., Smartt, S. J., & Trundle, C. 2007, A&A, 464, 289

Evans, C. J., Smartt, S. J., Lee, J.-K., et al. 2005, A&A, 437, 467

Eversberg, T., Lépine, S., & Moffat, A. F. J. 1998, ApJ, 494, 799

Fabricius, C., Bastian, U., Portell, J., et al. 2016, A&A, 595, A3

Ferrario, L., Pringle, J. E., Tout, C. A., & Wickramasinghe, D. T. 2009, MNRAS, 400, L71

Fukui, Y., & Kawamura, A. 2010, ARA&A, 48, 547

Fullerton, A. W., Gies, D. R., & Bolton, C. T. 1996, ApJS, 103, 475

Fullerton, A. W., Massa, D. L., & Prinja, R. K. 2006, ApJ, 637, 1025

Gaia Collaboration, Brown, A. G. A., Vallenari, A., et al. 2018a, A&A, 616, A1

Gaia Collaboration, Mignard, F., Klioner, S. A., et al. 2018b, A&A, 616, A14

Gamen, R., Barbá, R., Morrell, N., et al. 2007, Boletin de la Asociacion Argentina de Astronomia La Plata Argentina, 50, 105

Garcia, M., Najarro, F., & Herrero, A. 2011, Bulletin de la Societe Royale des Sciences de Liege, 80, 144

Garmany, C. D., Conti, P. S., & Chiosi, C. 1982, ApJ, 263, 777

Georgy, C., Ekstrom, S., Granada, A., et al. 2013, VizieR Online Data Catalog, 355

Georgy, C., Meynet, G., Walder, R., Folini, D., & Maeder, A. 2009, A&A, 502, 611

Godart, M., Simón-Díaz, S., Herrero, A., et al. 2017, A&A, 597, A23

Gontcharov, G. A. 2006, Astronomy Letters, 32, 759

Gräfener, G., Koesterke, L., & Hamann, W.-R. 2002, A&A, 387, 244

Grassitelli, L., Fossati, L., Simón-Diáz, S., et al. 2015, ApJ, 808, L31

Gray, D. F. 2005, The Observation and Analysis of Stellar Photospheres

Grin, N. J., Ramírez-Agudelo, O. H., de Koter, A., et al. 2017, A&A, 600, A82

Groh, J. H., Meynet, G., Ekström, S., & Georgy, C. 2014, A&A, 564, A30

Groh, J. H., Meynet, G., Georgy, C., & Ekström, S. 2013, A&A, 558, A131

Grunhut, J. H., Wade, G. A., Neiner, C., et al. 2017, MNRAS, 465, 2432

Haemmerlé, L., Eggenberger, P., Meynet, G., Maeder, A., & Charbonnel, C. 2016, A&A, 585, A65

Haiman, Z., & Loeb, A. 1997, ApJ, 483, 21

Hamann, J., Balbi, A., Lesgourgues, J., & Quercellini, C. 2009, jcap, 4, 011

Hanson, M. M. 1998, in Astronomical Society of the Pacific Conference Series, Vol. 131, Properties of Hot Luminous Stars, ed. I. Howarth, 1–13

Hartmann, L., & Stauffer, J. R. 1989, AJ, 97, 873

Heap, S. R., Lanz, T., & Hubeny, I. 2006, ApJ, 638, 409

Heger, A. 2012, in Astrophysics and Space Science Library, Vol. 384, Eta Carinae and the Supernova Impostors, ed. K. Davidson & R. M. Humphreys, 299

Heger, A., Langer, N., & Woosley, S. E. 2000, ApJ, 528, 368

Herbig, G. H. 1962, ApJ, 135, 736

Herrero, A., Kudritzki, R. P., Vilchez, J. M., et al. 1992, A&A, 261, 209

Herrero, A., Puls, J., & Najarro, F. 2002, A&A, 396, 949

Herrero, A., Simon-Diaz, S., Najarro, F., & Ribas, I. 2007, in Astronomical Society of the Pacific Conference Series, Vol. 367, Massive Stars in Interactive Binaries, ed. N. St.-Louis & A. F. J. Moffat, 67

Herrero, A., & Villamariz, M. R. 1999, in IAU Symposium, Vol. 193, Wolf-Rayet Phenomena in Massive Stars and Starburst Galaxies, ed. K. A. van der Hucht, G. Koenigsberger, & P. R. J. Eenens, 244

Hervé, A. 2015, in SF2A-2015: Proceedings of the Annual meeting of the French Society of Astronomy and Astrophysics, ed. F. Martins, S. Boissier, V. Buat, L. Cambrésy, & P. Petit, 381–384

Hillier, D. J. 1991, A&A, 247, 455

Hillier, D. J. 2012, in IAU Symposium, Vol. 282, From Interacting Binaries to Exoplanets: Essential Modeling Tools, ed. M. T. Richards & I. Hubeny, 229–234

Hillier, D. J., & Lanz, T. 2001, in Astronomical Society of the Pacific Conference Series, Vol. 247, Spectroscopic Challenges of Photoionized Plasmas, ed. G. Ferland & D. W. Savin, 343

Hillier, D. J., & Miller, D. L. 1998, ApJ, 496, 407

Hoeg, E., Bässgen, G., Bastian, U., et al. 1997, A&A, 323, L57

Høg, E., Fabricius, C., Makarov, V. V., et al. 2000, A&A, 355, L27

Holgado, G., Simón-Díaz, S., & Barbá, R. 2017, in Highlights on Spanish Astrophysics IX, ed. S. Arribas, A. Alonso-Herrero, F. Figueras, C. Hernández-Monteagudo, A. Sánchez-Lavega, & S. Pérez-Hoyos, 394–400

Holgado, G., Simón-Díaz, S., Barbá, R. H., et al. 2018, A&A, 613, A65

Howarth, I. D. 2004, in IAU Symposium, Vol. 215, Stellar Rotation, ed. A. Maeder & P. Eenens, 33

Howarth, I. D., Siebert, K. W., Hussain, G. A. J., & Prinja, R. K. 1997, MNRAS, 284, 265

Howarth, I. D., Walborn, N. R., Lennon, D. J., et al. 2007, MNRAS, 381, 433

Huang, W., & Gies, D. R. 2006, ApJ, 648, 580

Huang, W., Gies, D. R., & McSwain, M. V. 2010, ApJ, 722, 605

Hubeny, I., & Lanz, T. 1995, ApJ, 439, 875

—. 2011, TLUSTY: Stellar Atmospheres, Accretion Disks, and Spectroscopic Diagnostics, Astrophysics Source Code Library, ascl:1109.021

Hunter, I., Lennon, D. J., Dufton, P. L., et al. 2011, A&A, 530, C1

Hunter, I., Dufton, P. L., Smartt, S. J., et al. 2007, A&A, 466, 277

Hunter, I., Brott, I., Lennon, D. J., et al. 2008, ApJ, 676, L29

Iglesias, C. A., & Rogers, F. J. 1996, ApJ, 464, 943

Irrgang, A., Przybilla, N., Heber, U., et al. 2014, A&A, 565, A63

Janka, H.-T., Hanke, F., Hüdepohl, L., et al. 2012, Progress of Theoretical and Experimental Physics, 2012, 01A309

Kaufer, A., Wolf, B., Andersen, J., & Pasquini, L. 1997, The Messenger, 89, 1

Kennicutt, R. C., Kobulnicky, H. A., & Pizagno, J. L. 1998, in Bulletin of the American Astronomical Society, Vol. 30, American Astronomical Society Meeting Abstracts, 1354

Kharchenko, N. V., Scholz, R.-D., Piskunov, A. E., Röser, S., & Schilbach, E. 2007, Astronomische Nachrichten, 328, 889

Kippenhahn, R., Meyer-Hofmeister, E., & Thomas, H. C. 1970, A&A, 5, 155

Kippenhahn, R., Weigert, A., & Weiss, A. 2012, Stellar Structure and Evolution, doi:10.1007/978-3-642-30304-3

Kiriakidis, M., Fricke, K. J., & Glatzel, W. 1993, MNRAS, 264, 50

Kobulnicky, H. A., Kiminki, D. C., Lundquist, M. J., et al. 2014, ApJS, 213, 34

Kohley, R., Garé, P., Vétel, C., Marchais, D., & Chassat, F. 2012, in Proc. SPIE, Vol. 8442, Space Telescopes and Instrumentation 2012: Optical, Infrared, and Millimeter Wave, 84421P

Korn, A. J., Nieva, M. F., Daflon, S., & Cunha, K. 2005, ApJ, 633, 899

Kroupa, P., Famaey, B., de Boer, K. S., et al. 2010, A&A, 523, A32

Krumholz, M. R. 2009, High-mass star formation by gravitational collapse of massive cores:, ed. M. Livio & E. Villaver, 1–24

Krumholz, M. R., McKee, C. F., & Klein, R. I. 2005, Nature, 438, 332

Kudritzki, R. ., & Urbaneja, M. A. 2006, ArXiv Astrophysics e-prints, astro-ph/0607460

Kudritzki, R.-P. 1980, A&A, 85, 174

Kudritzki, R. P., Bresolin, F., & Przybilla, N. 2003, ApJ, 582, L83

Kudritzki, R.-P., Hummer, D. G., Pauldrach, A. W. A., et al. 1992, A&A, 257, 655

Kudritzki, R.-P., & Puls, J. 2000, ARA&A, 38, 613

Kudritzki, R.-P., Urbaneja, M. A., Bresolin, F., et al. 2008, ApJ, 681, 269

Kuiper, G. P. 1938, ApJ, 88, 429

Langer, N. 1991, in IAU Symposium, Vol. 143, Wolf-Rayet Stars and Interrelations with Other Massive Stars in Galaxies, ed. K. A. van der Hucht & B. Hidayat, 431

Langer, N. 1992, A&A, 265, L17

—. 2012, ARA&A, 50, 107

Langer, N., Cantiello, M., Yoon, S.-C., et al. 2008, in IAU Symposium, Vol. 250, Massive Stars as Cosmic Engines, ed. F. Bresolin, P. A. Crowther, & J. Puls, 167–178

Langer, N., & Heger, A. 1998, in Astronomical Society of the Pacific Conference Series, Vol. 131, Properties of Hot Luminous Stars, ed. I. Howarth, 76

Langer, N., Heger, A., & Fliegner, J. 1997, in IAU Symposium, Vol. 189, IAU Symposium, ed. T. R. Bedding, A. J. Booth, & J. Davis, 343–348

Langer, N., & Kudritzki, R. P. 2014, A&A, 564, A52

Larson, R. B. 2010, Reports on Progress in Physics, 73, 014901

Lee, U., Mathis, S., & Neiner, C. 2016, MNRAS, 457, 2445

Lefever, K., Puls, J., & Aerts, C. 2007, A&A, 463, 1093

Leitherer, C. 1998, in Stellar astrophysics for the local group: VIII Canary Islands Winter School of Astrophysics, ed. A. Aparicio, A. Herrero, & F. Sánchez, 527

Lennon, D. J., Lee, J.-K., Dufton, P. L., & Ryans, R. S. I. 2005, A&A, 438, 265

Lin, M.-K., Krumholz, M. R., & Kratter, K. M. 2011, MNRAS, 416, 580

Lindegren, L., Lammers, U., Bastian, U., et al. 2016, A&A, 595, A4

Lindegren, L., Hernández, J., Bombrun, A., et al. 2018, A&A, 616, A2

Lucy, L. B. 1976, ApJ, 206, 499

Lucy, L. B., & Solomon, P. M. 1970, ApJ, 159, 879

Luri, X., Brown, A. G. A., Sarro, L. M., et al. 2018, A&A, 616, A9

Maeder, A. 1980, A&A, 92, 101

—. 1987, A&A, 173, 247

Maeder, A., & Meynet, G. 1995, The Messenger, 80, 19

—. 2000a, A&A, 361, 159

—. 2000b, ARA&A, 38, 143

—. 2010, nar, 54, 32

Mahy, L., Rauw, G., De Becker, M., Eenens, P., & Flores, C. A. 2015, A&A, 577, A23

Maíz Apellániz, J., Alonso Moragón, A., Ortiz de Zárate Alcarazo, L., & The Gosss Team. 2017, in Highlights on Spanish Astrophysics IX, ed. S. Arribas, A. Alonso-Herrero, F. Figueras, C. Hernández-Monteagudo, A. Sánchez-Lavega, & S. Pérez-Hoyos, 509–509

Maíz Apellániz, J., & Barbá, R. H. 2018, A&A, 613, A9

Maíz Apellániz, J., Sota, A., Walborn, N. R., et al. 2011, in Highlights of Spanish Astrophysics VI, ed. M. R. Zapatero Osorio, J. Gorgas, J. Maíz Apellániz, J. R. Pardo, & A. Gil de Paz, 467–472

Maíz Apellániz, J., Sota, A., Morrell, N. I., et al. 2013, in Massive Stars: From alpha to Omega, 198

Maíz Apellániz, J., Alfaro, E. J., Arias, J. I., et al. 2015, in Highlights of Spanish Astrophysics VIII, ed. A. J. Cenarro, F. Figueras, C. Hernández-Monteagudo, J. Trujillo Bueno, & L. Valdivielso, 603–603

Maíz Apellániz, J., Sota, A., Arias, J. I., et al. 2016, ApJS, 224, 4

Markova, N. 2010, Publications de l'Observatoire Astronomique de Beograd, 90, 97

Markova, N., & Puls, J. 2008, A&A, 478, 823

Markova, N., Puls, J., & Langer, N. 2018, A&A, 613, A12

Markova, N., Puls, J., Repolust, T., & Markov, H. 2004, A&A, 413, 693

Markova, N., Puls, J., Scuderi, S., & Markov, H. 2005, A&A, 440, 1133

Markova, N., Puls, J., Simón-Díaz, S., et al. 2014, A&A, 562, A37

Martín-Fleitas, J., Sahlmann, J., Mora, A., et al. 2014, in Proc. SPIE, Vol. 9143, Space Telescopes and Instrumentation 2014: Optical, Infrared, and Millimeter Wave, 91430Y

Martins, F. 2018, A&A, 616, A135

Martins, F., Escolano, C., Wade, G. A., et al. 2012, A&A, 538, A29

Martins, F., Foschino, S., Bouret, J.-C., Barbá, R., & Howarth, I. 2016, A&A, 588, A64

Martins, F., & Palacios, A. 2013, A&A, 560, A16

Martins, F., & Plez, B. 2006, A&A, 457, 637

Martins, F., Schaerer, D., & Hillier, D. J. 2005, A&A, 436, 1049

Martins, F., Simón-Díaz, S., Palacios, A., et al. 2015a, A&A, 578, A109

Martins, F., Hervé, A., Bouret, J.-C., et al. 2015b, A&A, 575, A34

Mason, B. D., Hartkopf, W. I., Gies, D. R., Henry, T. J., & Helsel, J. W. 2009, AJ, 137, 3358

Massey, P., Bresolin, F., Kudritzki, R. P., Puls, J., & Pauldrach, A. W. A. 2004, ApJ, 608, 1001

Massey, P., Neugent, K. F., Hillier, D. J., & Puls, J. 2013, ApJ, 768, 6

Massey, P., Puls, J., Pauldrach, A. W. A., et al. 2005, ApJ, 627, 477

McErlean, N. D., Lennon, D. J., & Dufton, P. L. 1998, A&A, 329, 613

Mestel, L. 1965, QJRAS, 6, 161

Meynet, G. 1992, in Instabilities in Evolved Super- and Hypergiants, ed. C. de Jager & H. Nieuwenhuijzen, 173

Meynet, G., Ekstrom, S., Maeder, A., et al. 2013, in Lecture Notes in Physics, Berlin Springer Verlag, Vol. 865, Lecture Notes in Physics, Berlin Springer Verlag, ed. M. Goupil, K. Belkacem, C. Neiner, F. Lignières, & J. J. Green, 3

Meynet, G., Georgy, C., Hirschi, R., et al. 2011, Bulletin de la Societe Royale des Sciences de Liege, 80, 266

Meynet, G., & Maeder, A. 1997, A&A, 321, 465

—. 2000, A&A, 361, 101

Michalik, D., Lindegren, L., & Hobbs, D. 2015, A&A, 574, A115

Moffat, A. F. J. 2008, in Clumping in Hot-Star Winds, ed. W.-R. Hamann, A. Feldmeier, & L. M. Oskinova, 17

Mokiem, M. R., de Koter, A., Puls, J., et al. 2005, A&A, 441, 711

Mokiem, M. R., de Koter, A., Evans, C. J., et al. 2006, A&A, 456, 1131

Mokiem, M. R., de Koter, A., Vink, J. S., et al. 2007, A&A, 473, 603

Monteverde, M. I., & Herrero, A. 1998, Ap&SS, 263, 171

Morel, T., Hubrig, S., & Briquet, M. 2008, A&A, 481, 453

Morel, T., Castro, N., Fossati, L., et al. 2014, The Messenger, 157, 27

Morel, T., Castro, N., Fossati, L., et al. 2015, in IAU Symposium, Vol. 307, New Windows on Massive Stars, ed. G. Meynet, C. Georgy, J. Groh, & P. Stee, 342–347

Morton, D. C. 1967, AJ, 72, 313

Moss, C. 2001, in Astronomical Society of the Pacific Conference Series, Vol. 230, Galaxy Disks and Disk Galaxies, ed. J. G. Funes & E. M. Corsini, 487–490

Müller, P. E., & Vink, J. S. 2014, A&A, 564, A57

Najarro, F., Kudritzki, R. P., Cassinelli, J. P., Stahl, O., & Hillier, D. J. 1996, A&A, 306, 892

Negueruela, I., Steele, I. A., & Bernabeu, G. 2004, Astronomische Nachrichten, 325, 749

Norberg, P., & Maeder, A. 2000, A&A, 359, 1025

Oey, M. S., Parker, J. S., Mikles, V. J., & Zhang, X. 2003, AJ, 126, 2317

Ohkubo, T., Nomoto, K., Umeda, H., Yoshida, N., & Tsuruta, S. 2009, ApJ, 706, 1184

Owocki, S. P., Castor, J. I., & Rybicki, G. B. 1988, ApJ, 335, 914

Packet, W., Vanbeveren, D., De Loore, C., Sreenivasan, S. R., & De Greve, J. P. 1980, A&A, 82, 73

Patrick, L. R., Evans, C. J., Davies, B., et al. 2015, ApJ, 803, 14

Pauldrach, A. W. A., Hoffmann, T. L., & Lennon, M. 2001, A&A, 375, 161

Penny, L. R. 1996, ApJ, 463, 737

Perryman, M. A. C., Lindegren, L., Kovalevsky, J., et al. 1997, A&A, 323, L49

Petit, V., Owocki, S. P., Wade, G. A., et al. 2013, MNRAS, 429, 398

Petit, V., Keszthelyi, Z., MacInnis, R., et al. 2017, MNRAS, 466, 1052

Pettini, M. 2000, in The First Stars, ed. A. Weiss, T. G. Abel, & V. Hill, 305

Potter, A. T., Tout, C. A., & Eldridge, J. J. 2012, MNRAS, 419, 748

Prantzos, N. 2008, A&A, 489, 525

Preibisch, T., & Zinnecker, H. 2007, in IAU Symposium, Vol. 237, Triggered Star Formation in a Turbulent ISM, ed. B. G. Elmegreen & J. Palous, 270–277

Przybilla, N., Fossati, L., Hubrig, S., et al. 2016, A&A, 587, A7

Puls, J. 2017, in IAU Symposium, Vol. 329, The Lives and Death-Throes of Massive Stars, ed. J. J. Eldridge, J. C. Bray, L. A. S. McClelland, & L. Xiao, 435–435

Puls, J., Markova, N., Scuderi, S., et al. 2006, A&A, 454, 625

Puls, J., Springmann, U., & Lennon, M. 2000, A&AS, 141, 23

Puls, J., Sundqvist, J. O., & Markova, N. 2015, in IAU Symposium, Vol. 307, New Windows on Massive Stars, ed. G. Meynet, C. Georgy, J. Groh, & P. Stee, 25–36

Puls, J., Urbaneja, M. A., Venero, R., et al. 2005, A&A, 435, 669

Puls, J., Vink, J. S., & Najarro, F. 2008, A&A Rev., 16, 209

Puls, J., Kudritzki, R.-P., Herrero, A., et al. 1996, A&A, 305, 171

Ramírez-Agudelo, O. H., Simón-Díaz, S., Sana, H., et al. 2013, A&A, 560, A29

Ramírez-Agudelo, O. H., Sana, H., de Mink, S. E., et al. 2015, A&A, 580, A92

Ramírez-Agudelo, O. H., Sana, H., de Koter, A., et al. 2017, A&A, 600, A81

Raskin, G., Van Winckel, H., & Davignon, G. 2004, in Proc. SPIE, Vol. 5492, Ground-based Instrumentation for Astronomy, ed. A. F. M. Moorwood & M. Iye, 322–330

Repolust, T., Puls, J., & Herrero, A. 2004, A&A, 415, 349

Rivero González, J. G., Puls, J., Massey, P., & Najarro, F. 2012, A&A, 543, A95

Rivero González, J. G., Puls, J., & Najarro, F. 2011, A&A, 536, A58

Robertson, B. E., Ellis, R. S., Dunlop, J. S., McLure, R. J., & Stark, D. P. 2010, Nature, 468, 49

Rosen, A. L., Krumholz, M. R., & Ramirez-Ruiz, E. 2012, ApJ, 748, 97

Sabín-Sanjulián, C., Simón-Díaz, S., Herrero, A., et al. 2014, A&A, 564, A39

—. 2017, A&A, 601, A79

Sahlmann, J., Martín-Fleitas, J., Mora, A., et al. 2016, in Proc. SPIE, Vol. 9904, Space Telescopes and Instrumentation 2016: Optical, Infrared, and Millimeter Wave, 99042E

Salpeter, E. E. 1955, ApJ, 121, 161

Sana, H. 2013, in Massive Stars: From alpha to Omega, 26

Sana, H. 2017, in IAU Symposium, Vol. 329, The Lives and Death-Throes of Massive Stars, ed. J. J. Eldridge, J. C. Bray, L. A. S. McClelland, & L. Xiao, 110–117

Sana, H., & Evans, C. J. 2011, in IAU Symposium, Vol. 272, Active OB Stars: Structure, Evolution, Mass Loss, and Critical Limits, ed. C. Neiner, G. Wade, G. Meynet, & G. Peters, 474–485

Sana, H., Gosset, E., Rauw, G., Sung, H., & Vreux, J.-M. 2006, A&A, 454, 1047

Sana, H., de Mink, S. E., de Koter, A., et al. 2012, Science, 337, 444

Sana, H., Le Bouquin, J.-B., Lacour, S., et al. 2014, ApJS, 215, 15

Santolaya-Rey, A. E., Puls, J., & Herrero, A. 1997, A&A, 323, 488

Savaglio, S., K. Glazebrook Collaboration, & D. Le Borgne Collaboration. 2006, in American Astronomical Society Meeting Abstracts, Vol. 207, American Astronomical Society Meeting Abstracts #207, 16.18

Schneider, F. R. N., Langer, N., de Koter, A., et al. 2014, A&A, 570, A66

Schneider, F. R. N., Podsiadlowski, P., Langer, N., Castro, N., & Fossati, L. 2016, MNRAS, 457, 2355

Schneider, F. R. N., Ramírez-Agudelo, O. H., Tramper, F., et al. 2018, ArXiv e-prints, arXiv:1807.03821

Silich, S. A., Tenorio-Tagle, G., Terlevich, R., Terlevich, E., & Netzer, H. 2001, MNRAS, 324, 191

Simón-Díaz, S., Castro, N., Garcia, M., Herrero, A., & Markova, N. 2011a, Bulletin de la Societe Royale des Sciences de Liege, 80, 514

Simón-Díaz, S., Castro, N., Herrero, A., et al. 2011b, in Journal of Physics Conference Series, Vol. 328, Journal of Physics Conference Series, 012021

Simón-Díaz, S., Garcia, M., Herrero, A., Maíz Apellániz, J., & Negueruela, I. 2011c, in Stellar Clusters Associations: A RIA Workshop on Gaia, 255–259

Simón-Díaz, S., Godart, M., Castro, N., et al. 2017, A&A, 597, A22

Simón-Díaz, S., & Herrero, A. 2007, A&A, 468, 1063

—. 2014, A&A, 562, A135

Simón-Díaz, S., Herrero, A., Sabín-Sanjulián, C., et al. 2014, A&A, 570, L6

Simón-Díaz, S., Herrero, A., Uytterhoeven, K., et al. 2010, ApJ, 720, L174

Simón-Díaz, S., Stasinska, G., García-Rojas, J., et al. 2008, in Revista Mexicana de Astronomia y Astrofisica, vol. 27, Vol. 33, Revista Mexicana de Astronomia y Astrofisica Conference Series, 137–139

Simón-Díaz, S., Negueruela, I., Maíz Apellániz, J., et al. 2015, in Highlights of Spanish Astrophysics VIII, ed. A. J. Cenarro, F. Figueras, C. Hernández-Monteagudo, J. Trujillo Bueno, & L. Valdivielso, 576–581

Smith, Jr., H., & Eichhorn, H. 1996, MNRAS, 281, 211

Smith, K. C., & Howarth, I. D. 1998, MNRAS, 299, 1146

Smith, M. D. 2014, MNRAS, 438, 1051

Smith, N., Vink, J. S., & de Koter, A. 2004, ApJ, 615, 475

Sobolev, V. V. 1960, Soviet Ast., 4, 372

Sota, A., Maíz Apellániz, J., Morrell, N. I., et al. 2014, ApJS, 211, 10

Sota, A., Maíz Apellániz, J., Walborn, N. R., et al. 2011, ApJS, 193, 24

Spruit, H. C. 2002, A&A, 381, 923

Stahl, O., Mandel, H., Wolf, B., et al. 1993, A&AS, 99, 167

Steidel, C. 2014, Massive Stars and the Stellar and Nebular Abundance Scales in High Redshift Galaxies, Keck Observatory Archive LRIS, id.C247LA

Steidel, C. C., Giavalisco, M., Dickinson, M., & Adelberger, K. L. 1996, AJ, 112, 352

Sundqvist, J. O., Puls, J., & Owocki, S. P. 2014, A&A, 568, A59

Sundqvist, J. O., ud-Doula, A., Owocki, S. P., et al. 2012, MNRAS, 423, L21

Telting, J. H., Avila, G., Buchhave, L., et al. 2014, Astronomische Nachrichten, 335, 41

Tenorio-Tagle, G., Muñoz-Tuñón, C., Pérez, E., Silich, S., & Telles, E. 2006, ApJ, 643, 186

Teodoro, M., Damineli, A., Heathcote, B., et al. 2016, ApJ, 819, 131

Trundle, C., & Lennon, D. J. 2005, A&A, 434, 677

Tutukov, A. V., & Fedorova, A. V. 2010, Astronomy Reports, 54, 156

ud-Doula, A., & Owocki, S. P. 2002, ApJ, 576, 413

ud-Doula, A., Owocki, S. P., & Townsend, R. H. D. 2009, MNRAS, 392, 1022

ud-Doula, A., Sundqvist, J. O., Owocki, S. P., Petit, V., & Townsend, R. H. D. 2013, MNRAS, 428, 2723

Unsöld, A., & Weidemann, V. 1955, Vistas in Astronomy, 1, 249

Urbaneja, M. A., Herrero, A., Kudritzki, R.-P., et al. 2005, ApJ, 635, 311

Urbaneja, M. A., Kudritzki, R.-P., Bresolin, F., et al. 2008, ApJ, 684, 118

Vacca, W. D., Garmany, C. D., & Shull, J. M. 1996, ApJ, 460, 914

van Leeuwen, F. 2007, A&A, 474, 653

Villamariz, M. R., & Herrero, A. 2000, A&A, 357, 597

Vink, J. S. 2000, PhD thesis, Universiteit Utrecht ¡EMAIL¿jvink@phys.uu.nl¡/EMAIL¿

Vink, J. S., Brott, I., Gräfener, G., et al. 2010, A&A, 512, L7

Vink, J. S., de Koter, A., & Lamers, H. J. G. L. M. 1999, A&A, 350, 181

—. 2001, A&A, 369, 574

Vink, J. S., & Gräfener, G. 2012, ApJ, 751, L34

von Zeipel, H. 1924, MNRAS, 84, 665

Wade, G. A., Fullerton, A. W., Donati, J.-F., et al. 2006, A&A, 451, 195

Wade, G. A., Alecian, E., Bohlender, D. A., et al. 2009, in IAU Symposium, Vol. 259, Cosmic Magnetic Fields: From Planets, to Stars and Galaxies, ed. K. G. Strassmeier, A. G. Kosovichev, & J. E. Beckman, 333–338

Wade, G. A., Neiner, C., Alecian, E., et al. 2016, MNRAS, 456, 2

Walborn, N. R. 2009, Optically observable zero-age main-sequence O stars:, ed. M. Livio & E. Villaver, 167–177

Walborn, N. R., & Fitzpatrick, E. L. 1990, PASP, 102, 379

Walborn, N. R., Howarth, I. D., Herrero, A., & Lennon, D. J. 2003, ApJ, 588, 1025

Walborn, N. R., Howarth, I. D., Lennon, D. J., et al. 2002, AJ, 123, 2754

Walborn, N. R., Sana, H., Simón-Díaz, S., et al. 2014, A&A, 564, A40

Wickramasinghe, D. T., Tout, C. A., & Ferrario, L. 2014, MNRAS, 437, 675

Woosley, S. E., & Bloom, J. S. 2006, ARA&A, 44, 507

Woosley, S. E., Heger, A., & Weaver, T. A. 2002, Reviews of Modern Physics, 74, 1015

Yoon, S.-C., & Langer, N. 2005, A&A, 443, 643

Yorke, H. W. 1986, ARA&A, 24, 49

Yorke, H. W., & Sonnhalter, C. 2002, ApJ, 569, 846

Zinnecker, H., & Yorke, H. W. 2007, ARA&A, 45, 481

Zorec, J., & Briot, D. 1997, A&A, 318, 443